ISSN 0289-842X

# RIKEN Accelerator Progress Report

1994

vol. 28

理化学研究所
*The Institute of Physical and Chemical Research (RIKEN)*

# RIKEN Accelerator Progress Report 1994
January-December

理化学研究所
The Institute of Physical and Chemical Research (RIKEN)
Wako-shi, Saitama, 351-01 JAPAN

# CONTENTS

## 2. Atomic and Solid-State Physics

# I. PREFACE

This report summarizes research activities at the RIKEN Accelerator Research Facility for the year of 1994. The research program has been coordinated in the framework of the project entitled by Multidisciplinary Researches on Heavy Ion Science. It involves a variety of research fields; nuclear physics, atomic physics, nuclear chemistry, radiation biology, condensed matter physics in terms of accelerator or radiation, basic studies on energy production, basic studies on accelerator cancer therapy, material characterization, application to space science, accelerator engineering, laser technology and computational technology. The whole activities involve 12 laboratories in RIKEN and more than 400 researchers including outside users.

The research activities have steadily developed through the year at the major accelerator, the RIKEN Ring Cyclotron (RRC), and its subordinate accelerators, the energy-variable heavy ion linear accelerator (RILAC) and the K = 70 AVF cyclotron, which have altogether delivered a beam time (on the target) of more than 8000 hours.

Besides, this year should be marked as an epoch-making year for the Facility by having achieved approval of two major proposals, construction of an upgraded facility called the RIKEN Radioactive Beam Facility and setup of an international collaboration program on spin structure functions. Both of the projects are due to be initiated in FY 1995.

Continuous efforts have been taken to grade up the capabilities of the accelerators. Most importantly a project to drastically improve the beam intensities at RILAC is in progress. A set of 18 GHz ECR ion source and a frequency-variable RFQ is under construction to replace the upstream end of the accelerator. The completion is expected in 1995.

The heavy ion research program at the Facility has enjoyed another year of continuous development. Nuclear physics researches have heavily focused on the studies on unstable nuclei, in particular in terms of radioactive beam experiments. Studies on nuclear synthesis beyond the drip line and towards the super heavy elements have continued involving the identification of $^{10}$He and successful synthesis of Z = 106 isotopes through an incomplete fusion-like process, ($^{40}$Ar, $\alpha$xn). Spectroscopy on extremely neutron rich nuclei has made a further progress: Properties of soft dipole excitation and other excitation modes in halo (or skin) nuclei have been studied with a variety of direct reaction processes. Methods of laser spectroscopy and $\beta$-$\gamma$-neutron spectroscopy have been also employed for the study of nuclear structure. Studies have extended to heavier nuclei of a region around $^{32}$Mg including the radius measurement of a series of Na isotopes which were carried out at GSI. Exotic properties are anticipated for reactions induced by neutron rich nuclei. Results have been obtained on sub-barrier fusion reactions of this context. Radioactive-beam experiments offer unique opportunities to study reaction rates of astrophysical interest. Among others Coulomb dissociation cross section of $^{8}$B has been successfully measured in relation to the solar neutrino problem. The studies on unstable nuclei heavily depend on the development of the radioactive beams (RIB) at the Facility. Uniquely the Facility provides three different types of radioactive beams: Firstly intermediate-energy RIB by means of projectile fragmentation (PF) have been most frequently used, by amounting to about 40% of the whole RRC beam time. The second type of RIB is the spin-polarized beam which is also produced via PF process covering a wide range of nuclear species. The beam has been used to determine nuclear moments (g-factor and Q) of unstable nuclei ranging over a dozen of isotopes including exotic nuclei such as $^{17}$B. The third type of RIB is the high-spin isomer beam which is produced via reverse-kinematics fusion reaction. Beams of heavy isomers with spins close to 30 $\hbar$ are obtained with considerable intensities. Such beams were so far used to study Coulomb excitation of high-spin isomeric states.

In the field of nuclear physics spin-isospin response is another major subject, where reactions (d,$^{2}$He) and (d,d($0^{+}$)) as well as heavy-ion exchange reactions are primarily concerned. A wide acceptance and high resolution spectrometer, SMART, of Q-Q-D-D type and a spin-polarized ion source for deuteron have served for such experiments yielding well qualified informative results.

The heavy ion researches are extended over a variety of domains beside nuclear physics. Atomic physics has been pursued, enjoying an extremely wide energy range of heavy ions available with the ECR ion source, RILAC and RRC. Atomic collisions in the relativistic region have been studied at RRC. The first measurement has been performed of momentum distributions of relativistic electrons ejected by quasi-binary collisions of a target electron with a heavy projectile. A new technique of cold-target recoil-ion momentum spectroscopy (COLTRIMS) has been introduced to facilitate high-precision ( with a resolution better than 0.2 atomic unit) and high-efficiency spectroscopy on the ionization and electron transfer processes in ion-atom collisions. Beam foil spectroscopy of highly charged ions has been pushed forward to both heavier

elements and a new region of wave length. Nb and Zr ions were studied in the region of VUV while Ne ions were studied in the UV and visible regions. Basic information for laser and plasma applications is gained.

In nuclear chemistry remarkable development has continued in application of the methodology of multitracer. Multitracers have been extensively utilized in chemical, environmental and biological investigations. Twelve research items have been pursued involving a large number of groups from universities and other institutions. Among others a notable development has been attained in the study of trace elements in animal bodies. For instance behavior of more than 20 trace elements has been clarified in rats and mice under different conditions such as normal, Zn-deficient, and Vitamin D-excess. The data are useful not only for bioinorganic chemistry but also for dietetics, toxicology, pharmacology and medics in general. Another major effort has been paid to develop the setups for Coulomb excitation Mössbauer spectroscopy. A test experiment was successfully performed at the AVF Cyclotron using a $^{40}$Ar beam.

Heavy ion beams have offered a variety of means for material characterization such as PIXE, Rutherford scattering and channeling effects. Recently a project on slow positron spectroscopy using short lived isotopes was started at the AVF cyclotron. Heavy-ion beams are also useful to improve the property of material. In this context a new project on high-Tc superconducting materials has been started. The pinning effect of magnetic flux through superconducting materials caused by irradiation of high-energy heavy ions is under investigation.

Irradiation effects with heavy-ion beams are studied in several respects. One is concerned with radiation biology. Effects of high LET are studied for a variety of biological samples. As a recent development it has been proved for the case of a tabacco plant that heavy ion irradiation is strikingly effective to induce new types of mutagenesis as compared to the other standard mutagen treatments. Basic studies for heavy-ion-beam cancer therapy are continued in collaboration with National Institute of Radiological Science. Studies of curing probability are extensively performed with tumor-bearing mice. Recently an intriguing application of radioactive beam was tested in relation to the cancer therapy. Use of a radioactive beam may offer a possibility to gain real-time information on the range of the ions shooting the body, where the location of the stopped isotopes may be spotted by means of positron tomography. A simulation experiment using a radioactive beam of $^{11}$C was performed, demonstrating an encouraging perspective.

Another important domain on irradiation effects concerns the space technology. High-energy heavy ions from RRC serve as a good simulator of cosmic rays in space. Thus a broad range of samples are irradiated to study characteristic damages, including detectors and biological samples. In particular studies on electronic devices are made in collaboration with National Space Development Agency of Japan.

The Facility carries on an international research program on muon science in collaboration with the Rutherford-Appleton Laboratory. The muon beam facility at the proton synchrotron ISIS has been completed this year. It will start operation in early 1995 to accommodate versatile research programs using powerful pulsed muon beams.

Finally, having achieved approval of two new projects, the Facility is moving towards a new stage of global development. The project of the RIKEN Radioactive Beam Facility involves construction of superconducting separate-sector cyclotron with K-number around 2400 to work as the energy booster on top of the existing RRC. Beam energies of heavier elements are to become sufficiently high to produce PF radioactive beams over a drastically wide region of unstable nuclei. The cyclotrons are to be accompanied with dual rings of synchrotron to enhance the experimental perspectives. We anticipate that the new Facility could make a central contribution to the world community of next generation RIB science. Most optimistically the Facility would be completed somewhere around 2002 or 2003. Another project on relativistic-energy spin physics is formulated as the 2nd international research program following the muon project. It is to be carried out in collaboration with Brookhaven National Laboratory. The program aims at investigation of spin related properties of nucleons in terms of quark-gluon framework by facilitating spin-polarized proton beams in RHIC. This implies introduction of a new domain of physics into the whole RHIC program as well as a considerable expansion of the research area covered by our Facility.

Masayasu Ishihara
*Director*
*RIKEN Accelerator Research Facility*

# II. OPERATION OF ACCELERATORS

# RRC Operation

A. Goto, M. Kase, N. Inabe, T. Kageyama, I. Yokoyama, M. Nagase, S. Kohara, T. Nakagawa, K. Ikegami, O. Kamigaito, J. Fujita, H. Isshiki,* H. Akagi,* R. Ichikawa,* N. Tsukiori,* R. Abe,* K. Takahashi,* T. Maie,* T. Kawama,* T. Honma,* and Y. Yano

In this-year runs from November 1993 to October 1994, 32 kinds of combinations of ion species and energies were used for experiments, of which 13 kinds were new ones. The total beam time was 199.5 days. The AVF-RRC operation was performed for 147 days (74%) and the RILAC-RRC operation for 52.5 days (26%). The beam time of 162 days (81%) was devoted to nuclear physics experiments and that of 37.5 days (19%) to non-nuclear physics experiments. Table 1 summarises the characteristics of the accelerated beams. Figure 1 shows the plots of the ions accelerated so far in the available region of energy-mass space. Stand-alone use of the AVF cyclotron has routinely been made; its total beam time was additional 30.5 days.

Because of the following troubles, a total of 15 days of the scheduled machine time had to be cancelled. As for the AVF cyclotron, the deflector sometimes became not to work due to its unendurable leak current, a part of the RF slide-contacts of the movable shorting plate was melted and burned, and the vacuum leak occurred from the magnetic channel due to beam hitting. The first two troubles were also experienced last year. As for the RRC, one of the connectors (made of brass) for cooling of the main coils was broken due to corrosion, and the vacuum leak occurred between the aluminum

Table 1. RRC beams accelerated during Nov. 1993–Oct. 1994.

| Particle | Charge | RFF (MHz) | h | Injector | Energy (MeV/nucleon) | Beam time (days) |
|---|---|---|---|---|---|---|
| $H_2$ | 1 | 27.6 | 5 | AVF | 90† | 1 |
| | 1 | 29.0 | 5 | AVF | 100† | 0.5 |
| | 1 | 30.1 | 5 | AVF | 110† | 1 |
| | 1 | 30.45 | 5 | AVF | 113† | 1 |
| | 1 | 31.2 | 5 | AVF | 120† | 1.5 |
| | 1 | 32.6 | 5 | AVF | 135 | 3 |
| d | 1 | 32.6 | 5 | AVF | 135 | 4.5 |
| pol. d | 1 | 32.6 | 5 | AVF | 135 | 24 |
| $^{12}C$ | 6 | 27.9 | 5 | AVF | 92 | 7 |
| | 6 | 29.0 | 5 | AVF | 100 | 4 |
| | 6 | 32.6 | 5 | AVF | 135 | 14 |
| $^{13}C$ | 6 | 29.0 | 5 | AVF | 100† | 16 |
| $^{14}N$ | 7 | 24.6 | 5 | AVF | 70 | 0.5 |
| | 7 | 32.6 | 5 | AVF | 135 | 6.5 |
| $^{15}N$ | 7 | 30.5 | 5 | AVF | 115 | 11.5 |
| $^{16}O$ | 8 | 32.6 | 5 | AVF | 135 | 2 |
| $^{18}O$ | 8 | 29.0 | 5 | AVF | 100 | 22 |
| $^{20}Ne$ | 10 | 32.6 | 5 | AVF | 135 | 2 |
| $^{22}Ne$ | 10 | 30.1 | 5 | AVF | 110 | 12.5 |
| $^{24}Mg$ | 12 | 29.0 | 5 | AVF | 100 | 5 |
| $^{28}Si$ | 14 | 32.6 | 5 | AVF | 135† | 1 |
| $^{36}Ar$ | 5 | 18.8 | 11 | RILAC | 7.5† | 5 |
| $^{40}Ar$ | 5 | 18.8 | 11 | RILAC | 7.5 | 19.5 |
| | 6 | 18.6 | 10 | RILAC | 9† | 3.5 |
| | 14 | 32.5 | 9 | RILAC | 35† | 3.5 |
| | 17 | 28.1 | 5 | AVF | 95 | 6.5 |
| $^{84}Kr$ | 13 | 20.0 | 10 | RILAC | 10.5 | 0.5 |
| | 25 | 32.7 | 9 | RILAC | 36† | 2.5 |
| $^{136}Xe$ | 21 | 18.6 | 11 | RILAC | 7.4† | 8 |
| | 23 | 18.6 | 10 | RILAC | 9 | 1.5 |
| | 31 | 28.0 | 9 | RILAC | 26 | 2 |
| $^{170}Er$ | 24 | 18.0 | 11 | RILAC | 7† | 6.5 |
| | | | | | Total | 199.5 |

† New beams

* Sumijyu Accelerator Service, Ltd.

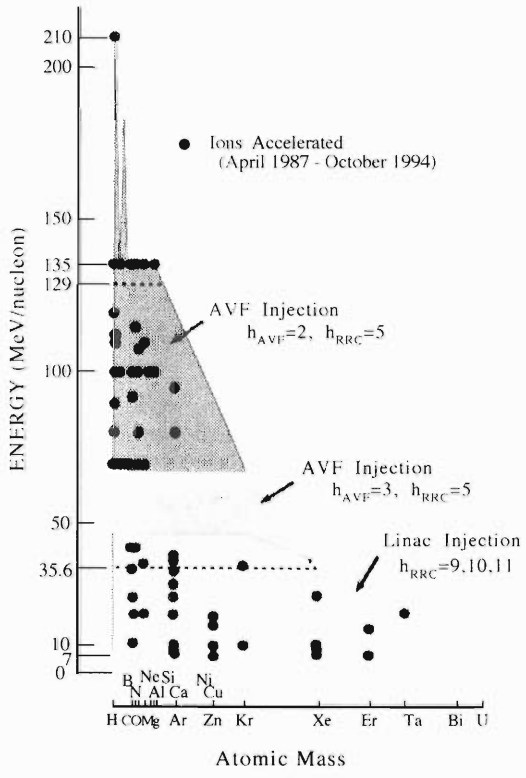


Fig. 1. RRC beams accelerated during Nov. 1993–Oct. 1994.

gasket and the ceramics that are used in the coaxial rf power feeder.

During the period of six-weeks overhauls in summer, the following big works were done. Firstly, we abandoned a total of 56 connectors (using O-rings) that were used inside the movable boxes of the rf resonators of the RRC for cooling of them, and instead directly connected cooling pipes by welding. Owing to this repair, the vacuum leak in the rf resonators, which sometimes troubled us before, have not occurred since then. The preesure inside the acceleration chamber is now about $10^{-6}$ Pa. Secondly, we replaced one of the three mini-computers (Mitsubishi M60/500) used for the control of the accelerator complex by a new one (Mitsubishi M60/AR), which is an upgraded machine of M60/500. The basic architecture of the control system has remained unchanged. Some component parts of the replaced computer will be stocked as spares for the remaining old two computers.

We have recently begun to make use of parasite-mode operation. The first trial was made between E3 and E6 experimental rooms, where the sub experiment on a counter test and the main experiment with RIPS were performed, respectively. Switching the beam delivery could be made in a second each time. A combination of the single-bunch selector on the injection beam line of the AVF cyclotron and the two beam detectors each using a micro-channel plate (MCP), which were developed last year, has routinely been used both as phase monitors for stabilizing the magnetic fields of the two cyclotrons and as monitors for single-turn extraction. A single-bunch selector functioning with a repetition rate of as high as 1 MHz has also successfully been developed using a high-speed semi-conductor device. We tried and succeeded in accelerating argon ions of lower energies in the AVF cyclotron (2.75 MeV/nucleon) with the third harmonic acceleration mode instead of the second to meet users' demand. This will enable us to cover the so far non-available region of energy-mass space from 40 to 70 MeV/nucleon as shown in Fig. 1, although only one in every three beam bunches can be accelerated by the RRC. The development of a high-density polarized $^3$He gas target system is also in progress.

A new injector system of the RILAC consisting of a single-stage high-field 18 GHz ECR ion source and a variable-frequency RFQ linac is now under fabrication for completion by the spring of the next year. As for the RFQ linac, a half-scaled model for the cold test of the cavity was completed at the end of the last year, and various measurements were made on its rf characteristics. The measurements showed that the model had good performance in accordance with the design.

# RILAC Operation

E. Ikezawa, M. Hemmi, T. Chiba, Y. Chiba, S. Kohara, T. Aihara,* T. Ohki,* H. Hasebe,* H. Yamauchi,* and Y. Miyazawa

RILAC has been in steady operation, and has supplied various kinds of ion beams for experiments. Table 1 gives the statistics of operation from Jan. through Dec. 1994. Table 2 summarizes the time sharing for individual research groups. The percentage of the beam time for RIKEN Ring Cyclotron (RRC) was about 42% of the total; ions of $^{36}Ar$, $^{40}Ar$, $^{84}Kr$, $^{130}Te$, $^{136}Xe$, and $^{170}Er$ accelerated by RILAC were injected to RRC. Table 3 gives the statistics of ions used in this year. We began accelerating $Zr^{12+}$, $Pd^{12+}$, $Te^{9+}$, and $Ce^{14+}$ at frequencies of 32, 28, 18.8, and 28 MHz respectively. The percentage of the beam time for metallic ions amounted to about 19% of the total.

This year we had the following machine troubles. (1) The tetrode (RCA-4648) used in the No. 5 final rf amplifier was replaced with a new one, because the emission currents from the filament have declined. The tube has been used for fourteen years. (2) A refrigerator and coolant oil for the 8 GHz ECR ion source were replaced with new ones because the plasma chamber of the ion source was not cooled very well. (3) A chamber for the electrostatic quadrupole lens of the ECR ion source had a small vacuum leak with the damage of diverged beams hit on it for long time. We changed the chamber into a spare one.

Table 1. Statistics of the operation from Jan. 1 through Dec. 31, 1994.

| | Day | % |
|---|---|---|
| Beam time | 167 | 45.8 |
| Frequency change | 11 | 3.0 |
| Overhaul and improvement | 55 | 15.1 |
| Periodic inspection and repair | 24 | 6.6 |
| Machine trouble | 0 | 0.0 |
| Scheduled shut down | 108 | 29.6 |
| Total | 365 | 100 |

Table 2. Beam time for individual research groups.

| | Day | % |
|---|---|---|
| Atomic physics | 43 | 25.7 |
| Solid-state physics | 6 | 3.6 |
| Nuclear chemistry | 7 | 4.2 |
| Radiation chemistry | 16 | 9.6 |
| Accelerator research | 25 | 15.0 |
| Beam transportation to RRC | 70 | 41.9 |
| Total | 167 | 100 |

Table 3. List of ions used in this year.

| Ion | Mass | Charge state | Day |
|---|---|---|---|
| He | 4 | 1 | 7 |
| C | 12 | 4 | 8 |
| N | 14 | 3 | 5 |
| O | 16 | 3 | 5 |
| Ne | 20 | 3, 4 | 8 |
| Ar | 36 | 5 | 5 |
| Ar | 40 | 5, 6, 8 | 63 |
| Kr | 84 | 13 | 10 |
| Zr | 90 | 12 | 4 |
| Zr | 91 | 12 | 2 |
| Nb | 93 | 12 | 4 |
| Pd | 106 | 12 | 1 |
| Te | 130 | 9 | 10 |
| Xe | 136 | 9, 15 | 24 |
| Ce | 140 | 14 | 1 |
| Er | 170 | 11 | 8 |
| Bi | 209 | 11, 19 | 2 |

We carried out the following machine improvements. (1) The power supplies for the drift tube magnets used in the No. 6 resonator and for the quadrupole magnets of the beam transport line were remodeled by replacing the obsolete power transistors with the modern ones. (2) In the rf system of six resonators, a wide band amplifier (output power of 500 W), and both of power supplies of the control grid (250 V, 2.5 A) and the screen grid (1.5 kV, 2.2 A) for the final vacuum tube have been replaced with new ones, because they were worn out after many years operation.

To further simplify and stabilize the operation of the accelerating voltage, both tuning and amplitude regulation circuits for each main resonator are newly designed and being manufactured at present.

We have tested to obtain metallic ions by use of a material such as Pd, $La_2O_3$, $TeO_2$, and $CeO_2$. Ion currents with these rods were very stable. At present we can supply ions of 10 gaseous and 41 solid elements.

* Sumijyu Accelerator Service, Ltd.

# AVF Cyclotron Operation

A. Goto, T. Kageyama, M. Kase, N. Inabe, S. Kohara, M. Nagase, T. Nakagawa, K. Ikegami, O. Kamigaito, I. Yokoyama, J. Fujita, H. Isshiki,* H. Akagi,* R. Ichikawa,* N. Tsukiori,* R. Abe,* K. Takahashi,* T. Maie,* T. Kawama,* T. Honma,* and Y. Yano

In this-year runs from November 1993 to October 1994, thirty-four kinds of combinations of ion species and energies were used for experiments, of which thirteen kinds were new ones. The total beam time was 177.5 days. The beam time for polarized deuterons amounted to 24 days, the longest among the accelerated beams. Table 1 summarizes the characteristics of the accelerated beams.

Stand-alone use of the AVF cyclotron has routinely been made while the RRC is operated with the RILAC beam injection. The total beam time for it was 30.5 days, about four times that of the last year. Those beams were used for the production test of slow positrons, measurement of nuclear fusion cross sections, and radioisotope production for Mössbauer spectroscopy and laser nuclear spectroscopy.

To meet users' demand for lower energies, we tried and succeeded in accelerating argon ions of 2.75 MeV/nucleon with the third acceleration mode instead of the second, for which the cyclotron was originally designed. The beam intensity was about 1e$\mu$A. This beam was used for the experiment of Mössbauer spectroscopy. We also tested to accelerate krypton ions with a mass-to-charge ratio of 4.2 at 4 MeV/nucleon. The beam intensity was as low as 10 nA, because the ECR ion source had an unknown trouble with respect to the beam intensity at that time. Taking account of the normal intensity of 20 $\mu$A from the ECR ion source for $^{84}Kr^{20+}$, however, the beam intensity from the cyclotron is expected to be about several hundreds of enA. The krypton ion is the heaviest that can be accelerated with the cyclotron.

Table 1. Ions accelerated with the AVF cyclotron during Nov. 1993–Oct. 1994.

| Particle | Charge | RF freq. (MHz) | Energy (MeV/nucleon) | Beam time (days) | Particle | Charge | RF freq. (MHz) | Energy (MeV/nucleon) | Beam time (days) |
|---|---|---|---|---|---|---|---|---|---|
| p | 1 | 19.35 | 9.9* | 0.5 | $^{12}C$ | 4 | 13.95 | 5.1 | 7 |
| | 1 | 23.0 | 14.0*† | 2.5 | | 4 | 14.5 | 5.5 | 4 |
| $H_2$ | 1 | 13.8 | 5.0† | 1 | | 4 | 16.3 | 7.0 | 14 |
| | 1 | 14.0 | 5.2* | 0.5 | $^{13}C$ | 4 | 14.5 | 5.5 | 16 |
| | 1 | 14.5 | 5.5† | 0.5 | $^{14}N$ | 4 | 12.3 | 4.0 | 0.5 |
| | 1 | 15.05 | 6.0† | 1 | | 5 | 16.3 | 7.0 | 6.5 |
| | 1 | 15.23 | 6.1† | 1 | $^{15}N$ | 4 | 15.25 | 6.1 | 11.5 |
| | 1 | 15.6 | 6.4† | 1.5 | $^{16}O$ | 5 | 16.3 | 7.0 | 2 |
| | 1 | 15.7 | 6.5*† | 0.5 | $^{18}O$ | 6 | 14.5 | 5.5 | 22 |
| | 1 | 16.3 | 7.0 | 3 | $^{20}Ne$ | 7 | 16.3 | 7.0 | 2 |
| | 1 | 16.3 | 7.0* | 6.5 | $^{22}Ne$ | 7 | 15.05 | 6.0 | 12.5 |
| d | 1 | 12.3 | 4.0* | 2.5 | $^{24}Mg$ | 7 | 14.5 | 5.5 | 5 |
| | 1 | 16.3 | 7.0 | 4.5 | $^{27}Al$ | 9 | 16.0 | 6.7* | 4 |
| | 1 | 18.5 | 9.0*† | 3.5 | $^{28}Si$ | 9 | 16.3 | 7.0† | 1 |
| | 1 | 19.0 | 9.5*† | 2 | $^{40}Ar$ | 11 | 15.4 | 2.8*† | 4.5 |
| pol. d | 1 | 16.3 | 7.0 | 24 | | 11 | 14.05 | 5.2 | 6.5 |
| $\alpha$ | 2 | 15.5 | 6.3*† | 3.5 | $^{84}Kr$ | 11 | 12.3 | 4.0† | — |
| | | | | | | | | Total | 177.5 |

* Served for stand-alone use of the AVF cyclotron.
† New beams

As a monitor for single-turn extraction, a combination of the single-bunch selector on the injection beam line and the beam detector with a micro-channel plate (MCP), which was developed last year, has routinely been used. This monitoring system is indispensable, in particular, for the acceleration of polarized deuterons. It has also been used as a monitor for stabilizing the magnetic field of the cyclotron.

During the past one year there have still been two kinds of serious troubles with respect to the following cyclotron components as in the last two years: a part of the RF slide-contacts of the movable shorting plate was melted and burned twice; and the deflector became not to work five times due to its unendurable leak current. In addition, the vacuum leak occurred from the magnetic channel due to beam hitting. In the summer-time overhaul, it was found that one of the bolts attaching the copper membrane to the sectors, the membrane covering trim coils in rough vacuum, was cut off by a mechanical stress and dropped down on the dee electrode.

* Sumijyu Accelerator Service, Ltd.

# Tandetron Operation

E. Yagi, T. Urai, and M. Iwaki

The Tandetron was operated for 85 days for experiments except for machine inspection, beam test, repair and so on in the period from Nov. 1, 1993 to Oct. 31, 1994.

The experimental studies on the following subjects were made.

(1) Rutherford Backscattering Spectroscopy (RBS)

(a) Behaviour of Kr atoms implanted into aluminium by a channelling method (Metal Physics Lab., at present, Muon Science Lab.).

(b) Behaviour of Xe atoms implanted into iron (Metal Physics Lab., at present, Muon Science Lab.).

(c) RBS analysis of Tb-implanted sapphire crystals (Surface Characterization Centre).

(d) Characterization of Ni films grown on MgO by biased dc sputter deposition (Metal Physics Lab., at present, Muon Science Lab.).

(2) Nuclear Reaction Analysis (NRA)

(a) Lattice location of hydrogen in niobium alloys by a channelling method (Metal Physics Lab., at present, Muon Science Lab.).

(3) Particle Induced X-ray Emission (PIXE)

(a) Application of PIXE to biomedical and material sciences: Trace element analysis using energy-dispersive X-ray spectrometry, and chemical state analysis using wave-dispersive X-ray spectrometry (Inorganic Chemical Physics Lab.).

# III. RESEARCH ACTIVITIES

# 1. Nuclear Physics

# Stochastic Variational Method for Few-Nucleon Systems

K. Varga and Y. Suzuki

[few-body systems, stochastic variational method.]

The investigation of the few-nucleon systems using realistic nucleon-nucleon interaction, derived from two-nucleon scattering data, is always in the centre of the interest as we want to know to what extent we can describe a nucleus as a system of interacting nucleons. The solution of the nuclear many-body Schrödinger-equation, however, is always a difficult task especially for few-fermion systems where the collective or statistical models are not applicable. We elaborated a fully microscopic approach based on a variational method with stochastic selection[1] of the important basis states. The wave function of the system is taken as antisymmetrized product of functions of relative motion between the nucleons. Various rearrangements are superposed to take into account various types of correlations among the nucleons and to describe the nonuniform structure of the few-nucleon systems. The functions of the relative motions are expanded in terms of nodeless harmonic oscillator functions of different size parameters. The matrix elements are evaluated analytically in a unified and systematic way in three steps: (i) Evaluating matrix elements with Gaussian packets in the single particle coordinate representation, (ii) Transforming to relative and center-of-mass coordinate representation and (iii) Transforming to nodeless harmonic oscillator function bases with definite angular momenta.

To test the accuracy of our approach we solved the three- and four-body Schrödinger equations using some simple model forces and then compared our results to other solutions in the literature. For this test purpose we used the Malfliet-Tjon (MT), Volkov (see Fig. 1), and Coulomb potential. (In case of Coulomb potential we used electron and positron instead of proton and neutron.) For three-body systems with MT potential we got $-8.257$ MeV and the dimension of the basis was about 80. For Coulomb potential our results is $-0.262005$ a.u. on dimension of 150. Both results agree in all digits with the best value in the literature.[1] For a four-nucleon system ($\alpha$ particle) with MT potential

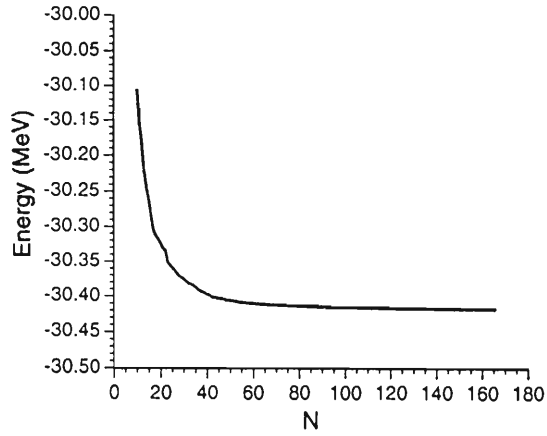


Fig. 1. Convergence of energy as a function of the number of basis states for a four-nucleon system with Volkov interaction.

our result is $-31.358$ MeV ($-31.357$ MeV on dimension of 1000 in Ref. 2) with 250 basis states. For the Coulomb interaction our result (0.51597 a.u.) agrees up to 5 digits at dimension of 300 with results of other calculations.

In summary, we tested our stochastic variational approach against the results of other few-body methods. Our results agree perfectly with those of other models even for Coulombic systems (negative positronium and dipositronium). Preliminary calculations show that this method works for five- and six-body systems as well. Encouraged by these results we plan to apply this method to few-nucleon systems with a realistic interaction.

References

1) K. Varga, Y. Suzuki, and R. G. Lovas: *Nucl. Phys.*, **A571**, 447 (1994).
2) See, for example, H. Kamada and W. Gloecke: *ibid.*, **A548**, 205 (1992), and the references therein.

# Microscopic Multicluster Description of Light Exotic Nuclei

K. Varga, Y. Suzuki, Y. Ogawa, and I. Tanihata

[exotic nuclei, cluster model, stochastic variational model.]

We have developed a microscopic multicluster model for the description of light neutron rich nuclei.[1] In this model a nucleus comprises several clusters (e.g. alpha particle, $^3$H, $^3$He, or single nucleon clusters), and the intercluster wave function is taken as a superposition of terms belonging to different arrangements, each defined by a set of Jacobi coordinates. Each term is then a superposition of products of nodeless harmonic oscillator functions (gaussians) of the individual Jacobi coordinates with different widths. The wave function constructed in this way is then considered a variational trial function. This wave function, however, contains prohibitively large number of overlapping terms (basis states). We use the stochastic variational method to select the "important" states: We select those basis states from a randomly chosen set, which contribute to the ground state energy substantially. In this way one can construct a flexible basis of low dimension.

We have successfully applied this model to microscopic description of $^6$He $= \alpha + \mathrm{n} + \mathrm{n}$ and $^8$He $= \alpha + \mathrm{n} + \mathrm{n} + \mathrm{n} + \mathrm{n}$ as three- and five-body systems.[2] The ground state energies are reproduced very well. We have calculated the proton, neutron and matter radii and densities. The momentum distribution of fragments arising from the two-neutron removal reactions is also determined. All results are in good agreement with experiments.

Recently, we are studying the $^9\mathrm{Li} = \alpha + {}^3\mathrm{H} + \mathrm{n} + \mathrm{n}$ and the $^9\mathrm{C} = \alpha + {}^3\mathrm{He} + \mathrm{p} + \mathrm{p}$ four-cluster systems. Various descriptions of $^{11}$Li assume a $^9\mathrm{Li} + \mathrm{n} + \mathrm{n}$ three-body model to understand the halo structure. Information, therefore, on the structure of $^9$Li is necessary to see to what extent we can approximate the $^9$Li as a passive core in the structure of $^{11}$Li. The interaction cross section and the magnetic moment of $^9$C have recently been measured and the measurement of the quadrupole moment is planned in the near future.

By describing all important subsystems of these four-cluster systems, such as $^8\mathrm{Li} = \alpha + {}^3\mathrm{H} + \mathrm{n}$, $^8\mathrm{B} = \alpha + {}^3\mathrm{He} + \mathrm{p}$, for example, we set the parameters of our model to independent data. The model, therefore, contains no free parameters for $^9$Li and $^9$C, and reproduces their ground state energies and root mean square radii reasonably well.[3] The magnetic and quadrupole moments, except for the magnetic moment of $^8$B and $^8$Li, are also reproduced well. The quadrupole moments of $^9$C are predicted to be $-5.04$ e fm$^2$ and $-6.11$ e fm$^2$. To explore the possible halo structure, the nucleon density distributions and the one- and two-nucleon removal amplitudes were determined (see Fig. 1).

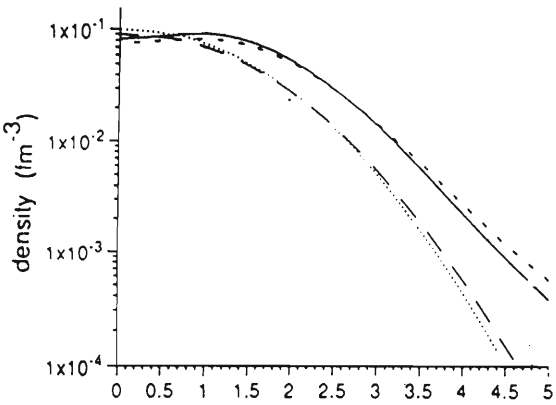


Fig. 1. Proton density distributions of $^9$C (short dashed line) and $^9$Li (dotted line), and neutron density distributions of $^9$C (long dashed line) and $^9$Li (solid line).

Another application of the model is the description of the Be isotopes. Starting from the $^8$Be, which has a well-known $\alpha + \alpha$ structure, by adding one neutron at a time, we study the $^9$Be,$^{10}$Be, $^{11}$Be and $^{12}$Be nuclei. It is interesting to investigate how the density distribution and the structure (e.g. cluster and shell model configurations) of these isotopes change as we increase the number of neutrons. The increase of the available experimental information on Be isotopes in these years attracts considerable attention of the theoretical nuclear structure physicist, and make it possible to check the model assumptions, and the results and the predictions of different models.

References

1) K. Varga, Y. Suzuki, and R. G. Lovas: *Nucl. Phys.*, **A571**, 447 (1994).
2) K. Varga, Y. Suzuki, and Y. Ohbayashi: *Phys. Rev.*, **C50**, 189 (1994).
3) K. Varga, Y. Suzuki, and I. Tanihata: submitted to *Phys. Rev.*, **C**.

# Configuration of the Two-Neutron Halo of $^{11}$Li and Gamow-Teller Transition†

T. Suzuki and T. Otsuka

[Neutron halo, GT $\beta$ decay.]

Effects of neutron halo as well as meson exchange currents (MEC) are studied for the Gamov-Teller (GT) $\beta$ transition, $^{11}$Li $(3/2^-_{g.s.}) \longrightarrow ^{11}$Be $(1/2^-, 0.32$ MeV). Effects of the halo of neutron ($\nu$) $p_{1/2}$ wave function in $^{11}$Li and $^{11}$Be on one-body transition matrix elements as well as on two-body meson exchange currents are studied. The $\nu p_{1/2}$ wave function is obtained in a Woods-Saxon well to reproduce the single-neutron separation energy ($S_n$), that is taken to be 160 keV[1,2] in $^{11}$Li. Calculated results are found to be insensitive to the variation of $S_n$ by ~30 keV. The shell model configuration amplitudes obtained with the three sets of the Cohen-Kurath interactions are used. Effects of the halo on the one-body terms are shown in Fig. 1. The halo reduces the GT matrix elements by 35–43% and is important to get close to the experimental log ft value.[3-5]

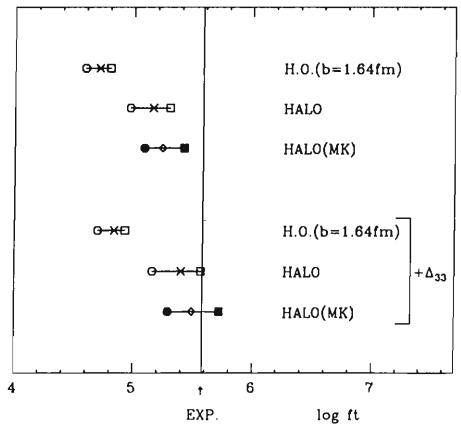


Fig. 1. Log ft values of the GT transition. The observed value (log ft = $5.58 \pm 0.01$[5]) is indicated by a vertical line with "EXP". Symbols ○, × and □ denote three sets of the Cohen-Kurath wave functions: POT(8-16), TBE(8-16) and TBE(6-16), respectively. Results with $p^5(sd)^2$ configurations admixed by the Millener-Kurath interaction are shown by symbols ●, ◇ and ■, which correspond to ○, × and □, respectively. Lower 3 sets of the results in the figure include the contributions from the $\Delta_{33}$-isobar exchange current, while upper 3 sets include only one-body terms.

We now extend the shell model space to include the sd-shell. Allowing 2 valence particles to be excited into the sd-shell by the Millener-Kurath interaction results in the increase of log ft by 0.08–0.12.

One-pion exchange currents due to $\Delta_{33}$-isobar excitations are also included. The halo affects the two-body terms in the GT matrix elements by 7–8%. The exchange currents further increase the calculated log ft value as shown in Fig. 1. We can conclude that the effects of the halo, the admixture of the sd-shell and the exchange currents are important to reduce deviations from the observed log ft value of the GT transition.

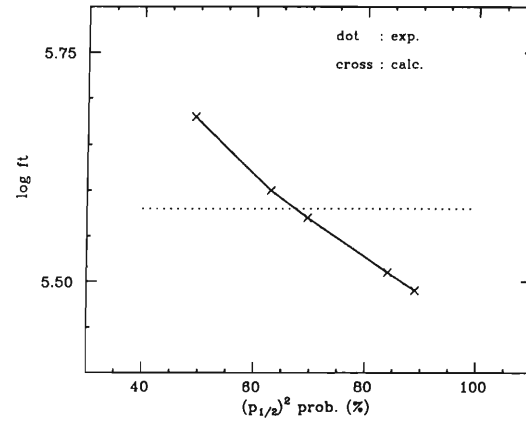


Fig. 2. Log ft values of the GT transition vs probability of the $\nu p^2_{1/2}$-configuration. Dotted points show the observed log ft value: log ft=5.58.

Finally, we discuss the configurations of the two-neutron halo in $^{11}$Li. What is the probability of $\nu p^2_{1/2}$ configuration in the halo of $^{11}$Li? We decrease the probability of $\nu p^2_{1/2}$ configuration by lowering the single-particle energies of the sd orbits. Calculated log ft values (see Fig. 2) increase almost linearly as the probability decreases down to ~60% and cross the observed value at ~65%. Thus, the GT transition is shown to play an indispensable role in identifying the structure of two-neutron halo of $^{11}$Li. It is indicated that the two neutrons forming the halo consisit of the $p^2_{1/2}$ configuration with 60–70%.

References

1) B. M. Young et al.: *Phys. Rev. Lett.*, **71**, 4124 (1993).
2) T. Kobayashi et al.: KEK Report, No. 91–22 (1991) (unpublished).
3) F. Ajzenberg-Selove: *Nucl. Phys.*, **A506**, 1 (1990); *ibid.*, **A433**, 1 (1985).
4) E. Roeckl et al.: *Phys. Rev.*, **C10**, 1181 (1974).
5) T. Bjornstad et al.: *Nucl. Phys.*, **A359**, 1 (1981).

† Condensed from the article in Phys. Rev., **50**, 555 (1994).

# Neutron Halo Effects in Direct Neutron Capture and Photodisintegration

T. Otsuka, M. Ishihara, N. Fukunishi, T. Nakamura, and M. Yokoyama*

[Neutron Halo, Direct Neutron Capture, $^{12}C(n,\gamma)^{13}C$.]

The direct neutron capture associated with E1 $\gamma$-ray emission is discussed for the capture into an s orbit with neutron halo. An application to the reaction $^{12}C(n,\gamma)^{13}C(1/2^+)$ is presented, demonstrating a novel and enormous enhancement in the capture cross section at low energy. The neutron halo is known to be one of the most prominent and exotic effects seen in the ground states of some unstable nuclei such as $^{11}Li$, $^{11}Be$, etc. It has been suggested that the neutron halo is not limited to exotic nuclei, and in fact can be seen in excited states of nuclei on or near the $\beta$ stability line as well. For instance, the first $1/2^+$ state of $^{13}C$ at Ex $\sim$ 3 MeV is predicted, by the recent Variational Shell Model calculation,[1] to have the neutron halo structure. We shall consider this $1/2^+$ state as an example, and demonstrate that the direct neutron capture cross section is indeed enhanced at lower energy due to the halo structure of this $1/2^+$ state of $^{13}C$ where the $2s_{1/2}$ neutron orbit actually has the halo feature. The present result is in a good agreement with recent experimental data obtained in Tokyo Institute of Technology by Nagai and his collaborators.[2] We would like to emphasize that the direct neutron capture provides us with a precious and probably unique experimental method to observe the halo structure in excited states (of stable nuclei). The astrophysical implication of this state is quite significant for instance for the inhomogeneous Big Bang models. The inverse process, i.e., photodisintegration is discussed also for an example $^{11}Be$ which is known to have the neutron halo in its anomalous ground state. A sharp but non-resonant peak near the threshold is obtained as an evidence of this neutron halo. This work has been published.[3]

References

1) T. Otsuka et al.: *Phys. Rev. Lett.*, **70**, 1385 (1993).
2) T. Ohsaki et al.: *Astrophys. J.*, **422**, 422 (1994).
3) T. Otsuka et al.: *Phys. Rev.*, **C49**, R2289 (1994).

* Department of Physics, University of Tokyo

# Deformed Woods-Saxon Potential Approach to the Structure of $^{11}$Be

A. Muta* and T. Otsuka

[Deformed Woods-Saxon potential, $^{11}$Be, halo, unstable nuclei.]

The halo structure is explained as a tunneling effect in a loosely bound system of single-particle potential. We consider the halo nucleus $^{11}$Be, including its strong deformation.

We first study the difference between the wave function in the Woods-Saxon potential and that in the square well potential, and find that the amplitude of $1s1/2$ halo structure depends strongly on potential diffuseness. In other words, the amplitude of halo wave function in the Woods-Saxon potential is larger than that in the square well potential. Hence the halo structure is a phenomenon sensitive not only to the loose binding but also to the potential diffuseness. On the other hand, deformation effect on the halo amplitude of $1s_{1/2}$ is small and this effect is more prominent in the wave function of the inner part. We calculate $\langle r^2 \rangle$ as a function of binding energy. For stable heavy nuclei, of which S(n) is more than 8 MeV, $\langle r^2 \rangle$ is mainly determined inside the nucleus. On the other hand, for a halo orbit of unstable nuclei $\langle r^2 \rangle$ is influenced largely by the density of the outer, i.e., tunneling part.

Our calculation with the axially symmetric deformed Woods-Saxon potential reproduces $1s_{1/2}$ halo structure of $^{11}$Be quite well with a reasonable spectroscopic factor ($= 0.77$)[1] as shown in Fig. 1[2] and Fig. 2.[3] Proton RMS radius, $Q_0$, halo radius $\sqrt{\langle r^2 \rangle_{halo}}$, and S(p) are also reproduced well. Figure 2 shows, through the E1 excitation scheme, that the halo structure of $1s_{1/2}$ depends on the potential diffuseness. Figure 3 exhibits the density distribution and one can see that the density distribution is strongly deformed. Furthermore, a cluster structure is seen in Fig. 3.

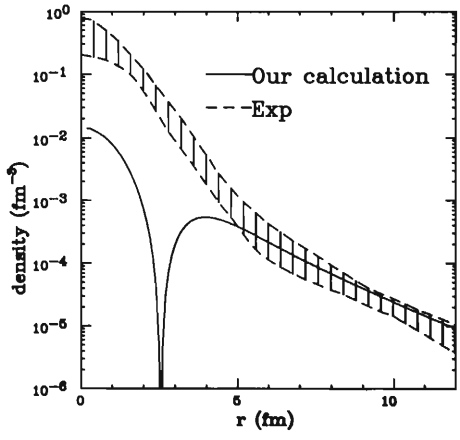


Fig. 1. Our calculation (solid line) using $1s_{1/2}$ wave function reproduces experimental data (dashed line) well. Spectroscopic factor of S = 0.77 is taken.[1]

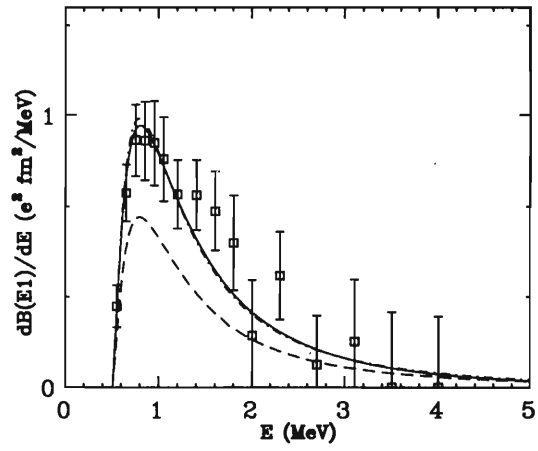


Fig. 2. dB(E1)/dE for the photodisintegration of $^{11}$Be as a function of the excitation energy E. The solid (dot-dashed) line is obtained by the spherical (deformed) Woods-Saxon potential and is in agreement with experimental data. The result obtained by a square well potential (dashed line) does not reproduce the experimental data.

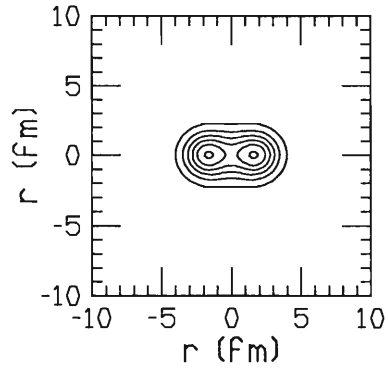


Fig. 3. Matter density contour plot of $^{11}$Be. Cluster structure and super deformation are seen.

* Department of Physics, University of Tokyo

References

1) B. Zweiglinski et al.: *Nucl. Phys.*, **A315**, 124 (1979).
2) M. Fukuda et al.: *Phys. Lett.*, **B268**, 339 (1991).
3) T. Nakamura et al.: *ibid.*, **B331**, 296 (1994).

# Beta-decay of Neutron-rich Nuclei $^{17}$B and $^{19}$C

H. Kitagawa, A. Ozawa, and H. Sagawa

[beta-decay, neutron-rich nuclei.]

Recently the beta-decay of neutron-rich nuclei ($^{17}$B, $^{19}$C, $^{19}$N) with large isospins was measured at the RIKEN Ring Cyclotron.[1] Nuclei of this mass region are theoretically interesting because the isospin symmetry is expected to be broken, e.g. spin-parities of the ground state of some of the mirror pairs are different each other. The purpose of this work is to specify the spin-parities which are unknown experimentally, and to investigate the configuration (especially the $s_{1/2}$-orbit in the sd-shell) of $^{19}$N through one-neutron stripping reaction to $^{18}$N + n.

The structure of the latter problem is as follows. By a little consideration, the ground state of $^{19}$C should have a positive parity. Due to the observed log$ft$ value, this beta decay is assumed to be allowed one, then the excited states of $^{19}$N are positive parity states, which have two holes in the p-shell. The observed negative parity states of $^{18}$N must have one hole or three holes in the p-shell. If the stripping of $^{19}$N to $^{18}$N + n is a single-step reaction, the $^{18}$N states concerning this stripping should have three holes. Then the question is why these observed three hole states are close to the ground state that should be a one-hole state.

We calculate energy levels, log$ft$ values and branching ratios of beta-decays using the shell model with the Millener-Kurath interaction. The model space is restricted to p- and sd-shells. We consider only allowed Gamow-Teller type beta-decay. Spectroscopic factors are calculated in order to estimate the strength of the stripping reaction of $^{19}$N to $^{18}$N + n. Though this shell model interaction file is designed for the states with up to one hole in the p-shell, we will be able to modify the interaction file in the shell model by fitting the observed values of two and three hole states.

We show the results of calculations in Figs. 1, 2, and Table 1. Energy difference between the ground states of $^{17}$B and $^{17}$C is well reproduced, although the excited states (with a negative parity) of $^{17}$C is not reproduced so well. Though the calculated log$ft$ values are well reproduced, the branching ratios are not reproduced. This would be because we cannot describe correct energy levels of the excited states with this interaction file of the shell model, i.e. the model space is small for this kind of nuclei. The calculated values of log$ft$ and the branching ratios of the decay of $^{19}$C seem well reproduced, but the energy differences between two levels which have different parities are not reproduced. As the calculated values of the spectroscopic factors are quite small, these stripping reactions are almost forbidden, different from the observed ones. Decomposing each excited state into one and three hole states, we find these states are almost one hole states. We need to make three hole components larger in order to reproduce the observed stripping scheme. Hence the orbits in sd-shell should be lower and closer to the p-shell, breaking the isospin symmetry.

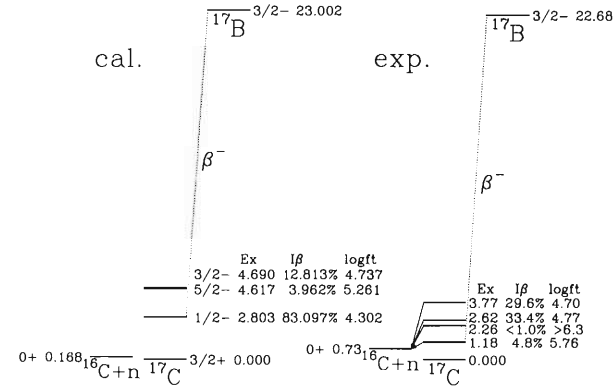


Fig. 1. Result of calculation for the decay of $^{17}$B.

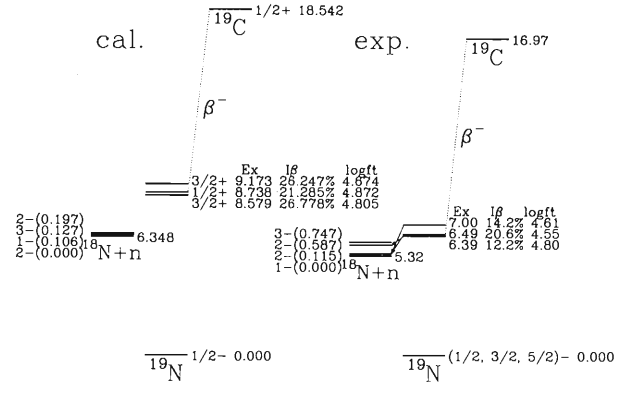


Fig. 2. Result of calculation for the decay of $^{19}$C.

Table 1. Calculated spectroscopic factors of $^{19}$N to $^{18}$N + n: $(s_j^{1/2})^2 \times 10^5$.

| $^{18}$N | | 2− | 1− | 3− | 2− |
|---|---|---|---|---|---|
| | $E_{ex}$(MeV) | 0.000 | 0.106 | 0.127 | 0.197 |
| $^{19}$N | 3/2 + (9.173) | 52 | 94 | 0 | 33 |
| | 1/2 + (8.738) | 4 | 32 | 0 | 4 |
| | 3/2 + (8.579) | 41 | 11 | 1 | 13 |

References

1) A. Ozawa et al.: to be published.

# Beta-decay of $^{17}$Ne and Isospin Symmetry

H. Kitagawa, A. Ozawa, and H. Sagawa

[beta-decay, isospin symmetry.]

Breaking of isospin symmetry might play an important role to understand the structure of "halo" nuclei. It is important to compare the mirror pairs (both the masses and the isospins are the same but $z$-components of the isospin are different.) in order to investigate the isospin symmetry breaking. Recently measured nuclear radii of the A = 17 isobars show asymmetry of the isospin in this system. Since the nuclear radii reflect the spatial expansion of the nucleon (it consists of matrix elements which contain expectation values of $r^2$.), it is rather difficult to discuss the isospin asymmetry in a quantitative way. We can see this asymmetry easily if we use the beta-decay strength, because it consists of matrix elements which contain expectation values of $r$ or 1.

The $\beta^+$-decay of the ground state of $^{17}$Ne to the first excited state of $^{17}$F has been measured by Borge et al. Since this state of $^{17}$F is very close to the one-proton threshold, it is considered as a candidate of a proton-"halo" state. With the value of beta-decay strength of mirror pairs, the asymmetry coefficient is defined[1] as

$$\delta = \frac{ft_+}{ft_-} - 1 = \frac{B(\mathcal{M})_-}{B(\mathcal{M})_+} - 1.$$

If the isospin symmetry is conserved, the value of $\delta$ must be zero.

Borge et al.[2] listed the value of $\delta$ for several mirror pairs with their result of $^{17}$F. In most of the pairs the values of $\delta$ are small positive numbers close to zero. This is considered as the result of the expansion of neutron wave functions compared with the proton ones. The value of $\delta$ of A = 17 pair is exceptionally large and negative. They concluded that this is due to the effect of the "halo"-proton of $^{17}$F.

We investigated theoretically the $\beta^+$-decays of $^{17}$Ne to both the ground and the first excited states of $^{17}$F by using the shell model for the configuration. The Skyrme Hartree-Fock wave function calculated with the SGII interaction is adopted for the single-particle wave functions. Since the ground state of $^{17}$Ne is close to the two-proton threshold, we considered this state as a two-proton "halo" state similar to the neutron "halo" of $^{11}$Li. Through the beta-decay strength, it is possible to clarify the configuration of $^{17}$Ne.

We calculated the $\beta^+$-decay matrix element using the Gamow-Teller type operator for $^{17}$Ne(1/2−) to the first excited state of $^{17}$F(1/2+), and the unique first forbidden operator for $^{17}$Ne to the ground state of $^{17}$F(5/2+). Main contribution of single-particle matrix elements is $p_{1/2} \rightarrow s_{1/2}$ for $^{17}$Ne $\rightarrow^{17}$ F(1/2+) and $p_{1/2} \rightarrow d_{5/2}$ for $^{17}$Ne $\rightarrow^{17}$ F(5/2+). We assumed the configuration of $^{17}$F is the same as that of $^{17}$O neglecting the proton-"halo" of the first excited state of $^{17}$F.

Table 1. Result of calculations for A = 17 system.

| $^{17}$Ne config. | same as $^{17}$N | $s_{1/2}$ only | $d_{5/2}$ only | exp. |
|---|---|---|---|---|
| $\delta$(1/2+) | 0.203 | −0.682 | > 1 | −0.55(9) |
| $\delta$(5/2+) | −0.026 | > 1 | −0.348 | not yet |
| Br(5/2+) | 43.4% | 0 | 64.6% | not yet |

We show the result of calculation in Table. 1. Three types of configurations of $^{17}$Ne are considered; the same configuration as that of $^{17}$N, the configuration restricting the sd-shell only to the $s_{1/2}$-orbit or only to the $d_{5/2}$-orbit. The latter two configurations break the isospin symmetry. For the beta-decay of $^{17}$Ne to $^{17}$F(1/2+), we can reproduce the observed value if we assume the $s_{1/2}$-orbit. If we use these restrictions to the $s_{1/2}$-orbit for the configuration of the 5/2+ state, the value of $\delta$ of $^{17}$Ne to $^{17}$F(5/2+) is very large. This is due to a suppression of the single particle matrix element of $p_{1/2} \rightarrow d_{5/2}$. Though this decay has not been measured yet, we can expect that the $s_{1/2}$ level is lower than the $d_{5/2}$ level and the isospin symmetry is broken in this pair. The measurement of the $\beta^+$-decay of $^{17}$Ne to the ground state of $^{17}$F is desired, because we can verify this assumption by the observed value.

References

1) I. S. Towner: *Nucl. Phys.*, **A216**, 589 (1973).
2) M. J. G. Borge et al.: *ibid.*, **A490**, 287 (1988); *Phys. Lett.*, **B317**, 25 (1993).

# Giant Resonances in Nuclei with Neutron Skin

M. Yokoyama,* T. Otsuka, H. Sagawa, and N. Fukunishi

[Neutron-rich nuclei, giant quadrupole resonance, exotic nuclei.]

The quadrupole, octupole, and dipole giant resonances in various nuclei are investigated in terms of the Hartree-Fock calculations and the random-phase approximation (RPA) using the Skyrme interaction consistently.

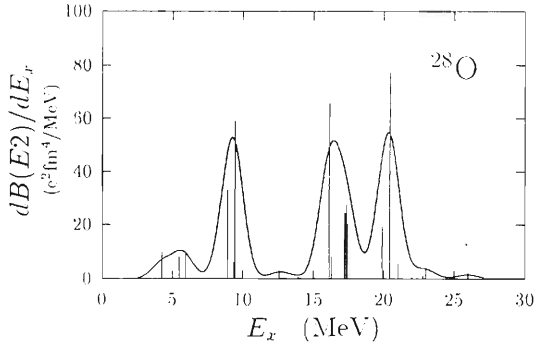


Fig. 1. $B(E2)$ of $^{28}$O obtained by means of the random-phase approximation (RPA) using the Skyrme III interaction. The peaks in the low energy region (5–18 MeV) are considered to be neutron-mode excitations.

It is seen in nuclei with neutron skin[1] that the average excitation energies are lowered from the standard mass number dependence and that neutron-mode excitations, which consist almost only of neutron contributions, lie below the primary (isoscalar or isovector) giant resonances. The neutron-mode excitations have large strength comparable with the primary giant resonances. It is also seen that the correlation energy is small in the neutron-mode because the proton-neutron interaction does not affect so much.

Proton-mode excitations can be seen in the proton-rich nuclei, but they are not so remarkable as in the neutron-rich nuclei.

References

1) N. Fukunishi, T. Otsuka, and I. Tanihata: *Phys. Rev.*, **C48**, 1468 (1993).

* Department of Physics, University of Tokyo

# Transfer and Fusion Reactions of Unstable Nuclei

K.-H. Kim,* T. Otsuka, and M. Tohyama

[Neutron skin, fusion reaction, transfer reaction.]

The transfer and fusion reactions are studied for reactions between a stable and an unstable nucleus with neutron skin, taking as examples the reactions $^{40}$Ca + $^{16,28}$O. The two-dimensional time-dependent Hartree-Fock (TDHF) method is used.[1)]

Figure 1 shows the impact-parameters as functions of the center-of-mass energy $E_{c.m.}$, for (a) $^{40}$Ca + $^{16}$O and (b)–(d) $^{40}$Ca + $^{28}$O reactions. The boundary between the fusion and other reactions is indicated by the solid line in (a) and (b). These boundaries are indicated by the dashed-dotted lines in (c) and (d). In (c) and (d), the boundary between the regions I and II is shown by the solid lines. The region I of (c) is the transfer of less than one neutron and that of (d) is the transfer of less than one proton. The region II is the transfer of more than one neutron (in the case of (c)) or proton (in the case of (d)), and III is the fusion region. All lines are drawn connecting points where calculations are carried out. The classical value of $b$ is shown by the dashed line.

It is shown that, in $^{40}$Ca + $^{28}$O reactions, the nucleon transfer is enhanced enormously for both protons and neutrons. However, the neutron skin does not enhance the fusion cross section contrary to the usual expectation.

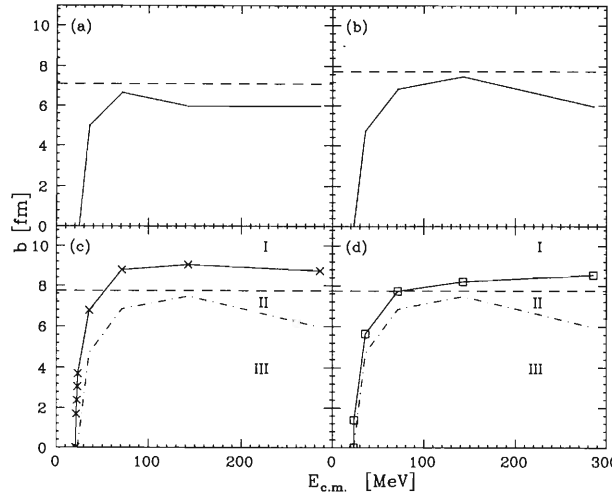


Fig. 1. Impact-parameter $b$ as a function of $E_{c.m.}$ for (a) $^{16}$O + $^{40}$Ca and (b)–(d) $^{28}$O + $^{40}$Ca reactions.

References

1) K. T. R. Davies and S. E. Koonin: *Phys. Rev.*, **C23**, 2042 (1981).
2) N. Fukunishi, T. Otsuka, and I. Tanihata: *ibid.*, **C48**, 1648 (1993).

* Department of Physics, University of Tokyo

# Mass Dependent Parameter Set of the Relativistic Mean Field Theory for Unstable Nuclei and Nuclear Matter

Y. Sugahara* and H. Toki

[Relativistic Mean Field, Unstable Nuclei.]

Recently, the unstable nuclear beam facilities are available in various laboratories in the world. These facilities push forcefully the boundaries of known nuclei toward the nuclear drip lines. Many interesting properties as neutron halo and neutron skin are found at the neutron drip lines and many more are being expected to be found.[1,2] Such information in turn provides strong constraint on the nuclear astrophysics, in particular, the supernovae and neutron stars. It is then an interesting project for theoreticians to work out a theory on unstable nuclei and nuclear matter. We need in this case large extrapolation, which is usually very difficult and a careful strategy should be made to make the theory reliable.

We consider "relativity" as a key word of success in describing the experimental data. Our strategy is therefore to choose the relativistic mean field (RMF) theory as the phenomenological theory with several parameters, which should describe unstable nuclei and nuclear matter. The form of the RMF theory is suggested by the microscopic theory, the relativistic Brueckner Hartree-Fock (RBHF) theory, which is able to reproduce the saturation property of nuclear matter.[3] The parameters of RMF are then obtained by using the experimental data including the unstable nuclei.

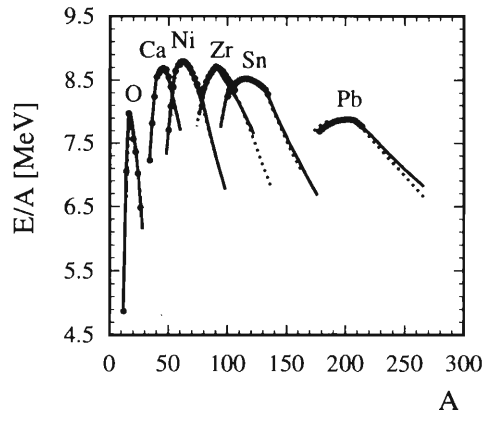


Fig. 1. Binding energies of the proton magic nuclei as a function of the mass number. The results of TMA are denoted by solid curves and those of NL1 by dotted curves and they are compared with the experimental values denoted by circles.

We tried first to get a single parameter set to describe all nuclei, but had to use two parameter sets for satisfactory results; TM1 for heavy nuclei ($Z \geq 20$) and TM2 for light nuclei ($Z \leq 20$).[4] We, therefore, decide to include mass dependence to all the coupling constants to get a parameter set for nuclei in all the mass region. The parameter set is called TMA. We show the binding energies for the proton magic nuclei as a function of the mass number in Fig. 1, in which the results of NL1 and the experimental data are plotted as comparison. We show also the proton and the neutron radii in Fig. 2.

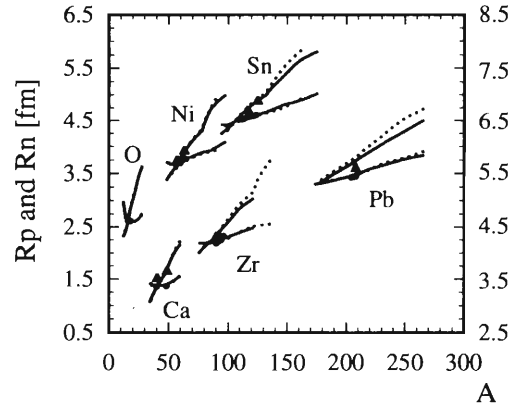


Fig. 2. Proton and neutron radii of the proton magic nuclei. The notations are the same as Fig. 1. The experimental values of proton radii are denoted by circles and those of neutron radii by the triangles.

We calculate then the profile of neutron star as a function of the central density. The critical mass of the neutron star is reduced to about twice the mass of the sun for TMA. The proton fraction is found pretty large even for the case of TMA, where the symmetry energy at the saturation density is moderate.

References

1) I. Tanihata et al.: *Phys. Rev. Lett.*, **55**, 2676 (1985).
2) I. Tanihata et al.: *Phys. Lett.*, **B289**, 261 (1992).
3) R. Brockmann and R. Machleidt: *Phys. Rev.*, **C42**, 1965 (1990).
4) Y. Sugahara and H. Toki: *Nucl. Phys.*, **A579**, 557 (1994).

* Department of Physics, Tokyo Metropolitan University

# Relativistic Mean Field Theory for Unstable Nuclei and the Birth of Neutron Stars

K. Sumiyoshi, D. Hirata, Y. Sugahara,* H. Suzuki, and H. Toki

[relativistic mean field theory, unstable nuclei, neutron stars.]

The recent advance in unstable nuclear beam experiments provides us with new knowledge on unstable nuclei away from the stability line.[1] Such extensive studies on unstable nuclei have also a potential to provide us with valuable information on the dense matter under the extreme conditions such as a neutron rich environment in neutron stars. Hence, it is important to construct a many body framework, which is reliable even for unstable nuclei, and apply the same framework to provide the equation of state (EOS), which is essential to clarify the mechanism of supernova explosions and the evolution of neutron stars.

We study the properties of unstable nuclei away from stability and the equation of state (EOS) for neutron stars and supernovae in the relativistic mean field (RMF) theory.[2-7] The lagrangian with the non-linear $\sigma$-$\omega$ terms of the RMF theory[5] is motivated by the recent success of the relativistic Brueckner Hartree Fock theory.[8] We use the parameter set TM1 determined by the fitting to the experimental data of nuclei including unstable ones. The RMF theory thus constructed reproduces successfully the binding energy of many nuclei other than used in the fitting.[2-5]

We show in Fig. 1 the calculated results of the root-mean-square radii of the distribution of protons and neutrons of Sn isotopes in the RMF theory with TM1. We also show the results of the Skyrme Hartree-Fock calculations[4] with the parameter set SIII for comparisons. The results of the RMF theory are in excellent agreement with experimental data for the radii for protons. The radii for neutrons are significantly different between the two calculations depending on the symmetry energy. This difference in the neutron rich region will be examined in more detail by future experimental studies.

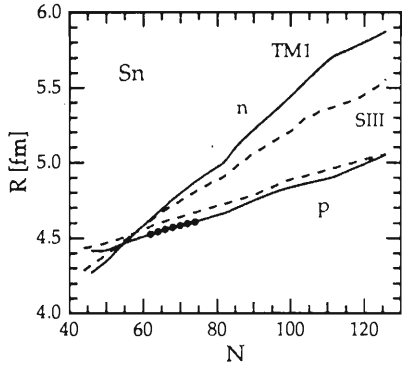


Fig. 1. The root-mean-square radii R of Sn isotopes as a function of the neutron number. The experimental data are shown by dots.

We then apply the EOS calculated in the same RMF theory[6,7] to the numerical simulation of the cooling of a protoneutron star just born in the supernova explosion.[9] We show in Fig. 2 the calculated time profile of the mean energy of neutrinos emitted from the protoneutron star during the cooling. Here we compare it with the case with the EOS having the reduced symmetry energy.

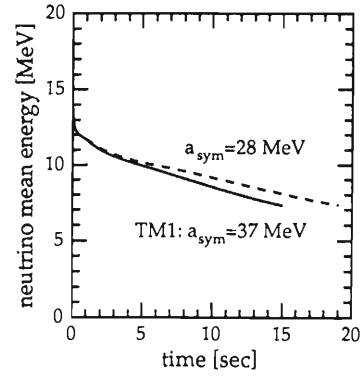


Fig. 2. The time profiles of the mean energy of supernova neutrinos in the two cases with different symmetry energies.

We found that the symmetry energy, which is essential to describe unstable nuclei, influences the thermal evolution of protoneutron stars and supernova neutrinos emitted in the supernova explosion. It would be interesting if we could examine the properties of supernova neutrinos by comparisons with the detection of the neutrino burst in future supernova explosions in terms of the EOS constrained by the unstable nuclei.

* Department of Physics, Tokyo Metropolitan University

References

1) I. Tanihata et al.: *Phys. Rev. Lett.*, **55**, 2676 (1985).
2) D. Hirata et al.: *Phys. Rev.*, **C44**, 1467 (1991).
3) D. Hirata et al.: *Phys. Lett.*, **B314**, 168 (1993).
4) K. Sumiyoshi et al.: *Nucl. Phys.*, **A552**, 437 (1993).
5) Y. Sugahara et al.: *ibid.*, **A579**, 557 (1994).
6) K. Sumiyoshi et al.: *Astrophys. J.*, **422**, 700 (1994).
7) K. Sumiyoshi et al.: *Nucl. Phys.*, **A581**, 725 (1995).
8) R. Brockmann et al.: *Phys. Rev.*, **C42**, 1965 (1990).
9) K. Sumiyoshi et al.: submitted to *Astron. Astrophys.*

# Study of the Triaxial Deformation in the Relativistic Mean Field Theory

D. Hirata, K. Sumiyoshi, B. V. Carlson, H. Toki, and I. Tanihata

[Nuclear Structure, binding energy, gamma deformation, relativistic mean field theory.]

The use of the radioative beam facilities has allowed us to study the nuclear structure of nuclei far from the stability line.[1,2] The studies of exotic nuclei display a large diversity of phenomena which could not be observed in the stable ones.[3]

The relativistic theories have been extensively applied in the last few years to nuclei and nuclear matter with remarkable success. The description of the ground state properties of the stable and unstable nuclei including the axial deformation, using the relativistic mean field theory (RMF) is extremely successful.[4-6]

Recently, the RMF theory has been applied to study the ground state properties of unstable nuclei such as Sr, Xe, Cs and Ba isotopes, under the axial symmetry assumption.[6,7] The results of the calculation were in good agreement with the experimental data for the neutron rich nuclei. However, in the proton rich side, the description was not as good and it was attributed to a transitional character in that region.[3] The non-relativistic calculations seem able to describe these isotopes when the triaxial deformation assumption is taken.

Recently, the RMF theory with the axial symmetry assumption, has been also applied to study the ground state properties of very rich neutron sulfur nuclei.[8] The results of the RMF calculation were compared with those obtained from the non-relativistic Hartree-Fock (HF) with Skyrme forces. However, the HF calculations were performed under the triaxial symmetry. It is therefore a challenge to extend the RMF theory to non-axially-symmetric configurations, that is the triaxial deformation, and to apply it to these nuclei.

The extension of the RMF theory from the axial symmetry to non-axially symmetric configurations is rather difficult. In order to simplify the calculations, we expanded the meson fields and the Dirac spinors in deformed basis. With those expansions, the Dirac equations were reduced to a complex hermitian matrix diagonalization problem and the meson fields to an inhomogeneous set of linear equations.

Due to the size of memory and cpu limit we had to truncate the expansion at $N = 8$ major shells for fermions and bosons. With this procedure we had to restrict our calculations to light systems.

Here, we present the results of the RMF theory with the triaxial symmetry for the $^{16}$O, $^{24}$Mg and $^{46\text{-}48}$S using the TM1 parameter set.[9] We performed constraint calculations with the quadrupole moments in order to obtain the energy surface on the ($\beta$,$\gamma$) plane. The deformation parameters $\beta$ and $\gamma$ were determined from the expectation values of the intrinsic quadrupole moments $\langle Q_\mu \rangle = \langle r^2 Y_{2\mu} \rangle$, where

$$\beta = \frac{4}{3\pi}(1.2A^{1/2})^2\sqrt{\langle Q_0\rangle^2 + \langle Q_2\rangle^2} \text{ and } \gamma = \sqrt{2}\frac{\langle Q_2\rangle^2}{\langle Q_0\rangle^2}.$$

Figure 1 shows the energy surfaces of these nuclei in the ($\beta$,$\gamma$) plane, where $\gamma$ runs from 0° to 60°. The horizontal axis corresponds to the prolate solution while $\gamma = 60°$ corresponds to the oblate solution.

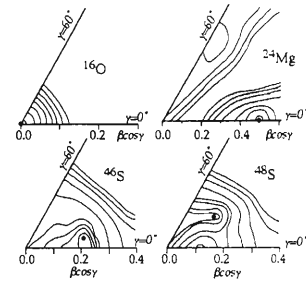


Fig. 1. The energy surfaces for $^{16}$O, $^{24}$Mg and $^{46\text{-}48}$S in the plane. ($\beta$,$\gamma$). The absolute minimum of the binding energy is denoted by a black dot.

In summary, we have applied the RMF theory under the triaxial symmetry on $^{16}$O and $^{24}$Mg nuclei in order to test the performace of the code for spherical and axial deformed nuclei. The results obtained with the new code are quite similar to those obtained using the axial and spherical codes and are in good agreement with the experimental data of charge rms radii, binding energies, and the quadrupole moment of Mg.

We have also performed the RMF theory calculations with the same assumption as the HF[8] for the very rich $^{46\text{-}48}$S isotopes and found that both are gamma soft deformed. The RMF calculations give $\gamma = 2.8°$ for $^{46}$S and $\gamma = 28.7°$ for $^{48}$S while the HF calculation gives $\gamma = 10°$ for $^{48}$S.

References

1) I. Tanihata et al.: *Phys. Rev. Lett.*, **55**, 2676 (1985).
2) I. Tanihata et al.: *Phys. Lett.*, **B289**, 261 (1992).
3) J. H. Hamilton: Treatise on Heavy-Ion Science, Vol. 8, ed. D. A. Bromley, Plenum, New York, p. 3 (1989).
4) R. Brockmann and R. Machleidt: *Phys. Rev.*, **C42**, 1965 (1990).
5) Y. K. Gambhir et al.: *Ann. Phys.*, (NY) **198**, 132 (1990).
6) H. Toki et al.: *Nucl. Phys.*, **A524**, 633 (1991); D. Hirata et al.: *Phys. Rev.*, **C44**, 1467 (1991); D. Hirata et al.: *Phys. Lett.*, **B314**, 168 (1993).
7) D. Hirata et al.: submitted to *Nuc. Phys.*
8) T. R. Werner et al.: *Phys. Lett.*, **B333**, 303 (1994).
9) Y. Sugahara and H. Toki: *Nucl. Phys.*, **A579**, 557 (1994).

# Effective Interaction in Asymmetric Nuclear Matter

N. Fukunishi

[Asymmetric nuclear matter.]

Properties of asymmetric nuclear matter play crucial roles in many branches of physics. Asymmetric nuclear matter is a virtual system which is composed of different number of protons and neutrons without the Coulomb interaction. Bulk properties of neutron-rich nuclei strongly relate to asymmetric nuclear matter. The equation of state for asymmetric nuclear matter is also important in the physics of neutron stars[1] and type-II supernova.[2]

We employ the non-relativistic Brueckner-Hartree-Fock (NRBHF) approach. It is well known that the NRBHF theory does not reproduce correct saturation properties for symmetric nuclear matter. Thus, some other approaches, for examples, the relativistic Brueckner-Hartree-Fock (RBHF) theory, have been proposed. However, studies of asymmetric nuclear matter in the NRBHF theory is meaningful because of the following three reasons.

(1) We are mainly interested in how properties of a many-nucleon system change according to the asymmetry ratio $\alpha = \frac{\rho_N - \rho_P}{\rho_N + \rho_P}$. Note that about 90% of the potential energy is reproduced in the NRBHF theory.

(2) More elaborated calculation within the non-relativistic framework given by Jiang et al.,[3] improves the discrepancy between theories and experiments.

(3) The predicted properties of asymmetric nuclear matter, for example, the density dependence of the symmetry energy, are different between the NRBHF and the RBHF theories.[4]

In the NRBHF theory, the G-matrix interaction, which is an effective interaction in the nuclear media, is calculated from the realistic nuclear forces as follows,

$$G(\omega) = V + V\frac{Q}{\omega - H_0}G(\omega).$$

$V$ implies a nuclear force. The Reid Soft Core interaction is used in this calculation. $Q$ means the Pauli operator which is the origin of the density-dependence of the G-matrix interaction. $\omega$ is the starting energy, i.e., the energy of the two nucleons in asymmetric nuclear matter. The starting energy is determined self-consistently in this framework and may change in asymmetric nuclear matter compared with the symmetric case. $H_0$ is an energy of the intermediate states. We employ the BBP prescription[5] for $H_0$. Similar calculations have been performed.[6,7] The main difference is that the present calculation treats the Pauli operator exactly. We calculated various quantities in this framework. We find that the correct treatment of the Pauli operator changes properties of asymmetric nuclear matter little.

We further examine the $\alpha$-dependence of the effective interaction (G-matrix interaction). Figure 1 shows the G-matrix interaction for the $^3S_1$ channel in which the strongest $\alpha$-dependence is seen. The G-matrix interactions are illustrated with the solid line ($\alpha = 0$) and the dashed line ($\alpha = 0.32$). Note that $\alpha = \frac{1}{3}$ corresponds to N = 2Z. (N is a neutron number and Z is a proton number.) Near the saturation density, the density-dependence of the G-matrix is very weak. This is one of the origins of this weak $\alpha$-dependence. The starting energy dependence of the G-matrix is rather strong for the $^3S_1$ channel. For $\alpha = 0.32$, the energy of a proton or a neutron changes significantly. However, the starting energy which is a sum of the proton and the neutron energy changes little. This is another origin of the observed weak $\alpha$-dependence. This calculation implies that the G-matrix interaction calculated in symmetric nuclear matter can be used for the asymmetric case.

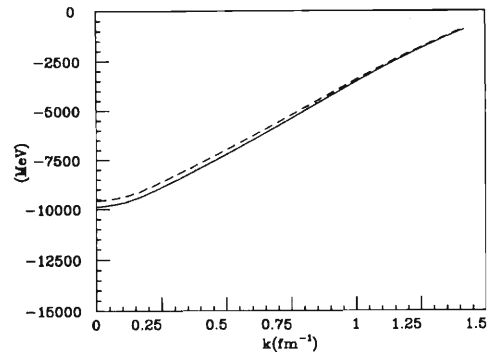


Fig. 1. G-matrix interactions for the $^3S_1$ channel ($k_F = 1.45$ fm$^{-1}$). The solid line shows the symmetric case and the dashes line indicates the asymmetric ($\alpha = 0.32$) case.

References

1) J. Nemeth and D. W. L. Sprung: *Phys. Rev.*, **176**, 1496 (1968); N. C. Chao, J. W. Clark, and C. H. Yang: *Nucl. Phys.*, **A179**, 320 (1972).
2) E. Baron, J. Cooperstein, and S. Kahana: *Phys. Rev. Lett.*, **55**, 126 (1985).
3) M. F. Jiang, R. Machleidt, and T. T. S. Kuo: *Phys. Rev.*, **C41**, 2346 (1990).
4) H. Huber, F. Weber, and M. K. Weigel: *Phys. Lett.*, **B317**, 485 (1993).
5) H. A. Bethe, B. H. Brandow, and A. G. Petschek: *Phys. Rev.*, **129**, 225 (1963).
6) I. Bombaci and U. Lombardo: *ibid.*, **C44**, 1892 (1991).
7) H. Q. Song, Z. X. Wang, and T. T. S. Kuo: *ibid.*, **C46**, 1788 (1992).

# Stationary Solution of Time Dependent Density Matrix Formalism

M. Tohyama

[density matrix formalism, ground state correlations, Lipkin model.]

We have recently reported realistic calculations for the damping of giant resonances[1] and for low-energy heavy-ion collisions,[2] based on the time dependent density matrix theory (TDDM). Although the obtained results are quite encouraging, these numerical calculations contain inconsistency in the treatment of the ground state: the Hartree-Fock (HF) ground state, which clearly is not a stationary solution of TDDM, is used as the initial ground state. An attempt to find a stationary solution of TDDM was made in Ref. 3 but was not quite successful. In this report we demonstrate that a better stationary solution of TDDM can be obtained through an adiabatic treatment of two-body interactions. We use the Lipkin model hamiltonian[4] which consists of $N$ fermions occupying two $N$-fold degenerate levels with energies $\epsilon/2$ and $-\epsilon/2$, respectively. The states in the upper level are labeled by quantum number $p = 1, 2, \ldots N$, while those in the lower level are labeled by $-p$. We solve the TDDM equations of motion for the Lipkin model, starting from the HF ground state and adiabatically turning on the two-body interaction:

$$V(t) = V(1 - e^{-t/\tau}). \tag{1}$$

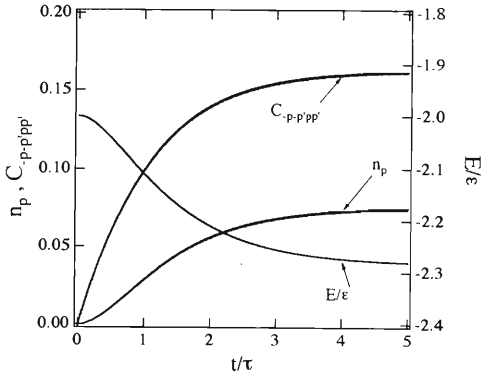


Fig. 1. Time evolution of $E$, $n_p$ and $C_{-p-p'pp'}$ in TDDM for an $N = 4$ system.

In Fig. 1 the occupation probability of the upper level $n_p$, the two-body correlation matrix $C_{-p-p'pp'}$ and the total energy $E$ are shown as a function of time for an $N = 4$ system with $|V|/\epsilon = 0.3$. Each of $n_p$, $C_{-p-p'pp'}$ and $E$ approaches a constant value at large $t$. We found that as long as $\tau \gg \hbar/\epsilon$, the solution at large $t$ becomes stationary and does not depend on $\tau$.[5] The obtained results of $E$ for various values of $|V|/\epsilon$ are compared with the exact ones in Fig. 2. The total energy $E$ in TDDM has the $|V|/\epsilon$ dependence similar to the exact one.

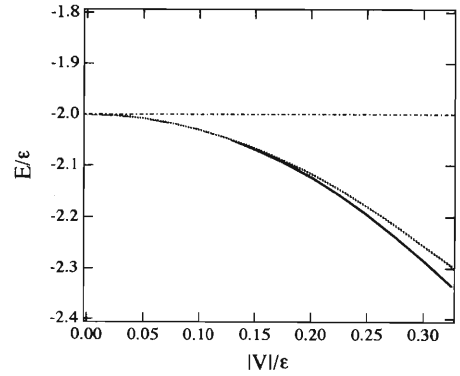


Fig. 2. Total energy as a function of $|V|/\epsilon$ for the $N = 4$ system. Solid line denotes the results of the TDDM calculation and dotted line the exact solution. Dot-dashed line indicates the HF result.

References

1) M. Gong and M. Tohyama: *Z. Phys.*, **A335**, 153 (1990).
2) M. Gong, M. Tohyama, and J. Randrup: *ibid.*, p. 331.
3) H. J. Lipkin, N. Meshkov, and A. J. Glick: *Nucl. Phys.*, **62**, 188 (1965).
4) M. Tohyama, P. Schuck, and S. J. Wang: *Z. Phys.*, **A339**, 341 (1991).
5) M. Tohyama: *Prog. Theor. Phys.*, **92**, L905 (1994).

# Strength for Isoscalar Modes in Diabatic Picture

S. Yamaji and H. Hofmann*

[Large Scale Collective Motion, Linear Response Theory, Diabatic Motion.]

We studied the collective response function as a function of the excitation energy for typical isoscalar modes.[1] We found that the strength function exhibits the usual low energy and giant resonance peaks at low temperatures whereas all the strength is concentrated in a low energy mode at temperatures higher than a temperature of around 1.5 MeV. Thus the vibrational inertia of slow motion turns into that of irrotational flow at high temperatures. According to the study in Ref. 2 this is largely due to the fact that the vibrations looked at are the ones about thermal equilibrium in true sense. It is described by the many-particle many-hole configurations which come into play through the coupling constant k expressed by

$$-k^{-1} = \frac{\partial^2 E(Q,S)}{\partial Q^2} + \chi(0),$$

where $E(Q,S)$ is the lowest possible energy specified by the collective variable $Q$ and the entropy $S$ in the quasi-static picture, and $\chi(0)$ is the static response.[1] In this sense the $E(Q,S)$ represents what in nuclear physics often has been associated to "adiabatic dynamics".

Still according to Ref. 2 completely different behaviour is to be expected if the coupling constant is evaluated in the "diabatic" picture with all occupation numbers frozen. For vibrations of this type the previous formulas in Ref. 1 can be taken over. The only change necessary is to replace $k$ by a diabatic coupling constant $k_{\rm di}$ whose value is given by the above expression with the quasi-static energy being replaced by the diabatic one $E_{\rm di}$(Q,S). The corresponding coupling constant $k_{\rm di}$ stays constant with excitation, rather than decreases as in the case of "adiabatic" motion (see Fig. 5 of Ref. 2).

In Fig. 1 we present a numerical computation, again for the same situation as in Ref. 1, but with $k$ replaced by $k_{\rm di}$. No shift of strength is seen. Only the giant peaks get broader at higher temperatures. This is traced back to the increasing single particle width with temperature.

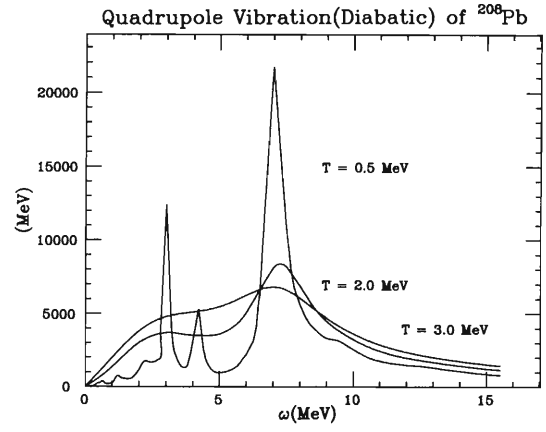


Fig. 1. Strength distribution for diabatic quadrupole vibrations.

References

1) H. Hofmann, S. Yamaji, and A. S. Jensen: *Phys. Lett.*, **B286**, 1 (1992).
2) D. Kiderlen, H. Hofmann, and F. A. Ivanyuk: *Nucl. Phys.*, **A550**, 473 (1992).

* Department of Physics, Technical University of Munich, Germany

# Possible Interpretation of Extremely Low Energy Odd Spin States

T. Horibata and N. Onishi

[$\gamma$-deformation, Tilted rotation, Wobbling motion.]

The dynamics of nuclear rotation including precession and wobbling is studied in order to make clear the mechanism dominating collective motions in nuclei, especially in the $\gamma$-unstable region, e.g., isotopes of tungsten or osmium. The wobbling motion is associated with triaxiality of nuclear deformation, and hence is likely to be strongly coupled with the fluctuation of $\gamma$-degrees of freedom. In fact, classical motions for a macroscopic model of the $\gamma$-soft rotor exhibit remarkable dynamics interweaving the $\gamma$-vibration and the wobbling motion, and are shown to possess a typical feature of nonlinear mechanical systems.[1] We investigated how these mechanisms manifest themselves in the collective state in the microscopic nuclear system.

Mikhailov and Janssen[2] suggested that the nuclear wobbling motion occurs as a result of Coriolis interaction pushing down odd spin states of the $\gamma$-vibrational band till it becomes close to the even spin yrast line. Following this idea, Matsuzaki discussed possible exsistence of the motion in $^{182}$Os based on the RPA calculation.[3] However those works are restricted within a linear vibration theory of the wobbling motion being slightly off from the stationary rotation along the principal axis of quadrupole deformation.

Recently we proceed a self-consistent three-dimensional cranking calculation,[4] and report the exsistence of tilted axis rotating states (TAR-states) in the crossing yrast band of the nucleus.[5] Figure 1 shows energy minima in the three dimensional potential surface for $^{182}$Os. Based on the symmetry properties, there are two minimum points at the mirror image positions with respect to the equator on the prime meridian. These minima represent the axes of stationary rotation in which wavefunction the symmetry of signature is broken down. The tunneling back and forth motion between the two points recovers a definite signature. Two solutions are obtained from the double-well model. The lowest solution corresponds to the Gerade state which is an even signature state and the other one is the next lowest Ungerade state which is an odd signature state. Namely,

$$\Psi_{\substack{\mathrm{G}\\\mathrm{U}}} = \int_{-\frac{\pi}{2}}^{\frac{\pi}{2}} f_{\substack{\mathrm{g}\\\mathrm{u}}}(\phi)\Psi_{\mathrm{T}}(\phi)d\phi \quad (f_{\substack{\mathrm{g}\\\mathrm{u}}}(-\phi) = \pm f_{\substack{\mathrm{g}\\\mathrm{u}}}(\phi)). \quad (1)$$

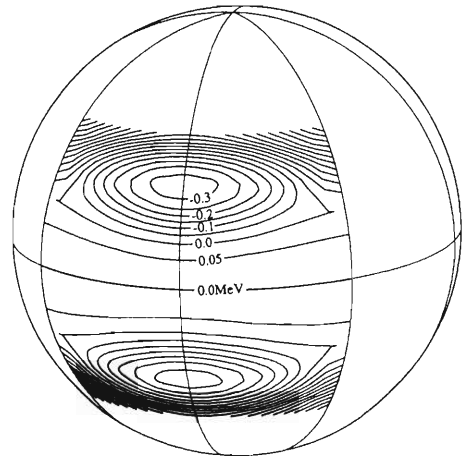


Fig. 1. Energy contour map of J = 15 sphere.

Therefore the Gerade and Ungerade solutions represent even and odd angular momentum yrast states, respectively. The energy defference gives the signature splitting. This result may have a different feature in contrast with the prediction by Mikhailov and Janssen. The existence of TAR solutions in yrast implies a possible new interpretation for the backbending phenomena in nuclei of $\gamma$-unstable region, and serves an explanation of abnormal spectra observed in the the odd-spin yrast-band in $^{182}$Os nucleus.

References

1) N. Onishi and D. Chang: *Nucl. Phys.*, **A557**, 301c (1993).
2) I. N. Mikhailov and D. Janssen: *Phys. Lett.*, **72B**, 303 (1978).
3) M. Matsuzaki: *Nucl. Phys.*, **A509**, 269 (1990).
4) A. K. Kerman and N. Onishi: *ibid.*, **A361**, 179 (1981); N. Onishi: *ibid.*, **A456**, 279 (1986).
5) T. Horibata and N. Onishi: *Phys. Lett.*, **B325**, 283 (1994); *RIKEN Accel. Prog. Rep.*, **27**, 14 (1993).

# The M1 Ttransitions and the New SU(3) in Superdeformed Nuclei

K. Sugawara-Tanabe, A. Arima, and N. Yoshida

[M1 transitions, Superdeformation.]

We have already proposed the idea that the quantization of alignment in superdeformation comes from the parity doublet (P-D) levels[1] by the addition of the pure "s" instead of the pseudo-spin "$\tilde{\mathbf{s}}$". The P-D levels are the two different parity single particle levels with the asymptotic quantum number representation, $[N, N, 0]\frac{1}{2}$ and $[N-1, N-2, 1]\frac{1}{2}$, which are almost degenerated in a deformed axially symmetric Nilsson potential around superdeformation, and the Fermi surface for $Z = 66$ or 80 and $N = 86$ or 112 locates near this degeneracy. Both of the P-D levels belong to the same supershell with $N_{sh} = N$. We found that the $L - S$ coupling scheme is restored in superdeformation not only for the P-D levels but also for all the other levels belonging to the same $N_{sh}$. This is caused by the strong coupling between the spin-orbit partners with small $\ell$ like $p1/2$ and $p3/2$, which influences the large $\ell$ spin-orbit partners through the strong coupling among the same spin-orbit coupled $\ell \pm 2$ levels. We also found that the effect of the unique-parity level, which is not taken into account in the pseudo-spin scheme, should not be neglected in superdeformed states. A good physical quantity to check this idea is the M1 transision rate, as M1 operator is proportional to spin. The M1 transition rate between the superdeformed bands in $^{193}$Hg was observed and the $g_K$ factor was extrapolated.[2] We calculated the M1 transition rate and found the several candidate levels which explain this experimental value of $g_K$ factor. Since we can neglect the effect of the spin-orbit interaction at superdeformation, we can construct a new SU(3) group introducing the new boson operators in the z-axis. We constructed 8 generators that fulfill the commutation relation of SU(3) from the byproduct of this set of boson operators in analogy to Elliot's SU(3) model.[3] This new SU(3) group corresponds to the space neglecting $\Delta N_{sh} \neq 0$ in contrast to Elliot's SU(3) where $\Delta N \neq 0$ is neglected. In $N_{sh}$ both positive and negative parity levels are degenerated and even $N_{sh}$ and $N_{sh} + 1$ have the same Casimir operator, and subsequently the new SU(3) is duplicate. Similarly we can construct a new SU(3) scheme in the hyperdeformation and the superdeformation in $^{132}$Ce region. In the former case SU(3) is triplicate and in the latter case it has six-degeneracy.

References

1) K. Sugawara-Tanabe, A. Arima, and N. Yoshida: *Nucl. Phys.*, **A570**, 291c (1994).
2) M. J. Joyce et al.: *Phys. Rev. Lett.*, **71**, 2176 (1993).
3) J. P. Elliot: *Proc. Roy. Soc. W*, **A245**, 128;562 (1958).

# Systematics of Alpha Q-values: Alpha Decay Life Times of Unstable Nuclei

H. Sato

[$\alpha$-decay Life.]

In the previous work,[1] we found that the $\alpha$ decay half life in a wide region of even-even nuclei can be reproducible with the method employed by Arima and Yoshida,[2] if a reliable theoretical S-factor and a realistic potential for the relative motion of the $\alpha$ and residual nucleus are taken into account. Here we extend the study to the systematics of $\alpha$ decay half lives of all the $\alpha$ decayable nuclei by applying the same method to the unstable nuclear system with the employment of a double folding potential for the relative motion of the $\alpha$ and residual nucleus, whose potential depth is obtained by solving the eigenvalue problem for the $\alpha$ Q value given by Tachibana, Uno, Yamada, and Yamada mass formula.[3] The density distributions of unstable nucleus are evaluated with a DDHF type variational calculation. Employing the node quantum number $N_r$ consistent with the single particle level scheme of a simple shell model, we calculate the $\alpha$ decay half life $T_{1/2}$ by $\ln 2\hbar/\Gamma_\alpha$ for all the $\alpha$ decayable nuclei by assuming the angular momentum L = 0, and summarize those in Fig. 1 as a function of Z and N. Figure 1 corresponds to the contour plots of the logarithms $\log_{10}(T_{1/2})$ at every 2 order difference in the $\alpha$ decay half life times $T_{1/2}$ in units of seconds. The dark area at the border in the contour plot of Fig. 1 shows the degeneracy of contour lines due to a drastic change of decay half life

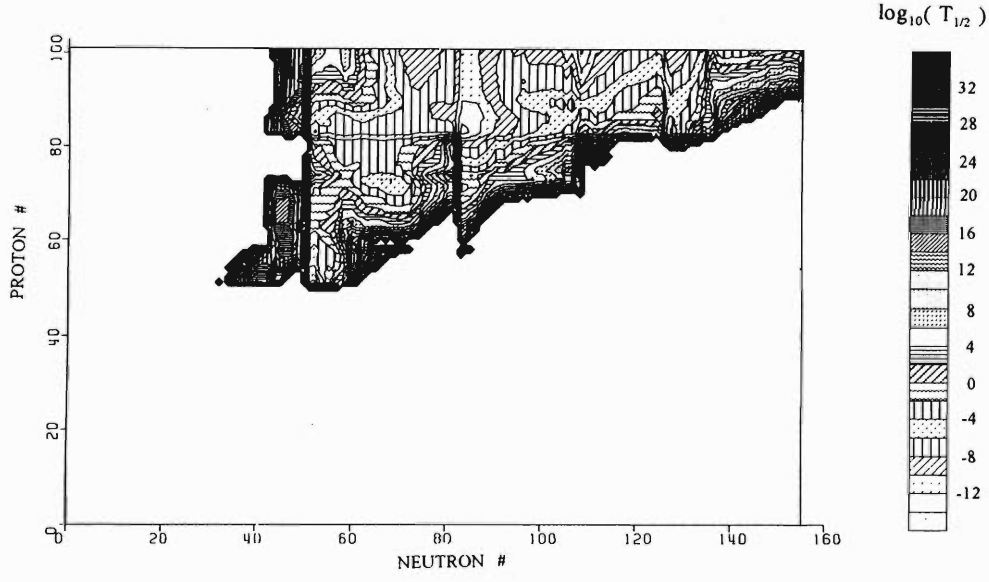


Fig. 1. The contour plots of the $\log_{10}(T_{1/2})$ of $\alpha$ decay half lives with S = 1 in units of seconds.

times. The cliffs can be seen at the border (i.e. the $\alpha$ drip line in nuclear chart) and also at magic numbers. The $\alpha$ decay half life times are drastically changed at magic numbers N = 50, 82, and 126. We compare the results with the $\beta$ deacy half life times predicted.

The author would like to thank Professor M. Ishihara for his encouragement.

References

1) H. Sato: *RIKEN Accel. Prog. Rep.*, **27**, 18 (1993).
2) A. Arima and S. Yoshida: *Phys. Lett.*, **B40**, 15 (1974); *Nucl. Phys.*, **A219**, 475 (1974).
3) T. Tachibana, M. Uno, M. Yamada, and S. Yamada: *At. Data Nucl. Data Tables*, **39**, 251 (1988).

# Shell Model on a Random Gaussian Basis

K. Varga

[shell model, alpha decay, stochastic variational model.]

A realistic study of alpha decay or cluster-decay process demands a reliable description of the motion of nucleons at the nuclear surface. The representation of a decaying state in the shell model requires handling of huge bases that is often beyond the capability of the computers.[1] This problem was recently circumvented by complementing the shell model with a cluster-model basis.[2,3] This cluster-configuration shell model, however, is difficult to apply. We therefore developed a new model, which is closer to the conventional shell model but in practical applications may be superior.

The new model[4] is essentially a shell model, in which the valence orbits are replaced by combinations of Gaussian functions of different size parameters, with exact Pauli projection off the core orbits. These gaussians are more flexible than the harmonic oscillator single-particle (s.p.) functions because their width parameters are free. A variational background can guarantee that they will be automatically chosen so as to suit to the problem considered. In particular, the gaussians can produce a more realistic fall-off in the surface, which is important for the description of decay processes. Moreover, in the interior the gaussians are able to simulate the effects of several oscillator shells. Note that the Pauli projection provides the gaussians with some, say $n_0$, nodes, so that n gaussians in the expansion of a s.p. function will involve s.p. orbits of $n_0, \cdots, n_0 + n - 1$ nodes. In spite of the inclusion of such high-lying shells, the problem may still remain tractable if the basis elements are carefully selected. We admit states in the basis depending on their contribution to the g.s. energy. This method of choosing random states as candidates for the basis is called the "stochastic variational method".[5]

To test this new model we applied for the description of the alpha decay of $^{212}$Po and compared the results to those of the previous model. The energy of the decay has been reproduced succesfully, the absolute decay width is slightly underestimated.

In summary, with the help of the stochastic variational method, a flexible shell-model wave function has been constructed for the ground state of $^{212}$Po using combinations of Gaussian functions as single particle orbits. The present model gives nearly as good a result for the alpha decay width as our former model, which is sharpened just to describe the alpha decay. The chief merit of the model presented here is its technical simplicity, which makes it easily applicable to other alpha or even to heavy-cluster decays.

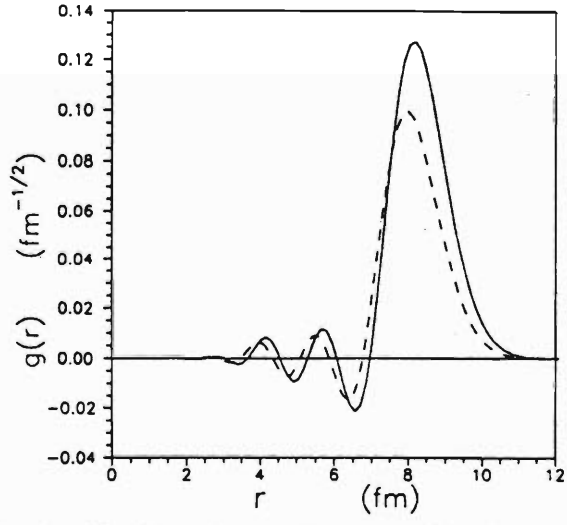


Fig. 1. The formation amplitude as a function of the distance between the alpha particle and the daughter nucleus. The solid line represents the cluster configuration shell model,[2,3] and the dashed line the result of the present model.[4]

References

1) I. Tonozuka and A. Arima: *Nucl. Phys.*, **A323**, 45 (1979).
2) K. Varga, R. G. Lovas, and R. J. Liotta: *Phys. Rev. Lett.*, **69**, 37 (1992).
3) K. Varga, R. G. Lovas, and R. J. Liotta: *Nucl. Phys.*, **A550**, 421 (1992).
4) K. Varga and R. J. Liotta: *Phys. Rev.*, **C50**, R1292 (1994).
5) K. Varga, Y. Suzuki, and R. G. Lovas: *Nucl. Phys.*, **A571**, 447 (1994).

# Σ-Hypernuclear Production Spectra on a $^9$Be Target

T. Harada and H. Kitagawa

[ Σ-hypernuclei, narrow width, $(K^-,\pi^-)$ reaction, DWIA, shell-model.]

The aim of this study is to understand theoretically the Σ-hypernuclear production by the $^9$Be$(K^-,\pi^-)$ reaction with the distorted-wave impulse approximation (DWIA). In this note, we discuss the structure of $^9_\Sigma$Be-hypernucleus within the shell-model approach, in order to determine the characteristic behavior of a Σ-hyperon in light nuclei.

The discovery of the long-lived Σ-hypernuclear state ($\Gamma \leq 8$ MeV) by the $^9$Be$(K^-,\pi^-)$ reactions at CERN made us excited about a narrow width puzzle,[1] because its ΣN→ΛN conversion width was expected to be $\Gamma\sim25$ MeV in nuclear matter.[2] Many efforts were made so as to understand narrow peaks. However, there had been such poor statistics in this data that we could not solve the puzzle. Recently, Σ-hypernuclear spectra measurements on a $^9$Be target at BNL were reported in better statistics[3]: There appears a broad (not narrow) peak at $B_{\Sigma^0}\sim12$ MeV in the continuum regions. In order to investigate theoretically the structure of $^9_\Sigma$Be-hypernucleus, we construct the nucleus-Σ optical potential by the folding model. The optical potential is obtained as

$$U_J^T(\mathbf{R}) = \left\langle \left[\Phi_{j_c}^{T_c}(^8\mathrm{Z}) \otimes \Sigma\right]_J^T \right| {}^{\mathrm{eff}}\hat{t}_{\Sigma\mathrm{N}}\left(\mathbf{r}-\mathbf{R};\rho\left(\left|\frac{\mathbf{r}+\mathbf{R}}{2}\right|\right)\right) \left| \left[\Phi'^{T_c'}_{j_c'}(^8\mathrm{Z}') \otimes \Sigma'\right]_J^T \right\rangle$$

where $\Phi_{j_c}^{T_c}(^8\mathrm{Z})$ is the Cohen-Kurath wave function of the $A = 8$ core-nucleus and $\mathbf{R}$ is the relative coordinate between the core-nucleus and the Σ-hyperon. ${}^{\mathrm{eff}}\hat{t}_{\Sigma\mathrm{N}}(\mathbf{r};\rho)$ denotes the effective ΣN interaction with density ($\rho$) dependence, which is derived from the Brueckner $g$-matrix calculation with Sigma-nucleon absorptive potential (SAP)[4] in a nuclear medium. Note that the real part of the optical potential is shallow and has a peculiar shape with a repulsive core near the nuclear center.

Let's consider the Σ-hypernuclear inclusive $\pi^-$ spectrum in $^9$Be$(K^-,\pi^-)$ reaction. We calculate the double-differential cross section within the DWIA framework by using the Green function method.[5] Figure 1 displays the calculated spectrum at $p_{K^-} = 720$ MeV/c within Σ single-particle description by the shell-model approach, together with the experimental data at CERN.[1] We find two peaks in the spectrum: The peak near $B_{\Sigma^0}\sim7$ MeV, above the $\Sigma^0$-emission threshold, comes from continuum states of $^8$B$(T = 0;\ J^\pi = 0^+,\ 2^+)\otimes\Sigma^0$. The second peak near $B_{\Sigma^0}\sim20$ MeV also originates from main configurations of $^8$Li-$^8$B-$^8$Be$(T = 1;\ J^\pi = 2^+,\ 1^+,\ 3^+)$ and $\Sigma^+$-$\Sigma^0$-$\Sigma^-$ in the continuum states. The calculated spectrum seems to be similar to the earlier CERN data, rather than the recent BNL data.

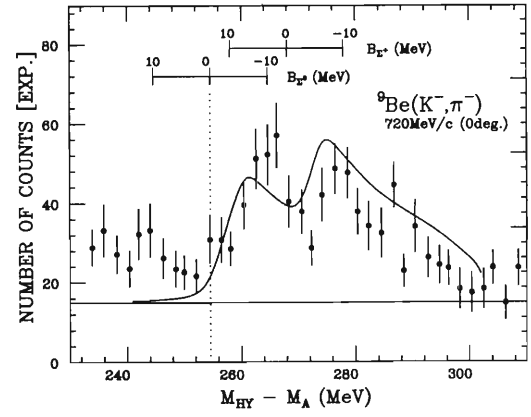


Fig. 1. The calculated $\pi^-$ spectrum by the $^9$Be$(K^-,\pi^-)$ reaction at $p_{K^-} = 720$ MeV/c is shown together with the experimental data at CERN.[1]

On the other hand, performing the microscopic cluster calculation[6] of α+3N+Σ in $^8_\Sigma$Be ($^8_\Sigma$Li), we showed that there appears a cluster phenomenon of $\alpha+^4_\Sigma$He ($\alpha+^4_\Sigma$H) as if it were the well-known di-molecular α+α structure of the $^8$Be ground state. It is far from the structure of $^8_\Lambda$Be ($^8_\Lambda$Li), where a Λ-hyperon plays a role of glue between α and 3N due to no $\pi$-$\rho$ exchange in the ΛN interaction. It should be noted that no clustering effect is taken into account in this shell-model calculation. Thus it is suggested that there should exist a cluster configuration of $\alpha+^4_\Sigma$He+n in $^9_\Sigma$Be. We might obtain a large enhancement near $B_{\Sigma^0}\sim12$ MeV in the $^9$Be$(K^-,\pi^-)$ reaction if such a cluster phenomenon is switched on.

In conclusion, we cannot reproduce the $^9$Be$(K^-,\pi^-)$ spectrum in the recent BNL data within the shell-model approach. The spectra shape might provide so valuable information for us to determine the behavior of the Σ-hyperon in light nuclei.

References

1) R. Bertini et al.: *Phys. Lett.*, **B90**, 375 (1980).
2) C. B. Dover, D. J. Millener, and A. Gal: *Phys. Rep.*, **184**, 1 (1989).
3) Sawafta et al.: Proc. of Int. Conf. on Hypernuclear and Strange Particle Physics, Vancouver, July 4–8, 1994, to be published.
4) T. Harada: *Nucl. Phys.*, **A547**, 165c (1992).
5) O. Morimatsu and K. Yazaki: *ibid.*, **A483**, 493 (1988).
6) S. Okabe, T. Harada, and Y. Akaishi: *ibid.*, **A514**, 613 (1990).

# Nuclear Mesonic Exchange Currents

C.-L. Lin and S. Yamaji

[One-photon exchange approximation, Δ-isobar, Nuclear exchange currents.]

The well known electrodynamic theory and its weaker interaction compared with that of strong interaction bring us one of the powerful methods, the electron scattering, to investigate electromagnetic properties as well as nuclear structures. At low energy the constituents of nucleus are hadrons, and the meson exchange takes responsibility of mutual interactions so as to form the nucleus. On the other hand, the kinds of mesons and isobars increase with increasing transferred energy and momentum. Among those particles, the dynamics of the Δ-isobar in the nucleus is one of the interesting problems in electronuclear physics. We stand on the framework of quantum hadrodynamics,[1] and investigate the roles of Δ-isobar in the mesonic exchange currents and their related electromagnetic properties. Both nuclear exchange currents and nuclear wave functions are derived from a Lagrangian which can bring the gauge invariance on our obtained exchange currents.

First of all, we have to look for an appropriate Lagrangian. The two important symmetry principles, the Lorentz invariance and the gauge invariance, show the way of how to reach our goal. And the differential cross section of the electron scattering which can be factorized into lepton and nuclear response tensors helps us to be able to tackle the target nucleus independent of the projectile. Further, in a position of quantum hadrodynamics, one can interpret the hadronic theory as an effective theory[2] of QCD so as to shelve the renormalization problem in the hadronic sector.[3] In addition, we treat both Δ-isobar and nucleon on equal footing, that is, the Δ-isobar is an independent particle inside the nucleus. Since the coupling between Δ-isobar and pion is stronger than that of Δ-isobar and ρ-meson, we consider only the pion, σ and ω mesons this time. The model Lagrangian is as follows:

$$
\begin{aligned}
L = \bar{\psi}\Bigg\{ & \Bigg( i\partial\!\!\!/ - e\Gamma^{\mu}_{N}\, A_{\mu} - g^{N}_{V}\gamma^{\mu}V_{\mu} \\
& + \frac{f_{\pi NN}}{m_{\pi}}\gamma^{\mu}\gamma_{5}\left(\tau_{i}D^{ij}_{\mu}\pi_{j}\right)\Bigg) - \left(m_{N} - g^{N}_{s}\phi\right)\Bigg\}\psi \\
& + \frac{1}{2}\left(\partial_{\mu}\phi\partial^{\mu}\phi - m^{2}_{s}\phi^{2}\right) - \left(\frac{1}{4}G_{\mu\nu}G^{\mu\nu} - \frac{1}{2}m^{2}_{V}V_{\mu}V^{\mu}\right) \\
& + \frac{1}{2}\left\{\left(D^{ij}_{\mu}\pi_{j}\right)\left(D^{\mu}_{ik}\pi^{k}\right) - m^{2}_{\pi}\vec{\pi}^{2}\right\} \\
& + i\bar{\Delta}^{\alpha}\left\{\sigma_{\alpha\beta}\left[\left(i\partial\!\!\!/ - e\Gamma^{\mu}_{\Delta}\, A_{\mu} - g^{\Delta}_{V}\gamma^{\mu}V_{\mu}\right)\right.\right. \\
& \left.\left. - \left(m_{\Delta} - g^{\Delta}_{s}\phi\right)\right]\right\}\Delta^{\beta} \\
& + \frac{g_{\pi N\Delta}}{m_{\pi}}\left\{\bar{\Delta}^{\alpha}\theta_{\alpha\beta}(\xi)\left[\tilde{\tau}^{i}(D^{\beta}_{ij}\pi^{j})\right]\psi + \text{h.c.}\right\} \\
& - \frac{1}{4}F_{\mu\nu}F^{\mu\nu}.
\end{aligned}
$$

The related physical quantities are defined as the following:

$$
\begin{aligned}
& F_{\mu\nu} \equiv \partial_{\mu}A_{\nu} - \partial_{\nu}A_{\nu}, \\
& \quad A_{\mu} = \text{electromagnetic field}, \\
& G_{\mu\nu} \equiv \partial_{\mu}V_{\nu} - \partial_{\nu}V_{\nu}, \\
& \quad V_{\mu} = \text{neutral vector meson } \omega \text{ field}, \\
& \Gamma^{\mu}_{N,\Delta} \equiv \gamma^{\mu}(F^{s}_{1,N,\Delta} + \tau_{3}F^{V}_{1,N,\Delta}), \\
& \quad F^{s,V}_{1,N,\Delta} = \text{electric form factor}, \\
& \quad \text{upper-script}\{s = \text{isoscalar},\ V = \text{isovector}\} \\
& \quad \text{lower-script}\{N = \text{nucleon},\ \Delta = \Delta\text{-isobar}\} \\
& D^{\mu}_{ij} \equiv \delta_{ij}\partial^{\mu} + e\varepsilon_{ij3}A^{\mu}, \\
& \theta_{\alpha\beta}(\xi) \equiv g_{\alpha\beta} - \xi\gamma_{\alpha}\gamma_{\beta},
\end{aligned}
$$

and $\psi$, $\pi_i$, $\phi$ and $\Delta^{\alpha}$ represent nucleon, pion, $\sigma$-meson and Δ-isobar field, respectively. The quantities $\tau_i$ and $\tilde{\tau}_i$ express respectively the spinor and vector-spinor isospins. Then we can easily get the nuclear electromagnetic currents in the one-photon exchange approximation. The parts generated by the Δ-isobar are:

$$
\begin{aligned}
J^{\mu}_{\Delta} = e\Bigg\{ & i\bar{\Delta}^{\alpha}\sigma_{\alpha\beta}\Gamma^{\mu}_{\Delta}\Delta^{\beta} \\
& - \frac{g_{\pi N\Delta}}{m_{\pi}}\left[\bar{\Delta}^{\alpha}\theta^{\mu}_{\alpha}(\xi)(\vec{\tilde{\tau}}\times\vec{\pi})_{3}\psi + \text{h.c.}\right]\Bigg\},
\end{aligned}
$$

where $\theta^{\mu}_{\alpha}(\xi) = g^{\mu}_{\alpha} - \xi\gamma_{\alpha}\gamma^{\mu}$, $\sigma_{\alpha\beta} = i[\gamma_{\alpha},\ \gamma_{\beta}]/2$, and $\xi$ is a parameter. The first term on the right hand side gives the one-body current, and the second term is the Δ-isobar exchange current. And the conservation of the whole electromagnetic currents is ensured with a couple of assumptions that each coupling is up to the first order, and the same isospin operators are used for all baryons. As to the nucleon wave functions, we have to solve the coupled equations obtained from the Lagrangian for all cooperated hadrons. Since, at this stage, the r-representation is better than the p-representation,[4] the electromagnetic currents should also have the same representation. For this purpose, we use the Rarita-Schwingers wave functions[5] for the Δ-isobar.

In order to study the role of Δ-isobar in electronuclear physics, we are calculating nuclear response functions using both nuclear wave functions and nuclear electromagnetic currents described above.

References

1) B. D. Serot and J. D. Walecka: Adv. Nucl. Phys., Plenum New York-London, **16**, 1 (1986).
2) M. Benmerrouche et al.: *Phys. Rev.*, **C39**, 2339 (1989).
3) K. Wehrberger: *Phys. Rep.*, **225**, 273 (1993).
4) G. B. West: *ibid.*, **18C**, 263 (1975).
5) W. Rarita and J. Schwinger: *Phys. Rev.*, **60**, 61 (1941).

# QCD Phase Transition in the Dual Ginzburg-Landau Theory

H. Suganuma, H. Ichie,* and H. Toki

[QCD phase transition, color confinement, dual Ginzburg-Landau theory.]

Color confinement is one of the most striking features of the nonperturbative QCD, and has been studied with much interest in the hadron physics. As for the confinement mechanism, 't Hooft proposed an interesting conjecture of monopole condensation under the abelian gauge fixing.[1] In this scheme, color confinement is realized by condensation of monopole-like objects, which naturally appear in QCD by the abelian gauge fixing.[1] This conjecture was strongly supported by recent studies based on the lattice gauge theory.[2,3] The dual Ginzburg-Landau (DGL) theory[4-6] is formulated as the infrared effective theory of QCD in terms of the QCD-monopole condensation. We have studied relevant nonperturbative features as color confinement, quark pair creation and dynamical chiral-symmetry breaking using the DGL theory.[4,5]

We investigate here the QCD phase transition at finite temperature in the DGL theory,[6] where the QCD-monopole condensate is an order parameter of color confinement. Although we include the dynamical effect of quarks in our framework, we concentrate in the pure gauge case because our main interest is color confinement property. In this case, the DGL theory is simply reduced to the ordinary Ginzburg-Landau theory in the superconductivity, so that we can easily derive its partition functional at finite temperature.[6] By investigating the effective potential at finite temperature (thermodynamical potential), we find the reduction of the QCD-monopole condensate at high temperature. We also consider a possible reduction of the self-interaction $\lambda$ between QCD-monopoles at high temperature according to the asymptotic freedom of QCD, and use a simple ansatz, $\lambda(T) = \lambda(T-\alpha \mathrm{Tc})/\mathrm{Tc}$, where $\alpha$ is chosen to reproduce $\mathrm{Tc} = 0.2$ GeV. As the semi-empirical quantity, we also calculate the string tension $k(T)$ at finite temperature.[4,6] We show in Fig. 1 the string tension $k(T)$. We find the reduction of the string tension at high temperature, which means the decrease of the confining force there. Quantitatively, our results with the variable $\lambda(T)$ almost reproduce the lattice QCD data shown by the black dots.[7]

In the DGL theory, there appear two important glueballs responsible for color confinement. One is the scalar QCD-monopole field, and the other is the axial-vector dual-gauge field.[4] They correspond to the Higgs field and the weak boson fields in the electro-weak standard theory, respectively. We show in Fig. 2 the masses of the two glueballs in the DGL theory.[6] One finds the large glueball-mass reduction near the critical temperature Tc.[6] It would be interesting to check our prediction by the lattice QCD and also by experiments.

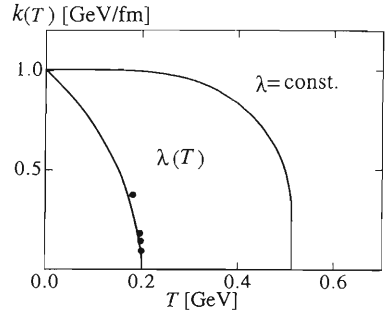


Fig. 1. The string tension $k(T)$ as functions of temperature $T$ for a constant $\lambda$ and a variable $\lambda(T)$. The lattice QCD data in the pure gauge are shown by the black dots.

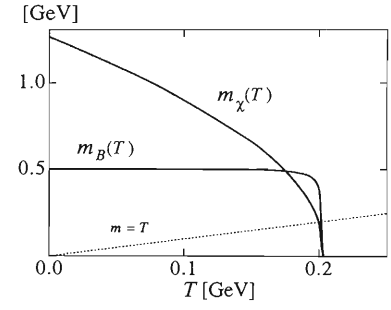


Fig. 2. The masses of glueballs at finite temperature. $m_B(T)$ and $m_\chi(T)$ denote the masses of the dual gauge gauge field and the QCD-monopole field, respectively. The dotted line denotes $m = T$. The phase transition occurs at the temperature where $m_B, m_\chi = T$.

References

1) G. 't Hooft: *Nucl. Phys.*, **B190**, 455 (1981).
2) A. S. Kronfeld, G. Shierholz, and U.-J. Wiese: *ibid.*, **B293**, 461 (1987).
3) T. Suzuki and I. Yotsuyanagi: *Phys. Rev.*, **D42**, 4257 (1990).
4) H. Suganuma, S. Sasaki, and H. Toki: RIKEN-AF-NP-164 (1994); *Nucl. Phys.*, **B** in press.
5) H. Toki, H. Suganuma, and S. Sasaki: *Nucl. Phys.*, **A577**, 353c (1994).
6) H. Ichie, H. Suganuma, and H. Toki: RIKEN-AF-NP-175 (1994).
7) M. Gao: *Nucl. Phys.*, **B9** (Proc. Suppl.), 368 (1988).

* Department of Physics, Tokyo Metropolitan University

# Measurement of Fusion Cross Section with Neutron Halo Nucleus $^{11}$Be

A. Yoshida, T. Fukuda, Y. Watanabe, C. Signorini, L. Mueller, F. Scarlassala, Y. Pu, Y. Mizoi, N. Aoi, M. Hirai, J. Nakano, H. Kobinata, Y. Nagashima, T. Nomura, and M. Ishihara

[sub-barrier fusion, neutron halo nucleus $^{11}$Be.]

The main motivation of this research is concerned with a possibility to observe the fusion cross sections of neutron halo nuclei (such as $^{11}$Be, $^{11}$Li) considerably larger or smaller than the one induced by the corresponding stable isotopes, due to the excitation of the soft dipole mode, neutron breakup, etc. These effects, in the case of the $^{11}$Li halo nucleus, have been recently discussed in various theoretical papers[1-3] with rather different predictions. As the beam intensity of $^{11}$Be is larger than that of $^{11}$Li by more than one order of magnitude, we first measured the excitation function of the fusion cross section in the systems $^{11,10,9}$Be + $^{209}$Bi with the same experimental setup. The fusion process has been identified via the detection of the delayed $\alpha$-particles emitted by the decay of the ground state of the evaporation residues populated after neutron evaporation. This technique has an advantage of clear identification of the fusion comparing with the measurement of fission in the same systems.

The beams of Be isotopes were produced by the fragmentation process of $^{13}$C primary beam with 100 MeV/u energy and 100 pnA intensity on a Be production target with 12 mm thickness. They were then separated by the RIPS projectile fragment separator, resulting in a purity of almost 100%. After the separation, an Al degrader plate was inserted in the beam line to reduce the secondary beam energy down to around the Coulomb barrier. A typical beam intensity of $^{11}$Be was 140 kcps with the energy of 50 MeV$\pm$37% (in fwhm) and with the beam size of around 5 cm in diameter. With this simple deceleration method, the distribution of the beam energy became wide, so that a TOF measurement was done event by event to determine the beam energy.

At the experimental target position, four $^{209}$Bi targets (500-700 $\mu$g/cm$^2$) evaporated onto a Mylar backing foil (70 $\mu$g/cm$^2$), were surrounded by 9 Si surface barrier detectors (SSD). Each detector had a size of 48 $\times$ 48 mm and a thickens of 300 $\mu$m and they covered a solid angle of about 30% of 4$\pi$. The time gate for the delayed $\alpha$-decay coincidence was 2 $\mu$s after the arrival of each beam particle. The neutron detector walls surrounded the target chamber in order to measure neutrons originating from breakup fusion events if any.

The $\alpha$-decays from $^{216}$Fr (E$\alpha$ = 9.01 MeV, $T_{1/2}$ = 700 ns), which originate from 4n,3n evaporation with $^{11,10}$Be beam respectively, and those from $^{215}$Fr (E$\alpha$ = 9.34 MeV, $T_{1/2}$ = 120 ns), which originate from 5n,4n,3n evaporation with $^{11,10,9}$Be beam respectively, were clearly observed with enough statistics to argue the fusion excitation function around the barrier region.

Figure 1 shows the measured fusion excitation function in the system of $^{11}$Be + $^{209}$Bi comparing with simple theoretical calculation. Both data and theory seem to agree well except for higher energy regions. It is also found that the measured fusion cross section of $^{10}$Be shows almost the same magnitude as $^{11}$Be, in paticular, near the barrier region. From these results, we can say that there is no strong indication of halo neutron effect (e.g. enhancement/suppression) for a fusion reaction near the barrier region which has been predicted by many theoretical calculations. Further detailed analysis is now in progress by using the data of neutron detectors in order to get information about the breakup fusion reaction.

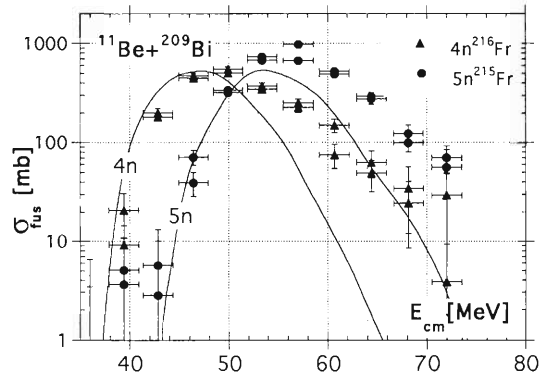


Fig. 1. The measured fusion excitation function. The x error bars indicate an energy binning size in the analysis which corresponds to the TOF energy resolution of around 1.5 MeV, and y error bars indicate only statistical errors. The solid lines indicate a theoretical calculation by the PACE2 evaporation code using a simple parameter set, in which the halo neutron effect of $^{11}$Be is not considered.

References

1) M. S. Hussein et al.: *Phys. Rev.*, **C46**, 377 (1992).
2) N. Takigawa et al.: *ibid.*, **C47**, 2470 (1993).
3) C. H. Dasso et al.: *ibid.*, **C50**, R12 (1994).

# Spectroscopy of $^{13}$Be Using $^{12}$Be Radioactive Beam

A. A. Korsheninnikov, E. Yu. Nikolskii, T. Kobayashi, D. V. Aleksandrov, M. Fujimaki, H. Kumagai, A. A. Ogloblin, A. Ozawa, I. Tanihata, Y. Watanabe, and K. Yoshida

[NUCLEAR REACTIONS, radioactive nuclear beam, $CD_2$, C($^{12}$Be,p), E/A = 55 MeV.]

We have performed spectroscopic studies of the heaviest known unstable beryllium isotope $^{13}$Be, which was observed for the first time in Ref. 1 and recently investigated in Refs. 2 and 3.

We have studied[4] under inverse kinematics the neutron transfer reaction d($^{12}$Be,p) at $E$ = 55 A MeV using the $^{12}$Be beam produced by the RIPS. Measurements were performed by the proton telescopes at backward angles ($\theta_p^{lab} \sim 115°$–$145°$) with targets $CD_2$ and C. The experimental setup is shown in Fig. 1. The proton spectrum from the $CD_2$ target is presented as a function of relative energy in the $n$+$^{12}$Be system, $E_{n-12Be}$, by a solid histogram in Fig. 2. The dashed histogram shows the contribution from carbon. This background corresponds to a low energy proton spectrum from the target-like source (fragmentation of the target or evaporation from the target-like system). The background does not allow to investigate in a reliable way the low-energy region in $^{13}$Be, where an intruder s-shell state can be expected from the extrapolation $^{17}$O → $^{15}$C → $^{13}$Be (inversion of $5/2^+$- and $1/2^+$-states). Figure 2 shows the known $^{13}$Be state at

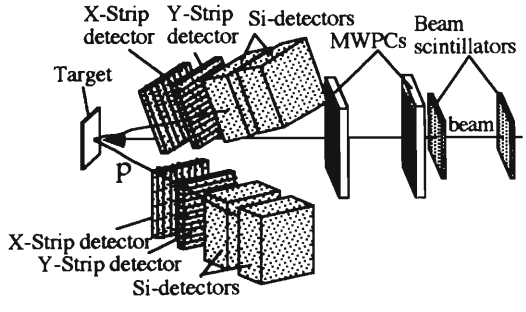


Fig. 1. Experimental setup.

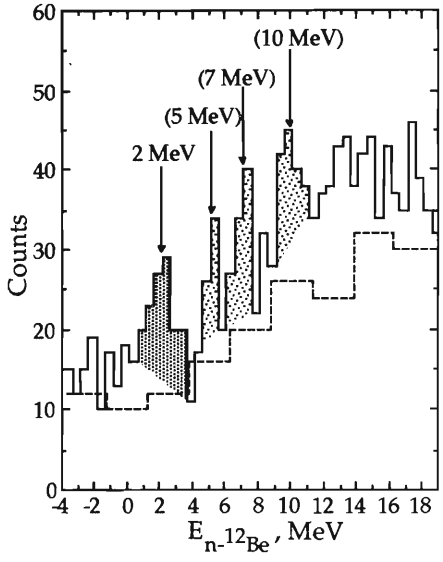


Fig. 2. Proton spectra from the reactions $CD_2$($^{12}$Be,p) (solid line) and C($^{12}$Be,p) (dashed line).

2 MeV above the $n$+$^{12}$Be threshold. In addition, three states of $^{13}$Be at 5, 7 and 10 MeV above the $n$+$^{12}$Be threshold were assigned tentatively. The 5 MeV state confirms the result of Ref. 2. The 7 MeV state differs from the tentative level, given in Ref. 2, at 8.5 MeV above the threshold.

References

1) D. V. Aleksandrov et al.: *Sov. J. Nucl. Phys.*, **37**, 474 (1983).
2) A. N. Ostrowski et al.: *Z. Phys.*, **A343**, 489 (1992).
3) S. Piskor et al.: *Z. Phys.*, **A**, to be published.
4) A. A. Korsheninnikov et al.: *Phys. Lett.*, **B**, in press.

# Excited States of $^{12}$Be in the Vicinity of He-Thresholds

A. A. Korsheninnikov, E. Yu. Nikolskii, T. Kobayashi, D. V. Aleksandrov, M. Fujimaki, H. Kumagai, A. A. Ogloblin, A. Ozawa, I. Tanihata, Y. Watanabe, and K. Yoshida

[ NUCLEAR REACTIONS, radioactive nuclear beam, p($^{12}$Be,p), p($^{12}$Be,p$^{12,11,10}$Be), p($^{12}$Be,p$^{8,6,4}$He), p($^{12}$Be,p$^{x}$He$^{x}$He), $E/A$ = 55 MeV, p($^{8}$He,p), $E/A$ = 33 MeV. ]

Previously excited levels in the neutron rich nucleus $^{12}$Be were investigated at excitation energies < 6 MeV. On the other hand, the region of thresholds for decay to helium isotopes attracts special attention (~10 MeV). In the vicinity of these thresholds, $^{12}$Be states can exist with an exotic cluster structure with He-like subsystems.

We have studied[1] the elastic and inelastic scattering $^{12}$Be+p at E = 55 $A$ MeV using the $^{12}$Be beam produced by the RIPS. To provide a proton target, we used $CH_2$. Protons were measured by two telescopes of solid state detectors at laboratory angles $\theta_p^{lab} \sim 50°$–80°. We also investigated the coincidence between protons and particles from the dissociation of $^{12}$Be (beryllium and helium isotopes as well as neutrons), which were measured using a charge fragment detection system (dipole magnet, drift chamber, hodoscope of plastic scintillators) and neutron walls (plastic scintillators).

A measured inclusive spectrum of protons is shown in Fig. 1. A strong peak from the elastic scattering is seen as well as the known state at 2.1 MeV. We also marked the other known states at 4.6 and 5.7 MeV, where some structure exists in the spectrum. In addition, there are new states at 8.6 and 10 MeV. It is stressed by the insert in Fig. 1 (summing over channels), where these states are clearly seen (note also the structure at ~13–14 MeV). The states are quite narrow, $\Gamma \leq 0.5$ MeV. Figure 2 shows that the 8.6 MeV state lies slightly below the first helium threshold, while the 10 MeV state is located above this threshold and close to the second helium threshold. Measuring proton spectra in coincidence with beryllium and helium isotopes, we obtained data, which show that the 10 MeV state has low partial width for decay to beryllliums, $\Gamma_{total}/\Gamma(^{12}\text{Be}^* \rightarrow {}^{x}\text{Be}) = 3.6 \pm 1.6$. One more state at ~14 MeV was observed, which also decays into heliums. Since the decay energy to beryllliums is much higher than the decay energy to heliums (Fig. 2), a difference in the penetration factors should be large, and thus the helium reduced width should be predominant in the states at 10 and ~14 MeV. So these levels likely have a cluster structure He+He. Since $^{6}$He and $^{8}$He consist of an $\alpha$-core plus weakly bound neutrons, these $^{12}$Be states can actually have an exotic structure $\alpha + \alpha + 4n$.

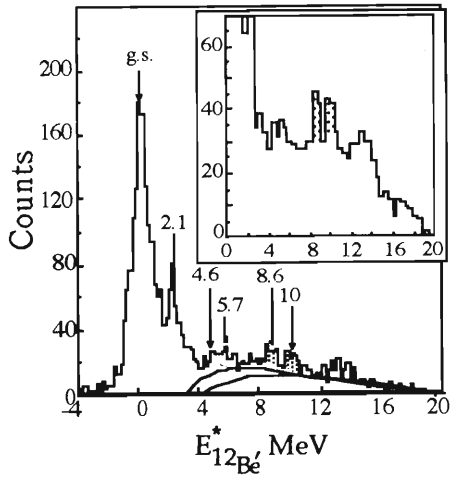


Fig. 1. Proton spectrum from p($^{12}$Be,p). Curves show possible backgrounds from the phase space p+$^{11}$Be+n and the n-n final state interaction in the channel p+$^{10}$Be+n+n.

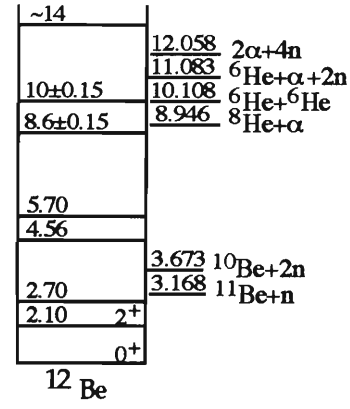


Fig. 2. Levels of $^{12}$Be.

References

1) A. A. Korsheninnikov et al.: *Phys. Lett.*, **B**, (1995).

# Systematic Behavior of Ejectile Spin Polarization in the Projectile Fragmentation Reaction

H. Okuno, K. Asahi, M. Ishihara, H. Ueno, H. Sato, J. Nakamura, T. Nakamura, F. Ambe, T. Ichihara, N. Inabe, M. Iwamoto, Y. Ohkubo, T. Kubo, Y. Kobayashi, A. Yoshida, M. Adachi, T. Shimoda, N. Takahashi, H. Miyatake, D. Beaume,[*1] D. Morrissey,[*2] and W.-D. Schmidt-Ott[*3]

[ NUCLEAR REACTIONS X($^{15}$N, $^{12}$B($^{13}$B))Y, $E/A$ = 70, 112 MeV/u; deduced spin polarization of $^{12}$B ($^{13}$B) nuclei from $\beta$-ray asymmetry. ]

Ejectile spin polarization $P$ in intermediate-energy projectile fragmentation has been measured for different targets and incident energies using RIPS fragment separator. In this report, we present the recent progress of the study on the polarization mechanisms.[1)]

Some representative results are shown in Fig. 1. The behavior of the polarization spectrum is mostly compatible with the prediction of the kinematical model of Ref. 2. In more quantitative discussions, however, we note that some aspects deviate from the model predication. In particular the model infers that the

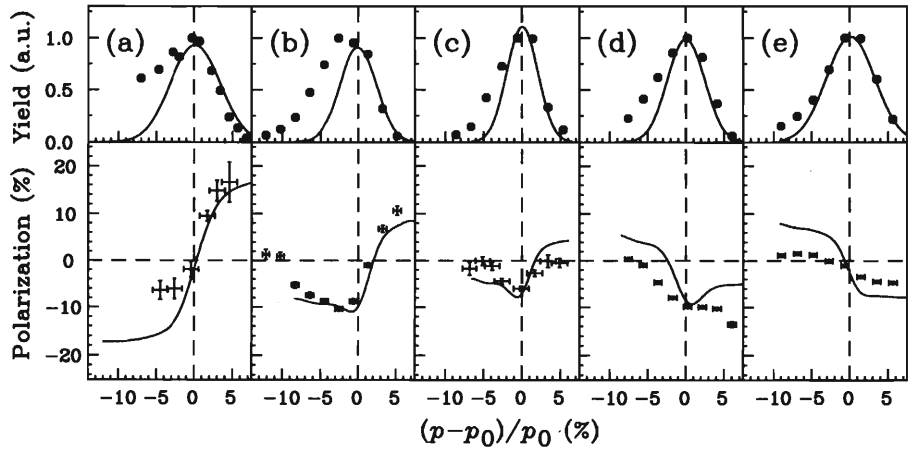


Fig. 1. Yield (upper part) and spin polarization (lower part) spectra as functions of fragment momentum $p$. for (a) $^{14}$N (39.4 MeV/u) + $^{197}$Au → $^{12}$B ($\theta_L$ = 5.0°) + X, (b) $^{15}$N (68.0 MeV/u) + $^{197}$Au → $^{13}$B ($\theta_L$ = 4.0°) + X, (c) $^{15}$N (109.6 MeV/u) + $^{197}$Au → $^{13}$B ($\theta_L$ = 2.0°) + X, (d) $^{15}$N (67.3 MeV/u) + $^{93}$Nb → $^{13}$B ($\theta_L$ = 2.5°) + X, (e) $^{15}$N (68.0 MeV/u) + $^{27}$Al → $^{12}$B ($\theta_L$ = 1°) + X.

yield weighted average of the polarization $\langle P \rangle$ should be zero and the zero-crossing of $P$ should occur at the momentum corresponding to the velocity of the projectile, $p_0$. These features are missing in many of the observed spectra, indicating a need for a modified theory.

A closer inspection of the angular momentum transfer mechanism clarified that the general feature that $\langle P \rangle$ tends to be negative can be accounted for if the removal of the nulceons occurs in a position away from the line connecting the center of the two nuclei. Solid curves in Fig. 1 show results calculated including such effects, reproducing gross behavior of the spectra rather well.

The appearance of large polarization around $p_0$ is particularly useful when the reaction is applied to produce spin polarized nuclear beams since one can employ a thick target and relatively wide momentum window to gain in the beam intensity. In fact, the phenomenon is exploited for the efficient measurements of nuclear moments of neutron-rich nuclei.[3)]

References

1) H. Okuno et al.: *Phys. Lett.*, **B335**, 29 (1994).
2) K. Asahi et al.: *ibid.*, **B251**, 488 (1990).
3) H. Ueno et al.: This report, p. 41 and p. 42.

*1 Institut de Physique Nucléaire, France
*2 NSCL, Michigan State University, USA
*3 II. Physikalisches Institut, Universität Göttingen

# Interaction Cross Sections and Radii of $^{11}$C and $^{12}$N

A. Ozawa, T. Kobayashi, D. Hirata, I. Tanihata, O. Yamakawa,[*1] K. Omata, K. Sugimoto,[*2] N. Takahashi, T. Shimoda, D. Olson,[*3] W. Christie,[*3] and H. Wieman[*3]

[ NUCLEAR REACTIONS Be,C,Al($^{11}$C,$^{11}$C)X, Be,C,Al($^{12}$N,$^{12}$N)X, $E/A$ = 730 MeV; measured interaction cross sections $\sigma_I$, deduced root mean square radii and effective deformation parameters. ]

The recent development of radioactive beams provides the new measurement of the radii of unstable light nuclei. On the other hand, a recent development of the detection technique of quadrupole moments provides the new measurement of quadrupole moments ($Q$) of light mirror nuclei. Some of the isospin dependence of matter radii were measured for $A$ = 6–12, 17.[1,2] In the present experiment, we have measured the interaction cross sections and radii of $^{11}$C and $^{12}$N on target nuclei Be, C, and Al around 730$A$ MeV. From the present experiment, we can obtain a complete set of radii and $Q$ of mirror nuclei in the mass number $A$ = 8, 11, 12, and 17. Thus, it becomes possible to compare the systematics between the radii and quadrupole moments for thease mirror nuclei. The systematics suggest the solution of the proton-halo problem of $^{8}$B, where the relatively large quadrupole moment, that suggests the proton-halo in the shell-model analysis,[3] conflicts no enhancement of the matter radius.[1]

The secondary beams of $^{11}$C and $^{12}$N were produced through projectile fragmentation of $^{18}$O and $^{20}$Ne primary beams (800$A$ MeV), respectively, that were accelerated by the Bevalac at the Lawrence Berkeley Laboratory. The secondary isotopes were produced in a production target of Be and were separated by their rigidity using the beam-line as described in a previous paper.[4] The interaction cross section was measured by a transmission method and the effective root-mean-square (RMS) radii are derived by the same manner as a previous paper.[4] The effective RMS matter radii are determined as, $2.12 \pm 0.06$ fm for $^{11}$C and $2.47 \pm 0.07$ fm for $^{12}$N.

Effective deformation parameters ($\beta_{\rm eff}$) are derived from the equation, $Q = Q_0[I(2I-1)]/[(I+1)(2I+3)]$ and $Q_0 = 0.7569 Z {R_0}^2 \beta_{\rm eff}(1 + 0.1577\beta_{\rm eff})$, where $I$ is the intrinsic spin and $R_0$ is the radius obtained from effective RMS charge radius. Isoscalar and isovector parts for $\beta_{\rm eff}$ are derived by $\beta_{\rm eff}{}^{\rm IS} = \beta_{\rm eff}{}^{+} + \beta_{\rm eff}{}^{-}$, and $\beta_{\rm eff}{}^{\rm IV} = \beta_{\rm eff}{}^{+} - \beta_{\rm eff}{}^{-}$, where + and − mean the signs of $T_z$. Obtained $\beta_{\rm eff}{}^{\rm IS}$ and $\beta_{\rm eff}{}^{\rm IV}$ are shown in Fig. 1. $\beta_{\rm eff}{}^{\rm IV}$ is almost zero in the present mass range, but $\beta_{\rm eff}{}^{\rm IS}$ shows the strong mass number dependence. $\beta_{\rm eff}{}^{\rm IV} \sim 0$ suggests that deformation is almost equal within a mirror pair. The relatively large deformation has been observed for $A$ = 8. This suggests that the relatively large quadrupole moment of $^{8}$B is due not to the proton-halo but to the relatively large deformation of the nucleus. In the shell model description, deformation can be described by effective charges for proton and neutron. Present results also suggest that the strong mass dependence of effective charges is necessary among such light nuclei.

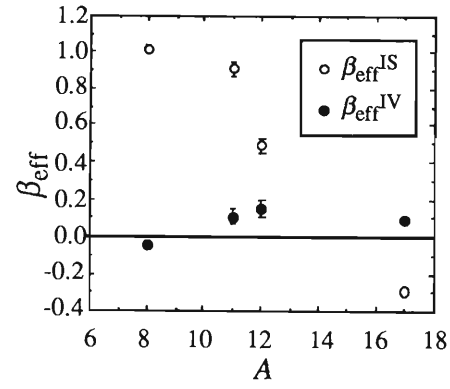


Fig. 1. The mass dependence of the effective deformation parameters. The Isoscalar part is shown by the open circle. The Isovector part is shown by the closed circle. The parts in the mass 11 and 12 are obtained from the present experiment.

References

1) I. Tanihata et al.: *Phys. Lett.*, **B206**, 592 (1988).
2) A. Ozawa et al.: *ibid.*, **B334**, 18 (1994).
3) T. Minamisono et al.: *Phys. Rev. Lett.*, **69**, 2058 (1992).
4) I. Tanihata et al.: *ibid.*, **55**, 2676 (1985).

*1 Fukui Prefectual University
*2 Osaka University
*3 LBL, Berkeley, U.S.A.

# Radii of Na Isotopes and the First Direct Evidence of Neutron Skin

T. Suzuki, K.-H. Behr,[*1] O. Bochkarev,[*2] A. Brünle,[*1] K. Burkard,[*1] L. Chulkov,[*2] P. Egelhof,[*1] H. Geissel,[*1] M. Golovkov,[*2] D. Hirata, H. Irnich,[*1] Z. Janas,[*1] H. Keller,[*1] T. Kobayashi, G. Kraus,[*1] G. Münzenberg,[*1] F. Nickel,[*1] S. Neumaier,[*3] A. Ozawa, A. Piechazek,[*1] E. Roeckl,[*1] W. Schwab,[*1] K. Sümmerer,[*1] K. Yoshida, and I. Tanihata

[Nuclear Structure, Neutron skins, Radioactive beams.]

From a series of experiment, it is suggested that thick neutron skins are formed in unstable neutron rich nuclei. Because no stable nucleus shows any of the decoupling phenomena, it is essential to find and study the decoupling for understanding the nuclear interactions as well as the nuclear matter of an asymmetric mixture of proton and neutron. Also a nucleus with neutron skin or halo is expected to show a variety of new collective excitations that are not expected in the stable nuclei.

Evidence of a neutron skin of thickness about 1 fm was presented by Tanihata et al. in $^{6}$He and $^{8}$He nuclei from the measurements of interaction cross sections and the two/four neutron removal cross sections.[1] Although it is not unreasonable, yet they had to assume that the correlation between valence neutrons in these nuclei is small or not very much different from that expected from a simple shell model.

We have measured the interaction cross sections of Na isotopes from $A = 20$ to 32. Sodium isotopes provide a unique opportunity, because the root-mean-square charge radii of Na isotopes were determined by the isotope shift measurement, and thus direct comparison of the charge and the neutron radii can be made.

The measurements are made at the FRS facility of the GSI in Germany. Beams of $^{20\text{-}23}$Na and $^{25\text{-}32}$Na at 900$A$ MeV were produced from Ar beam accelerated by the heavy-ion synchrotron SIS. The first half of the FRS is used to separate and identify the incident Na beams. The reaction targets of C with 7 and 4 g/cm$^2$ in thickness were used. Then the last half of the FRS was used to identify and to count the non-reacted nuclei in the target. This method provided the transmission measurement of the interaction cross sections.

The solid circles in Fig. 1 show the preliminary results of the determined interaction cross sections. The solid line in the figure shows the expected cross sections assuming the matter density distribution to be the same as the proton distribution except for the normalization scaled by $A/Z$. The proton distributions are calculated by a relativistic mean field (RMF) model that reproduces the isotope shifts very well.[2] The dotted line shows the cross section calculated with the matter density distribution obtained by the same RMF model. This model gives gradual growth of the neutron skin for neutron rich Na isotopes. It is seen that the observed interaction cross sections are much larger than the ones predicted from the proton density distribution and close to the RMF matter density distribution that has large neutron skins. The thickness of the neutron skin ($R^{n}_{rms}$ - $R^{p}_{rms}$) reaches 0.6 fm for $^{32}$Na.

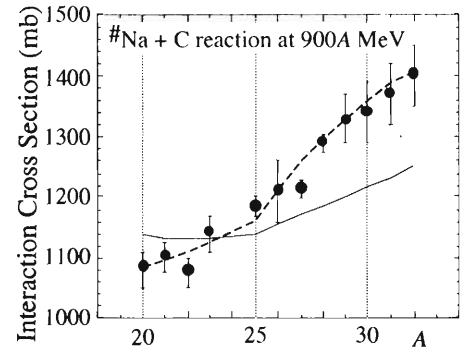


Fig. 1. Interaction cross section of Na isotopes.

References

1) I. Tanihata et al.: *Phys. Lett.*, **B289**, 261 (1992).
2) D. Hirata et al.: *Phys. Rev.*, **C44**, 1467 (1991).

*1 GSI, Darmstadt, Germany
*2 Kurchatov Institute, Russia
*3 TH Darmstadt, Germany

# Coulomb Excitation of $^{32}$Mg

T. Motobayashi, Y. Ikeda, Y. Ando, K. Ieki, M. Inoue, N. Iwasa, T. Kikuchi, M. Kurokawa, S. Moriya, S. Ogawa, H. Murakami, S. Shimoura, Y. Yanagisawa, T. Nakamura, Y. Watanabe, M. Ishihara, T. Teranishi, H. Okuno, and R. F. Casten*

[$^{208}$Pb($^{32}$Mg,$^{32}$Mg $\gamma$)$^{208}$Pb; Coulomb excitation, deduced $B$(E2).]

The Coulomb excitation of a very neutron-rich nucleus $^{32}$Mg to its $2^+$ state was studied using a radioactive beam of $^{32}$Mg at 49.2 MeV/nucleon on a $^{208}$Pb target.[1] The RIPS facility of the RIKEN Ring Cyclotron provided a $^{32}$Mg beam. A $^{208}$Pb target of 350 mg/cm$^2$ thickness was placed at the focal point of the RIPS system.

Scattered $^{32}$Mg nuclei were detected by a counter telescope placed 35 cm from the target in the air after passing through a 25 $\mu$m thick mylar window. The telescope consisted of five ion-implanted silicon detectors of 40×40 mm$^2$ effective area and 400 $\mu$m thickness. The particle was identified by the $\Delta E$-$E$ method, and was good enough for the present purpose of selecting $^{32}$Mg among other Mg-isotopes. The excitation to the $2^+$ state was identified by measuring the $\gamma$ ray deexcitation of the $2^+$ state in coincidence with the scattered $^{32}$Mg ions.

Sixty NaI(Tl) scintillators surrounded the target to detect the $\gamma$-rays. Each scintillator crystal is of rectangular shape with size 6×6×12 cm$^3$. The high granularity of the setup allows one to measure the angle of the $\gamma$ ray emission, which is useful in correcting large Doppler shifts of the $\gamma$ rays from the excited $^{32}$Mg that was moving with $v/c \approx 0.3$.

Figure 1 shows the $\gamma$-ray energy spectrum associated with the $^{32}$Mg + $^{208}$Pb inelastic scattering. It is obtained by a sum of spectra for all the NaI(Tl) scintillators after the Doppler shift correction. Accidental coincidence yield is subtracted in the energy spectrum shown in Fig. 1 by using the data obtained by setting a gate at the region beside the true-coincidence peak in the $^{32}$Mg-$\gamma$ time-difference spectrum. As clearly seen in the figure, only one photo-peak at 0.89 MeV corresponding to the $2^+ \rightarrow 0^+$ transition was observed.

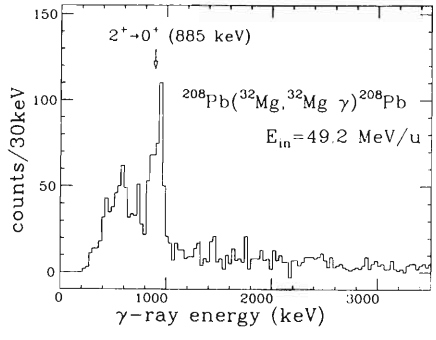


Fig. 1. Energy spectrum of $\gamma$ rays emitted from the $^{32}$Mg+$^{208}$Pb inelastic scattering at 49.2 MeV/u incident energy. The Doppler shift is corrected for.

An experimental deformation parameter $\beta = 0.512 \pm 0.044$ was extracted by comparing the predicted effective cross section with the experimental value obtained from the photo-peak yield. The theoretical effective cross section was obtained by a coupled channel calculation with a Monte Carlo simulation taking into accout the finite solid angle of the particle detector, $\gamma$ ray detection efficiency, multiple scattering in the target, and finite energy and angular spread of the incident beam. The error contains a possible uncertainty regarding the choice of the optical potential and that in the estimation of nuclear excitation amplitude, besides experimental uncertainties. This deformation parameter corresponds to $B(\mathrm{E2}) = 454 \pm 78$ e$^2$fm$^4$.

The present result agrees with 450 e$^2$fm$^4$ predicted in a shell model of Fukunishi, Otsuka and Sebe.[2] The prediction exhibits this large $B$(E2) value for $^{32}$Mg if the model space is extended to the p-f shell, and it reproduces the present data. On the other hand, no such large value is predicted with a limited model space where the valence nucleons are only in the s-d shell orbitals. This suggests a large mixture of the p-f shell orbitals for $^{32}$Mg and vanishing of the $N = 20$ shell gap, which result in large deformation. The same conclusion is obtained by comparing the present result with the $B$(E2) values calculated by the $N_\mathrm{p}N_\mathrm{p}$ scheme.[3] A good agreement is obtained for $^{32}$Mg (369 e$^2$fm$^4$) if the neutron number of 20 is not treated as a magic number, in contrast to the prediction with an $N = 20$ shell closure (68 e$^2$fm$^4$) that much underestimates the data.

The present result demonstrates the usefulness of Coulomb excitation at several tens MeV/nucleon, where large cross sections and availability of thick targets enable experiments with unstable nuclear beams of low intensity.

* Physics Department, Brookhaven National Laboratory, U.S.A.

References

1) T. Motobayashi et al.: Rikkyo Univ. Preprint, RUP-94-13; *Phys. Lett.*, in press.
2) N. Fukunishi, T. Otsuka, and T. Sebe: *Phys. Lett.*, **B296**, 279 (1992).
3) R. F. Casten and N. V. Zamfir: *Phys. Rev. Lett.*, **70**, 402 (1993).

# Beta-decay of Neutron Rich Nucleus $^{14}$Be

N. Aoi, M. D. Belbot, M. Hirai, E. Ideguchi, M. Ishihara, T. Kishida, J. J. Kolata, G. Liu, H. Miyatake, T. Nakamura, H. Okuno, H. Sakurai, S. Shimoura, T. Shirakura, T. Teranishi, Y. Watanabe, S. Yamamoto, A. Yoshida, and M. Zahar

[RADIOACTIVITY $^{14}$Be($\beta^-$), measured $\beta$-delayed neutron deduced log$ft$. $^{14}$B deduced level.]

A nucleus very far from the stability line often has a large $Q_\beta$ and decays into excited states of the daughter nucleus over a wide energy range, affording a rich domain of nuclear spectroscopy. In the case of extremely neutron rich nuclei, most of the final states are unstable with respect to neutron emission. Hence, neutron measurement provides a useful means to study the properties of $\beta$-decay.

We measured the energy spectrum of $\beta$-delayed neutron and $\gamma$-ray of very neutron rich nucleus $^{14}$Be.[1] A $^{14}$Be beam was provided by the RIPS (Riken Projectile-fragment Separator) at the RIKEN Ring Cyclotron using projectile fragmentation of 100A MeV $^{18}$O. The $^{14}$Be nuclei were implanted to five thin (300 $\mu$m) Si- detectors located at the final focal point with a typical intensity of $3 \times 10^2$ counts/sec. Emitted $\beta$-rays were detected by plastic scintillation counters placed on both sides of the Si-detectors. Energies of the delayed neutrons were measured by means of a time-of-flight method. The neutron flight path was set about 2 m so that the energy resolution of neutron was 1 MeV at 15 MeV. The energy threshold of the neutron detector was set at 200 keV. Delayed $\gamma$-ray energies were measured by two Ge detectors located at about 13 cm from Si-detectors.

In the measured neutron TOF spectrum shown in Fig. 1, we observed a strong peak at the energy of $282.7 \pm 1.7$ keV.

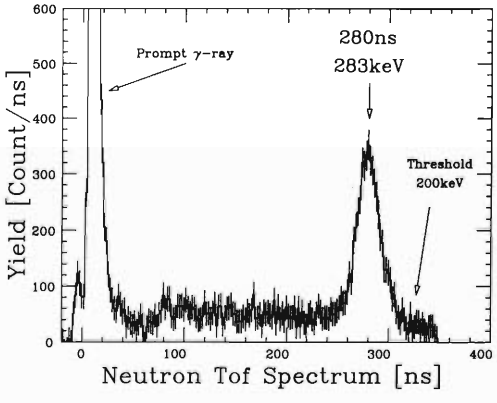


Fig. 1. TOF spectrum of neutron from $^{14}$Be. The sharp peak of approximately 7 ns is due t the prompt $\gamma$-ray. The peak at 280 ns corresponds to the neutron with energy of 283 keV.

The branching ratio corresponding to this strong peak is determined tentatively to be $63 \pm 15\%$. The detection efficiency for neutrons was obtained from the separated run using $^{17}$N beam whose neutron energies and neutron emission rate are well studied.[2]

The strong peak in the neutron spectrum may be related to two alternative possibilities of the decay scheme. The one candidate is the decay to a level just above the neutron threshold which is followed by neutron emission leading to the ground state of $^{13}$B without accompanying any g-emission (Fig. 2 case 1). The log$ft$ value correspond to this decay is $3.7 \pm 0.1$ which indicate that this decay is due to a allowed transition.

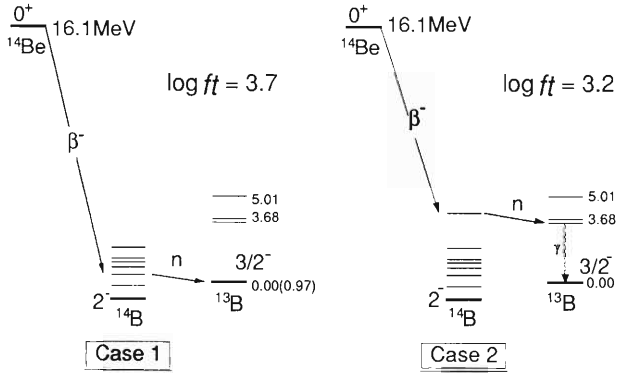


Fig. 2. Two candidates of the decay scheme of $^{14}$Be related to the 283 keV neutron. See text for further details.

The other possibility is the decay to a higher excited state of $^{14}$B, which decays to an excited state of $^{13}$B by emitting a neutron. In this case, $\gamma$-emission should take place successively (Fig. 2 case).[2] If we assume this scheme, the decay is ascribed to an allowed transition of log$ft$ $= 3.2 \pm 0.1$.

The analysis for the $\gamma$-ray energy-spectrum is now in progress, in expectation of information to distinguish between the alternative possibilities.

References

1) T. Kishida et al.: *RIKEN Accel. Prog. Rep.*, **27**, 46 (1993).
2) H. Ohm et al.: *Nucl. Phys.*, **A274**, 45 (1976).

# Beta-delayed Neutron Decay of $^{19}$C and Its Astrophysical Implications

A. Ozawa, R. N. Boyd, J. Kolata, F. Chloupek, G. Raimann, K. Yoshida, M. Fujimaki, T. Kobayashi, Y. Watanabe, I. Tanihata, S. Kubono, and K. Kimura

[RADIOACTIVITY $^{19}$C($\beta^+$ n); measured $\beta$-delayed $E_n$ and deduced $E_x$ in $^{19}$N.]

The $\beta$-delayed neutron decay of $^{19}$C has been studied mainly from the astrophysical interest using the time-of-flight (TOF) technique. In the previous report,[1] the motivation and the experimental setup for the present experiment were described in detail.

A typical $\beta$-delayed neutron spectrum is shown in Fig. 1. Several peaks have been identified as $\beta$-delayed neutrons from $^{17}$B and $^{16}$C, which are, respectively, a contaminant in the $^{19}$C beam and its daughter nucleus, by the independent experiment to study the $\beta$-delayed neutron decay of $^{17}$B. One $\beta$-delayed neutron peak from $^{19}$N, which is the daughter nucleus of $^{19}$C, has also been identified, since the neutron energy matches the energy difference between one of known excited states in $^{19}$O and the $^{18}$O + n threshold, and the peak shows the different time dependence from other peaks. Finally, three lines with energies of $E_n$(lab) = 1.49, 1.01, and 0.45 MeV belong to the $\beta$-delayed neutron decay of $^{19}$C. Half-lives obtained by the time spectra gated by the three lines ($T_{1/2} = 46 \pm 4$ ms) show the good consistency with the previous measurement ($T_{1/2} = 49 \pm 4$ ms).[2] All three lines in TOF are coincident with the $\gamma$-ray from the level with $E_x = 115$ keV in $^{18}$N. And the line with $E_n = 0.45$ MeV is coincident with the $\gamma$-ray from the level with $E_x = 587$ keV in $^{18}$N. Using the information, we assign newly obtained levels in $^{19}$N, as shown in Fig. 2. The closest level to the neutron emission threshold in $^{19}$N lies above ~1 MeV from the threshold. Thus, in the temperature range of interest,[3] these newly obtained levels do not affect the big bang nucleosynthesis in imhomogeneous models.

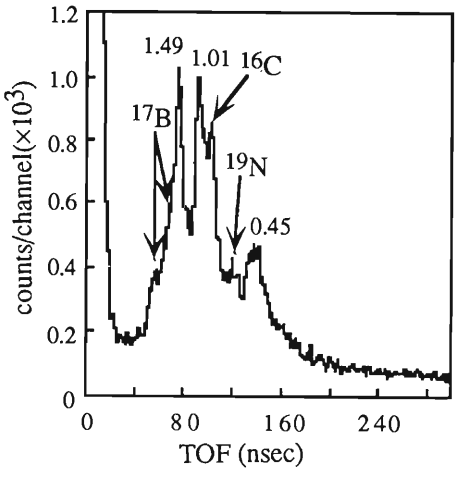


Fig. 1. Time of flight neutron spectrum following the $\beta$-decay of $^{19}$C. The neutron energies (in MeV) are given in the laboratory system.

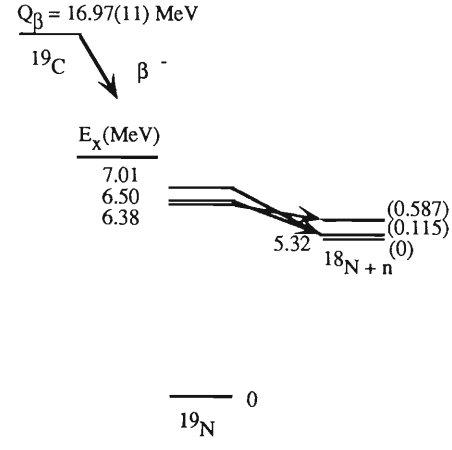


Fig. 2. Decay scheme of $^{19}$C.

References

1) A. Ozawa et al.: *RIKEN Accel. Prog. Rep.*, **27**, 45 (1993).
2) J. P. Dufour et al.: *Phys. Lett.*, **B206**, 195 (1988).
3) F. K. Thielmann et al.: Nuclei in the Cosmos, Springer-Verlag, Berlin, p. 147 (1992).

# Magnetic Moment of Proton Drip-Line Nucleus $^{9}$C

K. Matsuta, M. Fukuda, M. Tanigaki, T. Minamisono, Y. Nojiri, M. Mihara, T. Onishi, T. Yamaguchi, A. Harada, M. Sasaki, T. Miyake, S. Fukuda, K. Yoshida, A. Ozawa, T. Kobayashi, I. Tanihata, J. R. Alonso,* G. F. Krebs,* and T. J. M. Symons*

[ NUCLEAR REACTION $^{12}$C + $^{12}$C, $E = 67A$ MeV; measured $\beta$-ray asymmetry of $^{9}$C, nuclear magnetic resonance; deduced magnetic moment of $^{9}$C ground state. ]

The technique of polarized radioactive nuclear beams has been applied to the $\beta$-NMR study of the proton drip-line nucleus $^{9}$C($I^{\pi} = 3/2^{-}$, $T_{1/2} = 126$ ms). The magnetic moment of $^{9}$C was measured for the first time. With the known magnetic moment of $^{9}$Li, the present result gives us a pair of nuclear magnetic moments in the $A = 9$ isospin quartet ($I^{\pi} = 3/2^{-}$, $T = 3/2$), which is the first example of such pair magnetic moments for $T = 3/2$.

Polarized $^{9}$C nuclei were produced through the $67A$ MeV $^{12}$C + $^{12}$C collision at RIKEN's $K540$ cyclotron and separated by the RIPS (RIKEN Projectile Fragment Separator). The purified $^{9}$C nuclei were slowed down by an energy degrader and were implanted in a cooled Pt foil (30K) placed in a strong magnetic field $H_0 = 4.000$ kOe to maintain the polarization obtained through the reaction. The NMR of $^{9}$C was observed by means of the asymmetric beta-ray emission.

The NMR spectrum obtained by the polarization destruction method is shown in Fig. 1. By fitting a Lorenzian to the NMR spectrum, the resonance frequency was obtained as $\nu_L = 2827.3 \pm 0.4$ kHz. From the result, a preliminary value for the magnetic moment of $^{9}$C was obtained as $|\mu| = 1.3914 \pm 0.0005\ \mu_N$. The sign of $\mu(^{9}\mathrm{C})$ can be reasonably assumed to be negative for the further discussion. The obtained magnetic moment is very much quenched from the Schmidt value $-1.91\ \mu_N$. Using the iso-scalar moment analysis summarized by the relation; $\mu(T_z = -3/2) + \mu(T_z = +3/2) = J + 0.380\langle\sigma\rangle$, with the known magnetic moment $\mu(^{9}\mathrm{Li}) = 3.4391 \pm 0.0006\ \mu_N$,[1] the spin expectation value is obtained as $\langle\sigma\rangle = 1.44$. This value is unusually large compared with other even-odd nuclei and is very much deviated from the theoretical value $\langle\sigma\rangle = 1.0$ calculated using the Cohen-Kurath wave function with the free nucleon g-factors.[2] This discrepancy may be attributed to unknown anomalous structures of the proton drip-line nucleus.

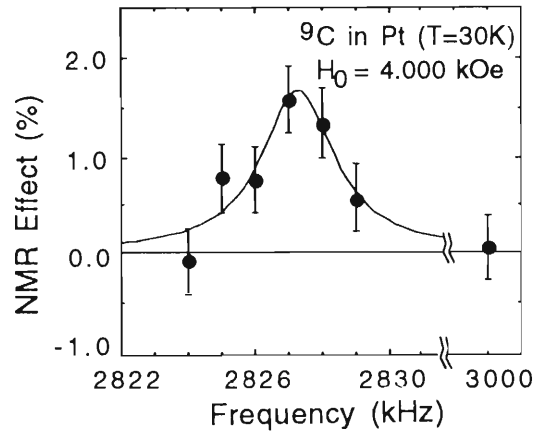


Fig. 1. NMR spectrum of $^{9}$C in Pt.

References

1) F. D. Correll et al.: *Phys. Rev.*, **C28**, 862 (1983).
2) H. Sagawa: private communication.

* LBL, Berkeley, U. S. A.

# Magnetic Moment of Very Neutron-rich Nucleus $^{17}$B

H. Ueno, H. Izumi, K. Asahi, H. Okuno, K. Nagata, H. Ogawa, M. Adachi, H. Sato, Y. Hori, A. Yoshida, N. Aoi, G. Liu, M. Ishihara, W.-D. Schmidt-Ott, T. Shimoda, H. Miyatake, S. Mitsuoka, and N. Takahashi

[ NUCLEAR REACTION $^{93}$Nb + $^{22}$Ne, $E/A$ = 110 MeV/nucleon; measured $\beta$-ray asymmetry of $^{17}$B, nuclear magnetic resonance; deduced magnetic moment of the ground state for $^{17}$B. ]

In order to investigate the effect of a large neutron excess on the nuclear tructure, we carried out the measurement of a magnetic moment for the very neutron-rich nucleus $^{17}$B which is supposed to be a neutron-halo nucleus.[1] The magnetic moment of $^{17}$B was determined by using a spin polarized radioactive beam from the projectile fragmentation reaction.[2] $^{17}$B ($J^\pi = \frac{3}{2}^-$, $t_{\frac{1}{2}}$ = 5.08 ms, $Q_\beta$ = 24 MeV) was produced with a beam of $^{22}$Ne on a 1.07 g/cm$^2$ thick $^{93}$Nb target at $E/A$ = 110 MeV/u. Fragments emitted at $\theta_L = 1.5 \pm 1.0°$ were analyzed in the projectile fragment separator RIPS, and were implanted in a Pt stopper, to which a static magnetic field of 1000 Gauss was applied. For the determination of the magnetic moment, we employed the adiabatic fast passage $\beta$-NMR method: The up/down ratio of $\beta$-ray yields from the implanted $^{17}$N was measured for several different frequency bins, over which the frequency of an oscillating field $B_1$ was swept.

In the first measurement, we performed a number of runs by changing the positions and width of the bins run by run, each resulting in a low-statistics spectrum. In such a situation the conventional method of analysis did not allow us to gather the data into a spectrum of significant statistics for deduction of a conclusive result for the magnetic moment. In order to overcome this difficulty we developed a new method of analysis in which all data are analyzed in terms of a probability distribution by respecting the characteristic feature of the adiabatic fast passage method. The probability distribution function derived by this method is shown in Fig. 1. This result was confirmed in the second measurement in which we concentrated on the frequency region suggested by the above result, as shown in Fig. 2. From these results we could determine the absolute value of $\mu$ within $\pm 3.5\%$ accuracy. We then carried out a precision measurement by dividing this region into seven pieces. The result is shown in Fig. 3. The result preliminarily derived from Fig. 3 is

$$|\mu| = 2.540 \pm 0.015 \ (n.m.).$$

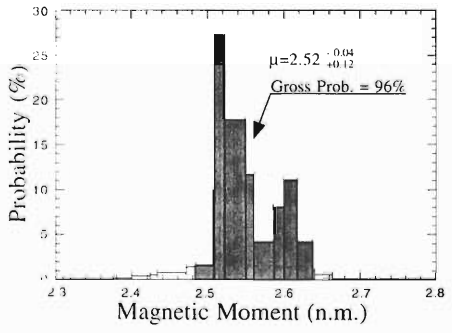


Fig. 1. Probability distribution function deduced by applying the newly developed method of analysis. See text.

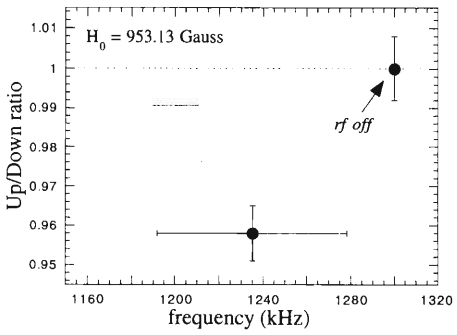


Fig. 2. The result of the second measurement.

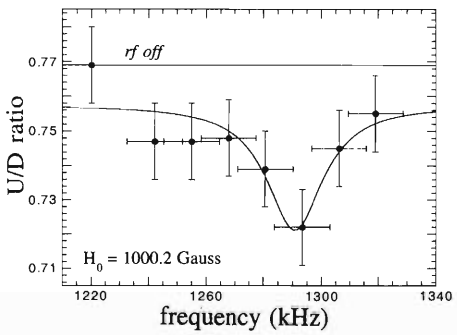


Fig. 3. NMR spectrum obtained from the last measurement.

## References

1) E. Litard et al.: *Europhys. Lett.*, **13**, 401 (1990).
2) H. Okuno et al.: *Hyperfine Interact.*, **78**, 97 (1993).

# Magnetic Moment of $^{17}$N

H. Ueno, H. Izumi, K. Asahi, H. Okuno, K. Nagata, Y. Hori, H. Sato, A. Yoshida,
G. Liu, N. Aoi, H. Ogawa, M. Adachi, and M. Ishihara

[ NUCLEAR REACTION $^{93}$Nb+$^{18}$O, $E/A = 70$ MeV/nucleon; measured $\beta$-ray asymmetry of $^{17}$N, nuclear magnetic resonance; deduced magnetic moment of the ground state for $^{17}$N. ]

Nuclear magnetic moment of $^{17}$N was determined by using a spin polarized radioactive beam from the projectile fragmentation reaction.[1] $^{17}$N ($J^\pi = \frac{1}{2}^-$, $t_{\frac{1}{2}} = 4.173$s, $Q_\beta = 8.680$ MeV) was produced with a beam of $^{18}$O at 70 MeV/u onto a $^{93}$Nb target of 428 mg/cm$^2$ thickness. Fragments emitted at $\theta_L = 2.5 \pm 1.0°$, after being isotope-separated by RIPS, were implanted in a carbon graphite stopper to which a static magnetic field of 2475 Gauss was applied. Nuclear magnetic resonance was observed through a change in the up/down asymmetry of $\beta$-rays emitted in the decay of $^{17}$N. The NMR spectrum obtained is shown in Fig. 1. The experimental magnetic moment $\mu$ was deduced from the dip position in the spectrum as

$$|\mu| = 0.352 \pm 0.002 \ (n.m.).$$

No correction was made for the Knight shift and chemical shift since their effects are considered to be smaller than the experimental error assigned to $\mu$ (the Knight shift is estimated as $K \sim 10^{-4}$ from the Korringa constant $T_1 \cdot T = 2.7 \times 10^4$ sec·K, and the chemical shift normally takes the order of $10^{-4} \sim 10^{-5}$).

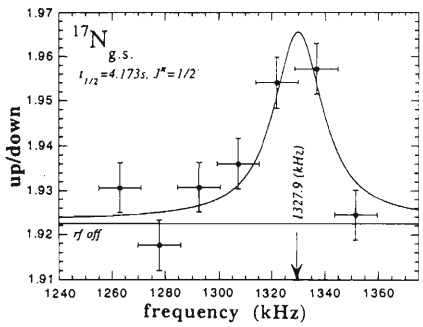


Fig. 1. NMR spectrum obtained for $^{17}$N. The up/down ratio of $\beta$-rays is plotted as a function of the frequency of an oscillating field.

In Fig. 2 the experimental value is compared with shell model calculations[2-4] based on the OXBASH program.[5] Here a negative sign is assumed for the $^{17}$N experimental value. The calculation with the *p-sd* cross shell interactions recently proposed by Warburton and Brown (referred to as WBP in Fig. 2)[2] reproduces the experimental value better than the one based on the Millener-Kurath interaction (MK).[3] In order to clarify effects of the neutron excitation to the *sd*-shell, the calculation with Cohen-Kurath interaction (CKPOT)[4] in the *p*-model space is also plotted. We note here the large outward deviation from the Schmidt value, representing the expected absence of the M1 core polarization for the $p_{\frac{1}{2}}$ orbit.[6] Thus the magnetic moments, in particular their deviation from the Schmidt values, of $^{17}$N and other odd-mass N isotopes may afford a sensitive test of *p-sd* cross shell interactions. In fact in the case of $^{17}$N the WBP model shows that the magnetic moment is largely determined by the admixture of the $|\pi(p_{\frac{3}{2}})^3(p_{\frac{1}{2}})^2 >^{J=\frac{3}{2}} \otimes |\nu(d_{\frac{5}{2}})^2 >^{J=2}$ configuration, for which the expectation value for $\mu$ amounts to 8 times that of the major components having proton configurations of $|\pi(p_{\frac{1}{2}}) >^{J=\frac{1}{2}}$ type. The contribution of such a configuration, involving the excitation of the sd-shell neutrons by the *p*-shell protons through the cross-shell interactions, may play an increasingly important role in the ground state of heavier N isotopes, and well deserves of further experimental investigation.

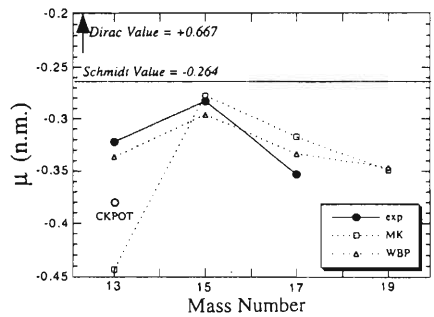


Fig. 2. Comparison of the experimental magnetic moments for N isotopes of odd mass with shell model calculations. MK: the Millener-Kurath *p-sd* cross shell effective interaction. WBP: the *p-sd* cross shell effective interaction recently proposed by Warburton and Brown. CKPOT: the calculation within a *p*-model space using the Cohen-Kurath *p*-shell effective interaction. See text.

References

1) K. Asahi et al.: *Phys. Lett.*, **B251**, 488 (1990).
2) E. K. Warburton and B. A. Brown: *Phys. Rev.*, **C46**, 923 (1992).
3) D. J. Millener and D. Kurath: *Nucl. Phys.*, **A255**, 315 (1975).
4) S. Cohen and D. Kurath: *ibid.*, **73**, 1 (1965).
5) B. A. Brown, A. Etchegoyen, and W. D. M. Rae: OXBASH, MSU Cyclotron Laboratory Report, No. 524 (1986).
6) H. Noya, A. Arima, and H. Horie: *Suppl. of Prog. Theor. Phys.*, No. 8, p. 71 (1958).

# Asymmetry Parameter of $^{23}$Mg Beta Decay

K. Matsuta, M. Fukuda, S. Fukuda, T. Minamisono, Y. Nojiri, T. Izumikawa, M. Tanigaki, M. Nakazato, M. Mihara, T. Onishi, T. Yamaguchi, T. Miyake, M. Sasaki, A. Harada, T. Ohtsubo, K. Yoshida, A. Ozawa, T. Kobayashi, I. Tanihata, J. R. Alonso,* G. F. Krebs,* and T. J. M. Symons*

[ NUCLEAR REACTION $^{197}$Au + $^{24}$Mg, $E = 91A$ MeV; measured $\beta$-ray asymmetry of $^{23}$Mg, nuclear magnetic resonance; deduced asymmetry parameter of $^{23}$Mg ground state transition. ]

Study of the weak vector coupling constant $G_V$ for mixed transitions provides a sharp test for the CVC (Conserved Vector Current) theory. The $G_V$ for a mixed transition is obtained from the beta-decay asymmetry parameter in combination with the half life of the transition. In the present experiment, the asymmetry parameter of $^{23}$Mg beta decay has been measured for the first time at RIKEN's K540 cyclotron using the technique of polarized radioactive nuclear beams.

The $^{23}$Mg nuclei were produced through projectile fragmentation of the $^{24}$Mg beam bombarding a Au target at $100A$ MeV. The $^{23}$Mg fragments produced at a deflection angle of 2° were separated using the RIPS (RIKEN Projectile Fragment Separator), and were momentum analyzed in the separator. Thus obtained polarized $^{23}$Mg nuclei were then implanted in a cooled thin Pt catcher foil placed in a strong magnetic field to maintain the polarization. The polarization effect was measured by means of asymmetric beta-ray emission for both the ground state transition and the transition to the first excited state. The transition to the excited state was tagged by the 440 keV gamma rays.

Figure 1 shows the obtained beta-ray asymmetries $AP$ ($A$: asymmetry parameter, $P$: polarization) for both beta-ray singles and beta-gamma coincidence events. Since the value $A_{ex}$ is known to be $-0.6$, the ratio of two asymmetries, $A_{ex}/A'_0 = 0.90 \pm 0.19$, gives asymmetry parameter for the ground transition as $A_0 = -0.65(13)$, which is in good agreement with the value $-0.55$ predicted from the CVC. More precise measurements are being planned in order to obtain the coupling constant $G_V$ with the accuracy of about 1%.

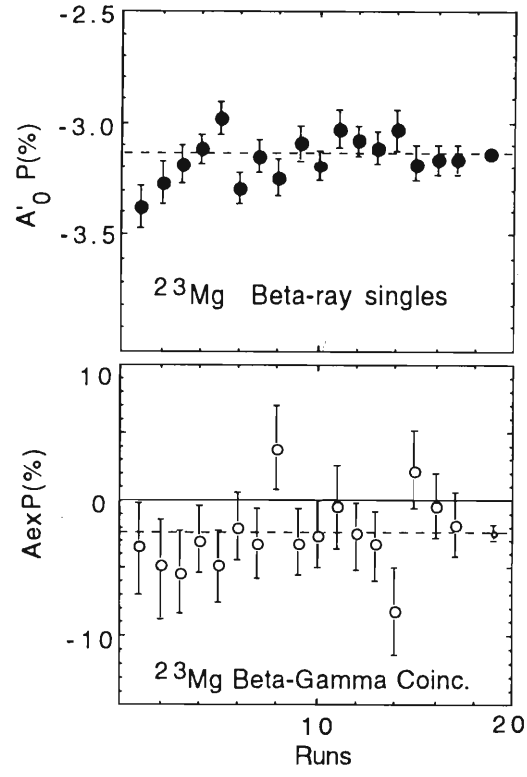


Fig. 1. Beta-ray asymmetries.

* LBL, Berkeley, U.S.A.

# Nuclear Moments of $^{179}$Ta

M. Wakasugi, W.-G. Jin, T. T. Inamura, T. Murayama, H. Katsuragawa,
T. Ishizuka, J.-Z. Ruan, and I. Sugai

[NUCLEAR MOMENTS (Static) $^{179}$Ta; measured $a, b$; deduced $\mu, Q$.]

We measured the hyperfine structure of radioactive isotope $^{179}$Ta ($T_{1/2} = 1.8\ y$) with a laser spectroscopy system using an argon-ion sputtering atomic beam source.[1] From the measurement, we determined magnetic dipole and electricquadrupole moments of the nuclear ground state.

A sample of $^{179}$Ta isotope was prepared by bombarding a natural Hf target (0.25 mm thick) with a 19 MeV deuteron beam from an AVF cyclotron. Reactions of $^{180}$Hf(d,3n) and $^{179}$Hf(d,2n) were used. The number of produced $^{179}$Ta atoms was about $5 \times 10^{14}$ atoms. The size of the d-beam spot on the Hf target was about 6 mm$^2$, and most of $^{179}$Ta atoms were mainly located at the depth shallower than 0.1 mm from the surface. That means the abundance of $^{179}$Ta in a volume of 0.6 mm$^3$ was about 20 ppm.

After cooling of short lived isotopes such as $^{177}$Ta, we set the radioactive sample together with a natural Ta sample in the laser spectroscopy system. First, we observed a hyperfine spectrum of a 540.3 nm transition from $^4F_{3/2}$ ground state to 18504.7 cm$^{-1}$ $^4D_{1/2}$ state of the stable isotope $^{181}$Ta to check wavelength of the laser and optimize geometrical conditions of the apparatus. The hyperfine spectrum is shown in Fig. 1(a). Next, we moved the sample so that the argon-ion beam hits the center of the d-beam spot on the radioactive sample. At this position, we measured the fluorescence spectrum at the same wavelength region as in Fig. 1(a), and it is shown in Fig. 1(b).

To identify hyperfine transition lines of $^{179}$TaI, we measured a background spectrum with an argon-ion beam by hitting a point outside of the d-beam spot and the spectrum is shown in Fig. 1(c). Then, hyperfine peaks of $^{179}$TaI have been identified as labeled by alphabets $a$ to $f$ in Fig. 1(b). From these peaks, we could determine the hyperfine splitting of the ground state $^4F_{3/2}$. Then hyperfine constants A and B of the ground state $^4F_{3/2}$ were determined to be $A^{179} = 492(1)$ MHz, and $B^{179} = -1043(10)$ MHz.

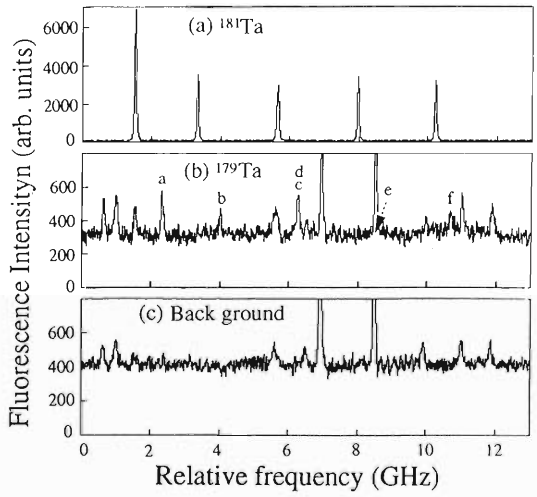


Fig. 1. Measured spectra of the 540.3 nm transition in $^{179}$Ta with reference spectra: The spectrum (a) was obtained when an argon-ion beam hits the natural Ta sample; the spectrum (b) was obtained for the center of d-beam spot on the radioactive sample; and the spectrum (c) for a point outside the d-beam spot on the radioactive sample.

Since A factor is proportional to the nuclear magnetic moment $\mu$, we derived the moment of $^{179}$Ta to be $\mu_I^{179} = +2.289(9)\ \mu_N$ using $A^{181}$ and $\mu_I^{181}$ previously known for $^{181}$Ta isotope.[2,3] A ratio of B factor of two isotopes should be equal to the ratio of the nuclear quadrupole moment $Q_s$. The moment $Q_s^{179}$ of $^{179}$Ta was also derived to be $Q_s^{179} = +3.37(4)$ b, using $B^{181}$ and $Q_s^{181}$ values.[2,3]

References

1) M. Wakasugi et al.: *Rev. Sci. Instrum.*, **64**, 3487 (1993).
2) W. G. Jin et al.: *Phys. Rev.*, **A50**, 1920 (1994).
3) P. Raghavan: *At. Data Nucl. Data Tables*, **42**, 189 (1989).

# Nuclear Moments of $^{180m}$Ta by Laser-RF Double-Resonance Spectroscopy

W.-G. Jin, M. Wakasugi, T. T. Inamura, T. Murayama, H. Katsuragawa, T. Ishizuka, and I. Sugai

[NUCLEAR MOMENTS (Static) $^{180m}$Ta; measured $a$, $b$; deduced $\mu$, $Q$.]

A typical refractory element Ta has a naturally occurring long-lived ($T_{1/2} > 1.2\times10^{15}$ y) spin ($I = 9$) isomer $^{180m}$Ta at 75.3 keV, whose abundance is 0.0123%. This exotic nuclide has attracted much interest in astrophysics as well as in nuclear structure physics. The nuclear magnetic dipole moment of $^{180m}$Ta was tentatively reported more than ten years ago[1] but the electric quadrupole moment is not known.

We developed a laser-rf double-resonance (LRDR) spectroscopic technique[2,3] using an innovative Ar-ion sputtering atomic beam source especially to study refractory elements.[4,5] In this paper we shall report a precise hyperfine structure (hfs) measurement of $^{180m}$Ta by means of LRDR.

Figure 1 shows the laser-induced fluorescence spectrum of the 540.3 nm (ground state $^4F_{3/2}$ – 18504.7 cm$^{-1}$ $^4D_{1/2}$) transition. Six strong peaks are hyperfine transitions in $^{181}$Ta; two small peaks indicated by $\alpha$ and $\beta$ are those in $^{180m}$Ta. The other hyperfine transitions in $^{180m}$Ta were masked by strong peaks of $^{181}$Ta.

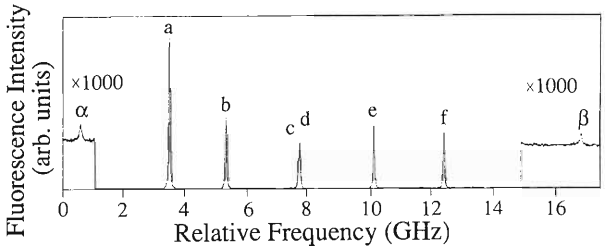


Fig. 1. Laser-induced fluorescence spectrum of the 540.3 nm transition in Ta.

For the LRDR measurement of $^{180m}$Ta, the laser frequency was fixed at one of hfs peaks, and change in the fluorescence intensity as a function of the rf was obtained by scanning the frequency applied to the rf loop. The measured LRDR spectra for the peaks $\alpha$ and $\beta$ are shown in Fig. 2(a) and (b), respectively. From the LRDR spectra, two hyperfine splittings of $\Delta\nu(F-F' = 19/2-21/2)$ and $\Delta\nu(15/2-17/2)$ of $^4F_{3/2}$ in $^{180m}$Ta were determined and thus the hfs constants

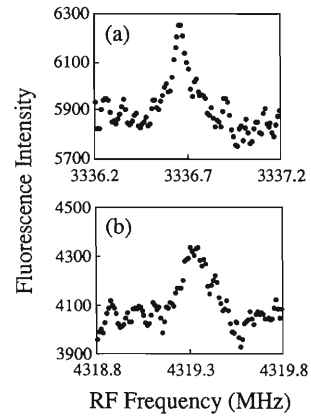


Fig. 2. RF resonance spectrum (a) for $F - F' = 19/2 - 21/2$ and (b) for $F - F' = 15/2 - 17/2$ in $^{180m}$Ta. Spectrum (a) was measured for the optical transition $\alpha$ in Fig. 1, and (b) for $\beta$.

$A$ and $B$ were precisely derived for the ground state $^4F_{3/2}$: $A = 402.9466(10)$ MHz and $B = -1533.056(15)$ MHz. Using the known hfs constants $A$ and $B$[6] and nuclear moments $\mu$ and $Q$[7] for $^{181}$Ta, we have the magnetic dipole moment $\mu^{180m} = 4.825(11)\ \mu_N$ and the spectroscopic quadrupole moment $Q^{180m} = 4.946(20)$ b for $^{180m}$Ta. The present dipole moment is in agreement with that given by Burghardt et al. within their experimental error;[1] the present accuracy is improved by a factor of five and the quadrupole moment was determined for the first time.

References

1) B. Burghardt et al.: *Phys. Lett.*, **B92**, 64 (1980).
2) W. G. Jin et al.: *Phys. Rev.*, **A50**, 1920 (1994).
3) M. Wakasugi et al.: *ibid.*, p. 4639.
4) M. Wakasugi et al.: *Rev. Sci. Instrum.*, **64**, 3487 (1993).
5) W. G. Jin et al.: *Phys. Rev.*, **A49**, 762 (1994).
6) S. Büttgenbach and G. Meisel: *Z. Phys.*, **244**, 149 (1971).
7) P. Raghavan: *At. Data Nucl. Data Tables*, **42**, 189 (1989).

# $^{27}$Al(d,$^2$He) Reaction Studied at $E_d$ = 270 MeV

T. Niizeki, H. Ohnuma, T. Yamamoto, K. Katoh, T. Yamashita, Y. Hara, H. Okamura, H. Sakai, S. Ishida, N. Sakamoto, H. Otsu, T. Wakasa, T. Uesaka, Y. Satou, S. Fujita, T. Ichihara, H. Orihara, H. Toyokawa, K. Hatanaka, S. Kato, S. Kubono, and M. Yosoi

[NUCLEAR REACTION $^{27}$Al(d,$^2$He), $E_d$ = 270 MeV.]

We have been studying Gamow-Teller strength distributions in the $T_z = +1$ channel ($GT_+$) for sd-shell nuclei by (d,$^2$He) reactions.[1,2] In this report we present the data on $^{27}$Al. The experiment was carried out using a 270 MeV deuteron beam from the RIKEN Ring Cyclotron and a large solid-angle, large momentum-acceptance magnetic spectrometer system SMART. The target was 39.4 mg/cm$^2$ thick self-supporting foil of aluminum. Details of the experiment were described in our previous reports.[1,2] Major modifications made since the report last year are the use of a helium gas-filled detector chamber and the use of improved optics to further reduce multiple scattering and to improve angular and energy resolutions. An overall energy resolution of about 600 keV has been obtained so far.

Figure 1(a) shows a sample small-angle spectrum from the $^{27}$Al(d,$^2$He)$^{27}$Mg reaction. This spectrum was obtained by dividing a spectrum measured at the spectrometer angle of 0° into smaller angular bins. The peaks indicated by triangles show forward rise, and are identified as being excited by GT transitions. In addition to those, there also seem to exist a number of very weak GT components in a high excitation energy region. States in $^{27}$Mg that can be excited by GT transitions should have $J^\pi$ of $3/2^+$, $5/2^+$ and $7/2^+$.

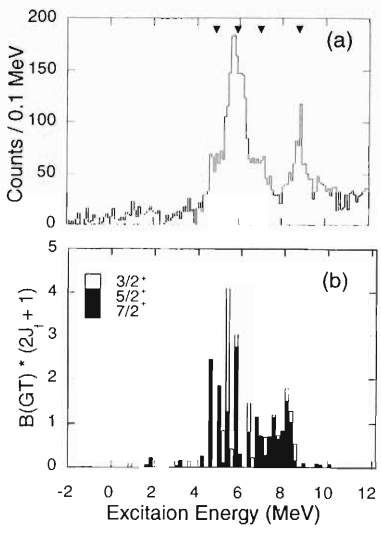


Fig. 1. Excitation energy spectrum (a) obtained at 0° for the $^{27}$Al(d,$^2$He)$^{27}$Mg reaction. Distribution of calculated reduced GT transition probabilities B(GT) is shown in (b).

There is a $3/2^+$ state at 0.98 MeV in $^{27}$Mg, and two $5/2^+$ states at 1.70 and 1.94 MeV.[3] The 0.98 MeV state is strongly fed[4] by the $\beta$ decay of the $5/2^+$ ground state of $^{27}$Na with a log $ft$ value of 4.3. These low-lying states are only very weakly excited in the (d,$^2$He) reaction. They are considered to be arising basically from higher-seniority $(d_{5/2})^{10}$ configurations coupled with an $s_{1/2}$ neutron. They should not therefore be excited by L = 0 in charge exchange reactions on $^{27}$Al, but should be strongly fed in the $\beta$ decay of $^{27}$Na. Such an interpretation agrees with the experimental observation.

Major portion of the GT strength is concentrated in two regions, one around 6 MeV and another around 9 MeV in excitation. The experimentally observed peaks in these regions look like composite peaks containing several unresolved peaks. These peak shapes are a little broader than, but very similar to, those observed in the $^{28}$Si(d,$^2$He)$^{28}$Al reaction as discussed in a separate report.[5]

Figure 1(b) shows the GT strength distribution calculated for the full sd-shell configuration by the OXBASH.[6] The B(GT) values are multiplied by $2J_f + 1$, and the bin size is 200 keV. Weak excitation of the low-lying states discussed above agrees with the shell-model calculation. The calculated GT strength distribution at least qualitatively reproduces the data: it gives two regions of concentrated strength separated by about 3 MeV.

The A = 27 nuclei studied here are about the middle of the sd-shell, and expected to have numerous states with small GT components. Indeed there are 40 states so far reported[3] between 4 and 8 MeV excitation energy in $^{27}$Mg, about three quarters of which have been assigned to be $3/2^+$, $5/2^+$ or $7/2^+$. According to the present data, however, the GT strength in $^{27}$Mg is not distributed over a wide region, but concentrated in narrow regions of excitation energy. Shell model calculations seem to be able to explain such concentration of the GT strength. Further analysis is in progress.

References

1) T. Niizeki et al.: *RIKEN Accel. Prog. Rep.*, **27**, 38 (1993), and references therein.
2) T. Niizeki et al.: *Nucl. Phys.*, **A577**, 37c (1994).
3) P. Endt: *ibid.*, **A521**, 1 (1990), and references therein.
4) D. Gullemaud-Mueller et al.: *ibid.*, **A426**, 37 (1984).
5) T. Niizeki et al.: This report, p. 47.
6) B. A. Brown, A. Etchegoyen, W. D. M. Rae, and N. S. Godwin: Program OXBASH (1984), unpublished.

# $GT_+$ Strength Distributions in N = 15 Isotones

T. Niizeki, H. Ohnuma, T. Yamamoto, K. Katoh, T. Yamashita, Y. Hara, H. Okamura, H. Sakai, S. Ishida, N. Sakamoto, H. Otsu, T. Wakasa, T. Uesaka, Y. Satou, S. Fujita, T. Ichihara, H. Orihara, H. Toyokawa, K. Hatanaka, S. Kato, S. Kubono, and M. Yosoi

[NUCLEAR REACTIONS: $^{26}$Mg, $^{27}$Al, $^{28}$Si(d,$^2$He), $E_d$ = 270 MeV.]

We have been studying Gamow-Teller strength distributions in the $T_z = +1$ channel ($GT_+$) for sd-shell nuclei by (d,$^2$He) reactions. We have obtained, in particular, the (d,$^2$He) spectra for the target nuclei $^{26}$Mg, $^{27}$Al, and $^{28}$Si, all of which have N = 14. The final nuclei $^{26}$Na, $^{27}$Mg, and $^{28}$Al are N = 15 isotones. Figure 1 shows spectra obtained at $\theta_{lab}$ = 0–1°, the same as shown previously,[1,2] except that those at $\theta_{lab}$ = 3–4° have been subtracted after suitable normalization. The L = 0 angular distributions are expected to decrease rapidly from 0° to 4°, while those with higher L stay roughly constant in this range. Therefore the spectra shown in Fig. 1 would be safely regarded as reasonable representations of the $GT_+$ strength distributions in final nuclei.

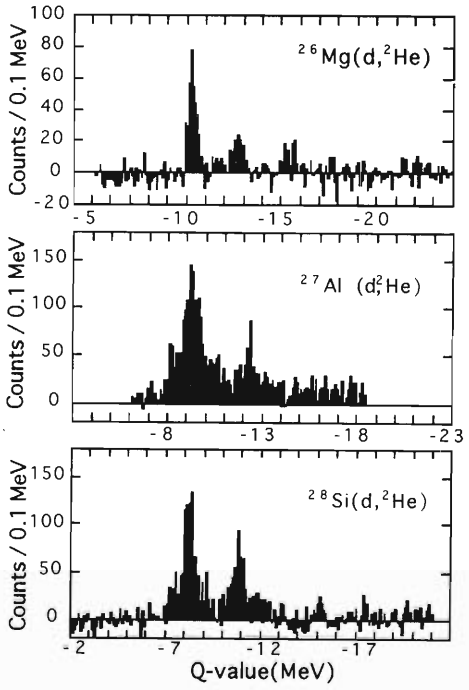


Fig. 1. Q-value spectra for the $^{26}$Mg, $^{27}$Al, $^{28}$Si(d,$^2$He) reactions at $E_d$ = 270 MeV obtained for the angular range between 0 and 1°. Those for 3–4° have been subtracted.

An interesting feature of these spectra is that all of them show quite similar distributions. There are only two strong peaks in each spectrum; the one at lower excitation energy is the strongest, followed by a medium peak 2–3 MeV higher in excitation. There possibly are several other weaker peaks. The strongest peak in $^{28}$Al is known to have satellite peaks on both sides.[2] The Q-values for the strongest peaks are about 11, 10, and 8 MeV for $^{26}$Na, $^{27}$Mg, and $^{28}$Al, respectively. The $GT_+$ distribution observed in the $^{27}$Al(d,$^2$He)$^{27}$Mg reaction is broader than the others, because final states with $J^\pi = 3/2^+, 5/2^+$, and $7/2^+$ can be excited by $GT_+$ transitions in this case, while only the $1^+$ states are excited from even-even targets. An additional reason for a broader distribution in $^{27}$Mg may be the low neutron separation energy of 6.4 MeV for this nucleus. The strong GT peaks are well below the neutron thresholds in the other two cases.

Full sd-shell shell-model calculations have been successful to describe various properties of nuclei over the entire region of sd-shell.[3] Indeed the $GT_+$ strength distribution in $^{26}$Na was found to be in reasonable agreement with the shell model prediction.[1] On the other hand, the $GT_-$ distribution observed in the $^{28}$Si(p,n)$^{28}$P reaction[4] could not be reproduced by the shell model: the experimental data show that major portion of the $GT_-$ strength is concentrated in a few peaks while the $GT_-$ strength is spread over a wide excitation energy region according to the shell model. The $^{28}$Si(d,$^2$He) data shown in Fig. 1 are almost identical to those for the mirror $^{28}$Si(p,n) reaction, and disagree with the shell model calculation. Although the results for $^{27}$Mg are somewhat uncertain due to the fact that there are more $GT_+$ states than in $^{26}$Na and $^{28}$Al, the shell model calculations at least qualitatively reproduce the data giving two regions of concentrated GT strength.[2]

Wider spreading of the GT strength toward the middle of the sd-shell, as suggested by the shell model calculation, seems more natural since there are more s-d particles and hence a wider configuration space available. However the present data combined with previous (p,n) data[4] clearly show that this is not the case for $^{28}$Si. The GT strength is concentrated in a few peaks even at the middle of the shell. The reason for such failure of the shell model is not clear at present. More detailed analysis of the experimental data and further theoretical investigations are under way.

References

1) T. Niizeki et al.: *Nucl. Phys.*, **A577**, 37c (1994).
2) T. Niizeki et al.: This report, p. 46.
3) B. A. Brown, A. Etchegoyen, W. D. M. Rae, and N. S. Godwin: Program OXBASH (1984), unpublished.
4) B. D. Anderson et al.: *Phys. Rev.*, **C43**, 50 (1991).

# Excitation of Spin-dipole States by the $^{12}C(^{12}C,^{12}N)^{12}B$ Reaction at $E/A = 135$ MeV

T. Ichihara, M. Ishihara, H. Ohnuma, T. Niizeki, T. Yamashita, K. Katoh, S. Kubono, M. Tanaka, Y. Fuchi, S. Takaku, H. Okamura, S. Ishida, and Y. Satou

[NUCLEAR REACTION $^{12}C(^{12}C,^{12}N)^{12}B$, $E/A = 135$ MeV.]

Giant resonances can be described as the collective motion of nucleons in a nucleus, or as coherent superpositions of one-particle one-hole excitations in a microscopic picture. Recent progress in shell-model theories has made it possible to carry out large-space microscopic calculations including 1 $\hbar\omega$ or even higher configurations for giant resonances in light nuclei such as $^{12}C$. Experimentally, charge-exchange reactions have been used extensively to reveal the isovector mode of giant resonances. However, very little information has been obtained about the spin-dipole resonances, which are characterized by the quantum numbers $\Delta S = 1$, $\Delta T = 1$ and $\Delta L = 1$.

Two broad peaks were observed at 4.5 MeV and 7.5 MeV in previous (p,n), (n,p) charge-exchange experiments on $^{12}C$.[1] DWBA analysis of their angular distributions indicated that these peaks were dominantly due to the $J^\pi = 2^-$ and $1^-$ components, respectively. They were interpreted as the members of the isovector spin-dipole resonance built on the ground state of $^{12}C$. In these reactions, however, both the spin-flip ($\Delta S = 1$) and non spin-flip ($\Delta S = 0$) components can be excited.

The $(^{12}C,^{12}N)$ reaction has a stringent selectivity of the spin and isospin transfer, i.e. $\Delta S = 1$ and $\Delta T = 1$, and can be utilized to pick up pure spin-flip components. It has been suggested that the $(^{12}C,^{12}N)$ reaction may become dominantly one-step in the region of $E/A > 100$ MeV. Indeed our recent study of the $^{12}C(^{12}C,^{12}N)^{12}B$ reaction leading to the $^{12}B$ ground state ($1^+$) at $E/A = 135$ MeV has shown an encouraging result.[2] In this paper we extend such a spectroscopic study to the region of giant resonances.

The experiment was performed using an $E/A = 135$ MeV $^{12}C$ beam from the ring cyclotron at the RIKEN Accelerator Research Facility. Outgoing particles were analyzed with the high-resolution spectrograph SMART. Figure 1 shows sample spectra at two different angles. The $^{12}B$ ground state (g.s.) as well as the bumps around $E_x = 4.5$ MeV and 7.5 MeV are strongly excited.

The deduced differential cross sections are plotted in Fig. 2 together with the results of the microscopic one-step DWBA analysis using the Franey-Love $t$-matrices and shell-model wave functions.[2]

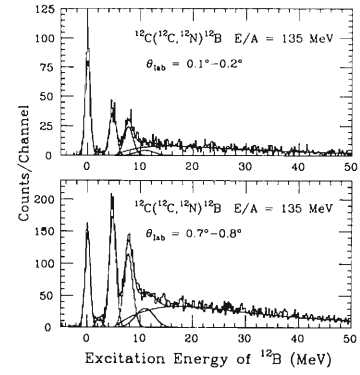


Fig. 1. Typical energy spectrum of the reaction.

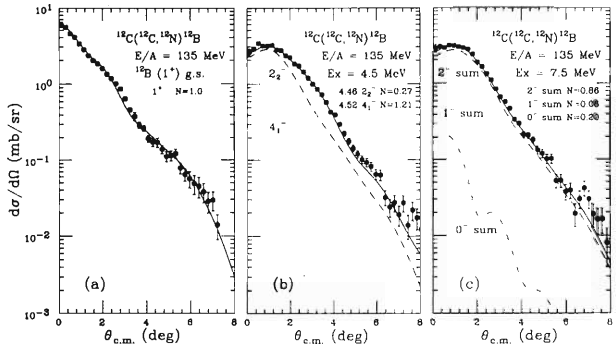


Fig. 2. Differential cross sections for each state.

An intriguing feature observed here is that the strength around 7.5 MeV comes mainly from the $2^-$ states. The discrepancy between the present analysis and the previous (n,p) and (p,n) results[1] can be considered to be due to the different selection mechanism of the reaction. The $(^{12}C,^{12}N)$ reaction selects only the $\Delta S = 1$ excitation whereas the (n,p) and (p,n) reactions involve both the $\Delta S = 1$ and $\Delta S = 0$ excitations.

References

1) X. Yang et al.: *Phys. Rev.*, **C48**, 1158 (1993), and references theirin.
2) T. Ichihara et al.: *Phys. Lett.*, **323**, 278 (1994); *Nucl. Phys.*, **A569**, 287c (1994); *ibid.*, **A577**, 93c (1994).

# Tensor Analyzing Power of the $^{12}C(\vec{d}, ^2He)^{12}B$ Reaction at 270 MeV

H. Okamura, S. Ishida, N. Sakamoto, H. Otsu, T. Uesaka, T. Wakasa, Y. Satou, S. Fujita, H. Sakai, T. Ichihara, K. Hatanaka, T. Niizeki, K. Katoh, T. Yamashita, Y. Hara, and H. Ohnuma

[ NUCLEAR REACTION $^{12}C(\vec{d}, ^2He)$, $E_d$=270 MeV, measured cross section and analyzing powers, DWBA analysis. ]

It is theoretically shown that the tensor analyzing powers of the $(\vec{d}, ^2He)$ reaction contain essentially the same nuclear information as the polarization-transfer observables of the nucleon-nucleus scattering.[1] Considering its unique selectivities, $\Delta S$=1, $\Delta T$=1, and $\Delta T_Z$=+1, the $(\vec{d}, ^2He)$ reaction should be a powerful tool for the study of the spin-flip dipole state, particularly in identifying $J^\pi$ of the residual nucleus ($2^-$, $1^-$, and $0^-$ for a $0^+$ target). It would be fascinating to know if the $0^-$ collective states were enhanced through their coupling to the pionic degrees of freedom in the nucleus.

The usefulness of the tensor analyzing power, however, has not been experimentally established. We have measured $A_{yy}$ and $A_{xx}$ of the $(\vec{d}, ^2He)$ reaction at 270 MeV on the $^{12}C$ target, the structure of which is well understood. The cross section and the vector analyzing power $A_y$ have been also measured for the study of the reaction mechanism. Details of the experimental procedure[2,3] and of the polarized deuteron beam[4] are described elsewhere.

The result is shown in Figs. 1 and 2. The data has been analyzed according to the prior-formalism of the DWBA theory for the three-body reaction. The calculation reproduces the data reasonably well. Details are discussed in Ref. 3.

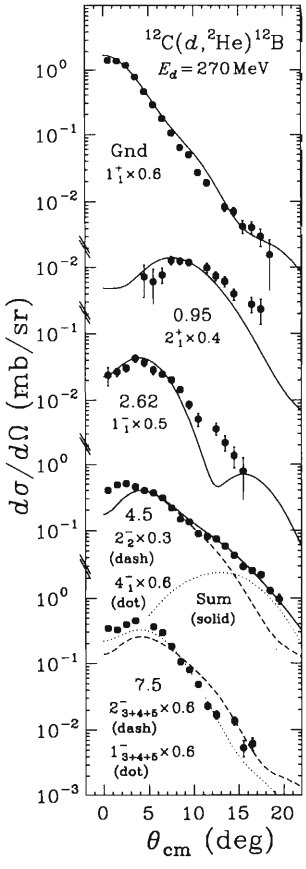


Fig. 1. Angular distributions of the cross section. The result of DWBA analysis is also presented normalized by the factor indicated for each state.

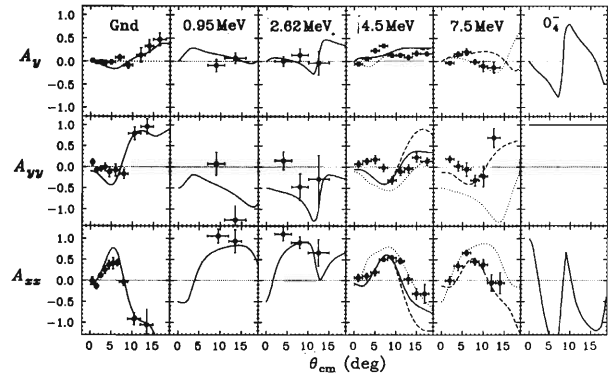


Fig. 2. Angular distributions of the analyzing powers with the result of DWBA analysis. The DWBA prediction for the $0^-_4$ state ($E_x$ = 14 MeV) is also presented for comparison.

References

1) D. V. Bugg and C. Wilkin: *Nucl. Phys.*, **A467**, 575 (1987).
2) H. Ohnuma et al.: *Phys. Rev.*, **C47**, 648 (1993).
3) H. Okamura et al.: *Nucl. Phys.*, **A577**, 89c (1994); *Phys. Lett.*, **B345**, 1 (1995); This report, p. 124.
4) H. Okamura et al.: *AIP Conf. Proc.*, **293**, 84 (1994); This report, p. 148.

# Production of High-Spin Isomer Beam

T. Kishida, S.-J. Chae, A. Ferragut, Y. Gono, E. Ideguchi, M. Ishihara, M. Kidera, J.-C. Kim, H. Kumagai, H. Kusakari, G. Liu, B.-J. Min, S. Mitarai, T. Morikawa, K. Morita, T. Murakami, M. Nakajima, A. Odahara, M. Ogawa, M. Oshima, M. Shibata, T. Shizuma, M. Sugawara, H. Tsuchida, A. Yoshida, and Y. Zhang

[ NUCLEAR REACTIONS, $^{16}O(^{136}Xe,7n)^{145}Sm$, $^{9}Be(^{170}Er,5n)^{174}Hf$, $^{27}Al(^{130}Te,9n)^{148}Tb$, $E_p$ = 7–10 MeV/u, Recoil Separator, High-Spin Isomer Beams. ]

The high spin isomer beam line of RIKEN Accelerator Facility is a unique apparatus in the world. This beam line provides a high spin isomer as a secondary beam, which enables us to study the nuclear high spin state of exotic condition. One of the important subjects is the search for off-yrast collective mode of the high spin isomer state by means of the Coulomb excitation. And another important subject is the production of very high spin states by means of secondary fusion reactions between the high spin isomer and the target nucleus.

The high spin isomer beams are produced via heavy-ion-induced fusion reactions of inverse kinematics. The fusion products, thus produced, recoil out into the forward direction and have large kinetic energies enough for the secondary reactions. In the first stage, a gas-filled system was used to enhance the secondary beam intensity by the charge state equilibration of the beams in the gas.[1,2] However, the effect of the multiple scattering in the beam line materials was too large to get a well- focused beam spot, and the beam transmission was limited. In the second stage, in order to improve the transmission, we developed a new system without filling gases and with the intermediate focal plane (F1) for the separation of the reaction products from the primary beam.[3] (See Fig. 1) As reported in Ref. 3, high spin isomer beams were produced via a Xe-induced reaction with, or without, filling gases, and the transmission without gases was measured to be 20–30% while that for the gas- filled system was about 10%.

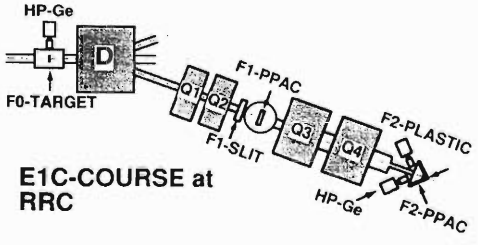


Fig. 1. Schematic diagram of the high-spin isomer beam facility.

In 1994, we produced three kinds of high spin isomer beams. (A) The high spin isomer of $^{145}Sm$ of $I^{\pi} = (49/2)^{+}$ was produced by the $^{16}O(^{136}Xe,7n)^{145}Sm$ reaction. A $SiO_2$ foil of about 2–3 mg/cm$^2$ was used as a production target. The primary beam intensity was 6–30 $\times$ 10$^9$ sec$^{-1}$. And the isomer yield was finally obtained to be about $5 \times 10^4$ sec$^{-1}$ by measuring the known $\gamma$-ray yields. (B) The K-isomer of $^{174}Hf$ of $K^{\pi} = 8^{-}$ was produced by the $^{9}Be(^{170}Er,5n)^{174}Hf$ reaction. A Be foil of 1.84 mg/cm$^2$ was used as a production target, and the primary beam intensity was 6–$12 \times 10^9$ sec$^{-1}$. The isomer yield was, then, $1.5–3 \times 10^3$ sec$^{-1}$. The Coulomb excitation of the K-isomer state was successfully observed with this beam. (C) The high spin isomer of $^{148}Tb$ of I = 27[4] was produced by the $^{27}Al(^{130}Te,9n)^{148}Tb$ reaction. The data of this experiment is now in analysis.

In the case of $^{145}Sm$, we encountered the difficulties that the production target would be destroyed by the heat emerged when the intensity of the primary beam was very large. We, therefore, have to use a target material like $^{9}Be$ or $^{27}Al$ which has large heat conductance. (For example, $^{145}Sm$ can be produced by the $^{9}Be(^{142}Ce,6n)^{145}Sm$ reaction.)

Furthermore, we plan to use a gas target system as a production target for further increase of the primary beam intensity. This high intensity high spin isomer beam will be a powerful tool for secondary fusion experiments to produce a cold high spin compound nucleus.

References

1) Y. Gono et al.: *RIKEN Accel. Prog. Rep.*, **26**, 12 (1992).
2) Y. Gono et al.: *Nucl. Phys.*, **A557**, 341c (1993).
3) T. Morikawa et al.: *RIKEN Accel. Prog. Rep.*, **27**, 31 (1993).
4) The value of spin is preliminary.

# Coulomb Excitation of $^{174}$Hf $K$-Isomer: $\gamma$-Ray Spectroscopy with High-Spin Isomer Beam

T. Morikawa, Y. Gono, K. Morita, T. Kishida, T. Murakami, E. Ideguchi, H. Kumagai, G. Liu, A. Ferragut, A. Yoshida, Y. Zhang, M. Oshima, M. Sugawara, H. Kusakari, M. Ogawa, M. Nakajima, H. Tsuchida, S. Mitarai, A. Odahara, M. Kidera, M. Shibata, J. C. Kim, S.-J. Chae, Y. Hatsukawa, and M. Ishihara

[ NUCLEAR REACTION, $^{9}$Be($^{170}$Er,5$n$)$^{174}$Hf, Recoil Separator, High-Spin Isomer Beams, $K$-Isomer, Secondary Reaction, Coulomb Excitation, $B(E2)$. ]

By using the high-spin isomer beam (HSIB),[1] a Coulomb excitation (COULEX) experiment of $^{174}$Hf $K^{\pi} = 8^{-}$ isomer was successfully carried out. This is the first application of the HSIB to the $\gamma$-ray spectroscopy in the secondary reaction.

A 7.0 MeV/u $^{170}$Er primary beam was provided by RIKEN Ring Cyclotron, and was incident on the production target of a 1.84 mg/cm$^2$ $^{9}$Be foil with an intensity of 1–2 pnA. The HSIB of $^{174}$Hf $K$-isomer was produced by the recoil separator system at E1C course,[2] and was delivered to the second target of a $^{208}$Pb foil of 2 mg/cm$^2$. Due to the small difference of the magnetic rigidity between the primary and secondary beams, the intensity of HSIB with reasonable purity was limited to 1.5–3 $\times$ $10^3$ pps on the second target. Eight HP Ge detectors at $\theta_{\gamma} = 135°$ and four PPAC's covering $15° \leq \theta_p \leq 65°$ were used to detect COULEX $\gamma$-rays and the scattered projectile, respectively, and the coincidence signal between them triggered the data acquisition system. Twenty-four NaI(Tl) scintillators were also placed surrounding the PPAC chamber to detect the delayed $\gamma$-rays deexciting the isomer following the prompt COULEX reaction.

The list-mode data were off-line sorted to extract the COULEX events of $^{174}$Hf isomers. Figure 1(a) shows a $\gamma$-ray spectrum obtained by the TOF (PPAC-RF) gate for the reaction products. As a background, the $^{170}$Er (primary beam) COULEX spectrum was also made by a different TOF-gate as shown in Fig. 1(b). The pure $\gamma$-ray spectrum of $^{174}$Hf COULEX in Fig. 1(c) was finally obtained after the background subtraction. In the $\gamma$-ray spectrum in Fig. 1(c), the prominent peak of $9^{-} \rightarrow 8^{-}$ transition was observed at 232 keV, as well as the rotational sequence of the ground state band (GSB) following the multiple-step excitation up to $8^{+}$ state. By gating on the NaI(Tl) delayed signals, the 232 keV transition was confirmed to feed the isomer. In contrast, the $10^{-} \rightarrow 8^{-}$ transition of $\Delta I = 2$ was not observed, which is consistent with the expectation for a rotational band of a large $K$ quantum number. Figure 2 summarizes the levels and transitions observed in the present experiment.

In order to estimate the $B(E2 : 8^{-} \rightarrow 9^{-})$ value, we used the ratio of cross sections, $\sigma(8^{-} \rightarrow 9^{-})/\sigma(0_g^{+} \rightarrow$

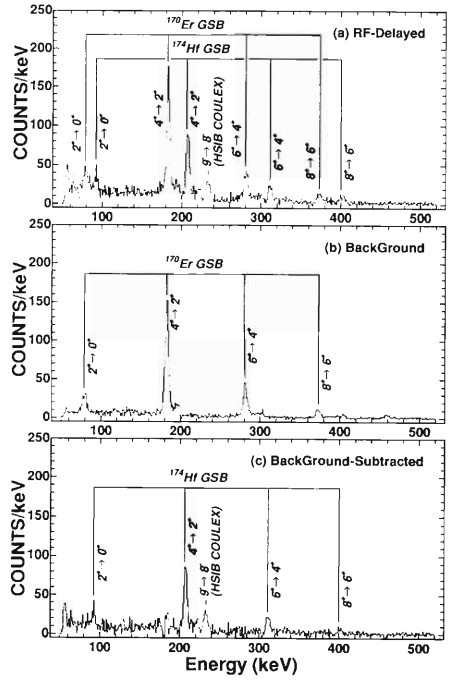


Fig. 1. Doppler-corrected $\gamma$-ray spectra gated by $^{174}$Hf (a) and $^{170}$Er (b) components in the TOF (PPAC-RF) distribution. The spectrum (c) is made by subtracting (b) from (a) with appropriate normalization.

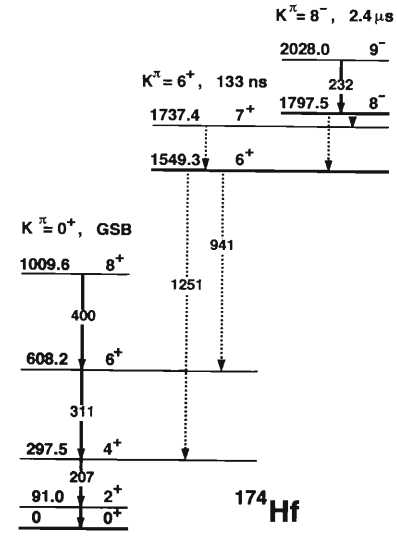


Fig. 2. A partial level scheme of $^{174}$Hf with the observed transitions indicated by solid lines. Dashed arrows are the transitions following the $^{174}$Hf $K^{\pi} = 8^{-}$ isomer decay.

$2_g^+$). The experimental value of this ratio was $0.57 \pm 0.50$, and is consistent with the theoretical value 0.51 which is calculated by assuming the $K^\pi = 8^-$ band as a rigid rotor with $Q_0 = 7.3$ b,[3] the same value as the ground state. From the present analysis, $B(E2 : 8^- \rightarrow 9^-)$ value was extracted to be $2 \pm 1$ $e^2\mathrm{b}^2$. Although the uncertainty is large, still it may be concluded that the $K^\pi = 8^-$ band has a collectivity as large as that of the GSB. The goodness of the $K$-quantum number is also suggested by the absence of the $\Delta I = 2$ transition.

In the hafnium and tungsten region, some $K$-isomers were recently reported[4,5] to severely violate the $K$-selection rule in their decay mode. In the case of $^{176}$W, the $K^\pi = 14^+$ isomer is reported[5] to decay directly to the $K^\pi = 0^+$ GSB member with a branching ratio of >30%, which clearly challenges our understanding for the high-$K$ isomers. It is, therefore, very important to directly measure the $B(E2)$ values and $Q$-moments of the isomer bands by HSIB COULEX. Although the quality of the present data is not sufficient for such an analysis, it is possible to improve it in the future experiments.

References


1) Y. Gono et al.: *Nucl. Phys.*, **A557**, c341 (1993).
2) T. Morikawa et al.: *RIKEN Accel. Prog. Rep.*, **27**, 31 (1993).
3) E. Browne: *Nuclear Data Sheets*, **62**, 1 (1991).
4) N. L. Gjørup et al.: private communication.
5) B. Crowell et al.: *Phys. Rev. Lett.*, **72**, 1164 (1994).

# High-Spin States in $^{148}$Tb

E. Ideguchi, Y. Gono, S. Mitarai, A. Odahara, M. Kidera, M. Sibata, M. Oshima, T. Morikawa, Y. Hatsukawa, S. Hamada,* H. Iimura,* M. Shibata,* T. Ishii,* and T. Kishida

[NUCLEAR REACTIONS, $^{141}$Pr($^{13}$C,6n)$^{148}$Tb, High-Spin Isomer Beams.]

The recent progress of the experimental teqniques using unstable nuclear beams has made it possible to study nuclear structures in the extreme state which was not attainable experimentally in the past. In order to investigate extremely high-spin states of nuclei, the development of high-spin isomer beams[1] is going on at RIKEN Ring Cyclotron. For the time being the available isomers as secondary beams are high-spin yrast traps in N = 83 isotones[2-7] and high-K isomers[8] in the Hf region.

In the N = 83 region the high-spin isomers were found systematically. Figure 1 shows the systematics of the high-spin isomer of N = 83 isotones. The excitation energies and half-lives of these high-spin isomers are almost the same, i.e. ~8 MeV and ~1 $\mu$s respectively. This suggests the resembling structure of these yrast traps in the isotones. In these isotones $^{148}$Tb is one of the candidates as a high-spin isomer beam which can be produced by the $^{27}$Al($^{130}$Te,9n)$^{148}$Tb reaction. The $^{27}$Al target is easy to handle and resistant to heat up. In this reaction good separation of the reaction products from the primary beam is obtained since the magnetic rigidity of their optimum charge states is much different. Therefore a detailed study to get the information of the yrast trap of $^{148}$Tb was performed.

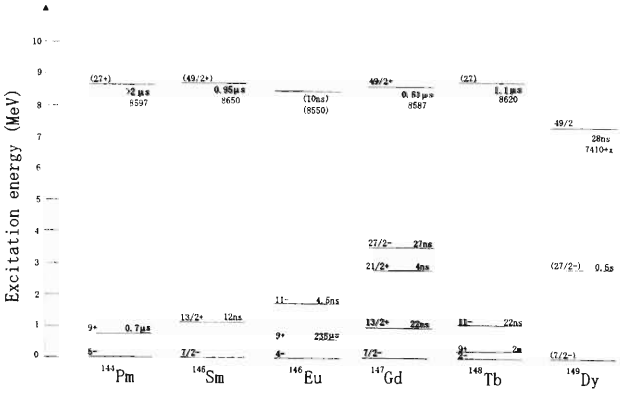


Fig. 1. The systematics of high-spin isomers of N = 83 isotones.

Broda et al.[9] reported the low lying level scheme of $^{148}$Tb and a half life of the high-spin isomer as 1.1 $\mu$s. But the decay scheme of the high-spin isomer was not established yet. The level structure above the high-spin isomer was not studied either.

In order to clarify the level structure of $^{148}$Tb an in-beam $\gamma$ experiment was carried out at the JAERI tandem accelerater facility. The high-spin states of $^{148}$Tb were populated by the $^{141}$Pr($^{13}$C,6n)$^{148}$Tb reaction. The $^{13}$C beams of 95, 98, 100 and 108 MeV were provided by the JAERI tandem accelerator. The self-supporting $^{141}$Pr foil target with the thickness of 4.7 mg/cm$^2$ was used. Six HPGe detectors with RIKEN BGOACS's were used. The detectors were placed at 4 different angles with respect to the beam axis, so that the information of the angular distribution and directional correlation (DCO) ratios could be obtained. From the analysis of the excitation function and the $\gamma$-$\gamma$ coincidence data a tentative level scheme was constructed up to the excitation energy of 11.8 MeV. And the spin of each state was assigned by the analysis of angular distribution of $\gamma$-rays. The half life of the high-spin isomer was confirmed to be 1.1 $\mu$s by the analysis of the time spectrum between $\gamma$-rays. Figure 2 shows the tentative level scheme so far constructed. The data analysis is still in progress.

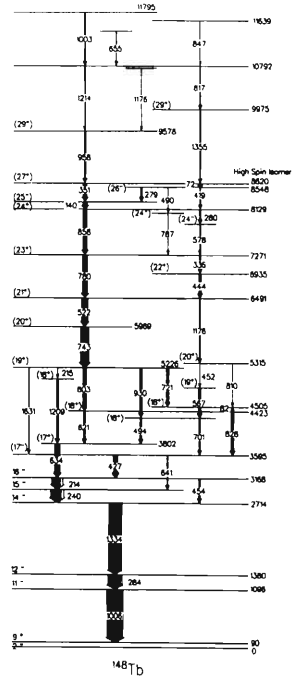


Fig. 2. Tentative level scheme of $^{148}$Tb.

* Japan Atomic Energy Research Institute

References
1) Y. Gono et al.: *Nucl. Phys.*, **A557**, 341c (1993).
2) T. Murakami et al.: *Z. Phys.*, **A345** 123 (1993).
3) A. Ferragut et al.: *J. Phys. Soc. Jpn.*, **62**, 3343 (1993).
4) A. Odahara et al.: *Z. Phys.*, **A350**, 185 (1994).
5) E. Ideguchi et al.: *Bull. Phys. Soc. Jpn.*, p. 108 (1993).
6) R. Broda et al.: *Z. Phys.*, **A305**, 281 (1982).
7) O. Bakander et al.: *Nucl. Phys.*, **A389**, 93 (1982).
8) T. Morikawa et al.: submitted to *Phys. Lett.*
9) R. Broda et al.: *Z. Phys.*, **A293**, 135 (1979).

# New Isomers in $^{174}$Hf

G. Liu, Y. Gono, T. Morikawa, E. Ideguchi, T. Kishida, K. Morita, H. Kumagai, A. Ferragut, A. Yoshida, M. Ishihara, T. Murakami, Y. Zhang, M. Oshima, Y. Hatsukawa, M. Sugawara, H. Kusakari, M. Ogawa, M. Nakajima, H. Tsuchida, S. Mitarai, A. Odahara, M. Kidera, M. Shibata, J.-C. Kim, and S.-J. Chae

[NUCLEAR REACTIONS $^{9}$Be($^{170}$Er, 5n)$^{174}$Hf, 7.0 MeV/u, Measured $E_\gamma$, $I_\gamma$, $\gamma\gamma$-coin.]

The N $\sim$ 106, Z $\sim$ 72 region is known to have many multi-quasiparticle isomers.[1] Take the Z = 72 (Hafnium) isotopic chain as an example, the isomeric state with spin and parity as $22^-$ in $^{176}$Hf, which corresponds to the 6 quasi-particle excitation, has been observed. For $^{174}$Hf, however, only the isomer of $14^+$ has been obeserved; although the states built on the $14^+$ isomer have been reported, they still remain uncertain.[2] More experimental data are required to understand the high spin isomer states of $^{174}$Hf.

The experiment was performed on the E1C high-spin isomer beam (HSIB) course[3] of the RIKEN Ring Cyclotron. The $^{174}$Hf was produced by the inverse-kinematic fusion reaction $^{9}$Be($^{170}$Er, 5n)$^{174}$Hf at the F0 target chamber, with the energy of $^{170}$Er beam being 7.0 MeV/u and the $^{9}$Be target thickness being 1.84 mg/cm$^2$. The $^{174}$Hf was selected and then transported to the F2 focal plane for measurement. The primary beam and other reaction products were eliminated by adjusting the slit at the F1 focal plane. The $\gamma$-$\gamma$ coincidence measurement of $^{174}$Hf was carried out by using two portable Ge detectors and one clover-type Ge with 4 units.[4] All the Ge detectors were calibrated with $^{152}$Eu and $^{133}$Ba $\gamma$-ray source.

The states built on the $14^+$ isomer have been reported with the first transition energy of 234 keV.[1,2] But such transition is not observed in our experiment. Figure 1 shows the delayed $\gamma$ spectrum with time-difference condition of $T_1$-$T_2$ > 500 ns subtracted by the spectrum with $T_1$-$T_2$ < $-$500 ns, and gated on the transitions of $K^\pi = 6^+$ band, which come from the decay of the $14^+$ isomer. There is no peak at 234 keV; the inconsistency indicates that the band built on the $14^+$ isomer still needs experimental data to confirm. Because the clover-type Ge detector was used in the $\gamma$-$\gamma$ coincidence measurement, the Compton effect becomes so serious that the background has many positive and negative bumps, and the real peak can be concealed in the background. Further analysis of the experimental data will be performed to eliminate such effect.

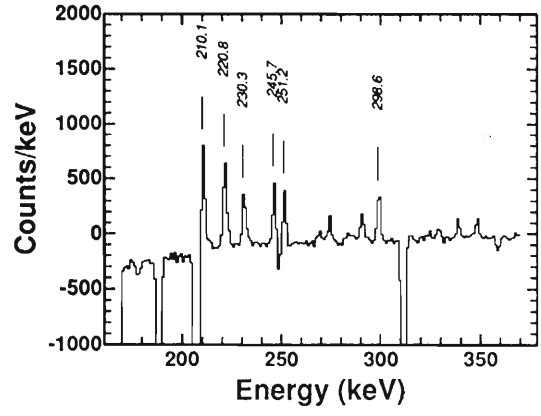


Fig. 1. The delayed $\gamma$ spectrum gated by the transitions of $K^\pi = 6^+$ band, including 231 keV, 269 keV, 443 keV, 520 keV, 552 keV, and 569 keV (see for details in the text). The positive peaks in the spectrum should be attributed to the transitions above $K^\pi = 14^+$ isomer and the negative peaks to the transitions below $K^\pi = 6^+$ isomer.

References

1) P. M. Walker: *Phys. Scripta*, **T5**, 29 (1983).
2) N. L. Gjorup et al.: Toronto Conf., p. 160 (1992).
3) T. Morikawa et al.: *RIKEN Accel. Prog. Rep.*, **27**, 31 (1993).
4) Catalog of Eurisys Mesures, France, 1994.

# Excitation Energy of Hot Nuclei Produced in $^{40}$Ar + $^{116}$Sn Reaction at $E/A$ = 30 and 37 MeV/u

K. Furutaka, K. Yoshida, A. Yajima,[*1] Y. Akeboshi,[*2] K. Matsuda,[*2] T. Murakami, J. Kasagi, T. Nakagawa, K. Yuasa-Nakagawa, Y. Futami, A. Galonsky, and G. Bizard

[ NUCLEAR REACTIONS: $^{40}$Ar + $^{116}$Sn at $E/A$ = 30, 36.4 MeV/u; measured neutron, proton and $\alpha$ particle energy spectra and angular distributions; moving source analysis. ]

To determine excitation energies of hot nuclei formed in heavy-ion fusion reaction and to study their properties, neutrons, protons and $\alpha$ particles emitted in $^{40}$Ar + $^{116}$Sn reactions at E/A = 30 and 37 MeV/u were measured in coincidence with heavy evaporation residues (ER).

Self-supporting foil of $^{116}$Sn (about 1mg/cm$^2$) was irradiated with 30 and 36.4 MeV/u $^{40}$Ar beams of about 15 enA served from the RIKEN Ring Cyclotron. Neutrons were detected with 22 liquid scintillation detectors placed between 30 and 155 deg. with respect to the beam axis and their energies were measured through the Time-of-flight (TOF) method. TOF lengths ranged from 0.8 m to 2.4 m. Overall time resolution was about 1.5 ns (FWHM) for prompt $\gamma$ rays. Protons and $\alpha$ particles were measured with $BaF_2$-plastic phoswich detectors,[1] in separate runs. Heavy residues were detected with 4 stacks of MCP-MCP-Si detector array placed ~10° with respect to the beam axis and mass $A_{ER}$ and velocity $V_{ER}$ of evaporation residues were deduced.

Events were divided into 4 bins according to $V_{ER}$ and examined separately. To deduce multiplicity $M_i$ and temperature parameter $\tau_i$, obtained spectra were analyzed using a Moving Source Model, in which isotropic Maxwellian volume (surface) emission of neutrons (protons and $\alpha$ particles) was assumed. Two emission sources were needed to reproduce the spectra: one is a pre-equilibrium-like source moving with roughly a half the beam velocity. The other is an equilibrium source moving with a similar velocity to $V_{ER}$.

From the obtained multiplicities and temperature parameters for the equilibrium source, thermal excitation energy $E_{th}$ was deduced using the following relation: $E_{th} = \sum_{i=n,p,\alpha} M_i(\langle E_i\rangle + E_{C,i} + B_i) + E_\gamma$, where $M_i$, $\langle E_i\rangle$, $E_{C,i}$, $B_i$ are multiplicity, average energy, Coulomb energy and binding energy, respectively. $E_\gamma$ is the energy removed through $\gamma$-ray emission. $\langle E_i\rangle = 3/2\tau_i$ for neutrons, while for protons and $\alpha$ particles $\langle E_i\rangle = 2\tau_i$.

In Fig. 1 the obtained excitation energies were plotted against $R = V_{obs}/V_{FMT}$ (bottom-up) together with energies obtained by using a usual kinematical relation based on the massive transfer model[2-4] (top-down), where $V_{FMT}$ is the velocity corresponding to full momentum transfer. As can be seen in the figure, the energy extracted by the present method is always smaller than that calculated from the massive transfer model, suggesting that in this incident energy region a simple massive transfer picture is no more valid.

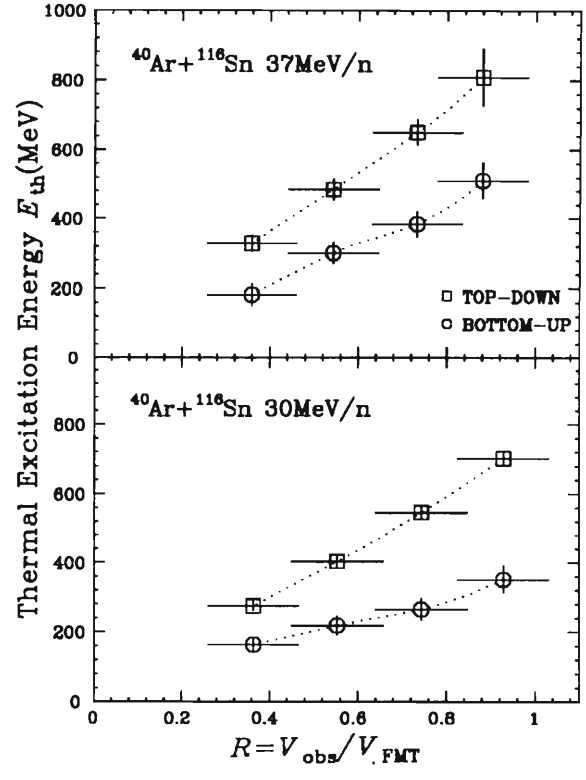


Thermal excitation energies calculated using multiplicities and average energies (○) are plotted against $R = V_{obs}/V_{FMT}$, together with those obtained by assuming a simple massive transfer model (□).

References

1) Y. Futami et al.: *Nucl. Instrum. Methods Phys. Res.*, **A326**, 513 (1993).
2) R. Wada et al.: *Phys. Rev.*, **C39**, 497 (1989).
3) A. Chbihi et al.: *ibid.*, **C43**, 652 (1991).
4) K. Yoshida et al.: *ibid.*, **C46**, 961 (1992).

*1 Toshiba Electric, Co.
*2 Mitsubishi Electric, Co.

# Angular Momentum Dependence of the Giant Dipole Resonance in Hot Nuclei

Y. Aoki, R. Sasaki, T. Ohtsuki, H. Yamazaki, J. Kasagi, K. Yuasa-Nakagawa, K. Furutaka, Y. Futami, K. Yoshida, T. Nakagawa, and T. Suomijarvi*

[ Heavy ion fusion reaction, Finite temperature nuclei, Giant dipole resonance, $\gamma$-ray multiplicity. ]

Our previous studies on the GDR in very hot nuclei[1] show that there exists a limiting temperature of nuclei for presence of GDR decay. In order to clarify the mechanism of the disappearance of GDR in hot nuclei, information on the GDR in the excitaion energy region between 150 and 200 MeV, especially on the angular momentum and excitation energy dependence of the resonance width, is very important. We have investigated properties of decay $\gamma$-rays emitted from nuclei at the excitation energy of about 150 MeV in the Ni, $^{92}$Mo, $^{116}$Sn + $^{40}$Ar reactions. Experiments were performed at the RIKEN Ring Cyclotron. Self-supporting foils were bombarded with $^{40}$Ar beams at $E/A$ = 7 MeV. High energy $\gamma$-rays from the fused compound nuclei were detected with two sets of high energy $\gamma$-ray detector consisting of 7 $BaF_2$ scintillators which were placed at 90° and 135° with respect to the beam direction at the distances of 15 cm from the target. In order to obtain a better detector response for high energy $\gamma$-rays, a lead collimator was placed in front of each detector, so that only the center scintillator was directly irradiated by the $\gamma$-rays from the target. The detector was covered by plastic scintillators to reject events due to cosmic-rays. A $BaF_2$ ball covering about 1/3 of $4\pi$ with 62 plastic-$BaF_2$ phoswich detectors[2] was used to measure low energy $\gamma$-rays and was served as a $\gamma$-ray multiplicity filter to select the angular momentum brought into the fused nuclei. Since light charged particles as well as $\gamma$-rays can be measured by the ball detectors, all the detectors are placed in a large scattering chamber (ASHRA), in order to obtain the correlation between the charged particle and the high energy $\gamma$-ray emissions.

Events due to neutrons and charged particles were rejected by the time-of-flight method together with a pulse shape analysis. High energy $\gamma$-rays were measured in coincidence with as many as 14 low energy $\gamma$-rays firing the ball detector. Spectra of high energy $\gamma$-rays corresponding to the different spin regions were obtained by setting a gate on observed distributions of the number of detectors fired by $\gamma$-rays ($M_\gamma$). In Fig. 1, 2, and 3, we show such spectra obtained in the Ni + $^{40}$Ar, $^{92}$Mo + $^{40}$Ar, and $^{116}$Sn + $^{40}$Ar reactions, respectively; open circles are data for $M_\gamma$ = 4 and 5, triangles for $M_\gamma$ = 6 and 7, and squares for $M_\gamma \geq 8$. As shown, all the spectra show a bump on an

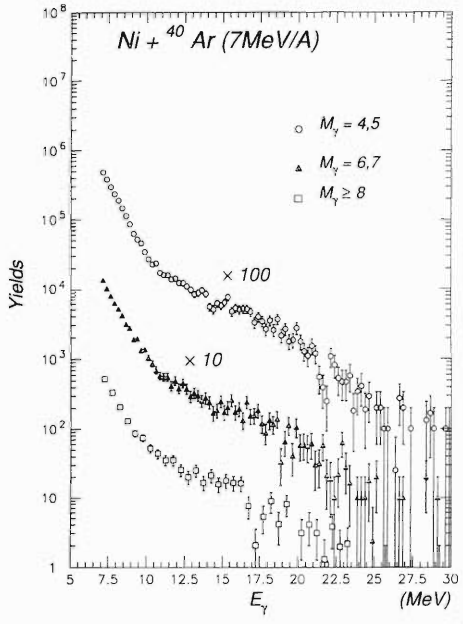


Fig. 1. Gamma-ray spectra obtained in the Ni + $^{40}$Ar reaction at $E/A$ = 7 MeV. Open circles show the spectrum for $M_\gamma$ = 4 and 5, triangles for $M_\gamma$ = 6 and 7, and squares for $M_\gamma \geq 8$.

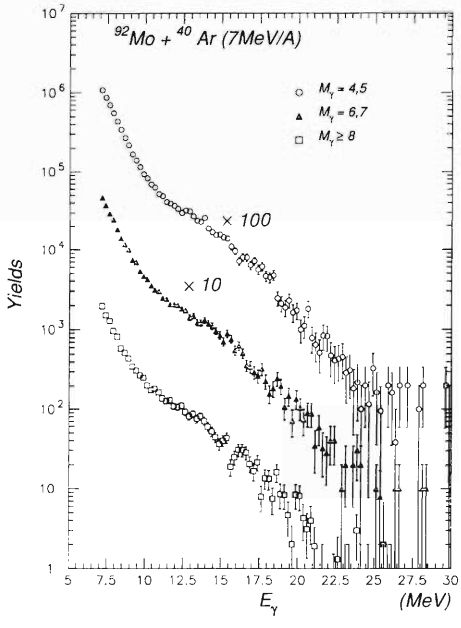


Fig. 2. Same as Fig. 1, except for spectra obtained in the $^{92}$Mo + $^{40}$Ar reaction.

* Institute de Physique Nuceaire, IN2P3-CNRS, Orsay, France

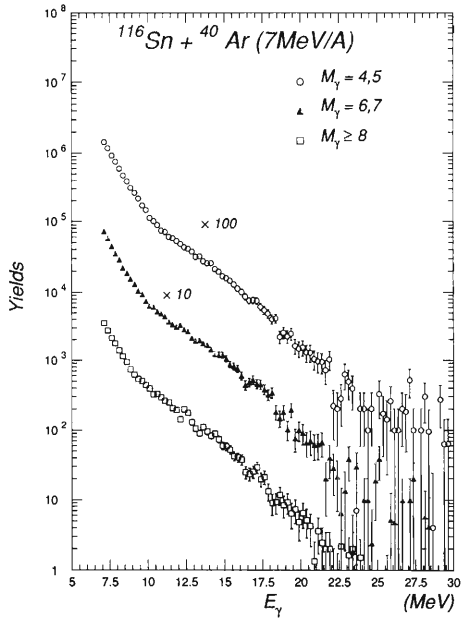


Fig. 3. Same as Fig. 1, except for spectra obtained in the $^{116}$Sn + $^{40}$Ar reaction.

exponentially fall-off curve for $E_\gamma > 10$ MeV, which is interpreted as arising from the decay of highly excited nuclei via GDR $\gamma$-ray emission. The high energy tail of the bump is less steep for the Ni + $^{40}$Ar reaction than for the other reactions. This observation is consitent with our understanding that the resonance energy becomes larger as the mass number decreases. The resonance energy depends on spin as well; it seems to decrease as $M_\gamma$ increases. In order to obtain the spin dependence of the resonance parameters quantitatively, the analysis with a statistical decay calculation is now in progress.

References

1) K. Yoshida et al.: *Phys. Lett.*, **B245**, 7 (1990); J. Kasagi and K. Yoshida: *Nucl. Phys.*, **A569**, 195c (1994).
2) Y. Futami et al.: *Nucl. Instrum. Methods Phys. Res.*, **A326**, 513 (1993).

# Development of Quasi-Monoenergetic Neutron Field with the Use of 80 to 135 MeV Protons Injected on Lithium

T. Nakamura, N. Nakao, M. Takada, E. Kim, M. Imamura, T. Shibata, Y. Uwamino, N. Nakanishi, S. Fujita, S. Nakajima, T. Ichihara, and T. T. Inamura

[ quasi-monoenergetic neutrons, p-Li reaction, TOF method, organic liquid scintillator, spallation cross section measurement. ]

Monoenergetic neutron fields are strongly needed for the measurement of neutron reaction cross sections, neutron penetration through matter, neutron detector efficiency and so on, since these data in the energy range above 20 MeV are quite poor. We developed a quasi-monoenergetic neutron field in the E4 beam line of RRC. $H_2^+$-ions of 80, 90, 100, 110, 120, and 135 MeV/nucleon energies were injected on a 1-cm thick $^7$Li target to produce quasi-monoenergetic neutrons at 0 degrees with respect to the proton beam axis. The neutron spectra were measured with a 12.7-cm-diam by 12.7-cm-long BC501A organic liquid scintillator placed 20 m away from the target. The spectra given by the TOF method are shown for 90, 100, 110, and 120 MeV proton energies in Fig. 1 and the lower energy parts of the spectra in Fig. 1 were analyzed by the unfolding method with the measured response function.[1] The peak neutron energies and FWHMs are 86.3, 96.5, 106.6, 116.7 MeV and 3.6, 3.3, 3.1, 2.9 MeV, respectively, for these four proton energies.

By irradiating these quasi-monoenergetic neutron beams, we measured the spallation cross sections of $^{12}$C(n,2n$\alpha$)$^7$Be, $^{27}$Al(n,spal)$^{22}$Na, $^7$Be and $^{209}$Bi(n,xn)$^{210-x}$Bi. The peak neutron fluence during sample irradiation was determined from the $^7$Be yield produced in the target by $^7$Li(p,n) reaction. The activities induced in the samples were measured with an HP-Ge detector. We found many radioisotopes of $^{207}$Bi, which were produced by $^{209}$Bi(n,3n) reaction down to $^{198}$Bi by $^{209}$Bi(n,12n), from the gamma-ray spectra and are now analyzing the measured spectra in order to get these cross section values from the reaction rates of identified isotopes and the neutron fluence.

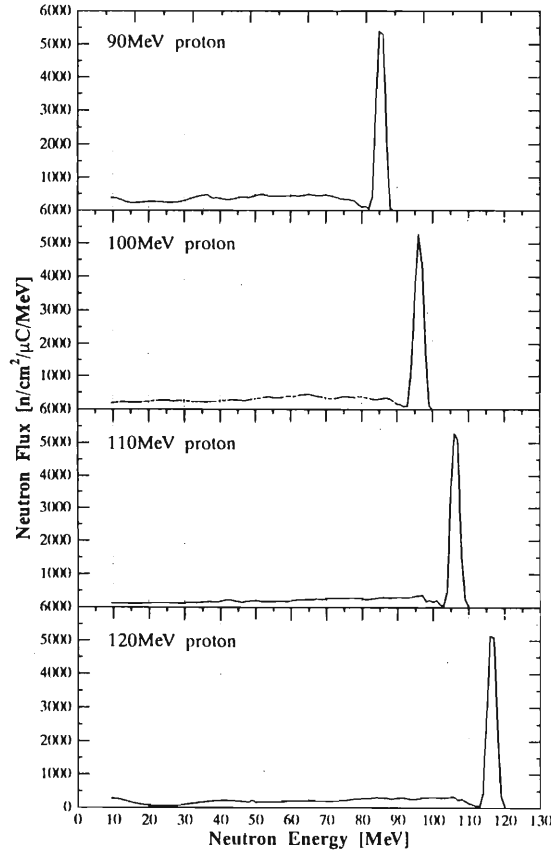


Fig. 1. Neutron spectra of 90, 100, 110, and 120 MeV p-Li reactions.

References

1) T. Nakamura et al.: *RIKEN Accel. Prog. Rep.*, **27**, 117 (1993).

# Muon Catalyzed Fusion in Thin Deuterium Films and Slow Negative Muon Production

P. Strasser, K. Ishida, S. Sakamoto,* K. Shimomura,* N. Kawamura,* and K. Nagamine

[Muon Catalyzed Fusion, Thin Solid Hydrogen Films, Slow Negative Muon Production.]

Muon catalyzed fusion of deuteron/deuteron reaction (dd-$\mu$CF) in thin deuterium films and slow negative muon emission[1] were investigated more intensively during the last experiment performed at the TRIUMF superconducting muon channel.

Two different contributions to the total fusion yield, i.e., one resulting from d$\mu$ atoms emitted from the primary $H_2/D_2$ layer via Ramsauer-Townsend effect and the other through "direct" muon stopping in the $D_2$ layer itself, were clearly distinguished in this last run. This was realized by comparing results with a thin deuterium layer ($\approx$0.8 mg/cm$^2$) deposited directly on the cold plate, and with those using the same deuterium layer thickness added to an $\approx$8 mg/cm$^2$ $H_2/D_2$ layer ($C_d \approx 10^{-3}$) (see Fig. 1). The ratio of "direct" fusion versus fusion via emitted d$\mu$ was found to be 0.19(4) at this target thickness, for a total fusion yield of $3.5(5) \times 10^{-4}$ per incident muons.

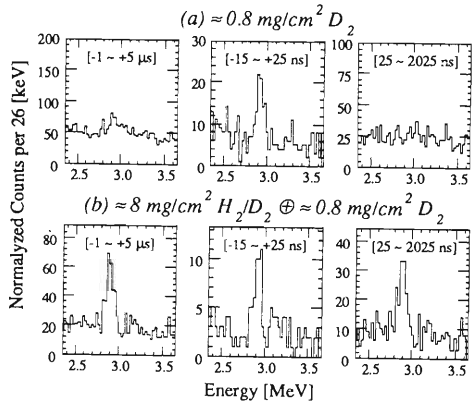


Fig. 1. SSB energy spectra: (a) with only $\approx$0.82 mg/cm$^2$ $D_2$, and (b) with $\approx$8 mg/cm$^2$ $H_2/D_2$ ($C_d \cong 0.001$) $\oplus$ $\approx$0.82 mg/cm$^2$ $D_2$.

The fusion proton time spectrum obtained with the pure deuterium target (see Fig. 2) shows a similar resonance behavior to that observed with warmer targets, and suggests that the quartet state is still resonant. However, the thermal energy of the target (3/2kT $\cong$ 0.4 meV) is far too low to reach the lowest resonance energy of $\sim$3 meV. An effective rate of molecular formation from F = 3/2 hyperfine state of 3.1(1.8) $\mu s^{-1}$ and an effective hyperfine conversion rate of 36(15) $\mu s^{-1}$ were extracted. The statistics being not sufficient enough, it is nearly impossible to discuss quantitatively these values. It is however close to the preliminary values obtained by Marshall et al.[2] with fusion neutrons in a similar experiment. The interpretation of the results is at present not clear, and the analysis, which has been so successful at higher temperatures in terms of hyperfine effects and muon molecular formation from thermalized d$\mu$, may be no longer adequate.

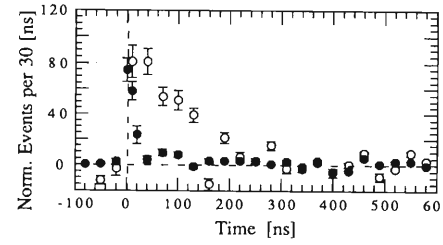


Fig. 2. Fusion proton time spectra with $\approx$8 mg/cm$^2$ $H_2/D_2$ ($C_d \cong 0.001$) $\oplus$ $\approx$0.82 mg/cm$^2$ $D_2$ (open circles) and with only $\approx$0.82 mg/cm$^2$ $D_2$ (closed circles).

Slow negative muon emission was also examined using an MCP detector. $\approx$10-keV muons collected by a large-acceptance spectrometer were successfully detected at the expected time-of-flight depending on the magnetic field settings (see Fig. 3). These slow muons are mainly produced by incident muons which are degraded through the target materials. The fusion yield in the $D_2$ layer being not sufficient enough, muons released after fusion can not yet be distinguished. It seems that nearly one order of magnitude is needed to identify the first slow muon re-emitted after dd-$\mu$CF. This can be realized by increasing the incident muon stopping number in the $H_2/D_2$ target, and by optimizing the $D_2$ layer thickness to maximize the yield of slow muons released from this layer.

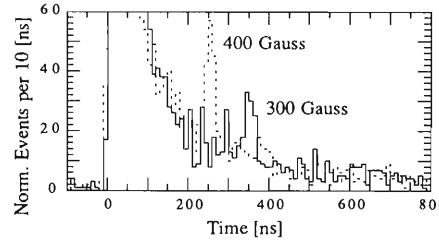


Fig. 3. Measured MCP time spectra with $\approx$8 mg/cm$^2$ $H_2/D_2$ ($C_d \cong 0.001$) $\oplus$ $\approx$0.34 mg/cm$^2$ $D_2$: (a) 300 Gauss and (b) 400 Gauss.

References

1) K. Nagamine et al.: *RIKEN Accel. Prog. Rep.*, **23**, 69 (1993).
2) G. M. Marshall et al.: *Hyperfine Interact.*, **82**, 529 (1993).

* Meson Science Laboratory, University of Tokyo

# 2. Atomic and Solid-State Physics

# Low-energy Electron Impact Ionization of Atomic Hydrogen

S. Watanabe and D. Kato*

Electron-impact ionization of hydrogen is one of the most fundamental processes involving one heavy and two light particles in disintegration without charge transfer. Theory has been considered largely incomplete because theoretical methods could evaluate cross sections with a far less precision than can the experiment.[1] Recently Bray and Stelbovics[2] have succeeded in bridging this long-standing gap from intermediate to high energies, however they left some gap on the low-energy side unresolved. It is our purpose to investigate the low-energy region rather close to the threshold.

It has been found that the Hyper-Spherical Close-Coupling method (HSCC), developed by J. Z. Tang et al.,[3] is applicable to the strongly correlated two-electron atomic system. However the HSCC suffers from a fundamental problem, that is, its incapability to represent the disintegration of the three-body system. In order to overcome this problem, we introduce a matching procedure as follows.

Suppose we enclose the internal region with a large enough box so as to contain all the dynamical information therein, and then project out the internal HSCC solutions to the delimited asymptotic solutions which satisfy the approximate Schrödinger equation,

$$\left(-\frac{1}{2}\nabla_1^2 - \frac{1}{2}\nabla_2^2 - \frac{1}{r_2} - E\right)\Psi \simeq 0 \qquad (r_1 \geq r_2) \quad (1)$$

where the effect beyond the monopole term is presumed negligible. Here let this box be a hypersphere of radius $R_m$. At $R > R_m$ we exclude the region where $r_2$ is greater than $r_m = R_m/\sqrt{2}$. This does not mean that the excluded region is entirely out of our consideration. It would mean instead we construct wave packets by integrating over suitable energy (or momentum) intervals so that the wave packets localized near the proton are formed.

Figure 1 shows the total ionization cross section $\sigma$ as well as $\sigma/E$, which is a more sensitive function of correlations, calculated in the combination of the HSCC with the matching procedure at energies up to 0.4 a.u. from the ionization threshold. The result is compared with the other theoretical results[2,4] and the Shah-Elliot-Gilbody experimental data.[1] The relative

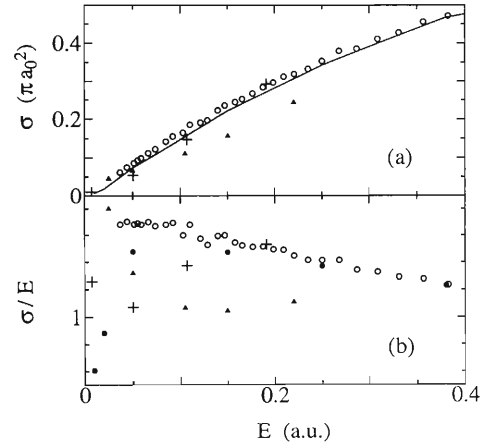


Fig. 1. (a) Total ionization cross sections. Solid line represents present work, and open circles experimental data from Shah-Elliot-Gilbody,[1] crosses the convergent close-coupling method,[2] and filled triangles the pseudo-state expansion method.[4] (b) $\sigma/E$, a function that reveals the details near the threshold. Filled circles represent present work, and the other symbols are as in (a).

difference in $\sigma$ between our result and the experiment is within a few % from $E = 0.1$ to 0.4 a.u. As for the function $\sigma/E$, our result is smooth whereas the Convergent Close-Coupling (CCC) result of Bray and Stelbovics[2] shows a noticeable fluctuation.

To conclude, we have succeeded in evaluating the low-energy ionization cross section with a precision comparable to that of the Shah-Elliot-Gilbody experiment down to ~0.1 a.u. The adiabatic basis functions adaptive to strong correlations should become progressively important for exploring even lower energy regions.

References

1) M. B. Shah, D. S. Elliott, and H. B. Gilbody: *J. Phys.*, **B20**, 3501 (1987).
2) I. Bray and A. T. Stelbovics: *Phys. Rev. Lett.*, **70**, 746 (1993) and private communications (1994).
3) J. Z. Tang, S. Watanabe, and M. Matsuzawa: *Phys. Rev.*, **A46**, 2437 (1992).
4) J. Callaway: *ibid.*, **A44**, 2192 (1991).

* Department of Applied Physics and Chemistry, University of Electro-Communications

# Mechanism of Enhancement of Some High-lying Resonance Series in Photoionization Spectra of Excited Helium

J.-Z. Tang and I. Shimamura

The study of high-lying doubly excited resonances of two-electron atoms is of fundamental and crucial importance for our understanding of strong electron–electron correlations in atoms in general. Experiments on photoionization have advanced to the stage of resolving these resonances of helium up to the manifold converging to the principal quantum number $n = 6$ of the inner electron.[1] Doubly excited states may be grouped into Rydberg series and these series may be characterized in terms of a set of approximate quantum numbers $K$, $T$, and $A$. Here, $K$ and $T$ are the quantum numbers pertaining to the angular correlation, while $A$ ($= +1, -1$, or 0, which are often abbreviated as $+$, $-$, or 0) pertains to the radial correlation.[2] Each member of these series may be specified by the notation $n(K,T)^A_{n'}$ with $n'$ the principal quantum number of the outer electron. Another often used quantum number is $v = (1/2)(n - 1 - K - T)$, which is the bending vibrational quantum number of the three-body system or the number of nodes in the angle $\theta_{12}$ between the position vectors $\mathbf{r}_1$ and $\mathbf{r}_2$ of the two electrons.

There exist nine (eleven) different $^1P^\circ$ Rydberg series of He below the $n = 5(6)$ threshold, of which only one series with the ground angular mode, i.e., $v = 0$, and with $A = +$ was observed in the photoionization experiment.[1] To elucidate this experimental finding, propensity rules, $\Delta v = 0$ and $\Delta A = 0$, were proposed on the basis of the nodal structure of the wave functions,[3] which affects significantly the dipole matrix elements. According to these rules, only Rydberg series of ground angular mode, $v = 0$, and with $A = +$ are populated dominantly for photoabsorption by $\mathrm{He}(1^1S)$. However, the rules $\Delta v = 0$ and $\Delta A = 0$ have never been tested experimentally on photoionization from excited states of helium.

In the present work, the hyperspherical close-coupling (HSCC) method[4] is used to compare the detailed structures in the photoionization spectra of $\mathrm{He}(1^1S)$ and $\mathrm{He}^*(2^1S)$ between the $\mathrm{He}^+(n = 4)$ and $\mathrm{He}^+(n = 6)$ thresholds; both the total photoionization cross section and partial cross sections for the production of $\mathrm{He}^+(n)$ are studied. Recall that the propensity rules were proposed on the basis of the correlation patterns or the nodal structures of the adiabatic wave functions. The two initial states, $\mathrm{He}(1^1S)$ and $\mathrm{He}^*(2^1S)$, have the same quantum numbers $K = 0$, $T = 0$, $n = 1$, and $v = 0$ and the same property $A = +$. Therefore the final states that are strongly excited must be common to both processes according to the propensity rule.[3] However, some doubly excited resonance series of excited angular modes that are either weak or unobservable in the ground-state spectrum are found to be greatly enhanced in the $\mathrm{He}^*(2^1S)$ spectrum. This corroborates that previously derived propensity rules do not apply, in fact, to photoionization of $\mathrm{He}^*(2^1S)$.

The physical reason of this result lies in the dependence of the electron-electron correlation pattern on the hyperradius $R$, which measures the size of the electron pair and is defined as $R = \sqrt{r_1^2 + r_2^2}$. The ground state, $\mathrm{He}(1^1S)$, is deeply bound. Thus its wave function concentrates in the small $R$ region, where the correlation pattern favors the dominant population of the final state of the ground angular mode. This is consistent with the experimental finding[1] and the propensity rule of Ref. 3. The metastable state, $\mathrm{He}^*(2^1S)$, on the other hand, is loosely bound and a significant portion of its wave function is concentrated in a larger-$R$ region, where the correlation pattern is so different from that in the small-$R$ region that the wave function may have a significant overlap with final Rydberg states with $v = 1$ as well as those with $v = 0$. This interpretation also suggests the generality of the enhancement of some resonance series in excited-state spectra.

Another effect of the electron-electron correlation in the initial state on the photoionization process has been observed in the partial cross sections $\sigma(n)$ for the production of $\mathrm{He}^+(n)$ ions. The calculated results show that for photoionization of the ground-state helium, the $n = 1$ partial cross section $\sigma(1)$ is dominantly large; while for photoionization of the metastable state helium, the $n = 2$ and 3 partial cross sections are dominantly large. The large $\sigma(3)$ implies that the electron–electron correlation is important for the metastable state $\mathrm{He}^*(2^1S)$ and that the independent-electron configuration $1s2s$ is inadequate.

An interesting feature of high-lying doubly excited resonance states is that the lowest one or more of those belonging to a series that converges to a threshold $\mathrm{He}^+(n)$ may lie below the threshold $\mathrm{He}^+(n - 1)$. Thus, as perturbers, these resonance states may interfere strongly with doubly excited resonance states belonging to the series that converge to the threshold $\mathrm{He}^+(n-1)$, resulting in overlapping resonances. Overlapping resonances near the $n = 5$ and 6 thresholds of $\mathrm{He}^+$ are studied and some resonances that are overlooked in the literature are uncovered. Details of this work have been published.[5]

References

1) M. Domke et al.: *Phys. Rev. Lett.*, **66**, 1306 (1991).
2) C. D. Lin: *Adv. At. Mol. Phys.*, **22**, 77 (1986).
3) H. R. Sadeghpour: *Phys. Rev.*, **A43**, 5821 (1991).
4) J.-Z. Tang et al.: *ibid.*, **A46**, 2437 (1992).
5) J.-Z. Tang and I. Shimamura: *ibid.*, **A50**, 1321 (1994).

# High-lying Doubly Excited Resonances in the Photodetachment of $H^-$

J.-Z. Tang and I. Shimamura

Doubly excited states of two-electron atomic systems, such as $H^-$, He, and $Li^+$, serve as prototypes for unraveling the nature of strong electron-electron correlations. Especially, those doubly excited states in which both electrons are highly excited exhibit their characteristic features. Recent high-resolution photoabsorption experiments have resolved clearly these high-lying doubly excited states of both He[1] and $H^-$.[2] Among the several computational methods for analyzing the detailed structures of these photoabsorption spectra, a hyperspherical close-coupling (HSCC) method[3] has been particularly successful in reproducing the experimental photoionization spectra of He.[4] A similar HSCC method combined with an analytic description of the wave function for the detached electron in the dipole field of excited hydrogen has been applied to the photodetachment of $H^-$ in the energy region of low-lying doubly excited resonances;[5] the source of the discrepancy among previously calculated resonance spectra just above the threshold for the production of the H atom in the $n = 2$ states has been clarified.

For a given total orbital angular momentum $L$, the total spin $S$, and parity $\pi$, each doubly excited state may be labeled by a set of quantum numbers $n\{v\}^A_{n'}$, or simply $v^A_{n'}$ when $n$ is evident. The principal quantum number $n$ is for the inner electron and $n'$ is for the outer electron. $A$ pertains to the radial correlation and may be represented by $+$, $-$, or 0. The bending vibrational quantum number $v$, representing the number of nodes in the angle $\theta_{12}$ between the position vectors $\vec{r}_1$ and $\vec{r}_2$ of the two electrons, pertains to the angular correlation.

We extend the work of Ref. 5 for application to the photodetachment spectra of $H^-$ involving high-lying doubly excited states up to the H($n = 7$) threshold. In Fig. 1(a), we show the calculated total cross section between the H($n = 5$) and H($n = 6$) thresholds. We see that some resonances with $A = -$ have also clear presence in the spectra with relatively large amplitudes but very narrow widths. Thus the modification of the propensity rule of Ref. 6 that we found for excited helium[4] is necessary also for the ground state of $H^-$ because it is only loosely bound.

The experimental partial cross sections[2] are compared in Fig. 1(b) with the calculated ones for the production of H($n = 5$) convoluted with the experimental energy resolution of 8.3 meV; a good agreement is seen over the whole spectrum. The narrow resonance $6\{0\}^-_7$ has a sizable cross section even after the convolution and is indeed observed in the experimental spectrum of Fig. 1(b). Narrower resonances with $A = -$ could

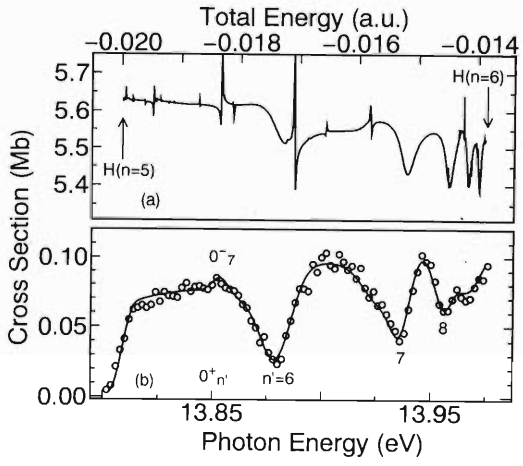


Fig. 1. Photodetachment spectra of $H^-$ between the $n = 5$ and 6 thresholds. (a) The total cross section. The narrow high peaks are resonances with $A = -$. (b) The partial one for the H($n = 5$) production (solid curve: convoluted with the experimental resolution of 8.3 meV; circles: experiment.[2] The states are labelled by $v^A_{n'}$.

be resolved clearly if the total photodetachment cross sections were measured with the same energy resolution.

Of particular interest among the calculated resonances are the Wannier ridge states $n\{0\}^+_n$, whose energies with respect to the double-electron-ionization threshold may be represented by the formula

$$E(n,n) = -(Z-\sigma)^2/(n-\mu)^2, \qquad (1)$$

where $Z$ is the nuclear charge and the screening parameter $\sigma$ and the quantum defect $\mu$ are parameters characteristic of the collective motion of the two electrons. We calculated and fitted the resonance energies for $H^-$, He, and $Li^+$ to Eq. (1). The results show that the screening parameter $\sigma$ is independent of $Z$. The quantum defect $\mu$ is found to be approximately proportional to $Z^{-1}$ even though the $Z$ values covered here are as small as $Z \leq 3$.

References

1) M. Domke, G. Remmers, and G. Kaindl: *Phys. Rev. Lett.*, **66**, 1306 (1992).
2) P. G. Harris et al.: *ibid.*, **65**, 309 (1990).
3) J.-Z. Tang, S. Watanabe, and M. Matsuzawa: *Phys. Rev.*, **A46**, 2437 (1992).
4) J.-Z. Tang and I. Shimamura: *ibid.*, **A50**, 1321 (1994).
5) J.-Z. Tang et al.: *ibid.*, **A49**, 1021 (1994).
6) H. R. Sadeghpour and C. H. Greene: *Phys. Rev. Lett.*, **65**, 313 (1990).

# The Energy Relaxation of Subexcitation Electrons in $H_2$ Gas

K. Kowari

Electrons with energies below the lowest electronic excitation threshold energy of the constituent molecule of a gas relax owing to elastic collisions, vibrationally inelastic collisions, rotationally inelastic collisions, and chemically reactive processes such as the electron attachment. These electrons are termed subexcitation electrons. The constituent molecules of a gas are taken to be in large excess. In previous papers,[1,2] we have carried out the time-dependent studies on the degradation and thermalization of the subexcitation electrons in $CH_4$[1] and $SiH_4$[2] with the method developed by Kowari et al.[1] The method is based on the Boltzmann equation with the Fokker-Planck operator for elastic collisions and a difference operator for inelastic collisions.

Thermalization and degradation of subexcitation electrons with initial energies of 1 eV, 3 eV and 5 eV in $H_2$ gas at a pressure of 1 atm and temperature of 300 K are studied with the numerical solutions of the Boltzmann equation. The collision term of the Boltzmann equation has the elastic term and inelastic term involving rotationally inelastic collisions as well as vibrationally inelastic collisions.

Figure 1 shows thermalization time with the initial energies of 1 eV. The solid curve represents the thermalization time which shows a change of the average energy of electrons obtained from the Boltzmann equation, and the dotted curve expresses the continuous-slowing-down approximation (CSDA) time. The thermalization time and CSDA time show a moderate agreement as a whole, and they agree very well in a short time range and deviate in a long time range.

The details of the present study will be described in Ref. 3. We give the summary on the details of the study as follows. Time evolution of the electron density distribution function, that of the cumulative degradation spectrum, and thermalization times are obtained. Time-dependent yields or collision numbers for rotationally and vibrationally inelastic processes are calculated by using the cumulative degradation spectrum. We extensively discuss the present thermalization times in comparison with experimental thermalization times and other theoretical values.

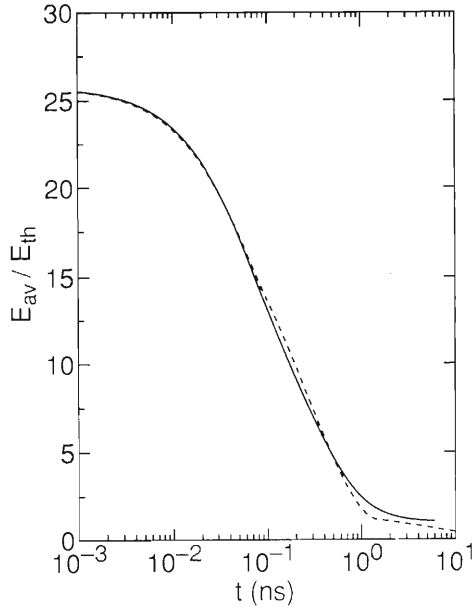


Fig. 1. The thermalization of the average electron energy in $H_2$ at 300 K; the initial electron energy in electron-volts is equal to 1. The dashed curve is the CSDA time.

References

1) K. Kowari, L. Demeio, and B. Shizgal: *J. Chem. Phys.*, **97**, 2061 (1992).
2) K. Kowari and B. Shizgal: *Chem. Phys.*, **185**, 1 (1994).
3) K. Kowari: to be published in *Phys. Rev.*, **A**.

# Single and Double Ionization of Helium by Slow Protons and Antiprotons

M. Kimura, I. Shimamura, and M. Inokuti*

The first series of atomic collision experiments using an antiproton ($\bar{p}$) beam of energy above 0.5 MeV was carried out in the low-energy antiproton ring (LEAR) at CERN.[1] In these experiments, the ratio $R_\sigma(\bar{p}) = \sigma^{++}/\sigma^{+}$ between double- and single-ionization cross sections $\sigma^{++}$ and $\sigma^{+}$ of He for $\bar{p}$ impact was found to be larger by a factor of two than that for proton ($p$) impact, $R_\sigma(p)$. Some theoretical attempts have been made to understand the conspicuous difference between $p$-impact and $\bar{p}$-impact double ionization.[2-5] The studies have shed light on the limitations of the independent-particle model and on the importance of electron correlation in these processes.

The recent upgrade in the LEAR facility has led to experiments by Hvelplund et al.[6] in a much lower energy regime down to 10 keV; see Fig. 1. The ratio $R_\sigma(p)$ decreased sharply as the energy decreased, while $R_\sigma(\bar{p})$ increased nearly monotonically. At 20 keV, $R_\sigma(\bar{p})$ was larger than $R_\sigma(p)$ by an order of magnitude.

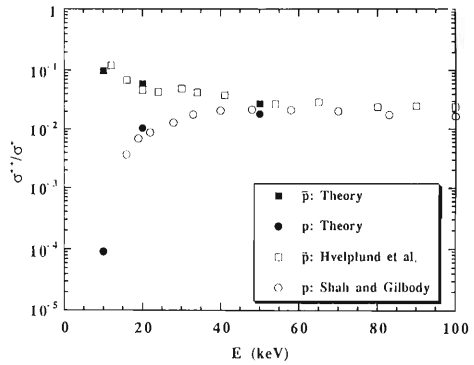


Fig. 1. Ratio of double to single ionization cross sections due to $p$- and $\bar{p}$-impact. Theoretical results are from the present work. The experimental results are taken from Ref. 7 for $p$ impact and from Ref. 6 for $\bar{p}$ impact.

Here we report the results of our investigation of double and single ionization for $p$ and $\bar{p}$ impact on the basis of a semiclassical molecular-state expansion method. In this method, the electronic motion is described quantum mechanically as a two-center molecular-state problem, and the relative motion between the two heavy particles is described classical mechanically. Discrete molecular electronic states were determined by the configuration-interaction method with the use of Slater-type orbitals as basis functions. Singly ionized continuum electronic states were obtained in the fixed-nuclei static-exchange approximation for elastic electron scattering from the neutral molecule $\bar{p}He^{+}$ or the molecular ion $(HeH)^{++}$. Those for doubly ionized states were constructed by using a perturbation method in which the interelectronic Coulomb potential is the perturbation and the terms up to the first order in the wave function are retained. The adiabatic wave-packet approach, which spans electronic continuum locally, was taken. A discretized sampling procedure, based on the Gauss quadrature, was used to select continuum states for the molecular-state expansion method. The number of channels included in the calculations was 150–250.

Figure 1 displays the present results for $R_\sigma$ along with the measurements for $\bar{p}$ impact by Hvelplund et al.[6] and for $p$ impact by Shah and Gilbody.[7] Good qualitative agreement between the theoretical and experimental results is seen. The present results clearly exhibit characteristic features of the increase and decrease in the ratios $R_\sigma$ for $p$ and $\bar{p}$ impact with decreasing energies. We examined details of each ionization probability (as a function of the impact parameter and the energy of the ejected electons), obtained from various test calculations. The presence of the positive charge deforms the electron cloud of He toward the incoming proton for charge transfer, and on further approach of the proton, some fractions of these electron distributions subsequently lead to single or double ionization by ladder-climbing the molecular states. For $\bar{p}$ impact, in contrast, the deformation of the electron cloud is in the opposite direction and the electronic binding energies decrease, which is the main mechanism for single ionization. The electron-electron interaction in the presence of $\bar{p}$ is of primary importance in the emission of another electron, leading to double ionization.

Details of this work were published elsewhere.[8]

* Argonne National Lab., U.S.A.

References

1) L. H. Andersen et al.: *Phys. Rev. Lett.*, **57**, 2147 (1986); *Phys. Rev.*, **A36**, 3612 (1987); *ibid.*, **A40**, 7366 (1989).
2) H. Knudsen and J. F. Reading: *Phys. Rept.*, **212**, 107 (1992).
3) L. Ford and J. F. Reading: *J. Phys.*, **B21**, L685 (1988); *ibid.*, **B23**, 2567; 3131 (1990).
4) J. McGuire: *Phys. Rev. Lett.*, **49**, 1153 (1982).
5) D. R. Schultz, R. E. Olson, and C. O. Reinhold: *J. Phys.*, **B24**, 521 (1991).
6) P. Hvelplund et al.: *ibid.*, **B27**, 925 (1994).
7) M. B. Shah and H. B. Gilbody: *ibid.*, **B22**, 3037; 3983 (1989).
8) M. Kimura, I. Shimamura, and M. Inokuti: *Phys. Rev.*, **A49**, R4281 (1994).

RIKEN Accel. Prog. Rep. **28** (1995)

# Ionization and Charge Transfer of Atomic Hydrogen in Collision with Multiply Charged Ions

N. Toshima

The close-coupling method has been widely used in various fields of atomic collision physics with the recognition that it is one of the most reliable and powerful theoretical approaches. It is mostly applied to scattering processes in the intermediate or low energy region, where the multiple scattering effect is so significant that perturbative approaches are not applicable. Although good agreement has been achieved with experimental data for various excitation and electron capture processes, extensive study of ionization processes has not been performed so far. The contribution of the continuum states is usually taken into account through discretized continuum states constructed by the diagonalization of the target and projectile Hamiltonians in terms of a set of square integrable basis functions. The purpose of inclusion of pseudocontinuum states has been in most cases to improve the description of the two-center nature of the electronic wave functions, and hence a sufficiently large number of positive-energy pseudostates have not been employed for the calculation of ionization cross sections.

Though the Slater-type orbitals have been mostly used for the construction of basis functions of the expansion, the existence of the electron translation factor (ETF), which accounts for the different translational motion of the two nuclei, makes impossible the analytic evaluation of the two-center matrix elements. Accurate numerical evaluation of the matrix elements becomes rather difficult when the collision energy is high owing to the rapid oscillation of ETF or when the states have many nodal structures. In the study of the Thomas mechanism, Toshima and Eichler[1] have avoided the difficulty in the numerical integration of the matrix elements by the introduction of the Gaussian-type orbitals (GTO) for the expansion. The GTO representation enables all the two-center matrix elements to be evaluated analytically with any desired accuracy regardless of the collision energy. It was demonstrated that the GTO representation is a very powerful method for the treatment of the processes in which continuum states play a decisive role. Most of the existing theoretical calculations of ionization cross sections of atomic hydrogen in collision with multiply-charged ions are based on perturbative approaches and their agreement with experimental data is not satisfactory at intermediate and low energy regions.[2] Toshima[3] investigated the ionization process in $C^{6+} + H$ collisions by the above-mentioned close-coupling method and he found that deep bound states of the projectile ion have a significant contribution to the ionization and excitation cross sections below 10 keV and the neglect of those states causes serious overestimation of the cross sections.

In this report we calculate ionization and electron capture cross sections for the collisions of atomic hydrogen with multiply-charged naked ions of the nuclear charges $Z = 2$–$8$,

$$\begin{aligned} A^{Z+} + H(1s) &\rightarrow A^{Z+} + p + e \\ &\rightarrow A^{(Z-1)+} + p \end{aligned}$$

by means of the close-coupling method based on the Gaussian-type-orbital expansion. The numbers of Gaussian-type orbitals and the ranges of the non-linear parameters are determined and optimized so as to produce the wave functions of all the bound states sufficiently accurately. With increasing the Gaussian orbitals still further, the eigenvalues of the pseudocontinuum states shift to lower energies as a whole and the spacings among them become smaller but the calculated ionization cross sections change little. The capture cross sections show more rapid convergence with increasing the number of Gaussian orbitals.

The contribution of the projectile continuum to the ionization is generally smaller than that of the target continuum and they show different dependence on the impact parameter. The impact parameter dependence of the ionization to the target continuum has resemblance to that of the excitation regardless of the collision energy while the ionization to the projectile continuum shows rather different behavior from that of the electron capture at low energies. The present calculations give ionization cross sections of atomic hydrogen systematically in good agreement with experimental data for various projectile charges in a wide energy range covering from the adiabatic transition region to the perturbative high-energy region. Simultaneously they produce highly reliable cross sections for excitation and electron capture. The details of the results are presented in a separate paper.[4]

References

1) N. Toshima and J. Eichler: *Phys. Rev. Lett.*, **66**, 1050 (1991); *Phys. Rev.*, **A46**, 2564 (1992); N. Toshima: *J. Phys.*, **B26**, L281 (1993).
2) M. B. Shah and H. B. Gilbody: *J. Phys.*, **B16**, L449 (1983).
3) N. Toshima: *ibid.*, **B27**, L49 (1994).
4) N. Toshima: *Phys. Rev.*, **A50**, 3940 (1994).

# Magnetization of Ferromagnetic Clusters

G. Bertsch,* N. Onishi, and K. Yabana**

Dynamics of small clusters, composed of a ferromagnetic material like iron, in the magnetic field of a Stern-Gerlach magnet (SG) has been studied experimentally through observations of the deflection profile.[1-4] The angular momentum of clusters is dominantly carried by nuclei constituting clusters. The relative motion of nuclei occuring in shape oscillation, is not expected to be important, and hence clusters may be considered to behave as a rigid-body. On the other hand, the magnetic moment of clusters coupled with the magnetic field, is due to the electron spin polarized to a certain direction. The coupling of the total electron spin with a rigid body is assumed to be so strong that the direction of spin polarization of electrons is frozen along an axis of the rigid-body.[5-7]

The dynamics is studied in classical mechanics. It is justified that, because the moment of inertia is extremely large, highly excited states of large angular momentum are populated at temperature of the beam source. Therefore the unit of angular momentum $\hbar$ is vanishingly small. An advantage of the analysis of the motion in terms of classical mechanics is to understand the associated dynamics more clearly and intuitively. We treat a simple case of an axially symmetric rotor in which the direction of magnetization is along the symmetry axis. The density of clusters in the beam is considered to be also small enough that they are isolated. For an isolated system of the simple model, the dynamical variables are separated into rotation, precession and nutation, and the motion is solved completely in analytic form.[8]

The variation of magnetic field, which takes place in entering into a SG magnet, is assumed to be small enough in comparison with a typical period of the motions; this is called the adiabatic assumption. In the assumption, an adiabatic invariance for the nutation is found, which relates the total angular momentum conserved outside of the magnet to the total energy in the magnet through adiabatic continuation. We derive a scaling law in which the magnetization and the deflection profile are functions of the magnetic field and the temperature only through the ratio of the magnetic field strength to the temperature $\mu_0 B/k_B T$ like in the Langevin formula of magnetization in the canonical ensemble. This scaling law implies that the model has not any structure giving a characteristic scale for energy and angular momentum. We also discuss two limits of weak-field and/or high-temperature and *vice versa*.

Our results reveal that a simple model such as a rigid-body with frozen electron spin is not able to explain the experimental data; the magnetization curve versus magnetic field strength has a dip at high temperature. Now we are working on an intermediate coupling model of electron spin with a rigid-rotor. The strength of coupling gives a certain temperature at which the structure change takes place in magnetization, and the scaling law may be violated.

References

1) D. M. Cox et al.: *Phys. Rev.*, **B32**, 7290 (1985).
2) W. de Heer, P. Milani, and A. Chatelain: *Phys. Rev. Lett.*, **65**, 488 (1990).
3) J. P. Bucher, D. C. Douglass, and L. A. Bloomfield: *ibid.*, **66**, 3052 (1991).
4) I. Billas, J. Becker, and W. de Heer: *Z. Phys.*, **D26**, 325 (1993).
5) P. J. Jensen and K. H. Bennemann: *ibid.*, p. 246.
6) A. Maiti and L. M. Falicov: *Phys. Rev.*, **B48**, 13596 (1993).
7) G. F. Bertsch and K. Yabana: *ibid.*, **A49**, 1930 (1994).
8) H. Goldstein: in Classical Mechanics, Addison-Wesley, p. 213 (1981).

* Institute for Theoretical Nuclear Physics, University of Washington
** Faculty of Science, Niigata University

# Lifetimes of the 3p $^2$P Levels of Na-like Nb

R. Hutton, S. Huldt, B. Nyström, I. Martinson, K. Ando,
T. Kambara, Y. Kanai, Y. Nakai, and Y. Awaya

We have used the techniques of beam-foil spectroscopy to investigate the atomic structure of Na-like Nb. The lifetimes of the 3p $^2$P levels have been investigated using the ANDC (Arbitrary Normalized Decay Curve) method of cascade correction. This was shown to be essential in a previous beam-foil study[1] of 3p $^2$P lifetimes for Na-like Ti, Fe, Ni, and Cu. The measurements presented here bridge the gap between the old work up to Na-like Cu and newer data from Träbert et al. for Na-like Xe and Au.[2]

The experiments were done using a beam of 183 MeV Nb ions provided by the RILAC. Details of the experimental setup can be found in Ando et al.[3] The beam-foil spectra of Nb showed the 3s $^2$S – 3p $^2$P$_{1/2,3/2}$ resonance doublets, at 135.1 Å and 182.7 Å, as well as the 3p $^2$P – 3d $^2$D lines at 109.57 Å and 131.69 Å. A section of the spectrum is shown in Fig. 1. The decay curves of the four Nb lines were measured carefully. Examples of the decay curves are shown in Fig. 2. As demonstrated earlier,[1] cascading from 3d levels to 3p levels must be corrected for, to avoid systematic errors in the 3p lifetime values. This was accomplished by using the ANDC method of Curtis et al.[4] which is based on joint analysis of the decay curves of the primary level (the lifetime which is to be determined) and of the levels that feed it. In the present work the ANDC analysis was performed by means of the CANDY computer code.[5] The lifetime values obtained in this way are $t = 29 \pm 2$ ps for the 3p $^2$P$_{3/2}$ level and $t = 70 \pm 5$ ps for the 3p $^2$P$_{1/2}$. These data are in excellent agreement with the theoretical values,[6] which are 28.55 ps and 68.77 ps for these levels.

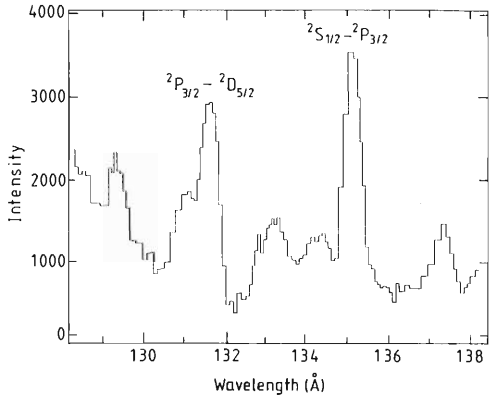


Fig. 1. This figure shows a small wavelength region of a beam-foil spectrum recorded for 183 MeV Nb.

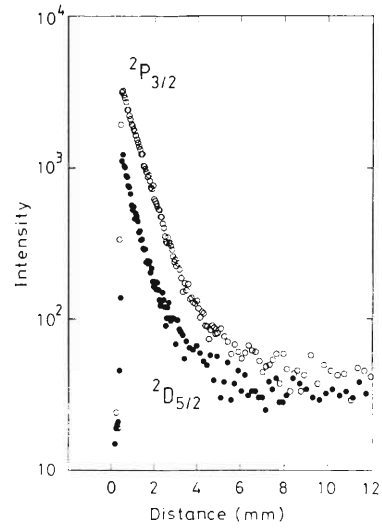


Fig. 2. Decay curves for the 3s $^2$S$_{1/2}$ – 3p $^2$P$_{3/2}$ and 3p $^2$P$_{3/2}$ – 3d $^2$D$_{5/2}$ transitions in Na-like Nb.

References

1) R. Hutton, L. Engström, and E. Träbert: *Phys. Rev. Lett.*, **60**, 2469 (1988).
2) E. Träbert, J. Doerfert, J. Granzow, R. Buttner, U. Staude, K. H. Schartner, P. Rymuza, P. H. Mokler, L. Engström, and R. Hutton: *Phys. Lett.*, **A188**, 355 (1994).
3) K. Ando et al.: *J. Spectr. Soc. Jpn.*, **41**, 370 (1992).
4) L. J. Curtis, H. G. Berry, and J. Bromander: *Phys. Lett.*, **A34**, 169 (1971).
5) L. Engström: *Nucl. Instrum. Methods*, **202**, 369 (1982).
6) C. E. Theodosiou and L. J. Curtis: *Phys. Rev.*, **A38**, 4435 (1988).

# Mg-like Intercombination Lifetimes for Zr and Nb

R. Hutton, S. Huldt, B. Nyström, I. Martinson, K. Ando,
T. Kambara, Y. Kanai, Y. Nakai, and Y. Awaya

Intercombination (spin-forbidden) transitions such as the $3s^2\ ^1S_0 - 3s3p\ ^3P_1$ line in Mg-like ions are of considerable interest in plasma diagnostics. For instance, the ratio of the intensities of close-lying allowed and spin-forbidden lines can be used to determine electron densities in plasmas. Also, calculation of these intercombination rates requires careful treatment of several factors, e.g., configuration mixing, spin-orbit interaction and relativistic effects.

In this work beam-foil studies were made for Mg-like Nb and also for the neighboring element Zr. In the latter case two isotopes, $^{90}$Zr and $^{91}$Zr, were investigated with the aim of searching for possible nuclear-spin induced effects on the decay of the $3s3p\ ^3P_1$ level. The beam-foil setup is described in Ando et al.[1] Because of their comparatively long lifetimes the intercombination lines are often weak features in complex spectra or even masked by stronger, allowed transitions. One of the unique properties of the beam-foil method is that time-delayed spectra[2] (recorded at a certain distance downstream from the foil) can be obtained. This feature can be used to enhance lines from long-lived levels. We used this property to identify the $3s^2\ ^1S_0 - 3s3p\ ^3P_1$ line in the Zr and Nb spectra.

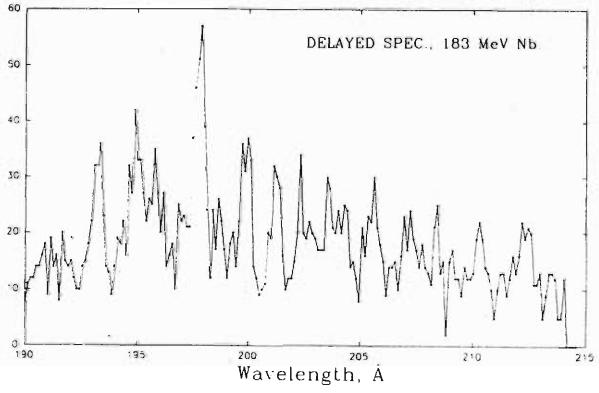


Fig. 1. Delayed spectrum for 2 MeV/nucleon Nb ions after foil excitation. The $3s^2\ ^1S_0 - 3s3p\ ^3P_1$ intercombination line is at 197.68 Å.

Such a spectrum for Nb is depicted in Fig. 1. The Mg-like intercombination line can be seen at 197.7 Å. Figure 2 shows decay curves measured for this transition both with and without a small (6 gauss) magnetic field to diverge beam related electrons; see Hutton et al.[3] The values we find for the lifetime of the $3s3p\ ^3P_1$ levels in both Zr and Nb are about 20% shorter than current theoretical values (e.g., Huang and Johnson[4]) This discrepancy is the subject of further experimental and theoretical investigation.

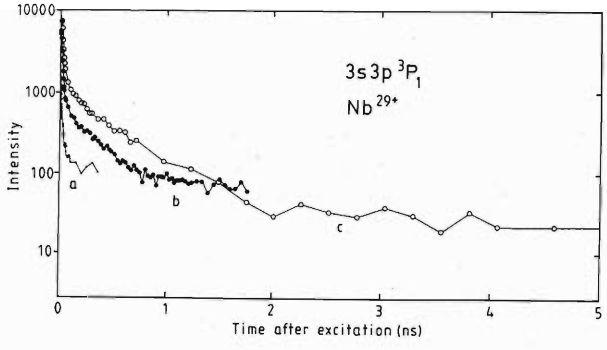


Fig. 2. Decay curve for the $3s^2\ ^1S_0 - 3s3p\ ^3P_1$ transition for Mg-like Nb recorded at a beam energy of 183 MeV. (a) Background decay (i.e., a decay curve taken in the position of no apparent line), (b) a decay curve taken with no magnetic field, and (c) a decay curve taken with a magnetic field to remove beam-related electrons.

References

1) K. Ando et al.: *J. Spectr. Soc. Jpn.*, **41**, 370 (1992).
2) E. Träbert: *Physica Scripta*, **48**, 699 (1993) and references therein.
3) R. Hutton et al.: Proc. Int. Conf. on the Physics of Highly Charged Ions (HCI), Vienna 1994. To be published in *Nucl. Instrum. Methods Phys. Res.*
4) K. N. Huang and W. R. Johnson: *Nucl. Instrum. Methods Phys. Res.*, **B9**, 502 (1985).

# Beam-Foil Spectra of Highly Charged Neon

K. Ishii, Y. Kimura, T. Nishida, and K. Ando

In this report we present the results of a beam-foil study of the spectra of highly charged neon ions in the visible and near UV regions. The spectra of NeVI-NeIX have been thus far studied in the VUV region.[1-5] The beam-foil method is efficient for populating states with high $n$ and $l$ quantum numbers in highly charged ions. The excited states thus created decay radiatively with emission of visible and near UV photons as well as VUV ones. The observation of the transition makes it possible to establish the high lying energy levels and to estimate the ionization potentials. This method has been used extensively; see e.g. Ref. 6 for chlorine, Ref. 7 for oxygen, and Ref. 8 for fluorine. Neon beams at the energy of 10 MeV from RILAC were sent through a thin carbon foil with a thickness of 10 $\mu g/cm^2$. The photon emission of the post foil beams was observed in perpendicular direction to the beam, by use of a monochromator (NIKON G-250) and a photomultiplier (Hamamatsu R585) in conjunction with the standard NIM modules. The photoelectron pulses were stored in a microcomputer together with the integrated beam current and the clock signals. The whole spectrum was recorded between 3000Å and 6000Å with a slit width of 0.5 mm. The partial spectrum recorded with higher resolution by refocusing the monochromator and by narrowing the slit width, is displayed in Fig. 1.

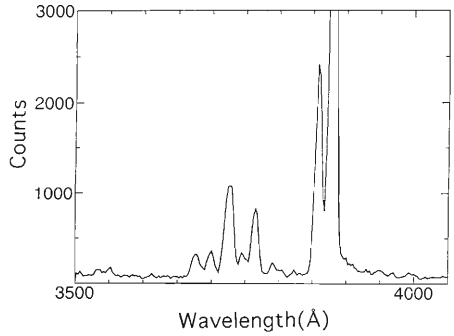


Fig. 1. Neon spectrum taken at 10 MeV.

The resolution is however not high enough to identify the individual lines of 2p3p–2p3d transition. In Table 1, the tentative assignment is listed. Further study is now in progress with emphasis on the higher resolution.

Table 1. Tentative assignment of observed lines.

| Wavelength (nm) | Transition | Ion(Sequence) |
|---|---|---|
| 567 | $n$=8–9 | VII (Be) |
| 529 | 7–8 | VI (B) |
| 480 | 9–10 | IX (He) |
| 466 | 10–12 | VIII (Li) |
| 456 | 9–11 | VII (Be) |
| 450 | 11–14 | VIII (Li) |
| 434 | 8–9 | VIII (Li) |
| 389 | 7i–8k | VII (Be) |
| 386 | 7h–8i | VII (Be) |
| 377 | | |
| \| | 2p3p–2p3d | VII (Be) |
| 367 | | |
| 331 | 8–10 | VII (Be) |

References

1) K. Bockasten, R. Hallin, and T. P. Hughes: *Proc. Phys. Soc.*, **81**, 522 (1963).
2) B. C. Fawcett and F. E. Irons: *ibid.*, **89**, 1063 (1966).
3) G. Tondello and T. M. Paget: *J. Phys.*, **B3**, 1757 (1970).
4) H. Hermansdorfer: *J. Opt. Soc. Am.*, **62**, 1149 (1972).
5) L. Barretle, D. J. G. Irwin, and R. Drouin: *Physica Scripta*, **12**, 113 (1975).
6) R. Hallin, J. Lindskog, A. Marelius, J. Pihl, and R. Sjödin: *ibid.*, **8**, 209 (1973).
7) B. Denne, L. Engström, S. Huldt, J. O. Ekberg, L. J. Curtis, K. Ishii, E. Veje, and I. Martinson: *ibid.*, **21**, 151 (1980).
8) L. Engström: *ibid.*, **29**, 113 (1984); *ibid.*, **31**, 379 (1985).

# Binary Encounter Electron Peaks for 0° Electrons in Collisions of $Bi^{q+}$

Y. Kanai, T. Kambara, M. Oura, Y. Nakai, T. M. Kojima, S. Kravis, and Y. Awaya

Previously, we studied the binary encounter electron (BEe) peaks in collisions of $Bi^{q+}$ on $H_2$, He, and Ar at 0° electron emission angle with varying incident charge states ($q$) and incident energies.[1-3] The BEe has been known as the electron emitted from the target essentially by the binary encounter collisions between the projectile ions and the target electron in the high energy ion-atom collisions. Recently, the shift $\Delta E_b$ in the peak energy from the value for pure binary collisions and the double differential cross sections of the BEe have been measured by many other groups to study the production mechanism of the BEe, and compared with the theoretical works quantitatively.[4] Theoretical calculations can explain the $q$ dependence of the double differential cross sections of the BEe in the simple collision system (bare and H-like ions on $H_2$, He). However, it is rather difficult to calculate them for complex collision systems involving the projectile ions with many electrons . We have measured the $q$ dependence of the double differential cross sections of the BEe in the collisions of $Bi^{q+}$ with $H_2$, He, and Ar, and compared it with that for simple collision systems to get the information of the production mechanism of the BEe. We have also measured the $q$ dependence of the BEe peak shift in the same collision systems in a wide range of $q(10 \leq q \leq 34)$. From the previous experiments,[1-3] we can say, qualitatively, that the features of the BEe peaks in the $Bi^{q+}$ collisions are as follows: (1) The peak intensity depends on the incident charge, (2) the peak shift depends on the incident charge, and (3) the peak width depends on the Compton profile of the target electrons. These features are almost the same as those of the BEe peaks in the simple collision systems. The presence of many orbital electrons of the projectile ions does not seem to affect the main features of the BEe peaks.

In this report, we present the $q$ dependence of the BEe peak shift for 0.8 MeV/nucleon $Bi^{q+}$ on $H_2$ and He collisions and compare it with a simple model, quantitatively.

The beams of $Bi^{q+}$ from the RILAC were magnetically analyzed, collimated by two sets of four-jaw slits system and focused on the target gas cell. Single collision conditions have been verified experimentally.

Figure 1 shows the $q$ dependence of the BEe peak shifts $\Delta E_b$, i.e., the difference between $4E_p m/M$ and the observed peak energy, where $E_p$ is the projectile energy, $m$ the electron mass, and $M$ the projectile mass. Here, we compare our results with the peak shift given by a simple model (the adiabatic tunneling model).[5] In this model, there is a characteristic distance $R_c$, called the tunneling distance. When the projectile ion comes to this distance from the target, the target electrons tunnel to a projectile continuum state. After that, the tunneled electrons collide with the projectile ion as free electrons having effective collision velocity $v_{eff} = (4v^2 - \Delta E_b)^{1/2}$. This model gives the energy shifts $\Delta E_b$ and $R_c$ as follows:

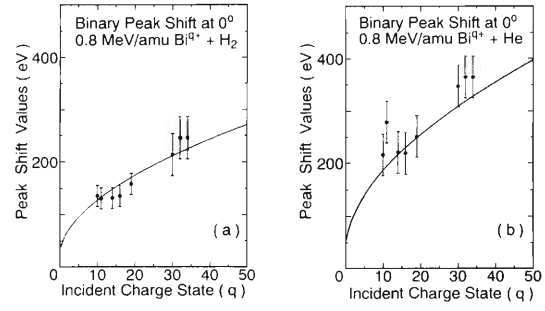


Fig. 1. Binary encounter peak shift in the collisions between 0.8 MeV/nucleon $Bi^{q+}(q = 10\text{–}34)$ and $H_2$, He. Circles: observed values. Solid line: adiabatic tunneling model. (a) $Bi^{q+}$ - $H_2$ system, (b) $Bi^{q+}$ - He system.

$$\Delta E_b = I_t + \frac{q_i}{R_c} + v^2 - v^2\sqrt{1 - \frac{2I_t}{v^2} - \frac{2q_i}{R_c v^2}} \quad \text{(a.u.)} \quad (1)$$

$$R_c = \frac{3}{4Z_2}\left(1 + \frac{16q_i}{3Z_2}\right) \quad \text{(a.u.)}. \quad (2)$$

Here, $I_t$ is the ionization potential of the target, $Z_2$ the target (effective) atomic number, and $v$ the collision velocity. Our results are shown in Fig. 1. The calculated peak shift values are also shown in Fig. 1 as the solid line. Our results are in good agreement with the prediction of the adiabatic tunneling model. In order to get the $q$ dependence of the double differential cross section of the BEe in this model, we need to calculate the double differential cross section of the binary encounter collisions between the free electron having $v_{eff}$ and the Bi ions.

By using heavy projectile ions with many electrons, we could observe clearly the incident charge state dependence of the BEe peak energy.

References

1) Y. Kanai et al.: Proc. 6th Int. Conf. on the Physics of Highly-Charged Ions (Manhattan, Kansas, 1992), edited by P. Richard, M. Stöckli, and C. D. Lin, AIP, New York, p. 315 (1993).
2) Y. Kanai et al.: *RIKEN Accel. Prog. Rep.*, **26**, 65 (1992).
3) Y. Kanai et al.: *ibid.*, **27**, 64 (1993).
4) M. Sataka et al.: *J. Phys.*, **B27**, L171 (1994).
5) P. D. Fainstein et al.: *Phys. Rev.*, **A45**, 6417 (1992).

# Binary Encounter Electron Production at Relativistic Collision Velocities

B. D. DePaola, Y. Kanai, P. Richard, Y. Awaya, T. Kambara, and Y. Nakai

Recently, there has been much interest in binary encounter electrons (BEe). These are electrons which are ejected from a target, generally in gas or vapor phase, following a "binary" collision with a fast projectile. That is, in a classical model, these are electrons which suffer an impulsive billiard-ball-like collision and are ejected with some distribution centered about a velocity which is (non-relativistically) twice that of the incoming projectile. The distribution in this simple model is just the initial momentum distribution of the target electron, projected onto the collision axis, i.e. the Compton profile. In this simple model, the cross section for BEe production is given by the Rutherford scattering formula.

This model, with some refinements, has been remarkably accurate in predicting BEe peak locations, shapes, and absolute, differential (in angle) cross sections. All experimental tests of this simple impulse model have been done at non-relativistic projectile energies. In the experiments described here, a highly charged ion beam was used to investigate BEe production, differential in angle, and at relativistic velocities, using solid targets. Thus, the experiments discussed here differ from those done previously in several significant ways. Specifically, it was desired to measure *relative* cross sections for BEe production as a function of electron emission angle. Also, it was desired to measure the shape of the BEe emission peak (within the resolution of the electron spectrometer) and the location of the BEe peak.

The apparatus used in these experiments consists of an ultra-high vacuum chamber, a remote-controlled foil positioner, and an electron spectrometer, whose entrance angle with respect to the projectile axis was remote-controlled. The projectile beam, 93 MeV/nucleon $Ar^{q+}$ ($q = 17, 18$) was passed through a thin carbon foil, followed by the electron spectrometer, and finally into a Faraday cup. Foils of various thickness, from 22 to 83 $\mu g/cm^2$, were used with no apparent difference observed in either the BEe peak width or position.

The electron spectrometer has been used at RIKEN in the past. It consists of a simple solenoid attached to specially shaped pole pieces. The electrons are made to pass between the pole pieces and are deflected through an angle related to their momenta before being detected in an electron multiplier (EM). The spectrometer has a momentum resolution of 3%. The spectrometer is scanned using an NEC pc-controlled power supply which sources a current through the solenoid. In scanning the spectrometer, counts from the EM are accumulated for a time proportional to the accumulated charge in the Faraday cup.

In Fig. 1 two typical electron spectra are shown. These are plots of accumulated electron counts versus spectrometer current (in Amperes). The spectra were taken at 0°, or along the projectile axis. The curve composed of circles is for $Ar^{17+}$ projectiles, while the curve composed of triangles is for $Ar^{18+}$ projectiles. In the $Ar^{17+}$ curve the sharp structure at about 0.25 Amps is the so-called cusp peak, corresponding to electrons captured or lost to the continuum of the projectile. At these velocities the cusp is almost entirely due to electron loss to the continuum, as evidenced by the

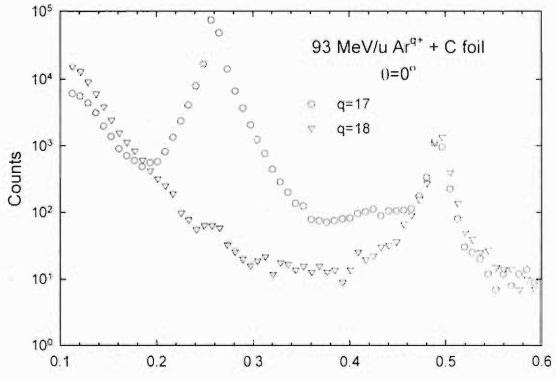


Fig. 1. Typical electron momentum spectra at 0°. The projectile is 93 MeV/nucleon $Ar^{q+}$. The circles are data for $q = 17$, while the triangles are for $q = 18$.

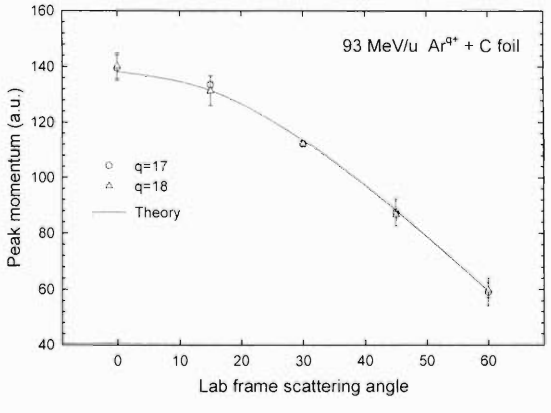


Fig. 2. The momentum of the peak of the binary encounter structure as a function of laboratory frame electron emission angle. The projectile is 93 MeV/nucleon $Ar^{q+}$. The circles are data for $q = 17$, while the triangles are for $q = 18$. The calculation is from a simple relativistic "billiard-ball" model.

almost complete lack of a cusp in the $Ar^{18+}$ data. Both curves show a structure at about 0.5 Amps. This is the so-called binary encounter electron peak, and was the focus of attention in this series of experiments.

In order to study the properties of the BEe peak as a function of emission angle, a series of spectra like those shown in Fig. 1 were taken over a range of emission angles from 0° to 60° (lab frame). Figure 2 shows a plot of the momentum of the peak of the BEe structure as a function of electron emission angle. Also shown in Fig. 2 as a solid line is the predicted location of the momentum of a free electron after suffering a billiard-ball-like collision with a 93 MeV/nucleon Ar projectile. The agreement is striking, indicating that the simple relativistic impulsive model is an accurate predictor of the final momentum of the scattered electron.

Analysis is currently underway to determine if the cross sections, differential in angle, are adequately described by Rutherford scattering, as is the case for lower velocity collision systems. It will also be interesting to see if the cross sections scale with projectile charge in the same way as in the lower velocity regime. It is well known that at lower velocities screening and interference effects are important in the BEe production cross sections. No relativistic theory for BEe currently exists, but it is thought that screening and interference effects should not be important at the velocities investigated here.

# Charge Distribution of Kr Ion Passing through Thin Carbon Foil at 36 MeV/nucleon

Y. Nakai, T. Kambara, Y. Kanai, T. M. Kojima, and Y. Awaya

We have measured the charge state distribution of Kr ion passing through a thin C foil for radiative electron capture (REC) X-ray experiments using $Kr^{36+}$ at 36 MeV/nucleon from RIKEN Ring Cyclotron. The charge state of Kr ion passing through the C foil was analyzed by the dipole magnet on the downstream of the C foil. A 2-dimensional position sensitive gas detector was located at the exit of the dipole magnet and used to count the Kr ions. The gas detector has a 1 mm spacing stripe electrode and a 2 mm spacing wire electrode for determination of horizontal and vertical position respectively, and has a cathode plane of conductive polymer foil. All the strips and wires on each electrode were connected each other with resistors. The position detection was accomplished by a charge division method. Its active area was 170 mm × 80 mm. The horizontal position spectrum is shown in Fig. 1.

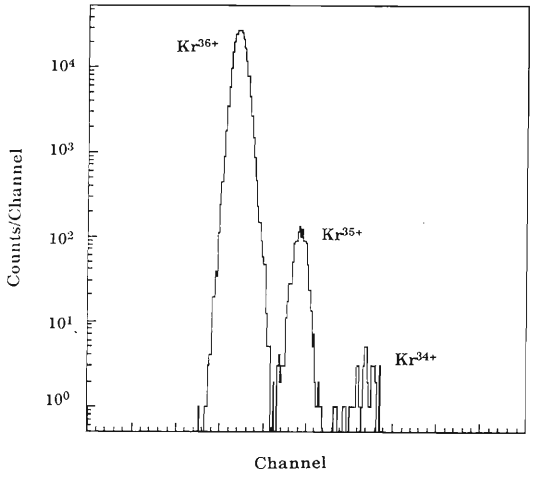


Fig. 1. The horizontal position spectrum. $Kr^{36+}$ and $Kr^{35+}$ peaks are shown.

The C foils of 10 $\mu g/cm^2$ and 20 $\mu g/cm^2$ were used. Moreover, the effective thickness along the beam axis was changed by tilting the 20 $\mu g/cm^2$ foil at 35°.

The number ratios between $Kr^{36+}$ and $Kr^{35+}$ and between $Kr^{35+}$ and $Kr^{34+}$ were measured. In the $Kr^{35+}$-$Kr^{34+}$ case, the fitting procedure was used for reduction of the yield of two charge states. The fraction of charge states less than 34+ was so small and we assumed the total number of incident particles was the sum of the numbers of $Kr^{34+}$, $Kr^{35+}$, and $Kr^{36+}$. The errors is only derived from the statistical one and the fitting procedure. The uncertainties of C-foil thickness and the absolute tilted angle are not exactly estimated yet. The fraction of charge state from 34+ to 36+ is shown in Fig. 2.

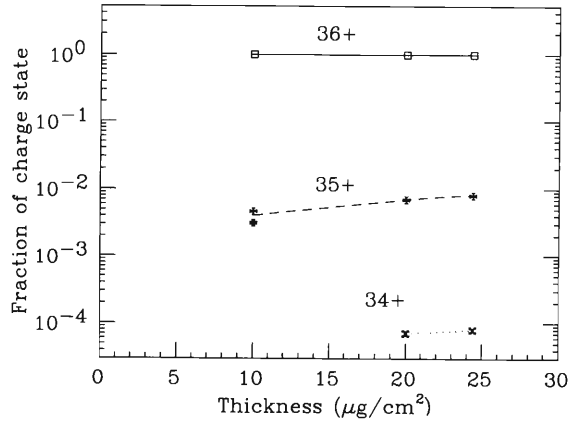


Fig. 2. The fraction of each charge state. The vertical error bars are smaller than symbol size. Two values at the thickness 10 $\mu g/cm^2$ are corresponding to the different runs. The uncertainties of foil thickness and absolute tilted angle of foils are not included in this figure.

# Momentum Distribution of Recoil Ions from 8.7 MeV $O^{7+}$-He Collisions

T. Kambara, Y. Awaya, Y. Kanai, Y. Nakai, T. M. Kojima, O. Jagutzki, and H. Schmidt-Böcking

We have measured the three-dimensional momentum distributions of the recoil ions from collisions between 8.7 MeV $O^{7+}$ ions and a target of He atoms in cases of pure ionization $O^{7+} + He \rightarrow O^{7+} + He^{+}$ and one-electron capture $O^{7+} + He \rightarrow O^{6+} + He^{+,2+}$ to study the dynamical processes between highly-charged heavy ions and few-electron atoms.

The longitudinal (parallel to the projectile) component of the recoil ion momentum from an ion-atom collision with velocity $v_p$ is expressed as:

$$p_{\parallel R} = -Q/v_p - n_e v_p/2 - \sum_{i=1}^{p} p_{\parallel ei} \quad (1)$$

where $Q$ is the Q value, $n_e$ is the number of the transferred electrons in the process, and $p_{\parallel e}$ is the longitudinal momentum of the ionized electrons. Therefore this component reflects the transfer of electrons and change of the total kinetic energy of the ions. The transverse components are expressed as:

$$p_{\perp R} = -p_{\perp P} - \sum_{i=1}^{p} p_{\perp ei} \quad (2)$$

and reflect the momentum transfer due to the projectile scattering and emitted electrons.[1)]

In the experiments, an $O^{3+}$ beam from RILAC passed a carbon foil to strip the electrons and the hydrogen-like $O^{7+}$ ions were selected. Then the momentum of the ions was analyzed by a bending magnet. The energy of the ions was about 8.7 MeV which corresponds to the velocity of 4.7 atomic unit (au) and momentum of $1.4\times10^5$ au. It was estimated that about 99.8% of the metastable ions decay before the target. The ion beam was collimated by a pair of slits and was led to a target chamber where it crossed a target of He gas. The target was a cooled gas jet which crosses the ion beam at about 90°. The momenta of the $He^{+}$ and $He^{2+}$ ions were analyzed by an electrostatic recoil-ion analyzer. The recoil ion analyzer with the gas jet target and an electrostatic recoil ion spectrometer are described elsewhere in this report.[2)] After the target, the oxygen ions in a charge state of 6+ or 7+ were selected by a dipole magnet and were counted by a parallel-plate avalanche counter (PPAC) with two-dimensional position sensitivity in coincidence with the three dimensional momentum of the recoil ions.

The transverse momentum $P_\perp$ distributions of $He^{+}$ ions for pure single ionization $O^{7+} + He \rightarrow O^{7+} + He^{+}$ are shown in Fig. 1. Figure 1(a) shows the $P_\perp$ distribution in the horizontal component obtained from the TOF measurement and (b) the vertical component from the detection position on the recoil ion detector. The centroid of the vertical distribution shifts upward by about 1.6 au due to mass motion of the target He atom in the jet with velocity of 450 m/s. The FWHM of the distribution is about 1 au for both the components. The momentum distribution of $He^{2+}$ is wider than that of $He^{+}$, but the yield of $He^{2+}$ was too small to determine the momentum distribution.

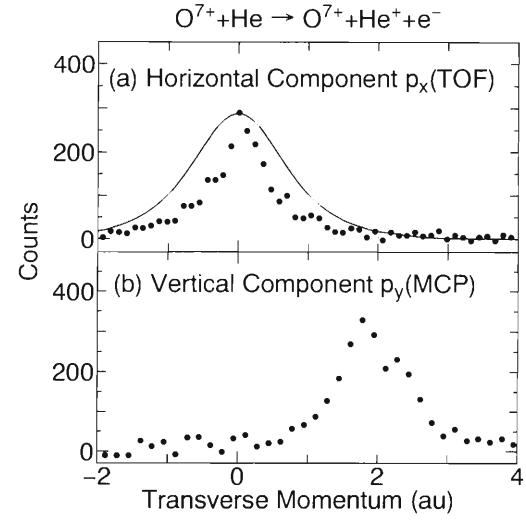


Fig. 1. Momentum distribution of recoil $He^{+}$ ions from pure ionization by 8.7 MeV $O^{7+}$: (a) is the horizontal component obtained from the time of flight measurement and (b) is the vertical component obtained from the vertical position of the ions at the MCP of the recoil ion analyzer. A curve in (a) shows the Compton profile of He atom experimentally obtained by Eisenberger. The abscissa is the momentum in atomic unit.

References

1) R. Dörner, V. Mergel, R. Ali, U. Buck, C. L. Cocke, K. Froschauer, O. Jagutzki, S. Lencinas, W. E. Meyerhof, S. Nüttgens, R. E. Olson, H. Schmidt-Böcking, L. Spielberger, K. Tökesi, J. Ullrich, M. Unverzagt, and W. Wu: *Phys. Rev. Lett.*, **72**, 3166 (1994).
2) O. Jagutzki, T. Kambara, Y. Nakai, Y. Awaya, and H. Schmidt-Böcking: This report, p. 129.

# Single Event Effect in Power MOSFETs by High-Energy Heavy Ion

S. Matsuda, S. Kuboyama, T. Akutsu, T. Hada, J. Aoki, T. Hirose, H. Ohira, T. Kohno, N. Inabe, T. Nakagawa, M. Kase, A. Goto, and Y. Yano

Power MOSFETs (Metal-Oxide-Semiconductor Field Effect Transistors) perform excellently as power switching devices. However, power MOSFETs have a possible catastrophic failure mode known as Single Event Burnout (SEB) phenomenon which is important to consider in space electronic applications.

The detailed mechanism for SEB was observed experimentally by the EPICS (Energetic Particle Induced Charge Spectroscopy) measurement system in previous work.[1] The experimental results were also confirmed with numerical simulation technique.

To prove the effect of a nuclear reaction on SEBs, SEBs were measured by EPICS with heavy ions which have the same LET but different energy. The selected ions were Kr and Xe and their characteristics are shown in Table 1.

Table 1. Characteristics of the ions used in this study.

| Ions | Energy [MeV] | LET [MeV/(mg/cm$^2$)] | Range [$\mu$m(Si)] |
|---|---|---|---|
| $^{84}$Kr | 924 | 27.5 | 127 |
| $^{134}$Xe | 3536 | 33.7 | 363 |

RIKEN Ring Cyclotron was used for the heavy ions irradiation. To avoid contaminant ions, a defocused direct beam without a scatterer such as Au foil was used. The incident beam was monitored by an SSD just adjacent to the sample device.

The sample device used in this study was 2SK725 manufactured by Fuji Electric Corp. The device has a maximum drain-source voltage rating ($V_{DS}$) of 500 V. The high voltage rating requires a relatively thick active layer ($\approx$40 $\mu$m of epi-layer). However, both ions have sufficient ranges to penetrate throughout the active region of the sample device.

Figures 1 and 2 show the EPICS spectra for Kr and Xe ions, respectively. At 50 V of $V_{DS}$, the first peak is in the same position. This fact comes from that the Kr and Xe ions have the same LET value. However, the observed SEB thresholds for Kr and Xe ions were 250 V and 95 V, respectively. Obviously the threshold voltage is not solely determined by LET of incident ions. For Kr ions, the $V_{DS}$ dependence of the EPICS spectra is normal as compared with another typical case. In previous work on Power MOSFETs, it was suggested that SEB was triggered when a collected charge exceeded a certain threshold charge $Q_{TH}$.[1] In contrast with the Kr ions, SEBs in Xe case are triggered although the second peak still remains below $Q_{TH}$. The fact will be explained by the nuclear reaction which deposits excess charges in the active layer of a semiconductor.

The effect of the nuclear reaction was experimentally proved.[2] The results suggest that a usual SEB immunity test as a function of LET should be carefully considered to simulate the actual space environment for high voltage devices which have a thicker sensitive layer.

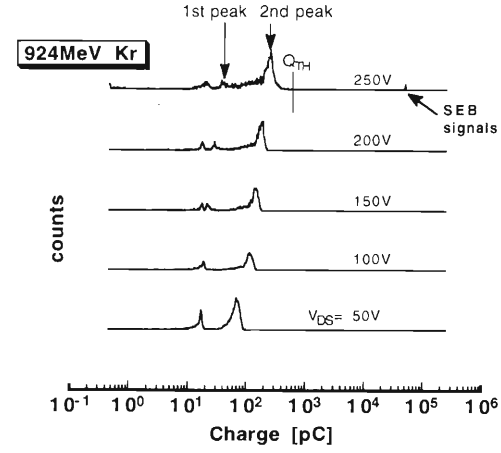


Fig. 1. EPICS spectra for 924 MeV Kr ions.

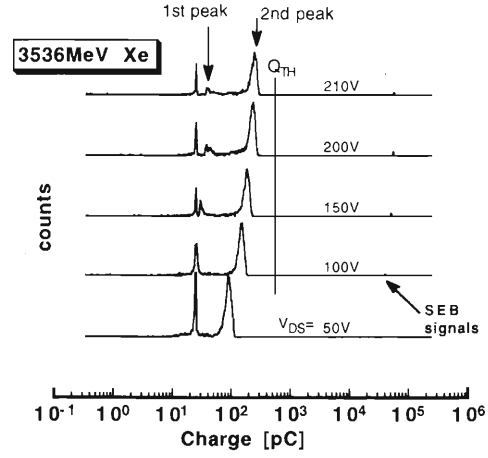


Fig. 2. EPICS spectra for 3536 MeV Xe ions.

References

1) S. Kuboyama et al.: *IEEE Trans. Nucl. Sci.*, **NS-39**, 1698 (1992).
2) S. Kuboyama: *ibid.*, **NS-41**, 2210 (1994).

# Laser Spectroscopy of Atoms in Superfluid Helium

M. Nakamura, Q. Hui, J. L. Persson, and M. Takami

Neutral atoms in superfluid helium (HeII) are known to be trapped in bubble-like cavities formed by a strong repulsive force between the atoms and surrounding helium atoms. The excitation and emission spectra of such bubble atoms exhibit peculiar spectra due to the coupling of atomic electronic states with the vibrational motion of the bubble. Almost all the bubble spectra have a very broad and largely blue-shifted excitation (absorption) band and emission lines close to free atomic lines with a typical width of 1–2 nm.[1] On the other hand, magnetic resonance and hyperfine transitions in the ground electronic states are known to have widths and resonance frequencies very close to those in free space.[2] One of the objectives of the present work is to develop an experimental technique to study the fine structure and magnetic moments of atoms with unstable nuclei in HeII.

We are currently studying optical properties of neutral atoms in HeII with lasers. A schematic diagram of the experimental set up is shown in Fig. 1. Neutral atoms are dispersed in HeII by laser ablation of solid metal samples immersed in HeII.[3,4] A pulsed YAG laser beam (355 or 532 nm, ~30 mJ/pulse) ablated the metal sample and produced a large number of small particles of the sample material. A second YAG laser beam (355 or 266 nm wavelength, ~10 mJ/pulse) with a few ms delay after ablation dissociated the particles to disperse neutral atoms in HeII. A pulsed dye laser was used to excite the atoms with a 50 ns–10 ms delay time after dissociation. The emission from the bubble atoms was detected by a photomultiplier through a 25 cm monochromator.

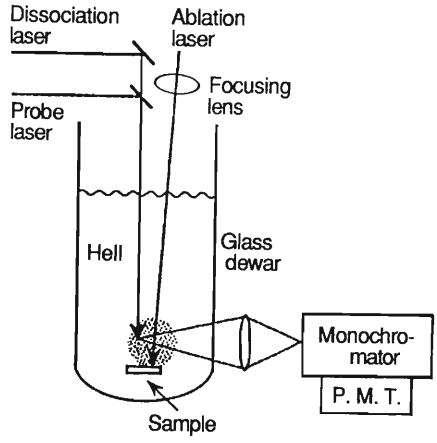


Fig. 1. Experimental set up.

So far we observed bubble spectra for a number of neutral atoms. A part of the experimental data including the group IIIa atoms are listed in Table 1. For the dynamics of bubble atoms, we measured radiative lifetimes for a number of atoms and found that most neutral bubble atoms have radiative lifetimes close to those in free space, but atoms in highly excited states or in an unidentified free-atom-like state show complex behavior.[5] The efficient quenching of the excited state by resonant radiation observed in Yb confirmed the rapid relaxation of bubble modes.[6] We also succeeded in the observation of highly excited states in Ca and Sr where the Coulomb potential is severely distorted by the existence of a bubble.

Table 1. New bubble transitions.

| Atom | Transition | Excitation[a] (nm) | Emission (nm) | Free space (nm) |
|---|---|---|---|---|
| Yb | $7s\ ^3S_1$–$6p\ ^3P_2$ | 670 | 770 | 769.9 |
| Ag | $5p\ ^2P_{1/2}$–$5s\ ^2S_{1/2}$ | 320 | 338 | 338.3 |
| Al | $4s\ ^2S_{1/2}$–$3p\ ^2P_{1/2}$ | 358 | 394 | 394.4 |
| Ga | $5s\ ^2P_{1/2}$–$4p\ ^2P_{1/2}$ | 368 | 403 | 403.3 |
| In | $6s\ ^2P_{1/2}$–$5p\ ^2P_{1/2}$ | 364 | 410 | 410.2 |

a) Center of broad absorption band.

References

1) H. Bauer et al.: *Phys. Lett.*, **A146**, 134 (1990).
2) T. Yabuzaki: private communication.
3) A. Fujisaki et al.: *Phys. Rev. Lett.*, **71**, 1039 (1993).
4) J. H. M. Beijersbergen et al.: *Phys. Lett.*, **A181**, 393 (1993).
5) Q. Hui et al.: *Z. Phys.*, **B**, in press.
6) Q. Hui et al.: *Laser Chemistry*, **15**, 221 (1995).

# Muonium Centers in Crystalline Si and Ge under Illumination

R. Kadono, A. Matsushita, R. M. Macrae, K. Nishiyama,* and K. Nagamine

An isolated hydrogen atom is the simplest interstitial impurity in crystalline semiconductors and therefore serves as a testing field for the basic understanding of atomic defects in these materials. Moreover, the recent revelation that atomic hydrogen can form chemical complexes with shallow impurities and thereby passivate their electrical activity (i.e., hydrogen passivation), of crucial importance in the processing of semiconductor devices, has prompted wider interest in the structure and kinetics of hydrogen isotopes and their complexes with other defect impurities. Unfortunately, compared with hydrogen complexes relatively little is known about isolated hydrogen in semiconductors. This is in marked contrast to the case of muonium (Mu, a bound state of $\mu^+$ and $e^-$) where it is widely investigated as an isolated center. Thus, the study of Mu centers serves as a complementary source of information on hydrogen isotopes in semiconductors. However, a standing issue of Mu study is that a considerable fraction of muons implanted into intrinsic Si/Ge at low temperatures are found as $\mathrm{Mu}^0_\mathrm{T}$ centers, i.e., those at the tetrahedral interstitial (T) site, while most calculations predict the bond-center (BC) site to be the adiabatic potential minimum for neutral muonium and hydrogen.[1)]

In order to get an insight into this problem we conducted a time-differential $\mu$SR experiment upon Si and Ge under illumination. A xenon flashlamp (0.5 $\mathrm{mJ/cm^2}$ per pulse, synchronized with the muon pulse) was used to illuminate the specimen with minimal heat load and conventional $\mu$SR measurements were performed under longitudinal field (LF) or transverse field (TF) conditions. The electronic state of the muon is determined through the magnetic field dependence of the (time dependent) positron decay asymmetry,

$$A(t) = A_0[f_\pm + f_\mathrm{T}P_\mathrm{T}(t,B) + f_\mathrm{BC}P_\mathrm{BC}(t,B)], \quad (1)$$

where $A_0$ is the experimental asymmetry, $f_\alpha$ is the relative yield of the charged state ($\mathrm{Mu}^\pm$), $\mathrm{Mu}^0_\mathrm{T}$, and $\mathrm{Mu}^0_\mathrm{BC}$ centers ($\alpha = \pm, \mathrm{T}, \mathrm{BC}$, satisfying $\sum_\alpha f_\alpha = 1$), and $P_\alpha(t,B)$ is the corresponding polarization function dependent on the time $t$ and external field $B$. The muon depolarization due to *cyclic charge exchange* (e.g., $\mathrm{Mu}^\pm \rightleftharpoons \mathrm{Mu}^0_\mathrm{T}$), which turns out to be the predominant process under illumination, is qualitatively the same as that due to *spin exchange interactions* involving the relevant neutral state (e.g., $\mathrm{Mu}^0_\mathrm{T}$) and the characteristics of the regime may thus be studied through the behavior of the neutral intermediate state.[2)]

We found that the charged state ($\mathrm{Mu}^\pm$) formed at high temperatures undergoes fast spin relaxation in both Si and Ge under illumination due to a cyclic charge exchange reaction with photo-induced carriers. In Si the $\mathrm{Mu}^0_\mathrm{T}$ state also collides effectively with carriers to induce reaction, while in Ge the neutral state is unreactive. In particular, in Si at low temperatures the $\mathrm{Mu}^0_\mathrm{T}$ center is rapidly converted into $\mathrm{Mu}^0_\mathrm{BC}$ with supervening fast spin relaxation under illumination. As shown in Fig. 1, the initial LF-$\mu$SR asymmetry at 8 K is reduced by illumination, indicating that $\mathrm{Mu}^0_\mathrm{T}$ has been transformed into $\mathrm{Mu}^0_\mathrm{BC}$ ($f_\mathrm{BC} = 0.5 \rightarrow 1$), and evidencing that the $\mathrm{Mu}^0_\mathrm{BC}$ state is the true ground state at low temperatures. The details are found elsewhere.[3)]

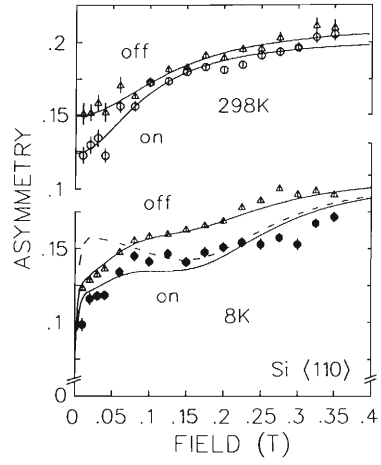


Fig. 1. Longitudinal field dependence of the initial asymmetry $A(t=0)$ in illuminated Si at 8 and 298 K. Solid curves at 298 K are fits to Eq. (1). At 8 K the dashed curve is calculated with $f_\mathrm{BC} = 1$ and the solid curve with further depolarization at the initial $\mathrm{Mu}^0_\mathrm{T}$ state.

References

1) See, for example, the review by C. G. Van de Walle, Hydrogen in Semiconductors, p. 585 (1991).
2) I. G. Ivanter and V. P. Smilga: *Zh. Eksp. Teor. Fiz.*, **60**, 1985 (1971) [*Sov. Phys. JETP*, **33**, 1070 (1971)].
3) R. Kadono, A. Matsushita, R. M. Macrae, K. Nishiyama, and K. Nagamine: *Phys. Rev. Lett.*, **73**, 2724 (1994).

* Meson Science Laboratory, Faculty of Science, University of Tokyo

# Annealing Behaviour of Kr Atoms in Kr-Implanted Aluminium

E. Yagi and M. Hacke

It has been demonstrated that heavy inert gas atoms (Ar, Kr, and Xe) implanted into metals at ambient temperature precipitate into micro-clusters, and that for high implantation doses they are in a solid phase (solid inert gas bubbles) epitaxially aligned to matrices.[1-3]

From previous channelling studies on Kr-implanted Al crystals, we obtained the following results. At the initial stage of implantation various types of complexes consisting of Kr atoms and vacancies ($V$) such as $KrV_4$, $KrV_6$ and larger ones are formed, and act as nucleation centres for the subsequent bubble formation.[4-6] The complexes $KrV_4$ and $KrV_6$ are stable up to about 400 K and 560 K, respectively. The formation of epitaxial solid krypton is enhanced by post-implantation irradiation at room temperature.[7] The solid krypton is also formed on annealing.[6]

The result described above on the stability of the complexes was obtained from isochronal annealing experiments of a $1 \times 10^{15}$Kr/cm$^2$ implanted specimen. However, it is desirable to demonstrate the stability of the $KrV_4$ more clearly, because the fraction of the $KrV_4$ complexes was small in the $1 \times 10^{15}$Kr/cm$^2$ implanted specimen, and the change in its fraction on annealing was small. Therefore, in the present study its stability is investigated by a channelling method in a $4 \times 10^{14}$Kr/cm$^2$ implanted specimen which contains a larger portion of $KrV_4$ complexes than in the $1 \times 10^{15}$Kr/cm$^2$ implanted specimen.

$Kr^+$ implantation was carried out at room temperature at 50 keV with a dose of $4 \times 10^{14}$Kr/cm$^2$. Channelling analyses were performed at room temperature with a 1.0 MeV $He^+$ beam in the as-implanted state and after annealing at 433 K for 30 min.

In the as-implanted state the Kr angular profile exhibits a shallow dip with nearly the same half-width as that of the corresponding channelling Al dip for the ⟨100⟩ and ⟨111⟩ channels, and a central peak superimposed on a shallow dip for the ⟨110⟩ channel. In the ⟨100⟩ Kr profile a small central peak is superimposed on the dip as shown in Fig. 1(a). The relative depth of the ⟨100⟩ Kr dip with respect to the corresponding Al dip is smaller than that of the ⟨111⟩ Kr dip. As previously reported,[4-7] these profiles can be interpreted as showing that the Kr atoms are distributed over substitutional ($S$), tetrahedral ($T$), octahedral ($O$), and random ($R$) sites. The observed small ⟨100⟩ central peak originates from the $T$-site occupancy, and the ⟨110⟩ central peak from the $T$- and $O$-site occupancies. As the fraction of the $O$-site occupancy is much larger than that of the $T$-site occupancy, the contribution of the $O$-site occupancy to the ⟨110⟩ central peak

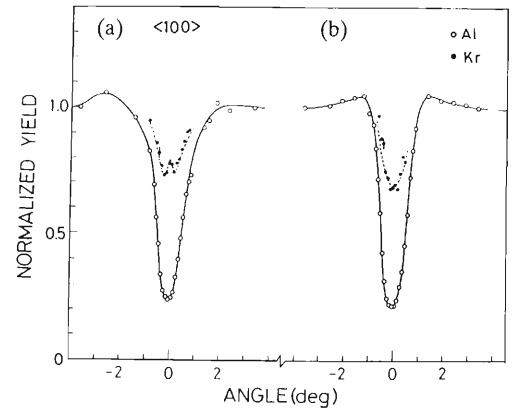


Fig. 1. ⟨100⟩ channelling angular profiles obtained for the $4 \times 10^{14}$Kr/cm$^2$ implanted specimen (a) in the as-implanted state, and (b) after annealing at 433 K for 30 min. The broken curves are Kr angular profiles calculated for the distribution of Kr atoms with (a) 20% at $S$, 6% at $T$, 19% at $O$ and 55% at $R$ sites, and (b) 20% at $S$, 19% at $O$ and 61% at $R$ sites. The solid curves were drawn only to guide the eye.

is much larger than that of the $T$-site occupancy.

After annealing at 433 K, the small ⟨100⟩ central peak disappears (Fig. 1(b)), and the relative depths of the ⟨100⟩ and ⟨111⟩ Kr dips become equal. The ⟨110⟩ central peak is still observed. The $T$-site occupancy has been interpreted to be a result of the interaction between Kr atoms and implantation-introduced vacancies: By trapping 4 vacancies a Kr atom is located at the centre (a $T$ site) of a vacancy tetrahedron. Therefore, the result described above can be explained in terms of the dissociation of $KrV_4$ complexes, and demonstrates that the $KrV_4$ is stable up to about 400 K. More detailed descriptions are given in Ref. 8.

References

1) A. vom Felde, J. Fink, Th. Müller-Heinzerling, J. Pflüger, B. Scheerer, G. Linker, and D. Kaletta: *Phys. Rev. Lett.*, **53**, 922 (1984).
2) C. Templier, C. Jaouen, J.-P. Rivière, J. Delafond, and J. Grilhé: *C. R. Acad. Sci. Paris*, **299**, Ser. II, 613 (1984).
3) J. H. Evans and D. J. Mazey: *J. Phys.*, **F15**, L1 (1985).
4) E. Yagi: *Phys. Stat. Sol.*, **a104**, K13 (1987).
5) E. Yagi: *Nucl. Instrum. Methods Phys. Res.*, **B39**, 68 (1989).
6) E. Yagi, I. Hashimoto, and H. Yamaguchi: *J. Nucl. Mater.*, **169**, 158 (1989).
7) E. Yagi: *Phys. Rev. Lett.*, **67**, 3804 (1991).
8) M. Hacke and E. Yagi: *J. Phys. Soc. Jpn.*, **64**(3), (1995), in press.

# Hyperfine Magnetic Field of $^{61}$Ni in Spinel Chromite $Cu_{0.9}Ni_{0.1}Cr_2O_4$

T. Okada, Y. Noro,* Y. Kobayashi, H. Kitazawa, and F. Ambe

About twenty years ago, we reported that in the $^{61}$Ni Mössbauer spectroscopy a large hyperfine magnetic field ($H_{hf}$) of 450 kOe for $^{61}$Ni was found at the tetrahedral (A) sites of $NiCr_2O_4$ with a spinel structure in contrast with the smaller $H_{hf}$ around 100 kOe at the octahedral (B) sites of $NiFe_2O_4$ etc.[1] After that, several groups reported $^{61}$Ni Mössbauer measurements of spinel oxides. In early times, the interaction of the magnetic moment of the nucleus with the electron spin and orbital moment was studied by E. Fermi and E. Segrè.[2] It is deduced from this interaction that $H_{hf}$ consists of three parts of Fermi contact, the orbital angular momentum and the magnetic dipole-dipole interaction. When the electron in the ground state has an angular momentum, the second part gives very large $H_{hf}$. Göring pointed out firstly that the large $H_{hf}$ of $^{61}$Ni at A sites of $NiCr_2O_4$ arose from the incompletely quenched orbital angular momentum[3] by the second order perturbation though the orbital angular momentum was quenched by the first order one. As any compounds except for $NiCr_2O_4$ and $NiCr_{2-x}Fe_xO_4$ have not been investigated, the $H_{hf}$ of $^{61}$Ni in various compounds has to be measured in order to elucidate the origin of these large $H_{hf}$. The specimen of $Cu_{0.9}{}^{61}Ni_{0.1}Cr_2O_4$ has a spinel structure tetragonally distorted (c/a = 0.92) due to the Jahn-Teller effect of $Cu^{2+}$ ions at the tetrahedral sites where the ground state of Ni ions is doubly degenerated and then the orbital angular momentum is still wholly alive. This paper purposes to measure the $H_{hf}$ of $^{61}$Ni ions in the doubly degenerated ground state.

The single line source of $^{61}$Cu ($\rightarrow$ $^{61}$Ni) was produced in the RIKEN AVF cyclotron. A powdered specimen of $Cu_{0.9}{}^{61}Ni_{0.1}Cr_2O_4$ was prepared by the conventional ceramic sintering method. The source and absorber were kept at the same temperature in a helium cryostat.

A Mössbauer spectrum of $Cu_{0.9}{}^{61}Ni_{0.1}Cr_2O_4$ taken at the liquid He temperature is give in Fig. 1. One can see the widely spread lines. The value of the internal magnetic field $H_{hf}$ amounts to 830 kOe, which is the largest one ever reported for $^{61}$Ni. In conclusion, we found the large $H_{hf}$ of $^{61}$Ni ions in the doubly degenerated ground state. It is considered that the large $H_{hf}$ of $^{61}$Ni at A sites of spinel oxides is caused by the orbital angular momentum because it is still wholly alive in the doubly degenerated ground state.

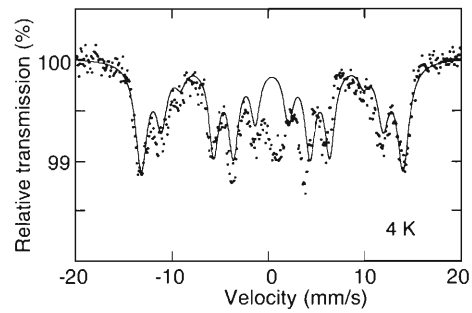


Fig. 1. $^{61}$Ni Mössbauer spectrum of spinel chromite $Cu_{0.9}{}^{61}Ni_{0.1}Cr_2O_4$ at 4 K. The solid line is the guide of eyes.

References

1) H. Sekizawa, T. Okada, S. Okamoto, and F. Ambe: *J. de Physique*, **32**, C1-326 (1971).
2) E. Fermi and E. Segrè: *Z. Physik*, **82**, 729 (1933).
3) J. Göring: *Z. Naturforsh.*, **A26**, 1929 (1971).

* Hitachi Image and Media System Laboratory

# $^{57}$Fe Mössbauer Studies of $YSr_2Cu_{3-x}Fe_xO_{7-y}$

T. Okada, Y. Kobayashi, T. Tatsumi,* and N. Yamada*

The Sr compound $YSr_2Cu_3O_{7-y}$ has a similar crystalline structure with a typical high-$T_c$ superconductor $YBa_2Cu_3O_{7-y}$ and is also superconductive. The elucidation of the resemble and different features between both compounds is attractive and significant to investigate the origin of a high-$T_c$ superconductivity. The Ba compounds $YBa_2Cu_{3-x}Fe_xO_{7-y}$, substituting Fe for Cu atoms in $YBa_2Cu_3O_{7-y}$, have been studied by many researchers. The Sr compounds $YSr_2Cu_{3-x}Fe_xO_{7-y}$ have been studied also and found that the solubility range of Fe atoms is $0.3 \leq x \leq 1.0$ when the Sr compounds are calcined in flowing $O_2$ gas.

Our attention is as follows:

(1) In spite of the similarity of the superconducting transition temperature between these compounds with Fe content $x = 0.3$, the Mössbauer spectra of these compounds are different. It is expected that the difference of a microstructure in these compounds can be clarified by the analysis of the Mössbauer data.

(2) For the highly Fe substituted compounds, e.g. $YSr_2Cu_2Fe_1O_{7-y}$ ($x = 1$), new magnetic ordering states are expected. We studied the magnetic states in the compound by means of the magnetization and the Mössbauer measurements.

The typical Mössbauer spectra of the powder specimen $YSr_2Cu_{2.7}Fe_{0.3}O_{7-y}$ in a temperature range from 4 K to 296 K are shown in Fig. 1. The spectra at 296 K can be analyzed with three doublets arising from the quadrupole splitting (QS). The sites occupied by Fe ions can be classified into three sites. The isomer shifts (IS) of two sites are nearly zero and the IS of the other site is +0.27 mm/s. The IS of the former are near the value for $Fe^{3+}$ ions in highly covalent oxides (Cu(1) site). The IS of the latter is the ordinary value for $Fe^{3+}$ ions in oxides (Cu(2) site). The area ratio of the three sites in Mössbauer spectrum differs remarkably from that of the Ba compounds $YBa_2Cu_{2.7}Fe_{0.3}O_{7-y}$. It means that the number of $Fe^{3+}$ ions occupied in Cu(1) sites increases in the Sr compound. As shown in Fig. 1(e), the spectrum at 4 K can be explained by a superposition of two magnetically split sextets. In the sharp sextet (A) the value of the hyperfine magnetic field ($H_{hf}$) is around 450 kOe, and the values of $H_{hf}$ in the very broaden sextet (B) are widely distributed around 200 kOe. The magnitudes of $H_{hf}$ in the B sextet are smaller than that in the Ba compound. Furthermore, the values of $H_{hf}$ in B sextet decrease more rapidly with increasing temperature than that in the Ba compound.

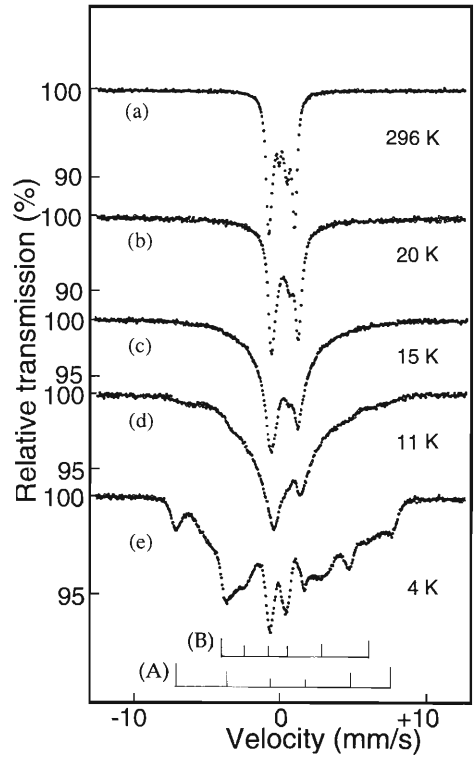


Fig. 1. Mössbauer spectra of $YSr_2Cu_{2.7}Fe_{0.3}O_{7-y}$ at various temperatures.

In summary, (1) the number of $Fe^{3+}$ ions occupied in Cu(1) sites increases in the Sr compound $YSr_2Cu_{2.7}Fe_{0.3}O_{7-y}$, and the magnetic interaction of these ions is weaker than that in the Ba compound $YBa_2Cu_{2.7}Fe_{0.3}O_{7-y}$, and (2) though figures are not shown here, the temperature dependence of $H_{hf}$ and that of the magnetization in the highly Fe substituted compounds are similar to those in the spin glass.

* Department of Applied Physics and Chemistry, The University of Electro-Communications

# 3. Radiochemistry and Nuclear Chemistry

# Multitracer Study on Transport and Distribution of Metal Ions in Rice Plant

S. Ambe, Y. Ohkubo, Y. Kobayashi, M. Iwamoto, and H. Maeda

Although plants grow on soil containing various elements, little is known about uptake and accumulation of metal elements other than those regarded as essential ones. Human activities have led to the contamination of soil not only with heavy elements but also with radioactive isotopes. Elements artificially introduced to the environment can change the equilibrium in nature and their behavior in partition between soil and water often differs from that of elements originally existing in soil, which would affect the uptake of elements by plants. Therefore, it is very important to investigate the uptake and distribution of metal ions in plants and to evaluate the quantities of accumulation of stable elements and radioactive isotopes.

This paper reports on a study of the uptake and distribution of various metal elements by means of the multitracer technique. Rice (*Oryza sativa* cv. Nihonbare) plant was hydroponically cultivated in a nutrient solution containing a multitracer prepared from a gold target.[1,2] Distributions of various elements among leaves, stems, and roots were determined by $\gamma$-ray spectroscopy of each part of the plants.

The amount of radioisotopes taken up by each part of the plants is represented as percentage distribution obtained by dividing the radioactivity in one part of a plant by the total amount of radioactivity added to the culture media. Figure 1 shows the percentage distribution of elements among various parts of the rice plant which was transplanted 2 weeks after germination into a nutrient solution containing a multitracer and grown for 3 days. A large fraction of the radioisotopes of Sc, Mn, Fe, Co, Zn, As, Rb, Sr, Y, Zr, Te, Ba, Ce, Eu, Gd, Tb, Tm, Yb, Lu, Hf, Ir, and Pt was found in the roots and only a small fraction in the stems. Among them, the rare-earth elements showed relatively high distribution in the roots. In the leaves, appreciable amounts of Mn, Co, Zn, Rb, Sr, and Ba were detected.

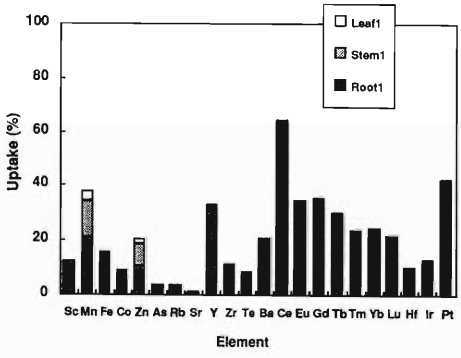


Fig. 1. The percentage distribution of metal elements among various parts of the rice plant grown in a nutrient solution for 3 days.

The rice plant cultured in a nutrient solution containing the multitracer for 14 days showed an increase in the uptake of the elements by roots, stems, and leaves (Fig. 2). Essential elements Mn and Zn were concentrated in the leaves, showing an almost complete uptake from the nutrient solution. Although Fe is also an essential element, the amount of iron in the stems and leaves was less than the detectable limit. This indicates that the plants have stored enough Fe during the preceding culture stage. An increase in the amount of As, Rb, Sr, Te, and Ba in the stems and leaves was observed compared to the 3-day culture. The amounts of rare earth elements in the roots also increased with time but they were not detected in the leaves. The distribution of lanthanides in the roots was found to decrease in the order of increasing atomic number.

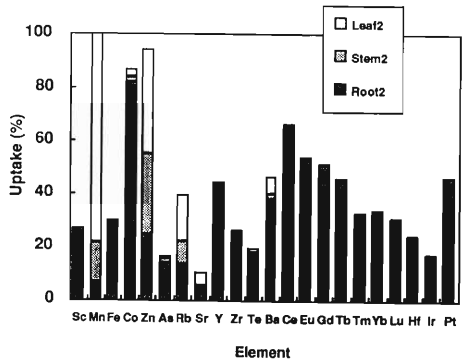


Fig. 2. The percentage distribution of metal elements among various parts of the rice plant grown in a nutrient solution for 14 days.

References

1) S. Ambe, S. Y. Chen, Y. Ohkubo, Y. Kobayashi, M. Iwamoto, and F. Ambe: *Chem. Lett.*, **1991**, 149.
2) S. Ambe, S. Y. Chen, Y. Ohkubo, Y. Kobayashi, M. Iwamoto, M. Yanokura, and F. Ambe: *Anal. Sci.*, **7**, Suppl., 317 (1991).

# Multitracer Study on Transport and Distribution of Metal Ions in Soybean Plant

S. Ambe, Y. Ohkubo, Y. Kobayashi, M. Iwamoto, and H. Maeda

Transport and distribution of metal ions in soybean plants were studied using multitracers produced by irradiating an Au target by 135 MeV/nucleon $^{12}C$, $^{14}N$, and $^{16}O$ ions accelerated by RIKEN Ring Cyclotron. The multitracer prepared from the target by solvent extraction consisted of radioisotopes of the following elements: Be, Na, Sc, Mn, Fe, Co, Zn, Se, Rb, Sr, Y, Zr, Nb, Ag, Te, Ba, Ce, Pm, Eu, Gd, Tb, Tm, Yb, Lu, Hf, Ir, and Pt.

Soybean plants (*Glycine max* L. Merrill cv. Okuharawase) were grown in a nutrient solution containing a multitracer. Distributions of various elements among seeds, leaves, stems, and roots were determined by $\gamma$-ray spectroscopy of each part of the plants. For comparison, soil cultivation was also performed.

Soybean plants 50 days after the start of germination were grown in a multitracer nutrient solution for 30 days. The results of analysis of the $\gamma$-ray spectra of the roots, stems, leaves, pods, and seeds are shown in Fig. 1. In the edible part, namely in seeds, Mn, Co, Zn, Rb, Sr, and Ba were detected. The pods showed uptake of the same elements as those in the seeds. Rb, Sr, and Ba were found to be distributed among all parts of the plant, similar to the distribution of the essential elements Mn and Zn. Be, Zr, Nb, Ru, Rh, Ag, and rare-earth elements were predominantly found in the roots. The distribution pattern of lanthanides in the roots is similar to that for the rice plants.[1)]

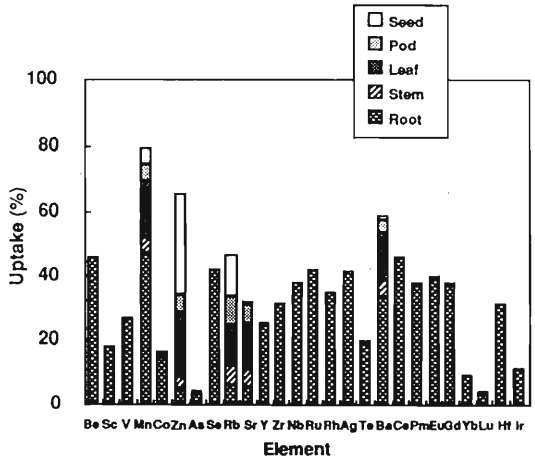


Fig. 1. The percentage distribution of metal elements among various parts of the soybean plant grown in a nutrient solution for 30 days.

Soybean plants grown on the soil were harvested about 2 months after the start of germination. The seeds were still immature. The roots were carefully collected and washed to remove soil. Figure 2 shows distribution of elements among various parts of the plants. The number of elements detected in the roots is smaller than that for soybean plants grown in the nutrient solution. Mn, Zn, Se, Rb, and Sr were found in the stems, leaves, pods, and seeds as in the case of the hydroponic culture. However, the percentage distribution of all elements was smaller by a factor of $10^{-3}$–$10^{-2}$ compared to that of the soybean plants grown in the nutrient solution.

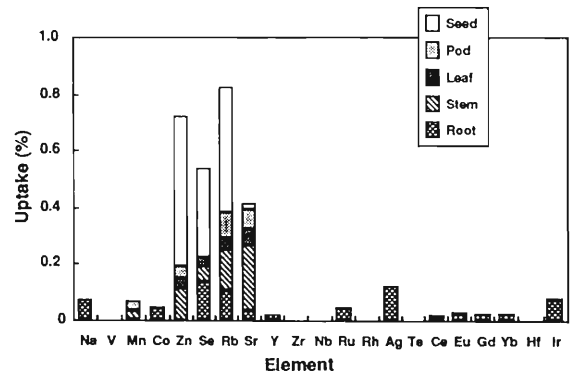


Fig. 2. The percentage distribution of metal elements among various parts of the soybean plant grown on soil for 2 months.

This difference is explained by the low distribution of metal ions in soil water and the dilution of radioisotopes with corresponding elements in soil. The distribution of Se is quite similar to that of essential element Zn. This suggests that Se is required for germination and growth of the plant.

References

1) S. Ambe, Y. Ohkubo, Y. Kobayashi, M. Iwamoto, and H. Maeda: This report, p. 83.

# The Study of Behavior of Various Elements in Atmosphere-plant System by Multitracer Technique

T. Shinonaga, S. Ambe, S. Enomoto, H. Maeda, M. Iwamoto, T. Watanabe, and I. Yamaguchi

The behavior of various elements in atmosphere-plant system is being studied by a multitracer technique.

In recent years, pollution in environment has become serious problems for human lives. These problems mainly occur by industrial wastes and products, automotive exhaust gases, and soot. The recent remarkable problem is the radioisotopes leaked into atmosphere from the atomic reactors and one of the obvious example is the accident of Chernobyl Reactor which occurred on April 26, 1986. After the accident, a large number of radionuclides were injected into the atmosphere and they brought many risks to lives especially in Europe. After this accident, many investigations have been reported for the problem of spread radionuclides, e.g., for long-lived radionuclides such as $^{129}$I ($T_{1/2} = 1.6 \times 10^7$ y) in the atmosphere and the rainwater.[1] These radionuclides may nfluence human bodies directly or possibly through the plants and the animals as food. Wagner reported the radio ecological investigation on the food-chain, such as air-soil-vine-wine determining contents of $^{137}$Cs at different locations in Germany before and after the Chernobyl accident.[2] These results clearly show the fact that the pollutants in atmosphere are taken in human bodies through the food-chain.

The most of previous studies which concern the problem of the pollution in plants were performed in the field observing a few elements, but the mechanism of the absorption of elements in the atmosphere into plants is not yet well known. This mechanism could also be important for understanding a complicated circulation system of elements on the earth.

In this study the absorption of various elements in the air by plants and soil is experimentally investigated using a radioactive multitracer. As the first step, the relative amount of elements absorbed in each part of plant is determined. These results will be considered to provide a base of estimation of the factors in the mathematical model for the behavior of elements in the plant-soil-atmosphere system. The depth-profiles of absorbed elements in soil are also analyzed.

For the production of multitracer, the Au target irradiated with $^{14}$N at the RIKEN Ring Cyclotron was dissolved in aqua regia and Au ions were finally removed from the 3 mol dm$^{-3}$ HCl solution by extraction with ethyl acetate, and the carrier-free and salts-free multitracer was prepared. This multitracer solution in an evaporating dish was put on the soil covered with parafilm in a closed (excepted a hole covered with a glass fiber filter together with a membrane filter) acryl box. In the multitracer solution, cellulose powder (> 300 mesh) was supplied and the solution was dried. The used plants were Soybean and Komatsuna. They were cultivated in this acryl box installed in a biotron with the radionuclides at 23 °C under exposure of 20000 lux light of fluorescent lamps for 12 h a day during 30–80 days for Soybean and 10–20 days for Komatsuna, respectively. About 8 liter of air was overblown per day at the upper and near the surface of soil covered with parafilm to make similar condition to floating dust. The tube for supplying water was put under the soil to avoid the leaching effect of the elements by water, and about 100 ml of distilled water was given per day. The monitors were similarly made to each plant by a glass fiber filter and they were set up beside each plant.

After the plants were grown up, they were taken out and separated each part: root, leaf, stem, seed, pod for Soybean, and leaf and root for Komatsuna. Some of the stems and beans were cut in inner part and outer part. After they were washed with diluted HCl solution in an ultrasonic wave bath, the $\gamma$-ray was measured for each part of the plants.

For the depth-profiles of soil, three test tubes of 2 cm dia., 14 cm height were inserted in the soil at some distances from the dish containing the multitracer, and the $\gamma$-ray was measured for 2 cm depth from the surface and further each 4 cm part of depth, respectively.

The observed elements were Be, Sc, V, Cr, Mn, Co, Zn, As, Se, Rb, Sr, Y, Ru, Ag, In, Sn, Te, Ba, Ce, Eu, Gd, Yb, Lu, Hf, Re Ir, and Pt. The measurement has been finished and the analysis is now being carried out.

References

1) M. Paul, D. Fink, G. Hollos, A. Kaufman, W. Kutschera, and M. Magaritz: *Nucl. Instrum. Methods Phys. Res.*, **B29**, 341 (1987).
2) A. Wagner: Bundesforschungsanstalt für Ernährung, Karlsruhe, Germany, p. 205 (1989).

# Study on Uptake and Excretion of Trace Elements in Rats using the Multitracer Technique

M. Yanaga, S. Enomoto, R. Hirunuma, R. Furuta, K. Endo, A. Tanaka, S. Ambe, M. Tozawa,* and F. Ambe

The isotopic tracer method is useful in science, technology, medicine and many other fields. If a number of radioactive tracers are used simultaneously, it is possible to determine the characteristic behaviour of different elements under an identical experimental condition. In the present study, the multitracer technique, which was established at RIKEN a few years ago,[1,2] was applied to an investigation of the uptake and excretion behaviour of trace elements in rats.

A multitracer solution was obtained from a gold foil target irradiated with $^{14}$N-ion beam accelerated by the RIKEN Ring Cyclotron. The target was dissolved in aqua regia and the solution was evaporated to dryness. After the residue was dissolved in 3M HCl, gold ions were removed by extraction with ethyl acetate. The remaining aqueous phase was again evaporated to dryness and adjusted to pH 3 with dilute HCl for administration to rats.

The multitracer solution was orally administered to three seven-weeks-old male Wistar rats. A half ml of the solution was used for each rats. Feces and urine were collected at 8 h and then at 24-h intervals after administration. The radioactivities of them were measured with pure Ge detectors. The spectra were analysed with BOB code[3] on a FACOM M1800 computer. The observed $\gamma$-rays were assigned to various nuclides according to their energies and half-lives.

In the multitracer solution used in this study, radioisotopes of many kinds of elements were included: e.g., Be, Sc, Mn, Co, Zn, As, Se, Rb, Sr, Y, Zr, Ce, Eu, Gd, Tb, Er, Tm, Yb, Lu, Hf, W, and Re. In Fig. 1, rates of excretion are summarised for five of those elements for one of the rats. Excellent agreement was found in the excretion rates among the rats. As shown in Fig. 1, a very small amount of rhenium was found in feces, which means that rhenium was entirely absorbed into the body. The excretion behaviour for Re to urine was found to be quite unique. More than 80% of rhenium was eliminated in urine within only one day. Further experiments on elimination of rhenium to urine showed that the excretion was composed of at least two phases. Namely, more than 85% of Re was excreted with a half-life of about 3 h but 3–5% of Re with a day-order half-life irrespective of whether a carrier material ($KReO_4$, 0.2 mg/rat) was included in the administered solution or not. In those experiments, most of rhenium remaining in the rats' body (<7%) was found in hair and a trace amount (<0.01%) was found in bone.

Interesting behaviour was also found in the excretion rate for tungsten. Fifty to 90% of tungsten was absorbed into the body; then, 80–90% of the absorbed tungsten was eliminated in urine within one day. No $\gamma$-rays due to tungsten were detected in any organs and tissues 6 days after administration.

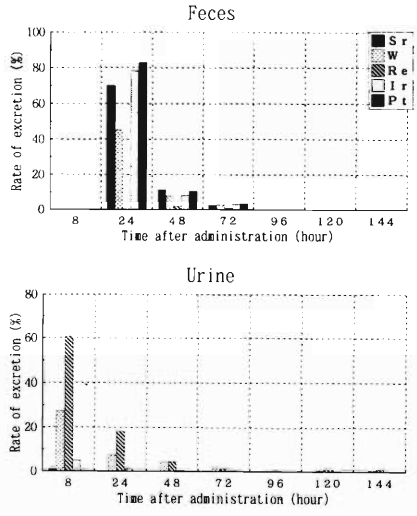


Fig. 1. Rates of excretion of Sr, W, Re, Ir, and Pt to feces and urine for one of the three rats studied.

Excretion behaviour of Mn, Co, Zn, As, Se, Rb, Sr, Ir, and Pt is in general compatible with previous works on uptake and excretion of these elements by animals,[4,5] which guarantees the reliability of the multitracer experiments. For example, as shown in Fig. 1, more than 15% of strontium was absorbed and only a small portion of it was excreted in urine. This element was found only in bone. It is known that the gastrointestinal tract is the main route of entry into body and the fraction absorbed via intestine is 30%, and that 99% of body burden is deposited in bone.[5]

The $\gamma$-rays due to Be, Zr, Hf and rare earth elements were not detected in organs and tissues. There were no peaks of these elements in any spectra of urine except for Hf which was detected in a minute amount (<0.1%). This means that these elements were not or only a little absorbed into rats. It is reported that gastrointestinal absorption of soluble or insoluble beryllium is thought to be minimal because the alkalinity of the gastrointestinal tract causes precipitation of beryllium, and it is suggested that only 0.006% of ingested beryllium was absorbed.[5]

* Dept. Chem., The Jikei University School of Medicine

References

1) S. Ambe et al.: *Chem. Lett.*, **1991**, 149.
2) S. Ambe et al.: *Anal. Sci.*, **7**, Suppl., 317 (1991).
3) H. Baba et al.: *J. Nucl. Sci. Technol.*, **8**, 1227 (1972).
4) H. Sakurai and H. Tanaka eds.: Seitaibiryougenso, Hirokawa Publishing Co., Tokyo (1994).
5) H. G. Seiler, A. Sigel, and H. Sigel eds.: Handbook on Metals in Clinical and Analytical Chemistry, Marcel Dekker, Inc., New York (1994).

# Multitracer Study on Distribution of Radioactive Nuclides in Rats: Metabolism and Accumulation in Various Tissues, Organs and Body Fluids

S. Enomoto, M. Yanaga, R. Hirunuma, K. Endo, S. Ambe, and F. Ambe

Data obtained from radioactive tracer experiments on biological systems generally show considerable variation due to the peculiarity of individual samples. Use of a multitracer[1] in a given biological system enables us to obtain information on the behavior of trace amounts of many kinds of radioactive nuclides in various tissues, organs or body fluids simultaneously under strictly identical conditions, suggesting that effects of both peculiarities of samples and variation in experimental conditions can be minimized.

In the present study, the uptake and distribution of radioactive isotopes in various tissues, organs and body fluids of rats were examined by means of the multitracer technique to clarify the behavior and role of different elements.

Hydrochloric acid solution containing a multitracer was prepared from gold foil irradiated with N-14 beam of 135 MeV/nucleon from RIKEN Ring Cyclotron and was adjusted to pH 3. The solution was administered orally to Wistar rats (male) which were seven weeks old. The rats were sacrificed after several days. The tissues, organs, body fluids and excretions were weighed and their radioactivities were determined by $\gamma$-ray spectrometry. Identification and determination of isotopes were done on the basis of their energies and half-lives. The results are given in percentage of orally administrated dose per gram of tissues, organs and body fluids (uptake rate, %/g).

From the analysis of $\gamma$-ray spectra, distributions of 23 elements, namely Be, Mn, Co, Zn, As, Se, Rb, Sr, Y, Zr, Ce, Eu, Gd, Tb, Er, Tm, Yb, Lu, Hf, W, Re, Ir, and Pt, were determined. Typical results at 6 days after administration are shown in Fig. 1. The results and discussion are given below, with the elements being tentatively divided into the following six groups based on the classification of the periodic table.

(1) Rubidium (alkaline metal) was found to be distributed widely among various tissues, organs and body fluids. High concentrations were found in liver, spleen, kidney and skeletal muscle. The chemical similarity of rubidium to potassium is considered to allow use of the former as a substitutive tracer for the latter to some extent. These results suggest that rubidium is essentially an intracellular ion, physiologically most similar to potassium since it is distributed throughout the body in a very similar manner. Distribution of rubidium in whole blood was mostly found in erythrocytes. From this study, rubidium is found to be eliminated very slowly from the body.

(2) Strontium (alkaline earth metal) was found in high concentrations in bone. The result suggests that the distribution of strontium was similar to that of calcium. The results have also demonstrated that intestinal absorptions of strontium and calcium are comparable, which leads to the hypothesis that these elements share a common carrier system in the intestinal wall, probably with a greater affinity for calcium.

(3) 3d-Transition elements such as Mn, Co, and Zn were distributed in organs based on their individual characteristics. Among the elements, zinc was found in every organ as well as blood, and high concentrations of it were observed in liver, kidney and spleen. The absorption of zinc ions mainly occurs in the small intestine, especially in the jejunum, while its absorption in the duodenum and the stomach seems to be very low.[2] Zinc is essential for the structure, reg-

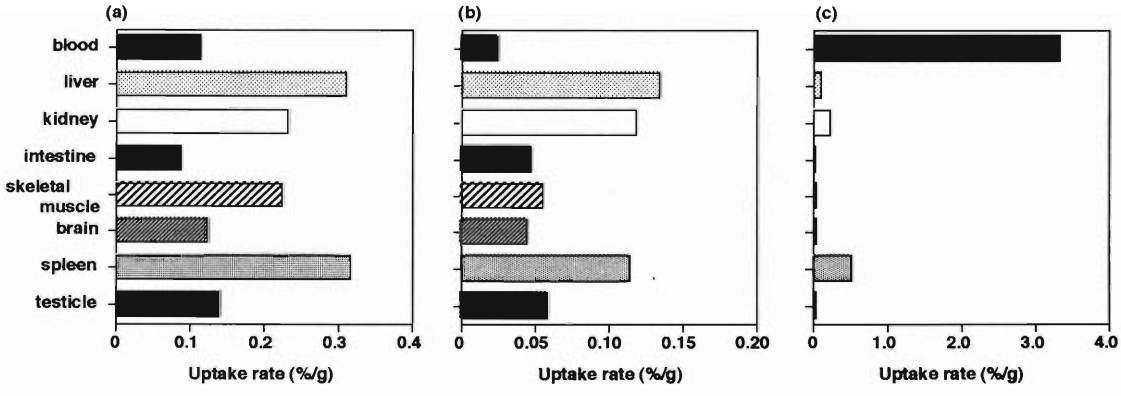


Fig. 1. Uptake rate (%/g) of rubidium (a), zinc (b) and arsenic (c) in various tissues, organs and body fluids in a rat.

ulation, and/or the catalytic action of many enzymes and it influences the activity of over 300 enzymes.[3] In accordance with this, we found that zinc was widely distributed in various tissues, organs and body fluids. On the other hand, orally administrated manganese does not concentrate in specific organs. In general, the absorption level of manganese is lower in animals which have reached adulthood.[4]

(4) All the radioactivities of rare earth elements (Y, Ce, Eu, Gd, Tb, Er, Tm, Yb, and Lu) and Be, Zr, Hf were eliminated in feces. These results indicate that these elements were not absorbed by the digestive organs including intestine.

A detailed discussion is given in Ref. 5.

(5) Of the 5d-transition metals, W, Re, Ir, and Pt were determined, and each was found to exhibit characteristic behavior. Intestinal absorptions of tungsten and rhenium were rapid. They were likewise rapidly transferred to blood and then to kidneys for filtration and removal from the body. However, rhenium was retained partly in rat hair 6 days after administration. In contrast, platinum and iridium were absorbed by liver, kidney, and intestine. These metals are reported to bind with metallothionein in liver and kidney.[6] The above result is compatible with this binding characteristic.

(6) The absorption of arsenic (group V) and selenium (group VI) was also investigated. Selenium was found to be widely distributed in every organ, and the highest concentration of which was detected in kidney, liver, blood, testicles, and intestine. Selenium is involved in some important biochemical reactions and is found in a number of proteins.[7] Accordingly, we found that selenium was widely distributed in various tissues, organs and body fluids. On the other hand, arsenic was found mainly in blood. Arsenic combines with sulfhydryl groups of many enzymes.[8] Arsenic is a strong hemolytic poison, with erythrocytes being the target. We found that arsenic is bound to protein ($\alpha_1$-globulin) in serum and to the globulin part of hemoglobin in erythrocytes.

These results suggest that when applied to a given biological system, the multitracer technique is a powerful tool to obtain information on the behavior of trace amounts of elements in various tissues, organs and body fluids.

References


1) S. Ambe et al.: *Chem. Lett.*, **1991**, 149.
2) L. Thunus and R. Lejeune: Handbook on Metals in Clinical and Analytical Chemistry, edited by H. G. Seiler, A. Sigel, and H. Sigel, Marcel Dekker, New York, p. 667 (1994).
3) R. J. Cousins: *Physiol. Rev.*, **65**, 238 (1985).
4) L. S. Maynard and D. D. Joel: *Life Sci. Stal.*, **28**, 96 (1977).
5) M. Yanaga et al.: This report, p. 86.
6) R. P. Sharma and I. R. Edwards: *Biochem. Pharmacol.*, **32**, 2665 (1983).
7) R. J. Magee and B. D. James: Handbook on Metals in Clinical and Analytical Chemistry, edited by H. G. Seiler, A. Sigel, and H. Sigel, Marcel Dekker, New York, p. 551 (1994).
8) R. Iffland: *ibid.*, p. 237.

# Distribution and Behavior of Trace Elements in Zinc Deficient Rats Using the Radioactive Multitracer Technique

S. Enomoto, M. Yanaga, R. Hirunuma, K. Endo, S. Ambe, and F. Ambe

The concentration variation of one particular element generally affects the concentrations and physiological effects of other substances, including other inorganic elements. This multidimensional interdependence has been known qualitatively for a few of elemental nutrients.[1] However, the multidimensional interdependence of many trace elements in living bodies is still not clear. Two components can interact by mutually promoting synergistic effects or by competing and suppressing antagonistic effects. Use of a radioactive multitracer in a given biological system enables us to obtain information on the multidimensional interdependence of many trace elements in various tissues, organs or body fluids simultaneously under strictly identical conditions, suggesting that effects of both peculiarities of samples and variation in experimental conditions can be minimized.

In the present study, the uptake and distribution of radioactive isotopes in various tissues, organs and body fluids of zinc deficient rats and normal rats were examined by means of the multitracer technique to clarify the behavior and role of different elements. Zinc is the second most abundant transition element in the animal organisms, following iron; zinc also plays an important role in many processes of metabolisms of living beings. More than 300 different zinc-proteins are known. These include numerous essential enzymes which catalyze the metabolic conversion or degradation of proteins, nucleic acids, lipids, porphyrin precursors and other important bioorganic compounds. It is thus not surprising that zinc deficiency leads to severe pathological effects and is expected to affect the behavior of other trace elements greatly.

A saline solution containing a multitracer was prepared from a gold foil irradiated with N-14 beam of 135 MeV/nucleon from RIKEN Ring Cyclotron. The solution was injected intravenously to normal or zinc deficient Wistar rats (male) which were seven weeks old. The rats were sacrificed after 4 days. The tissues, organs, body fluids and excretions were weighed and their radioactivities were determined by $\gamma$-ray spectrometry. Identification and determination of isotopes were done on the basis of their energies, half-lives and peak areas. The results are given in percentage of intravenously injected dose of tissues, organs and body fluids (uptake %).

From the analysis of $\gamma$-ray spectra, distributions of Sc, V, Mn, Co, Zn, Rb, Sr, Y, Ce, Eu, Gd, Tm, Yb, Lu, Hf, Re, Ir, and Pt were determined. Concerning the Zn distribution in zinc deficient rats, the uptakes in testicle, skin and bone were smaller than those in normal rats; however, the uptakes in other tissues and blood were larger. Other various trace elements also demonstrated characteristic behavior. Noteworthy is that distributions of Pt and Ir in zinc deficient rats are quite different from those in normal rats. In the case of normal rats, Pt and Ir are classified in the same behavioral group (the platinum group), because these elements behave in a similar manner in an animal body.[2] However, when we administrated them to zinc deficient rats, the uptakes of Ir in skeletal muscle, skin, hair, and plasma were larger than those of Pt by a factor of about 2–3. These results suggest that zinc deficiency contributes to conformational changes or affinity changes on transport proteins or enzymes which interrelate with the uptakes of Pt and Ir. The distributions of various rare earth elements (REE) exhibited similar behavior in both normal and zinc deficient rats. The uptakes of REE in various tissues, such as liver and kidney, were correlated with changes in the ionic radius of REE. The uptakes of "light" REE increased with increasing ionic radius, however, there were not a marked tendency in those of "heavy" REE. These results suggest that the uptakes of light REE, whose ionic radii are near that of calcium, are interrelated with the calcium transport systems in cytoplasmic membrane. In contrast, the uptakes of REE in bone were different from those in other tissues. The heavy covalent REE in bone were accumulated to a greater extent than the light REE. The uptakes of light REE were decreased with increasing ionic radius. These results also indicate that heavy covalent REE are adsorbed on hydroxyapatite that reacts with enzymes such as alkaline phosphatase and light REE are non-specifically adsorbed on connective tissues in surface of bone.

These results suggest that when applied to a given biological system, the multitracer technique is a powerful tool to obtain information on the behavior of trace amounts of elements and the multidimensional interdependence of various elements in various tissues, organs and body fluids.

References

1) H. Sigel, A. Sigel, and H. G. Seiler: Handbook on Metals in Clinical and Analytical Chemistry, Marcel Dekker, New York, p. 1 (1994).
2) K. H. Konig and M. Schuster: *ibid.*, p. 521.

# Tissue Distribution of 16 Elements in Mice: An Application of Multitracers to Animal Experiments

R. Amano, M. Nobuta,* M. Sakamoto,* R. Tsujioka,* S. Enomoto, and F. Ambe

We are now developing the radioactive multitracer technique in the metabolism study of a number of trace elements in animals. First we examined here the tissue distribution of carrier-free multitracers in mice and discuss on their usefulness in animal experiments.

A multitracer solution was obtained from the silver foil target irradiated with $^{14}N$ beam accelerated in RIKEN Ring Cyclotron. The preparation procedure was given elsewhere.[1,2] After evaporation of the carrier-free multitracer solution containing hydrochloric acid, a physiological saline solution was added to prepare the multitracer solution for injection. Male ddY mice (body weight 25–35 g) were injected intraperitoneally with 0.2 mL of the final preparation. At 4 different time, namely, 3, 24, 72, and 168 hr after administration of the multitracers, the mice were killed under ether anesthesia and approximately 0.3 mL of blood was collected. After this, brain, cardiac muscle, lung, liver, spleen, pancreas, kidney, skeletal muscle and bone were excised. These tissues and the blood were weighed immediately and freeze-dried. The dried tissues and blood samples were measured by $\gamma$-ray spectrometry with pure Ge detectors against an appropriate standard to obtain the percentage of injected dose per gram of tissue (%dose/g). The radionuclides were identified by the $\gamma$-ray energies and half lives. Tissue distribution of the radionuclides was evaluated in terms of the percentage of injected dose per gram of tissue (the tissue uptake rate, %dose/g).

The tissue uptake rates of Be, Sc, V, Cr, Mn, Fe, Co, Zn, As, Se, Rb, Sr, Y, Zr, Ru, and Rh were obtained for the 9 tissues and blood in mice. We now brief some preliminary results concerning vanadium as an example. Table 1 summarizes the tissue uptake rates of radioactive V in the tissues and blood. Each value represents the mean of four mice. Figure 1 shows the time course of the uptake rates for 4 tissues. The values for bone at 24, 72, and 168 hr after injection were 6.03, 8.73, and 5.65 %dose/g, respectively. These values were much larger than those for other organs. Vanadium is not generally noted as a bone-seeking element. The multitracer technique enables simultaneous tracing of other elements concerned with bone and extensive comparison of these elements under a strictly identical condition.[3] Figure 2 compares the bone uptake rates of V, Sr, Zr, Y, Rh, Ru, and Se. The values of V resembled those of Sr, Zr, and Y, but not those of Rh, Ru, and Se. From these results it has been found that vanadium may play an important role in the bone metabolism. We have mainly mentioned above the results concerning vanadium as an example. We really obtained similar results on 15 other elements in the present work, which will be reported and discussed later.

Table 1. Tissue uptake rate of radioactive V in mice at 3, 24, 72, and 168 hr after intraperitoneal injection.

| Tissue | V | | | |
|---|---|---|---|---|
| | 3 hr | 24 hr | 72 hr | 168 hr |
| Blood | 2.94 ± 0.15 | 0.86 ± 0.19 | n.d. | n.d. |
| Brain | 0.09 ± 0.05 | 0.06 ± 0.00 | n.d. | n.d. |
| Cardiac muscle | 0.84 ± 0.28 | 0.74 ± 0.10 | 0.47 ± 0.16 | 0.34 ± 0.11 |
| Lung | 1.09 ± 0.21 | 0.66 ± 0.11 | 0.35 ± 0.06 | 0.22 ± 0.04 |
| Liver | 2.53 ± 0.63 | 1.50 ± 0.24 | 0.79 ± 0.12 | 0.76 ± 0.26 |
| Spleen | 0.48 ± 0.17 | 0.69 ± 0.28 | 0.51 ± 0.23 | 0.24 ± 0.09 |
| Pancreas | 0.64 ± 0.23 | 0.55 ± 0.27 | 0.42 ± 0.17 | n.d. |
| Kidney | 6.47 ± 1.83 | 2.28 ± 0.35 | 1.86 ± 0.05 | 0.83 ± 0.19 |
| Bone | 3.65 ± 0.90 | 6.03 ± 1.58 | 8.73 ± 2.24 | 5.65 ± 1.58 |
| Skeletal muscle | 0.61 ± 0.13 | 0.27 ± 0.17 | 0.24 ± 0.03 | 0.15 ± 0.03 |

n.d.: not detected

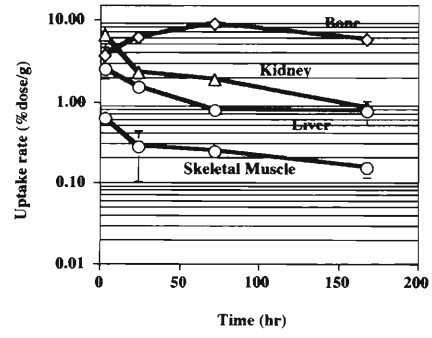


Fig. 1. Time course of the tissue uptake rates of radioactive V in mice.

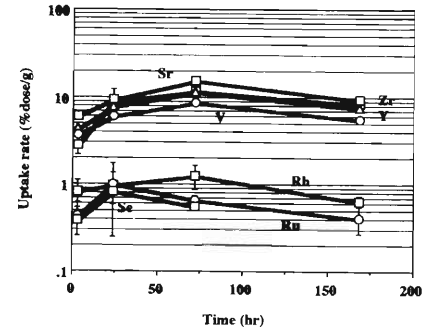


Fig. 2. Time course of the uptake rates of V, Sr, Zr, Y, Rh, Ru, and Se in mouse bone.

In conclusion, we want to emphasize the advantages of the multitracer technique over the conventional single tracer technique: the multitracer method enables simultaneous tracing of many elements in the identical organ and a strict comparison of their biobehavior.

References

1) S. Ambe et al.: *Chem. Lett.*, **1991**, 149.
2) S. Ambe et al.: *Anal. Sci.*, **7**, Suppl., 317 (1991).
3) F. Ambe: *RIKEN Review*, No. 4, p. 31 (1994).

* School of Allied Medical Professions, Kanazawa University

RIKEN Accel. Prog. Rep. **28** (1995)

# Studies on Transcuticular Movement of Multitracer from Plant Leaf Surfaces

T. Watanabe, K. Matsumoto, S. Ambe, and I. Yamaguchi

The surface of plants is generally covered with cutile which plays an important role in their growth for prevention of transpiration, invasion of microbes and foreign substances and for morphogenesis. The transcuticular movement of radionuclides as a foreign substance is an interesting matter relating to the uptake, distribution and accumulation in plants via rainfall of those contained in fall-outs.

To investigate the transcuticular penetration and translocation of radionuclides on/in plants, the authors have carried out a preliminary study of the transcuticular movement of $^{137}$Cs applied as an aqueous droplet onto the leaves of chinese cabbage. The result showed that $^{137}$Cs firstly penetrated into the cuticle under the droplet, then passed across it to translocate inside the leaf tissue acropetally and basipetally, and finally distributed in the stems, leaves and roots other than the leaf applied. To analyze quantitatively the translocation proccesses of various kinds of radionuclides, five $\mu$l of the multitracer solution was applied onto the leaf surfaces of chinese cabbage and mugwort at the fifth leaf stage. Then, the amounts of each radionuclide in the malutitracer translocated into the fractions of cuticle, applied leaf, other leaves and roots were periodically measured. The calculation is now underway using computers.

# Simultaneous Analysis of Solid-Liquid Adsorption Behavior of Various Elements using Radioactive Multitracer: Activated Carbon Fiber and Non-ionic Macro-reticular Copolymer

S. Shibata, K. Watari,* Y. Noda,* S. Ambe, Y. Ohkubo, M. Iwamoto, Y. Kobayashi, M. Yanokura, H. Maeda, and F. Ambe

Activated carbon and non-ionic macro-reticular (MR) copolymers have been reported to be effective adsorbents for a number of organic substances in aqueous solutions, but not enough attention has been paid to the adsorption of inorganic substances.[1,2] We reported previously the adsorption behavior of 36 inorganic elements on Kynol ACF-1605-15 (novoloid-based activated carbon fiber) and Amberlite XAD-7 (non-ionic MR copolymer) in 0.01–10 mol·dm$^{-3}$ solutions of HCl and LiCl using a radioactive multitracer prepared by irradiation of Au or Ag foil with a heavy ion beam.[3]

We continued the study on the adsorption behavior of various elements on these adsorbents using a multitracer obtained from irradiated Fe foil. In separation of the reaction products after the irradiation of iron with 135 MeV/nucleon $^{16}O^{6+}$, iron was extracted with isopropyl ether from 8 mol·dm$^{-3}$ HCl. The aqueous layer was evaporated to dryness. The residue was dissolved in 1 mol·dm$^{-3}$ HCl. Other experimental methods were mentioned in a previous report.[3]

Figure 1 shows the adsorption profiles of 42 elements in log-log plotting of Kd against the concentration of $Cl^-$. The authors are now studying the adsorption behavior of other elements using the multitracer prepared from other targets, such as Zn and Sn.

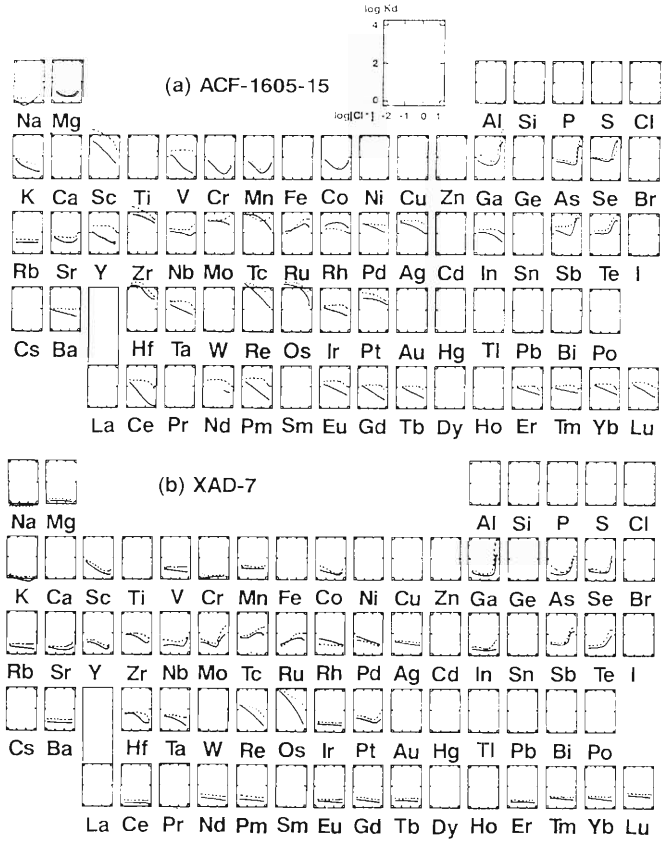


Fig. 1. Effect of $Cl^-$ concentration in HCl (—) and LiCl (···) on Kd values of elements for ACF-1605-15 (a) and XAD-7 (b).

References

1) K. Watari, K. Imai, S. Shibata, and M. Miura: *J. At. Energy Soc., Jpn.*, **26**, 384 (1984).
2) S. Shibata, K. Watari, and K. Kaneko: *Radioisotopes*, **39**, 26 (1990).
3) S. Shibata et al.: *RIKEN Accel. Prog. Rep.*, **27**, 83 (1993).

* National Institute of Radiological Sciences

# Studies on the Ion Exchange Adsorption Behavior of Strongly Acidic Resin NAFION and its Application to Analytical Chemistry

N. Ito, H. Harakawa, Y. Saito, K. Kimura, S. Ambe, M. Iwamoto, H. Maeda, and F. Ambe

Radioactive multitracer solutions, in a carrier- and salt-free condition, prepared from gold[1-5] foil irradiated with 135 MeV/nucleon $^{14}N$ ions were used for the titled studies in a NAFION-$HNO_3$ system after being converted to a nitric acid solution. The NAFION-501 resin, manufactured by DuPont, is a perfluorinated polymer containing ~5 mmol $g^{-1}$ sulfonic acid groups. Because of the strong acidity of the resin, a comparison of its exchange behavior with that of a common cation exchange resin attracts much attention.

The resin, commercially available as a cylindrical shape of ca. 1 mm$\phi \times 3$ mm, was crushed with a stamp mill at liquid nitrogen temperature, passed through a 50–120 mesh screen, and used. Into a small polyethylene bottle, 0.1 ml of the multitracer solution and 2.4 g of the resin were introduced, and the acidity of the system was adjusted to 0.1, 0.3, 1, 3, 5, and 10 mol $dm^{-3}$ with nitric acid and distilled water, thereby making the volume of the solution to 10 ml. The contents of the bottle were shaken vigorously at 25 °C with an 8-shape mode shaker. Time of the shaking was 75 hours. After filtration, $\gamma$-ray spectrometry was carried out for both phases.

The distribution ratios (D) of alkali metal, alkaline earth metal and rare earth element (Fig. 1a) were obtained, decreasing with slopes of the valence number on log-log plotting as nitric acid concentration increased, which is characteristic of the ion exchange. D's for Hf and Zr (Fig. 1b) were relatively low at 0.1 mol $dm^{-3}$ nitric acid concentration, while in other concentrations, those decreased with slopes of $-2$ approximately. It is thought that Hf and Zr mainly exist as $HfO^{2+}$ and $ZrO^{2+}$ in 0.3 ~ 10 mol $dm^{-3}$ nitric acid concentrations and the low D values at 0.1 mol $dm^{-3}$ concentration would be due partially to their hydrolytic species.

An ion exchange separation using a NAFION resin column was carried out with 0.1, 0.3, and 5 mol $dm^{-3}$ nitric acid concentrations. Twelve % of Hf and 5% of Zr were eluted at 0.1 mol $dm^{-3}$ nitric acid without adsorption, corresponding to the above lower D values at low concentrations of nitric acid. Pt (60%) was also passed through the column. Alkali metal and alkaline earth metals were separated from each other in order of D values at 0.3 mol $dm^{-3}$ nitric acid, and finally other multi-valent elements including rare earths and the rest of Hf and Zr were eluted at 5 mol $dm^{-3}$.

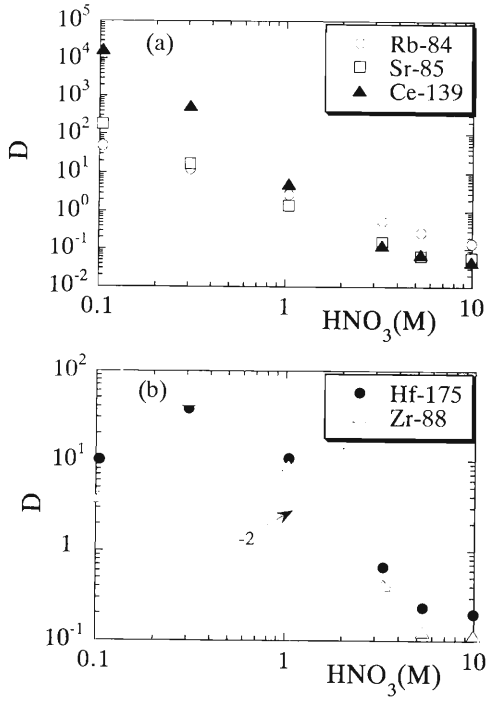


Fig. 1. Relationship between D and acidity of nitric acid. (a) Rb, Sr, and Ce. (b) Zr and Hf.

References

1) S. Ambe, S. Y. Chen, Y. Ohkubo, Y. Kobayashi, M. Iwamoto, M. Yanokura, and F. Ambe: *RIKEN Accel. Prog. Rep.*, **25**, 95 (1991).
2) S. Ambe, S. Y. Chen, Y. Ohkubo, Y. Kobayashi, M. Iwamoto, M. Yanokura, and F. Ambe: *Anal. Sci.*, **7**, Suppl., p. 317 (1991).
3) S. Ambe, S. Y. Chen, Y. Ohkubo, Y. Kobayashi, M. Iwamoto, and F. Ambe: *RIKEN Accel. Prog. Rep.*, **24**, 73 (1990).
4) S. Ambe, S. Y. Chen, Y. Ohkubo, Y. Kobayashi, M. Iwamoto, M. Yanokura, and F. Ambe: *Chem. Lett.*, **1991**, 149.
5) T. Bamba, H. Harakawa, Y. Saito, K. Kimura, T. Yaita, S. Shibata, S. Ambe, Y. Ohkubo, M. Iwamoto, Y. Kobayashi, M. Yanokura, H. Maeda, and F. Ambe: *RIKEN Accel. Prog. Rep.*, **26**, 88 (1992).

# Influence of Metal Humate Formation on the Adsorption of Multitracer on Kaolinite

Y. Takahashi, Y. Minai, S. Ambe, M. Iwamoto, H. Maeda, F. Ambe, and T. Tominaga

Humic acid, a naturally-occurring organic polyacid, is soluble in neutral aqueous solutions and capable of forming stable complexes with some cations through a variety of its functional groups. Therefore, humic acid may influence migration in the environment of metal cations such as lanthanides and trivalent actinides.[1,2] We have used the multitracer technique to study interactions between various ions and humic acid.[3] Kaolinite is a typical clay mineral which adsorbs metal cations in the environment. The presence of humic acid in aquifer, however, may reduce the adsorption of ions on kaolinite by complex formation. The influence of humate formation on the adsorption of multitracer on kaolinite is given in this report.

Multitracer was produced by spallation reaction of Au with $^{12}C$ or $^{14}N$ at RIKEN Ring Cyclotron and was prepared as 3 M HCl solution.[4,5] The HCl solution was converted to 0.001 M perchloric acid solution for the following experiments. Humic acid solution (5 m$\ell$, 50 mg/$\ell$), kaolinite (10 mg), and multitracer solution were mixed and shaken for a week. After centrifugation, the aqueous phase was filtered with a membrane filter (pore size, 0.45 $\mu$m). Then $\gamma$-ray spectra of the filtrates were recorded with a pure Ge detector coupled with a 4096 channel multi-channel analyzer. Photopeak intensities of the radionuclides in the aqueous phase were determined with a routine (BOB) on a FACOM M780 computer. Percentages of the dissolved species of Co, As, Rb, Sr, Y, Zr, Ag, Ba, Ce, Eu, Gd, Yb, Lu, Hf, Re, Ir, and Pt in each sample were obtained by comparing the photopeak intensities with those for the multitrader solution injected.

In all samples, humic acid was also adsorbed on kaolinite,[6] and fractions of dissolved humic acid were obtained spectrophotometrically as shown in Fig. 1.[7] Rubidium (alkali metal), and As or Re (forming oxoacids) were not adsorbed on kaolinite; addition of humic acid did not affect their adsorption behavior. This indicates that those ions do not make complexes with humic acid. Barium (alkaline-earth metal) may be partially present as a humate complex, since the pH dependence of Ba adsorption was almost similar to that of humic acid: the percentage of the dissolved species decreased at pH = 4–5 and increased at pH > 7. Yttrium and the lanthanides (Ce, Eu, Gd, Yb, Lu) form stable complexes with humic acid, since their dissolved percentages were identical with those of humic acid. Both humic acid and the rare earths were adsorbed in low pH region and were dissolved at pH > 6. The presence of humic acid made the pH dependence of adsorption of rare earths the opposite to that in the humic acid-free system. It means that the interaction of the clay mineral with humic substances modifies the adsorption property of the mineral. As shown in Fig. 1, humic acid apparently enhances the dissolution of Hf; identical results were obtained with Zr. However, much less amount of Hf or Zr was dissolved when humic acid was added after Hf or Zr had been adsorbed on kaolinite. Adsorption behavior of the tetravalent ions differs from that of rare earth ions: dissolved fractions of rare earths were identical irrespective of the order of addition of humic acid and tracers. It suggests that a surface complex of Hf or Zr on kaolinite is more stable than a humate complex. When humic acid is added before the addition of tracers, the humic acid coating on kaolinite may prevent adsorption of Hf or Zr on kaolinite. These results show that Hf or Zr exists as a hydrolyzed species in the aqueous phase, or on kaolinite. Humic acid indirectly influences the adsorption behavior of Hf and Zr on kaolinite.

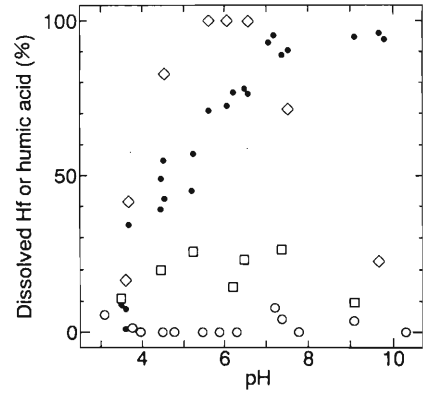


Fig. 1. Percentages of dissolved species of Hf and humic acid when the following solution (5 m$\ell$) was contacted with kaolinite (10 mg). (○: without humic acid, □: humic acid was added after addition of Hf, ◇: humic acid was added before addition of Hf, ●: humic acid)

References

1) Y. Minai et al.: Proc. 3rd. Int. Symp. Adv. Nucl. Energ. Res., p. 229 (1991).
2) Y. Takahashi et al.: *J. Radioanal. Nucl. Chem. Lett.*, **186**, 129 (1994).
3) Y. Minai et al.: Proc. Int. Trace Anal. Symp., p. 71 (1994).
4) S. Ambe et al.: *Chem. Lett.*, **1991**, 149.
5) S. Ambe et al.: *Anal. Sci.*, **7**, Suppl., p. 317 (1991).
6) Y. Takahashi et al.: Mat. Res. Soc. Symp. Proc., in press.
7) Y. Takahashi et al.: in preparation.

# Adsorption Behavior of Lanthanides Affected by Humate-complex

T. Ozaki, Y. Takahashi, Y. Minai, S. Ambe, M. Iwamoto, H. Maeda,
F. Ambe, and T. Tominaga

Humic acid is a naturally-occurring polyacid which can combine with various metal cations. The polyacid may greatly influence the distribution of several metals in the environment. We have studied the adsorption behavior of several metal ions on hematite and the influence of metal humate formation on the adsorption by using the multitracer technique. The multitracer technique permits us to ditermine the characteristic behavior of different elements under strictly identical experimental conditions and to make a precise comparison of the adsorption behavior among them.

A multitracer solution (3M HCl) was obtained from a gold target irradiated with a $^{12}C$ beam accelerated with RIKEN Ring Cyclotron. After evaporating up the multitracer solution to remove hydrochloric acid, 0.001M perchloric acid was added to prepare the multitracer solution for further experiments. Hematite ($\alpha$-$Fe_2O_3$) was added to a solution containing a multitracer. The pH of the solution was adjusted with dilute NaOH or $HClO_4$. The suspended solution was shaken for 1 week at room temperature. After centrifugation, the supernatant solution was filtered by a membrane filter (0.45 um) to remove $\alpha$-$Fe_2O_3$ thoroughly. The $\gamma$-ray spectra of the supernatant were measured with a pure Ge detector coupled with a 4096-channel multi analizer.

In Fig. 1 is shown the pH dependence of adsorption of Rb and Eu. In the absence of humic acid, Rb was not adsorbed significantly on hematite in the pH range studied. Europium attained complete adsorption in the alkaline region. In Fig. 1 (b and d) were shown adsorption curves of Rb and Eu in the presence of humic acid in the initial solution studied. Humic acid was almost adsorbed in the acidic pH range and decreased its adsorption with the increase in pH. Comparison of these adsorption curves with those of Rb and Eu in the absence of humic acid indicated that the adsorption of Rb was not infulenced by the addition of humic acid while the adsorption of Eu became similar to that of humic acid. Similar results were obtained for the other lanthanides acquired by the multitracer method. The observed behavior of lanthanides may suggest the high stability of humate-complexes in solution.

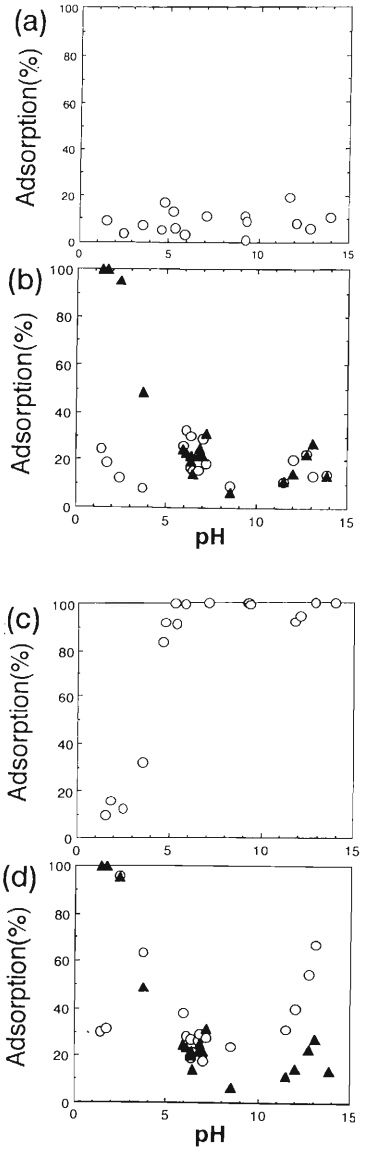


Fig. 1. Adsorption of Rb, Eu (○) and humic acid (▲) on hematite (hematite: 100 mg; volume of solution: 4 mℓ) Rb(a) and Eu(c) in humic acid free solutions; Rb(b) and Eu(d) in humic acid solutions.

# Production of Multitracer Nuclides by Irradiation with an $^{40}$Ar Beam

M. Iwamoto, S. Ambe, Y. Ohkubo, Y. Kobayashi, H. Maeda, and F. Ambe

At present, lighter heavy ions such as C, N, and O are used in combination with Ge, Ag, and Au targets in production of multitracers by RIKEN Ring Cyclotron.[1-6] In this method, each target material requires a specific elaborate treatment. If much heavier ions are used as projectiles in combination with different targets and catcher foil for production of multitracer nuclides, it is expected that a large part of product nuclides are recoiled out of the target and can be collected by catcher foil placed behind the target. Using appropriate catcher foil of a common material, the same simple separation method is available for different targets. Last year we reported the results of an experiment with a $^{84}$Kr beam.[7] This year irradiation with an $^{40}$Ar beam was studied.

The target was Ag-, Ta-, and Au- foil and the catcher was 25 mm-thick Al foil. The target assemblies were irradiated by 40 MeV/nucleon $^{40}Ar^{15+}$ ions using Falling Ball Irradiation System.[1] The average beam intensity was about 10 enA and irradiation time was 40–60 min. Details of experimental conditions for the targets are summarized in Table 1.

Table 1. Irradiation conditions.

| Target | Thickness ($\mu$m) | Duration (h) | Total amount of electricity ($\mu$C) |
|---|---|---|---|
| Cu | 20 | 0.67 | 10.1 |
| Ag | 10 | 0.67 | 14.2 |
| Au | 25 | 1.00 | 41.7 |

After the irradiation, the target and catcher foil were analyzed by direct $\gamma$-ray spectroscopy with pure Ge-detectors. Yield calculation of product nuclides was made by BOB code[8] and related programs. Assignment of the nuclides was performed on the basis of the energy of $\gamma$-rays and half-life.

Tables 2, 3, and 4 show the percentage of radionuclides found in the Al catcher foil, that is, the yield in catcher foil divided by the total yield for Cu-, Ag-, and Au-target respectively. The high yield of $^{24}$Na in the catcher foil is ascribed to fragmentation of $^{27}$Al nuclei in the foil. These preliminary results already demonstrate the effectiveness of this catcher foil method.

Table 2. Percentage of radionuclide found in Al catcher foil for Cu target.

| Nuclide | % |
|---|---|
| Na-24 | 100* |
| Sc-44d | 37 |
| Sc-47 | 28 |
| Mn-52 | 22 |

Table 3. Percentage of radionuclide found in Al catcher foil for Ag target.

| Nuclide | % | Nuclide | % |
|---|---|---|---|
| Na-24 | 93* | Sr-83 | 29 |
| As-71 | 34 | Y-87m | 25 |
| As-72 | 36 | Zr-86 | 28 |
| Se-73 | 35 | Zr-89 | 31 |
| Br-77 | 30 | Nb-90 | 21 |
| Kr-79 | 79 | Ru-97 | 12 |
| Rb-81 | 29 | Rh-101m | 8 |

Table 4. Percentage of radionuclide found in Al catcher foil for Au target.

| Nuclide | % | Nuclide | % |
|---|---|---|---|
| Na-24 | 93* | Te-119 | 17 |
| Mg-28d | 100 | Xe-125 | 12 |
| Sc-44m | 100 | Cs-129 | 25 |
| Cu-67 | 100 | La-132 | 16 |
| Zn-69m | 100 | Ce-135 | 14 |
| As-72 | 22 | Gd-147 | 15 |
| Se-73 | 18 | Dy-155 | 16 |
| Br-77 | 100 | Dy-157 | 16 |
| Y-87m | 100 | Er-160d | 10 |
| Zr-89 | 20 | Tm-165 | 13 |
| Nb-90 | 20 | Hf-173 | 6 |
| Mo-93m | 20 | | |

* $^{24}$Na produced from the catcher foil is included.

References

1) S. Ambe et al.: *Chem. Lett.*, **1991**, 149.
2) S. Ambe et al.: *Anal. Sci.*, **7**, Suppl., 317 (1991).
3) M. Iwamoto et al.: *ibid.*, p. 313.
4) S. Ambe et al.: *Appl. Radiat. Isot.*, **43**, 1533 (1992).
5) S. Ambe et al.: *Radiochim. Acta*, **63**, 49 (1993).
6) S. Y. Chen et al.: *J. Radioanal. Nucl. Chem. Lett.*, **186**, 113 (1994).
7) M. Iwamoto et al.: *RIKEN Accel. Prog. Rep.*, **27**, 79 (1993).
8) H. Baba et al.: *J. Nucl. Sci. Technol.*, **8**, 1227 (1972).

# Target Residues from the Interaction of Copper with 40 MeV/nucleon $^{40}$Ar Ions

W. Li,* X. Yin,** S. Ambe, Y. Ohkubo, Y. Kobayashi, M. Iwamoto, H. Maeda, X. Zhang,** Q. Luo,** and F. Ambe

The interaction of natural copper with lighter heavy ions, $^{12}$C and $^{20}$Ne, of intermediate energy has been studied systematically[1-3] with $\gamma$-ray spectrometry. In this work we extend the similar measurement to the interaction of copper with 40 MeV/nucleon $^{40}$Ar ions.

Irradiation was performed on the RIKEN Ring Cyclotron. By using the thick-target thick-catcher foil technique, cross sections and average forward ranges, FW, were determined for the target residues. Further analysis of the experimental data was carried out in the Institute of Modern Physics, Academia Sinica, China.

In terms of an assumption on Gaussian charge distribution, the mass yield distribution was calculated from the cross sections of the target residues. In $^{12}$C induced reaction of copper over a 20–45 MeV/nucleon energy range, we utilized the fireball model to generate the mass transfer, the momentum transfer and the excitation energy for each process of complete and incomplete fusion. When coupled with the sequential binary decay model, GIMINI code, the theoretical calculations were in good agreement with the mass yield distribution measured experimentally. In this work a similar calculation was carried out. However, theoretical calculations, as seen in Fig. 1, failed to reproduce the experimental mass yield distribution from the $^{40}$Ar + $^{nat}$Cu reaction at 40 MeV/nucleon.

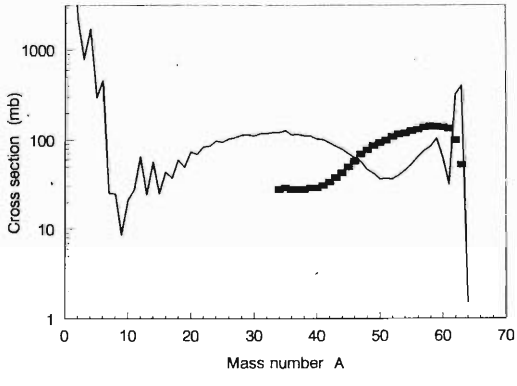


Fig. 1. Mass yield distribution in $^{40}$Ar + $^{nat}$Cu reaction (solid line is the calculations with the GIMINI code).

To estimate the linear momentum transfer in the collisions with $^{40}$Ar ions, the FW values were converted to recoil velocities of the residues, $v_{//}$, in initial collisions using, the ZBL transport equation. Resulting $v_{//}/v_{CN}$ values are shown in Fig. 2 as a function of mass loss, $\Delta$A, from the target, where $v_{CN}$ is the velocity of the presumed nucleus. Following Ref. 1 and Ref. 3, the maximum recoil velocity corresponding to central collision was extracted from Fig. 2. Assuming that the intermediate energy heavy ion reaction could be depicted as an incomplete fusion process, a preliminary mass of the composite system was deduced from the fractional velocity transfer $v_{//}/v_{CN}$. Thus the linear momentum transfer was obtained. The fractional linear momentum transfer corresponding to central collision was calculated to be 0.30 for the collision of copper with 40 MeV/nucleon $^{40}$Ar ions. When compared with the similar results from the collisions of copper with $^{12}$C and $^{20}$Ne ions, it is found that the fractional momentum transfer corresponding to central collisions decreases with increasing projectile mass at the same projectile velocity. However, the linear momentum transferred from the projectile to struck nucleus for the collision with $^{40}$Ar ions is higher than those in cases of $^{12}$C and $^{20}$Ne ions. As a result, the maximum nuclear temperature in central collisions reaches the value of about 5.5 MeV.

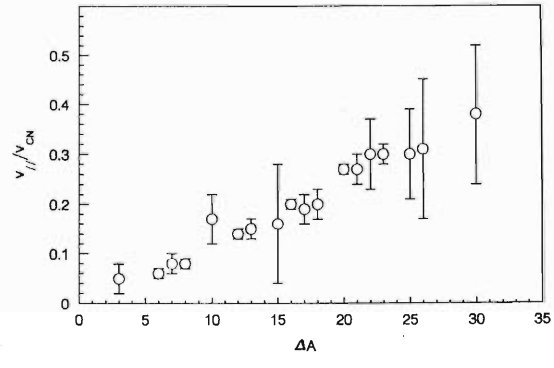


Fig. 2. Fractional velocity transfer $v_{//}/v_{CN}$ as a function of mass loss, $\Delta$A, from the target.

References

1) L. Pienkowski et al.: *Phys. Rev.*, **C43**, 1331 (1991).
2) J. P. Whitfield et al.: *ibid.*, **C47**, 1636 (1993).
3) L. Wenxin et al.: submitted to *Phys. Rev.*, **C**.

* Shanghai Institute of Nuclear Research, Academia Sinica, China
** Institute of Modern Physics, Academia Sinica, China

# The Mass Yield Distribution of Target Residues from the Interaction of Iron with 135 MeV/nucleon $^{12}$C Ions

Z. Qin,* W. Li,** L. Zhao,* W. Wen,* Q. Luo, T. Sun,* S. Ambe, Y. Ohkubo, M. Iwamoto, Y. Kobayashi, H. Maeda, and F. Ambe

Nuclear reactions induced by intermediate-energy heavy ions have been extensively investigated. The mass distribution of target residues is one of the most important characteristics of nuclear collisions induced by energetic heavy ions. In this work, the mass yield distribution of target residues has been studied for the interaction of iron with 135 MeV/nucleon $^{12}$C ions.

The experiment was performed on the RIKEN Ring Cyclotron. The target stack consisted of three pieces of ~15.7 mg/cm$^2$ thick natural iron foil. The purity of target material was 99.9%. The stack was mounted in a ball made of aluminum and set in the irradiation site of the Falling Ball Irradiation System. Following the irradiation, the middle target foil was assayed with a calibrated HPGe $\gamma$-ray spectrometer at RIKEN. The data process was completed at the Institute of Modern Physics, Lanzhou, China.

The mass yield distribution was obtained from the measured cross sections on the basis of the Gaussian charge distribution. The experimental results are compared with calculations based on the statistical multifragmentation model[1] (Fig. 1) and the modified sequential binary decay model[2] (Fig. 2), respectively. The calculations based on both of the theoretical models agree with the experimental mass yield distribution. It indicates that the target residues (A > 40), being described by using statistical theory, originate from the decay of equilibrated compound-like nuclei. This is the common basis between the two models. The largest difference between the two theoretical models lies in the prediction concerning mass yields in a lower mass region (A < 30). It is interesting that the experimental mass yields at this region are slightly lower than calculated results of the fusion fragmentation model considering multifragmentation, while higher than those of the sequential binary decay model. Similar to a lot of physical experiments, the radiochemical measurements based on off-line $\gamma$ ray spectra can hardly distinguish the validity of the sequential binary decay model and the multifragmentation model in the description of disassembly of hot nuclei. The deviation described above perhaps confirms that the intermediate mass fragments with a mass number less than 30 are the source of multifragmentation in the disassembly of hot nuclei. This issue is worthy of further study.

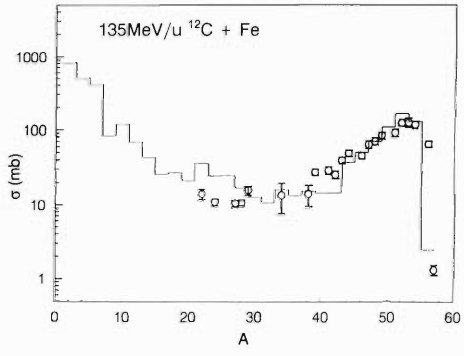


Fig. 1. Comparison of experimental results with the fusion fragmentation model (as histogram).

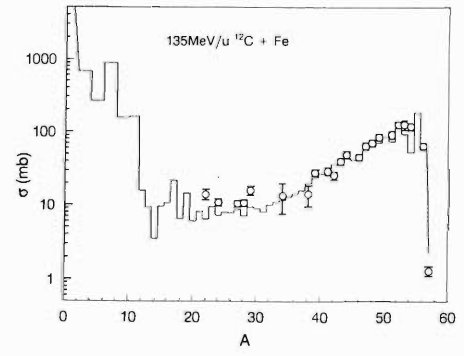


Fig. 2. Comparison of experimental results with the modified sequential binary decay model (as histogram).

References

1) S. Benhao, Z. Yuming, and Z. Xiaoze: *Phys. Rev.*, **C40**, 2680 (1989).
2) R. J. Charity et al.: *Nucl. Phys.*, **A340**, 371 (1988).

* Institute of Modern Physics, Academia Sinica, Lanzhou, China
** Shanghai Institute of Nuclear Research, Academia Sinica, Shanghai, China

# Angular Distribution of Recoil Products in the Heavy-Ion Reaction of Gold

M. Furukawa, A. Shinohara, K. Mukai, T. Muroyama, A. Yokoyama, S. Kojima, T. Saito, Y. Ohkubo, and F. Ambe

Angular distributions of recoil products were measured for the heavy-ion reaction of gold at the E3b course of the RIKEN Ring Cyclotron. The target was self-supporting 240 $\mu$g/cm$^2$-thick Au metal foil made by a spattering method, and set at the center of a Lucite cylindrical chamber, in the interior of which Mylar film was put on to catch the recoil products. The ions used were 35 and 95 MeV/nucleon $^{40}$Ar and 70 and 135 MeV/nucleon $^{14}$N. The irradiations were done for 3 to 4 hours in the beam current ranging from 50 to 200 enA. The catcher foil was divided into 8 peaces along the scattering angle, and subjected to the off-line $\gamma$-ray measurement.

The relative angular distribution of the recoil product was obtained from the main $\gamma$-ray intensities observed in the individual catcher foils. The results for the Au + $^{14}$N (135 MeV/nucleon) system were presented in Fig. 1 for some products in peripheral, spallation and fission reaction regions. The angular distributions for the peripheral reaction (target like products) showed side peaking distribution; those for the spallation region had a narrow forward peak; the products mainly from fission were distributed over a wide angle. The data analysis is in progress for 35 and 95 MeV/nucleon-$^{40}$Ar and 135 MeV/nucleon-$^{14}$N beam experiments, and the measurement has been still continued for a 70 MeV/nucleon-$^{14}$N beam experiment.

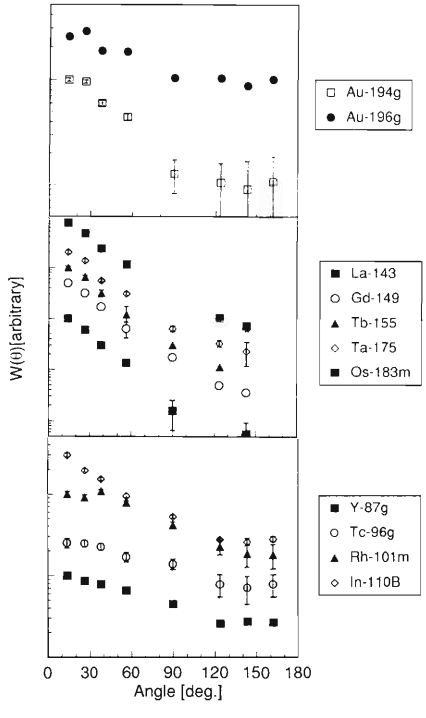


Fig. 1. Angular distributions of the recoil products in the Au + $^{14}$N (135 MeV/nucleon) system.

We have data for the mean recoil ranges measured in the previous experiments,[1] which are available for estimation of the mean linear momentum transfer to the product. We can deduce the moving frame angular distribution from the momentum transfer if having obtained the velocities of the recoil product in the moving frame. Figure 2 shows preliminary results for the translated distributions in the fission region. In this analysis we assumed the total kinetic energy of the fission fragments obtained by Viola's systematics. Some distributions showed 90° symmetric shape, and the other ones were distorted shape. The 90° symmetric distribution corresponds to the slow fission passing through the equilibrated intermediate nucleus, while the distorted one may result in the fast fission. However, further consideration on the translation method for the moving frame in addition on more detailed data analysis will be required in order to discuss the property of fission in this energy region.

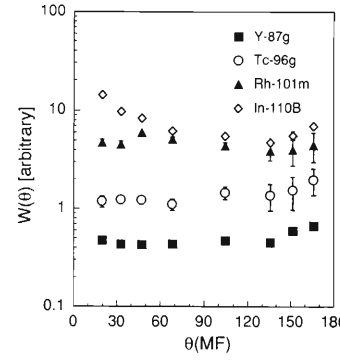


Fig. 2. Moving frame angular distributions for the products in the fission region.

Such a fission process, as well as the competition with the spallation reaction, provides important information on the mechanism of hot nucleus formation in the collision step and the succeeding equilibrium state or its decay process. We will discuss the above from the beam and energy dependence of the angular distribution, which will be obtained in the present experiments, and from the mean recoil ranges and mass yield distributions measured previously.

References

1) E. Taniguchi et al.: *Radiochim. Acta*, **62**, 163 (1993); J. Kurachi et al.: *RIKEN Accel. Prog. Rep.*, **26**, 94 (1992).

# Incomplete Fusion of the $^{141}$Pr Induced by 38–95 MeV/u $^{40}$Ar Ions

K. Mukai, A. Yokoyama, T. Saito, H. Baba, Y. Ohkubo, A. Shinohara, and M. Furukawa

We have studied the $^{141}$Pr + $^{40}$Ar reaction at various energies ranging from 38 through 95 MeV/nucleon, and found that the incomplete fusion plays an important role in the intermediate energy region (20–30 MeV/nucleon). We performed the experiments at RIKEN Ring Cyclotron by the radiochemical methods. $^{141}$Pr foils were bombarded with $^{40}$Ar ions at beam energies of 38, 59, and 95 MeV/nucleon. After the irradiation, the samples were assayed by the Ge $\gamma$-ray spectrometry. The details of experiments are described elsewhere.[1)]

From the results, the mean projectile recoil ranges ($FW$) are obtained, where $F$ is the fraction of the radioactivity collected in the forward foil and $W$ is the target thickness in mg/cm$^2$. Then we deduced recoil velocities of product nuclei and the linear momentum transferred (LMT) from the projectile to the target nucleus using the range-energy table calculated with the OSCAR code.[2)]

As an example, the LMT at a bombarding energy of 38 MeV/nucleon as a function of the product mass is shown in Fig. 1. The LMT takes the maximum value around $A$ = 100 to 110, and this mass region corresponds to the peak position of the mass distribution originated from the incomplete fusion. From the results, the average LMT values were deduced at various bombarding energies. As the beam energy increases, the average LMT decreases almost linearly.

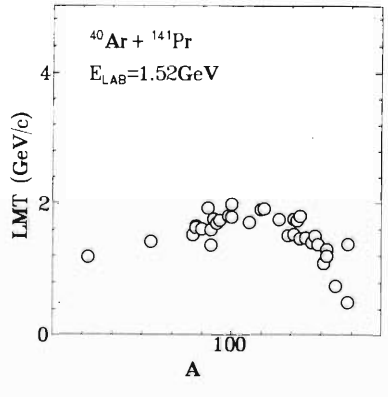


Fig. 1. The longitudinal momentum along beam direction at the bombarding energy of 38 MeV/nucleon as a function of the product mass number.

Regardless of the target-projectile combination, it was reported that the LMT obeys Leray's systematics:[3)]

$$\tilde{\rho} = 1 \quad \text{for} \quad V_{\rm rel} \geq 0.1$$
$$\tilde{\rho} = -1.904 V_{\rm rel} + 1.19 \quad \text{for} \quad V_{\rm rel} \leq 0.1$$

where

$$V_{\rm rel} = \sqrt{\frac{2(E_{\rm cm} - V_{\rm c})}{\mu}}.$$

The averaged LMT values as a function of $V_{\rm rel}$ are plotted in Fig. 2 as ratios to those on the assumption of full momentum transfer. There is a discrepancy between the systematics and the observed values. The data from Refs.[4,5)] are also plotted in the same figure. The figure demonstrates that the projectile dependence is more remarkable than the target dependence.

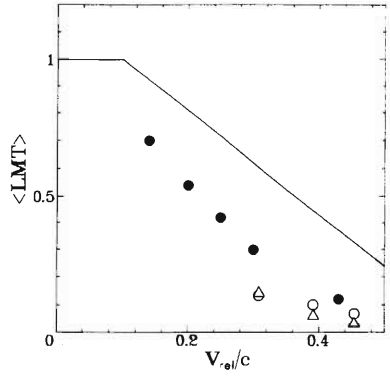


Fig. 2. Comparison of the average LMT with the Leray systematics. The symbols represent the projectile-target combinations: (●) $^{12}$C + $^{nat}$Cu,[4)] (○) $^{40}$Ar + $^{141}$Pr, and (△) $^{40}$Ar + $^{nat}$Cu.[5)]

The LMT is very useful to help us in understanding the incomplete fusion mechanism. But the systematics taking the dependence on both projectile and target into consideration would further refine our understanding of the incomplete fusion mechanism.

References

1) K. Takesako et al.: *OULNS Ann. Rept.*, p. 122 (1992).
2) K. Hata and H. Baba: INDC(NDS)-195-GZ, p. 131 (1981); JAERI-M, p. 88 (1988).
3) S. Leray: *J. Phys.*, **C4**, 275 (1986).
4) J. P. Whitfield and N. T. Porile: *Phys. Rev.*, **C47**, 1636 (1993).
5) E. Taniguchi et al.: *Radiochim. Acta*, **62**, 163 (1993).

# TDPAC of $^{99}$Ru in $YBa_2Cu_3O_{6.8}$ and $YBa_2Cu_3O_6$

Y. Ohkubo, Y. Kobayashi, S. Ambe, K. Harasawa, T. Okada, F. Ambe, K. Asai, and S. Shibata

Using TDPAC and Mössbauer techniques, we measured the hyperfine fields at $^{99}$Ru in $YBa_2Cu_3O_{6.8}$ and $YBa_2Cu_3O_6$. We have then found that the parent nuclide $^{99}$Rh exclusively occupies the Cu-1 site of both oxides and that there are two and one types of oxygen coordination around $^{99}$Ru in $YBa_2Cu_3O_{6.8}$ and $YBa_2Cu_3O_6$, respectively, corresponding to the observed electric field gradients (EFG's).[1] In this report, we describe our conclusion on the oxygen coordination.

The EFG at $^{99}$Ru is produced by the valence and closed-shell electrons of the probe atom; the surrounding oxygen ions distort the spherically symmetric distribution of the closed-shell electrons of the probe atom and then contribute to the EFG. In order to determine the oxygen coordination around $^{99}$Ru, we refer to the results of a point charge lattice sum calculation for $(FeO_n)^{-m}$ in $YBa_2Cu_3O_{7-\delta}$.[2] This calculation deals only with the closed-shell electron contribution and is thus not considered to give accurate values of the largest principal axis component of the EFG, $V_{zz}$. However, from the combined studies of EXAFS and Mössbauer spectroscopy on $YBa_2(Cu_{1-x}Fe_x)_3O_{6.9}$, we consider that the calculation reproduces the relative magnitudes of $V_{zz}$ at $^{57}$Fe with respect to the oxygen coordination, indicating that the magnitude of EFG due to the valence electrons correlates to that due to the closed-shell electrons; this is because the neighboring ions certainly influence the distribution of the valence electrons of the probe atom through the chemical bonding. We note that $^{57}$Fe occupies the Cu-1 site of $YBa_2Cu_3O_{7-\delta}$ and is considered to take approximately the same valence of +4 irrespective of $\delta$, and that $^{99}$Ru in the same matrix is constantly tetravalent. Therefore, we may apply the lattice sum calculational results for $^{57}$Fe to the case of $^{99}$Ru.

The calculation for $^{57}$Fe in $YBa_2Cu_3O_{7-\delta}$ immediately leads to the assignments for $^{99}$Ru in $YBa_2Cu_3O_{6.8}$ and $YBa_2Cu_3O_6$ shown in Table 1. Using a notation of $V_{zz}(^{99}\text{Ru-4})$, for example, for $V_{zz}$ at $^{99}$Ru with the 4-fold oxygen coordination, we notice that $V_{zz}(^{99}\text{Ru-4})$ and $V_{zz}(^{99}\text{Ru-3})$ are essentially equal to $V_{zz}(^{57}\text{Fe-4})$ and $V_{zz}(^{57}\text{Fe-3})$, respectively, while $|V_{zz}| = 0.7 \times 10^{22}$ V/m$^2$ at $^{99}$Ru in $YBa_2Cu_3O_{6.8}$ is about two times smaller than $V_{zz}(^{57}\text{Fe-5})$, from which we assign $|V_{zz}| = 0.7 \times 10^{22}$ V/m$^2$ at $^{99}$Ru in $YBa_2Cu_3O_{6.8}$ to the 6-fold oxygen coordination.

Table 1. $V_{zz}$'s for various local oxygen configurations around $^{57}$Fe and $^{99}$Ru at room temperature.

| Coordination number | $V_{zz}$ at $^{57}$Fe (calc.)[a] ($10^{22}$ V/m$^2$) | $\lvert V_{zz}\rvert$ at $^{57}$Fe (obs.)[b] ($10^{22}$ V/m$^2$) | $\lvert V_{zz}\rvert$ at $^{99}$Ru (obs.)[c] ($10^{22}$ V/m$^2$) |
|---|---|---|---|
| 2 | −2.9 | | |
| 3 | −2.2 | 1.62 | 1.7 |
| 4 | 2.2 | 2.36 | 2.3 |
| 5 | 1.2 | 1.27 | |
| 6 | 0.4 | | 0.7 |

[a] Point charge lattice sum calculations by Kimball et al. (Ref. 2).
[b] Reference 3. [c] This work.

In Fig. 1 are plotted the $V_{zz}(T)/V_{zz}(0)$ at $^{99}$Ru in $YBa_2Cu_3O_{6.8}$ and in $YBa_2Cu_3O_6$ versus $T^{3/2}$, together with those at $^{57}$Fe in $YBa_2(Cu_{1-x}Fe_x)_3O_7$ (dashed line: $|V_{zz}| \approx 1.3 \times 10^{22}$ V/m$^2$ at 293 K).[4] The solid lines are least-squares ones fitted to our data. In the temperature range we studied, the $V_{zz}$'s at $^{99}$Ru roughly follow the empirical expression obtained for noncubic metals, $V_{zz}(T)/V_{zz}(0) = [1 - \beta T^{3/2}]$; thermal motions of the lattice ions average EFG, reducing $V_{zz}$ with increasing temperature. The coefficient $\beta$ is proportional to $(M\Theta_D^2)^{-1}$, where $M$ and $\Theta_D$ are the mass of the vibrating ions and the Debye temperature. From the obtained $\beta$ values, we conclude that the thermal motion of the heavier probe atom is more effective than that of the lighter oxygen in averaging EFG at high temperatures and that as the coordination number increases, more restrictions are imposed on the motion of $^{99}$Ru, making the $\beta$ value smaller. This conclusion on the behavior of the $\beta$ value is reasonable and supports our assignment of the oxygen coordination around $^{99}$Ru.

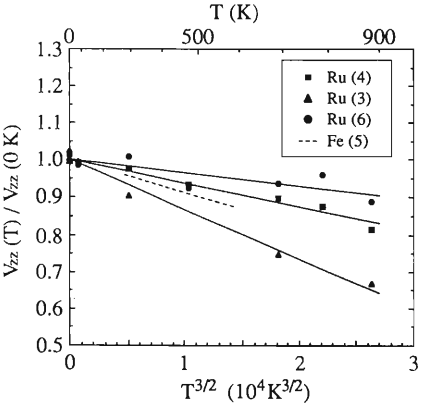


Fig. 1. Temperature dependence of $V_{zz}$ at $^{99}$Ru in $YBa_2Cu_3O_{6.8}$ and $YBa_2Cu_3O_6$ together with that at $^{57}$Fe in $YBa_2(Cu_{1-x}Fe_x)_3O_7$ (dashed line: $|V_{zz}| \approx 1.3 \times 10^{22}$ V/m$^2$ at 293 K).[4]

References

1) Y. Ohkubo, Y. Kobayashi, K. Harasawa, S. Ambe, T. Okada, K. Asai, S. Shibata, M. Takeda, and F. Ambe: *Hyperfine Interact.*, **84**, 83 (1994).
2) C. W. Kimball, J. L. Matykiewicz, H. Lee, J. Giapintzakis, A. E. Dwight, B. D. Dunlap, J. D. Jorgensen, B. W. Veal, and F. Y. Fradin: *Physica C*, **156**, 547 (1988).
3) M. G. Smith, R. D. Taylor, and H. Oesterreicher: *Phys. Rev.*, **B42**, 4202 (1990).
4) E. B. Saitovitch, R. B. Scorzelli, I. S. Azevedo, and H. Micklitz: *ibid.*, **B41**, 2103 (1990).

# A New Set-up for In-Beam Mössbauer Spectroscopy at RARF

Y. Yoshida, Y. Kobayashi, K. Yukihira,* K. Hayakawa,* H. Häßlein, S. Nasu, and F. Ambe

Short-lived nuclei beams produced by Coulomb excitation and other nuclear reactions such as $^{56}$Fe($d$, $p$)$^{57}$Fe are opening a new field in materials science[1-5]:

(1) Single isolated atoms can be observed in any host matrix with no restriction of the solubility of the probe atoms.

(2) In an in-beam Mössbauer experiment, the Mössbauer $\gamma$-rays are detected within the lifetime of the Mössbauer excited state ($\tau$ = 140 ns for $^{57}$Fe) after implantation of every excited probe nucleus. This provides not only a unique measuring-time-range of about 100 ns for solid state physics and chemistry, but also atomistic information on electronic states and lattice vibrations at different lattice sites.

(3) Atomic jump processes on substitutional and/or interstitial sites can be followed even in inert gas solids at different temperatures. A study on the jump processes of Fe atoms in solid Ar is in progress using a new in-beam system at RARF described below.

(4) Since the time-bunched-pulsed heavy-ions beam is employed in the experiment, it is also possible to study dynamic effects just after the implantation by measuring spectra with different time windows.

Recently, we have completed a new set-up for the in-beam Mössbauer spectroscopy at the E7C beam-line connected with AVF cyclotron,[6] as shown in Fig. 1. This system consists of three parts; main chamber, sample preparation room, and vacuum chambers with a Faraday-cup. Using a DOS/V-PC machine located in the measurement room, we can monitor and control the whole measuring system; all experimental parameters such as the temperature and the position of specimens, the degree of vacuum in the whole chamber, and the manipulation of pumping systems and all vacuum valves. The $\gamma$-rays from the 14.4 keV Mössbauer level of $^{57}$Fe are detected by two parallel-plate avalanche counters (PPAC) which are filled with acetone gas of 25 mbar. The fast timing signals from the PPACs are amplified and used for the $\gamma$-ray counting. The data are collected and processed by the same computer.

In our first beam time, we used $^{40}Ar^{11+}$ ions with a total energy of 100 MeV for Coulomb excitation of $^{57}$Fe. The performance of the in-beam Mössbauer spectrometers and the on-line operations of all other instruments were checked and confirmed. However, both the time structure and the intensity of the pulsed Ar beam available at the time were still far below our demand. Further developments on the beam structure and the intensity at AVF cyclotron are highly desirable to achieve an in-beam Mössbauer experiment. In order to get higher S/N we have been developing new PPACs using FeTi and FeAl evaporated films.

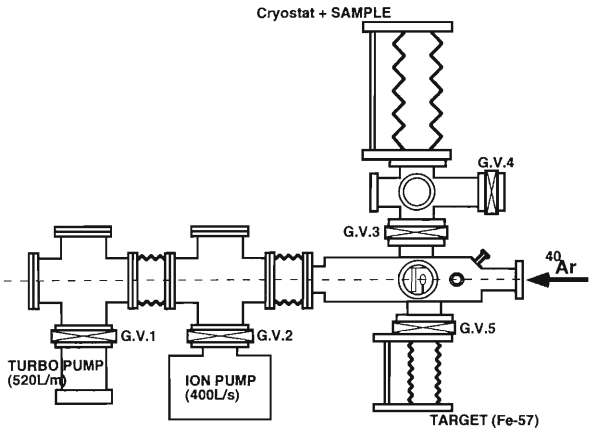


Fig. 1. The in-beam Mössbauer system located at the beam-line in E7 experimental hall.

References

1) M. Menningen, R. Sielemann, G. Vogl, Y. Yoshida, K. Bonde-Nielsen, and G. Weyer: *Europhys. Lett.*, **3**, 927 (1987).
2) Y. Yoshida, M. Menningen, R. Sielemann, G. Vogl, G. Weyer, and K. Schroeder: *Phys. Rev. Lett.*, **61**, 195 (1989).
3) Y. Yoshida: *Hyperfine Interact.*, **47**, 95 (1989).
4) R. Sielemann and Y. Yoshida: *ibid.*, **68**, 119 (1991).
5) P. Schwalbach, S. Laubach, M. Hartick, E. Kankeleit, B. Keck, M. Menningen, and R. Sielemann: *Phys. Rev. Lett.*, **64**, 1274 (1990).
6) Y. Kobayashi, Y. Yoshida, H. Häßlein, S. Nasu, and F. Ambe: *RIKEN Accel. Prog. Rep.*, **27**, 111 (1993).

* Shizuoka Institute of Science and Technology

# Extraction of Intense Slow Positron Beam from Various Targets Irradiated with $p^+$ and $d^+$ Ions

Y. Itoh, K. Lee, I. Kanazawa, N. Oshima, T. Nakajyo, A. Goto, N. Nakanishi, M. Kase, and Y. Ito

The production of intense slow positron beams ($> 10^8$ $e^+$/sec) is motivated by the prospect of its broad applications. For the past decades most positron studies have been performed using $^{22}$Na of $\beta^+$-decay radioisotope because of its long life time (2.67 yr.) and proper intensity. The maximum intensity of the slow positrons from commercially available $^{22}$Na is less than $10^6$ $e^+$/sec with moderation efficiency of $\approx 10^{-4}$.[1] More intense slow positron beam (more than $\approx 10^8$ $e^+$/sec) is needed to develop applications such as a positron reemission microscope (PRM), low energy positron diffraction (LEPD) *etc.* from their present preliminary stage to practical performance. For the last several years LINAC has been used[2,3] to obtain high intensity slow positrons of $\geq 10^7$ $e^+$/sec by pair production. However the slow positron beam from LINAC has a pulsed structure and thus it must be given a further beam processing, and moreover the system is expensive and of a large non-laboratory scale. On the other hand, production of $\beta^+$-decay radioisotopes using a cyclotron has several advantages. A high intensity direct current (DC) slow positron beam ($\approx 10^8 \sim 10^9$ $e^+$/sec) is directly obtained from a relatively inexpensive compact system.

Using the RIKEN AVF cyclotron, various targets were irradiated with a proton or deuteron beam to produce $\beta^+$-decay radioisotopes. Using a well annealed W film (with a thickness of 10 $\mu$m) as a moderator, slow positrons were extracted at 30° backward to the incident ion beam. This geometry was chosen to allow for (1) extraction of the slow positrons during the ion beam irradiation and (2) the use of various kinds of target materials. We produced $\beta^+$-decay radioisotopes from various targets such as boron nitride (BN), aluminum (Al), carbon (C), and silicon nitride ($Si_3N_4$) using a proton or deuteron beam from the RIKEN AVF Cyclotron. The reactions that lead to the formation of the $\beta^+$-decay radioisotopes are $^{11}$B(p,n)$^{11}$C and $^{14}$N(p,$\alpha$)$^{11}$C for BN, $^{27}$Al(p,n)$^{27}$Si for Al, $^{12}$C(d,n)$^{13}$N for carbon, $^{28}$Si(d,n)$^{29}$P and $^{14}$N(d,n)$^{15}$O for $Si_3N_4$. Table 1 summarizes the slow positron counts emitted from each target at different beam energies and three different geometries of the moderator for BN and Al targets. The intensity of the slow positron beam is strongly dependent on the target materials, energy of the ion beam, condition of the moderator and geometry of the target holder. In the current stage we obtained $5.6 \times 10^4$ $e^+$/sec per 4 $\mu$A of proton beam from a boron nitride target. We expect slow positron counts of $>10^{6-7}$ $e^+$/sec with proper selection of a target and energy of irradiation ion beam, target geometry and good condition of the moderator. From the preliminary experiments we conclude that the condition of the moderator is one of the major factors for the emission of slow positrons. Therefore, in the future experiments a newly designed chamber equipped with an in-situ moderator annealing system will be used to obtain a better condition of the moderator. The number of the slow positrons was determined in a gated beam operation mode, where the ion beam irradiation was switched on and off at short intervals (typically 1 sec) and the coincidence counts of the annihilation $\gamma$-ray were measured while the beam was off. The signal to noise ratio drastically increased by 3 orders of magnitude in this method. This implies that a short length of beam guiding line as in the previous system will not become an obstacle to perform actual experiment if the gated beam operation is applied.

Table 1. Measured slow positron counts from each target irradiated with different ion beam energies and different types of moderator and conditions.

Proton beam

| Energy of $p^+$ beam | Targe | Current of $p^+$ beam | $e^+$ counts measured at the operated $\mu$A | Type of Moderator (Condition) | Expected $e^+$ counts at max current (20 $\mu$A) |
|---|---|---|---|---|---|
| | BN | 4 $\mu$A | $1.3 \times 10^4$ $e^+$/sec | Model-1 | $6.5 \times 10^4$ $e^+$/sec |
| 7 MeV | BN | 5 $\mu$A | $8.5 \times 10^2$ $e^+$/sec | Model-2 (Used) | $3.4 \times 10^3$ $e^+$/sec |
| | BN | 4.4 $\mu$A | $4.5 \times 10^3$ $e^+$/sec | Model-3 (New) | $2.0 \times 10^4$ $e^+$/sec |
| | Al | 4.4 $\mu$A | 0 | Model-2 (Used) | 0 |
| 10 MeV | BN | 3.6 $\mu$A | $1.02 \times 10^4$ $e^+$/sec | Model-3 (Used) | $5.7 \times 10^4$ $e^+$/sec |
| | Al | 3.6 $\mu$A | $5.5 \times 10^2$ $e^+$/sec | Model-2 (Used) | $3.1 \times 10^3$ $e^+$/sec |
| 14 MeV | BN | 4.0 $\mu$A | $7.8 \times 10^3$ $e^+$/sec | Model-2 (Used) | $3.9 \times 10^4$ $e^+$/sec |
| | BN | 4.0 $\mu$A | $5.6 \times 10^4$ $e^+$/sec | Model-2 (New) | $2.8 \times 10^5$ $e^+$/sec |

Deuteron beam

| Energy of $d^+$ beam | Targe | Current of $d^+$ beam | $e^+$ counts measured at the operated $\mu$A | Type of Moderator (Condition) | Expected $e^+$ counts at max current (10 $\mu$A) |
|---|---|---|---|---|---|
| | Carbon | 1.3 $\mu$A | $4.2 \times 10^3$ $e^+$/sec | Model-2 (New) | $3.2 \times 10^4$ $e^+$/sec |
| 8 MeV | $Si_3N_4$ | 1.3 $\mu$A | $3.4 \times 10^3$ $e^+$/sec | Model-2 | $2.6 \times 10^4$ $e^+$/sec |

## References


1) E. Gramsch, J. Throwe, and K. G. Lynn: *Appl. Phys. Lett.*, **51**, 1862 (1987).
2) L. D. Hulett, T. A. Lewis, D. L. Donohue, and S. Pendyals: Proc. 8th Int. Conf. on Positron Annihilation, Gent, p. 586 (1989).
3) Y. Ito, M. Hirose, S. Takamura, O. Sueoka, I. Kanazawa, K. Mashiko, A. Ichimiya, Y. Murata, S. Okada, M. Hasegawa, and T. Hyodo: *Nucl. Instrum. Methods Phys. Res.*, **A305**, 269 (1991).

# Positronium Formation and Annihilation in Porous Silicon

Y. Itoh, H. Murakami, and A. Kinoshita*

We have previously reported the existence of a long lived positronium in a porous silicon made by anodization of a silicon crystal.[1-3] It has been found that the annihilation rate of a positronium is temperature dependent. The effects of gas atmosphere and temperature dependence on positronium annihilation in porous silicon have been examined in this experiment. The longest component is shorter in oxygen atmosphere than those in vacuum and in nitrogen because of the ortho-para conversion process in the oxygen condition.

Table 1 shows the lifetime and S-parameter of the three components in porous silicon, measured in oxygen, nitrogen, air, and vacuum. The oxygen gas caused a drastic decrease in the longest lifetime. Most molecules of oxygen are absorbed in the pore space, or on its surface. The amount of oxygen dissolved additionally into the bulk layer at 300 K is thought to be negligible compared with that in the pores. We consider that the ortho-positronium with lifetime $\tau_3$ is free in the pore and collides with the pore surface and the introduced gas molecules, since $\tau_3$ changes through oxygen exposure. The shortened lifetime in an oxygen atmosphere is reasonably understood in terms of the spin conversion of ortho-positronium, following the interaction with oxygen molecules in the pores or on the pore surface. Nitrogen had no effect on the ortho-para conversion. We are progressing the experiments on the temperature dependence positron/positronium annihilation under a designated gas atmosphere such as oxygen, nitrogen and the others. Positron annihilation spectroscopy will be a tool to make the surface state of porous silicon and elucidate the photoluminescence mechanism.

Table 1. Lifetime and S-parameter of porous silicon in different gas conditions.

| Atmosphere | $\tau_1(I_1)$ ps(%) | $\tau_2(I_2)$ ps(%) | $\tau_3(I_3)$ ps(%) | S-parameter |
|---|---|---|---|---|
| In Nitrogen (1 atm) | 201 (48) | 356 (36) | 36000 (16) | 0.491 |
| In Vacuum ($8 \times 10^{-9}$Pa) | 234 (68) | 472 (11) | 35900 (21) | 0.517 |
| In Air (1 atm) | 237 (69) | 556 (9) | 22000 (22) | 0.603 |
| In Oxygen (1 atm) | 264 (77) | 654 (8) | 10200 (15) | 0.628 |

References

1) Y. Itoh, H. Murakami, and A. Kinoshita: *J. de Phys.*, **IV**, **3**, 193 (1993).
2) Y. Itoh, H. Murakami, and A. Kinoshita: *Appl. Phys. Lett.*, **63**, 2798 (1993).
3) Y. Itoh, H. Murakami, and A. Kinoshita: *RIKEN Accel. Prog. Rep.*, **27**, 92 (1993).

* Department of Science and Engineering, Tokyo Denki University

# 4. Radiation Chemistry and Radiation Biology

# Time and Depth Resolved Dynamics of Excited States in Ion Track in Condensed Matter

K. Kimura, T. Yoshikane, and H. Kumagai

1) Dynamics of core and self-trapped excitons produced in ion irradiated $BaF_2$ and CsCl.

Recently, above crystals are of interest not only as new scintillators for high energy physics but also as crystals presenting new exciton luminescence. Studies on luminescence mechanisms and exciton dynamics have been carried out using synchrotron radiation and energetic electron. The new luminescence band at 220 nm was assigned to transitions of valence electrons to the hole of the outermost inner shell and named the Auger-electron-free luminescence (AEFL). Another luminescence band at 310 nm was assigned due to the self trapped exciton (STE) similar to those for alkali halide crystals. We have studied on dynamical effects of ion-irradiation of the exciton luminescence, with development of techniques for fast luminescence decay measurements (SISP) of 100 ps resolution, using incident ions of comparatively low energies of about 2.0 MeV/nucleon. Some of new findings for $BaF_2$ have been reported already: excitation-density dependent shortening of the lifetime of AEFL and its mechanism[1]; similar shortening for STE, but a different mechanism i.e. the STE-STE exchange interaction.[2] In this report, further new findings and results on a CsCl crystal are mentioned briefly. Kinetics on AEFL of ion-irradiated $BaF_2$ enabled us to estimate the formation efficiency of the core hole $Ba^{3+}$. Figure 1 shows the efficiency per a nucleon as a function of LET (linear energy transfer) of various projectiles. There appeared a minimum evidently at LET due to N-ion. This may be explained by a mechanism that the core hole is formed by the Fano-type charge exchange process, namely, the transient pseudo molecular orbital formation between a projectile and a $Ba^{2+}$; the efficiency of the MO formation is the lowest in case of N-ion. A new finding for STE of $BaF_2$ is on unusual temperature effect on the luminescence decay. Figure 2 shows that with decreasing temperature the decay times are shortened from several ns to about 400 ps with no prominent change in the intensity. This temperature effect is reverse to results for photoirradiation by synchrotron radiation that the decay time of about 1 $\mu$s at room temperature is lengthened to about 10 $\mu$s at 50 K. The results may suggest that the STE is formed much densely with decreasing temperature because of decreasing rate of hole migration, resulting in an increase in the exchange interaction. This situation seems to induce the stimulated luminescence.

Ion induced AEFL of a CsCl crystal also showed so large excitation-density effect that the decay time at the initial stage was 150 ps at room temperature in

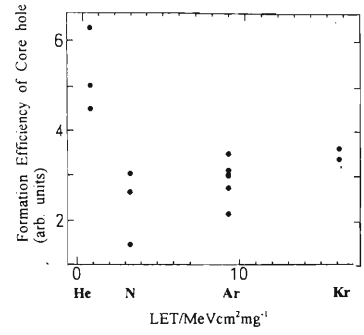


Fig. 1. Formation efficiency of the core hole $Ba^{3+}$ per a nucleon as a function of LET.

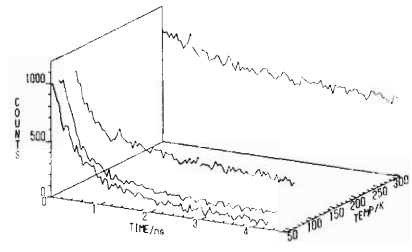


Fig. 2. Temperature dependence of the decay of STE in 2.0 MeV/nucleon He-ion irradiated $BaF_2$.

contrast with 880 ps for VUV irradiation. However, the decay time was increased considerably with decreasing temperature although the dependence in case of $BaF_2$ was scarce. On the other hand, ion-induced STE of CsCl presented very short decay constants, which were nearly independent of temperature. These results may be explained by substansially the same models as which succeeded in the case of $BaF_2$, but detailed analyses are going on.

2) Track-depth resolved dynamics of excited states.

Bragg-type curves were measured successfully for excited states produced in a dense Ar gas presessurized closely at the critical temperature, which is an extended study of preveous one on dense He.[3] The measurements are to be carried out systematically using various projectiles and rare gases to elucidate the basic track effect as a space of high-density excitation.

References

1) K. Kimura and J. Wada: *Phys. Rev.*, **B48**, 15535 (1993).
2) K. Kimura: *Nucl. Instrum. Methods Phys. Res.*, **B90**, 100 (1993); K. Kimura and H. Kumagai: *Radiat. Eff. Def. Solids*, **126**, 45 (1993).
3) K. Kimura: *Phys. Rev.*, **A47**, 327 (1993).

# Measurements of Heavy Ion Beam Qualities

N. Matsufuji, T. Kanai, H. Tomura, T. Kohno, A. Fukumura, F. Soga, and K. Kawachi

When shaping the range of heavy ion therapy beam at HIMAC, incident nuclides are broken into some fragmented particles by the bombardments with range-shifter made of lucite plates. It is important to know about the quality of the beam such as the composition of the beam and/or the contribution of each fragmented nuclide to LETs to make our treatment-planning more precise. For this purpose, fragmented particles were measured for the beams of carbon 135 MeV/nucleon and neon 135 MeV/nucleon with changing the thickness of lucite variously.

Figure 1 shows a schematic diagram of a detector system. The system was based on the counter-telescope method. A beam monitor made of a plastic scintillator was located at the most upstream position to count the number of incident particles. A coincidence detector was composed of a plastic scintillator of 5.0 mm in diameter and positioned at the downstream of the lucite target to distinguish fragmented particles from noises. A proportional counter and a silicon semiconductor detector were used as ΔE counters to measure the energy loss ΔE in the detectors. At the end of the beam line, a BGO scintillator was utilized as an E counter to measure total energy E. The BGO crystal had a cylindrical form, 15.0 mm in diameter and 15.0 mm in length. The measurements were carried out in E5 experimental room of the RIKEN Ring Cyclotron accelerator facility.

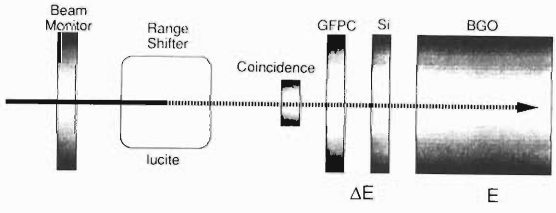


Fig. 1. The schematic diagram of the detector system.

Figure 2 illustrates an example of E-ΔE scatter plots for the incidence of carbon beam with target thickness of 28.97 mm in water-equivalence. The abscissa represents the total energy E measured by BGO detector and the ordinate denotes the energy loss ΔE from the Si semiconductor detector. Fragmented particles were well discriminated by the difference of the kind of nuclide.

Fluence spectra of each nuclide were derived by normalizing the number of particles included in each belt of E-ΔE scatter plots by the number of incident particles. Figure 3 displays the fluence of each nuclide for the incidence of carbon beam. The values calculated by Sihver and Kanai are also plotted for the sake of comparison.

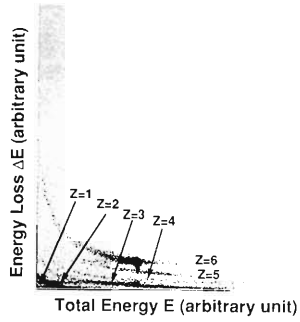


Fig. 2. The scatter plot of the total energy E and the energy loss ΔE for the incidence of carbon 135 MeV/nucleon beam.

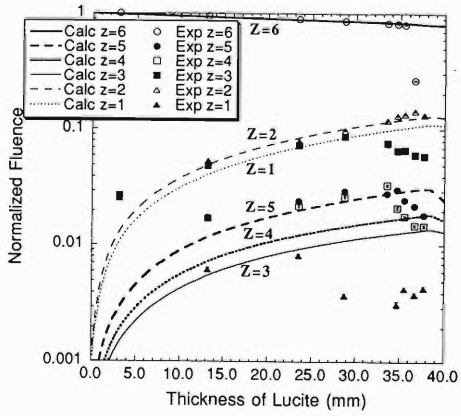


Fig. 3. Fluence spectra of fragments emitted by the incidence of carbon 135 MeV/nucleon beam.

Macroscopic reaction cross sections Σ were deduced from the fluence of incident nuclide. The Σ is expressed as an exponent of the following equation:

$$\frac{N}{N_0} = \exp(-\Sigma x),$$

where $x$ is the thickness of the target, $N_0$ is the number of incident particles and $N$ is the number of survived incident particles. Results are summarized in Table 1.

Table 1. Macroscopic reaction cross sections with a lucite target ($m^{-1}$).

| Beam | Experiment | Calculation |
|---|---|---|
| C 135 MeV/nucleon | 6.71 | 5.14 |
| Ne 135 MeV/nucleon | 8.52 | 7.06 |

These results indicate that incident heavy ion particles are more disintegrative comparing with calculated expectations. Precise analyses for the reason of this tendency and other beam qualities such as LET spectra for each nuclide are now in progress.

# The Profile of Chemical Damages in Polymers Induced by Heavy-ion Irradiation

Y. Hama, K. Hamanaka, H. Matsumoto, and F. Yatagai

The relationship between the energy transfer profile of heavy ion and the profile of chemical structural change in polymeric materials has not yet been clear enough. This may be important in the study on biological effects of heavy ions. The present study is concerning the depth profile of the chemical damages in polyethylene irradiated by 135 MeV/nucleon $C^{6+}$ from RIKEN Ring Cyclotron.

The samples used in this work were low density polyethylene (LDPE) and high density polyethylene (HDPE). They were formed in a slab of 2 mm thick by heat press. On irradiation, an enough number of slabs were piled up so that the thickness of the whole samples was longer than the range of the heavy ion.

Irradiation was carried out in air at room temperature with $C^{6+}$ of 135 MeV/nucleon.

The sample irradiated was sliced along the cross-section to get a thin film of a few hundreds of $\mu$m for the micro-FT-IR measurement. We could obtain the depth profile of chemical changes in heavy-ion irradiated LDPE and HDPE with a micro-FT-IR apparatus with which it is possible to detect the IR spectrum in a minimum area of 10 $\mu m \times 10$ $\mu$m.

The predominant species produced by heavy-ion irradiation were carbonyl group, trans-type double bond and hydroxy group. Figure 1 shows the depth profile of carbonyl groups and trans double bonds produced in HDPE. The carbonyl groups show very strange absorption in the vicinity of both surfaces of each slab compared with the inner region, and the envelope of yields of the carbonyl groups shows a kind of the Bragg curve. The depth profile of the trans double bond also looks like the Bragg curve.

The generation mechanism of the predominant species could be considered as follows: It has been known that alkyl radical is the predominant radical produced in polyethylene by $\gamma$-irradiation. In addition, the allyl radical is produced slightly. In our previous study, it has been found that most of oxidation takes place in the vicinity of the surface when the slab of PE was irradiated in air by $\gamma$-ray. It has been considered from this result that most alkyl radicals produced by $\gamma$-irradiation disappear by the reaction with oxygen molecules to create carbonyl groups in the vicinity

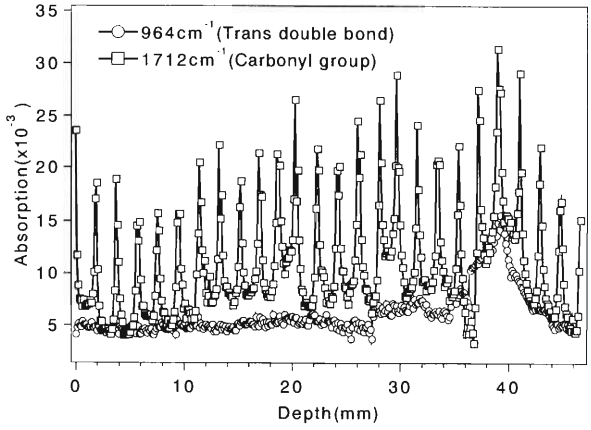


Fig. 1. The depth profile of the IR absorption due to carbonyl group and trans double bond for HDPE irradiated by 135 MeV/nucleon $C^{6+}$ in air at room temperature.

of the surface and that they disappear by recombination to create crosslinks in inner region. On the other hand, allyl radicals disappear by the reaction with oxygen molecules, although they are stable in vacuum at room temperature.

It may be considered that a reaction similar to the one on $\gamma$-irradiation takes place also on heavy-ion irradiation. That is, a large number of carbonyl groups observed in the vicinity of surface in each slab is considered to come from the reaction of alkyl radicals with oxygen molecules, though slight oxidation due to allyl radicals occurs. Moreover, alkyl radicals are considered to disappear by the recombination before they react with oxygen molecules which diffuse into the inner region. Therefore, the carbonyl groups produced in the inner region in each slab come from the oxidation of allyl radicals. This consideration leads to a conclusion that the relative yield of allyl radical to alkyl radical should be larger than that on $\gamma$-irradiation. This is supported by the fact that the G value for production of trans-double bonds also is larger than that on $\gamma$-irradiation. These results suggest that the chemical reaction processes on heavy-ion irradiation are affected by ionization or excitation in high density which is due to high LET.

# Radiation Effects of Ion-particles on Various DNA Structures (2)

S. Kitayama, M. Kikuchi,* K. Nakano, M. Suzuki, T. Takahashi, and H. Watanabe*

Ionizing radiation including accelerated particles induces various damages in DNA such as hydroxylation of base and sugar, disruption of phosphodiester bonds, etc. However, living cells repair the most of them except lethal damage which has not been clearly identified. Due to the technical limitation in analyzing the change of molecular structure of long DNA, the biological effects of radiation have been studied mostly on the strand breakage of DNA whose molecular weights are less than $10^8 (\sim 1.5 \times 10^5$ base pairs).

Recent technichal progress in the analysis of large DNA such as pulse field gel electrophoresis (PFGE) makes it possible to measure the molecular change of long DNA bigger than $\sim 10^7$ base pairs.

Even though a prokaryotic cell has no nucleus its single molecule of double-stranded DNA, corresponding to one chromosome, is folded extensively within a small cell envelope. Many cellular constituents are thought to be associated with the folded DNA. It is still unknown whether any segments of chromosomal DNA molecule are evenly attacked by radicals produced by radiations or whether cell constituents protect it or enhance the radiation damages on it. Following the studies reported last year (1), we continued such experiments to confirm the differrent radiation effecs on "naked", "folded" or "packaged" DNA. In order to prevent free diffusion of such DNA, cells were solidified with agarose and treated with or without lysozyme, RNase and/or proteinase. We confirmed by electronmicroscopic observation that DNA, after removals of RNA and proteins, is still enveloped in an agarose hole whose diameter is almost the same as that of intact cells (data not shown). Therefore, it can be thought that even in the "naked" sample DNA is still folded in a small space corresponding to the single cell. Therefore, the name of a "folded" sample must be changed to a "cell wall and RNA free" sample as a more appropriate terminology.

In order to compare the radiation effects of N-ions ($\sim$135 MeV/$\mu$, data presented last year[1]), Ar-ions ($\sim$95 MeV/$\mu$, Fig. 1(a)) and $^{60}$Co $\gamma$-rays (Fig. 1(b)) on these three folded forms of DNA, cells of *Deinococcus radiodurans* were solidified with agarose (DNA is still "packaged" in a cell with its constituents). Before irradiation the cells were lysed with lysozyme in the presence of RNase ("cell wall & RNA free") followed by proteinase K treatments ("naked"). RNA and proteins were removed by incubation with these enzymes following the irradiation and DNA was digested with a restriction endonuclease, Not I. The digested fragments (Not I fragments) were analysed by PFGE as shown in Fig. 1.

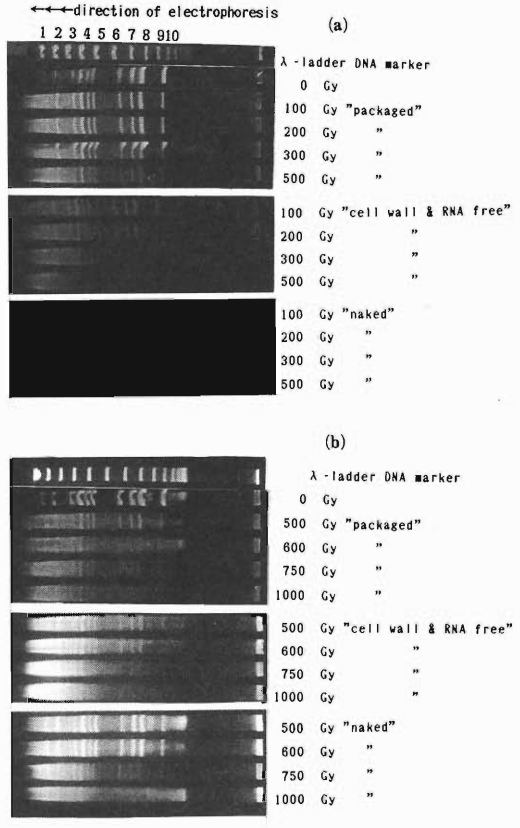


Fig. 1. Disappearance of Not I fragments in three different folded forms of DNA after the irradiation with $Ar^+$-ions(a) and $\gamma$-rays(b). Molecular weights of the $\lambda$-ladder DNA size standard shown in the figure are as follows(bp): 1 = 48.5 k, 2 = 97.0 k, 3 = 145.5 k, 4 = 194.0 k, 5 = 242.5 k, 6 = 291 k, 7 = 339.5 k, 8 = 388.0 k, 9 = 436.5 k, 10 = 485.0 k.

Several conclusions can be drawn from the figure; (1) Among the three folded forms of DNA the most sensitive to these radiations is that which is in a "cell wall and RNA free" sample. (2) Irradiation with the ions disrupt Not I fragments more efficiently than $\gamma$-rays. (3) Among the Not I fragments the biggest fragment (ca 480 kbp) is more sensitive to radiations than the others (400, 390, 360, 324, 255, 240, 225, 215, 109, 102, 100 kbp). After completing more detailed experiments these results will be analyzed quantitatively using densitometer tracing.

References

1) S. Kitayama et al.: *RIKEN Accel. Prog. Rep.*, **27**, 100 (1993).

* Japan Atomic Energy Research Institute

# Analysis of Mutations in the Human *HPRT* Gene Induced by Accelerated Heavy-ion Irradiations

Y. Kagawa,* F. Yatagai, M. Suzuki, Y. Kase, A. Kobayashi,* M. Watanabe, and F. Hanaoka

A knowledge of the specificity of mutation induced by a variety of mutagens has proved useful for better understanding of the molecular mechanisms of mutagenesis. In the past decade, a vast amount of data has been generated concerning cell death, mutation, chromosomal aberreation etc. by means of accelerated heavy-ions. Suzuki et al.[1] have already reported hypoxanthine phosphoribosyltransferase (HPRT) mutations obtained from the carbon-ion irradiation of human embryo cells. The initial energy of C-ion 135 MeV/n was degraded to adjust the linear energy transfer (LET) to 39, 68, 124, or 230 keV/mm when the cells were irradiated.

In this report, we investigated DNA sequence alterations in HPRT cDNA of mutant clones recovered from 230 keV/$\mu$m carbon-ion irradiations. The genomic DNA of these mutants have already been shown to represent normal electrophoretograms when they are amplified by multiplex PCR.

We extracted mRNA and genomic DNA from 6-thioguanine (6-TG) resistant mutants by a procedure described previously.[1] After reverse-transcripting mRNA to cDNA, the HPRT structural gene was amplified by PCR and sequenced by dideoxy method. Southern hybridization was carried out on EcoRI or PstI digested genomic DNA utilizing an exon6 region (258bp) as a probe.

Eighteen HPRT cDNAs of mutant clones obtained from 230 keV/mm carbon-ion irradiation were sequenced. As shown in Table 1, deletions of exon6 (83bp, 403–485) were the most frequent mutational events (10 clones), and the deletion of both exon6 and exon8 (77bp, 533–609) was next most frequent (6 clones), followed by base substitutions (2 clones: $^{415}$ACT → GCT, Thr → Ala, $^{7}$ACC → ATC, Thr → Ile). For comparison, we also characterized the 10 spontaneous *HPRT* mutatants by the same methods. In contrast, the most frequent mutational events of spontaneous mutants were base substitutions (5 clones) followed by deletions of both exon2 and exon3 (2 clones) and frameshift (2 clone). One remaining clone was unidentified, but this clone did not represent any deletions of exons.

Table 1. Comparison of mutational events.

| Class of mutation | Incidence | |
|---|---|---|
| | C-ion (230 keV/$\mu$m) | Spontaneous |
| Base substitution | 2 (11%) | 5 (50%) |
| Frame shift (base addition) | 0 | 2 (20%) |
| Deletion | 16 (89%) | 2 (20%) |
| exon6 | 10 | 0 |
| exons 6 and 8 | 6 | 0 |
| exons 2 and 3 | 0 | 2 |
| unidentified (point mutation) | 0 | 1 (10%) |
| Total | 18 (100%) | 10 (100%) |

Because all these mutants have been certified by the multiplex PCR analysis to have all exons on their genome, these deletions were supposed to be due to the translocation of each exon region or the abnormal mRNA splicing. Analyses of intron regions upstream exon6 and exon8 by genomic Southern, DNA sequencing and restriction enzyme digestion suggested that the above deletions induced by 230 keV/$\mu$m carbon-ion were due to the abnormal mRNA splicing. We need to confirm the possibility that these observed characteristics are specific to the effect of a heavy-ion.

References

1) M. Suzuki, M. Watanabe, T. Kanai, Y. Kase, F. Yatagai, T. Kato, and S. Matsubara: *Adv. in Space Res.*, in press.

* Toray Research Center Inc.

# Induction of Apoptosis in CHO Cells Exposed to Accelerated Neon Ions

H. Sasaki, F. Yatagai, Y. Furusawa, T. Kanai, and F. Hanaoka

Radiation-induced death of cultured mammalian cells is divided into reproductive and interphase death. The former is observed among cell progenies during several generations after exposure to moderate doses of X rays less than 10 Gy, whereas the dose more than 10 Gy is required for the latter to occurr. Heavily X-irradiated CHO (Chinese hamster ovary) cells stopped cell progression at the G2 phase and became giant. Since caffeine has been shown to override G2 block, we examined if caffeine could induce these giant cells to enter mitosis. Although they soon rounded up upon addition of caffeine as if they entered mitosis, they, when stained, showed nuclear condensation which led to apoptotic changes including fragmentation of nucleus as well as internucleosomal DNA. Furthermore, caffeine-induced apoptosis was suppressed by the incubation at the nonpermissive temperature of FT210 cells which have a ts defect in cdc2 H1 kinase,[1,2] suggesting the CDC2-dependent chromatin condensation required for nuclear condensation during apoptosis of heavily irradiated cells destined to undergo interphase death.

We previously found by means of the time-lapse photography that HeLa cells exposed to $\alpha$ particles from $^{241}$Am underwent interphase death more frequently than those exposed to X rays at the dose corresponding to the same survival level.[3] In the present preliminary study, the dose dependence of apoptosis induction in CHO cells was compared between X rays and monoenergetic Neon ions at Bragg peak (135 MeV/n, LET: 100 KeV/$\mu$m) generated by RIKEN Ring Cyclotron. After exposure to graded doses of X rays or Neon ions, cells were incubated for 24 h and then treated with caffeine (5 mM) for 2 h. Fraction of induced apoptotic cells was determined by counting round cells with condensed nuclei. The results in the Fig. 1 show that apoptotic

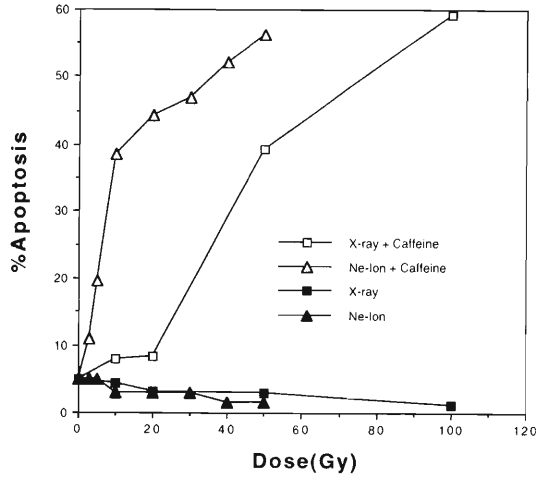


Fig. 1. Dependence of caffeine-induced apoptosis on dose of X ray and Neon ion in CHO cells.

cells increase linearly with dose of Neon ions within the range less than 10 Gy where they are scarecely seen in X-irradiated cells. High incidence of apoptosis in cells exposed to relatively low doses of Neon ions may be due to the formation of locally multiply damaged sites (LMDS) in target molecules (DNA). These facts suggest a predisposition to interphase death of heavy-ion irradiated cells. Evaluation of dependence of apoptosis induction on dose is now in progress using a more precise method.

References

1) C. Mineo et al.: *Exp. Cell Res.*, **167**, 53 (1986).
2) J. P. H. Th'ng et al.: *Cell*, **63**, 313 (1990).
3) H. Sasaki: *Radiat. Res.*, **99**, 311 (1984).

# Biological Effectiveness of Heavy-Ion Beams on Cultured Mammalian Cells

Y. Furusawa, K. Fukutsu, K. Ando, H. Ohara, F. Yatagai, and T. Kanai

The relative biological effectiveness (RBE) is thought to be given by a simple function of the linear energy transfer (LET), which is described as a linear-dimensional energy-deposit density. The three-dimensional energy-deposit density is different according to the types of accelerated ions when their LETs are the same, because of the difference in the velocities and electric charges of the accelerated ions. The cross sections between the ions and energy-absorbing materials, such as living cells, are different based on the target sizes of the irradiated cells, the truck structure of the accelerated ions, the target-truck distance, and so on. Thus, the biological effectiveness to the same LET ion beams may vary according to the types of ions and cells. To obtain the difference among the ion species as well as among the cell strains, we exposed V79 cells (from Chinese hamster) and HSG cells (from human salivary grand tumor) to several types of ion beams having various LETs under both aerobic and hypoxic conditions.

The cell-killing efficiency of HSG and V79 cells was measured with various LET beams of $^{3}$He, $^{12}$C, and $^{20}$Ne ions under both aerobic and hypoxic exposure conditions. For the irradiation of heavy-ion beams, the medical cyclotron at the National Institute of Radiological Sciences ($^{3}$He ions and $^{12}$C ions at a high-LET region) and the RIKEN Ring Cychrotron ($^{12}$C and $^{20}$Ne) were used as the sources of ion beams. Details concerning the irradiation systems were reported previously.[1] The survival curves of V79 cells for lower LET beams had large shoulders (3.8 Gy as $D_q$, at 20 keV/$\mu$m for aerobic condition), and that of HSG cells had small shoulders (1.2 Gy for the $^{3}$He-ion and 1.8 Gy for the $^{12}$C-ion at 20 keV/$\mu$m for the aerobic condition); the shoulders were reduced by an increment of the LET. The survival curves under both aerobic and hypoxic conditions were analogous for the same LET beam. The survival-curve parameters were numerically determined by using the Linear Quadratic Model as a fitting method, rather than the theoretical model of the survival fraction; the $D_{10}$ (dose required to reduce the survival to 10%) was obtained for each experiment. In this report, the cell survivals are discussed based only on $D_{10}$, since it was a stable parameter for our experiments.

Summaries of the $D_{10}$ values versus the LET for HSG and V79 cells under both aerobic and hypoxic conditions are given in Fig. 1; these details were reported previously.[2,3] The $D_{10}$ values were, for all cases, decreased with an increments of LET to a minimum at about 100–300 keV/$\mu$m, and then increased in a much higher LET region. The LET-$D_{10}$ curves of the V79 cells for $^{3}$He-, $^{12}$C-, and $^{20}$Ne-ions were separated. Based on the Figs. 1 and 2 in the middle (30–90 keV/$\mu$m) LET region, the lowest $D_{10}$ at the same LET radiation was found by the $^{3}$He-ion rather than by other ion-beams. The minimum value of $D_{10}$ was, however, not found for the $^{3}$He-ion. Because of limits of the LET range due to the irradiation apparatus, sufficient experiments for finding the minimum $D_{10}$ for the $^{3}$He ion were not possible. The $D_{10}$ values were lowest for the $^{3}$He ions, middle for the $^{12}$C ions and highest for the $^{20}$Ne ions at the same LET in the lower LET region in the figures. Analogous figures were found for HSG cells. The LET $D_{10}$ curves produced by the $^{3}$He ion for the HSG cells were lower than those produced for the V79 cells by the other ions. In

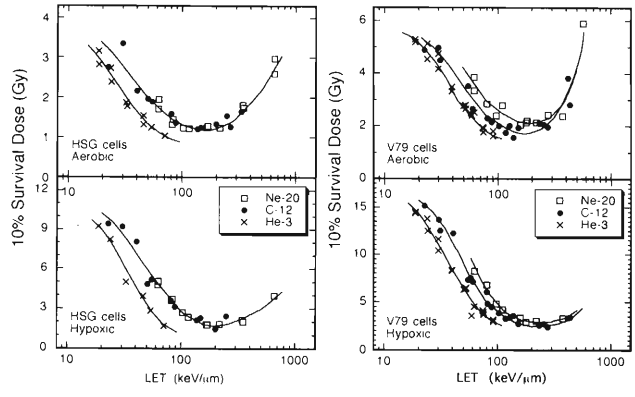


Fig. 1. Inactivation action spectra for HSG and V79 cells as represented by a 10% survival dose vs. the LET for $^{20}$Ne, $^{12}$C, and $^{3}$He ion-beams in aerobic and hypoxic irradiation conditions.

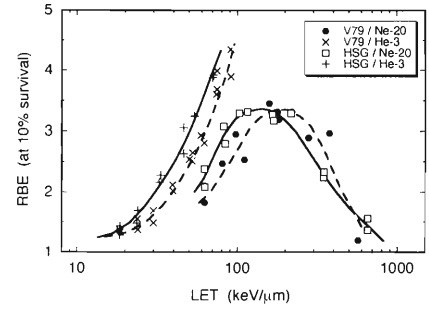


Fig. 2. Difference of the RBE (relative biological effectiveness) between HSG and V79 cells for $^{20}$Ne and $^{3}$He ion beams.

the curves for HSG cells by the $^{12}$C-ion and $^{20}$Ne-ions, it was hard to find any difference between each other. It is difficult to clear to give a reason for this; it may be caused by a difference in the target size of these two cell strains and truck structures of the ion beams. This difference due to exposed ions and cell strains is summarized as an expression of the RBE in Fig. 2 by using some data from the $^{3}$He-ion and $^{20}$Ne-ion beam experiments. In the figure, not only the difference produced by the ions described above, but a difference due to the cell strains, could also be found. The RBE curves of V79 cells for $^{3}$He-ions were shifted to a much higher LET region compared with that of the HSG cells. The same figures could also be found for the $^{20}$Ne ions.

References


1) T. Kanai et al.: NIRS-M-91, HIMAC-004; 1, Natl. Inst. Radiol. Sci., Chiba (1993).
2) Y. Furusawa et al.: Proc. 2nd Workshop on Phys. Biol. Res. Heavy Ion., eds. K. Ando and T. Kanai, NIRS-M-90, HIMAC-003; 11, Natl. Inst. Radiol. Sci., Chiba (1992).
3) Y. Furusawa et al.: Proc. 3rd Workshop on Phys. Biol. Res. Heavy Ion., eds., K. Ando and T. Kanai, NIRS-M-90, HIMAC-006; 34, Natl. Inst. Radiol. Sci., Chiba (1993).

# DNA Double Strand Breaks Induced with 135 MeV/nucleon Ne Beam

M. Murakami, K. Eguchi-Kasai, H. Itsukaichi, F. Yatagai, and T. Kanai

Heavy ion particles densely ionize substances that are just around these tracks. Considering this point, the biological effect by heavy ion particles may be different from the one by X-ray. We are interested in the mechanism of induction of DNA double-strand breaks on mammalian cells.

For the purpose of analyzing DNA double-strand break induction by heavy ion particles, the mouse LTA cells were irradiated with Ne beam accelerated by RIKEN Ring Cyclotron (the initial energy was 135 MeV/nucleon). After irradiation, cells were counted and were analyzed by the pulsed-field gel electrophoresis. The pulsed-field gel electrophoresis can separate the mega-base order large size DNA fragment. Cells were irradiated with neon beam, and were fixed into agarose plugs. The plugs were treated by proteinase K at 50 °C for 24 hr. The samples were electrophoresed for 68 hr at 15 °C and 60V with a Hexafield Horizontal Gel Electrophoresis apparatus with an electrical field alternating every 30 min. After the electropholesis, the gel was stained with ethidium bromide and visualized.

Double-strand DNA breaks were observed by the pulsed-field gel electrophoresis (Fig. 1). The amount of DNA double-strand breaks increased as the doses increased. For the DNA repair assay, the irradiated cells were incubated for 4 hr at 37 °C and then the cells were treated for the sample of pulsed-field gel electrophoresis. The amounts of DNA double strand breaks after 4 hr incubation were decreased. DNA repair was observed in this condition.

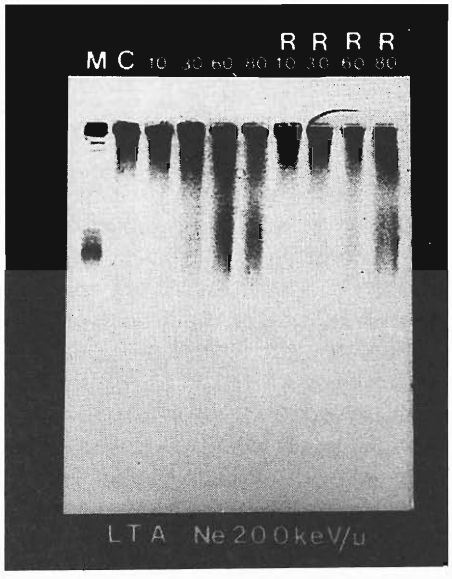


Fig. 1. DNA double-strand breaks induced by Ne-beam (LET = 200 keV/$\mu$m) irradiation. M; DNA marker -1.9mega-base-pair (*S. cerevisiae*), C; unirradiated control, 10; Ne beam irradiated with 10Gy, 30; 30Gy, 60; 60Gy, 80; 80Gy, R10; 4 hr incubation after irradiation with 10Gy of Ne beam (repair-10Gy), R30; repair-30Gy, R60; repair-60Gy, R80; repair-80Gy.

# Effects of Charged-particle Beams on 11 Mammalian Cell Lines

K. Eguchi-Kasai, M. Murakami, H. Itsukaichi, K. Fukutsu, T. Kanai, Y. Furusawa, K. Sato,* H. Ohara, and F. Yatagai

It can be noted that it is not simple double strand breaks (dsb) but non-reparable breaks that are associated with high biological effectiveness in the cell killing effect for high LET radiation. Here, we have examined the effectiveness of low (initial energy = 12 MeV/u) or high (135 MeV/u) energy charged particles on cell death in 11 mammalian cell lines including radiosensitive mutants. The dose, required to obtain 10% cellular survival, $D_{10}$, was calculated by regression analysis of survival curves according to a linear-quadratic model. When $D_{10}$ doses of charged particles were plotted against those of X-rays, a linear correlation was obtained (Fig. 1). Fitted lines were calculated by a computer using linear regression analysis. The slope of the fitted line has the inverse dimension of relative biological effectiveness (RBE). This value may relate to a theoretically maximal value of RBE of each particle beam. The slope varied depending on the radiation quality, generally showing larger values for low LET He ion and smaller values for high LET C or Ne ion. This should mean that RBE value is small for low LET He ion and is large for high LET C or Ne ion. This is generally observed for the survival of many mammalian cells except in a very high LET region. The RBE of particles having LET above 100 keV/$\mu$m was not necessarily large. RBE values of Mix beam are smaller than those expected from single irradiation by monoenergy particles of the same LET. It should be noticed that the points of radiosensitive mutants were located in the lower left corner of the figure. These radiosensitive cell lines were M10 and SL3-147. They were deficient in DNA dsb repair and showed lower RBE values against any particle beam if compared with their parent cell lines. Their RBE values were very close to unity, independent of the LET or the kinds of particles. On the other hand, human ataxia-telangiectasia fibroblasts, irs 1 and irs 2 cells, that were also radiosensitive but known as proficient in dsb repair, showed moderate RBE values. These 3 cell lines showed radioresistant DNA synthesis. Therefore this

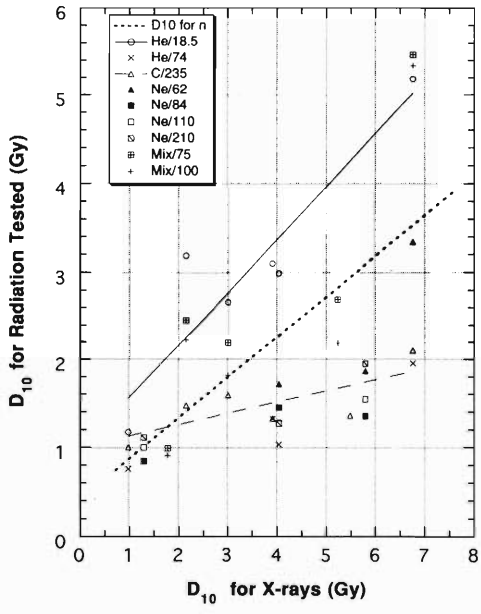


Fig. 1. Comparison of the cell killing effects among the charged particles. Dotted line represents the regression line for neutrons. Cell lines used were M10, SL3-147, AT5BIVA, irs1, irs2, L5178Y, HSG, MRC5sv1TG, R1, LTA, and V79 (from sensitive to resistant). The numbers following "He" or "C" in the figures were the LETs in keV/$\mu$m. For example, He/75 means the data after irradiation with He (LET $\approx$ 75 keV/$\mu$m). Mix means two-step-irradiations, 1st with He (12 MeV/nucleon, about 18 keV/$\mu$m) followed by C (12 MeV/nucleon, about 200 keV/$\mu$m) ions.

fact may be an important key to explain the killing of cells by high LET radiation. These experimental findings suggest that the DNA repair system does not play a major role against the attack of high LET radiations. Therefore, we hypothesize that a main cause of the cell death induced by high LET radiations is due to non-reparable dsb, which are produced at a higher rate compared with low LET radiations.

* Division of Radiation Hazards, National Institute of Radiological Sciences

# Effects of 135 MeV/nucleon Carbon Ion on Cultured Cells Derived from Squamous Cell Carcinoma

H. Itsukaichi, H. Ohara, K. Eguchi-Kasai, T. Kanai, K. Sato,* and F. Yatagai

In tumor tissue, there are many clones of cells with different radiation sensitivity against low LET radiations. For cancer therapy by ion beams, it should be important to predict the sensitivity to charged particles of such cells. We have been examined the radiosensitivity of 19 cell lines against X-ray and some kinds of high LET radiations. R1 cells which are derived from mouse squamous cell carcinoma[1] were chosen as one of radio-resistant cell lines. Here, we have examined the effect of low (initial energy = 12 MeV/nucleon) or high (135 MeV/nucleon) energy ion beams on the cell death of R1 cells.

Dose survival curves after irradiation with 135 MeV/nucleon C-ion beams are shown in Fig. 1 together with X-ray data. C-ion beams were more effective to kill R1 cells than X-rays as far as tested. Curves for the LET over 60 keV/$\mu$m have 2 phases, initial sensitive and second resistant phase. The ratio of resistant population increased with LET up to 167 keV/$\mu$m. This resistant population was not observed for fast neutrons (data not shown) or X-ray. This may be due to a technical problem. Studies about this phenomenon are now in progress. Inactivation cross section ($\sigma$) was calculated from $D_{37}$ which is the dose required to obtain 37% cellular survival. $D_{37}$ was obtained by regression analysis of survival curves according to a linear-quadratic model for the initial slope of survival curves. $\sigma$ increased with LET up to 200 keV/$\mu$m and looked to be saturated at 400 keV/$\mu$m (Fig. 2). $\sigma$-LET curve of R1 cells agreed with that of V79 cells (data not shown).

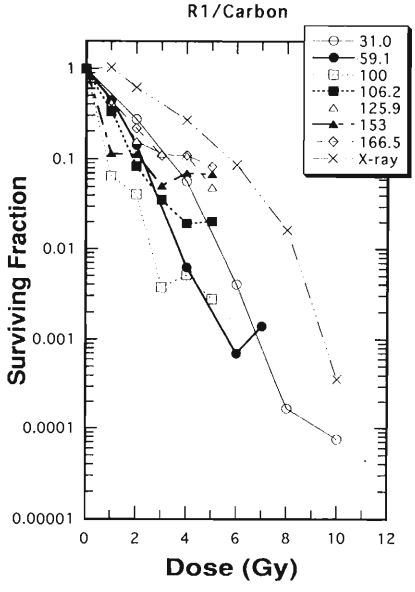


Fig. 1. Dose-survival curves of R1 cells. The numbers following symbols in the figure were the LETs of C-ion beams in keV/$\mu$m.

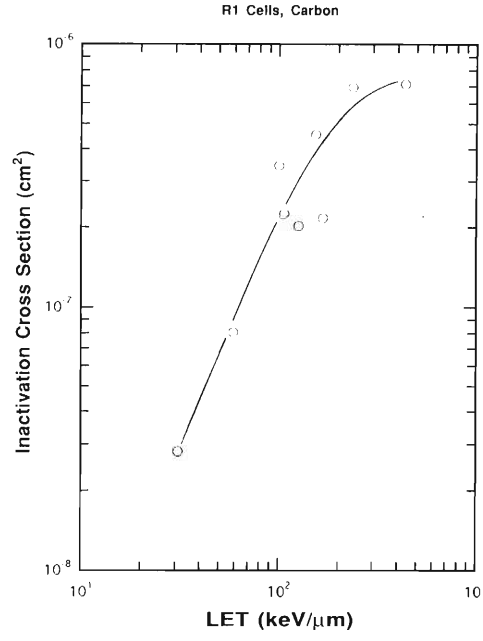


Fig. 2. Inactivation cross section of C-ion beams.

References

1) M. Miura and T. Sasaki: *Radiat. Res.*, **123**, 171 (1990).

* Division of Radiation Hazards, National Institute of Radiological Sciences

# Sensitivity of Normal Human Skin Fibroblasts after Carbon Ion Irradiation

H. Maezawa, T. Mori,* F. Yatagai, T. Kanai, and S. Inokuchi*

Knowledge for characteristics of normal tissue damages is important in successful radiotherapy with heavy ions. The study was conducted to know RBEs (relative biological effectiveness) of the lethal sensitivity, and the repair of lethal damages in human skin fibroblasts and keratinocytes after irradiation with heavy-ions. This paper reports the results in fibroblasts exposed to carbon ion.

Normal fibroblasts (HSF) were grown to a stationary phase in T25 flasks and irradiated with carbon ion accelerated to 135 MeV/nucleon in RIKEN Ring Cyclotron. Using the monoenergetic ion beam, the LETs were selected by inserting absober platès of appropriate thickness. Cell survival after irradiation was determined from the colony forming ability. Figure 1 shows the survival of fibroblasts after carbon-ion irradiation. The shoulder of the survival curves after irradiation by a carbon beam above 58.4 keV/$\mu$m of the dose averaged LET was reduced or disappeared depending on the LET, compared to the shoulder after irradiation with Co-60 gamma-rays. RBE at a given LET was difined as the ratio of the dose required for 10% survival with the ion beams to that with Co-60 gamma rays. Resulted RBE at 22, 58.4, 97, 106.7, and 266.8 keV/$\mu$m were 1.42, 2.40, 3.74, 3.81, and 2.76, respectively. PLD repair has been investigated with the delayed plating technique in which cells were

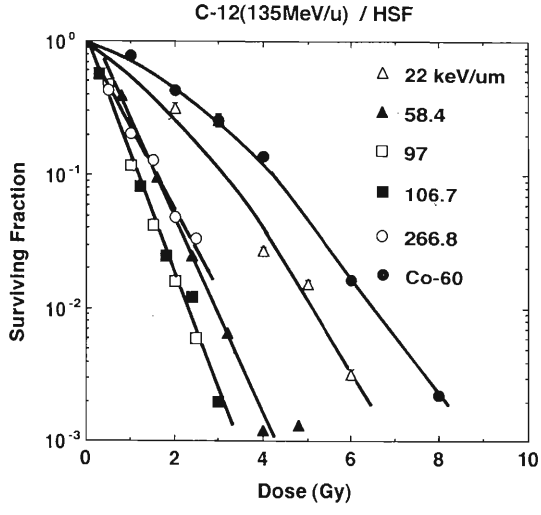


Fig. 1. Survival curves of fibroblasts irradiated with carbon ion and Co-60 gamma rays.

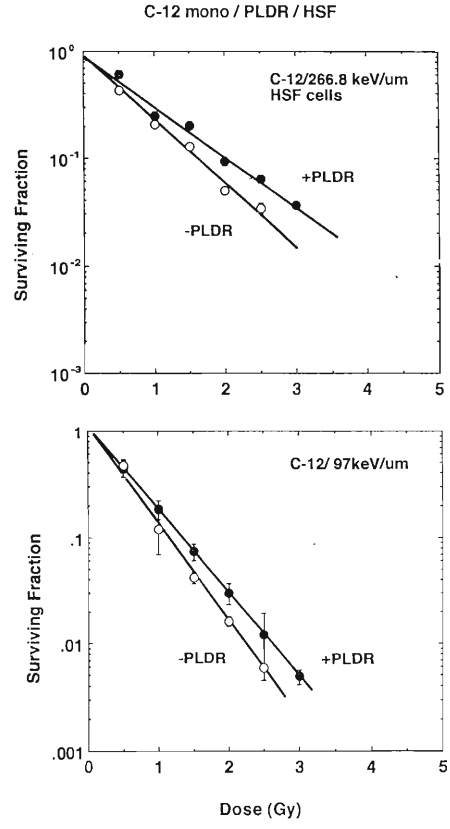


Fig. 2. Survival curves of stationary phase fibroblasts replated immediately after carbon-ion irradiation (−PLDR) and at 24 hrs after (delayed plating, +PLDR).

replated at 24 hr (37 °C) after irradiation. The survival after the delayed plating was higher as compared with that immediately after irradiation with carbon ion at 97 and 266.8 keV/$\mu$m (Fig. 2). PLD repair was clearly observed. The recovery ratio was calculated from the survival after the delayed plating to a given dose, which reduced survival to 1% when cells were replated immediately after irradiation. Recovery ratios (1.6 at 97 keV/$\mu$m and 2.7 at 266.8 keV/$\mu$m) in cells irradiated with carbon ion were smaller than that (5.6) in cells irradiated with Co-60 gamma rays.

Present results suggested that carbon ion above 58 keV/$\mu$m produced less repairable damages in fibroblasts as compared with Co-60 gamma-rays.

* School of Medicine, Tokai University

# Mutation Caused by Heavy Ion Particles and X-rays

N. Shigematsu,* H. Ito, S. Yamashita, K. Toya,* A. Kubo,* F. Yatagai, and T. Kanai

The purpose of this study is to compare X-rays and heavy ion particles irradiation with regard to their effects on cell killing and mutation induction. We also studied how their irradiation procedures (single and fractionation) would affect cell survival and mutation.

V79 cells were irradiated by the heavy ion beam from RIKEN Ring Cyclotron or by X-rays from MBR-1520R (Hitachi) and cell survivals were calculated by colony assay. After one or two weeks expression periods, the mutation frequencies at the *hprt* locus were calculated from the numbers of colonies formed in media supplemented with 6-thioguanine (10 $\mu$g/ml). The effects of the fractionation (3 hr interval) of radiation on the cell survival and the mutation frequencies were also examined.

The $D_0$ values for 150 kV X-rays, 20 keV/$\mu$m carbon beam, 80 keV/$\mu$m carbon beam and 80 keV/$\mu$m neon beam were 2.2 Gy, 1.8 Gy, 1.0 Gy, and 1.4 Gy, respectively (Fig. 1). As shown in Fig. 2 the extremely higher mutation was caused by the heavy ion beam compared with X-rays. A neon beam caused less mutation than a carbon beam under the same LET conditions. Both cell killing effect and the mutation induction were enhanced when LET of a carbon beam was increased 4 times (20 to 80 keV/$\mu$m). Our results indicate that the heavy ion beam therapy had more

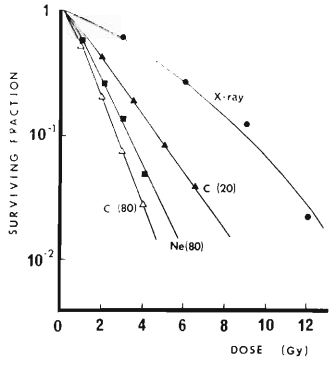


Fig. 1. Survival curves for X-rays and heavy ion beams (carbon 20 and 80 keV/$\mu$m and neon 80 keV/$\mu$m).

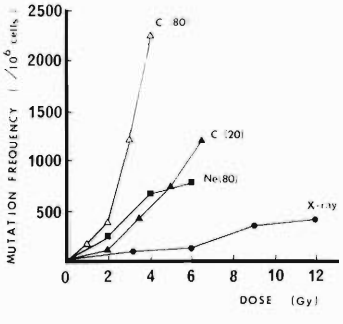


Fig. 2. Mutation frequencies per $10^6$ cells irradiated with X-rays and heavy ion beams (carbon 20 and 80 keV/$\mu$m and neon 80 keV/$\mu$m).

* Dept. Radiol., School of Medicine, Keio University

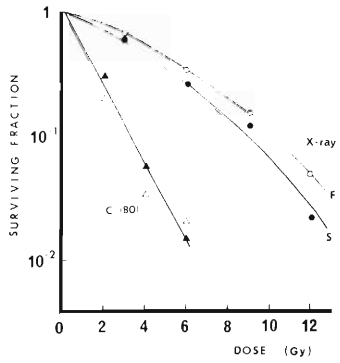


Fig. 3. Survival curves for X-rays single (●), X-rays fractionated (○), carbon single (▲) and carbon fractionated (△) irradiation.

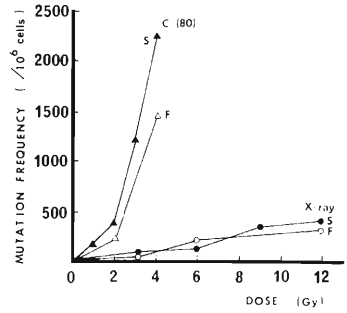


Fig. 4. Mutation frequencies for X-rays single (●), X-rays fractionated (○), carbon single (▲) and carbon fractionated (△) irradiation.

powerful cell killing effect than X-rays while it caused the high risk for mutation induction. A neon beam has small mutation induction effect comparing with a carbon beam while the similar cell killing effect can be expected from each of them. Comparison between single and fractionated irradiation was shown in Figs. 3 and 4. A carbon beam had no significantly different effects on cell killing between single and fractionated irradiation whereas X-rays had. When the carbon beam irradiation was fractionated, the mutation frequency was reduced although the survival curve was not affected. When X-rays was used the mutation frequency was almost the same in each way.

We concluded as follows:

(1) The mutation frequency was extremely high for the cells which were irradiated with a heavy ion beam compared with X-rays.

(2) The mutation frequency was increased when the LET of a carbon beam was increased.

(3) The mutation frequency was less for a neon than a carbon beam, suggesting that neon is a favorable beam for the heavy ion therapy especially when treating with higher doses.

(4) When the cells were irradiated with a heavy ion beam the fractionated procedure made it possible to reduce the mutation frequency without decreasing the cell killing effect.

# Effects of Accelerated Carbon-Ion on the Induction of Dominant Lethality in the Teleost Fish, *Oryzias latipes*

Y. Hyodo-Taguchi,* T. Kanai, S. Minohara, and Y. Furusawa

The dominant lethal mutation test with mice has been considered one of the most important methods for the estimation of the mutagenic effects of chemicals on higher animals. In the small teleost fish, *Oryzias latipes*, it has been reported that the dominant lethal mutation test by using the hatchability of eggs is useful for estimation of the mutagenic effects of radiation and chemicals.[1] In the present experiment, we have studied the genetic effects of heavy ion on the male germ cells of the fish by using the dominant lethal test system.

One of albino strains of medaka (*bi-3R*) was used. A single pair of the adult fish lays a cluster of 10–40 eggs almost every morning in a laboratory aquarium if the fish were kept at 26 °C. During the period of 6–9 days before irradiation, the numbers of fertilized and unfertilized eggs laid by each pair and the hatchability of the fertilized eggs were examined to determine non-irradiation control value. The male of each pair was irradiated with carbon-ion (135 MeV/u) accelerated by the RIKEN Ring Cyclotron. The fish were exposed to heavy ion of 2, 5, and 10 Gy at the mid position of spread-out bragg peak (dose average LET = 70 keV/$\mu$m). The irradiated fish were transported to the NIRS and each fish was kept with a non-irradiated female in an aquarium containing 2l of water. Each pair was kept under conditions of about 26 °C and 14-h light/10-h dark cycle and observed every day. The numbers of fertilized and unfertilized eggs laid by each fish were counted every morning and each cluster of fertilized eggs was incubated separately in a petridish at 26 °C. The incubation medium (D.W. containing 0.0001% methylene blue) was changed every day and dead embryos were removed. In the non-irradiated control, most embryos hatched 7–10 days after fertilization. The numbers of dead embryos and newly hatched fry were counted every day in each cluster. The hatchability was calculated as the percentage of hatched embryos per fertilized eggs. The hatchability of the non-irradiated control was 92 ± 1%; the relative hatchability rate (RHR) was calculated as follows: (hatchability of the given group)/(hatchability of the control group) × 100. Dominant lethal rates were calculated as 100 minus RHR. The maturation stage at which spermatogenic cells were irradiated was judged by the time between irradiation and fertilization.[2]

Thirty-one pairs of fish irradiated with carbon beam were examined to estimate fertility and hatchability of eggs laid for 30 days. A considerably high level of the fertility of the male fish was kept within 10 days after irradiation in all irradiated groups. At 20 and 30 days after irradiation a marked decrease in the fertility was observed in the C-beam 10 Gy-irradiated group. The hatchability changes showed that (1) the hatchability of eggs fertilized by irradiated males reduced markedly within 3 days after irradiation, and the effects were dose-dependent and (2) the effects of irradiation decreased if the interval between irradiation and fertilization became longer than 4 days. From these hatchability data, the dose-associated increase of production of the dominant lethality was observed in each spermatogenic cell stage in medaka after heavy ion irradiation; a dose-dependent increase in the dominant lethality was found for sperm, spermatid and spermatocytes within this dose range, whereas no marked increase of the dominant lethality could be found for spermatogonia. Mature sperm was the most sensitive among the various stages of spermatogenetic cells. The high and low inducibility of dominant lethal in sperm and spermatogonia, respectively, was reported in this fish after X-irradiation.[1,3]

On the basis the present results and the previous results from X-irradiated fish, it seems to be evident that the effect of carbon-beam on the induction of dominant lethality was about 2 times higher than that of X-rays for sperm and spermatid of the fish.

References

1) N. Egami, A. Shimada, and A. Hama-Furukawa: *Mutat. Res.*, **107**, 265 (1983).
2) N. Egami and Y. Hyodo-Taguchi: *Exp. Cell Res.*, **47**, 665 (1967).
3) A. Shima and A. Shimada: *Proc. Natl. Acad. Sci. USA*, **88**, 2545 (1991).

* National Institute of Radiological Sciences

# Biological Dose Distribution of Carbon-12 Spread-Out-Bragg-Peak for Tumor Controls

K. Ando, S. Koike, M. Iizuka, T. Aruga, N. Hori, T. Kanai, S. Minohara, M. Sudou, and F. Yatagai

The clinical trial of heavy charged particle therapy started June 23, 1994 at National Institute of Radiological Sciences. Biological effectiveness of therapeutic beams against tumors inactivation is of great concern for designing a range modulator which generates Spread-Out-Bragg-Peak (SOBP). A range modulator for 135 MeV/nucleon carbon-12 was designed by T. Kanai, and has been proven to exert fairly homogeneous cell kills against cultured V79 cells.[1] We here investigated and reported whether or not the SOBP made by the range modulator could also achieve homogeneity in tumor controls. (Materials and Methods) The NFSa fibrosarcomas were transplanted into hind legs of syngeneic C3H male mice. Seven through eight days after transplantation when leg tumors grew to 7–8 mm in diameter, mice locally received single doses of irradiation to their leg tumors. Desired tumor positions within 3-cm SOBP were obtained by placing thick Lucite plates in front of tumors. Cs-137 gamma ray was used to reference to obtain relative biological effectiveness (RBE) of carbon-12. After irradiation, tumors were (a) monodispersed by trypsin to serve lung colony assay for determining cell survivals, (b) measured by calipersonce a week up to 4 months to serve for tumor control assay ($TCD_{50/120}$). A total of 1050 mice were used for the experiments. (Results) Leg tumors were located at three SOBP positions; proximal-(LET = 61 keV/$\mu$m), middle-(LET = 78 keV/$\mu$m) and distal-(LET = 108 keV/$\mu$m) SOBP. (Fig. 1). Unmodulated plateau (LET = 23 keV/$\mu$m) was also included. Radiosensitivity of the tumor cells determined by lung colony assay showed that $D_0$ values for distal-, middle-, proximal-SOBP, and unmodulated plateau were 1.12, 1.48, 1.49, and 2.68 Gy, respectively. $D_0$ for gamma ray was 4.22 Gy.

Tumor control probabilities for each position of SOBP were determined 120 days after irradiation. $TCD_{50/120}$, i.e., radiation dose required for 50% of tumors controlled, was 32.5, 34.9, 37.1, and 56.4 Gy for distal-, middle-, proximal-SOBP and unmodulated plateau, respectively. RBEs of carbon-12 relative to gamma ray ($TCD_{50/12}$ = 83.2 Gy) were 2.56, 2.38, 2.24, and 1.48 for distal-, middle-, proximal-SOBP and unmodulated plateau, respectively.

Biological effect at each SOBP was obtained by comparing biological doses (i.e., the product of physical dose and RBE) between SOBP and unmodulated plateau, and used to evaluate homogeneity of tumor inactivation within SOBP. As for lung colony assay, biological effects at surviving fraction (SF) of 0.5 down to 0.1 , was ranging between 2.2 and 2.69, indicating fairly homogeneous effectiveness within 3-cm SOBP. Tumor control assay also resulted in homogeneity similar to colony assay; biological effects for tumor controls were 2.25, 2.2, and 2.05 for proximal-, middle- and distal-SOBP (Fig. 2).

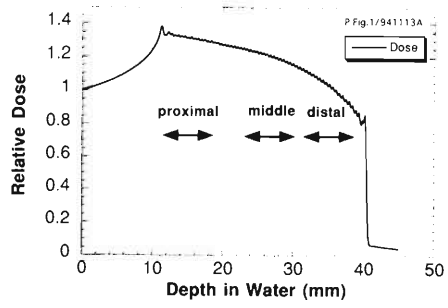


Fig. 1. Positioning of tumors within 3-cm Spread-Out-Bragg-Peak for 135 MeV/nucleon carbon-12. Arrow length corresponds to tumor thickness.

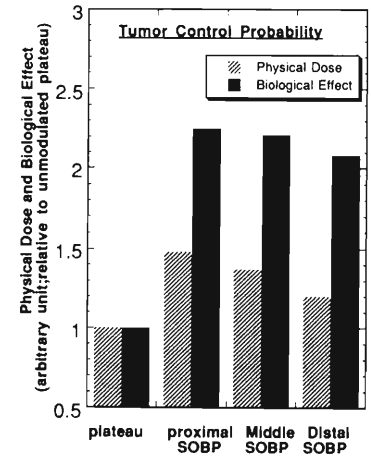


Fig. 2. Distribution of biological effectiveness within Spread-Out-Bragg-Peak. Biological effectiveness is normalized by unmodulated plateau beam.

It is concluded that homogeneous cell kills of a mouse tumor was achieved by the range modulator design of which was based on the data of Chinese hamster cells in vitro.

References

1) T. Kanai and Bio-Phys. Group of RIKEN Ring Cyclotron Users: Proc. 3rd Workshop on Physical and Biological Research with Heavy Ions, eds. K. Ando and T. Kanai, NIRS-M-99, HIMAC-006, Natl. Inst. Radiol. Sci., p. 7 (1993).

# 5. Instrumentation

# Production of a Low-Energy Polarized Neutron Beam

K. Sagara, N. Nishimori, T. Fujita,* H. Akiyoshi,* K. Maeda, and H. Nakamura*

To produce a 10–18 MeV polarized-neutron beam whose polarization is precisely known, a neutron-beam generator using $D(\vec{d},\vec{n})^3He$ reaction and a deuteron beam polarimeter using $^3He(\vec{d},p)^4He$ reaction have been developed. In this energy range, $D(\vec{d},\vec{n})^3He$ reaction has the highest figure of merit for the $\vec{n}$-beam production and $^3He(\vec{d},p)^4He$ reaction has high analyzing powers which vary smoothly with the incident energy and the scattering angle. The generator and the polarimeter will be combined with an intense $\vec{d}$-beam from the RIKEN AVF cyclotron to make high-precision polarized-neutron experiments on, for example, $\vec{n}+d$ scattering.

Figure 1 shows a $D_2$ gas target for the $\vec{n}$-beam production and a $^3He$ gas target for the $\vec{d}$-beam polarimeter. A number of background neutrons were greatly reduced by adopting heavy metals for a beam slit (W), for 3-$\mu$m-thick window foils of the target gas cells (Ta) and for a $\vec{d}$-beam stopper (Ta). The walls of the gas cells were made thin to reduce the scattering of neutrons by them.

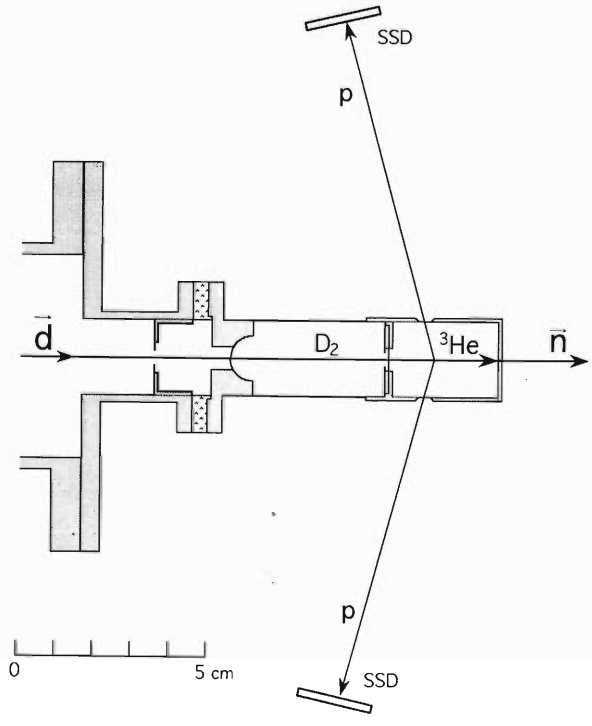


Fig. 1. A polarized-neutron-beam generator using $D(\vec{d},\vec{n})^3He$ reaction and a deuteron-beam polarimeter using $^3He(\vec{d},p)^4He$ reaction. The $\vec{d}$-beam is stopped on the bottom of the $^3He$-gas cell.

For example, a 12-MeV $\vec{n}$-beam in the 0° direction is generated by $D(\vec{d},\vec{n})^3He$ reaction at $E_d = 9$ MeV. The energy spread of the $\vec{n}$-beam comes mainly from the $\vec{d}$-beam energy loss of 140 keV in the $D_2$ target of 2 bar × 4 cm in thickness. As the continuum neutrons from $D(\vec{d},n)pd$ reaction have energies below 6.77 MeV, their contributions may be well separated by the TOF technique. The $\vec{n}$-beam flux in a solid angle of $\pm 1.5° \times \pm 3°$ is estimated to be $6 \times 10^6$ particles/sec for a 5 $\mu$A $\vec{d}$-beam.

When the deuteron spin axis is in the y (up) direction, the polarization of the $\vec{n}$-beam ($p_y^n$) is expressed as

$$p_y^n = \frac{3}{2} p_y^d K_y^y(0°) \Big/ \left[1 - \frac{1}{4} p_{yy}^d A_{zz}(0°)\right].$$

The vector and tensor components of the $\vec{d}$-beam polarization, $p_y^d$ and $p_{yy}^d$, are measured by the $^3He(\vec{d},p)$ polarimeter. We have already made accurate measurements of the analyzing powers $A_y$ and $A_{yy}$ of $^3He(\vec{d},p)$ reaction in the range of $E_d = 6.6$–$15.4$ MeV. As $p_y^n$ is mainly determined by $p_y^d$, the polarimeter counters (Fig. 1) are placed at the angle for the maximum of $A_y$. By this polarimeter, the $\vec{d}$-beam polarization can be determined within an accuracy of 0.6%.

Precise measurement of $K_y^y(0°)$ and $A_{zz}(0°)$ of $D(\vec{d},\vec{n})^3He$ reaction is in progress at Kyushu University tandem accelerator lab. The $\vec{n}$-beam polarization $p_y^n$ is measured using $^4He(\vec{n},n)$ scattering. The liquid helium target (used also as a scintillator) has already been installed and the measurement of $p_y^n$ has been started using the $A_y = 1$ (theoretically maximum) point of $^4He(\vec{n},n)$ scattering at 12 MeV.

A high-intensity polarized-neutron beam of energy of 10–18 MeV whose polarization (about 0.5) is known to within about 1% will be available in the near future.

* Department of Physics, Kyushu University

# Germanium Counter Telescope for Gamma-Ray Position Sensitive Detection

Y. Gono, E. Ideguchi, K. Miyazaki, T. Morikawa, T. Kishida, and M. Ishihara

We reported last year the concept as well as the results of simulation calculations of a Ge counter telescope.[1] A segmented Ge (S-Ge) detector has been produced following our specifications and delivered by a company, URISYS MESURES. This special detector is prepared to be used to give position information by a signal of Compton scattering. Then an energy information is given by summing signals of both Compton scattering in S-Ge and a totally absorbed signal in a Ge detector placed behind the S-Ge.

The first test was made to check energy resolution of each segment. In this test a highly integrated linear amplifier was developed in the tandem laboratory in Kyushu university. Four linear amplifiers were assembled in one span NIM chassis. This type of amplifier was prepared to handle 25 signals from every segment independently. Amplifier gains were adjusted to give a same pulse height for each segment though each preamplifier gives much different pulse height for a fixed energy $\gamma$-ray. Then energy resolutions were checked for every segment and the resulted values are given in Fig. 1.

| | | | | |
|---|---|---|---|---|
| 1 2.7 keV | 2 2.6 keV | 3 2.7 keV | 4 2.7 keV | 5 2.7 keV |
| 6 2.5 keV | 7 2.7 keV | 8 2.5 keV | 9 2.5 keV | 10 2.4 keV |
| 11 2.4 keV | 12 2.5 keV | 13 2.5 keV | 14 2.6 keV | 15 2.5 keV |
| 16 2.4 keV | 17 2.6 keV | 18 2.8 keV | 19 2.5 keV | 20 2.5 keV |
| 21 2.3 keV | 22 2.6 keV | 23 2.6 keV | 24 2.5 keV | 25 2.7 keV |

Fig. 1. FWHM of each segment at 1.33 MeV.

These values are not much different from the values measured using commercially available spectroscopy amplifiers which have 1 channel for one span NIM chassis.

The summed $\gamma$-ray spectrum was also tested. In this case a 20% HPGe detector was used as a rear detector with NaI(Tl) anti-Compton shield. A $^{152}$Eu $\gamma$-ray standard source was used. The resulted spectrum is shown in Fig. 2 with a spectrum taken by an S-Ge alone. Two spectra are shown by normalizing the peak heights of 1408 keV peaks in both spectra. The low energy continuum back ground in the summed spectrum is significantly reduced as expected.

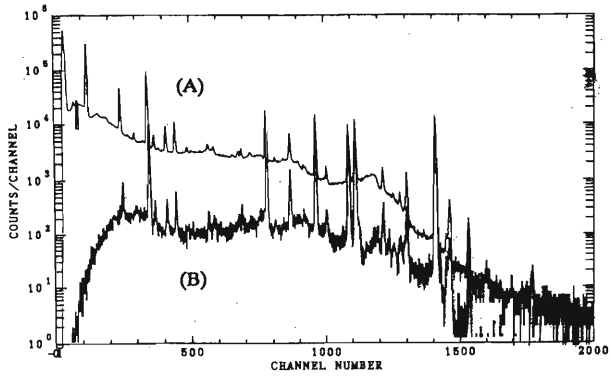


Fig. 2. $\gamma$-ray spectra taken in singles mode (A) by an S-Ge alone and a summed mode (B).

As a conclusion it was proved that a Ge counter telescope by using an S-Ge as a $\Delta$E counter works to reduce considerably a back ground and to give position information simultaneously. Also it may be worthwhile to point out that this detector can be used as an efficient polarimeter of $\gamma$-rays.

References

1) E. Ideguchi et al.: *RIKEN Accel. Prog. Rep.*, **27**, 121 (1993).

# A New Position Sensitive Silicon Detector for Experiments of Super Heavy Nucleus Search

M. Kurokawa, T. Motobayashi, H. Murakami, T. Uchibori, A. Yoshida,
K. Morita, Y. Pu, and T. Nomura

A new position sensitive silicon detector has been developed for super heavy nucleus-search experiments. In the experiments, a heavy element can be identified by measuring the energy of its successive $\alpha$ decays. To reduce accidental correlation the detector should have high position resolution. The detector developed is a double-sided position-sensitive silicon detector as illustrated in Fig. 1. The total effective area is 64 mm × 64 mm. The energy signal is extracted from the front side electrodes, and two-dimensional position information, x and y in this figure, is obtained from the front and back sides, respectively.

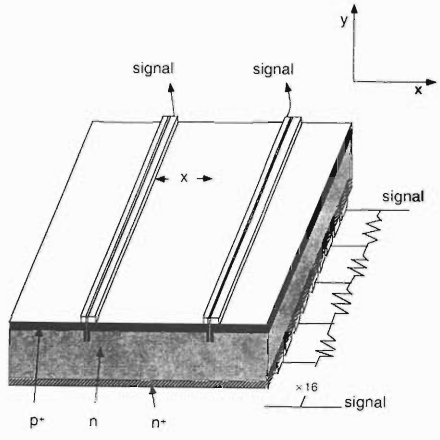


Fig. 1. Schematic view of the detector.

The front surface of the detector is divided into 12 resistive strips. This small number of the strips is intended to achieve a small total dead space which is formed between the strips, as well as to reduce the number of electronics. To obtain more precise x information than the width of a strip, the charge division method is employed. In contrast to the usual design where the charges are extracted from the top and bottom ends of a strip, two readout electrodes are running along the side edges of a strip. Because the position resolution is inversely proportional to the resistance between electrodes,[1] a high surface resistivity of around 10 kΩ2 was required in the present design. This was realized by the "shallow doping" technique in the implantation process. The doping density is almost ten times lower than the normal level.

The back side of the detector is designed to be a microstrip structure. The total number of electrodes is 128 and eight resistance chains are formed by connecting every other strips up to 16 with 120 Ω resistance. Signals are read out from the two ends of the chain.

To reduce the position resolution, the difference between the position signals corresponding to a fusion product $^{205}$Fr from the $^{40}$Ar + $^{169}$Tm reaction and its $\alpha$ decay was measured. The results are shown in Fig. 2. The energy dependence of the position resolution is roughly expressed as 1/E. This position resolution (x × y) of the newly developed detector is better than that of the detector[2] used in the previous experiment[3] by a factor of 100. This detection system was used in the experiment of $^{232}$Th + $^{40}$Ar reaction.

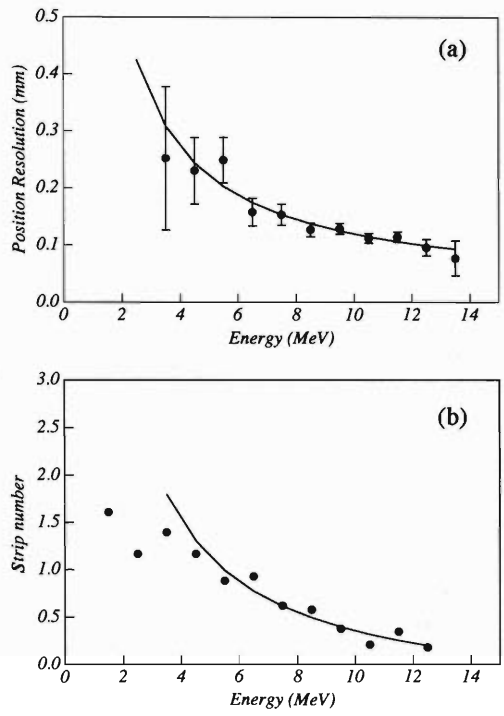


Fig. 2. Energy dependence of horizontal (a) and vertical (b) position resolution.

References

1) F. Eland and R. Sareen: *IEEE Trans. Nucl. Sci.*, **NS-21**, 75 (1974).
2) M. Kurokawa et al.: *RIKEN Accel. Prog. Rep.*, **25**, 120 (1991).
3) T. Nomura: Proc. Workshop on Heavy-Ion Reactions with Neutron-Rich Beams, ed. M. Ishihara, World Sci., p. 269 (1993).

# Status of the Detector System at SMART-FP1

H. Okamura, S. Ishida, N. Sakamoto, H. Otsu, T. Uesaka, T. Wakasa, Y. Satou, H. Sakai, T. Niizeki, K. Katoh, T. Yamashita, and T. Ichihara

The first focal plane (FP1) of the SMART spectrograph is primarily used to measure the $(d,^2\mathrm{He})$ reaction. The energy resolution as well as the $^2$He-detection efficiency was significantly improved by the newly fabricated detector system.[1] The angular resolution, however, was still very bad due to the large magnification in the vertical direction. This is a serious drawback since $(d,^2\mathrm{He})$ is a three-body reaction and the precise angular information, particularly for the light target, is required to determine the excitation energy as well as the scattering angle.

In the "standard" optics which has been used so far, the field strength of the $Q$-magnet is chosen so that the scattered particles with the central momentum are focussed in the vertical direction. Although the large angular acceptance is maintained in the wide momentum range, the angular resolution at the central momentum is significantly deteriorated due to the multiple-scattering by the vacuum window and by the wire chambers.

The new optics has been introduced as a compromise between the better angular resolution and the large acceptance. The field of the $Q$-magnet is chosen to be relatively strong so that the scattered particles are focussed at the high-momentum side in the vertical direction. Also the focal plane is shifted upstream, to the area between the two wire chambers, which will lead to the improved momentum resolution. The property of the new optics has been studied by using the elastically scattered protons from a gold target at $E_p = 135$ MeV. The result is summarized in Table 1 compared with the standard optics. The quality of data for the $(d,^2\mathrm{He})$ reaction is significantly improved by using the new optics as is shown in Fig. 1.

Table 1. Summary of optics properties at $E_p = 135$ MeV.

| | Standard optics | New optics |
|---|---|---|
| | *Magnetic Field* | |
| $PQ_1$ | 353.0 Gauss/cm | 392.6 Gauss/cm |
| $PQ_2$ | 163.6 Gauss/cm | 189.2 Gauss/cm |
| $PD_1$ | 7241 Gauss | |
| | *Acceptance* | |
| $\Delta\theta$ | $\leq$100 mrad[a)] | 84 mrad |
| $\Delta\varphi$ | $\leq$200 mrad[a)] | 156 mrad |
| $\Delta\Omega$ | $\leq$20 msr[a)] | 13.1 msr |
| $\Delta p$ | $\pm$12% | +6/$-$8 % |
| | *Resolution* | |
| $\delta\theta$ | 4 mrad | 4 mrad |
| $\delta\varphi$ | 5–30 mrad[a)] | 5 mrad |
| $\delta p/p$ | 1-3 $\times 10^{-3}$[a)] | $1 \times 10^{-3}$ |
| | $(d,^2\mathrm{He})$-*Resolution* | |
| $\langle\delta\mathrm{E}\rangle$ | $\delta(E_1 + E_2) = 700$ keV | $\delta E_x = 460$ keV[b)] |
| $\langle\delta\theta\rangle$ | unknown | 9 mrad[b)] |

[a)] $\Delta\Omega$, $\delta_\varphi$ and $\delta p/p$ depend on $p$ in the standard optics.
[b)] obtained from the three-body calculation.

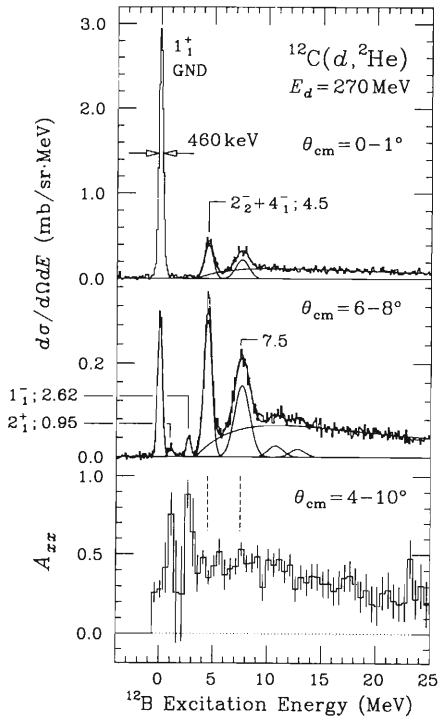


Fig. 1. Typical excitation energy spectra of the $(d,^2\mathrm{He})$ reaction obtained with the new optics.

Also the polarized deuteron beam has become available at SMART. By using the Wien filter, the polarization axis can be rotated to the normal or sideway direction of the scattering plane at any angle of the beam swinger.[2] A polarimeter has been installed at the exit of the beam swinger and the polarization at the target is directly measured.[2] The polarimeter target can be quickly inserted and removed by using a pneumatic actuator, which allows the periodical monitor of the beam polarization during the experiment. This feature was used in the first measurement of the analyzing powers of the $(d,^2\mathrm{He})$ reaction. Details of the experiment are described elsewhere.[3]

References

1) H. Okamura et al.: *RIKEN Accel. Prog. Rep.*, **27**, 113 (1993).
2) H. Okamura et al.: *AIP Conf. Proc.*, **293**, 84 (1994); *RIKEN Accel. Prog. Rep.*, **27**, 130 (1993); This report, p. 148.
3) H. Okamura et al.: *Nucl. Phys.*, **A577**, 89c (1994); *Phys. Lett.*, **B345**, 1 (1995); This report, p. 148.

# Construction of the Deuteron POLarimeter DPOL at the Second Focal Plane of SMART

S. Ishida, H. Okamura, N. Sakamoto, H. Otsu, T. Uesaka, T. Wakasa, Y. Satou, S. Fujita, H. Sakai, T. Ichihara, T. Niizeki, K. Katoh, T. Yamashita, Y. Hara, and K. Hatanaka

Polarization transfer measurement for inelastic deuteron scattering is one of the most efficient probes of isoscalar spin excitations which we have little information up to now. Spin flip probability $S_1$ in the $(d,d')$ reaction will be a signature of spin excitations as $S_{nn}$ is in the $(p,p')$ reaction.[1,2] $S_1$ is written, in terms of polarization observables, as

$$S_1 = \frac{1}{9}(4 - P^{y'y'} - A_{yy} - 2K_{yy}^{y'y'}),$$

where $yy$ denotes the tensor polarization and $P^{y'y'}$, $A_{yy}$ and $K_{yy}^{y'y'}$ are the tensor polarizing power, the tensor analyzing power and the tensor-tensor polarization transfer, respectively. Thus measurements of the tensor-polarization observables are needed to extract $S_1$ via the $(\vec{d},\vec{d'})$ reaction.

We are constructing the Deuteron POLarimeter DPOL at the second focal plane (FP-2) of the SMART spectrograph to measure the polarization of scattered deuterons. It is designed to measure all the vector ($it_{11}$) and tensor ($t_{20}$, $t_{21}$ and $t_{22}$) polarization components by utilizing following three reactions. (Table 1)

Table 1. Reactions and corresponding components of analyzing power.

| Reactions | Analyzing powers |
|---|---|
| 1 : $d + {}^{12}\mathrm{C} \rightarrow d + {}^{12}\mathrm{C}$ | $iT_{11}$ |
| 2 : $d + p \rightarrow {}^{2}\mathrm{He}\ (2p) + n$ | $T_{20}$ and $T_{22}$ |
| 3 : $d + p \rightarrow d + p$ | all components |

These reactions are measured semi-inclusively. The

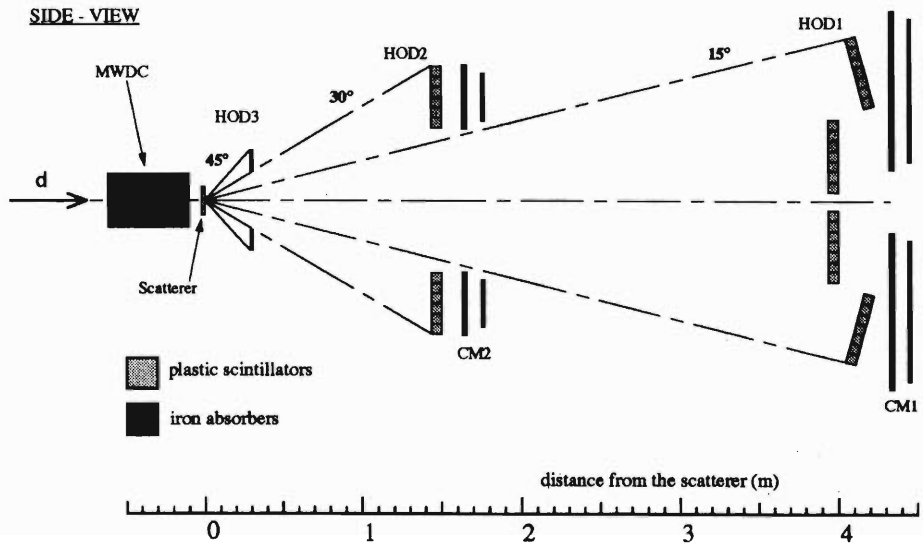


Fig. 1. A cross sectional view of the Deuteron POLarimeter DPOL. Details are described in the text.

geometry of DPOL is shown in Fig. 1. Note that the reaction plane of SMART is vertical because a scattering angle is changed by using a beam swinger system.

A multiwire drift chamber (MWDC) and trigger plastic scintillators ($0.5 \times 18 \times 80$ cm$^3$ and $1.0 \times 18 \times 80$ cm$^3$) are used for detecting scattered deuterons. These plastic scintillators containing C and H are also used as active scatterers for double scattering. The polarimeter-system consists of three hodoscopes, HOD1 (28 times $6.5 \times 6.5 \times 220$ cm$^3$), HOD2 (12 times $6.5 \times 6.5 \times 220$ cm$^3$) and HOD3 (2 times $1.0 \times 13 \times 100$ cm$^3$), and two calorimeters, CM1 (6 times $1.0 \times 29 \times 220$ cm$^3$ with 1.8 cm thick iron absorbers) and CM2 (2 times $1.0 \times 29 \times 220$ cm$^3$ with 1.8 cm thick iron absorbers). For all hodoscopes and calorimeters, plastic scintillators are used and they are viewed at both ends by photomultiplier tubes.

Three kinds of triggers for double scattering events

corresponding to the three different reactions are made. For the $^{12}$C($d$,$d_0$) event, calorimetry using iron absorbers and scintillators is employed to identify deuterons. For the $^{1}$H($d$,$^{2}$He) and $^{1}$H($d$,$d$) event, two charged particles are detected in coincidence.

The first experiment for testing the polarimeter-system has been recently performed with a 270 MeV polarized deuteron beam extracted from the RIKEN Ring Cyclotron.

Three combinations of the beam polarization were used in this experiment and their ideal values of vector and tensor polarization are ($p_Z$,$p_{ZZ}$) = (0,−2), (−1,+1) and (+1,+1), respectively. The polarization axis was controlled with the Wien filter downstream of the ion source so that it lay on the normal or sideway direction of the scattering plane at FP-2. The beam polarization was monitored by using the $d + p$ scattering at 270 MeV and typically 60–65 % polarization of the ideal value was obtained throughout the experiment.

Figure 2 shows the preliminary results of the effective analyzing powers for the $^{12}$C($d$,$d_0$) events. Large $iT_{11}$ values are obtained, which is consistent with the result of POMME.[3] Further analysis and improvement of the polarimeter are now in progress.

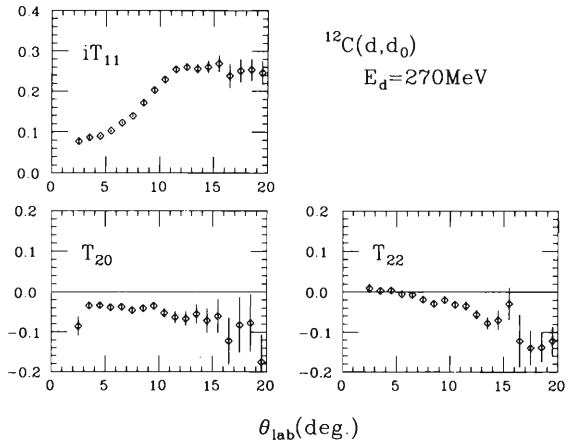


Fig. 2. Preliminary results of the effective analyzing powers of DPOL for the $^{12}$C($d$,$d_0$) events.

References

1) S. Ishida et al.: *Phys. Lett.*, **B314**, 279 (1993).
2) M. Morlet et al.: *ibid.*, **B247**, 228 (1990).
3) B. Bonin et al.: *Nucl. Instrum. Methods Phys. Res.*, **A288**, 389 (1990).

# PPAC for Beam Profile Monitor at the RIPS

H. Kumagai and K. Yoshida

A position sensitive parallel plate avalanche counter (PPAC) was constructed as a focus-plane detector for the secondary beam separator RIPS.[1] Two PPAC's were placed at the first and the second focus planes (F1 and F2) of the RIPS to measure x- and y- positions and time-of-flights of beam particles. Other two PPAC's were set in front of the third focus plane (F3) in order to obtain the beam profile at F3 where the user target was set up.

The structure of electrodes of the PPAC is shown in Fig. 1. As seen, the electrodes provided a sensitive area of $100 \times 100$ mm$^2$ and were composed of an anode and two cathodes which were used to determine the position of x- and y- direction. They were placed in parallel with 4 mm apart from one another in order of x-cathode, anode, and y-cathode. The anode was made of 2.5 $\mu$m polyester foil, both sides of which were covered with a 40 $\mu$g/cm$^2$ gold. The cathode was a 2.5 $\mu$m thick polyester foil on which 50 gold stripes were deposited to 80 $\mu$g/cm$^2$ in thickness. The width of stripes was 1.6 mm with a 0.4 mm inter-stripe gap. All the contiguous stripes were connected each other with 510 $\Omega$ chip resistors. The detection of positions was accomplished by the charge division technique for the charges induced on the cathode strip by avalanche.

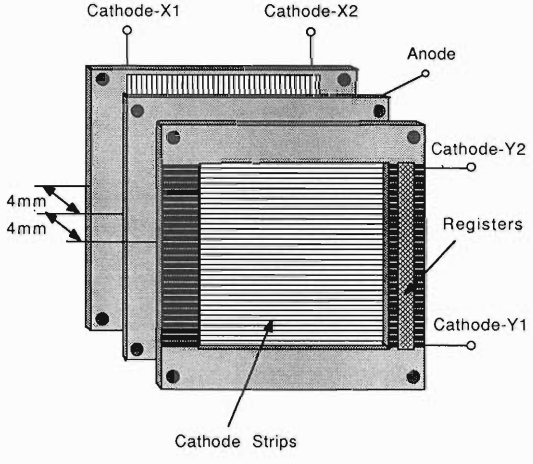


Fig. 1. The structure of electrodes.

The electrodes were placed in a small aluminum box ($184 \times 160 \times 48$ mm$^3$) in which isobutane of 6–10 Torr was filled as a counter gas. The entrance- and exit-windows were made of 4 $\mu$m polyester foil coated with 50 $\mu$g/cm$^2$ aluminum. The PPAC was operated with the anode bias of 600–800 V.

The signals from both ends of the resistor array of the cathode were amplified by a charge sensitive pre-amplifier and a shaping amplifier ($\tau$ = 2.5 $\mu$s) and were sent to CAMAC ADC's. The signals were analyzed by a PC9801 personal computer. One- and two-dimensional position spectra could be displayed on a monitor screen in real time mode. In the spectra, the peaks corresponding to the stripes were well separated. The position resolution obtained was 2 mm, although the FWHM of the peaks was much smaller than that. This resolution was enough for measuring the beam profile at F1 and F2. For the profile at F3, however, the resolution was not so good since the profile was deduced by the extrapolation from the position information of two PPAC's located at the upstream of F3.

The time signal was obtained from the anode signal by using a fast amplifier (rising time <1 ns, gain = 500) and a constant fraction discriminator. The time resolution of 0.46 ns (FWHM) was achieved for 41 MeV/nucleon $^{18}$O. The particle identification was accomplished with the timing information from the PPAC and the energy loss signals from the SSD ($50 \times 50 \times 0.3$ mm$^3$) which was placed just after the PPAC.

The PPAC's were installed in RIPS five years ago and since then they have been worked well. In order to improve the position resolution, new PPAC's ($100 \times 100$ mm$^2$ and $150 \times 100$ mm$^2$) are now under construction. The position resolution is expected to be less than 1 mm by using the cathodes with stripes of 1 mm width.

References

1) T. Kubo, M. Ishihara, N. Inabe, H. Kumagai, I. Tanihata, K. Yoshida, T. Nakamura, H. Okuno, S. Shimoura, and K. Asahi: *Nucl. Instrum. Methods Phys. Res.*, **B70**, 309 (1992).

# Polarized Xe Stopper for the Measurement of Magnetic Moment of Unstable Nuclei

H. Sato, Y. Hori, K. Mochinaga, M. Adachi, and K. Asahi

Polarized unstable nuclear beams produced by the projectile fragmentation reaction are very useful tools for the measurement of magnetic and quadrupole moments of unstable nuclei. Up to now, our group has succeeded in measuring magnetic and quadrupole moments of several neutron-rich nuclei produced at RIPS.[1,2] It is also true, however, that the above method of polarization based on the projectile fragmentation is not applicable to a certain class of nuclides. For example in the case of $^{11}$Be, the nucleus of considerable interest exhibiting the neutron halo and the anomalous spin and parity, no appreciable polarization was obtained in our previous experiments using the above method.

In this report we discuss a new method of obtaining polarized unstable nuclei, which comprises the implantation of fragment nuclei in a highly polarized stopper and the subsequent transfer of the host nuclear polarization to them through dipole-dipole interaction. Recently, it has been reported that a $^{129}$Xe solid whose nuclear spins are highly polarized can be produced and its spin relaxation time becomes very long in a certain condition (about 500 hours at 1 kG and 4.2 K).[3] We consider this material as a good candidate for the polarized stopper, which would provide a large spin polarization and a long relaxation time. We begin our study for obtaining the polarized Xe solid by polarizing gaseous Xe.

The $^{129}$Xe nuclear spin can be polarized by spin exchange with a polarized Rb atom. In this method, the Rb atomic spin is polarized by resonance absorption of a circularly polarized light of 795 nm wave length, and its polarization is transferred to the $^{129}$Xe nuclear spin during the formation of a Rb-Xe van der Waals molecule.[4] The $^{129}$Xe polarization $P_{Xe}$ depends on the Rb polarization $P_{Rb}$, the spin exchange rate $\gamma_{se}$ and the wall relaxation rate $\Gamma_w$. The time evolution of the $^{129}$Xe polarization is written as

$$P_{Xe} = P_{Rb}\{\gamma_{se}/(\gamma_{se} + \Gamma_w)\}[1 - \exp\{-(\gamma_{se} + \Gamma_w)t\}]$$

if we start the optical pumping at $t = 0$.

We started the experiment to polarize gaseous $^{129}$Xe nuclei. A natural Xe gas (26.4% $^{129}$Xe) of 610 Torr was contained in a cylindrical glass cell (2.2 cm in diameter, 4 cm or 8 cm long) together with an $N_2$ gas of 50 Torr and a small amount of Rb. The glass cell was illuminated by a circularly polarized light generated by a 2 W Ti:sapphire laser. The $^{129}$Xe polarization thus obtained through the optical pumping was determined experimentally by measuring its magnetization with an adiabatic fast passage NMR method (Fig. 1).

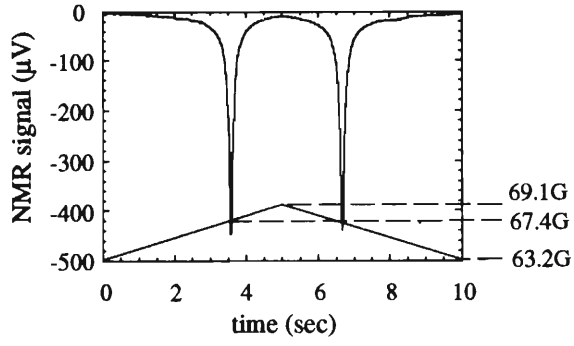


Fig. 1. Typical adiabatic fast passage NMR signal of polarized $^{129}$Xe gas. The signal shown by the curve represents the transverse polarization which appears when the resonance condition is met. In this case, the signal height corresponds to $P_{Xe} = 3.5\%$. As indicated at the bottom by the solid line, the magnetic field is swept through the resonance condition twice.

We made several glass cells and measured the $^{129}$Xe polarization. Up to now, a polarization of 3.5% has been reached. We also measured the spin relaxation rate and the Rb polarization. As a result, we found that the relatively small value of $P_{Xe}$ was due to a small Rb polarization, which may stem from a loss of the laser power due to reflection on the surface of the glass cell or from Rb oxidation due to possible impurities in Xe gas. We are improving the system in order to get higher $^{129}$Xe polarization. We also plan to construct an apparatus for producing a polarized Xe solid for the measurement of the magnetic moment of $^{11}$Be.

References

1) H. Okuno et al.: *Hyperfine Interact.*, **78**, 97 (1993).
2) H. Ueno et al.: *ibid.*, **84**, 371 (1994).
3) M. Gatzke et al.: *Phys. Rev. Lett.*, **70**, 690 (1993).
4) G. D. Cates et al.: *Phys. Rev.*, **A45**, 4631 (1992).

# A Recoil-Ion Momentum Spectrometer for Atomic Physics Experiments

O. Jagutzki, T. Kambara, Y. Nakai, Y. Awaya, and H. Schmidt-Böcking

In order to investigate many-particle reaction dynamics in atomic collisions a novel high-resolution technique has been developed, which determines the momentum and the charge state of the slowly recoiling target ions. Using a very cold and localized supersonic gas jet target a momentum resolution of better than 0.1 atomic unit (a.u.) is obtained by measuring the recoil-ion time-of-flight and the recoil-ion trajectory. Due to a detection efficiency of nearly $4\pi$ this technique is well suited for many-particle coincidence measurements and enables various highly differential experiments in atomic physics.

Such a Recoil-Ion Momentum Spectrometer was installed and tested at RILAC in collaboration with the Institute for Nuclear Physics of the University Frankfurt. Target gas (He, Ne, Ar, ...) is precooled to a temperature of 30 K (for He) at a pressure between 200 and 1000 hPa by a standard cryo-generator. The precooled gas expands through a 30 $\mu m\phi$ nozzle forming a supersonic gas jet. Special care has to be taken to meet the criteria for the supersonic expansion. Due to the properties of the supersonic expansion, the target gas is cooled to an internal temperature of about 0.1 K. This corresponds to a Maxwellian momentum spread for helium atoms of less than 0.1 a.u. in any direction, thus enabling spectroscopy of a helium ion recoil momentum with such precision. The center part of the gas jet passes after 6 mm through a 0.5 mm skimmer hole into the target chamber and is thus collimated to a narrow beam. The ionizing projectile beam (e.g. from RILAC) intersects the gas jet defining a target region limited by the size of the spatial overlap between gas jet and projectile beam.

This target is located in the extraction region of the spectrometer (see Fig. 1). The spectrometer consists of this extraction region, a field free drift zone and a two-dimensional position sensitive multi-channel-plate detector with a wedge-and-strip anode (PSCD). Recoiling ions produced in collisions of the projectiles with the gas jet atoms are extracted by a well-defined weak electrical field (typical of 1 V/cm). Then the ions pass a field free drift region and are detected on the PSCD. Special care has to be taken to ensure proper field conditions in the spectrometer. The extraction region is shielded by wires defining potential lines to guarantee a homogeneous field. All surfaces are coated with carbon to avoid contact potentials.

From the trajectory and flight time of an ion it is possible to determine the transferred recoil momentum in the collision by applying simple equations. The

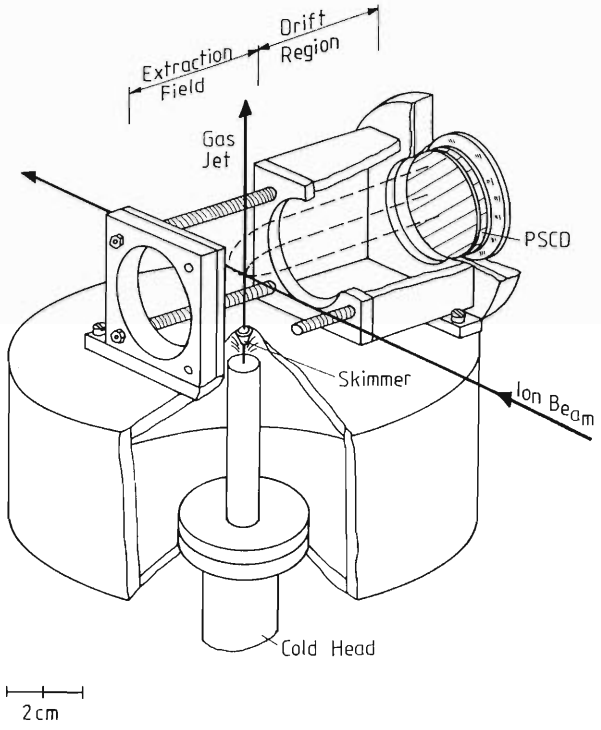


Fig. 1. Sketch of the recoil-ion momentum spectrometer.

trigger for the time-of-flight measurement can be the detection of the outgoing projectile or the use of a pulsed beam. The electrical field can be selected so that different charge states can be separated, and that the recoil determination with $4\pi$ is unambiguous for all three dimensions. The finite size of the target restricts the attainable momentum resolution. However, it is possible to reach for all three dimensions the maximum precision limited by the Maxwellian momentum spread due to the finite internal gas jet temperature. Transverse to the jet axis, the resolution can be even better.

At RIKEN and several other atomic physics facilities a variety of different experiments are currently in progress to exploit the unique opportunities offered by this novel high precision spectroscopy method.[1-3]

References

1) V. Mergel et al.: accepted for publication in *Phys. Rev. Lett.*
2) J. Ullrich et al.: accepted for publication in Comments in *At. Mol. Phys.*
3) T. Kambara et al.: This report, p. 75.

# Attenuation Length of Scintillation Photons in Liquid Rare Gases and their Mixtures

K. Masuda, N. Ishida, T. Doke, H. Okada, T. Komiyama, K. Hasuike, M. Shinoda, M. Sato, K. Terasawa, T. Kato, M. Suzuki, and M. Kase

Liquid xenon (LXe) is very suitable for radiation detectors of gamma-rays and energetic particles because of its large density and high atomic number. LXe can be operated not only as ionization detectors but also as scintillators. It has a large light yield ($6.8 \times 10^4$ photons/MeV) and fast decay time (3–20 ns).[1] Therefore it will be possibly used in nuclear and particle physics in near future. The critical factors for detection of LXe scintillation photons are the reflection of the scintillation light (174 nm) on detector walls and the attenuation length of the light in the liquid.

In order to investigate the above factors separately, we have developed an almost complete anti-reflector, which has a zigzag shaped surface so that the incident light does not go out from the surface due to multiple reflection.[2] An 80 cm long scintillation detector was used and the reflector was installed in the chamber. To measure the attenuation length, heavy ions from the RIKEN Ring Cyclotron were entered at different positions in the chamber. The scintillation photons produced in the liquid were detected by a photomultiplier after the wavelength in a VUV region was shifted to visible with sodium salicylate coated on a Pyrex window. Ions of $^{12}C$ and $^{14}N$ with the energy of 135 MeV/nucleon and $^{15}N$ with the energy of 115 MeV/nucleon were used. Ranges of ion tracks in the liquids are estimated to be 20 mm to 40 mm, depending on the combination of incident ion and liquid. Details of the apparatus including a gas purification system are described in a previous report.[3]

Previously[3] the attenuation length of scintillation photons in LXe was reported to be about 30 cm which is rather short compared with the value we expected. Therefore we have measured the attenuation lengths in other rare gas liquids and their mixtures to understand the result for LXe.

The light yields obtained experimentally were normalized to the solid angle for photon detection and plotted in Fig. 1 as a function of the distance between the heavy ion beam and the Pyrex window. From the position dependence of the relative light intensity, the attenuation lengths were calculated. The values are 68 cm in liquid argon (LAr), 84 cm in liquid krypton (LKr), 30 cm in LXe, 200 cm in LAr + Xe (3%) and 130 cm in LKr + Xe (3%). These results are summarized in Table 1. The table shows a matrix of the host liquids and the wavelengths of the scintillation.

The wavelengths of the scintillation are 128 nm, 147 nm and 174 nm in LAr, LKr and LXe, respectively. In Ar-Xe mixture or Kr-Xe mixture with enough concentration of Xe, the wavelength of the scintillation is converted to 174 nm from Xe excimers through the energy transfer from Ar or Kr molecules to Xe.

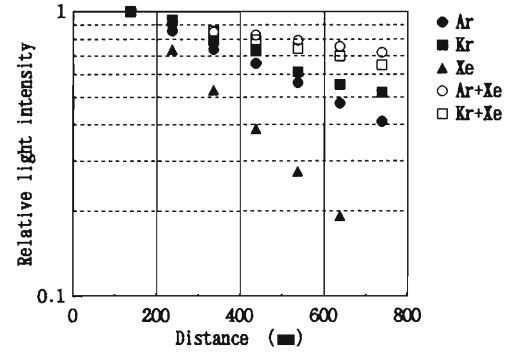


Fig. 1. The measured light intensity divided by the solid angle versus the distance between the ion track and the Pyrex window. The relative light intensity is normalized to unity at the distance of 137 mm.

Table 1. The attenuation lengths in cm of the scintillation photons.

| Liquid | Wavelength | | |
|---|---|---|---|
| | 128 nm | 147 nm | 174 nm |
| Argon | 68 | — | 200 |
| Krypton | — | 84 | 137 |
| Xenon | — | — | 30 |

Comparing the results for different wavelengths in the same host liquid, which means the same molecular structure and the same temperature, one can see that the scintillation light with the longer wavelength has the longer attenuation length both in LAr and LKr. One of possible explanations for this tendency may be the Rayleigh scattering of photons with liquid atoms. The scattering cross section has the wavelength dependence as the inverse forth power under an approximation, and the relation of the attenuation lengths experimentally obtained for different wavelengths is consistent with the scattering. If the present light attenuation is due to the scattering, one can collect most of photons including scattered photons by using reflectors on the detector wall or by doping the liquid with wavelength shifters. So, further study to measure the light collection with reflection mirrors will be done.

References

1) T. Doke: *Portugal Phys.*, **12**, 9 (1981).
2) N. Ishida et al.: submitted to *Nucl. Instrum. Methods.*
3) K. Masuda et al.: *RIKEN Accel. Prog. Rep.*, **27**, 116 (1993).

# A Blow-in Type Windowless Gas Target

K. Sagara, A. Motoshima,* H. Akiyoshi,* N. Nishimori, and K. Maeda

A new-type windowless gas target has been designed to produce a fairly thick target having a low gas-consumption rate. As shown in Fig. 1, the gas is blown into a target cell from both the upstream and downstream ends of the cell (cylindrical sections of 6 mm in diameter) through inclined narrow gaps. The gas back-flowing out of the cylindrical sections is pumped out by two mechanical booster pumps (MBP1-2) and by three turbo-molecular pumps (TMP1-3).

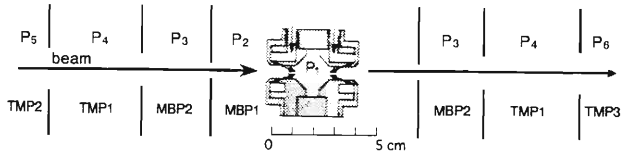


Fig. 1. A blow-in type windowless gas target. The back-flowing gas is evacuated by two mechanical booster pumps (MBP) and three turbo-molecular pumps (TMP). A blow-out gas target is realized by injecting the gas through the side wall at target center.

In the differentially-pumped windowless gas targets[1] so far developed, the gas is blown out from the center of the target cell. The present blow-in gas target (BIGT) is superior to the previous blow-out gas target (BOGT) in confining the gas. Figure 2 shows that the gas ($N_2$) pressure at the target center, p1 (see Fig. 1), of BIGT is about twice higher than p1 of BOGT when the pressure p2 (see Fig. 1) is the same. This means that the target thickness of BIGT is about twice thicker than that of BOGT for the same gas flow rate, if the gas distribution is the same in the both cases. The gas pressure along the beam axis was measured using the elastic scattering of protons at 90°. Figure 3 shows clearly that BIGT has a desirable flat-top distribution whereas BOGT has a gradually-dumping distribution.

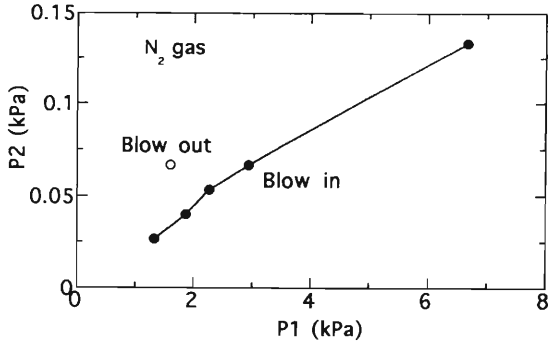


Fig. 2. Gas pressure p1 at the target center versus the pressure p2 at the first pumping section (see Fig. 1).

The present pumping speeds of MBP1 and MBP2 are 330 and 600 $m^3$/hr, respectively, and that of each TMP is 520 l/s. For $N_2$ gas, the maximum of the pressure p1 is now limited to 1.6 kPa by the pumping speed of TMP1. To increase p1 for $N_2$ ($^4$He) up to 4 (2) kPa, some of the pumps need to be replaced by more powerful ones. The effective target length is about 3 cm at present (see Fig. 3). It is easy to increase the length up to, for example, 10 cm. The $N_2$-gas thickness of 4 kPa × 10 cm corresponds to 0.5 mg/$cm^2$.

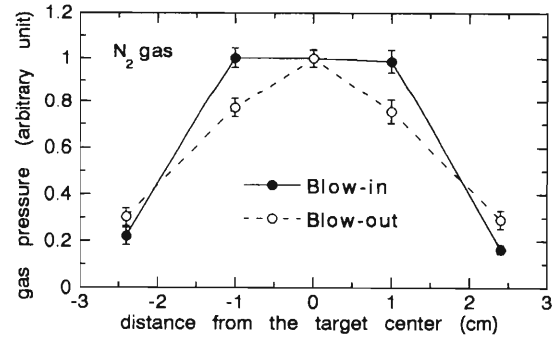


Fig. 3. Target gas pressure along the beam axis.

From the present data, the gas-flow for BIGT of 4-kPa $N_2$ is estimated to be about 0.8 $m^3$/hr, which is considerably less than the flow of 25 $m^3$/hr necessary for a $N_2$-gas jet target of 0.5 mg/$cm^2$ in thickness.[2]

BIGT will be useful for low-energy experiments such as in astro-nuclear physics, and for secondary-beam production with very high-intensity primary beams. It also has a possibility to be used as a charge stripper for intense heavy-ion beams.

References

1) J. Bussiere and J. M. Robson: *Nucl. Instrum. Methods*, **91**, 103 (1971).
2) G. Bittner et al.: *ibid.*, **161**, 1 (1979).

* Department of Physics, Kyushu University

# Observation Program of Cosmic Ray Ions with the First Brazillian Scientific Satellite

T. Kohno, T. Imai, H. Kato, I. Yamagiwa, and K. Nagata

The first Brazillian scientific satellite is planned to be launched on October 1996. We plan to promote a joint experiment for cosmic ray observation in collaboration with University of Campinas (UNICAMP) and National Institute of Space Research (INPE: Instituto Nacional de Pesquisas Espaciais). The planned orbit is a sun synchronous circular orbit with 800 km altitude and 99° inclination. This is a piggyback satellite of a main remote sensing satellite. The total payload is only 10 kg, and three or four instruments will be accepted to be onboard. Because of the very severe condition of weight, we concentrate our purpose on the observation of elemental composition of anomalous cosmic ray (ACR) where C - Ne will play an important role.

It is already confirmed that the ACRs are singly ionized whereas the galactic cosmic rays (GCRs) are fully stripped nuclei. Therefore the magnetic rigidity of ACR in the geomagnetic field is much greater than that of GCR in the same energy range. That means ACRs can be observed at a low latitude where GCRs cannot come from the outer space. This is a great merit for a near earth orbiting satellite such as this case.

From our former experience,[1] we know that elemental separation for medium nuclei (C,N,O,Ne) is possible even if we do not use position sensitive detectors if we limit the acceptance angle ($\theta$ in Fig. 1) within some limited value. We can save the electronic circuit weight by omitting PSDs (reducing the number of signals). Shown in Fig. 1 is a cross sectional view of the telescope. As shown here, we adopt a bidirectional entrance structure so that we can double the geometric factor by adding only one more $\Delta E$ detector. This method is usually very difficult to use because we have to clear the field of view for two opposite directions. But it is rather not so difficult in case of the satellite of a very small size, one side of the satellite being not too larger than the size of the telescope itself.

If we take the value of $\theta$ to be very small, the particle identification umbiguity due to pathlength distribution in the penetrating detector can be very small, that means good resolution. But we can get only a very small geometric factor, that means very small collecting power which leads to poor satistics. And if we take large $\theta$, the resolution becomes bad vice versa. In order to obtain the optimum value of $\theta$, we carried out numerical simulations assuming isotropic entrance and cosmic ray abundance of elements. We show one of the results of this simulation in Fig. 2. We decided $\theta$ to be 25° from these results of simulation. The geometric factor for this design is $\sim 3\ \mathrm{cm}^2 \cdot \mathrm{sr}$.

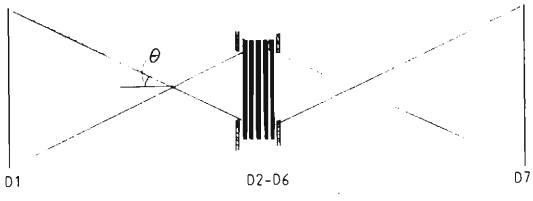


Fig. 1. Cross sectional view of the telescope. Particles coming in from both sides can be observed.

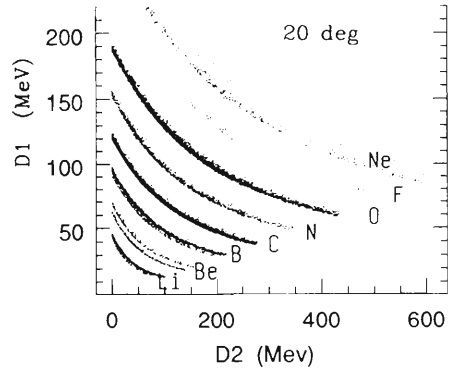


Fig. 2. One of the results of numerical simulation for the particle separation ability of the telescope. Only particles heavier than helium are originated. This is a scatter plot of energy losses in D1 vs. D2 for the events stopped in D2 for the case of $\theta = 20°$. We can see that the elemental separation up to Ne is clearly possible.

The telescope consists of two thin $\Delta E$ detectors located at the front of both sides and five $E$-detectors located at the midst of them (Fig. 1). The $\Delta E$ detector has an effective area of 48 mm × 48 mm and a thickness of 0.25 mm. The $E$-detector has a size of 28 mm × 28 mm and a thickness of 1 mm. The observable energy by this assembly is 14-54 MeV/nucleon for O for example. The total weight will be ~3 kg together with the telescope and electronics. We need to carry out nuclear calibration of the whole instrument by using heavy ion beams from RRC before launch.

References

1) T. Kohno et al.: *J. Phys. Soc. Jpn.*, **60**, 3967 (1991).

# Collinear Resonance Ionization Spectrometer with Diode and UV Lasers

M. Kubota,* H. Katsuragawa, T. Minowa,* and H. K. Uematsu**

In a past decade we have been developing a highly sensitive detection method and efficient atomizers for metal elements in resonance ionization spectroscopy.[1,2] As a next step we are constructing a collinear resonance ionization spectrometer with a diode laser and a UV laser.

The experimental setup is shown in Fig. 1. A collinear beam arrangement is employed because this arrangement is capable of doppler tuning. A Li ion beam supplied with a surface ion source is neutralized in a charge exchange cell. The first step excitation of the resulting Li atomic beam is carried out with a 670.8 nm diode laser which corresponds to the $^2S$–$^2P$ transition of Li. The second step excitation of Li atoms to ionization continuum is achieved with a $N_2$ laser radiation (377.1 nm). In this manner Li atoms are ionized again and a resonance ionization spectrum of Li can be observed by high-resolution diode lasers.

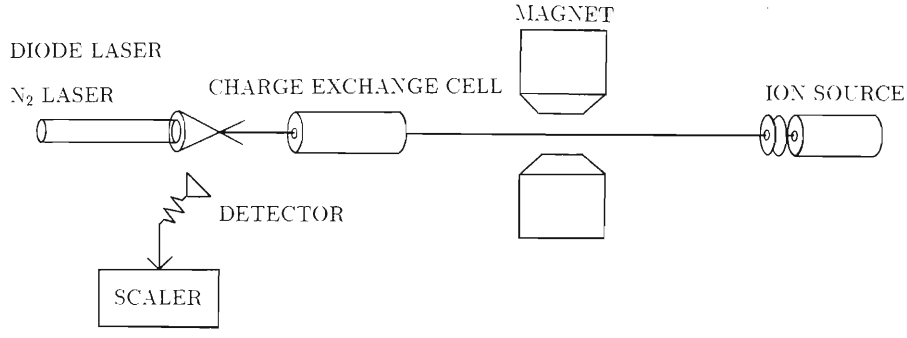


Fig. 1. Schematic diagram of collinear resonance ionization spectrometer.

Now the surface-ionization ion source is running and the maximum ion current of 200 nA has been attained for Ba. For Li the maximum ion current is estimated to be a few nA. Neutralization of a Ba ion beam in the charge exchange cell has been successfully performed.

References

1) T. Minowa et al.: *Rev. Sci. Instrum.*, **60**, 3280 (1989).
2) H. Katsuragawa et al.: *ibid.*, **64**, 265 (1993).

* Faculty of Science, Toho University
** Tokyo Gakugei University

# Design of Tritium Gas Handling System for Muon Catalyzed Fusion Experiment at RIKEN-RAL Muon Facility

T. Matsuzaki, K. Ishida, I. Watanabe, K. Nagamine, M. Kato,* K. Kurosawa,*
M. Hashimoto,* M. Tanase,* and H. Kudo**

For the muon catalyzed fusion ($\mu$CF) experiment at RIKEN Muon Facility of Rutherford Appleton Laboratory in U.K., a high purity D-T gas target, free from $^3$He component, is in preparation in order to perform precise measurements of $\alpha$-sticking probability in a $\mu$CF cycle. The $^3$He is a daughter nucleus of tritium (T) and does terminate the $\mu$CF cycle because a negative muon is captured by a doubly electrically charged $^3$He nucleus. For this $\mu$CF experiment, a tritium gas handling system has been designed and is now under construction.

The proposed flow diagram and the inner layout of the equipment are shown in Figs. 1 and 2. The gas handling system is constructed in a glove box and contains the following equipments; a tritium gas cylinder, a duterium gas cylinder, uranium getters, a palladium

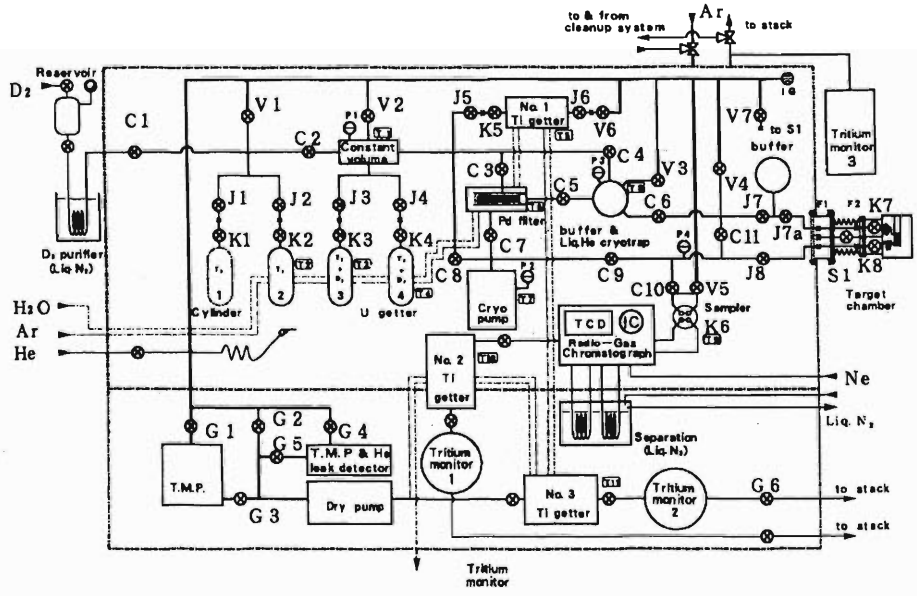


Fig. 1. Proposed flow diagram of the tritium gas handling system.

filter, a cryo-trap, a cryopump, titanium getters, a radio-gas chromatograph, a buffer tank of a constant volume, buffer tanks, in-line tritium monitors, a glove box tritium monitor, a turbo molecular pump, a dry pump, a helium leak detector, and their control system. A tritium clean-up system employing ZrFe getters to circulate the glove box inner gas (Ar), which is not shown in the figure, is connected to the glove box for possible leakage of tritium gas.

The target gas purification is performed by utilizing a uranium getter, a cryopump, a palladium filter and a cryo-trap. The radio-gas chromatograph includes an ion chamber to make hydrogen isotope analysis.

The gas handling system is installed in RIKEN Muon Facility and is directly connected to the $\mu$CF target chamber, where gas purification to remove $^3$He component and formation of the D-T gas mixtures are conducted at the experiment site.

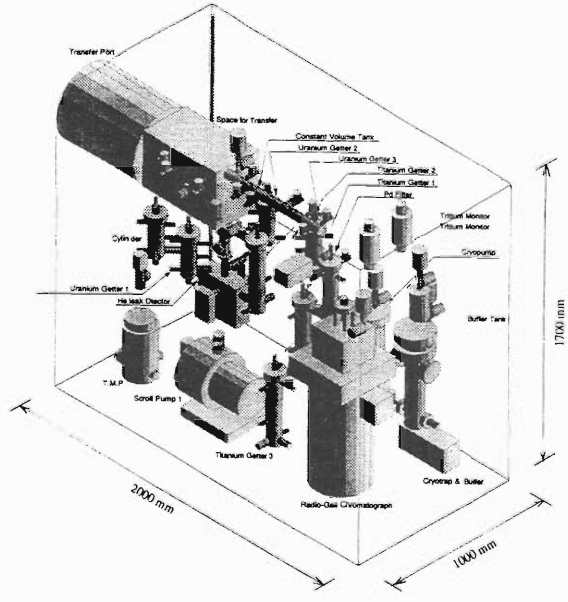


Fig. 2. Proposed layout of the equipment in glove box.

* Department of Radioisotopes, Japan Atomic Energy Research Institute
** Department of Chemistry, Tohoku University

# Production Tests of Radioisotope Beam by SLOW Beam Channel

T. Matsuzaki, R. Kadono, K. Ishida, A. Matsushita, and K. Nagamine

A low-energy radioisotope beam channel "SLOW" has been developed at RIKEN Ring Cyclotron. The main goal of this beam line was not only for the study of emission mechanisms of various low-energy ions from a characterized metal surface of the primary target, but also for the generation of radioactive ion beams for surface-physics studies of the secondary target. The detailed design, construction and performance are described in Ref. 1.

After the various improvements of the beam line,[2] the test experiments were performed to produce radioactive ions from a tungsten metal surface by the nuclear reactions using argon and nitrogen beams from RRC.

For the primary target, two types of tungsten foil were used; a foil with a thickness of 50 $\mu$m and a multi-folded foil with an effective thickness of 500 $\mu$m (25 $\mu m \times 20$). The targets were directly heated up to 2000 K by introducing a DC current and were irradiated by $^{40}$Ar beam (95 MeV/A) and $^{14}$N beam (135 MeV/A) to observe the produced ions by nuclear reactions. The vacuum at the targets was $10^{-7}$ to $10^{-8}$ torr during the beam irradiation. In the experiment, hydrogen and oxygen gases were introduced to the target in order to change the surface condition and then the produced ion yields were measured.

In the obtained spectra, alkaline ions naturally existing at the target surface were clearly observed but any significant signals of the ions associated with nuclear reactions by the beam irradiation were not observed.

In the transmitting type target employed in this experiment, the nuclei which are originally produced by the target fragmentation mechanism in thin target materials were expected to be thermally diffused to the surface to make surface ionization. The possibility of this process was proved to be very small in the experiments. Another experiment using fully or partially beam stopping type targets should be conducted to investigate the possibility of this process.

The production yield which is known experimentally was found out to be much smaller compared with the E7 room background, even after the installation of a radiation shield around the detection point. The room background was proved to be dominated by the components from the switching magnet and the beam dump in E7. The best way to solve the problem is considered to extend the SLOW beam line in order to transport the produced ions to a low background area to determine the yields precisely. The detector should be also modified to minimize the effective volume to improve the S/N ratio.

From the technical point of view to produce radioactive beams more effectively, a major modification might be required for the SLOW beam channel; the production part of radioactive nuclei and their ionization part should be separated like ISOLDE at CERN where the ionization part is expected to contain various types of ionization device.

After some relevant modifications of the SLOW beam channel, this experimental program will be restarted.

References

1) T. Matsuzaki et al.: *Nucl. Instrum. Methods Phys. Rev.*, **B70**, 101 (1992).
2) T. Matsuzaki et al.: *RIKEN Accel. Prog. Rep.*, **27**, 112 (1993).

# Construction of a Heat-Pipe Oven System for Laser Spectroscopy of Radioactive Isotopes

H. Maeda and F. Ambe

The heat-pipe oven was originally developed by Vidal and Cooper[1] for the purpose of confining metal vapors in an optical cell to perform a variety of spectroscopic measurements on metal atoms. The significant feature of this device is that a homogeneous vapor of well-defined temperature, pressure, and optical path length can be generated and confined in a cell for a considerably long period of time without losing any transparency of optical windows. Since temperature, pressure, and optical path length of the confined vapor can be controlled easily and measured accurately, the heat-pipe oven is available for quantitative spectroscopic measurements of atoms. Also, to use this device is advantageous for the detection and measurements of an extremely small amount of atoms. This is because, firstly, atoms are confined inside of the cell and, secondly, the thermionic diode, an extremely sensitive detector for ionized atoms, is optimally applicable.[2,3] It should be noted that the heat-pipe oven in conjunction with the thermionic-diode detector has also been a well established tool for high-resolution Doppler-free spectroscopy of alkali-metal and alkaline-earth-metal atoms.[4]

Recently, we have constructed a heat-pipe oven system to investigate radioactive isotopes, radioactive decays, nuclear reactions, etc., by the methods of laser spectroscopy. There are many important experiments that will be possible if adequate numbers of radioactive atoms of interest are confined in an optical cell for a sufficiently long time. One example is the laser spectroscopy of nuclear decay fragments.[5] Employing the heat-pipe oven in such experiments is very promising due to the several characteristic features described above.

Figure 1 shows the schematic diagram of our experimental setup. Briefly, it is composed of two pulsed Ti:$Al_2O_3$ lasers pumped by the second harmonic of a Q-switched Nd:YAG laser with a maximum output power of 200 mJ per pulse at 532 nm and repetition rate of 10 Hz, a heat-pipe oven, and a data-acquisition system which consists mainly of an amplifier, a gated integrator, and a personal computer. The Ti:$Al_2O_3$ laser has a tuning range from 690 to 950 nm with a maximum power of about 20 mJ per pulse and a linewidth of less than 0.1 $cm^{-1}$. A design of the heat-pipe oven is basically similar to that described in Ref. 1. It is equipped with a 3.5-cm-inside-diameter, 90-cm-long stainless-steel tube which has a 5-cm-long glass portion in the middle and optical windows at both ends. The tube is connected to a vacuum system so that it is evacuated up to $10^{-6}$ Torr and filled with $10^{-2}$–10 Torr of He buffer gas. This buffer gas and water coolings at both ends of the tube play a role to prevent the deposition of metal on the windows. The tube is heated electrically up to about 650 K. For measuring and detecting spectral lines of atoms we employ a photomultiplier as well as a thermionic diode ion detector. In particular, to activate the thermionic diode detector a 0.5-mm-diameter tungsten wire is inserted along the center of the tube and negatively biased (a few V) through a 100-kΩ load resistor. In this manner the pipe acts as a diode with a tungsten wire being the cathode and the wall of the pipe being the anode. Then changes in the diode current due to ion formation is detected as voltage changes through a 0.01-μF capacitor.

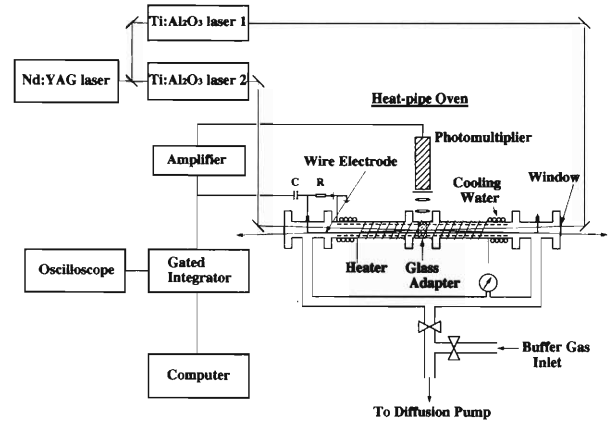


Fig. 1. A schematic diagram of the experimental setup.

As a preliminary experiment we have successfully observed the multiphoton ionization spectrum of stable $^{133}Cs$ atoms. Application of the setup to investigate the radioactive atoms is now under progress.

References

1) C. R. Vidal and J. Cooper: *J. Appl. Phys.*, **40**, 3370 (1969).
2) K. C. Harvey: *Rev. Sci. Instrum.*, **52**, 204 (1981).
3) D. C. Thompson and B. P. Stoicheff: *ibid.*, **53**, 822 (1982).
4) See, for example, K. Niemax: *Acta Phys. Pol. A*, **61**, 517 (1982).
5) See, for example, V. S. Letokhov: Laser Photoionization Spectroscopy, Academic Press, Orlando, p. 106 (1988).

# 6. Material Analysis

# *In situ* Analysis of Liquid Samples by Vertical Beam PIXE

J. Kawai and K. Maeda

Particle-induced X-ray emission (PIXE) spectrometry has an advantage that it is sensitive to heavy metals in a light element matrix such as liquid or biological samples. Liquid samples are one of the good targets of PIXE, and the beam should be vertical and the measurement should be carried out under a non-vacuum condition.

We have constructed a vertical beam line at RILAC for measuring PIXE of liquid samples. The horizontal ion beam was bent by a magnet, and came out in air through aluminum exit foil (6 $\mu$m) as shown in Fig. 1. The details of the exit foil have been described earlier.[1] The aluminum foil was insulated from ground level of the beam line to measure the current of ion beam going through the foil. The detector used was an Si(Li) solid state detector. The ion beam current measured by a Faraday cup was 10–100 nA/cm$^2$ for 8 MeV $He^+$ in vacuum. The ion energy at the surface of liquid after traveling in aluminum foil and air was estimated to be 20% lower than that of in vacuum. The integral beam current was monitored by currents induced in the aluminum foil and in the sample.

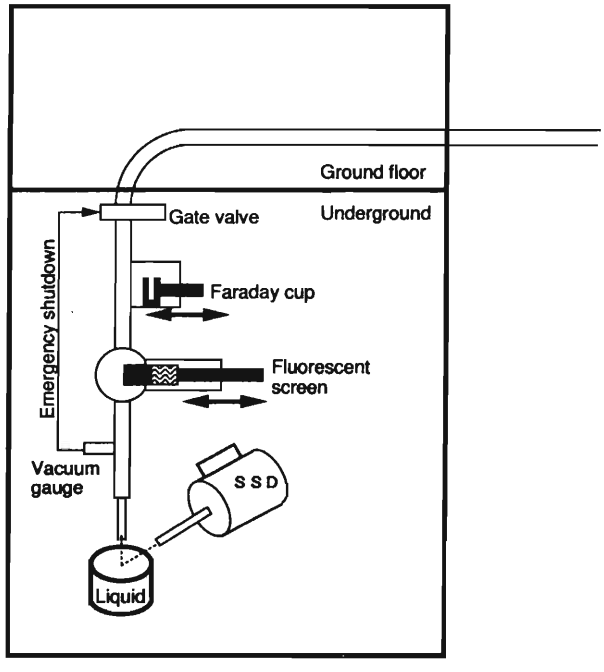


Fig. 1. Schematic illustration of the experimental setup.

The samples measured were, (1) aqueous solutions of various concentrations of $Cu^{2+}$, $Sr^{2+}$, $Ca^{2+}$, and $Cr^{3+}$ (30–10000 ppm) with $NO_3^-$, (2) milk, and (3) "Du Zhong" tea (Tochuu-cha). The samples (2) and (3) were expected to have a high $Ca^{2+}$ concentration. Recently in Japan, "Du Zhong" tea is one of the healthy beverages. Representative measured spectra of samples (2) and (3) are shown in Fig. 2. The concentrations determined from the calibration curve made by the aqueous solutions of various concentrations of $Cu^{2+}$, $Sr^{2+}$, $Ca^{2+}$, and $Cr^{3+}$ ions were $Ca^{2+}$ 1100 ppm (nominal, 1000 ppm), $K^+$ 890 ppm, and $Cl^-$ 250 ppm for milk, and $Ca^{2+}$ 70 ppm for Du Zhong tea.

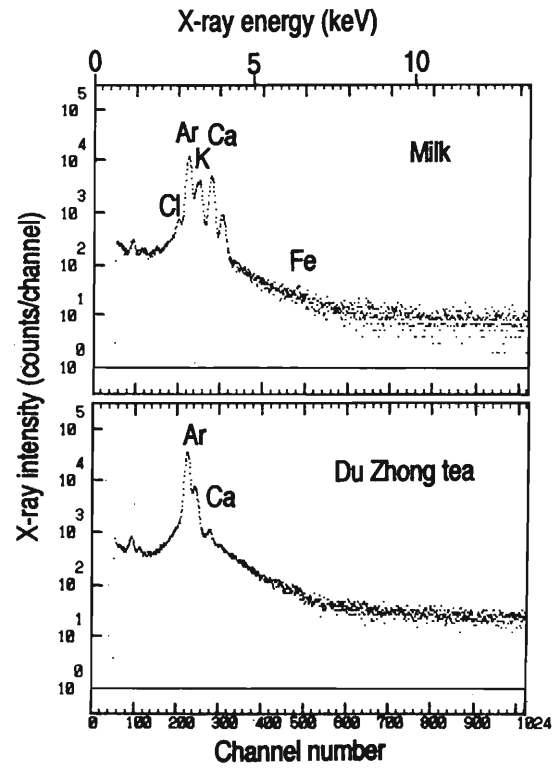


Fig. 2. Representative PIXE spectra of milk and "Du Zhong" tea.

References

1) Y. Sasa, K. Maeda, and M. Uda: *RIKEN Accel. Prog. Rep.*, **24**, 127 (1990).

# X-ray Satellite Caused by Radiative Auger Effect

K. Maeda and J. Kawai

In highly-sensitive element analysis by X-ray spectrometry, satellite X-rays often obstruct the detection of trace elements. We have reported low-energy satellites accompanying the main Kα line in X-ray spectra excited by He-ion (8 MeV) impact.[1] In this report, measurements of the same satellites excited by an X-ray tube are reported.

Samples were high purity metallic Ti, V, Fe, Cu, and Zr, and powders of $CaF_2$, $TiO_2$, and RbF. X-ray spectra were measured with a conventional X-ray fluorescence (XRF) spectrometer of Bragg type [Rh anode tube (30 kV and 10–40 mA) and Ge(111) or LiF(200) analyzing crystal].

Representative XRF spectra are shown in Fig. 1 along with the spectrum obtained by the He-ion impact. A weak broad peak was observed in the energy region corresponding to K-LL Auger transitions in all these spectra. The energies and intensities of the peak relative to the Kα line measured by the three different procedures were almost the same. From the peak energy, intensity and spectral shape, these peaks were attributed to the K-LL RAE (radiative Auger effect) satellites.

The K-LL RAE satellite was found in all spectra measured here. The intensities of the RAE satellites are summarized in Table 1 with the reproducibility (standard deviation) of the measurements. The data obtained by the He-ion impact is also given in the table. The integrated intensity was estimated after subtracting the background and correcting the matrix effects and detection efficiency. The range of integration was fixed to be twice of the energy separation between the highest ($^3P_2$ K-$L_3L_3$) and lowest ($^1S_0$ K-$L_1L_1$) Auger energies. The K-LL RAE/Kα intensity ratio was between 0.05–0.2% for elements of atomic number Z = 20–40. This means that neglect of the K-LL RAE satellites will introduce a serious error in trace analysis. There was no significant difference in the intensity ratio due to the differences of chemical species and excitation methods.

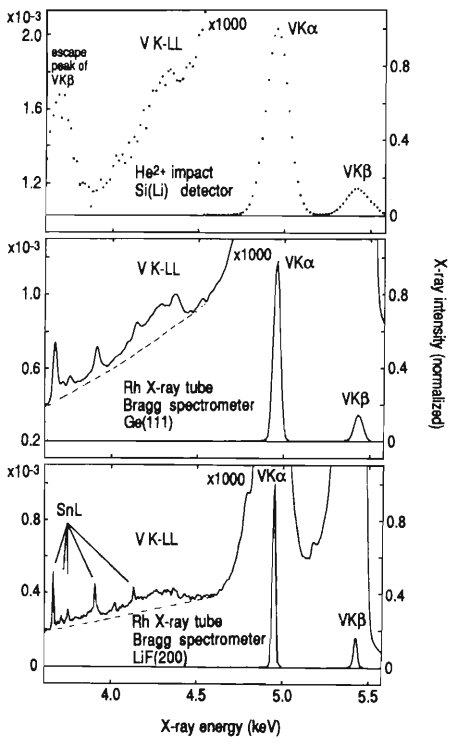


Fig. 1. X-ray spectra in the low-energy region of V Kα obtained from vanadium metal. L X-rays of Sn were considered to be emitted from the sample holder.

Table 1. Relative intensity of the K-LL RAE satellite to that of the $K\alpha_{1,2}$ line.

| Z | Element | Sample | Excitation source | X-ray spectrometer | Integrated intensity (%) |
|---|---|---|---|---|---|
| 20 | Ca | $CaF_2$ | Rh X-rays | Ge crystal[a]-PC[b] | 0.09±0.01 |
| | | | He ions | Si(Li) SSD | 0.17±0.03 |
| 22 | Ti | Ti | Rh X-rays | Ge crystal-PC | 0.20±0.05 |
| | | $TiO_2$ | Rh X-rays | Ge crystal-PC | 0.17±0.03 |
| | | Ti | Rh X-rays | LiF crystal[c]-PC | 0.22±0.02 |
| | | $TiO_2$ | Rh X-rays | LiF crystal-PC | 0.19±0.02 |
| 23 | V | V | Rh X-rays | Ge crystal-PC | 0.19±0.03 |
| | | | Rh X-rays | LiF crystal-PC | 0.23±0.03 |
| | | | He ions | Si(Li) SSD | 0.20±0.04 |
| 24 | Cr | Cr | He ions | Si(Li) SSD | 0.12±0.02 |
| 25 | Mn | Mn | He ions | Si(Li) SSD | 0.08±0.02 |
| 26 | Fe | Fe | Rh X-rays | LiF crystal-PC | 0.05±0.01 |
| | | | He ions | Si(Li) SSD | 0.07±0.01 |
| 29 | Cu | Cu | Rh X-rays | LiF crystal-PC | 0.20±0.01 |
| 37 | Rb | RbF | Rh X-rays | LiF crystal-PC | 0.05±0.01 |
| 40 | Zr | Zr | Rh X-rays | LiF crystal-PC | 0.05±0.01 |

[a] Bragg spectrometer with a flat Ge(111) analyzing crystal.
[b] proportional counter.
[c] Bragg spectrometer with a flat LiF(200) analyzing crystal.

## References

1) K. Maeda and J. Kawai: *RIKEN Accel. Prog. Rep.*, **26**, 130 (1992).

# Analysis of Trace Elements in Fish Otoliths by In-Air PIXE

N. Arai,* W. Sakamoto,* and K. Maeda

Fish otoliths in the inner ear detect or control the acceleration and position of the fish and are composed of a calcium carbonate-protein or calcium-phosphate-protein matrix as a needle aragonite crystal. Trace elements in the otoliths were known to be a good indicator of ambient environment. Many studies have been therefore carried out using SEM-EDX or SEM-WDX. Gunn et al.[1] reviewed these analytical techniques and reported that EDX systems were not suitable for quantitative analysis of trace elements (<5000 ppm) in otoliths and WDX systems were able to measure elements such as Ca, Na, Sr, K, S, and Cl to levels of several hundreds ppm, but the analyses damaged specimens and caused pitting and chemical change. We adopted in-air PIXE (Particle Induced X-ray Emission) in trace elements analysis of otoliths from several species of teleost fish.

Otoliths were removed from juvenile red sea bream, *Pagrus major*, and rockfish, *Sebastes schlegeli*. The red sea breams were reared in three different sea-farming stations, Momoshima (MS) and Hakatajima (HT) in the Seto Inland Sea and Miyazu (MZ) in the Sea of Japan. Two different origins of rockfish were examined; one was reared in Miyako sea-farming station and the other was caught in Miyako Bay in Iwate Prefecture. Otoliths surfaces were not cut nor polished and bombarded in air by a 1.6 MeV proton beam generated in the Tandetron accelerator of RIKEN. Two types of graphite collimators, 1- and 3-mm in diameter, were used in order to regulate the spot size of the proton beam. These collimators were insulated from an aluminum exit nozzle using a polyethylene sheet. The proton beam was brought out from the vacuum system into air through a 6-$\mu$m thick Al foil, and traveled 10-mm in air to the target. Path lengths in air and the Al foil caused a reduction in the proton energy from 1.6 MeV down to 1.16 MeV and spread the beam spot to diameter of about 1.2 mm. The beam intensity was monitored by collecting charge from the Al foil. X-rays emitted from the target were detected with a lithium-drifted silicon, Si(Li), made by EG&G Co. through a 74-$\mu$m Al absorber in order to attenuate X-ray intensities of CaK$\alpha$ and CaK$\beta$ and an 8-$\mu$m thick beryllium window. The distance was 19 mm between the top of the Si(Li) crystal and the beam spot on the target. The detector position was kept at 135° with respect to the incident beam direction. PIXE spectra were measured by monitoring a beam current and accumulated for a total beam charge of 10–20 $\mu$C. The PIXE spectral intensities were analyzed after subtracting background by means of the computer program BATTY in PIXAN.[2] Concentrations of trace elements in the otoliths were estimated with the aids of theoretical X-ray yield calculated by the computer program THICK in PIXAN. Experimental errors were examined by using standard argillaceous SRM-1C certified by the NIST.

Table 1 shows concentrations of trace elements in otoliths from red sea bream.[3] There is a significant difference between concentrations of Sr ($P < 0.0001$) and Zn ($P < 0.01$). This difference appears due to ambient seawater temperatures, i.e. MS: 26.6 °C, HT: 22.0 °C and MZ: 22.7 °C. Table 2 shows concentrations of trace elements in the rockfish otoliths. There is a clear difference between reared fish Sr concentrations and wild ones ($P < 0.001$). Although we have no direct environmental data to explain this difference, it is important that we can distinguish artificial fish from wild fish by means of the analysis.

Table 1. Number of specimens and mean trace element concentrations in otoliths from red sea bream reared in three stations, ppm ± s.e.[3]

| Station | N | Sr[a)] | Fe | Mn | Zn[a)] |
|---|---|---|---|---|---|
| MS | 29 | 2332±41 | 248±35 | 68±12 | 128±15 |
| HT | 27 | 1752±32 | 194±31 | 60±6.6 | 65±9.5 |
| MZ | 36 | 1635±32 | 170±14 | 43±4.9 | 103±10 |

[a)] Kruskal-Wallis test, Sr: $P < 0.0001$, Zn: $P < 0.01$.

Table 2. Number of specimens and mean trace element concentrations in wild rockfish otoliths and reared ones, ppm ± s.e.

| | N | Sr[a)] | Fe | Mn | Zn |
|---|---|---|---|---|---|
| Wild | 19 | 1719±44 | 63±15 | 9±1.5 | 45±6.4 |
| Reared | 13 | 1547±36 | 41±7.4 | 9±1.9 | 36±5.9 |

[a)] Student's t-test, $p < 0.001$.

References

1) J. S. Gunn, I. R. Harrowfield, C. H. Proctor, and R. E. Thresher: *J. Exp. Mar. Biol. Ecol.*, **158**, 1 (1992).
2) E. Clayton: PIXAN: The Lucas Heights PIXE Analysis Computer Package, AAEC/M113 (1986).
3) N. Arai, W. Sakamoto, and K. Maeda: *Fisheries Science*, **61**, 43 (1995).

* Faculty of Agriculture, Kyoto University

# Microstructure and Chemical Composition of Duckbilled Dinosaur Eggshell

K. Tazaki,*1 M. Aratani, S. Noda,*2 P. J. Currie,*3 and W. S. Fyfe*4

A dinosaur eggshell with preserved embryonic bones has provided a clear record of micro-structure, mineralogy and chemistry of the eggshell. Six fragments of a duckbilled dinosaur eggshell collected from Alberta, Canada, were analyzed using X-ray powder diffraction, a scanning electron microscope (SEM), an energy dispersive analyzer, a transmission electron microscope (TEM), and heavy-ion probe Rutherford scattering.[1)] Radial and tangential thin sections of two shell specimens showed two layers which were mainly composed of calcite with traces of apatite and aragonite. Silicate and iron oxides were also precipitated on outer surfaces, whereas apatite was precipitated between the two layers by diagenesis (Fig. 1). The presence of Fe, Cu, and Zn, detected by energy dis-persive analysis, suggests the presence of hematite, goethite, pyrite and Cu-Zn oxides which were a result of fossilization. Under the SEM, structural eggshell morphotype shows characteristic features of hadrosaurs, including irregular pore canals, columns, and crescent-shaped mammillary layers and cones. The outer surfaces of the shells show the typical columnar structure with pore openings. The organic material on the inner surface of the eggshell showing a mesh-like structure is interpreted as a fossilized membrane (chorion) of the eggshell. This would be the first record of such a delicate fine structure. Mosaic and lamellar deformation features of calcite show 3.85 Å(102) lattice images, apparent from high-resolution TEM. Rutherford scattering analysis reveals that the eggshell contains C, O, Si, Ca, Fe, and some heavy elements, together with a trace of iridium.[2)] The presence of iridium and the pathological repetition of layers of Hadrosauria's eggshell may suggest that gradual environmental changes adversely affected the reproductive process.

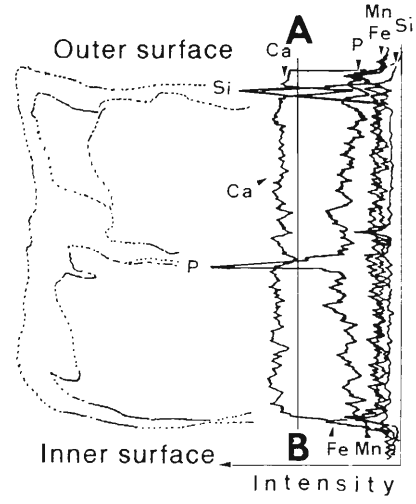


Fig. 1. EDX line scanning analyses of the dinosaur eggshell sample 2; RTMP 87.79.85 at line A-B. High Si with Fe elements concentrated on outer surface, whereas high P with Ca elements concentrated between two layers.

References

1) K. Tazaki, M. Aratani, S. Noda, P. J. Currie, and W. S. Fyfe: *Sci. Rep. Kanazawa Univ.*, **39**, 17 (1994).
2) M. Aratani and M. Yanokura: *RIKEN Rev.*, No. 4, p. 39 (1994).

*1 Department of Earth Sciences, Kanazawa University
*2 Institute of Industrial Science and Technology, Shimane
*3 Royal Tyrrell Museum of Paleontology, Canada
*4 Department of Earth Sciences, University of Western Ontario, Canada

# Heavy-ion Rutherford Scattering Applied to the Investigation of Fire Causes

K. Sato, H. Honda,* J. Ushimaru,* M. Yanokura, K. Maeda, and M. Aratani

Heavy-ion Rutherford Scattering (HIRS) has been applied to the investigation of fire causes.[1-3] The Tokyo Fire Department performs a thorough investigation for decision of fire causes. Recently, fires caused by one-push igniter types of gas tables have increased in number, and occupied ranks within the upper third in the Tokyo Metropolis.

Usually, we observe soot deposited on the surface of a brass rod for ignition of the gas table with microscope to decide whether gas has been burned or not before the fire. But, this method is not advantageous, because even soot might have been burned by fire in cases above a certain scale.

Thus we have employed the HIRS as an available method. The HIRS method enables us to decide whether the gas table has caused fire or not, depending on the distribution of oxygen atoms in the surface layer of the brass rod. The rod is equipped in the gas control valve and has a diameter of 3 mm and a length of 39.5 mm.

A 50 MeV $Ar^{6+}$ beam of about 250 nA was used as incident particles. The beam size was 0.2 mm × 2 mm. We set a sample holder with the brass rod on the center of a scattering chamber, and a slit was located in front of the sample holder. Detector A for recoiled hydrogen, oxygen and carbon ions was located at 30° to the incident argon ion beam. Detector B for scatterd argon ions was set at 40° (Fig. 1).

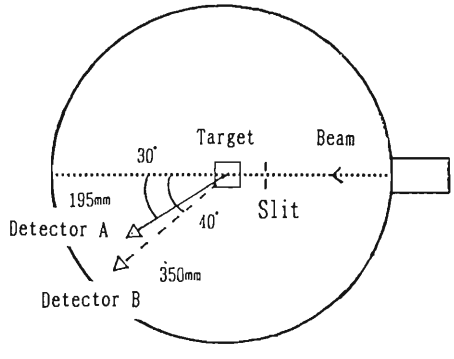


Fig. 1. Experimental apparatus.

Figure 2 was obtained with the gas table (in use before fire) that was subjected to an artificial fire.

The spectra are able to be transferred to the ratio of oxygen atoms to zinc and copper atoms (Fig. 3). Oxygen contents were graded into three levels, A, B, and C, and they corresponded to the three regions on the brass sample.

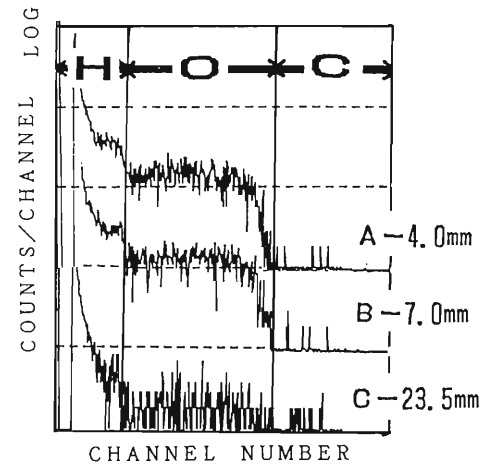


Fig. 2. Spectra for a standard sample prepared by an artificial fire.

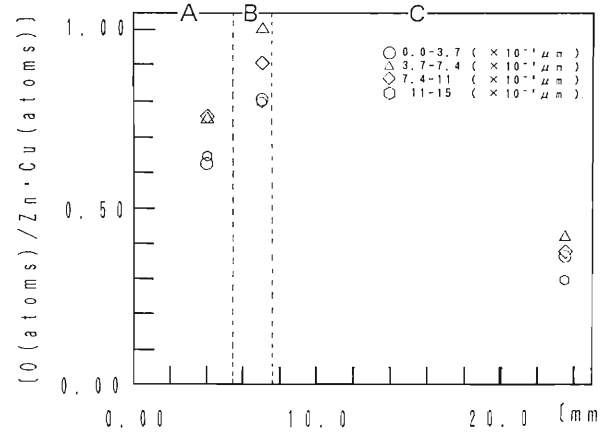


Fig. 3. Oxygen atom distribution in the surface layer of a brass rod.

References

1) K. Sato, H. Honda, J. Ushimaru, M. Yanokura, and M. Aratani: Proc. May Meet. Jpn. Fire Soc., p. 62 (1994).
2) K. Sato, H. Honda, J. Ushimaru, M. Yanokura, and M. Aratani: Proc. 38th Symp. Radiochem., p. 157 (1994).
3) K. Sato, H. Honda, J. Ushimaru, M. Yanokura, and M. Aratani: Proc. 48th Conf. Natl. Fire Engineer, p. 47 (1994).

* Tokyo Fire Department

# RBS Study of Tb-Implanted Sapphire (I)

M. Kumagai and M. Iwaki

A study has been made of the luminescence during Tb-implantation in $Al_2O_3$. The substrates used were colorless and transparent single-crystal $Al_2O_3$ with the (1–102) surface. The surfaces of all wafers were mechanically polished before ion implantation. The $Tb^+$ ion implantation was performed at an energy of 100 keV with fluences between $1 \times 10^{13}$ and $1 \times 10^{17}$ $Tb/cm^2$ at room temperature. The beam current density was about 0.05 $\mu A/cm^2$. The luminescence owing to $Tb^{3+}$ from Tb-implanted $Al_2O_3$ was seen during Tb-implantation.

In order to clarify the mechanism of ion beam induced luminescence of Tb-implanted $Al_2O_3$, the composition, damage and Tb-lattice sites in the Tb-implanted layers of $Al_2O_3$ have been estimated by Rutherford backscattering spectroscopy (RBS). RBS spectra have been measured at room temperature by using 1.5 MeV $He^+$ ions with a scattering angle of 150°.

Figure 1 shows the spectra obtained at an approximately random direction of an implanted specimen with $3.5 \times 10^{16}$ $Tb/cm^2$. The depth profile of implanted $Tb^+$ showed a Gaussian-type distribution. The Tb-dose calculated from the spectra is in good agreement with the nominal value of the implanted dose. The

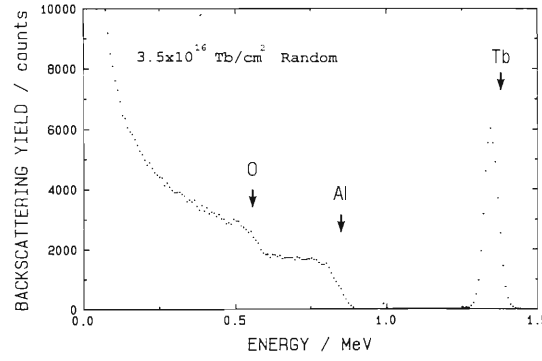


Fig. 1. Random spectra obtained for $Al_2O_3$ with $3.5 \times 10^{16}$ $Tb/cm^2$.

standard deviation calculat from the FWHM of the Tb spectra is about 21.1 nm, which disagrees with the predicted value of about 6.2 nm by the TRIM-90 code. The depth corresponding to the Tb peak in the spectra is about 19.6 nm, which shows a smaller value than the projected range of Tb of about 23.4 nm predicted from the TRIM calculation.

# 7. Miscellaneous

# Design of a Moisture Monitor Based on H-D Exchange in a Glass Surface Layer

T. Nozaki,* T. Kobayashi,* M. Aratani,** and M. Yanokura

Using heavy-ion ERDA and RBS, we formerly studied on the cation-by-hydrogen replacement in glass surface layers (less than a few micrometer thickness) and on the H-D exchange in them. The rates of the two reactions were highly dependent on the glass composition, and the exchange for some soda-lime silicate glass was found to be very slow at room temperature but almost completed in an hour at 80 °C.[1] Based on these results, we have designed a time-integration monitor unit for moisture in dry soils; it is shown in Fig. 1. A chip of the deuterium-replaced soda-lime glass, a crop of a highly soluble salt (e.g., LiCl, $CaCl_2$, KI, or NaBr), and a known, small amount of $D_2O$ are contained in a small box (e.g., 1.5 cm diameter, 2 cm height) with a window of a porous membrane.

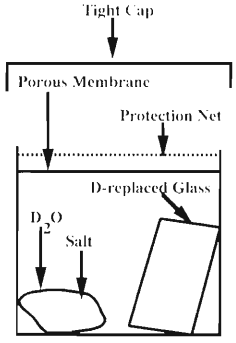


Fig. 1. A monitor unit for moisture vapour pressure in the soil.

Let us first assume that (1) the temperature and the moisture vapour pressure outside are constant, (2) the permeation constant through the film, I, is the same for $H_2O$ and $D_2O$ vapours, and the permeation is slow enough as compared with the time for the entering $H_2O$ to mix with the $D_2O$ and for the outgoing $D_2O$ to diffuse away. Then we can set up a pair of simultaneous differential equations,

$$\begin{aligned} -\mathrm{d[D]/dt} &= \mathrm{I\,V_{in}[D]/([H]+[D])}, \\ \mathrm{d[H]/dt} &= \mathrm{I\,V_{out} - I\,V_{in}[H]/([H]+[D])}, \end{aligned} \quad (1)$$

where [D] and [H] are the quantities of D and H as water in the box, and $V_{in}$ and $V_{out}$ are the water vapour pressures inside and outside of the box, respectively. Equations (1) can be solved easily, and give the relation,

$$\mathrm{[H]/[D]} = \{1 + (R-1)t/\tau\}^{R/(R-1)} - 1, \quad (2)$$

where $R = V_{out}/V_{in}$ and $\tau = ([H]+[D])/I\,V_{in}$. Figure 2 shows the relationship between [H]/[D] and R for some values of $t/\tau$. Fairly linear dependence is seen of [H]/[D] on R and $t/\tau$, for [H]/[D] < 0.3 and $\tau < 0.5$.

* School of Hygienic Sciences, Kitasato University
** Institute for Environmental Sciences

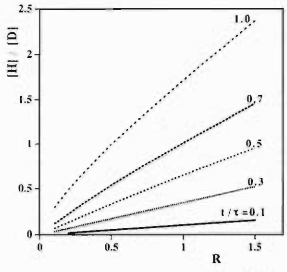


Fig. 2. Dependence of H/D ratio in the monitor box on the moisture vapour pressure and exposure time. For R and $\tau$, see text.

The value of I can be obtained from the weight gain of well dried molecular sieves separated by the membrane from an atmosphere of a saturated salt solution. For a given I, $\tau$ and R can be varied by selecting the salt and the quantity of initial $D_2O$. Now, ultrafiltration membranes of various characteristics are commercially available. A disposable set of ultrafiltration under centrifugation consisting of a tiny box with the membrane can be used for our set with little modification. After being exposed to the environment, the monitor box is capped tightly and kept at 80 °C for an hour. The [H]/[D] ratio in the glass surface is then measured by ERDA. The ERDA spectrum for H and D of uniform distributions can be obtained as rectangles under a measurement condition close to the condition we have used for a long time. From such spectra, we can obtain the [H]/[D] value easily and reliably. A value between 0.05 to 0.25 is suitable for the measurement, owing to the higher sensitivity of H than D in ERDA.

The effect of temperature change in practical use is not so serious, because the temperature changes less in the soil than its outside and because I for a real gas is proportional to the 0.6th to 0.8th power of temperature. Also, a saturated solution of any salt, being attached under the cap, can be used as a reference sample for the monitoring. The vapour pressure in the soil of desert lands often seems to be given by a saturated solution of some salt.

There are other possible uses of deuterated glasses for moisture monitoring. For example, a bare chip of deuterated Pyrex glass might be used for moisture minotoring at a high temperature range (150 to 230 °C).[2]

References

1) T. Nozaki et al.: *Heavy Ion Accel. Syst. Sci. Rep.* (Tokyo Inst. Tech.), **5**, 50 (1990).
2) T. Kobayashi et al.: *RIKEN Accel. Prog. Rep.*, **27**, 100 (1994).

# IV. NUCLEAR DATA

# Status Report of the Nuclear Data Group

Y. Tendow, A. Yoshida, Y. Ohkubo, A. Hashizume, and K. Kitao

The Nuclear Data Group has been continuing the following data activities since previous years.[1)]

(1) Nuclear reaction cross-section data (EXFOR)

Compilation of nuclear reaction cross sections induced by charged particles into the EXFOR format has been continued. At the launching point of our group in 1983, the scope of compilation was confined to the nuclear reaction cross sections to produce only 20 radioisotopes commonly used in biomedical fields including $^{11}$C, $^{13}$N, $^{15}$O, $^{18}$F, $^{28}$Mg, $^{52}$Fe, $^{67}$Ga, $^{68}$Ge, $^{74}$As, $^{77}$Br, $^{82}$Br, $^{77}$Kr, $^{81}$Rb, $^{82m}$Rb, $^{111}$In, $^{123}$Xe, $^{127}$Xe, $^{123}$I, $^{124}$I, and $^{125}$I. We have afterward widened the range of radioisotopes to some extent and also started to search comparatively important data not yet contained in the EXFOR master file until that time.

A considerable amount of old data not included in the EXFOR master as well as the data appeared in recent journals have been picked up and stocked in a queue library and the compilation is in progress at the same time.

(2) Evaluated Nuclear Structure Data File (ENSDF)

We have been participating in the ENSDF compilation network coordinated by the Brookhaven National Nuclear Data Center (NNDC). The evaluation and compilation of A = 120 mass chain is now in progress. A = 129 evaluation has come back from the review at NNDC and is now in post-review by us. Mass chains A = 127 and 118 are now in the stage of review at NNDC.

The Table of Isotopes (8th edition) is scheduled to be published by LBL and a draft of the part A = 118 through 129 has been sent from them for a pre-review by the Japanese group.

(3) Nuclear Structure Reference file (NSR)

We are engaged in collecting and compiling secondary references (annual reports, conference proceedings, etc.) appeared in Japan since the previous year into the Nuclear Structure Reference (NSR) file and sending it to NNDC.

The compilation of 1993 annual reports has been completed and sent to NNDC. Secondary sources surveyed this year are the following annual reports (in code name in NSR); RIKEN (*RIKEN Accel. Prog. Rep.*), JAERI-TV (*JAERI Tandem & V.D.G.*), INS (*INS Univ. Tokyo*), UTTAC (*Univ. Tsukuba Tandem Accel. Center*), RCNP (*Res. Center Nucl. Phys., Osaka Univ.*), OULNS (*Osaka Univ. Lab. Nucl. Study*), and CYRIC (*Cyclo. Radioisot. Center, Tohoku Univ.*).

(4) Others

The IAEA Advisory Group Meeting on the Coordination of the Nuclear Data Centers was held at the OECD Nuclear Energy Agency in Paris on 25–27 April 1994. A proposal for restructuring of the going cooperation network was made at the meeting and another Special Meeting was given at NDS IAEA on 31 October–1 November to discuss and adopt a new agreement for the general restructuring of the international nuclear data cooperation.

Recent developments in performance of desktop PC and peripheral storage equipments should bring revolutionary improvements in the use of nuclear data as well as in the evaluation or compilation methods of these data bases. Whole ENSDF data base, along with the NSR files, the Table of Isotopes (8th edition) and other special data bases such as Evaluated High-Spin Data File (EHSDF), Evaluated Nuclear Chart Data File (ENCDF) etc. are going to be disseminated in a single CD-ROM disk. The disk should also include softwares which provide interactive access to them literally, numerically and graphically on PC's with Macintosh, Windows or UNIX platform. Because of the rapidly increasing quantity of information, nuclear data are to be published more and more on electronic media such as CD-ROM from now onwards.

References

1) Y. Tendow, A. Yoshida, Y. Ohkubo, A. Hashizume, and K. Kitao: *RIKEN Accel. Prog. Rep.*, **27**, 127 (1994).

# Evaluation of Nuclear Structure Data of A=120

A. Hashizume,* K. Kitao, and Y. Tendow

The experimental nuclear data concerning the mass number 120 have been collected and evaluation was made so as to obtain a reliable new data-set file. The last evaluation was published in 1987.[1] The cut-off date of data collections of this publication was march 1986. This evaluation was made for the data collected from 205 references cited therin. Since then, 62 studies were reported to the end of 1993. The new file is a revised edition of the old one.

The file is consisted of 4 new data-sets, 17 revised data-sets and 44 data-sets which remained essentially unchanged. The new data-sets are the adopted levels in $^{120}$Pd,$^{120}$Pd $\beta$-decay and $^{238}$U($^{7}$Li,f). Here a data-set means a set of data for an adopted level, a decay or a reaction defined by incident and outgoing particles.

After the compilation of data, the evaluation was made. For example, $\gamma$-ray data were tested by Rits'-rule and intensity balance. Energies of excited states were obtained from the least-squares analysis. Spins and parities of states proposed by authors are tested by the log-ft in case of $\beta$-decay. In the course of evaluation, a group of computer programmes which are commonly used in mass chain evaluators in the world was generated to make and to check the data-sets.

The changes common for all new data-sets are following.

(1) Because new mass evaluation has been made by Audi and Wapstra in 1993, the Q-values of decays, $\beta$-ray energies and log-ft values were changed.

(2) The values of Ref. 2 were generally adopted for dipole- and quadrupole-moments because systematic corrections were applied to the original data.

(3) The cross-references were made for adopted data so as to make clear the correspondence to each data-set follwoing a new rule to make the file.

Figure 1 shows, for an example, a comparison of states in $^{120}$Te followed by $^{120}$I decay for old and new files.

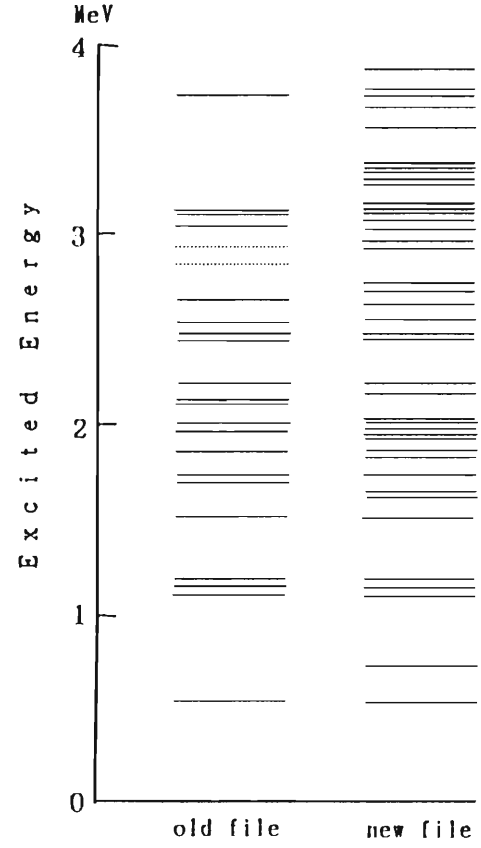


Fig. 1. The states in $^{120}$Te excited by $^{120}$In decay.

References

1) A. Hashizume and Y. Tendow: *Nucl. Data Sheets*, **52**, 641 (1987).
2) P. Raghavan: *At. Data Nucl. Data Tables*, **43**, 189 (1989).

* Japan Atomic Energy Relations Organization

# V. DEVELOPMENT OF ACCELERATOR FACILITIES

# Status of RIKEN 10 GHz Electron Cyclotron Resonance Ion Source (ECRIS)

T. Nakagawa, T. Kageyama, M. Kase, A. Goto, and Y. Yano

Recently, we modified the RIKEN 10 GHz ECRIS by introducing so-called plasma cathode method to the first stage structure to increase the beam intensity of highly charged ions from gaseous elements[1] In this paper, we report the effect of this method to produce the highly charged ions from solid materials.

To produce the ions from solid materials, ceramic rods were inserted into the plasma regions through an open space between poles of a sextuple magnet in the second stage and heated to obtain the sufficient vapor pressure. The supporting rod for a solid material was cooled by the water to prevent the temperature rising of the supporting rod. In the case of MgO, $Al_2O_3$, and ZrO, the diameter and length were 4 and 200 mm, respectively. The NiO rod was rectangular prism with a base 4 mm × 4 mm and a length of 40 mm. The gas pressures of the first, second, and extraction stages were $1.0 \times 10^{-5}$, $5 \times 10^{-7}$, and $8 \times 10^{-8}$ Torrs, respectively. The RF power of the second stage was about 500 W. Extracted voltage was 10 kV. Under this condition, we obtained the average beam intensity of 80 e$\mu$A for $Al^{7+}$ ions. Maximum current of $Ai^{7+}$ was 100 e$\mu$A for short time. This value was about three times as high as that without using the plasma cathode method. The consumption rate of the rod was about 0.01 mm/min. Figure 1 shows beam intensities of the highly charged Mg, Al, Ni, and Zr ions for each charge state. Closed and open circles are with and without using plasma cathode method. The beam intensity was strongly enhanced by using it. The beam intensity of $Al^{8+}$ ions increased from 15 to 60 e$\mu$A . In the case of the $Ni^{18+}$, beam intensity increased from 4 to 12 e$\mu$A. The beam intensity of Mg ions was relatively lower than those of Al ions. The melting temperature of MgO is about 2800 °C, which is higher than that of $Al_2O_3$ (about 2000 °C). It seems that the temperature and density of electrons are still not enough to obtain the intense beam of highly charged ions produced from the solid materials having a higher melting temperatures such as MgO.

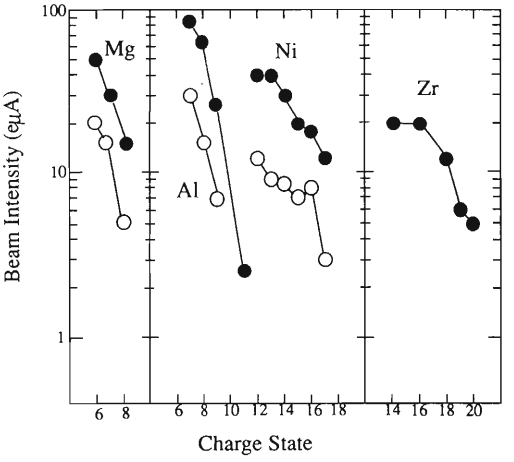


Fig. 1. Charge state distributions of Mg, Al, Ni, and Zr ions. Closed and Open circles are the beam intensity with and without using the plasma cahtode method.

References

1) T. Nakagawa, T. Kageyama, M. Kase, A. Goto, and Y. Yano: *Jpn. J. Appl. Phys.*, **32**, 1335 (1993).

# Status of the RIKEN Polarized Ion Source

H. Okamura, N. Sakamoto, T. Uesaka, H. Sakai, K. Hatanaka, K. Ikegami, J. Fujita, M. Kase, A. Goto, and Y. Yano

An important progress of the ion source development in this year is the improvement of the polarization degree. The present level of the polarization is summarized in Table 1.

Table 1. Summary of polarization.

| | | pure vector | | pure tensor | | | pure $J_Z$ | |
|---|---|---|---|---|---|---|---|---|
| Theor. value | $p_Z$ | $+\frac{2}{3}$ | $-\frac{2}{3}$ | 0 | 0 | 0 | +1 | −1 |
| | $p_{ZZ}$ | 0 | 0 | +1 | −2 | +1 | +1 | +1 |
| States at SX#1-exit | | 1,2,3 | | | | | | |
| | SFT#1 | | | | | 2→6 | 3→5 | |
| | WFT#1 | | | 1→4 | 1→4 | | | |
| States at SX#2-exit | | 1,2,3 | | 2,3 | 2,3 | 1,3 | 1,2 | |
| | SFT#2 | 3→6 | | 2→6[a] | 3→5[a] | | 2→6 | |
| | WFT#2 | | 1→4 | | | | | 1→4, 2→3 |
| States at ECR | | 1,2,6 | 2,3,4 | 3,6 | 2,5 | 1,3 | 1,6 | 3,4 |
| Present value | $p_Z$ | +0.57 | −0.55 | | | | +0.76 | −0.61 |
| | $p_{ZZ}$ | [b] | | +0.77 | −1.23 | +0.58 | +0.67 | +0.46[c] |
| Previous value | $p_Z$ | +0.40 | −0.43 | | | | +0.49 | −0.45 |
| | $p_{ZZ}$ | [b] | | — | −0.92 | — | +0.45 | +0.39[c] |

[a] Transitions 2→6 and 3→5 for the SFT#2 are switched by periodically changing the magnetic field while the frequency of the generator is kept constant.

[b] The input power to the WFT#2 cavity is set to less than 0.4 W to keep $p_{ZZ}$ negligibly small.

[c] $p_{ZZ}$ increases as increasing the input power to the WFT#2 cavity and reaches a maximum at the power greater than 1 W.

The possible sources causing the polarization reduction are: (1) a relatively strong radial component of the ECR magnetic field; (2) insufficient pumping of the ECR plasma region; (3) low efficiency of the RF transitions; and (4) insufficient dissociation degree of the dissociator.

Concerning the ECR ionizer, the radial component of the magnetic field has been reduced by increasing the inner diameter of the sextupole magnet from 90 mm to 120 mm. This resulted in the decrease of the field gradient from 122 Gauss/cm$^2$ to 53 Gauss/cm$^2$. It should be noted that the axial field is typically 800 Gauss at the plasma region to meet the ECR condition ($B_0$ = 874 Gauss) for the 2.45-GHz micro wave.

While the reduced radial field will minimize the influence of the transverse components on the polarization, the increase of the diameter of ionizing region, which is significantly larger than the atomic beam diameter, will cause an increase of the unpolarized background. Expecting the improved pumping of the plasma region, the diameter of the plasma chamber has been increased from 70 mm to 110 mm. Also a Ti sublimation pump has been installed in addition to the previously installed Ti-pump and the cryogenic pump, yielding the total pumping speed of 4000 $\ell$/s for hydrogen.

Concerning the RF transition units, the magnet system with tapered- and background-coils has been introduced so that the optimum gradient and strength of the magnetic field can be obtained. A typical field distribution is shown in Fig. 1. The dependence of the polarization on the magnetic field has been carefully studied as well as the dependence on the RF power fed to the cavity (see footnotes of Table 1).

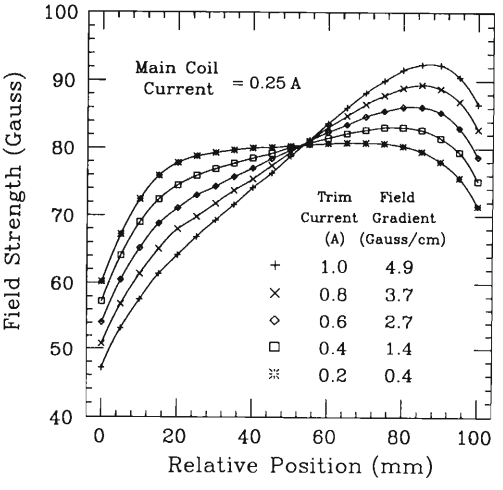


Fig. 1. Magnetic field distribution of the SFT#2.

Although the polarization degree is satisfactorily good in most cases, relatively low polarization is observed for the mode using the SFT#1. This is probably attributed to the low efficiency of the first sextupole magnet (SX#1) in selecting the spin-up states of the electron. At present, the pure-$J_Z$ modes are not practically used for the experiment.

Concerning the dissociator, we tried to extract the dissociation degree by measuring the $D/D_2$-ratio of the atomic beam with the QMA. But the recombination rate in the QMA-chamber, which causes an uncertainty in the dissociation degree, was found to be significantly large. Instead, the performance of the dissociator has been studied by using a compression tube which was calibrated by the $D_2$ gas flow and was installed in the middle of the ECR chamber. It should be noted that the previously used compression tube was uncalibrated and was installed upstream of the ionizer.[1] The flux of the atomic beam into the 25-mm aperture has been obtained to be $2.3 \times 10^{16}$ atoms/s. This sufficiently high intensity implies that the dissociation degree is fairly large and not causing the reduction of the polarization.

The current problem of the ion source operation is the short lifetime of the insulators, particularly at the

beam-extraction section and at the Wien filter. Since the $N_2$ buffer gas is fed in to maintain the stable ECR plasma, an intense beam of nitrogen ions with various charge states and with a huge emittance is extracted. It hits the electrodes and yields a large amount of metallic vapor, rapidly deteriorating the insulators. Recently all components of the extraction electrode which were made of stainless steel have been replaced by aluminum ones. The amount of metallic vapor is significantly reduced and the ionizer can be operated without maintenance for more than a couple of months. Modification of the electrode of the Wien filter is currently underway.

Also we have modified the transport beam-line to the AVF (injector) cyclotron expecting the improved beam transmission. Although it is not sufficiently tuned, the beam with the intensity of 3.5 $\mu$A has been obtained at the exit of the AVF cyclotron.

The spin-direction control is stably operated owing to the monitoring system of the single-turn extraction.[2,3] Figure 2 shows an example of tuning the Wien filter angle. The polarization is measured at 270 MeV and the polarimeter installed at the beam distribution corridor (D-room) is operated very efficiently and reliably. A new polarimeter which also uses the $d + p$ scattering as polarimetry[4] has been installed at the exit of the beam swinger of the spectrograph SMART. It moves with the beam swinger and thus directly measures the polarization at the target. The $CH_2$ target can be quickly inserted and removed by using a pneumatic actuator, which allows the periodical monitor of the beam polarization during the experiment.

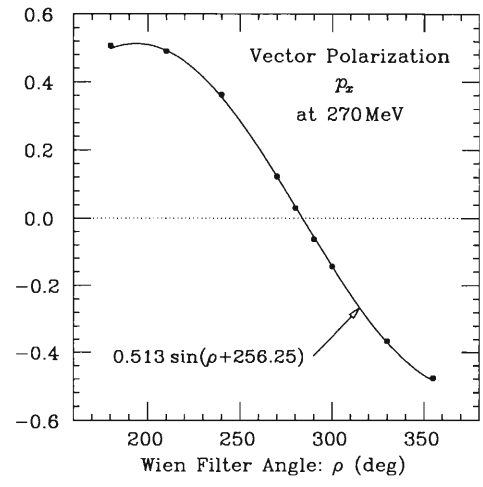


Fig. 2. Dependence of $p_x$ on the Wien filter angle, when the beam is purely vector-polarized and the spin direction is rotated by 90°. The data is neatly fitted by a sine function and its amplitude shows that the polarization degree, 77%, is not reduced. The statistical errors are well within the size of the data points.

References

1) H. Okamura et al.: *AIP Conf. Proc.*, **293**, 84 (1994); *RIKEN Accel. Prog. Rep.*, **27**, 130 (1993).
2) N. Inabe et al.: *RIKEN Accel. Prog. Rep.*, **27**, 133 (1993).
3) T. Kawama et al.: *ibid.*, p. 135.
4) N. Sakamoto et al.: *ibid.*, p. 39.

# Modeling of ECRIS Beam-Intensity Upgrading-Technologies

M. Niimura, T. Kageyama, T. Nakagawa, A. Goto, and Y. Yano

Progress was made in fundamental understanding of physics for upgrading the beam-intensity (total-current and current-density) of high-charge-state (HCS) ions available from an ECR ion source (ECRIS) and its extraction/transport optics. Due to the restriction of space, only the total-current upgrading-technologies such as (i) electron (e-) beam injection, (ii) wall-coating, and (iii) gas-mixing will be discussed here. Currently, the upgrading factor ($\eta$) defined by the ratio of beam intensities 'with' to 'without' upgrading-technologies is approximately $\eta(z) \leq 10$ after (i) and (ii) are combined for argon ions, for instance, at the charge state, $z \leq 14$. The physical model studied here seems to provide knowledge on how to increase $\eta$ beyond the present status.

Which property does actually upgrade the total beam-current? In order to answer such a fundamental question and to investigate the individual roles of electron density ($n_e$), temperature ($T_e$) and ion confinement time ($\tau$) separately, we have developed an analytic code that can compute the charge state distribution (CSD) under different parameters. The outline is following.

The rate of increase of the z-times ionized ion density, $n_z$ (where $z = 1,2,3,\ldots,Z_n$), is given by

$$\frac{dn_z}{dt} = [n_e S_{z-1,z}]\, n_{z-1} - [n_e S_{z,z+1} + n_o \rho_{z,z-1} v_i + 1/\tau]\, n_z + [n_o \rho_{z+1,z} v_i]\, n_{z+1}. \quad (1)$$

The first and third bracket terms in Eq. (1) are production rates of $n_z$ ions due to the electron impact against $n_{z-1}$ type particles (G1) and due to the charge exchange of $n_{z+1}$ ions with $n_o$ (G2), respectively, while the second term consists of loss rates of $n_z$ ions due to the ionization (L1), charge exchange (L2), and ion diffusion (L3) processes.

$S_{z-1,z} \equiv \langle \sigma_{z-1,z} v_e \rangle$ in Eq. (1) is the ionization rate coefficient or an averaged $\sigma v$ per particle averaged over Maxwellian distribution of the electron thermal velocity. Since we are interested in the HCS ions ($z \geq 4$), the stepwise electron impact ionization cross-section can be expressed by a simple form:[1] $\sigma_{z-1,z} = a_z q_z (ln\, U_z/U_z)\, (E_\infty^{z-1})^{-2}$ [cm$^2$]. Here, $U_z \equiv \varepsilon / E_\infty^{z-1} \geq 1$, $\varepsilon \equiv (1/2) m_e v_e^2$, Bethe coefficients $a_z q_z = 4.5 \times 10^{-14}$ because $z \geq 4$, and $E_\infty^{z-1}$ is the ionization (or binding) energy of $z-1$ type particles. The Maxwellian averaging results[1]

$$S_{z-1,z} = \frac{3.02 \times 10^{-6}}{T_e^{3/2}} \lambda\, E_1\left(\frac{1}{\lambda}\right), \quad \text{if} \quad \lambda \equiv \frac{T_e(\text{eV})}{E_\infty^{z-1}} \quad (2)$$

The exponential integral, $E_1(1/\lambda)$, appeared above has no analytic form except for the limit, $\lambda \to 0$. We thus have numerically derived relevant expressions:

$$E_1\left(\frac{1}{\lambda}\right) \equiv \int_{1/\lambda}^{\infty} \frac{e^{-x}}{x} dx = \lambda \exp\left(-\frac{1}{\lambda}\right) \quad (0 \leq \lambda \leq 0.5) \quad (3)$$

$$= -0.097 + 0.343\,\lambda - 0.015\,\lambda^2 \quad (0.5 \leq \lambda \leq 11.43) \quad (4)$$

$$= 1.863 \quad (\lambda \geq 11.43) \quad (5)$$

Figure 1 shows the numerically integrated $E_1(1/\lambda)$, whose polynomial form and saturation value are given by (4) and (5), respectively. These approximations were found quite satisfactory compared with more rigorous calculation done by Lots (his Fig. 4).[1] The L1 and G1 are now calculable.

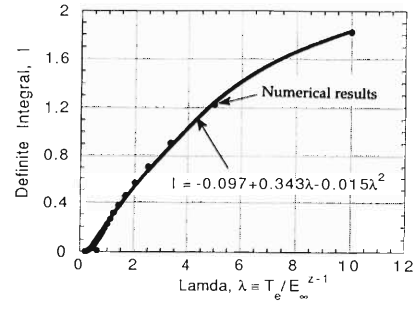


Fig. 1. Numerically evaluated exponential integral, $I \equiv E_1(1/\lambda)$, used for the calculation of $S_{z-1,z}(\lambda)$.

As for the charge exchange cross-section, we have used the Muller-Salzborn expression[2]: $\rho_{z,z-1} = 1.43 \times 10^{-12} z^{1.17} / (E_\infty^o)^{2.76}$ [cm$^2$] where $E_\infty^o$ is the first ionization potential of neutrals ($n_o$). The loss L2 takes place when z-ions collide with $n_o$, where the relative velocity of encounter is essentially the ion thermal velocity, $v_i$.

On the other hand, L3 $\equiv n_z/\tau$ is inversely proportional to the ion lifetime, $\tau \equiv L/v_i$ (L: effective wall distance). Within this report, we assume $\tau$ to be independent of z. The case $\tau$(HCS)$\geq\tau$(LCS) will be studied elsewhere.

At the steady-state ($dn_z/dt = 0$) the rate equation (1) is in the form: $[A_{z,z-1}]n_{z-1} - [A_{z,z}]n_z + [A_{z,z+1}]n_{z+1} = 0$. The matrix equation for the first 5-species can be expressed as

$$\begin{pmatrix} A_{11} & A_{12} & 0 & 0 & 0 \\ A_{21} & A_{22} & A_{23} & 0 & 0 \\ 0 & A_{32} & A_{33} & A_{34} & 0 \\ 0 & 0 & A_{43} & A_{44} & A_{45} \\ 1 & 2 & 3 & 4 & 5 \end{pmatrix} \times \begin{pmatrix} n_1 \\ n_2 \\ n_3 \\ n_4 \\ n_5 \end{pmatrix} = \begin{pmatrix} -A_{10} n_o \\ 0 \\ 0 \\ 0 \\ n_e \end{pmatrix} \quad (6)$$

The last row is the charge neutrality condition.

Firstly, the complete 18 × 18 matrix elements $A_{ij}$ have been computed for argon ($\mu$ = 40) ion system under the RIKEN f = 10 GHz ECRIS conditions: p = 1.8 × $10^{-6}$ [Torr], $n_{oi} \equiv 9.66 \times 10^{18} p/T(K) = 5.79 \times 10^{10}$ [$cm^{-3}$], $n_e \equiv 1.24 \times 10^{-8} f^2 = 1.24 \times 10^{12}$ [$cm^{-3}$], $n_o = n_{oi}/2 = 2.90 \times 10^{10}$ [$cm^3$], $\alpha \equiv n_e/(n_e + n_o) = 97.7\%$, $T_e$ = 500 eV, $T_i$ = 0.5 eV, $v_i \equiv 9.79 \times 10^5 T_i/(\mu)^{1/2} = 1.09 \times 10^5$ [cm/s], R = 10 cm, and $\tau = R/v_i = 91.7$ $\mu$s. Then, the 18 simultaneous equations were solved by a Gaussian elimination method.

Figure 2 presents computer results of CSD, where a monotonical decay of $n_z$ with respect to z is characteristic for both curves with diffusion loss, $1/\tau = 1.09 \times 10^4 s^{-1} \neq 0$. However, magnitude of $n_z$ increases when $n_e$ is raised. This means that the total beam-current, $I_z = Zen_z v_{es} S$ ($v_{es}$: escape velocity) will be upgraded if all the electrons externally "injected" via technologies (i)-(iii) are ECR heated and thermalized to the same $T_e$ = 500 eV as the background plasma. What happens if they were not heated? Then, the density of hot electrons won't increase. However, if the e-beam injection could trap ions indefinitely so that no diffusion loss takes place ($1/\tau = 0$), a significant upgrading much greater than the previous $n_e$ effect can be expected; *e.g.*, $\eta = \infty$ at z = 12. This is evident in Fig. 2 by comparing the $1/\tau = 0$ with $1/\tau \neq 0$ curve with $n_e = 1.24 \times 10^{12}$ $cm^{-3}$.

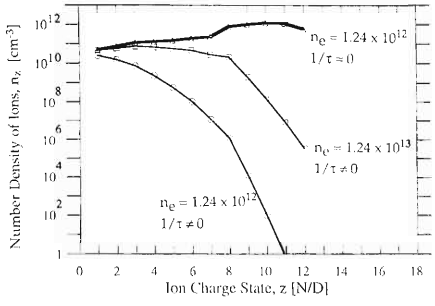


Fig. 2. Theoretical CSD in log-scale with and without the ion diffusion loss ($1/\tau$) and the effect of various $n_e$.

Figure 3 shows linear plots of two $1/\tau = 0$ curves together with one $1/\tau \neq 0$ curve. It is evident from

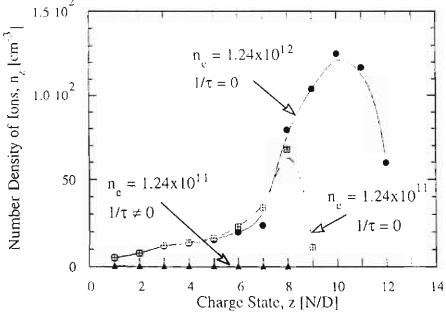


Fig. 3. Theoretical CSD in linear-scale, for argon ions at $T_e$ = 500 eV, similar to the case of Fig. 2.

Figs. 2 and 3 show that those $1/\tau = 0$ curves characteristically increase with z, and the peak shifts towards higher-z to attain a higher-$n_z$ as $n_e$ is raised, followed by a decay due to the increase of L2 at large-z. On the other hand, if charge exchanges were negligible beside L3 = 0, then $n_z/n_{z-1} \approx G1/L1 = S_{z-1,z}/S_{z,z+1}$ which is always an increasing function with z. Such a condition (L2 = L3 = 0) may be satisfied when $v_i$ or $(T_i)^{1/2}$ is lowered via the technology (iii), since L2, L3 $\sim v_i$. For this case, the $n_z$ will start decaying abruptly, regardless of $n_e$, after a certain z at which $\lambda \equiv T_e/E_\infty^{z-1} \leq 1$, as observed by Antaya.[3)]

Figure 4 shows one of our experimental results, where a tuning was made only for $Ar^{11+}$ ions, while applying technologies (i) and (iii). Although quite similar with $1/\tau = 0$ curves in Fig. 3, whether this is representing the case of L3 = 0 or L2 = L3 = 0 is yet to be confirmed; the tuning for all z's may result in a profile similar to the $1/\tau \neq 0$ curves seen in Fig. 2. Since L3 is actually scaled by $v_i/\phi$, the L3 = 0 condition may be satisfied if a potential-dip, ($\partial\phi/\partial r \geq 0$), is created via the technology (i).

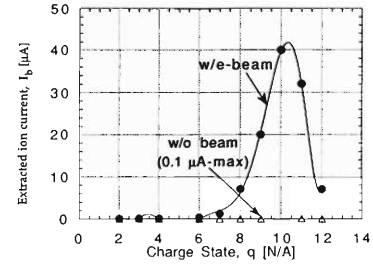


Fig. 4. Experimental CSD in linear-scale for argon ions, after correcting the overlapping effects at z = 10 and 5.

Among the upgrading technologies, either L3 = 0 or L2 = L3 = 0 type is more beneficial than the large-$n_e$ type for the sake of AVF cyclotrons which accept only the particle at z ≥ M/4. We presently inject ions with z close to the minimum z = M/4 (=10 for argon) into cyclotrons by automatically assuming that the beam-current always decreases with z. However, present study has revealed that the CSD can increase with z and its peak can shift towards higher-z under loss-less cases; one can then accelerate ions with z higher than now without sacrificing the beam-current. Conclusion: The effect of large-$\tau$ can be much greater than that of increasing $n_e$ by an order of magnitude which requires a raise of RF frequency by 3-times (to 30 GHz if 10 GHz now). The technology (i) lowers the hight of the plasma potential with a dip-$\phi$ on the axis, thereby reducing the ion diffusion loss while raising $n_e$.

References

1) W. Lotz: *Z. Physik*, **216**, 241 (1968).
2) A. Muller and E. Salzborn: *Phys. Lett.*, **62**, 351 (1997).
3) T. A. Antaya: *J. de Phys. C1*, **50**, C1-707 (1989).

# Development of High-$T_e$ ECRIS Plasma Diagnostics

M. Niimura, A. Goto, and Y. Yano

The averaged excitation rate coefficients of helium (HeI) lines have been calculated for the first time beyond the range of previous calculation[1] limited by $T_e \leq 100$ eV. The result indicates that the electron temperature ($T_e$) of ECR ion sources (ECRIS) can be measured spectroscopically up to $T_e = 1000$ eV, by utilizing the helium atoms left from turbomolecular pumping.

ECRIS plasmas are characterized by a high-$T_e$ plasma, which is a pre-requisite for production of high charge-state (z) ions. In a thermal plasma, $T_e \geq 1.44E_\infty^{z-1}$ should be achieved if more than 50% of the electrons should participate in the production of z-ions from (z−1)-ions with the ionization potential, $E_\infty^{z-1}$(=539 eV for Ar, z = 11). A non-perturbing $T_e$ monitor is thus needed in order to readjust machine parameters for the efficient, stable ion beam production throughout the course.

On the other hand, ECRIS plasmas are practically a dual-gas plasma; mixing of a supporting gas with the target gas is a common practice for the purpose to enhance the extracted ion beam-current. Our idea is to utilize one of the light gas atoms like HI and HeI as a $T_e$ monitor. This would not raise the ECRIS working pressure (typically $10^{-6}$ Torr) since one can use HI or HeI left over in the vacuum system. High-$T_e$ low-$n_e$ (typically $10^{11\sim12}$ cm$^{-3}$) characteristics of the ECRIS plasma tend to satisfy the condition of tenuous plasma model[2] used below.

As is well known, the $h\nu_{mn}$ photon emission due to the m→n (m > n) line transition has the intensity expressed by $I_{mn} = (1.6 \times 10^{-19}/4\pi)(h\nu_{mn})A_{mn}N_m$ [W/cm$^3$ sr]. Also known is that in a low-$n_e$ plasma the radiative decay rate balances with the collisional excitation rate, i.e., $A_{mn}N_m = N_e\langle\sigma_{nm}v\rangle N_n$, where $\sigma_{nm}$ is the n→m collisional excitation cross section. This is called corona model, which is valid if $T_e \geq 10$ eV in the plasma with $n_e = 1.24 \times 10^{12}$ cm$^{-3}$ (critical density of 10 GHz ECRIS). Particularly, if $T_e \gg \Delta E_{1m}$, a tenuous plasma condition holds meaning that the population of lower transition level is close to that of ground level ($N_n \sim N_1$). Then, $I_{mn} = (1.6 \times 10^{19}/4\pi)\ (h\nu_{mn})\ N_e\langle\sigma_{nm}v\rangle N_1$. Lees[3] has experimentally confirmed the proportionality of $I_{mn}$ against $N_e$, $N_1$, and $\sigma_{nm}$ during his $\sigma_{nm}$ measurement. Therefore, the relative line intensity (RLI) ratio of m→n transition to m'→n' (m' > n') transition is given by

$$x_o \equiv \frac{I_{mn}}{I_{m'n'}} = \frac{\Delta E_{nm}}{\Delta E_{n'm'}} \cdot \frac{\langle\sigma_{nm}v\rangle}{\langle\sigma_{n'm'}v\rangle}. \quad (1)$$

Here, $\Delta E_{nm}$[eV] $\equiv h\nu_{mn} \equiv 1239.8/\lambda_{mn}$ (where $\lambda_{mn}$ is the wavelength of m→n emission in units of nm). The factor $(\Delta E_{nm}/\Delta E_{n'm'})$ is missing from the Sovie's expression[1] of $x_o$. The term $\langle\sigma_{nm}v\rangle$ in Eq. (1) denotes the averaged excitation rate coefficient per particle defined by

$$\langle\sigma_{nm}v\rangle \equiv \int_{\Delta E_{nm}}^{\infty} \sigma_{nm}(\varepsilon)\, v(\varepsilon)\, g(\varepsilon)\, d\varepsilon \ \ [\mathrm{cm}^3/\mathrm{s}]. \quad (2)$$

Here, $v(\varepsilon)$ is the impacting electron velocity expressed by the kinetic energy, $\varepsilon = (1/2)mv^2$, and $g(\varepsilon)$ is the Maxwellian distribution in the 3-D energy space:

$$g(\varepsilon)d\varepsilon \equiv \frac{2}{T_e}\sqrt{\frac{\varepsilon}{\pi T_e}}\exp\left(\frac{-\varepsilon}{T_e}\right)d\varepsilon, \ \int_0^\infty g(\varepsilon)\, d\varepsilon = 1. \quad (3)$$

Using $d\varepsilon = mvdv$, Eq. (3) can be reduced to a more familiar form: $(m/2\pi T_e)^{3/2}\ \exp(-mv^2/2T_e)4\pi v^2 \equiv g(v)dv$, where $4\pi v^2$ is a volume element in the spherical coordinates. Substituting (3) and $v(\varepsilon) \equiv (2\varepsilon/m)^{1/2}$ in to Eq. (2) we obtain

$$\langle\sigma_{nm}v\rangle \equiv \sqrt{\frac{8}{\pi m}}T_e^{-1.5}\int_{\Delta E_{nm}}^{\infty} \varepsilon\, \sigma_{nm}(\varepsilon)\exp\left(\frac{-\varepsilon}{T_e}\right)d\varepsilon. \quad (4)$$

Here, $\Delta E_{nm}$ is the threshold energy to observe a finite $\sigma_{nm}$, and $(8/\pi m)^{1/2} = 6.68 \times 10^7$ when $T_e$ and $\varepsilon$ are in eV.

Our objective is to evaluate Eq. (4) for various atomic lines in the range of $T_e$ relevant to ECRIS. McWhirter[4] has evaluated $x_o$, but only for $T_e \leq 100$ eV (like Sovie's case) and for 471.3 nm ($2^3$P-$4^3$S) and 492.1 nm ($2^1$P-$4^1$D). Sovie[1] has later pointed out that the $\sigma_{nm}$ of D(diffuse)-series has a peculiar pressure dependence so that use of McWhirter's $x_o$ may lead erroneous $T_e$, while the $\sigma_{nm}$ of S(sharp)-series has no such a peculiarity over the range, 0–130 mTorr. This pressure range covers well the ECRIS working range, 0–0.01 mTorr.

Figure 1 shows two profiles of the experimentally

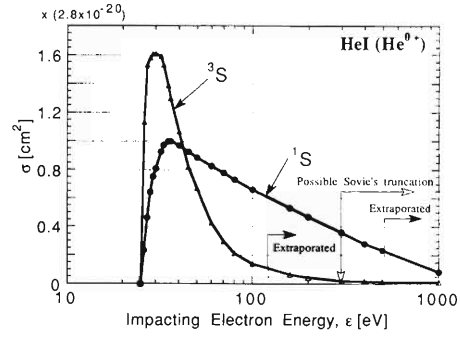


Fig. 1. Averaged excitation cross sections of HeI singlet-singlet ($^1$S) and triplet-triplet ($^3$S) lines. Symbols are data points read from Lees' experimental curves.[3]

observed $\sigma_{mn}(\varepsilon)$ of HeI lines in the S-series:[3] the $^1$S and $^3$S denote 443.7 nm ($5^1S \rightarrow 2^1P$) and 412.1 nm ($5^3S \rightarrow 2^3P$) transitions, respectively. These profiles are self-similar when the series of the upper state is same. The $^1$S and $^3$S profiles peak at $\varepsilon = 36$ eV and 30 eV, respectively, and the ratio of peak values is $\sigma(^3S)/\sigma(^1S) = (4.5 \times 10^{-20})/(2.8 \times 10^{-20}) = 1.607$. Lees' experimental curves of $\sigma_{mn}(\varepsilon)$ terminate after a certain $\varepsilon$, but they obviously ought to continue till $\sigma_{mn}(\varepsilon) = 0$. In Fig. 1 a smooth extrapolation was thus performed for $^1$S and $^3$S curves in the range of $\varepsilon \geq 500$ eV and $\varepsilon \geq 120$ eV, respectively. We suspect that Sovie[1] has prematurely truncated both $^1$S and $^3$S curves at around $\varepsilon = 300$ eV, as marked in Fig. 1, since he did not multiply the factor of $(\Delta E_{nm}/\Delta E_{nm'})$ in (1), but ended up with $x_o$ agreeable with ours.

The curve of $\sigma_{mn}(\varepsilon)$ may be approximated by either Bethe approximation of $\sigma = a \ln(\varepsilon)/\varepsilon$ type or Wooley-Allen approximation of $\sigma = (a/\varepsilon)[b - (1/\varepsilon)]$ type,[5] where a and b are constants. However, within the present work frame we have evaluated Eq. (4) numerically. Figure 2 presents the numerically evaluated excitation rate coefficients for the $^1$S and $^3$S transitions as a function of $T_e$.

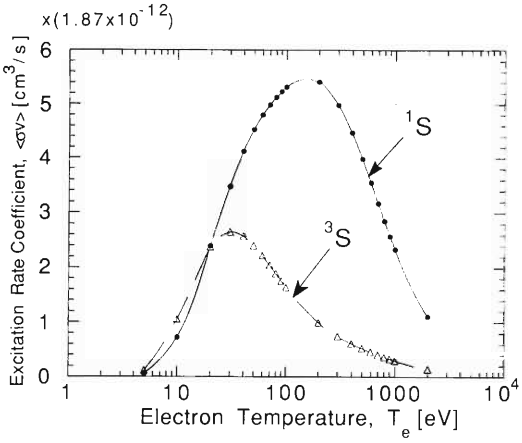


Fig. 2. Excitation rate coefficients of Eq. (4) as a function of $T_e$ for both $^1$S and $^3$S transitions.

Taking the ratio of the two curves presented in Fig. 2, and multiplying it by a factor of $(\Delta E_{nm}/\Delta E_{n'm'}) = 2.79$ eV/3.00 eV $= 0.93$, we have obtained the curve of $x_o \equiv I_{4437}/I_{4142}$ as shown in Fig. 3 over a wide range of $5 \leq T_e \leq 2000$ eV. This graph should be useful in the plasma diagnostics for determining $T_e$ from measured $x_o$, up to 1000 eV; resolution deteriorates above 1000 eV.

For the sake of comparison of our result with Sovie's, the portion of $T_e \leq 100$ eV has been re-plotted in linear scale in Fig. 4. A fairly good agreement is evident between the two curves. However, we can say that the same result as ours may be reached even after truncating the $\sigma_{nm}(\varepsilon)$ at around $\varepsilon = 300$ eV if the multiplication factor $(\Delta E_{nm}/\Delta E_{n'm'})$ was neglected in Eq. (1).

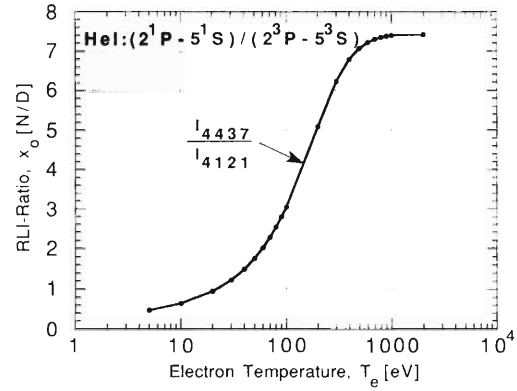


Fig. 3. The computed RLI-ratio, $x_o(T_e) = I_{4437}/I_{4142}$ which can determine $T_e$ in the range, $20 \leq T_e \leq 1000$ eV.

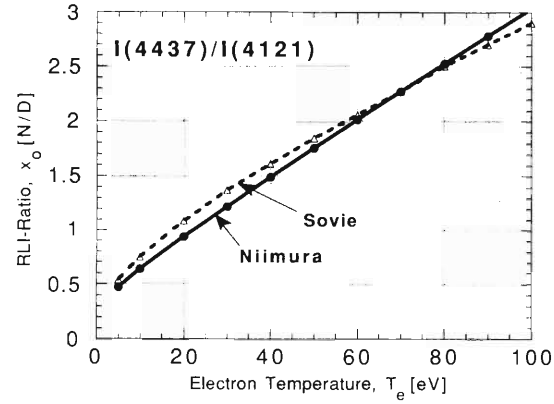


Fig. 4. Comparison of our result with Sovie's in the domain $0 \leq T_e \leq 100$ eV.

In conclusion, we could extend the temperature range so that $T_e$ of up to 1000 eV can be measured by a non-perturbing method. The hot-component of $T_e$ (or $T_{eh}$) in many two-temperature ECRIS is within this range. The energy analyzer diagnostics[6] determined $T_{eh} = 240$ eV for a typical ECRIS plasma, Caprice. The charge state distributions of the LBL and RIKEN 10 GHz ECRIS agree well with theoretical predictions, if $T_{eh} \sim 500$ eV.

References


1) R. J. Sovie: *Phys. Fluids*, **7**, 613 (1964).
2) R. Wilson: *J. Q. Spec. Rad. Transf.*, **2**, 447 (1962).
3) J. H. Lees: *Proc. Roy. Soc.* (London), **A137**, 173 (1943).
4) R. W. P. McWhirter: Plasma Diagnostic Techniques, Academic Press, New York, p. 201 (1965).
5) H. V. Regemorter: *Astrophys. J.*, **136**, 906 (1962).
6) K. S. Golovanivsky and G. Melin: *Rev. Sci. Instrum.*, **63**, 2886 (1992).

# Construction of a High Density Polarized $^3$He Gas Target

T. Uesaka, M. Wakasugi, T. Wakui, and A. Minoh

A high density polarized $^3$He gas target system has been constructed. The $^3$He nucleus is polarized by a spin-exchange reaction with a polarized Rb atom. The polarized Rb atom is produced by optical pumping using a circularly polarized laser beam. Our goal is to realize more than 60% polarization of $^3$He at a gas density of about 10 atoms at room temperature.

To achieve high polarization, both long relaxation time and high laser power are necessary. The $^3$He polarization at equilibrium is expressed as follows:

$$P_{^3\mathrm{He}} = \frac{\gamma_{SE}}{\gamma_{SE}+\Gamma} P_{Rb} \tag{1}$$

$$= \frac{\gamma_{SE}}{\gamma_{SE}+\Gamma} \frac{\gamma_{opt}}{\gamma_{opt}+\Gamma_{SD}}, \tag{2}$$

where $\gamma_{SE}$ is the spin exchange rate between Rb atom and $^3$He nucleus, $\Gamma$ the total spin relaxation rate, $P_{Rb}$ the polarization of Rb, $\gamma_{opt}$ the optical pumping rate, and $\Gamma_{SD}$ the spin destruction rate of Rb atom. From Eq. (2), the conditions to obtain high polarization are found to be

$$\gamma_{SE} \gg \Gamma, \tag{3}$$

$$\gamma_{opt} \gg \Gamma_{SD}. \tag{4}$$

Figure 1 shows a schematic view of the target system. As a pumping laser, we chose a 4W laser diode (Spectra Diode Labs SDL-2382-P1), whose wavelength is 798 nm at room temperature and spectral width 1.3 nm. The divergent beam from the laser diode is formed by lenses to have a proper beam envelope at the target cell. Circular polarization is produced by a $\lambda/4$ plate.

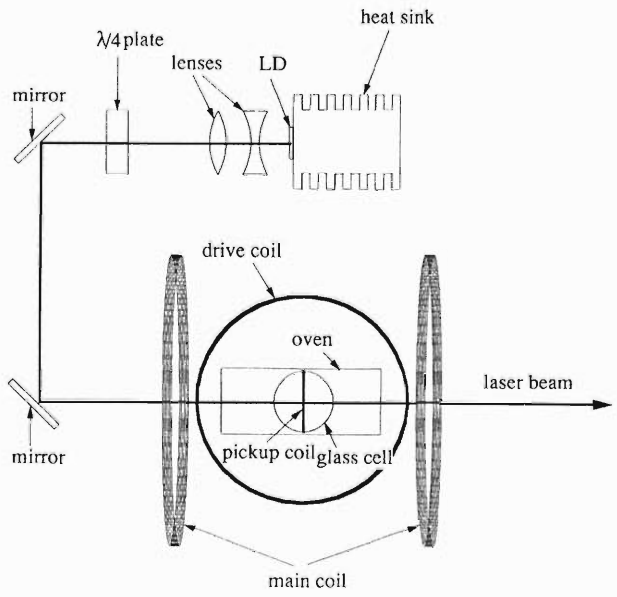


Fig. 1. Schematic view of target system.

The target cell, which is made of aluminosilicate glass (Corning1724), is heated up in a 180 °C oven to control the density of Rb atoms in the cell.

The polarization of $^3$He is measured with the adiabatic fast passage NMR (AFP-NMR) technique. The AFP-NMR system consists of 3 sets of coils: main coils, drive coils and a pickup coil. They are set perpendicular to one another. Main coils produce a static field (B $\sim$ 30 Gauss) and the drive coils provide an RF field ($\omega \sim$ 100 kHz). When the static field which is swept slowly coincides a resonance (B $= \omega/\gamma$, where $\gamma$ is a gyromagnetic ratio), spin of the $^3$He nucleus is flipped and the signal which is proportional to the polarization of $^3$He nucleus occurs in the pickup coil. The main coils are designed so that inhomogeneity of the static field is sufficiently small ($\Delta B/B \leq 10^{-3}$) in the volume of the target cell, to suppress the relaxation caused by the field inhomogeneity.

Two Major relaxations are caused by a cell wall and impurities in the bulk gas. To reduce the wall relaxation, cleaning procedure of the cell is very important: first, we remove ferromagnetic contaminants on the surface of glass cell with nitric acid. Next, we get rid of organic impurities with acetone. Finally, the cell is cleaned in ethanol with a ultrasonic cleaner.

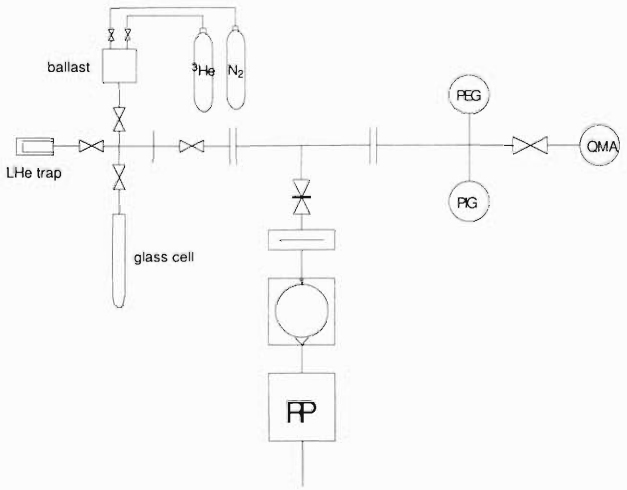


Fig. 2. Cell making system.

The vacuum system for gas filling was designed to reduce the impurities in the bulk gas (Fig. 2). A quadrupole mass analyzer is very useful to monitor components of the residual gas. A ballast and a liquid helium trap are devices to purify $^3$He gas.[1] The ultimate pressure of this system is $9.3 \times 10^{-9}$ Torr. The cell is baked at 250 °C in the vacuum for several days. The glass ampule which contains Rb is broken in the vacuum and the Rb is chased to the cell by a heating

gun. After that, a small amount of nitrogen gas, used as a quench gas, is frozen into the cell. A $^3$He gas purified through the ballast and the liquid helium trap is transferred to the cell at last.

The construction of the whole system has been completed, and a preparation for the first cell production is now in progress.

References

1) N. R. Newbery et al.: *Phys. Rev.*, **A48**, 4411 (1993).

# Monitoring System of Single Turn Extraction in Cyclotrons

M. Kase, N. Inabe, I. Yokoyama, T. Kawama,* A. Goto, and Y. Yano

In order to get a high-quality beam from the RIKEN Ring Cyclotron (RRC), it is essential to realize the single turn extraction in the two cyclotrons (AVF cyclotron and RRC). As for RRC, the single turn extraction can be easily judged[1] in both cases of the injections from AVF cyclotron and RILAC. In this year, the system was extended, involving the monitoring of the single turn extraction in the AVF cyclotron. And the beam phase measurement becomes possible at the same time.

The principle of monitoring the single turn extraction is illustrated in Fig. 1. A beam bunch, which is accelerated in the extraction orbit of the AVF cyclotron, is divided into two parts by a septum electrode of a deflector in the case of the double turn extraction. These two fragments from one bunch appear in the extraction beam line, being separated by a time difference of $2 \times T_0$ ($T_0$ is the period of rf in the AVF cyclotron) because the harmonic number of the AVF cyclotron is 2. Normally the fragment is paired with a complementary fragment from the adjacent turn, forming one beam bunch apparently, although their energies are slightly different. However, at the transient time when a beam starts or stops, these fragments appear separately, as shown in Fig. 1.

The beams are stopped partially (500 ns duration) and periodically (about 10 kHz) by a beam chopper in the injection beam line of the AVF cyclotron. Since the beam loss due to this effect is less than 1%, this beam modulation can be continued all the time, even during an experiment. The beam chopper is capable of switching on and off the beam completely within the duration of $2 \times T_0$.[2] A time structure of chopped beam from cyclotrons has been continuously monitored with two sets of probes with a micro-channel plate (MCP),[1] one is at the location of beam line just after the AVF extraction, and the other just after the RRC extraction. The block diagram of electronics is shown in Fig. 2. Two sets of preset counters are newly employed as a delay generator up to 100 $\mu$s.

A typical time spectrum obtained at the extraction beam line of the AVF cyclotron is shown in Fig. 3. The small peaks appearing in the duration of beam-switched-off are mainly due to the multi-turn extraction. When the single turn extraction is completely realized, these small peaks disappear except those due

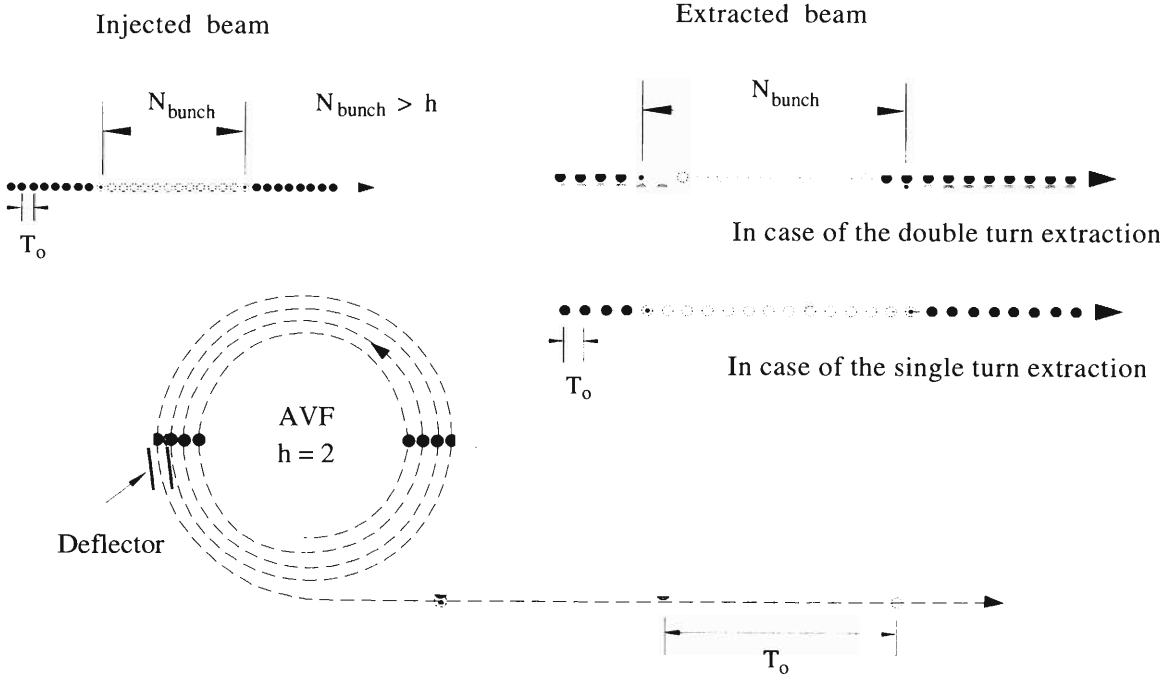


Fig. 1. A conceptional illustration of the principle of monitoring the extraction in the AVF cyclotron. The solid circles show the bunch of full beam, while smaller ones are partial bunch due to the transient effect of the chopping. The number of bunches, which are cut by the beam chopper, should be greater than the harmonic number (denoted by h) in this scheme.

* Sumitomo Heavy Industry Ltd.

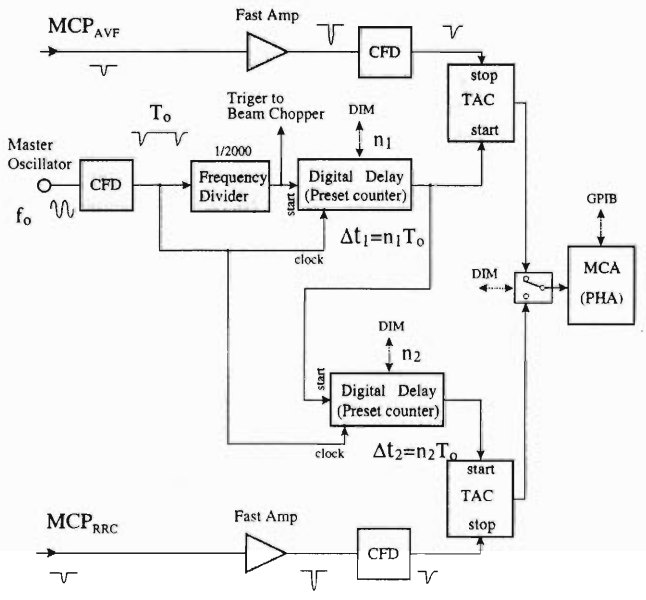


Fig. 2. A block diagram of electronics. Arrows with dotted line show the remote connection to a host computer (Mitsubishi M60/500). The numbers of $n_1$ and $n_2$ are the preset values to the counter used as a delay generator.

to the transient imperfection of the beam chopping. In this way, one can know quantitatively how the single turn extraction is realized inside the AVF cyclotron.

The turn numbers inside the cyclotrons are obtained from the values of delay time, $\Delta t_k = n_k T_0$ (k = 1 for the AVF and k = 2 for the RRC) in Fig. 2, if the delay time of signals in cables and the flight time of beam outside the cyclotrons are taken into consideration. The position instability of peaks in the spectrum

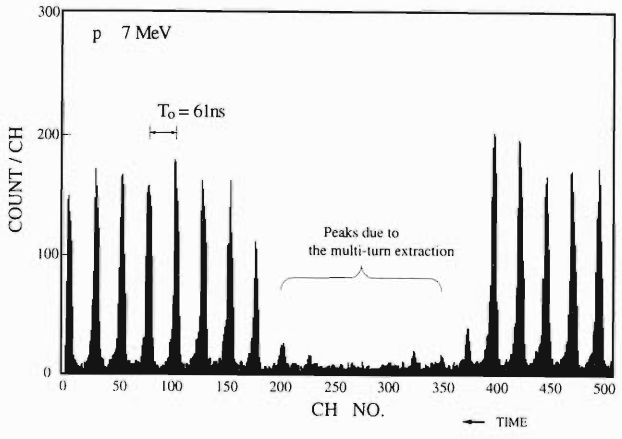


Fig. 3. An example of time spectrum of 7 MeV proton beam measured with MCP probe at the exit of the AVF cyclotron. The spectrum involving a moment of beam-off structure was found after searching an appropriate value for $n_1$ in Fig. 2, and was stored in an MCA for 1000s. The peaks, which appear every 61 ns, are corresponding to one beam bunch.

due to the drift of the delay-time was improved after the new digital delay generator was employed. It means that the measurements in the same system work also as a phase monitor which tells us how much magnetic fields drift inside the cyclotrons.[1)]

References

1) M. Kase, T. Kawama, T. Nakagawa, N. Inabe, I. Yokoyama, A. Goto, and Y. Yano: Proc. 9th Symp. on Accelerator Science and Technology, Tsukuba, Aug., p. 474 (1993).
2) N. Inabe et al.: *RIKEN Accel. Prog. Rep.*, **27**, 133 (1993).

# Study of the Beam Transport between the AVF and Ring Cyclotrons

N. Inabe, T. Honma, M. Kase, A. Goto, and Y. Yano

We studied the optics of the beam-transport line between the AVF and the Ring Cyclotrons (RRC) to improve efficiency of beam transmission in the line. Figure 1 shows the transport line. At first we measured an emittance of the beam extracted from the AVF Cyclotron (AVF). And then we searched one of the best solutions for the optics.

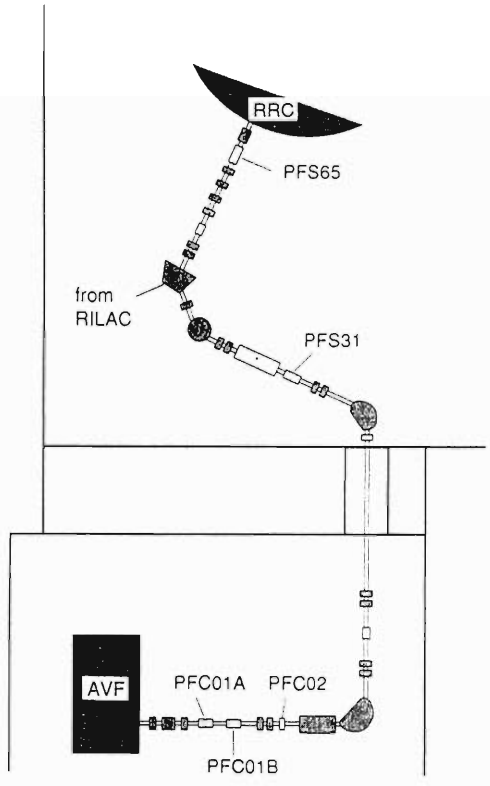


Fig. 1. Schematic drawing of the transport line between the AVF and the RRC.

Measurement of the emittance was performed with the beams of $^{22}Ne^{10+}$ 5.3 MeV/u and $^{14}N^{7+}$ 7.0 MeV/u. The emittance of transverse beam $\varepsilon$ is represented by using matrix elements of a $\sigma$ matrix as;

$$\varepsilon^2 = \sigma_{11}\sigma_{22} - \sigma_{12}{}^2. \quad (1)$$

The relation between $\sigma$-matrices after ($\sigma_o$) and before ($\sigma_i$) passing through the transport line is given by a transfer matrix of the transport line (R),

$$\sigma_o = R\sigma_i R^T. \quad (2)$$

Since $\sigma_{11}$ equals the square of a beam size, $\sigma_i$ can be obtained from the measurement of beam sizes corresponding to several transfer matrices and also the emittance can be calculated from Eq. (1). We changed the transfer matrix by two methods. One is performed by changing the field strength of the quadrupole magnet (Q-magnet) located just before a beam profile monitor. Another is done by changing a measuring point for the fixed field strength of all Q magnets in the line. By the former, the emittance of $^{22}Ne^{10+}$ 5.3 MeV/u beam was measured at PFC01A, PFS31, and PFS65. By the latter, that of $^{14}N^{7+}$ 7.0 MeV/u was measured at the straight section after the AVF using three profile monitors located at PFC01A, PFC01B, and PFC02. In the measurement we took care so that the intensity did not decrease with changing the strength of the Q-magnet.

The results of the measurements are shown in Table 1. For the horizontal direction of $^{22}Ne^{10+}$, the measured emittances at PFS31 and PFS65 are almost in good agreement with each other. The one from PFC01A is rather larger than those from PFS31 and PFS65. The reason might be due to two peaks of the profile clearly appearing at PFC01A since the beam was not extracted with single turn at that time. To check accuracy of the measured emittances at PFC01A and PFS31, we compared each beam size of the transport line calculated from the obtained $\sigma_i$ with the measured one. The beam sizes which were calculated using the result of PFS31 almost reproduced the measured ones but those from PFC01A did not. We also compared the emittance measured at the location of PFS31 with that of $^{14}N^{7+}$ beam. They were in good agreement with each other. From the analysis we conclude that the beam emittance extracted from the AVF is $\sim 7\pi$ mm*mrad in the horizontal plane. In the vertical plane the emittances of $^{22}Ne^{10+}$ beam measured at PFC01A, PFS31 and PFS65 are not in good agreement to one another. The emittance measured at PFC01A was close to that of $^{14}N^{7+}$ beam. For the vertical direction we also performed the same analysis as for the horizontal direction. The beam sizes calculated using the result of $^{14}N^{7+}$ beam almost reproduced the measured ones but those using the others did not reproduce so well. From the analysis we adopt $\sim 7\pi$ mm*mrad as the emittance of the vertical direction.

Table 1. Measured emittances.

| | | Emittance ($\pi$*mm*mrad) | |
|---|---|---|---|
| | Location | Horizontal | Vertical |
| $^{22}Ne^{10+}$ 5.3 MeV/u | PFC01A | 14 | 9 |
| | PFS31 | 7 | 15 |
| | PFS65 | 6.5 | 25 |
| $^{14}N^{7+}$ 7.0 MeV/u | | 7.9 | 7.6 |

With the measured emittance, we searched a solution for the optics of the transport line. Using the parameter searched, the transmission of the beam from PFS31 to PFS65 was raised up particularly and total transmission for the beam line amounted to more than 90%. Because the shape of the beam emittance depends on the way of extraction of the beam from the AVF, we must tune the AVF so as to extract the beam with almost the same shape of emittance. That is performed by checking the beam pattern of extracted region and the beam profile at PFC01A.

The obtained parameter is also applied to all kinds of beams and the transmission between the AVF and the RRC is more than 90% for all the beams.

# Development of a New Type of Single-Bunch Selector

N. Inabe, M. Kase, I. Yokoyama, A. Goto, and Y. Yano

A new type of single-bunch selector reported in the last progress report has been developed so as to have a high repetition rate.[1] Since the repetition rate of the old system (25 kHz) was limited by the talent of the switching module, we constructed a new switching module and raised the repetition rate up to 1 MHz. Figure 1 shows a schematic drawing of the circuit of the

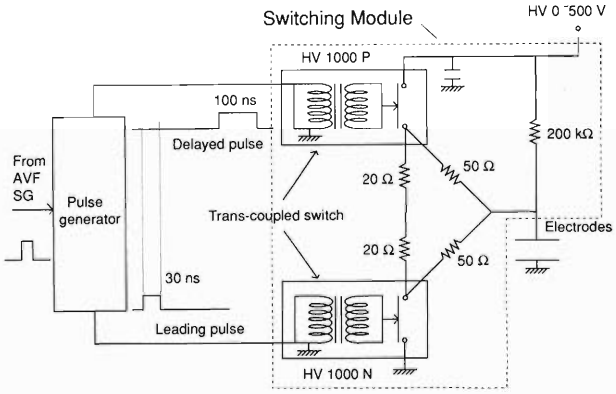


Fig. 1. Schematic drawing for the circuit of the new switching module.

switching module. As shown in Fig. 1, the switching module has two trans-coupled switches with repetition rate of 1 MHz (HV 1000 P, N), which are sold from DEI inc in USA. One is for the charge-up of the electrode and the other for the discharge. To avoid an electrical oscillation between two switches and the electrode, we inserted two 20 ohm resisters and two 50 ohm ones. Two pulses for the switches are made by a pulse generator located at upstream of the switching module. One is a leading pulse which is sent to the switch for discharge and the other is a delayed pulse which is sent to the one for charge. The difference of time when each pulse arrived at each switch corresponds to the duration of the chopped beam. Characteristics of the pulse made by the new switching module are summarized in Table 1. Although the voltage of the pulse is lower than that of the old one, it is high enough to make a single selection because the voltage to be needed is 500 V. Also the duration time is as short as that of the old one. From the properties it is shown that the new switching module can make a pure single bunched beam as the old one can. The system was also newly installed between the polarized ion source (PIS) and the AVF cyclotron (AVF).

Table 1. Characteristics of the pulse made by the new system.

| | |
|---|---|
| Voltage | 0–500 V (DC) |
| Repetition rate | $< 1$ MHz |
| Rise time | 15 ns |
| Duration time | 100–250 ns |

A performance study of the single-bunch selector was carried out for the 7.45 KeV $H_2^+$ beam from the PIS which was accelerated to 7 MeV/nucleon by the AVF with an RF frequency of 16.3 MHz and to 135 MeV/nucleon by the Ring Cyclotron (RRC) with an RF frequency of 32.6 MHz. The setup is shown in Fig. 2. A duration time during which the voltage between the electrodes was switched off was 150 ns. Voltage of the electrodes was 470 V. The variable delay connected with the switching module was adjusted so as to get the purest single bunched beam for the RRC. Time structures of the beam after the AVF and RRC were measured by using a time of flight (TOF) between a reduced RF signal and a timing signal of micro channel plates (MCP's) with a target.[2]

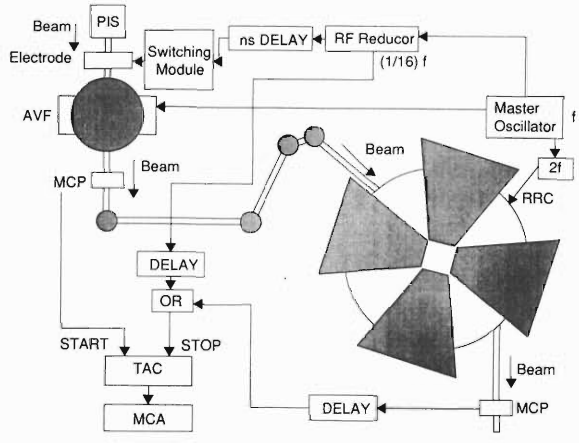


Fig. 2. Setup for a performance test of the single-bunch selector.

Figure 3 shows a typical example of the TOF spectrum of the AVF. The main peak in Fig. 3 is due to a single bunched beam to be extracted. The peak next to the main one is due to the next bunch of the main one. The existence of the other two peaks means that the same bunch inside the AVF cyclotron is extracted with two-turns. Production mechanism of those peaks is explained in Ref. 1. The result of the many peaks in the spectrum might be caused by the adjustment of the variable delay that is suitable to the RRC. In fact, using the system we obtained the single bunched beam as shown in Ref. 1 by adjustment of the variable delay for the AVF and by singleturn extraction from the AVF.

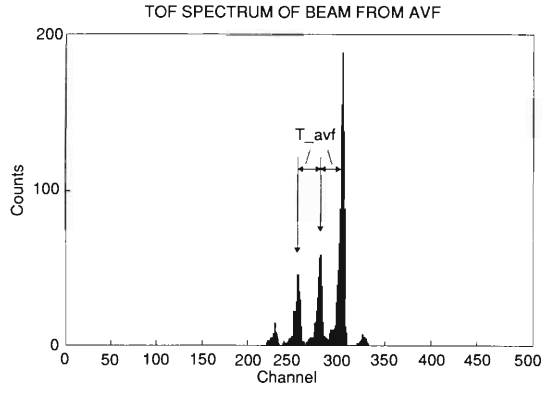


Fig. 3. An example of time spectra of the beam extracted from the AVF cyclotron. T_avf means the RF period of the AVF cyclotron.

Figure 4 shows a typical example of the TOF spectrum of the RRC. The main peak in Fig. 4 is made by the single bunched beam to be extracted. The peaks next to the main one are due to the next bunches of the main one. The two small peaks correspond to another turn of the RRC (right side) and that of the AVF (left side). The purity of the single bunched beam is ~80%.

Production mechanism of those peaks is explained in Fig. 5. As shown in Fig. 5, in principle, the other turn of the AVF gives a bad effect to the single bunched beam extracted from the RRC but the peak of the turn is not so strong. This might be due to bad transmission of the RRC for the turn.

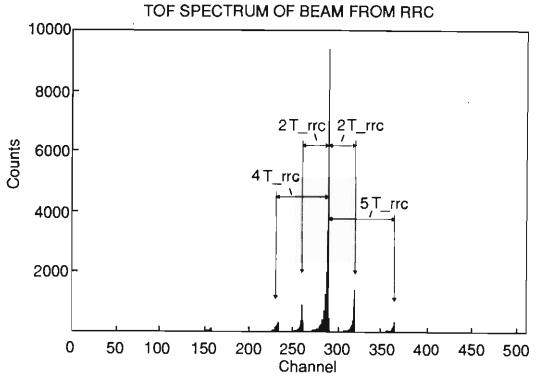


Fig. 4. An example of time spectra of the beam extracted from the RRC. T_rrc means the RF period of the RRC.

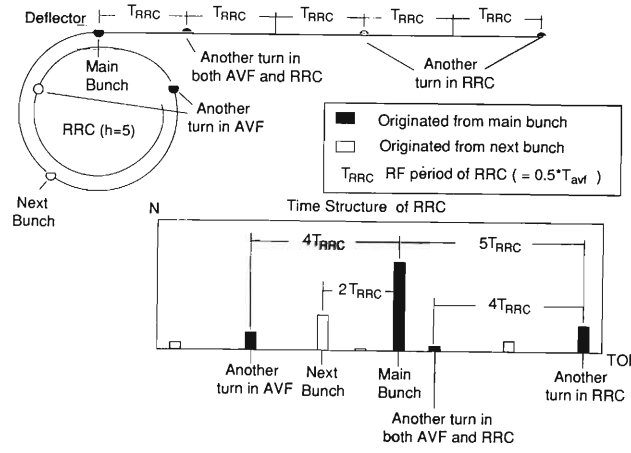


Fig. 5. Time structure of the beam from the RRC for two bunches with two-turns extraction in both the AVF and the RRC.

The value of the purity is large enough for usual experiments but not for those which need low background. The next step of the system is to get a purer single bunched beam. For the purpose it is planned for the frequency of the buncher located at upstream of the AVF to be 1.5 times as large as that of AVF.

References

1) N. Inabe et al.: *RIKEN Accel. Prog. Rep.*, **27**, 133 (1993).
2) T. Kawama et al.: *ibid.*, p. 135.

# Replacement of Computer for the RRC Control

M. Kase, A. Goto, and Y. Yano

The Ring Cyclotron (RRC), the AVF cyclotron, and the heavy ion linac (RILAC) have been controlled by means of a network of three mini-computers (Mitsubishi M60/500).[1] About 10 years have passed after the first installation of these computers, and now it becomes gradually difficult to continue a maintenance contract with a computer maker due to a shortage of spare parts of these computers. Thus we decided to change the computer#1 (the oldest one of the three) into a new one (Mitsubishi M60/AR), which is an upgraded machine of M60/500, without changing a basic architecture of the control system.

The computer#1, which was designed originally to be used for a program development, has been used for continuous monitoring, such as beam qualities, rf voltages and phases, temperatures at many points of the whole accelerator site, and also used for storage of these data in its memories. The computer#2 has been used for control of RILAC via a GPIB interface. The computer#3 has been a main control computer connected with the whole devices of the RRC and the AVF cyclotron via a DIM-CIM system through a CAMAC.[1]

The replacement was done in the following way; A new computer (M60/AR) was installed in a place of the computer#1 which was removed this time, and is used as the main control computer instead of the computer#3. The CAMAC system including a serial high way driver (SHD) board is unchanged. Man-machine interfaces at the control console, such as touch panels and graphic displays, are the same as before. All the control programs, which have been developed by RIKEN staffs, are still available in the new system. The computer#3 is used in turn instead of the computer#1, being also standby as a backup computer to the main control one. It can be connected back shortly, since old connection cables are kept remain under a floor of the control room. Some component parts of the computer#1 are stocked nearby as spare ones and will be used in case when some troubles occur with the old two computers in the future.

A comparison of performance of M60/500 and that of M60/AR is given in Table 1. The new system has two direct memory access (DMA) channels in order to lighten the main cpu load under the condition of multi-task processing. Since the new system supports the standard network, it is easily connected with other computers. The final configuration of the new control system is shown in Fig. 1.

Table 1. A comparison of the performance.

| | M60/500 | M60/AR |
|---|---|---|
| Processor number | 1 | 2 |
| Command speed | 3.7 MIPS | 9.7 MIPS |
| Main memory size | 5 MB | 32 MB |
| DMA channel | 0 | 2 |
| Disk memory size | 700 MB | 1.4 GB |

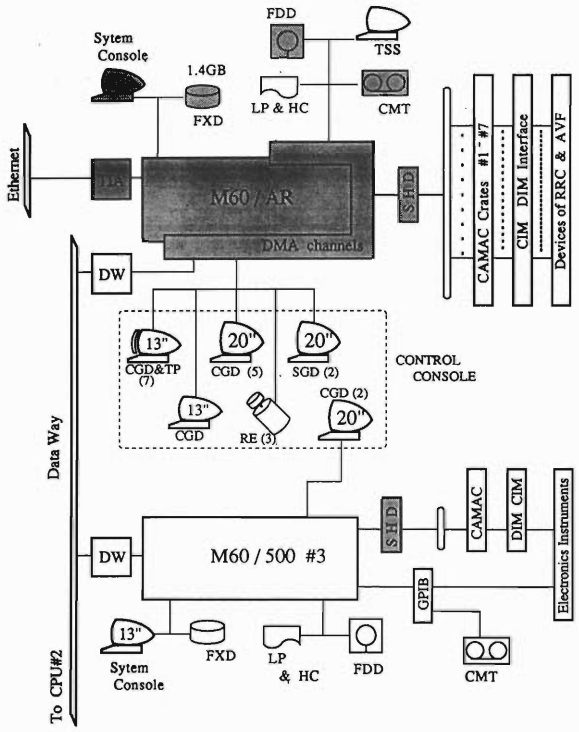


Fig. 1. The new control system of the RIKEN Ring Cyclotron and the AVF cyclotron. The shadowed parts are installed newly at this replacement. Figures in parentheses are the number of devices. FXD; fixed disc memory, FDD; floppy disc driver, CGD; color graphic display, TP; touch panel, RE; rotary encoder, PP; page printer, HC; hard copy, SHD; serial high way driver, CMT; cartridge magnetic tape, TSS; terminal, DW; data way controller.

The replacement of hardware was done during a shutdown period in this summer. The software installation was completed before the end of September. The final adjustment to improve the performance between the CAMAC system and the computer is now in progress.

References

1) T. Wada, J. Fujita, I. Yokoyama, T. Kambara, and H. Kamitsubo: *Sci. Papers I. P. C. R.*, **79**, 28 (1985).

# Construction of a New Injector System for RILAC

A. Goto, O. Kamigaito, Y. Miyazawa, M. Hemmi, N. Inabe, M. Kase, T. Nakagawa, T. Chiba, S. Kohara, and Y. Yano

A new injector system of RILAC is being constructed in order to increase beam intensities of heavy ions by one or two orders of magnitude. The system consists of a high-field, high-frquency ECR ion source, a variable frequency RFQ linac, and a beam transport system between them. Figure 1 shows a schematic drawing of the system. Details of each part are described in Refs. 1, 2, and 3, respectively.

Main characteristic features of the designed ECR ion source are as follows: (1) it is operational at 18 GHz, (2) it is of a single-stage type, (3) both of the axial mirror field and the radial hexapole field are high enough for not only the fundamental-frequency operation but also the twice-frequency operation, and (4) the plasma cathode method[4] is applied to it. The reason for adopting the single-stage type is that very high

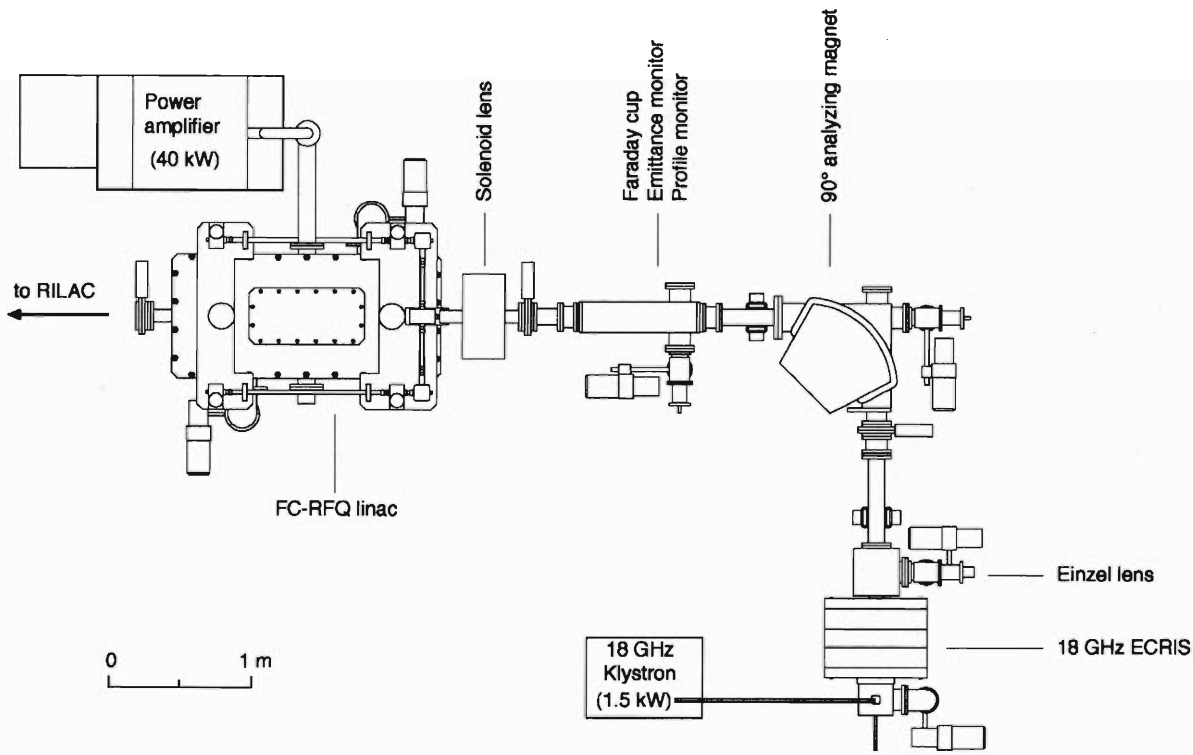


Fig. 1. Schematic drawing of a new injector system of RILAC.

charge states are not necessary for RILAC, and that this type has high performance for low charge states in contrast to a two-stage type. Beams are extracted with a maximum voltage of about 10 kV.

The RFQ linac is required to have the same function as that of the existing 450 kV Cockcroft-Walton terminal. It is designed to accelerate ions with a range of m/q = 7–28 up to 450 keV/q in the CW mode. The operational frequency should be varied between 17 MHz and 35 MHz, which is one of the most important problems to be solved in the design of the RFQ linac. We have adopted a "folded coaxial" RFQ (FC-RFQ) structure,[2] because it allows the cavity to be tunable in a wide range of frequencies and to be compact even in the low frequency region below 20 MHz. The FC-RFQ structure can also enables the intervane voltage to be flat enough to obtain high beam-transmission efficiency. A half-scaled model for the cold test was completed at the end of the last year and the measurements showed that the model had good performance in accordance with the design. The power losses are expected to be 6 kW at 17 MHz and 34 kW at 35 MHz.

The beam transport system between the ECR ion source and the FC-RFQ linac consists of an Einzel lens, a 90° bending magnet, and a solenoid magnet. This combination enables it to analyze beams with different m/q's and match the emittance of a selected beam to the acceptance of the FC-RFQ linac. Beam diagnostic

devices such as a Faraday cup, a beam profile monitor, and a beam emittance monitor will also be installed.

The new injector system is now being fabricated at the factory of SHI (Sumitomo Heavy Industries, Ltd) for completion by the spring of the next year. The beam test will be made at RIKEN before the installation on the due site of RILAC.

References


1) T. Nakagawa et al.: This report, p. 165.
2) O. Kamigaito et al.: This report, p. 168; O. Kamigaito, A. Goto, Y. Miyazawa, T. Chiba, M. Hemmi, M. Kase, and Y. Yano: *Jpn. J. Appl. Phys.*, **33**, L537 (1994).
3) N. Inabe et al.: This report, p. 166.
4) T. Nakagawa et al.: *Jpn. J. Appl. Phys.*, **32**, L1335 (1993).

# Design of RIKEN 18 GHz Electron Cyclotron Resonance Ion Source (ECRIS)

T. Nakagawa, T. Kageyama, A. Goto, N. Inabe, O. Kamigaito, M. Nagase, T. Chiba, M. Hemmi, M. Kase, Y. Miyazawa, E. Ikezawa, and Y. Yano

To increase the beam intensity of heavy ions accelerated by RILAC,[1] we have designed a new 18 GHz ECRIS. A schematic overview of the ECRIS is shown in Fig. 1.

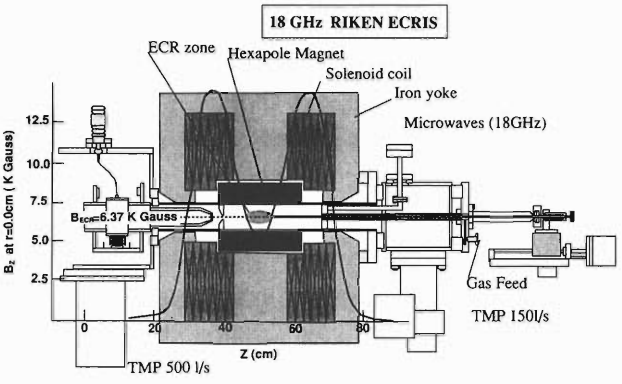


Fig. 1. Schematic drawing of the 18 GHz ECRIS and typical magnetic field distribution.

The axial confinement of the plasma is obtained by two solenoid coils which provide a magnetic mirror. The source is completely enclosed by an iron york in order to reduce the current of solenoid coils. The expected power consumption is about 90 kW. The coils are independently powered.

The mirror ratio has a nominal value of 2.7. In order to optimize the magnetic confinement of the plasma, we used the hexapole magnet structure proposed by Halbach.[2] The hexapole magnet consists of 24 segments made of Nd-Fe-B permanent magnets. The outer diameter (OD) and inner diameter (ID) are 180 and 80 mm, respectively. All of the segments are made of a material with high coercitivity (NEOMAX-40 Sumitomo Special Metals Co., LTD.). The design of the magnetic structure has been optimized by using the computer code PANDIRA. The field strength at the surface of the magnet is about 1.4 T. To protect the hexapole magnet from demagnetization by high temperature, a water cooled plasma-chamber with ID = 75 mm OD = 80 mm has been constructed. The water-cooled haxapole housing protects the permanent magnet from the high temperature caused by the solenoids.

We have chosen a microwave frequency of 18 GHz because it is the highest frequency that can be obatined by a commercially available klystron tube and applied for 2 $\omega_{ce}$ (electron cyclotron resonance frequency) mode operation.

The high vacuum of the plasma chamber is very important to produce the intense beam of highly charged ions.[3] This may be due to the effect of recombination of the ions. In the case of 18 GHz ECRIS, the plasma chamber is evacuated with the 500 and 150 l/s turbo molecular pumps. Using this pumping system, the ultimate vacuum of the plasma chamber will be of the order of $10^{-8}$ Torr.

In order to produce the highly charged ions from solid materials, the matrials are directly inserted into the plasma axially using a same method as described in Ref. 4.

To inject heavy ions into RILAC from the ECRIS, it will be connected with a new type variable energy RFQ[5] which is designed as an injector for RILAC.

References

1) M. Odera et al.: *Nucl. Instrum. Methods*, **227**, 187 (1984).
2) K. Halbach: *ibid.*, **187**, 109 (1981).
3) T. Nakagawa, T. Kageyama, M. Kase, A. Goto, and Y. Yano: *Jpn. J. Appl. Phys.*, **32**, 1335 (1993).
4) E. Ikezawa et al.: Proc. 8th Symp. on Accelerator Science and Technology, 1991, Saitama, p. 73 (1991).
5) O. Kamigaito et al.: This report, p. 168.

# Design of a Beam Transport Line between the 18 GHz ECRIS and the RFQ Linac

N. Inabe, M. Kase, O. Kamigaito, Y. Miyazawa, M. Hemmi, T. Chiba,
A. Goto, Y. Batygin, and Y. Yano

We designed a beam transport line between 18 GHz ECR ion source[1] and RFQ linac (RFQ)[2] that will be newly installed as a pre-injector of the RILAC. Figure 1 shows the transport line. In the design we required two conditions for the transportation of the beam. One is to separate a beam from the other unnecessary particles from the ion source and another is to match the emittance of the beam to the acceptance of the RFQ. From the conditions we separated the transport line into two sections: a beam analyzing section and a matching section. The beam analyzing section consists of a dipole magnet and drift spaces before and after it. In the section the end point is the analyzing point of the beam. The matching section consists of solenoid and drift spaces before and after it. The entrance of the section is the analyzing point and the exit the entrance of the RFQ. As shown in Fig. 1 the transport line has a beam diagnostic system such as a profile monitor, slits, and a Faraday cup around the analyzing point. Two vacuum pumps (350 l/s) are used. The designed vacuum pressure is less than $10^{-7}$ Torr.

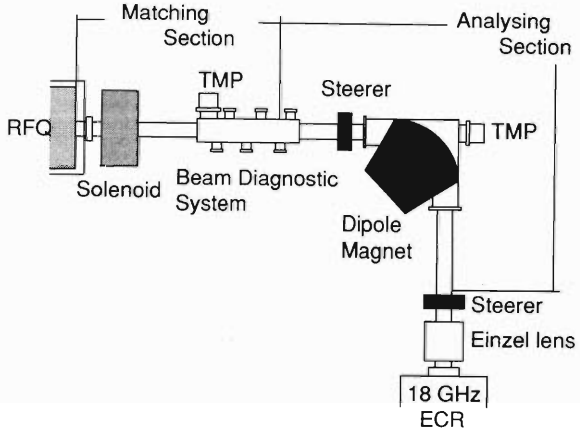


Fig. 1. Schematic drawing of the beam transport line between the 18 GHz ECR ion source and the RFQ linac.

For the search of the parameters such as drift lengths and strength of the solenoid we used the computer code TRANSPORT. The properties of the beam such as emittance, dispersion, and size was calculated by the code. In the calculation the emittance of the beam at the exit of the ion source was assumed to be a standard ellipse of $\pi$*5 mm*29.0 mrad and the momentum spread, $\Delta p/p$, to be 0. The half width of the beam of 5 mm corresponds to the radius of the extraction hole of the ion source. The object of the optics was chosen at the starting point of the analyzing section, since using another computer simulation code we confirmed that the shape of the emittance at this object point could be made to be the same as that from the ion source by locating an einzel lens after the ion source. The maximum magnetic rigidity was taken to be 76.13 kG*cm, which is the same as the designed value for the RFQ. In the cal-culation we did not take account of the space charge effect.

The parameters of the analyzing section such as drift lengths and edge angles of the dipole magnet were searched under the conditions of mass separation ($M/\Delta M$) > 100 and double focus at the analyzing point. For the dipole magnet we chose the same size as for the analyzing magnet between the 10 GHz ECR ion source and the AVF cyclotron (500 mm in radius, 80 mm in gap and 90° in bending angle). The reason for the choice is that the both maximum rigidities are similar to each other.

The parameters of the matching section such as strength and effective length of the solenoid and drift lengths were searched under the condition that the phase ellipses for the beam in both horizontal and vertical directions of the beam should lie into those of acceptance of the RFQ. As an additional condition we

Table 1. Designed parameters of the components in the beam transport line.

| | |
|---|---|
| **Distances** | |
| Object point ~ | |
| entrance of the dipole magnet | 1.1 m |
| Exit of the dipole magnet ~ | |
| analyzing point | 1.1 m |
| Analyzing point ~ | |
| entrance of the solenoid | 1.0 m |
| Exit of the solenoid ~ | |
| entrance of the RFQ linac | 0.37 m |
| **Magnets** | |
| Dipole | |
| Radius | 0.5 m |
| Bending angle | 90.0° |
| Maximum magnetic field | 1.6 kG |
| Edge angle (entrance and exit) | 28.7° |
| Gap | 80 mm |
| Solenoid | |
| Inner radius | 45 mm |
| Outer radius | 305 mm |
| Effective length | 0.25 m |
| Real length | 0.31 m |
| Maximum magnetic field | 6.3 kG |

required that the total lengths of the section should be as short as possible. The reason to choose the solenoid as a matching element is that the phase ellipses of the beam in the horizontal and vertical directions are similar at the entrance of the section and that the RFQ has the same acceptance in the both directions. Moreover it was because choice of the solenoid led the section to be compact. The magnetic field of the solenoid was calculated by the computer code POISSON. From the calculation we determined the real length of the solenoid for the required effective length and strength.

From the search we obtained the parameters of the transport line. The parameters are summarized in Table 1. The maximum designed fields of the dipole magnet and the solenoid have 10 $\sim$ 20% margin of the required maximum fields.

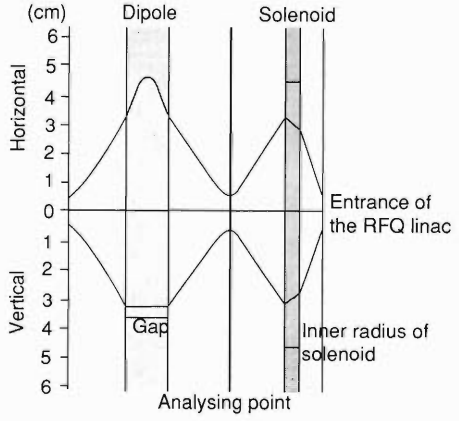


Fig. 2. Calculated envelope of the beam from the ECR ion source to the RFQ linac.

Figure 2 shows the envelope of the whole transport line. It is shown that the clearance of the beam for each aperture is large enough. The dispersion and magnification in the horizontal direction at the analyzing point are 2.20%/cm and $-0.98$, respectively. From the values of dispersion and magnification, $M/\Delta M$ is about 200 and it is large enough for the required one. Figure 3 shows the phase ellipses of the beam in the horizontal and vertical directions and the acceptance of the RFQ. As shown in Fig. 3, the ellipses of the beam are wrapped in those of acceptance of the RFQ and the matching between the emittance of the beam and the acceptance of the RFQ is very good.

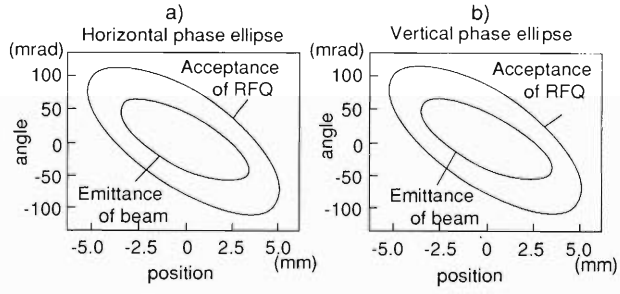


Fig. 3. Phase ellipses of emittance of the beam and the acceptance of the RFQ linac at the entrance of the RFQ linac: a) in the horizontal direction and b) in the vertical one.

## References

1) T. Nakagawa et al.: This report, p. 165.
2) O. Kamigaito et al.: This report, p. 168.

# Cold Model Test of the Variable Frequency RFQ Resonator

O. Kamigaito, A. Goto, Y. Miyazawa, T. Chiba, M. Hemmi, S. Kohara, M. Kase, and Y. Yano

Cold model test of the resonator of the variable frequency RFQ linac, designed as a new injector for RILAC, has been performed. This RFQ will accelerate ions with a range of $M/q$ = 7–28 to the final energy of 450 keV/$q$ in the cw mode, by varying the operational frequency from 17 MHz to 38 MHz. With the 18 GHz-ECRIS,[1] the RFQ injector is expected to greatly increase the intensity of the heavy ion beams for RILAC in the near future.

The RFQ resonator is based on the "folded-coaxial (FC)" structure.[2] This RFQ has the following distinct advantages. Firstly, the resonator can be made very compact even in the low frequency region below 20 MHz. Secondly, the operational frequency is changed widely with a movable shorting plate. Thirdly, the intervane voltage can be made flat enough to obtain high beam-transmission efficiency.

Figure 1 shows a schematic drawing of the RFQ resonator. Horizontal vanes are held by front and rear supports fixed on the base plate. Vertical vanes are fixed on the inner surfaces of a rectangular tube which surrounds the horizontal vanes. This tube is supported by four ceramic pillars placed on the base plate. A stem suspended from the ceiling plate is in electrical contact with the rectangular tube. A shorting plate placed around the stem can be moved vertically, which varies the resonant frequency. Radio-frequency power is fed into the resonator through the side wall by a capacitive feeder. A capacitive tuner is set on the opposite side wall and two capacitive pickup monitors are set on the base plate.

The resonator is separable into upper and lower parts, as shown in Fig. 1. The horizontal vanes and the rectangular tube with the vertical vanes are rigidly fixed inside the lower part. The upper part containing the stem and the shorting plate can be removed as an unit. This separable structure permits accurate alignment of the vanes and easy maintenance.

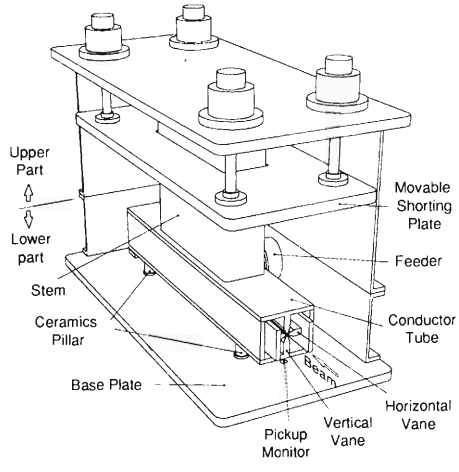


Fig. 1. Schematic drawing of the RFQ resonator. The size of the half-scale model is about 850 mm (L) × 350 mm (W) × 500 mm (H).

Figure 2 shows the schematic drawing of the magnetic flux of the fundamental mode. The flux surrounds the stem, rectangular tube and the horizontal vanes. The direction of the flux is reversed at the middle of the vanes, and the magnetic field vanishes there.

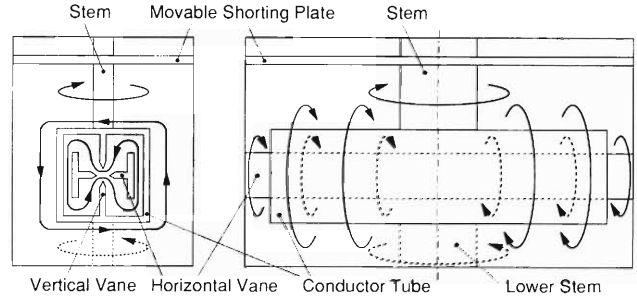


Fig. 2. Schematic drawing of the magnetic flux of the fundamental mode of the RFQ resonator. The lower stem is installed only in the high frequency operation.

In order to investigate the rf characteristics of the resonator, a half-scale model has been made of copper (C1100). The fabrication procedure for the real RFQ linac was also studied in the design of the model resonator. In the initial measurements, the vanes having a constant bore radius and the ceramic pillars made of Macor were used. The vanes have been aligned within the accuracy of 30 $\mu$m.

Figure 3 shows the measured resonant frequency of the fundamental mode along with the calculated values using the computer code MAFIA. The resonant frequency varies from 34.0 to 70.0 MHz by changing the position of the shorting plate by a stroke of 330 mm, which means that the actual operational frequency will range from 17.0 to 35.0 MHz. The resonant frequencies of the higher modes appear over 200 MHz, well separated from that of the fundamental mode.

Figure 4 shows the measured Q-values and the shunt impedances of the fundamental mode. The MAFIA calculations are also shown in the figure. The calculation overestimates the measured values by 30–50%. This is considered to result from the fact that the calculation does not realistically treat the roughness of the wall surface and the imperfectness of the electric contact. From these measurements, the power losses of the real RFQ linac are expected to be 6 kW at 17 MHz and 34 kW at 35 MHz.

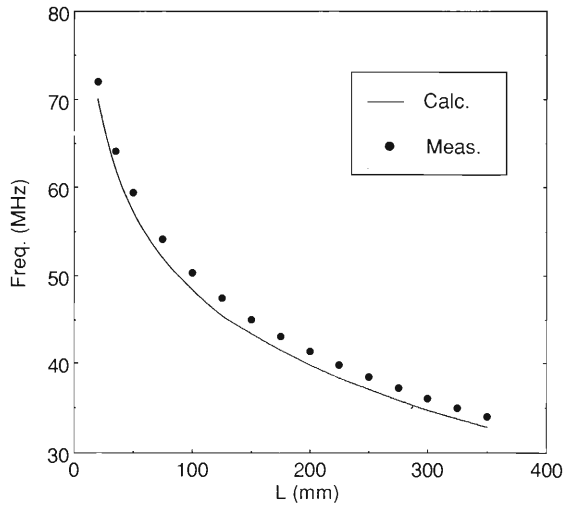


Fig. 3. Measured resonant frequencies (closed circles) and the values calculated using MAFIA (solid line) of the fundamental mode for the half-scale model. L denotes the distance in mm between the top surface of the rectangular tube and the bottom surface of the movable shorting plate.

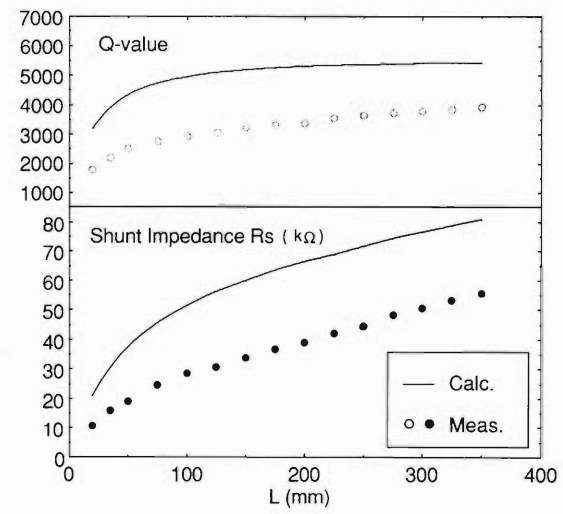


Fig. 4. Measured Q-values (open circles) and the shunt impedances (closed circles) of the half-scale model. The solid lines indicate the MAFIA calculations.

The intervane voltage distributions along the acceleration axis were measured with a perturbation method. They were found to be in good agreement with the MAFIA calculations. The imbalance among the intervane voltages in the four quadrants was ±2% at most.

Next, we replaced the un-modulated vanes with modulated ones and measured the rf characteristics. The modulated vanes have been fabricated by using the NC ball-end-mill machine within the accuracy of 30 $\mu$m. The resonant frequencies have risen up by about 1% and little change has been found in the Q-values and the shunt impedances. Ceramic materials were also examined by measuring the Q-values with pillars made of several types of $Al_2O_3$ and AlN being installed. At the present, ceramic pillars of $Al_2O_3$(Kyocera A479) are to be used in the real RFQ linac.

If we install an additional stem as shown in Fig. 2, the power losses can be reduced in the high frequency region above 35 MHz because the rf electric current is shared by the two stems. This lower stem is installed only in the high frequency operation. We have installed two kinds of lower stem in the half-scale model and measured the Q-values. As shown in Fig. 5, the operational frequency is restricted in the high frequency region but the Q-values are larger than those only with the upper stem. This result shows that the operational frequency can be extended to 38 MHz with the power loss of 34 kW.

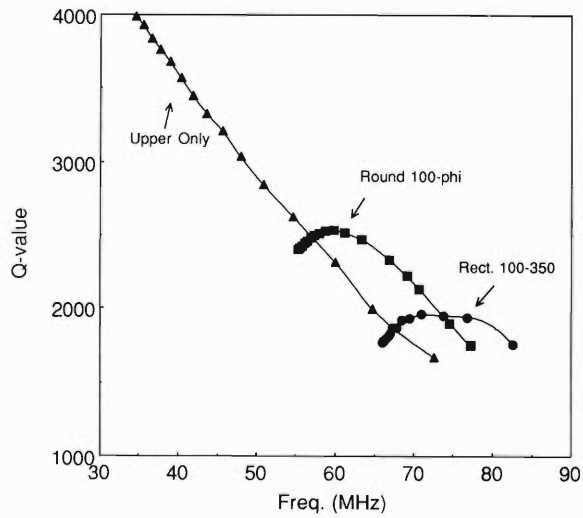


Fig. 5. Measured Q-values of the half-scale model of the RFQ resonator. The triangles are the Q-values using only the upper stem. The rectangles and the circles are the ones using lower stems of different shapes.

The design of the real RFQ linac is under progress by taking these results into account.

References

1) T. Nakagawa et al.: This report, p. 165.
2) O. Kamigaito, A. Goto, Y. Miyazawa, T. Chiba, M. Hemmi, M. Kase, and Y. Yano: *Jpn. J. Appl. Phys.*, **33**, L537 (1994).

# Hollow Beam Formation in the Extraction Region of ECRIS

Y. Batygin, A. Goto, and Y. Yano

Beam quality of a heavy ion accelerator complex is mostly defined by the extraction region of ion source where a space charge and a nonlinear external focusing field are essential. The extraction region of the 18 GHz ECR ion source which is under construction to upgrade RIKEN Accelerator Research Facility consists of an extraction electrode under the voltage of $U_{ext} = 10$ kV followed by a three-electrode Einzel lens (see Fig. 1). After passing the lens, the beam has to be focused into a spot with a diameter of 10 mm to be matched with the following transport system.

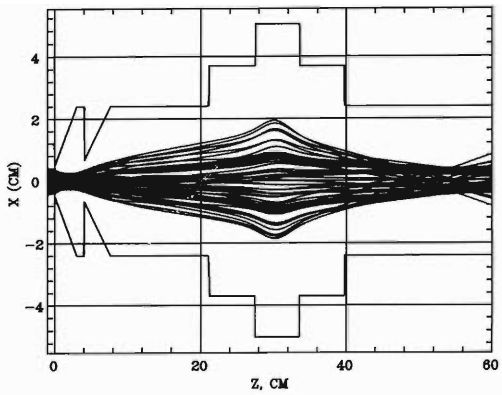


Fig. 1. Particle trajectories in the extraction region of the 18 GHz ECR ion source.

Numerical calculation of beam extraction was performed with the computer program BEAMPATH.[1] Ion trajectories start from a concave plasma emitting surface within the beam convergence angle $\theta$ defined by an aspect ratio R/d of extraction region and a ratio of beam perveance $P = I/U_{ext}^{3/2}$ to Child-Langmuir perveance $P_0 = (4\pi/9)\varepsilon_0(R^2/d^2)(2q/m)^{1/2}$ of one dimensional diode:[2]

$$\theta = -0.625\frac{R}{d}\left(\frac{P}{P_0} - 1\right). \quad (1)$$

For the expected value of beam current I = 100 $\mu$A of $Ar^{+5}$ the flow of particles is not space charge dominated and therefore initial convergence of the beam $\theta = -0.075$ is mostly defined by the focusing properties of extraction region.

The value of normalized beam emittance $\varepsilon$ is defined by the magnetic field fulfilling the ECR resonance condition $2\omega_L = \omega_{RF}$ and ion temperature $T_i$ due to ionization processes in plasma:

$$\varepsilon = 2R\sqrt{\frac{kT_i}{mc^2} + \left[\frac{\omega_L R}{2c}\right]^2}, \quad (2)$$

where $k = 8.617 \times 10^{-5}$ eV·K$^{-1}$ is Boltzmann's constant and $\omega_L = qB/2m$ is Larmor's frequency. For the considered case of the 18 GHz ECR ion source the resonant value of magnetic field is B = 0.637 T. The normalized beam emittance of an $Ar^{+5}$ beam with the temperature $kT_i = 3$ eV is:

$$\varepsilon = 2\times5\times10^{-3}\times\sqrt{0.8\times10^{-10} + 10^{-9}} = 3.3\times10^{-7}\pi \text{ m rad}. \quad (3)$$

The beam emittance is mostly defined by the value of magnetic field.

Particle trajectories obey the equations of motion derived from a single particle Hamiltonian:

$$H = \frac{1}{2m}\left[p_r^2 + \left(\frac{P_\theta}{r} - qA_\theta\right)^2 + p_z^2\right] + q(U_f + U_c), \quad (4)$$

where $p_r$, $P_\theta$ and $p_z$ are components of momentum of the particle, $U_f$ is a potential of the focusing field, $U_c$ is a space charge potential of the beam and $A_\theta = Br/2$ is a vector potential of the magnetic field. From computer simulation of the beam extraction problem in the ECR ion source it follows that the beam can obtain hollow structure in the time of crossover (see Fig. 2). The same phenomenon was observed in high perveance electron guns[3] and under focusing of an electron beam

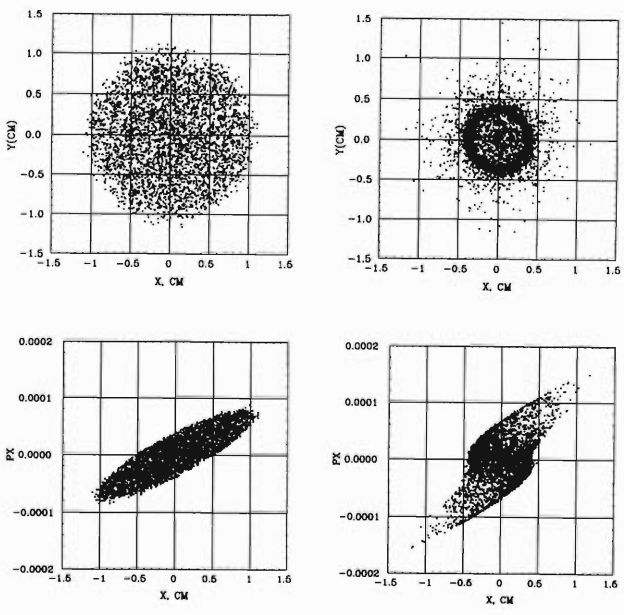


Fig. 2. Cross section of the beam (top) and phase space projections of particles (bottom) at z = 16 cm (left column) and at z = 60 cm (right column).

by short solenoid lenses with large aberrations.[4] For more details, let us consider the following analytical model.

The particles are born in the magnetic field of ECR ion source, hence every particle has non-zero value of azimuthal component of canonical momentum:

$$P_\theta = q\, B_z \frac{r^2}{2}. \tag{5}$$

After the solenoid the particles pass through the focusing lens and then move in a drift space. Electric field of the lens provides focusing which consists of a linear term G and higher order terms. We restrict our consideration to the first nonlinear term of electric field $G_3$. The transverse equation of motion of a particle in this region is given by

$$\frac{d^2r}{dt^2} = \frac{P_\theta^2}{m^2 r^3} - \frac{q}{m}[G(z)\, r + G_3(z)\, r^3 + \ldots]. \tag{6}$$

We assume the thin lens approximation which means that the length of the lens is small in comparison to the focal length. Therefore the radius of particle $r_o$ is not changed during the time of passing through the lens $t_1$. Equation (6) can be integrated to obtain the relationship between the initial and the final radii of particle in the drift region:

$$r^2 = r_0^2\{[1 - f(r_0)\tau]^2 + \tau^2\}, \tag{7}$$

where $\tau = \omega_L t$ is a dimensionless time of particle drift and the following notations are used:

$$\begin{aligned} &f(r_0) = (1 + \delta\, r_0^2)\tau_1;\ \delta = \frac{G_3}{G - \frac{m}{q}\omega_L^2}; \\ &\tau_1 = \left(\frac{\frac{q}{m}G}{\omega_L^2} - 1\right) t_1 \omega_L. \end{aligned} \tag{8}$$

To find the beam density redistribution let us assume that the number of particles dN inside a thin ring (r, r + dr) is constant during the drift of the beam, hence the particle density $\rho(r) = dN/(2\pi r dr)$ at any z is connected with the initial density $\rho(r_0)$ by the equation $\rho(r)dr^2 = \rho(r_0)dr_0^2$ or:

$$\rho(r) = \rho(r_0)\frac{1}{\tau^2 + 2\, r_0^2\, \tau\, \tau_1 \delta\, (\tau\, f - 1) + (\tau\, f - 1)^2}. \tag{9}$$

From this relationship it follows that changing of the beam profile is observed when a nonlinear term of the focusing field is not zero ($\delta \neq 0$). The linear focusing lens ($\delta = 0$) conserves the beam profile and changes only sizes of the beam. Introducing the nonlinear component of focusing field results in beam intensity redistribution according to the above formula and finally in hollow beam formation.

The hollow beam profile formation can be understood from the fact that spherical aberration of an electrostatic lens always increases focusing of particles in comparison with the ideal linear focusing.[5] As a sequence the peripheral particles in the drift region move faster to the axis than the inner beam particles. It results in a most populated boundary of the compressed beam than the core of the beam at the point of crossover.

Hollow beam formation is accompanied by emittance growth of the beam due to nonlinearity of a focusing lens. In the considered case the effective root-mean-square emittance

$$\varepsilon = 4\sqrt{< x^2 >< P_x^2 > - < xP_x >^2} \tag{10}$$

is increased by 1.3 times (see Fig. 2). For keeping the quality of the beam obtained from an ion source the nonlinearity of the focusing lenses have to be minimized.

References


1) Y. Batygin: Proc. EPAC92, Berlin, p. 822 (1992).
2) J. Kim, J. Whealton, and G. Schiling: *J. Appl. Phys.*, **49**, 517 (1978).
3) M. Reiser: Theory and Design of Charged Particle Beams, Wiley, New York (1994).
4) P. Loschialpo et al.: *J. Appl. Phys.*, **57**, 10 (1985).
5) J. D. Lawson: The Physics of Charged Particle Beams, Clarendon Press, Oxford (1977).

# Beam Dynamics Study in Variable Frequency RFQ Linac for RILAC

Y. Batygin, A. Goto, O. Kamigaito, and Y. Yano

An RFQ linac is characterized by the high transmission efficiency of particles and a large value of transversal acceptance which allows us to use it for acceleration of charged particle beams with high current and low initial energy. The RFQ structure designed for upgrading the RIKEN Linear Accelerator (RILAC)[1] is aimed to accelerate ions in a large range of charge to mass q/m ratio. Acceleration of different kinds of ions in the structure with a given value of intervane voltage U is performed by the change of operational frequency f and energy W of the beam fulfilling the conditions of invariance of acceleration gradient and geometry of the channel:

$$\frac{\sqrt{W}}{f} = \text{const}; \quad \frac{q}{m}\frac{U}{f^2} = \text{const}. \tag{1}$$

Latest study of $H^-$ beam dynamics in Ground Test Accelerator[2] under a space charge dominated regime shows that the transmission efficiency observed in experiment was significantly lower than it was expected from calculations (73% instead of 90% under the beam current of 37 mA). Possible sources for it were found to be higher order terms in RFQ potential and image charges. The purpose of this work is to examine how the transmission efficiency and other beam parameters are influenced by different representation of the designed RFQ field in the case of two lowest-order RFQ terms both neglecting space charge and under a high value of beam current including image forces. Multipole effects of RFQ potential can be investigated after choice of an exact shape of electrodes.

Beam dynamics in RFQ accelerator is studied using the general-purpose particle-in-cell code BEAMPATH.[3] The beam is represented as a collection of a large number of modeling particles (macro particles). The problem is solved in a right-hand Cartesian coordinate system (xyz). Particle trajectories obey the equations of motion followed from a single particle Hamiltonian:

$$\dot{\vec{p}} = -\frac{\partial H}{\partial \vec{r}}; \quad \dot{\vec{r}} = \frac{\partial H}{\partial \vec{p}}$$
$$H = \frac{1}{2m}(p_x^2 + p_y^2 + p_z^2) + q(U_{RFQ} + U_c) \tag{2}$$

where $\vec{p} = (p_x, p_y, p_z)$ is a momentum of the particle, $\vec{r} = (x, y, z)$ is a radius-vector of the particle, $U_{RFQ}$ is a potential of the radio frequency quadrupole structure, $U_c$ is a space charge potential of the beam. For integration of the equations of motion the second order method is used:

$$\vec{P}_{ISTEP+1/2} = \vec{P}_{ISTEP-1/2} + \vec{E}_{ISTEP}{}^{*}\,DT$$
$$\vec{r}_{ISTEP+1} = \vec{r}_{ISTEP} + \vec{v}_{ISTEP+1/2}{}^{*}\,DT. \tag{3}$$

The electric potential of the RFQ structure is given by the expression:[4]

$$U_{RFQ} = -\frac{U}{2}\left[\chi\left(\frac{x^2 - y^2}{a^2}\right) + \frac{4T}{\pi}I_o(kr)\sin(kz)\right] \cdot \sin(2\pi ft + \varphi_o) \tag{4}$$

where $\chi$ and T are focusing and acceleration efficiency respectively, and $k = 2\pi/\beta\lambda$ is a wave number.

Space charge field of the beam is calculated at each time step from the Poisson's equation in the system of coordinates, moving with the bunch:

$$\frac{\partial^2 U_c}{\partial x^2} + \frac{\partial^2 U_c}{\partial y^2} + \frac{\partial^2 U_c}{\partial z^2} = -\frac{\rho(x, y, z)}{\varepsilon_o}. \tag{5}$$

The Dirichlet boundary conditions for potential $U_c$ are imposed on the surface of an infinite pipe and periodic conditions in longitudinal direction are assumed. The region occupied by the bunch of particles is divided into uniform rectangular meshes of dimension NX·NY·NZ. Charge of every particle is distributed among the nearest eight nodes inversely proportional to the distance from particle to each node. For obtaining a solution of Poisson's equation the space charge density of the beam and unknown potential functions are represented as Fourier series:

$$U_{ijk} = \sum_{u=1}^{NX-1}\sum_{v=1}^{NY-1}\sum_{w=0}^{\frac{NZ}{2}-1}\left\{\left[\widetilde{U^{(c)}_{uvw}}\cos\left(\frac{2\pi wk}{NZ}\right) + \widetilde{U^{(s)}_{uvw}}\sin\left(\frac{2\pi wk}{NZ}\right)\right]\cdot\sin\left(\frac{\pi ui}{NX}\right)\cdot\sin\left(\frac{\pi vj}{NY}\right)\right\} \tag{6}$$

analogously for $\rho$ (x,y,z). Calculation of series (6) is performed using the Fast Fourier Transformation (FFT) method. Space charge and potential expansion coefficients are connected by an algebraic relationship followed from Poisson's equation:

$$\widetilde{U^{(c,s)}_{uvw}} = \left[\left(\frac{\pi u}{a}\right)^2 + \left(\frac{\pi v}{a}\right)^2 + \left(\frac{2\pi w}{\beta\lambda}\right)^2\right]^{-1} \widetilde{\rho^{(c,s)}_{uvw}} \tag{7}$$

which gives the solution of the space charge problem. Parameters of the numerical model used in simulation

Table 1. Parameters of the numerical model.

| | |
|---|---|
| Number of macroparticles | $10^4$ |
| Spatial grid NX·NY·NZ | $64 \times 64 \times 256$ |
| CPU storage requirement | 8 MBt |
| Integration step DT·f | 1/40 |
| Total number of integration steps | 1600 |
| CPU time (for VAX Alpha): | |
| I = 0 | 10 min. |
| I = 1 mA | 535 min. |

are listed in Table 1.

Four different types of RFQ field representation were compared in calculations: (i) linear variation of acceleration efficiency T, focusing efficiency $\chi$ and aperture of the channel a along the structure (PARMTEQ - type field[5]); (ii) a step-wise function of above parameters assuming the values of $\langle a_i \rangle = 0.5(a_{i-1} + a_i)$ and $\langle T_i \rangle = 0.5(T_{i-1} + T_i)$ equal to mean values over each cell; (iii) a step-wise function of parameters assuming the values of $\langle a_i \rangle = 0.5(a_{i-1} + a_i)$ and $\langle m_i \rangle = 0.5(m_{i-1} + m_i)$ equal to mean values over each cell; (iv) a step-wise function assuming all parameters are equal to the designed values at the end of each cell $T_i$, $\chi_i$, $a_i$.

Table 2. Beam parameters in RFQ structure. (A/Z = 5, f = 40 MHz)

| RFQ field approximation: | Linear (PARMTEQ-type) | | Step-wise ($\langle a_i \rangle$,$\langle T_i \rangle$) | | Step-wise ($\langle a_i \rangle$,$\langle m_i \rangle$) | | Step-wise ($T_i$,$\chi_i$,$a_i$) | |
|---|---|---|---|---|---|---|---|---|
| | I = 0 | I=1 mA | I = 0 | I=1 mA | I = 0 | I=1 mA | I = 0 | I=1 mA |
| Transmission efficiency, | 0.94 | 0.87 | 0.94 | 0.86 | 0.92 | 0.78 | 0.86 | 0.70 |
| Initial emittance $\pi$ mm mrad | 0.3 | 0.3 | 0.3 | 0.3 | 0.3 | 0.3 | 0.3 | 0.3 |
| Final emittance, $\pi$ mm mrad | 0.36 | 0.40 | 0.35 | 0.39 | 0.39 | 0.44 | 0.42 | 0.45 |
| Energy spread dW/W | 0.034 | 0.023 | 0.034 | 0.025 | 0.034 | 0.024 | 0.023 | 0.018 |
| Bunch length | 36° | 28° | 30° | 30° | 31° | 24° | 50° | 38° |

In Table 2 the results of simulation of the beam with A/Z = 5 are presented. The value of transmission efficiency obtained with a linear change of RFQ field along the structure agrees well with PARMTEQ prediction (94% for zero beam current and 90% for I = 1 mA). The step function of RFQ field representation gives smaller values of transmission efficiency especially for the space charge dominated regime.

Most of the particle losses are observed in transverse directions in the region between buncher and accelerating section. This region is characterized by a sharp increase of electrode modulation which results in a quick change of acceleration gradient along the structure and non adiabatic oscillation of particles. Small changes of parameters T, $\chi$ due to different representation of RFQ field results in deviation in synchronous phase of the bunch and mismatch of the beam with the channel. Beam losses in the longitudinal direction are much smaller (typically 2% for zero beam current and 4% for beam current I = 1 mA).

Further optimization of the acceleration structure is required to improve the beam transmission efficiency and to reduce the transverse beam emittance growth in RFQ linac.

References


1) O. Kamigaito et al.: This report, p. 168.
2) O. R. Sander et al.: Performance Report on the Ground Test Accelerator RFQ, presented at LINAC94, Tsukuba, Abstracts of LINAC94, p. 69 (1994).
3) Y. Batygin: Proc. EPAC92, Berlin, F.R.G., p. 822 (1992).
4) I. M. Kapchinsky: Theory of Resonance Linear Accelerators, Harwood, New York, U.S.A. (1985).
5) PARMTEQ code, Los Alamos National Laboratory.

# Construction of the RIKEN-RAL Muon Facility

K. Nagamine, T. Matsuzaki, K. Ishida, I. Watanabe, and R. Kadono

The construction of the RIKEN muon facility at Rutherford Appleton Laboratory (RAL) which was started in 1990 came to the final completion stage at the end of 1993. The first beam is scheduled in the fall of 1994.†

The rapid-cycling, high intensity proton synchrotron of the ISIS accelerator of Rutherford Appleton Laboratory (RAL), which was constructed for a spallation neutron source, is most suited for the pulsed muon generation. The ISIS can produce 800 MeV protons in a double pulse time structure (70 ns width, 340 ns separation and 50 Hz repetition) at an average current of 170 $\mu$A.

The final form of the RIKEN-RAL muon facility is shown in Fig. 1 which is almost identical to the original design proposed in 1990. The high intensity protons which have the double pulse time structure produce pions which are, after momentum selection, injected into a 5.5 m long, 12 cm bore and 5 T superconducting solenoid. During the passage in the solenoid field, intense pulsed muons are produced via pion decay in flight. The double pulse structure of the muons which is inconvenient to most of the muon science experiments is changed into two beams of a single pulse structure by a magnetic kicker system, each of which is fed into a separate experimental part (port 3 and port 1 or port 2).

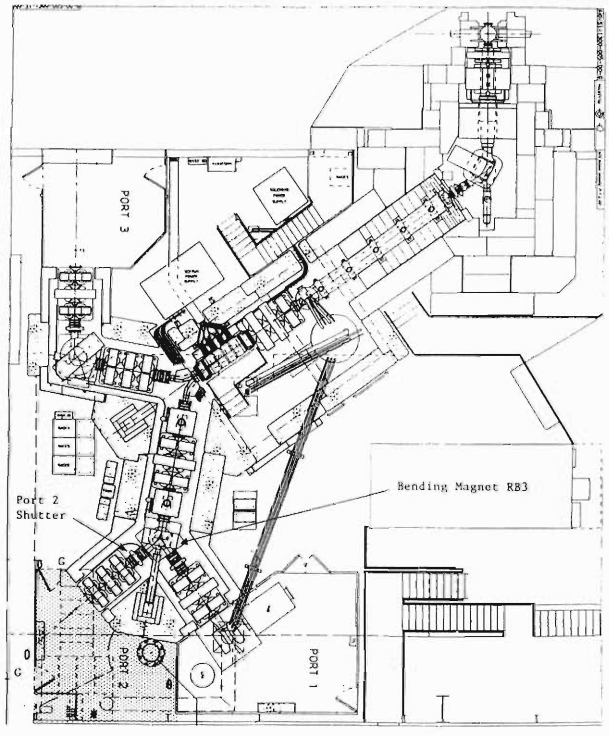


Fig. 1. Schematic layout of RIKEN muon facility at RAL.

In the fall of 1993, the superconducting solenoid and associated supercritical He cooling system was completed at the final location of the site. As described separately, the pulsed magnetic kicker system was completed in March 1994. The rest of the facility inculding the septum magnet placed after the kicker, dc separator, etc. were all completed in the spring of 1994. Various installation works including services and cablings will be completed in the summer of 1994.

The expected muon intensity is shown in Fig. 2, showing the world strongest pulsed muon facility to be realized at the RIKEN-RAL muon facility.

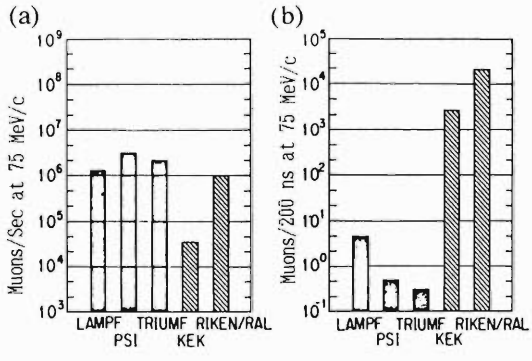


Fig. 2. Comparison of muon intencity at world-wide facilities; (a) average integrated intensity per sec and (b) instanteneous muon intensity.

† Note added in proof. The first beam was successfully generated on Nov. 9, 1994 with a confirmation of the achievement of expected intensity and quality.

# Optics Design for the RIKEN-RAL Muon Channel

K. Ishida, K. Nagamine, T. Matsuzaki, I. Watanabe, and G. H. Eaton*

RIKEN is constructing a high intensity pulsed muon beam channel at the ISIS facility of Rutherford Appleton Laboratory (RAL).[1] There, a rapid cycle proton syncrotron (800 MeV, 50 Hz) of high intensity (200 $\mu$A) has been used mainly for a spallation neutron source. Our muon channel will take the pions generated from the intermediate target placed upstream of the main target. As the best beam channel for the negative muon production, we have adopted the beam channel with a decay section of superconducting solenoid like PSI or UTMSL/KEK.[2,3]

The muon beam channel consists of four main parts, namely, a pion production target, a pion injection system, a solenoid decay section, and a muon extraction system. Muons will be delivered to two of the three experimental ports simultaneously (port 3 and port 1 or port 2).[1]

(1) The pion production target is a 10 mm thick graphite. The number of generated pions $N_\pi$ is expressed as

$$
\begin{aligned}
N_\pi &= N_C \times I_p \times d^2\sigma/d\Omega dp \times \Delta\Omega\, \Delta p \\
I_p &= 1.25 \times 10^{15}/\mathrm{sec}\ (200\ \mu\mathrm{A}) \\
N_C &= 6 \times 10^{23}/\mathrm{mol} / 12\ \mathrm{g/mol} \times 2.25\ \mathrm{g/cm^2} \\
&= 1.12 \times 10^{23}/\mathrm{cm^2} \\
&\quad (10\ \mathrm{mm} = 2.25\ \mathrm{g/cm^2} \\
&\qquad \text{thick carbon target}) \\
d^2\sigma/d\Omega dp &= (d^2\sigma/d\Omega dE_\pi)(dE_\pi/dp),
\end{aligned}
$$

where $I_p$ is the proton beam intensity, $N_C$ is the number of carbon nuclei in the target, and $d^2\sigma/d\Omega dE_\pi$ is the differential pion production cross section at 90 degrees to the proton beam. The pion production cross section was taken from the data of LAMPF (730 MeV).[4] Some enhancement of the cross section may be expected at 800 MeV. Typical number of generated pions was estimated to be $1.3 \times 10^8$/sec in a phase space of 100 mr $\times$ 100 mr and a momentum width of 121 MeV/c $\pm$ 5%.

(2) The pion injection system consists of two quadrupoles and a bending magnet to select the pion momentum. It is designed to have an acceptance of $\Delta\Omega = 75$ msr and $\Delta p = 10\%$.

(3) In the solenoid decay section the solenoid is used for confining the muons produced from the decay of the pions in the solenoid. The muons may be produced in any direction and at any place along the solenoid. With the help of the solenoid, the exit of the solenoid can be considered as a muon source.

(4) The muon extraction system is essentially a QQQ-B-QQQ-B-QQQ system, where Q is a quadrupole magnet and B a bending magnet. In Fig. 1 is shown the typical beam envelope in the muon extraction system for port 2. Each triplet quadrupole works as a lens, and the bending magnets are placed at the two nodes. Additionally, a kicker system[5] is placed in the straight section after the first triplet (QQQ). Also two DC separators with cross field coils were installed to remove positrons and electrons in the beam.

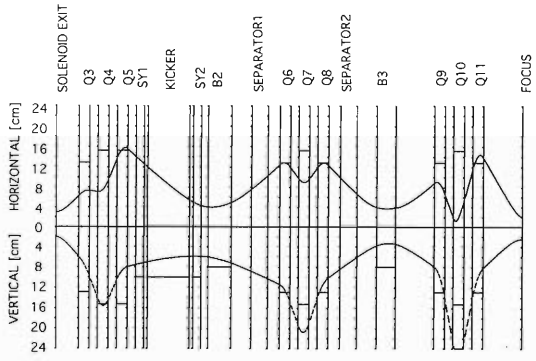


Fig. 1. Beam envelope in the extraction system for port 2. The initial phase ellipse is $\Delta x = \pm 30$ mm, $\Delta x' = \pm 80$ mr, $\Delta y = \pm 20$ mm, $\Delta y' = \pm 80$ mr, $\Delta p = \pm 5\%$.

The expected intensities of the muon beam for various momenta were calculated and are shown in Fig. 2. The first muon beam was succesfully produced in 9th November of 1994. A detailed beam tuning is now in progress.

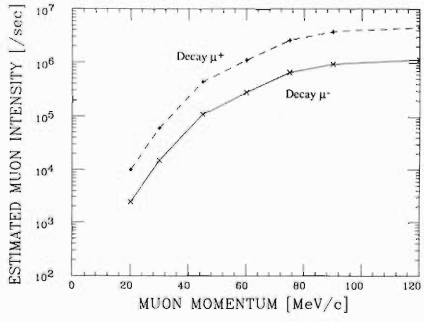


Fig. 2. Expected muon beam intensity for the RIKEN Muon Channel.

References

1) K. Nagamine et al.: This report, p. 174.
2) G. Vecsey: SIN Report, PR-75-002 (1973).
3) K. Nagamine: *Hyperfine Interact.*, **8**, 787 (1981).
4) D. R. F. Cochran et al.: *Phys. Rev.*, **D6**, 3085 (1972).
5) I. Watanabe et al.: This report, p. 176.

* Rutherford Appleton Laboratory

# Development of a Pulsed Kicker Magnet for the RIKEN-RAL Muon Beam Line

I. Watanabe, K. Ishida, T. Matsuzaki, K. Nagamine, and E. G. Sandels

A RIKEN Muon Beam Facility is being constructed at Rutherford-Appleton Laboratory (RAL) in UK.[1] Intense double pulsed muon beams which have wide momentum from 20 MeV/c to 120 MeV/c will become available at the new RIKEN facility. The separation of the double pulse is about 340 nsec from peak to peak and the width of each single pulse is about 70 nsec with the repetition rate of 50 Hz. The RIKEN muon facility consists of a pion injection system, a superconducting solenoid magnet, a muon extraction system and three muon experimental areas.[1] A fast pulsed kicker magnet is installed in the muon extraction system. In case of the low momentum beam, the double pulsed muon beam is separated by the kicker magnet and each single muon pulse is delivered to the two muon experimental areas simultaneously. The first muon pulse passes through the kicker magnet without magnetic field and the second pulse is deflected by the kicker magnetic field. To achieve a good separation of the muon pulse, the kicker magnetic field should be established within 250 nsec pulse separation time by the pulsed high current. In this paper the development of the fast kicker magnet is reported.

Figure 1 shows the electrical circuit of the kicker system. The kicker system consists of a PFN circuit, a fast switching thyratron, power cables and the magnet. The PFN circuit consists of 18 sections of the combination of capacitors and coils, and has a characteristic impedance of 6.73 Ω. The 7-coaxial cables with 50 Ω impedance are used in parallel. The thyratron is CX1725A (EEV, UK), and has a standing voltage of 70 kV. Both of the PFN circuit and the thyratron are cooled by air. The PFN is discharged by the thyratron. When the discharged pulse comes into the magnet, the reflection of the pulsed voltage occurs at the magnet end because of the magnet inductance resulting in the doubling of the voltage at the coil. This reflection causes the doubling of the current which passes through the magnet coil. This is the advantage of this circuit system compared with the impedance matching type system. The discharge current comes into the magnet through the sheath of the power cable and the return current from the magnet comes into the PFN through the inner conductor of the power cable and is absorbed in a dump resistor at the other side of the PFN circuit. The dump resister is soaked in oil and the oil is cooled by water through a heat exchanger. Since any additional inductance in the circuit would increase the rise time of the kicker magnetic field, these inductance should be minimized. For instance, the cathode of the thyratron is earthed to reduce the floating inductance around thyratron as shown in Fig. 1.

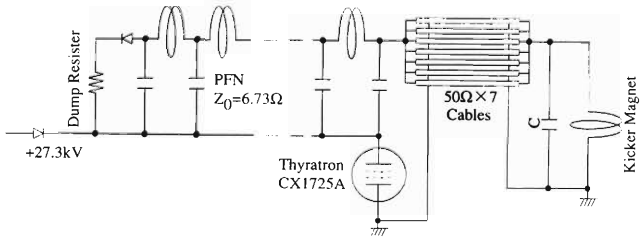


Fig. 1. Electric circuit diagram of the kicker system.

The kicker magnet consists of four unit magnets of the same structure.[2] Figure 2 shows the unit kicker magnet. The unit magnet is made of ferrite pieces of 40 mm thickness, and designed to be a "C"-type structure. The aperture of the unit magnet is 250L × 200H (mm) and the length along the beam line is 200 mm. The total length of the kicker magnet is 800 mm. A single turn coil made of pure Cu plate is wound around a ferrite core. All of the ferrite pieces are supported directly and individually by ceramic supports. The outside surface of the ferrite core is covered by a thin Cu plate to prevent the leakage of the magnetic field with the help of the eddy current in the Cu plate. A thick Cu plate (Mirror Plate) is installed at the open side of the "C"-type structure to prevent the leakage field and to homogenize the magnetic field.[2] Some capacitors are installed in parallel to the magnet coil as shown in Figs. 1 and 2.[2] The rise time of the magnetic field is improved because of the over shoot of the discharge current which is due to the impedance mismatch of these capacitors in the magnet. The main parameters of the kicker magnet are as follows;

| | |
|---|---|
| Charge up voltage | 27.3 kV |
| Maximum current | 4030 A |
| Magnetic field strength | 0.02 Tm |
| Bending angle | 7.6 ° |
| Rise time | < 200 nsec. |
| Flat top | > 300 nsec. |

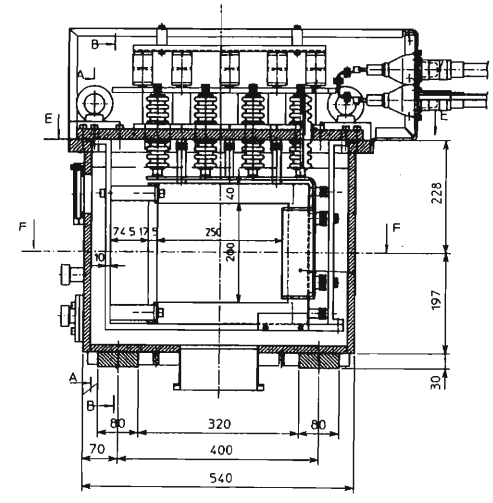


Fig. 2. Unit kicker magnet. View from the upstream side of the beam line.

Figure 3 shows an integrated kicker magnetic field along the muon beam path. The kicker field was measured in the air at a half of the maximum current. The double pulsed muon beam structure which is calculated from the proton beam structure is also shown in the figure to clarify the relationship between the muon beam and the kicker field. At the tail of the first muon pulse the magnetic field starts to rise. After the establishment of the flat top of the field the second muon pulse comes into the kicker. The flat top of the field is kept during the passage of the second pulse. The rise time from 5% to 95% was less than 200 nsec and the flat top was kept for about 300 nsec. Therefore, it is concluded that the kicker magnet has enough capability to separate the double pulsed muon beam.

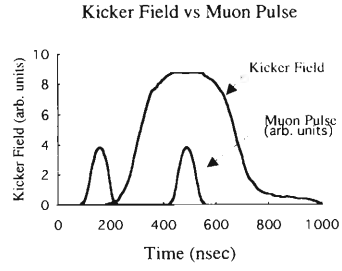


Fig. 3. Relationship between the calculated double pulsed muon beam and the measured integrated kicker magnetic field.

Figure 4 shows the distribution of the integrated kicker field along the axis from the coil to the mirror plate including the beam center. Each data is shown by a percentage deviation from the measured value at the beam center. The field distribution shows the symmetric distribution. Although the magnetic field decreases slightly at the both ends of the axis, it is confirmed by the beam trajectory calculation[3] that more than 90% muons can be transported in the homogeneous region.

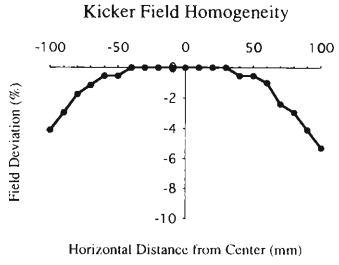


Fig. 4. Distribution of the integrated kicker magnetic field.

The integrated kicker field was measured to be 35% larger than the one estimated from the coil current and the ferrite length, indicating the expansion of the effective field length. The 2-dimensional field calculation[3] indicated that there was a leakage field from the magnet edge along the beam line in the real case and this leakage field increased the effective length of the kicker magnetic field. Based upon the calculation the effective length of the kicker magnetic field should be about 1.38 times as large as the designed one and this expansion is the same with the one observed from the field measurement. This expansion will help to transport higher momentum muons than originally expected. It is concluded that this kicker magnet can be in use for the muon beam with the momentum up to 65 MeV/c.

Figure 5 shows a result of the kicker magnet operation test at RAL using the real double pulsed surface muon beam. As the trigger timing of the discharge was changed from the early to the late, the first pulse was kicked away and disappeared with no change of the pulse structure of the second pulse, and then the second pulse disappeared when the first pulse recovered. Therefore, it was confirmed that each single muon pulse could be completely transported by the kicker magnet.

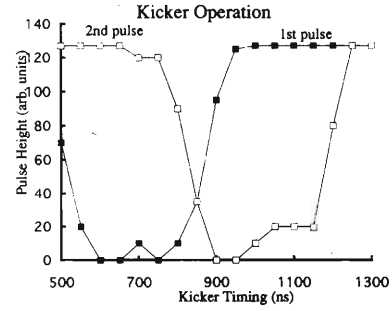


Fig. 5. Separation of the surface muon beam (25.4 MeV/c) by operating the kicker magnet.

## References

1) K. Nagmine et al.: *Hyperfine Interact.*, **87**, 1091 (1994).
2) E. G. Sandels: private communication.
3) K. Ishida: private communication.

# Conceptural Design of Accelerator Complex for RIKEN RI Beam Factory

Y. Yano and A. Goto

The RARF proposes "*RIKEN RI Beam Factory*" as a next facility-expanding project. The factory takes the aim at providing RI (Radioactive Isotope) beams of the whole mass range with the world-highest intensities in a wide energy range up to several hundreds MeV/nucleon. This short report describes a conceptual design of an accelerator complex most suitable for realizing the factory.

The best means to generate such RI beams is the utilization of the so-called "projectile fragmentation". In general, the reaction cross section for this projectile fragmentation steeply enhances with increasing an energy of a primary beam up to 100 MeV/nucleon, and it saturates above around this energy. Thus, in order to efficiently generate RI beams of the whole mass range using this method, firstly, primary-beam energies are required to exceed at least 100 MeV/nucleon even for very heavy ions such as uranium. Due to this condition, the availability of RI beams at the RARF is presently restricted to their mass less than around 60. Yet it should be noted that much higher energies up to 1 GeV/nucleon are not very advantageous because of the saturation effect in the cross sections mentioned above. Secondly, needless to say, intensities of primary beams must be as high as possible. Thirdly, from the cost-effectiveness point of view, the existing machines should be exploited and utilized as much as possible. Based upon these considerations, we propose an accelerator complex as illustrated in Fig. 1 which possesses such acceleration performance that a 150 MeV/nucleon uranium-beam with 0.5 p$\mu$A is obtainable.

A new injector composed of a frequency-tunable

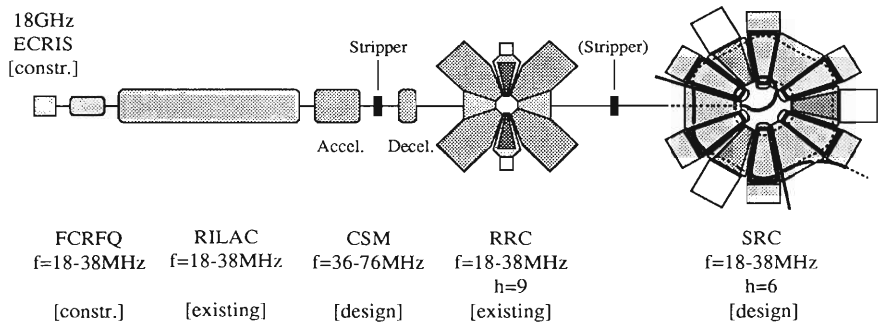


Fig. 1. Proposed accelerator complex for the RIKEN RI Beam Factory.

folded-coaxial RFQ linac (FCRFQ)[1] equipped with an 18 GHz ECR ion source (ECRIS-18)[2] is under construction in order to greatly upgrade the RILAC performance especially in the beam intensity. We use this machine as the initial-stage of the accelerator complex.

A high-intensity heavy-ion d.c. beam produced by the ECRIS-18 is bunched and accelerated by the FCRFQ with transmission efficiency of about 90% even at 1 mA. The value of the efficiency was calculated by the computer code PARMTEQ. This pre-accelerated beam is fully accepted and accelerated by the existing RILAC.

The output beam from the RILAC is passed through a charge-state multiplier (CSM, under design) to reduce its magnetic rigidity without velocity gain and injected into the existing RRC. The CSM consists of an accelerator, a charge stripper and a decelerator. The accelerator and decelerator are of frequency-tunable IH linacs, whose operational radio-frequencies are two times that of the RILAC to double an acceleration gradient. In the present design a maximum gap voltage is set to be 340 kV, and total lengths of these linacs are 8 meters (the partition into two or three units are necessary) and 3.7 meters, respectively. Transmission efficiency through the CSM depends only on charge state distributions behind the charge stripper foil because the 6-dimensional emittance of the RILAC beam is already adiabatically dumped so as to be fully captured by the acceptance of the CSM linacs. We estimate the yield of a given charge state in terms of Shima's formula[3] which is reliable in the relevant energy region. The CSM is a decisive device to obtain a higher-intensity or higher-energy very-heavy-ion beam in the proposed accelerator scheme; with this device the magnetic rigidity of a most-probable charge-state beam can be decreased down to the acceptable value

of the RRC even when the injection velocity into the RRC is increased.

Velocity of the RRC output beam is amplified by a factor of 2.4 with a six-sector superconducting ring cyclotron (SRC, under design), when the mean extraction radius (5.70 m) of the SRC is taken to be 2.4 times the mean injection radius (2.37 m). This mean injection radius is 2/3 times the mean extraction radius of the RRC. To meet a good matching condition, the harmonic number in the SRC is taken to be 6 as that in the RRC is 9. The preliminary calculation of betatron-frequency excursions implies that when we set the sector angle to be 20 degrees the maximum attainable energy is limited to be around 500 MeV/nucleon to avoid the crossing over $\nu_z = 1.0$ resonance.

Here, we illustrate acceleration of a uranium-ion beam up to 150 MeV/nucleon. The rf frequency of the RILAC is 25.5 MHz. A $^{238}U^{19+}$ beam with an intensity ($I^{ECR}$) of 60 e$\mu$A from the ECRIS-18 (this intensity is extrapolated from the 10 GHz CAPRICE data) is accelerated by the RILAC-CSM to 1.31 MeV/nucleon ($E^{RILAC}$). In the CSM the charge state is increased from $19^+$ ($q^{ECR}$) to $49^+$ ($q^{CSM}$). The yield of $49^+$ and the transmission efficiency of the FCRFQ are estimated to be 0.17 and 0.94, respectively, and thus a beam intensity of 0.5 p$\mu$A is to be obtained. This beam intensity ($I^{SRC}$) is preserved up to the final energy, provided that the transmission efficiency of both of the RRC and the SRC is 100% (this can be achieved by the *off-centering acceleration technique* which is routinely used for the RRC). The RRC output energy ($E^{RRC}$) is 21.7 MeV/nucleon, and the SRC final energy ($E^{SCR}$) is 150 MeV/nucleon. The SRC sector field ($B^{SRC}$) is needed to reach 5.48 T. Similarly, the maximum beam intensities for typical gaseous elements are attainable as listed in Table 1.

Table 1. Prospects of SRC beams.

| | RF frq | $q^{ECR}$ | $I^{ECR}$ | $E^{RILAC}$ | $q^{CSM}$ | $E^{RRC}$ | $E^{SRC}$ | $I^{SRC}$ | $B^{SRC}$ |
|---|---|---|---|---|---|---|---|---|---|
| | MHz | | e$\mu$A | MeV/u | | MeV/u | MeV/u | p$\mu$A | tesla |
| $^{16}O$ | 38.0 | 5 | 875 | 2.92 | 8 | 50.2 | 500 | 160 | 4.4 |
| $^{40}Ar$ | 35.0 | 7 | 880 | 2.48 | 16 | 42.1 | 370 | 43 | 4.7 |
| $^{84}Kr$ | 32.0 | 11 | 280 | 2.07 | 28 | 34.8 | 280 | 6 | 4.8 |
| $^{129}Xe$ | 29.0 | 14 | 165 | 1.70 | 35 | 28.3 | 210 | 2 | 5.0 |
| $^{238}U$ | 25.5 | 19 | 60 | 1.31 | 49 | 21.7 | 150 | 0.5 | 5.5 |

Quite high beam intensities can be provided especially for light ions, but use of such primary beams is not realistic from a viewpoint of the radiation-shielding-problem. We consider that a primary-beam intensity of 1 p$\mu$A is sufficient to generate RI beams in the whole mass region with desirable intensities: These primary beams will give us possibility to create and identify as many as one thousand kinds of new isotopes.

References


1) O. Kamigaito et al.: This report, p. 168.
2) T. Nakagawa et al.: This report, p. 165.
3) K. Shima et al.: *At. Data Nucl. Data Tables*, **51**, 174 (1992).

# Double Storage Rings for Multi-Use Experimental Storage Rings Proposed for RIKEN RI Beam Factory

T. Katayama, J. Xia, Y. Rao, Y. Yuan, and Y. Yano

A new type of experimental facility, MUSES (Multi-Use Experimental Storage Rings) is proposed for RIKEN RI beam factory.[1] It consists of Double Storage Rings (DSR) and a small-sized Accumulator-Cooler Ring (ACR): The DSR is followed by the ACR. This MUSES is installed downstream from an RI-beam generator for the Superconducting Ring Cyclotron (SRC). The DSR permits various types of unique colliding experiments: ion-ion merging or head-on collisions; collisions of electron and ion (stable or RI) beams; internal target experiments; and atomic and molecular physics with cooled electron beams. On the other hand, the ACR functions exclusively for the accumulation and cooling of RI beams as well as for the acceleration and radiation damping of electron beams: i.e., RI or electron beams are improved in quality by the ACR, and are injected into the DSR.

This report outlines the DSR. As for the ACR, refer to Ref. 2.

Figure 1 shows a conceptual view of the DSR. The two rings of the same specifications as shown in Table 1 are vertically stacked. Each lattice structure takes the form of a racetrack to accommodate two long straight sections. These straight sections of one ring vertically intersect those of the other ring at two colliding points. The ring circumference is 178.7 m, which is 5 times the extraction circumference of the SRC. The maximum $B\rho$-value becomes 12.76 Tm when a dipole field strength is 1.5 T at the maximum. If high-energy ion beams are demanded, the DSR serves as an ion synchrotron as well. The maximum energy is given, for example, to be 3.0 GeV for protons; 1.2 GeV/nucleon for light ions of q/A = 0.5; and 0.82 GeV/nucleon for $U^{92+}$ ions. For electrons the ACR boosts them up to the maximum energy of 2.5 GeV, and these electrons are stored in the DSR. In the present lattice structure, the betatron tune values are 6.335 (horizontal) and 5.763 (vertical). The operating beam energy is kept to be under the transition energy, since the transition gamma is as high as 4.86. At the colliding points the beta-function amplitudes are 0.6 m for both directions. The field-free section near the colliding points where experimental detector systems are installed is 5.0 m in length. These two long straight sections are dispersion-free.

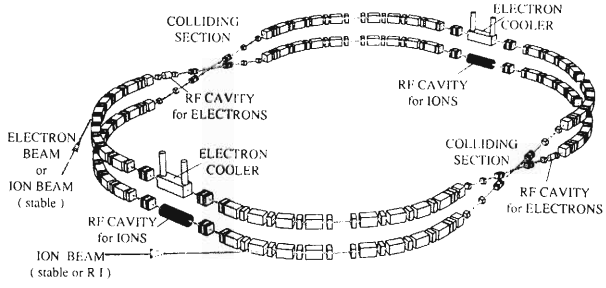


Fig. 1. Conceptual view of the DSR.

Table 1. Parameters of the DSR.

| | |
|---|---|
| Circumference $C$ (m) | 178.694 |
| Max. $B\rho$ (Tm) | 12.76 |
| Average radius $R$ (m) | 28.44 |
| Radius of curvature $\rho$ (m) | 8.506 |
| Max. beam energy (GeV/u) | |
| Proton | 3.00 |
| Ion (q/A = 0.5) | 1.20 |
| (q/A = 0.387) | 0.82 |
| Electron | 2.50 |
| Betatron tune values ($Q_x/Q_y$) | 6.350/5.763 |
| Momentum compaction | 0.0424 |
| Transition $\gamma$ | 4.859 |
| Max. betatron amplitude ($\beta_x/\beta_y$, m) | 22.0/13.5 |
| Max. dispersion function ($D_x/D_y$, m) | 3.023/0.666 |
| Betatron amplitude at interaction point ($\beta_x^*/\beta_y^*$, m) | 0.600/0.600 |
| Length of field-free section at colliding section (m) | 5.016 |

One of the key researches planned in the DSR is the colliding experiment of an electron beam with an RI beam: in one ring of the DSR, 2.5 GeV electrons are accumulated and collided with an RI beam stored in the other ring. This electron energy is determined so as to obtain a sufficiently short de-Broglie wave-length of 0.2 fm in the rest frame of the RI beam. To keep a sufficiently long Toushek lifetime, the RF voltage of 2.0 MV is applied to the electron beam. The detailed specifications of stored electron beams in the DSR are given in Table 2. The number of stored electrons amounts up to $1.9 \times 10^{12}$ particles. The typical colliding luminosity for the electrons and RI ions is estimated to be $5.6 \times 10^{26}/\mathrm{cm}^2/\mathrm{sec}$., provided that $1 \times 10^7$ particles of RI ions are stored. In order to further improve the luminosity, installation of a powerful pulsed heavy-ion source e.g. a laser ion source, and use of the electron cooling (the parameters are given in Ref. 2) in the DSR should be considered.

Other experiments such as ion-ion merging collisions at small angles are also envisaged. The luminosity is expected to be around $1 \times 10^{26}/\mathrm{cm}^2/\mathrm{sec}$. when the

Table 2. Parameters of the stored electron beam.

| | |
|---|---|
| Max. stored beam energy $E_{max}$ (GeV) | 2.5 |
| Max. stored beam current $I$ (A) | 0.5 |
| Max. stored No. of electrons $N$ | $1.86 \times 10^{12}$ |
| Injection energy $E_i$ (GeV) | 2.5 |
| Beam emittance at 2.5 GeV ($\varepsilon_x/\varepsilon_y$) (nm.rad) | 707.0/349.7 |
| Energy spread $\Delta E/E$ | $7.09 \times 10^{-4}$ |
| Bunch length $\sigma$ (cm) | 2.17 |
| RF voltage $V_{RF}$ (MV) | 2.0 |
| Revolution frequency $f_{rev}$ (MHz) | 1.677 |
| RF frequency $f_{RF}$ (MHz) | 503.3 |
| Harmonic No. $h$ | 300 |
| Toushek lifetime at 2.5 GeV (sec.) | $4.06 \times 10^5$ |
| Synchrotron radiation loss at 2.5 GeV (keV/turn) | 423 |

number of stored ions are assumed at the space charge limit of $4 \times 10^{12}$ particles.

For internal target experiments in the DSR, the stochastic cooling method is used. The band width is conservatively assumed at 500 MHz, and the feedback gain is 130 dB which is limited by an available wide-band RF power of 100 kW. Some details are given in Table 3.

Table 3. Parameters of the stochastic cooler.

| | |
|---|---|
| Cooling time (sec.) | |
| Longitudinal | 1 |
| Transverse | 15 |
| Band width $W$ (MHz) | 500 |
| Ambient temperature $T$ (K) | 18 |
| Total microwave power $P$ (kW) | 100 |

References

1) Y. Yano et al.: This report, p. 178.
2) T. Katayama et al.: This report, p. 182.

# Accumulator-Cooler Ring for Multi-Use Experimental Storage Rings Proposed for RIKEN RI Beam Factory

T. Katayama, J. Xia, Y. Rao, Y. Yuan, and Y. Yano

Supposing that RI beams possessing relatively low quality of emittances are accumulated in the DSR[1] up to the space-charge limit, the acceptance of the DSR is required to be intolerably large. Thus, we are investigating the net cost-effectiveness for introducing an extra small-sized Accumulator-Cooler Ring (ACR) before the DSR. This ACR functions exclusively for the accumulation and cooling of RI beams as well as for the acceleration and radiation damping of electron beams: *i.e.*, RI or electron beams are improved in quality by the ACR, and are injected into the DSR. With the ACR, the acceptance required for the DSR is significantly reduced.

Taking the accumulation and cooling of an extremely neutron-rich $^{132}Sn^{50+}$ (a double-magic nucleus of 40 sec. in half-life) beam of 210 MeV/nucleon for an example, we give some specifications of the ACR. This RI beam is produced via the projectile fragmentation of a primary beam of $^{136}Xe$ ions with a peak current of 2 p$\mu$A (see Ref. 2). Typical beam characteristics are estimated: The production rate is nearly $1 \times 10^7$ particles per sec.; the momentum spread is $\pm 0.1\%$; the phase width relative to RF frequency is $\pm 10$ degrees; and the transverse emittances are 4.5 $\pi$ mm.mrad in both horizontal and vertical directions.

The above RI beam is stored in the ACR, firstly with the conventional multi-turn injection method. About $1 \times 10$ particles are injected for each one turn revolution, because the orbit frequency is nearly 1 MHz. Provided that the acceptance of horizontal phase space of the DSR is designed to be 125 $\pi$ mm.mrad, and that the dilution factor is 1.25, after 22-turn injection the emittance of the stored beam becomes as large as the full acceptance. At this moment, the number of the stored particles increases up to $2 \times 10^2$ particles. Secondly, the stored particles are RF-stacked: The RF voltage of 24 kV is applied, and the frequency is swept from 29.12 MHz (corresponding to 210 MeV/u) to 29.44 MHz. This frequency sweep brings about changes in the beam momentum and average radius by 1.8% and 17 mm, respectively. This multi-turn-injection plus RF-stacking process is repeated at 10 Hz. During this process the RF-stacked beam continually undergoes the electron cooling at the top energy. Typical parameters of the electron cooler is tabulated in Table 1. The longitudinal and transversal cooling times are estimated to be as short as 0.1 sec. and 10 sec., respectively. After a sufficiently longer period than the intrinsic half-life, the number of the coasting particles accumulated in the ACR amounts up to the equilibrium value of $1 \times 10^5$. The momentum spread and emittances become less than 0.15% and nearly 1 $\pi$ mm.mrad, respectively. This high-quality stored beam is fast extracted, and is injected into the DSR by one turn.

Table 1. Paramters of the electron cooler.

| | |
|---|---|
| Maximum electron energy (keV) | 300 |
| Maximum cooled ion energy (MeV/u) | 500 |
| Maximum electron current (A) | 10 |
| Cathod diameter (mm) | 5.81 |
| Electron diameter at cooling section (mm) | 50 |
| Length of cooling section (m) | 3.0 |
| Cooling time (sec.) for 210 MeV/u $^{132}Sn^{+50}$ | |
| Longitudinal ($\Delta p/p = 0.1\%$) | 0.1 |
| Transverse ($\varepsilon = 125\ \pi$ mm.mrad) | 10 |

The ACR serves also as an electron synchrotron to accumulate electrons from a 0.5 GeV linac and to boost them up to 2.5 GeV. At the initial energy of 0.5 GeV, the radiation damping is induced: The damping times are estimated to be 0.5 sec. for the transverse direction, and 0.26 sec. for the longitudinal direction, which are short enough for accumulating electrons. The acceleration up to 2.5 GeV is done within 1 sec., and the equilibrium transverse emittances become as small as 0.43 nm.rad for the horizontal direction and 0.11 nm.rad for the vertical direction. The number of stored electrons is estimated to amount up to about $2 \times 10^{12}$ particles. This top-energy electron beam is fast extracted and injected into the DSR by one turn.

The optimization of parameters of the ACR is under way.

References

1) T. Katayama et al.: This report, p. 180.
2) Y. Yano et al.: This report, p. 178.

# VI. RADIATION MONITORING

# Leakage Radiation Measurements in the Ring Cyclotron Facility

S. Fujita, N. Nakanishi, S. Nakajima, M. Watanabe,* H. Ohishi,* K. Tanaka,*
Y. Uwamino, and T. T. Inamura

The measurements of leakage radiation were carried out with three kinds of beams: 135 MeV/u deuteron and $^{28}$Si beams, and 113 MeV proton beam. The beam intensities were 200 pnA for proton, 10 pnA for deuteron, and 4 pnA for $^{28}$Si. The beams were stopped at an iron target in the beam distribution corridor.

Leakage radiation of neutrons from the corridor was measured with four neutron dose rate meters, TPS-451S's (Aloka). The beam current at the target was read with a current integrator (ORTEC 439) and recorded with a personal computer. Figures 1-(a), (b), and (c) show the target point and positions where leakage radiation was measured in this experiment. The positions, 1Fc and B2c, are on the first floor and 2nd basement floor just right upper and under the target point, respectively. Leakage of neutrons was detected at the several points outside of the building. Results are summarized in Table 1. Dose rates were normalized with respect to the beam intensity of 1 p$\mu$A.

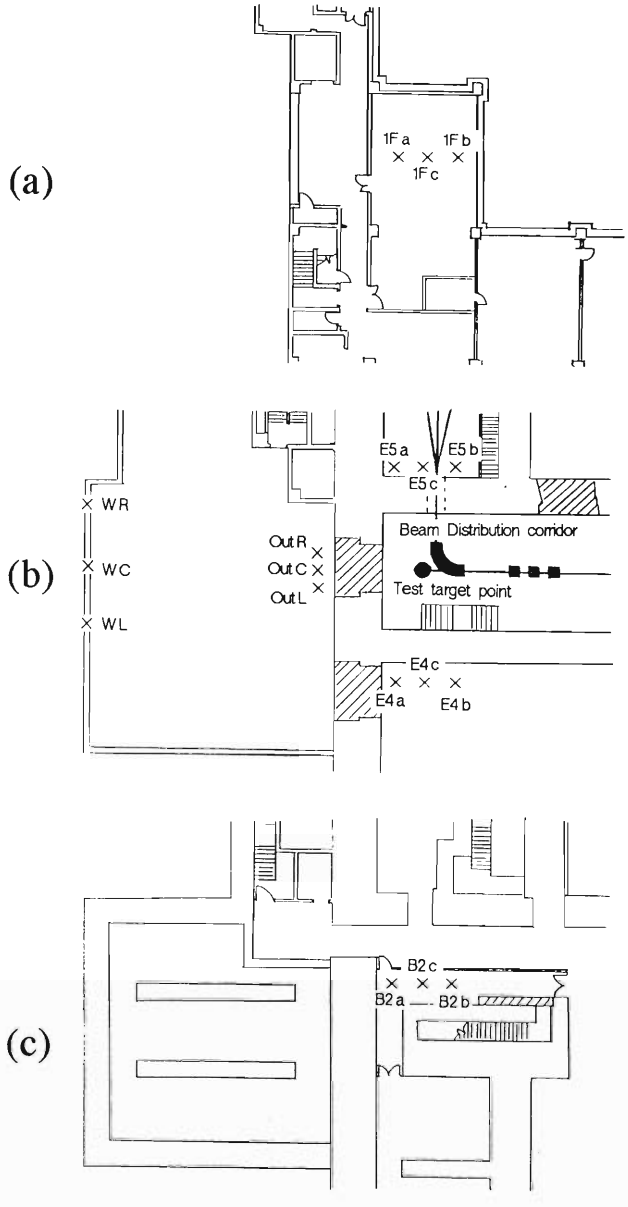


Fig. 1. Partial layout of the RIKEN Ring Cyclotron facility where the leakage radiation measurement was made. (a) Part of the 2nd basement floor; (b) Part of the 1st basement floor; (c) Part of the 1st floor. The target point is denoted by a closed circle. Leakage-radiation-dose measuring points are denoted by ×.

Table 1. Dose rates of neutron leakage radiation from a target point in the beam distribution corridor. [see Figs. 1-(a), (b), and (c)].

| Measured date | May. 19 - 20, 1994 | Oct. 1 - 2, 1994 | Oct. 16 - 17, 1994 |
|---|---|---|---|
| Accelerated Particle | d | $^{28}$Si | p |
| Energy | 135 MeV/u | 135 MeV/u | 113 MeV |
| measured position | dose rate ($\mu$Sv/h)/(p$\mu$A) | dose rate ($\mu$Sv/h)/(p$\mu$A) | dose rate ($\mu$Sv/h)/(p$\mu$A) |
| 1F a | 1.47E+00 | 3.88E+00 | 2.71E-02 |
| 1F c | 1.11E+00 | | 2.15E-02 |
| 1F b | | 3.48E+00 | 1.22E-02 |
| E5 a | 2.66E+02 | 2.81E+02 | 1.04E+01 |
| E5 c | 1.38E+02 | 1.32E+02 | 1.31E+01 |
| E5 b | 3.40E+02 | 2.45E+02 | 4.84E+01 |
| E4 a | 6.07E+01 | 1.05E+02 | 3.59E+00 |
| E4 c | 3.99E+01 | 5.93E+01 | 2.75E+00 |
| E4 b | 1.77E+01 | 2.35E+01 | 1.16E+00 |
| B2 a | 2.28E+02 | 2.37E+02 | 9.10E+00 |
| B2 c | 1.65E+02 | 2.05E+02 | 9.20E+00 |
| B2 b | 8.82E+01 | 7.35E+01 | 5.45E+00 |
| Out R | 1.46E+03 | 1.05E+03 | 5.20E+00 |
| Out C | 2.11E+03 | 1.38E+03 | 3.80E+00 |
| Out L | 1.58E+03 | 1.04E+03 | 5.20E+00 |
| W R | | 2.47E+01 | 1.82E-01 |
| W C | | | 2.70E-01 |
| W L | | 5.45E+01 | 2.26E-01 |

On the other hands, the automatic monitoring of leakage radiation using a computer (MX-3000) was also done continuously during this year. From the accumulated data for leakage neutrons, the radiation levels have been found to be less than the safety limit in the controlled area (1 mSv/week) and at the boundary of the controlled area (0.3 mSv/week) through the whole year. Leakage of neutrons has been recorded with one of the environmental monitors in the above deuteron experimental period. This radiation level, however, is far less than the safety limit (1 mSv/year) required at the boundary of the facility.

* Faculty of Science and Technology, Chuo University

# Residual Activities in the Ring Cyclotron Facility

S. Fujita, M. Watanabe,* H. Ohishi,* K. Tanaka,* N. Nakanishi, Y. Uwamino, and T. T. Inamura

Residual activities were measured at various points in the Ring Cyclotron facility. The measurements were performed during the routine overhaul period and after almost every beam time. In the following we describe significant activities observed in the measurements.

Just after the last experiment of the spring term, which was carried out with an $^{18}O^{8+}$ beam of 100 MeV/u in the E6 experimental vault from August 2 to 8, the routine overhaul started. The dose rates caused by the residual activities in the Ring Cyclotron and the injector AVF cyclotron were measured on Aug. 23 and 30, during the overhaul period. The results are shown in Figs. 1 and 2 along with the detection points.

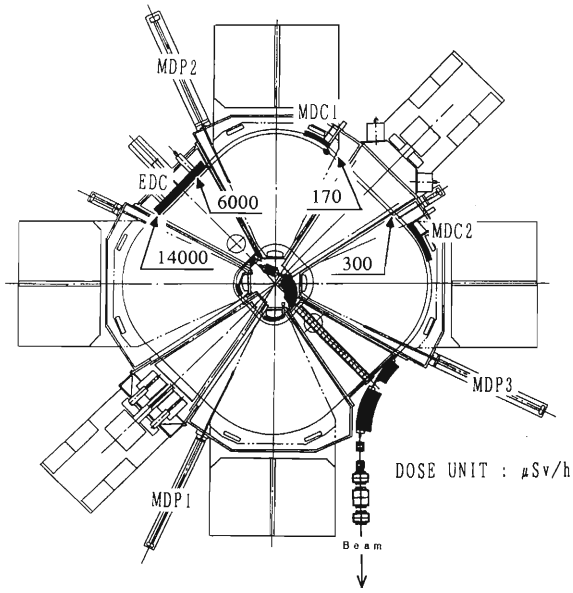


Fig. 1. Detection points around the RIKEN Ring Cyclotron: EDC, the electrostatic deflection channel; MDC1, the magnetic deflection channel 1; MDC2, the magnetic deflection channel 2; MDP1, the main differential probe 1; MDP2, the main differential probe 2; MDP3, the main differential probe 3. Indicated numerals are dose rates in units of $\mu$Sv/h.

In the period from Oct. 1, 1993 to Sep. 30, 1994, residual activites were measured along the beam lines with portable ionization chambers. The points a-y in Fig. 3 denote the places where the dose rates exceed 50 $\mu$Sv/h. Table 1 summarizes the observed dose rates along with the dates on which the measurements were performed. The maximum dose rate was found to be 50000 $\mu$Sv/h at the production target chamber of RIPS, denoted by point l in Fig. 3.

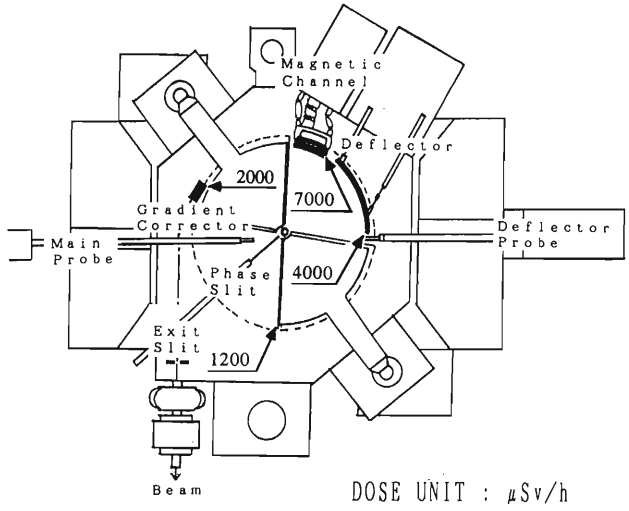


Fig. 2. Dose rates measured inside the injector AVF cyclotron. They are given in units of $\mu$Sv/h.

Table 1. Summary of the residual activities measured along the beam lines with ionization-chamber survey meters. The points a-y indicate the detection points shown in Fig. 3.

| Detection point | Measured dose rate ($\mu$Sv/h) | Date |
|---|---|---|
| a | 400 | Aug. 15, 1994 |
| b | 300 | Aug. 15, 1994 |
| c | 100 | Aug. 15, 1994 |
| d | 1500 | Feb. 8, 1994 |
| e | 110 | Nov. 29, 1993 |
| f | 800 | Nov. 29, 1993 |
| g | 350 | Apr. 4, 1994 |
| h | 220 | Apr. 4, 1994 |
| i | 60 | July 20, 1994 |
| j | 1400 | July 20, 1994 |
| k | 230 | July 20, 1994 |
| l | 50000 | Apr. 4, 1994 |
| m | 120 | Apr. 4, 1994 |
| n | 50 | Dec. 7, 1993 |
| o | 120 | Dec. 7, 1993 |
| p | 120 | May 2, 1994 |
| q | 56 | Aug. 16, 1994 |
| r | 110 | Oct. 12, 1993 |
| s | 50 | Oct. 28, 1993 |
| t | 120 | July 28, 1994 |
| u | 800 | Dec. 7, 1993 |
| v | 400 | May 18, 1994 |
| w | 120 | May 18, 1994 |
| x | 150 | May 18, 1994 |
| y | 80 | May 18, 1994 |

* Faculty of Science and Technology, Chuo University

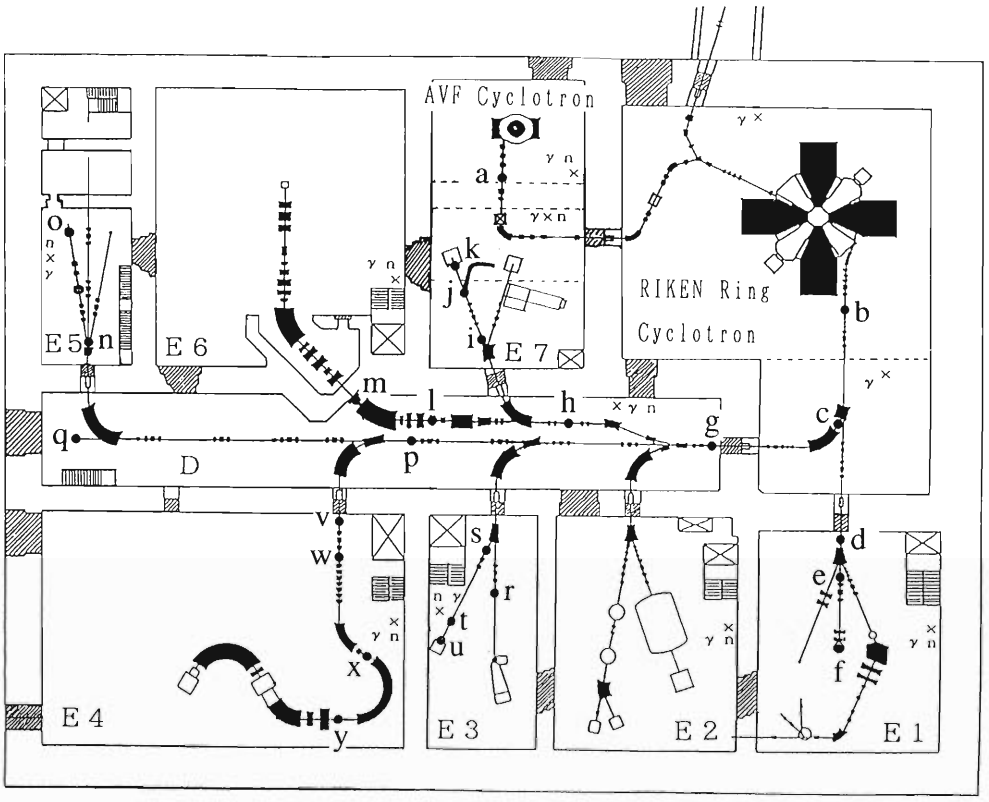


Fig. 3. Layout of the RIKEN Ring Cycrotron facility as of 1994. Monitoring positions are denoted by ×. Detection points of residual activities along the beam lines are denoted by a-y.

At almost all the detection points, larger values of the residual activities were observed compared to those of the previous report.[1] This is due to the increase of the beam intensities since last year.

References

1) S. Fujita, K. Tanaka, M. Watanabe, N. Nakanishi, and T. Inamura: *RIKEN Accel. Prog. Rep.*, **27**, 169 (1993).

# A Film Badge Reading System for the Radiation Safety Control

S. Fujita and N. Nakanishi

The radiation safety control system of the Ring Cyclotron Facility has worked steadily since 1986, performing radiation protection control continuously and automatically.[1)]

Since the facility was completed, a card-operated gate-bar system has been employed in the controlled area. In this system, when one enters into and leaves from the controlled area, all he has to do at the gate is to insert his own ID card into a card reader. A host computer (MX-3000) confirms that he is a good registrant and then opens the gate, recording the entering time together with his name in its memory. According to the radiation protection rules of the facility, he is required to have his own film badge (denoted by FB, hereafter) with him inside the area and to record a place and purpose of his work there when he enters. These rules had not been followed very much by users, since the system could not check them. Thus, we started to improve this situation.

In 1988, a personal computer PC9801 was installed at the entrance gate of the controlled area in order to input the place and purpose easily. But the place and purpose could not be recorded correctly, because the computer had not been connected with the existing radiation safty control system.

In 1993, the card readers were replaced with FB-readers. The procedure to keep records for entering and leaving the controlled area was much improved by introducing the FB-reading system. In the new system, no one can enter the controlled area without bringing his FB and inputting his own record. First, one has to show his FB to a FB reader at the entrance gate bar. Then the selection menue only for him starts automatically on a display of the PC9801. He can easily input the place where he is going and the purpose of his work there with a touch panel on the display. The computer stores these data and transfer them to the host computer (MX-3000). Finally the MX-3000 confirms the person and opens the gate bar.

Figures 1 and 2 show the photograph and the block diagram of the FB-reading system.

The system has a lot of new functions as follows:

(1) Display of names of all persons in the controlled area,

(2) Display of the message for the available interval of the film badge,

(3) An unallowed person is restricted to enter the controlled area and the display shows the message for the reason,

(4) Automatical register of in-out data for the controlled area,


Fig. 1. The photograph of the film badge reading system.

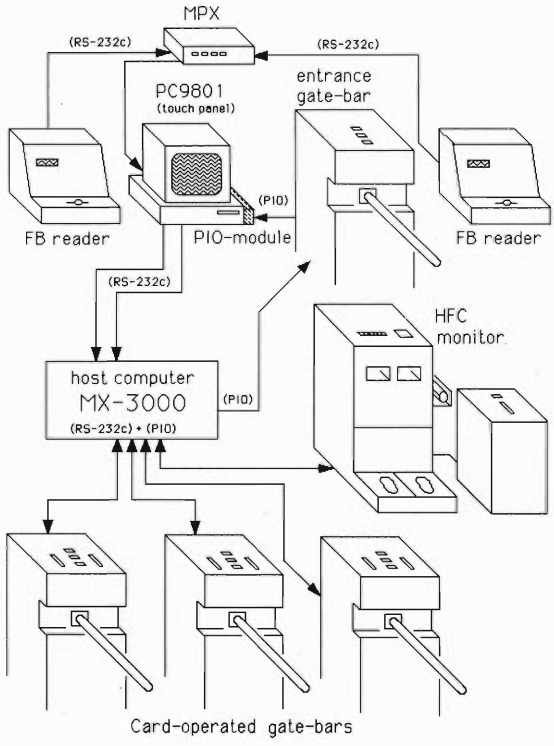


Fig. 2. The schematic block diagram of the film badge reading system.

(5) Automatical recovery from the system error between the card-operated gate-bar and the personal computer, and so on.

Now we are planning to install new film badge readers for all gate-bars in the Ring Cyclotron Facility.

References

1) I. Sakamoto, S. Fujita, T. Wada, and H. Takebe: *RIKEN Accel. Prog. Rep.*, **20**, 206 (1986).

# Measurement of Activities Induced by 135 MeV/u $^{28}$Si Incident on an Iron Target with the Activation Method

N. Nakanishi, S. Nakajima, S. Fujita, T. Minemura,* and M. Watanabe*

A series of measurements have been carried out for 135 MeV/u various incident particles on a thick iron target with the activation method in order to get information on the incident particle dependence of a neutron yield.

Here, the activity induced in metals by neutrons produced by 135 MeV/u $^{28}$Si beams incident on a thick iron target is briefly presented. Seven metals of C, Al, Fe, Co, Ni, In, and Au are used as neutron detectors and 11 reactions are adopted as the probe of activation intensity. These metal detectors were placed at scattering angles of 0, 30, 60, 90, 120, and 140 degs. Gamma rays were measured after irradiation. Details of the experiment are described elsewhere.[1] Figure 1 shows the angular dependence of induced activities in the detectors through various nuclear reactions. The activity is basically represented as the product of a neutron activation cross section and the neutron number produced by an incident particle. In this kind of experiment, only the activity is obtained. Thus, we must have information on activation cross sections of employed detectors in order to get the information of the neutron yield and vice versa. The reactions and characteristics of detectors are also given in Ref. 1.

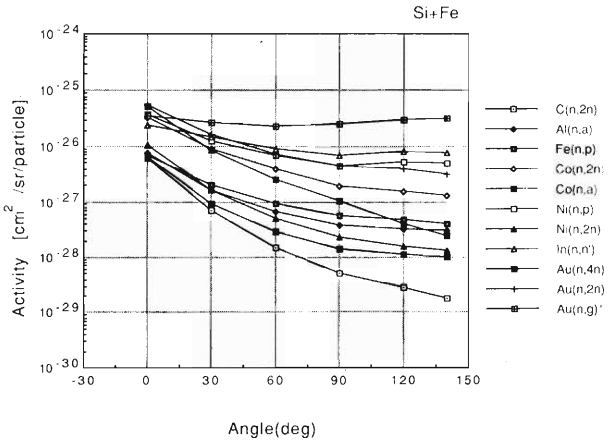


Fig. 1. Angular distributions of activities of 11 isotopes produced by 135 MeV/u $^{28}$Si incident on a thick iron target.

Unfortunately, activation cross sections are known at most up to several tens MeV only in a neutron energy, while even energetic neutrons whose energies are much higher than energies per nucleon of incident beams are emitted from a target in the case of incidence of composite particles. To get activation cross sections at high neutron energies, we are now going on experiments using protons with specific high energies at which neutron flux data exist.

Hereafter, the activity will be unfolded using newly obtained activation cross sections, and the neutron flux will be evaluated and a further mechanism producing neutrons in the target will be examined based on the intra-nuclear cascade evaporation model.

References

1) N. Nakanishi et al.: Proc. 9th Symp. on Accel. Sci. and Tech., Tsukuba, p. 425 (1993).

* Faculty of Science and Technology, Chuo University

# Neutron Dose Equivalent near a Thick Iron Target Induced by 135 MeV/n Ions

S. Nakajima, N. Nakanishi, and S. Fujita

We once measured an angular distribution of the neutron dose equivalent around a thick iron target using a commercially available rem counter when the target was being bombarded by a 135 MeV/nucleon $^{14}$N beam. Since then, we have observed the dose equivalent near the target at a right angle to the beam direction every time when an experiment using the activated-foil method was done. A part of these results is shown in Fig. 1. The figure shows that there is some incident particle dependence in the dose equivalent.

According to a text,[1] a dose equivalent of neutrons produced by protons of energy below 1 GeV on a thick iron target is roughly described by equations:

$$\phi(\theta) = 864 \times 5000(1 - e^{-q})/(\theta + 40/\sqrt{E})^2 \mathrm{Sv/h/p}\mu\mathrm{A}$$

at 1 m distance, and

$$q = 3.6E^{1.6},$$

where E is an incident proton energy in GeV and $\theta$ an angle in degree.

The angular distribution calculated by the equation is also plotted in Fig. 1. The magnitude is a few times larger in the case of $^{14}$N than the calculation for protons, but the shape of them resembles each other. This indicates that the dose equivalent induced by heavy ions can also be described by a similar equation with a slight modification including the incident particle dependence. When such an equation is found, a total neutron flux will be able to be obtained by a simple measurement of the dose equivalent using a rem counter.

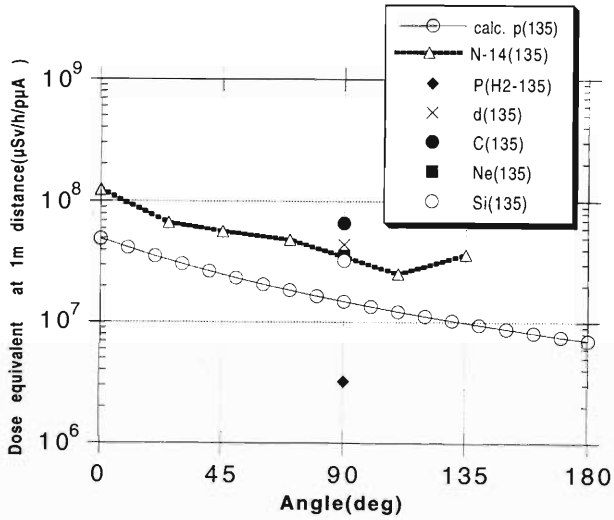


Fig. 1. Neutron dose equivalent measured with a commercially available rem counter and that calculated for protons.

But a commercially available rem counter clearly catches only a small fraction of produced neutrons, then an ingenious invention is necessary to obtain an accurate dose equivalent.

References

1) A. H. Sullivan: A guide to radiation and radioactivity levels near high energy particle accelerators, Nuclear Technology Publishing, Ashford, Kent, GBR (1992).

# VII. LIST OF PUBLICATIONS

## 1. Accelerator development and accelerator physics


Y. K. Batygin: "A Structured-Modular Approach to Software Design for High Current Beam Dynamics Simulation", AIP Conf. Proc. 297, Los Alamos, p. 196 (1994).

Y. K. Batygin: "Particle Distribution Generator in 4D Phase Space", *ibid.*, p. 419.

M. Niimura and R. J. Churchill: "Current Scaling of Projectile Velocities with and without a Snowplow Effect in Electromagnetic Launchers", *IEEE Trans. Magnetics*, **29**, 1249 (1994).

S. Wakasa, K. Fukuda, T. Takagi, and N. Nakanishi: "Design of an Ultra Compact Cyclotron for Particle Induced X-Ray Emission", *Int. J. PIXE*, **3**, 329 (1993).

O. Kamigaito, A. Goto, Y. Miyazawa, T. Chiba, M. Hemmi, M. Kase, and Y. Yano: "Design of a New Type of Variable-Frequency Radio-Frequency Quadrupole Linac with a Folded-Coaxial Resonator", *Jpn. J. Appl. Phys.*, **33**, L537 (1994).

M. Niimura and H. Amemiya: "Effect of Charged Dust in a High-energy Electron Beam", Proc. Int. Symp. on Dust and Dirty Plasma, Noise, and Chaos in Space and in the Laboratory, Plenum Press, New York, p. 33 (1994).

O. Kamigaito, A. Goto, Y. Miyazawa, T. Chiba, M. Hemmi, S. Kohara, M. Kase, and Y. Yano: "Design of a New Type of Variable-Frequency RFQ Linac with a Folded-Coaxial Resonator", Proc. 19th Linear Accelerator Meeting in Japan, Tokai, p. 84 (1994).

O. Kamigaito: "Design of a Variable Frequency RFQ Linac for RILAC", *RIKEN Rev.*, No. 4, p. 65 (1994).


## 2. Nuclear physics and nuclear instrumentation


K. Sumiyoshi and H. Toki: "Relativistic Equation of State of Nuclear Matter for the Supernova Explosion and the Birth of Neutron Stars", *Astrophys. J.*, **422**, 700 (1994).

O. V. Bochkarev, A. A. Korsheninnikov, E. A. Kuzmin, I. G. Mukha, L. V. Chulkov, and G. B. Yankov: "NN-Interaction in the Final State of Three-Particle Decays of Nuclei $^{6}$He($2^+$), $^{6}$Li($2^+$, T = 1), and $^{6}$Be($2^+$)", *Bull. Rus. Acad. Sci. Phys.*, **57**, 932 (1993).

I. Tanihata: "Application of Radioactive Nuclear Beams", *Butsuri*, **49**, 433 (1994).

K. Matsuta, A. Ozawa, Y. Nijiri, T. Minamisono, M. Fukuda, S. Momota, T. Ohtsubo, S. Fukuda, K. Sugimoto, I. Tanihata, K. Yoshida, K. Omata, J. R. Alonso, G. F. Krebs, and T. J. M. Symons: "Beta-NMR Detection of Beta-Emitting Fragment $^{43}$Ti", *Hyperfine Interact.*, **78**, 123 (1993).

K. Matsuta, A. Ozawa, Y. Nijiri, T. Minamisono, M. Fukuda, S. Momota, T. Ohtsubo, S. Fukuda, K. Sugimoto, I. Tanihata, K. Yoshida, K. Omata, J. R. Alonso, G. F. Krebs, and T. J. M. Symons: "Fragment Polarization of $^{43}$Ti in the $^{43}$T + C Collision", *ibid.*, p. 127.

K. Matsuta, A. Ozawa, Y. Nijiri, T. Minamisono, M. Fukuda, S. Momota, T. Ohtsubo, S. Fukuda, K. Sugimoto, I. Tanihata, K. Yoshida, K. Omata, J. R. Alonso, G. F. Krebs, and T. J. M. Symons: "Production of Unstable Nuclei Far from the Stability Line: Its Scope on Limitations", *ibid.*, p. 1219.

K. Ishida, S. Sakamoto, Y. Watanabe, T. Matsuzaki, and K. Nagamine: "X-ray Studies of Muon Transfer Reactions from Hydrogen to Helium", *ibid.*, **82**, 111 (1993).

H. Ueno, H. Okuno, K. Asahi, H. Sato, T. Kubo, T. Nakamura, N. Inabe, A. Yoshida, Y. Ohkubo, M. Adachi, T. Ichihara, M. Ishihara, T. Shimoda, H. Miyatake, N. Takahashi, and W.-D. Schmidt-Ott: "Spin-polarized Radioactive Beams and $\beta$-NMR Experiments", *ibid.*, **84**, 371 (1994).

K. Nagamine, T. Matsuzaki, K. Ishida, I. Watanabe, and R. Kadono: "Construction of RIKEN-RAL Muon Facility at ISIS and Advanced $\mu$SR", *ibid.*, **87**, 1091 (1994).

I. Tanihata: "Physics Wit Radioactive Nuclear Beams", New Frontiers in Nuclear Physics (Lecture Notes of JSPS-INS International Spring School), edited by S. Homma, Y. Akaishi, and M. Wada, World Scientific, p. 241 (1993).

A. S. Dem'yanova, H. G. Bohlen, B. Gebauer, S. A. Goncharov, A. A. Korsheninnikov, Ch. Langner, M. von Lucke-Petsch, W. von Oertzen, A. A. Ogloblin, O. Ya. Osadchy, A. N. Ostrovski, M. Wilpert, and Th. Wilpert: "Rainbow Scattering of Radioactive Nuclei and the Isospin Dependence of the Nucleus-Nucleus Potential", *Nucl. Phys.*, **A553**, 727c (1993).

A. A. Korsheninnikov, B. V. Danilin, and M. V. Zhukov: "Possible Existence of $^{10}$He as Narrow Three-body Resonance", *ibid.*, **A559**, 208 (1993).

A. A. Korsheninnikov and T. Kobayashi: "Main Mechanisms in Fragmentation of the Exotic Nucleus $^{6}$He", *ibid.*, **A567**, 97 (1993).

J. Kasagi and K. Yoshida: "Giant Dipole Resonances in Very Hot Nuclei", *ibid.*, **A569**, 195c (1994).

T. Ichihara, T. Niizeki, H. Okamura, H. Ohnuma, H. Sakai, Y. Fuchi, K. Hatanaka, M. Hosaka, S. Ishida, K. Kato, S. Kato, H. Kawashima, S. Kubono, S. Miyamoto, H. Orihara, N. Sakamoto, S. Takaku, Y. Tajima, M. H. Tanaka, H. Toyokawa, T. Uesaka, T. Yamamoto, T. Yamashita, M. Yosoi, and M. Ishihara: "Spin-Isospin Resonances Observed in the (d,$^{2}$He) and ($^{12}$C,$^{12}$N) Reactions at $E/A$ = 135 MeV", *ibid.*, p. 287c.

K. Sugawara-Tanabe, A. Arima, and N. Yoshida: "The Spin-orbit Interaction and SU(3) Generators in Su-

perdeformation", *ibid.*, **A570**, 291c (1994).

K. Varga, Y. Suzuki, and R. G. Lovas: "Microscopic Multicluster Description of Neutron-halo Nuclei with a Stochastic Variational Method", *ibid.*, **A571**, 447 (1994).

T. Niizeki, H. Ohnuma, T. Yamamoto, K. Katoh, T. Yamashita, Y. Hara, H. Hanaki, H. Okamura, H. Sakai, S. Ishida, N. Sakamoto, H. Ohtsu, T. Wakasa, T. Uesaka, Y. Satou, T. Fujita, T. Ichihara, H. Orihara, H. Toyokawa, S. Kato, S. Kubono, and M. Yosoi: "Spin-Isospin Strength Distribution in Sd-Shell Nuclei Studied by (d,$^2$He) Reactions at Ed = 270 MeV", *ibid.*, **A577**, 37c (1994).

H. Okamura, S. Ishida, N. Sakamoto, H. Otsu, T. Uesaka, T. Wakasa, Y. Satou, S. Fujita, H. Sakai, T. Niizeki, K. Katoh, T. Yamashita, Y. Hara, H. Ohnuma, T. Ichihara, and K. Hatanaka: "Study of the Spin-Dipole State via the (d,$^2$He) Reaction at 270 MeV", *ibid.*, p. 89c.

T. Ichihara, M. Ishihara, H. Ohnuma, T. Niizeki, Y. Tajima, T. Yamamoto, K. Kato, S. Katoh, T. Yamashita, Y. Fuchi, S. Kubono, M. H. Tanaka, H. Okamura, S. Ishida, T. Uesaka, Y. Satou, and T. Fujita: "($^{12}$C,$^{12}$N) Reaction at $E/A$ = 135 MeV as a Probe of Spin-Isospin Excitation", *ibid.*, p. 93c.

H. Toki, H. Suganuma, and S. Sasaki: "Magnetic Monopole Condensation for Confinement and Chiral Symmetry Breaking," *ibid.*, p. 353c.

I. Tanihata: "Neutron Skin and Neutron Halo", *Parity*, **9**, 42 (1994).

O. V. Bochkarev, A. A. Korsheninnikov, E. A. Kuzmin, I. G. Mukha, L. V. Chulkov, and G. B. Yankov: "Spectrum of Neutrons from the Three-Particle Decay of $^6$He($2^+$) and Its Structure", *Physics of Atomic Nuclei (former Sov. J. Nucl. Phys.)*, **57**, 1281 (1994).

M. Louvel, A. Genoux-Lubain, G. Bizard, R. Bougault, R. Brou, A. Buta, H. Doubre, D. Durand, Y. El Masri, H. Fujiwara, K. Hagel, T. Hamadai, F. Hanappe, S. C. Jeong, G. M. Jin, S. Kato, J. L. Laville, C. Le Brun, J. F. Lecolley, S. M. Lee, T. Matsuse, T. Motobayashi, A. Peghaire, J. Peter, R. Regimbart, F. Saing-Laurent, J. C. Steckmeyer, and B. Tamain: "Rapid Decrease of Fragment Emission Time in the Range of 3–5 MeV/u Excitation Energy", *Phys. Lett.*, **B320**, 221 (1994).

M. Tohyama: "Giant Resonances in a Neutron Rich Nucleus", *ibid.*, **B323**, 257 (1994).

T. Ichihara, M. Ishihara, H. Ohnuma, T. Niizeki, Y. Yamashita, T. Yamamoto, Y. Fuchi, S. Kubono, M. H. Tanaka, H. Okamura, S. Ishida, S. Miyamoto, and H. Toyokawa: "Charge Exchange Reaction $^{12}$C($^{12}$C,$^{12}$N)$^{12}$B at $E/A$ = 135 MeV", *ibid.*, p. 278.

T. Horibata and N. Onishi: "Tilted Axis Rotating States in $^{182}$Os Yrast", *ibid.*, **B325**, 283 (1994).

A. A. Korsheninnikov, K. Yoshida, D. V. Aleksandrov, N. Aoi, Y. Doki, N. Inabe, M. Fujimaki, T. Kobayashi, H. Kumagai, C.-B. Moon, E. Yu. Nikolskii, M. M. Obuti, A. A. Ogloblin, A. Ozawa, S. Shimoura, T. Suzuki, I. Tanihata, Y. Watanabe, and M. Yanokura: "Observation of $^{10}$He", *ibid.*, **B326**, 31 (1994).

T. Nakamura, S. Shimoura, T. Kobayashi, T. Teranishi, K. Abe, N. Aoi, Y. Doki, M. Fujimaki, N. Inabe, N. Iwasa, K. Katori, T. Kubo, H. Okuno, T. Suzuki, I. Tanihata, Y. Watanabe, A. Yoshida, and M. Ishihara: "Coulomb Dissociation of a Halo Nucleus $^{11}$Be at 72$A$ MeV", *ibid.*, **B331**, 296.

A. Ozawa, T. Kobayashi, H. Sato, D. Hirata, I. Tanihata, O. Yamakawa, K. Omata, K. Sugimoto, D. Olson, W. Christie, and H. Wieman: "Interaction Cross Sections and Radii of Mass Number $A$ = 17 Isobars ($^{17}$N, $^{17}$F, and $^{17}$Ne)", *ibid.*, **B334**, 18 (1994).

H. Okuno, K. Asahi, H. Sato, H. Ueno, J. Kura, M. Adachi, T. Nakamura, T. Kubo, N. Inabe, A. Yoshida, T. Ichihara, Y. Kobayashi, Y. Ohkubo, M. Iwamoto, F. Ambe, T. Shimoda, H. Miyatake, N. Takahashi, J. Nakamura, D. Beamel, D. J. Beaumel, W.-D. Schmidt-Ott, and M. Ishihara: "Systematic Behavior of Ejectile Spin Polarization in the Projectile Fragmentation Reaction", *ibid.*, **B335**, 29 (1994).

M. Wakasugi, W. G. Jin, T. T. Inamura, T. Murayama, T. Wakui, H. Katsuragawa, T. Ariga, T. Ishizuka, and I. Sugai: "Precision Measurement of the Hyperfine Structure and Nuclear Moments of $^{180m}$Ta by Laser-rf Double-resonance", *Phys. Rev. A*, **50**, 4639 (1994).

S. Hirenzaki, T. Suzuki, and I. Tanihata: "General Formula for the Coalescence Model", *Phys. Rev. C*, **48**, 2403 (1993).

A. Elmaani, J. M. Alexander, N. N. Ajitanand, R. A. Racey, S. Kox, E. Latard, F. Merchez, T. Motobayashi, B. Noren, C. Perrin, D. Rebreyend, T. U. Chan, G. Auger, and S. Groult: "Breakup of Intermediate-mass Fragments, $^8$Be and $^6$Li, Formed in the Reaction $^{40}$Ar + Ag at 7.8$A$ and 17$A$ MeV", *ibid.*, p. 2864.

A. Elmaani, J. M. Alexander, N. N. Ajitanand, R. A. Lacey, S. Fox, E. Liatard, F. Merchez, T. Motobayashi, B. Noren, C. Perrin, D. Rebreyend, T. U. Chan, G. Auger, and S. Groult: "Lifetime of Well Characterized Hot Nuclei via Small-Angle Particle-Particle Correlations: $^{40}$Ar + Ag ($E/A$ = 7.8 and 17 MeV)", *ibid.*, **49**, 284 (1994).

O. Hashimoto, H. Hamagaki, T. Kobayashi, Y. Shida, I. Tanihata, O. Yamakawa, N. Yoshikawa, S. Nagamiya, J. A. Bistirlich, K. M. Crowe, T. J. Humanic, M. Justice, J. O. Rasmussen, and Y.-W. Xu: "Projectile Rapidity Pions in 775 MeV/Nucleon $^{139}$La + $^{12}$C and $^{139}$La + $^{139}$La Reactions", *ibid.*, p. 420.

T. Otsuka, M. Ishihara, N. Fukunishi, T. Nakamura, and M. Yokoyama: "Neutron Halo Effect on Direct Neutron Capture and Photodisintegration", *ibid.*, p. R2289.

M. V. Zhukov, A. A. Korsheninnikov, and M. H. Smedberg: "Simplified $\alpha$ + 4n Model for the $^{8}$He Nucleus", *ibid.*, **50**, R1 (1994).

K. Varga, Y. Suzuki, and Y. Ohbayashi: "Microscopic Multicluster Description of the Neutron-rich Helium Isotopes", *ibid.*, p. 189.

T. Suzuki and T. Otsuka: "Configuration of the Two-Neutron Halo of $^{11}$Li and Gamow-Teller Transition", *ibid.*, p. R555.

K. H. Kim, T. Otsuka, and M. Tohyama: "Transfer and Fusion Reactions of Unstable Nuclei", *ibid.*, p. R566.

K. Varga and R. J. Liotta: "Shell Model on a Random Gaussian Basis", *ibid.*, p. R1292.

T. Motobayashi, N. Iwasa, Y. Ando, M. Kurokawa, H. Murakami, J. Ruan (Gen), S. Shimoura, S. Shirato, N. Inabe, M. Ishihara, T. Kubo, Y. Watanabe, M. Gai, R. H. France III, K. I. Hahn, Z. Zhao, T. Nakamura, T. Teranishi, Y. Futami, K. Furutaka, and Th. Delbar: "The Coulomb Dissociation of $^{8}$B and the $^{7}$Be(p,$\gamma$)$^{8}$B Reaction at Low Energies", *Phys. Rev. Lett.*, **73**, 2680 (1994).

D. Hirata, H. Toki, I. Tanihata, K. Sumiyoshi, Y. Sugahara, and R. Brockmann: "Relativistic Mean Field Theory for Unstable Nuclei", Proc. 3rd Int. Conf. on Radioactive Nuclear Beams, edited by D. J. Morrissey, p. 247 (1993).

A. A. Korsheninnikov, K. Yoshida, D. V. Aleksandrov, N. Aoi, Y. Doki, N. Inabe, M. Fujimaki, T. Kobayashi, H. Kumagai, C.-B. Moon, E. Yu. Nikolskii, M. M. Obuti, A. A. Ogloblin, A. Ozawa, S. Shimoura, T. Suzuki, I. Tanihata, Y. Watanabe, and M. Yanokura: "Experimental Study of Neutron Rich Helium Isotopes", *ibid.*, p. 357.

K. Matsuta, A. Ozawa, Y. Nojiri, T. Minamisono, M. Fukuda, S. Momota, T. Ohtsubo, S. Fukuda, K. Sugimoto, I. Tanihata, K. Yoshida, K. Omata, J. R. Alonso, G. F. Krebs, and T. J. M. Symons: "Production and Polarization of Beta-Emitting Projectile Fragment $^{43}$Ti", *ibid.*, p. 377.

T. Nakamura, T. Kobayashi, M. Fujimaki, N. Inabe, T. Kubo, T. Suzuki, I. Tanihata, Y. Watanabe, A. Yoshida, T. Teranishi, N. Aoi, Y. Doki, M. Ishihara, S. Shimoura, N. Iwasa, K. Katori, and K. Abe: "Coulomb Dissociation of $^{11}$Be", *ibid.*, p. 383.

A. Ozawa, T. Kobayashi, H. Sato, I. Tanihata, O. Yamakawa, K. Omata, K. Sugimoto, N. Takahashi, T. Shimoda, D. Olson, W. Christie, and H. Wieman: "Interaction Cross Sections and Radii of Mass Number $A$ = 17 Isobars ($^{17}$N, $^{17}$N, and $^{17}$Ne)", *ibid.*, p. 395.

I. Tanihata: "Study of Light Exotic Nuclei Using Radioactive Nuclear Beams", Proc. of Int. School-Seminar on Heavy Ion Physics, edited by Yu. Ts. Oganessian, Yu. E. Penionzhkevich, and R. Kalpakchieva, **1**, 3 (1994).

W. Benenson, D. Bazin, J. H. Kelley, D. J. Morrissey, N. A. Orr, R. Ronningen, B. B. Sherrill, M. Steiner, M. Thoennessen, J. A. Winger, S. J. Yennello, B. M. Young, I. Tanihata, X. X. Bai, N. Inabe, T. Kubo, C.-B. Moon, S. Shimoura, T. Suzuki, R. N. Boyd, K. Subotic: "Isomer Production in Fragmentation Reactions", Proc. 10th Winter Workshop on Nuclear Dynamics, "Advance in Nuclear Dynamics", Snowbird, Utah, USA, Jan. 16–22, 1994, edited by J. Harris, A. Mignerey, and W. Bauer, World Scientific, p. 175 (1994).

S. Yamaji, A. S. Jensen, and H. Hofmann: "Isoscalar Vibrational States in Hot Nuclei", *Progr. Theor. Phys.*, **92**, 777 (1994).

M. Tohyama: "Stationary Solution of a Time Dependent Density Matrix Formalism", *ibid.*, p. L905.

H. G. Bohlen, B. Gebauer, M. von Lucke-Petsch, W. von Oertzen, A. N. Ostrovski, M. Wilpert, Th. Wilpert, H. Lenske, D. V. Alexandrov, A. S. Demyanova, E. Nikolskii, A. A. Korsheninnikov, A. A. Ogloblin, R. Kalpakchieva, Y. E. Penionzhkevich, and S. Piskor: "Solution of the $^{10}$Li-Puzzle", *Z. Phys.*, **A344**, 381 (1993).

K. Varga, R. G. Lovas, and R. J. Liotta: "Absolute Alpha-Decay Width of $^{212}$Po in a Mixed Shell-and-Cluster Model", *ibid.*, **A349**, 345 (1994).

K. Varga, R. G. Lovas, and Y. Suzuki: "Microscopic Multicluster Description of Neutron Halos", *ibid.*, p. 347.

A. Odahara, Y. Gono, S. Mitarai, E. Ideguchi, M. Kidera, M. Shibata, T. Morikawa, T. Kishida, K. Morita, A. Yoshida, H. Kumagai, Y.-H. Zhang, A. Ferragut, T. Murakami, M. Oshima, H. Iimura, M. Shibata, S. Hamada, H. Kusakari, M. Sugawara, M. Ogawa, M. Nakajima, B.-J. Min, J.-C. Kim, S.-J. Chae, and H. Sagawa: "High-Spin States of $^{145}$Sm", *ibid.*, **A350**, 185 (1994).

## 3. Atomic and solid-state physics

M. Inokuti, M. Kimura, M. A. Dillon, and I. Shimamura: "Analytic Representation of Cross-Section Data", *Adv. Atom. Mol. Opt. Phys.*, **33**, 215 (1994).

H. Qiu, E. Yagi, G. Safran, B. Pecz, P. B. Barna, and M. Hashimoto: "RBS Study of the Ni Film and Ni/Si(100) Interface Prepared by Biased dc Sputter-Deposition", *Bull. Univ. Electro-Commun.*, **7**, 41 (1994).

E. Yagi: "Channelling Study on the Lattice Location of Hydrogen in Metals Utilizing a Nuclear Reaction", *Hyperfine Interact.*, **84**, 43 (1994).

R. Kadono, A. Matsushita, K. Nishiyama, and K. Nagamine: "Relaxed Excited States and Anomalous Hyperfine Structure of Muonium Centers in KBr", *ibid.*, p. 271.

R. Kadono, S. Fujii, A. Matsushita, K. Nagamine, K. Nishiyama, and S. Tanigawa: "Quantum Diffusion of Muonium in GaAs with Shallow Donor Impurities", *ibid.*, **85**, 79 (1994).

R. Kadono, J. H. Brewer, K. Chow, S. R. Kreitzman, Ch. Niedermayer, T. M. Riseman, J. W. Schneider, and T. Yamazaki: "Critical Behavior of Electric Field Gradient in MnSi Probed by Muon Level-Crossing Resonance", *ibid.*, p. 259.

R. Kadono, A. Matsushita, K. Nishiyama, and K. Nagamine: "Muon Radiolysis in Alkali Halides", *ibid.*, **87**, 979 (1994).

E. A. G. Armour, M. Plummer, and I. Shimamura: "Differential Scattering and Rotational Excitation in Low-Energy Positron-$H_2$ Collisions", *ibid.*, **89**, 309 (1994).

S. Kuboyama, S. Matsuda, T. Kanno, and T. Hirose: "Single Event Burnout of Power MOSFE's Caused by Nuclear Reactions with Heavy Ions", *IEEE Trans. Nucl. Sci.*, **NS-41**, 2210 (1994).

I. Hashimoto, J. Mitani, Y. Miyazaki, H. Yamaguchi, E. Yagi, and M. Iwaki: "Recrystallization of Kr in Kr-Implanted and Annealed Aluminum", *J. Nucl. Mater.*, **203**, 269 (1993).

N. Toshima: "Unexpectedly Large Contribution of $C^{5+}$ Deep Bound States in $C^{6+}$ + H Collisions", *J. Phys. B*, **27**, L49 (1994).

N. Nakamura, T. Nabeshima, Y. Kanai, S. Kitazawa, M. Koide, H. A. Sakaue, S. Ohtani, K. Wakiya, H. Suzuki, T. Takayanagi, Y. Awaya, and T. Kambara: "Ejected Electron Spectra from the Triplet States of $O^{4+}$ ($1s^2 3l3l'$) Produced by $O^{6+}$ + $O_2$ Collisions", *ibid.*, p. L785.

H. Qiu, H. Nakai, M. Hashimoto, G. Safran, M. Adamik, P. B. Barna, and E. Yagi: "Epitaxial Growth and Characterization of Ni Films Grown on MgO(001) by Biased Direct-Current Sputter Deposition", *J. Vac. Sci. Technol.*, **A12**, 2855 (1994).

M. Terasawa, T. Mitamura, T. Kohara, K. Ueda, H. Tsubakino, A. Yamamoto, Y. Awaya, T. Kambara, Y. Kanai, M. Oura, and Y. Nakai: "Influence of High Energy Heavy Ion Irradiation on Magnetic Flux Pinning in $La_{1.85}Sr_{0.15}CuO_4$", *Physica*, **235/240**, 2805 (1994).

J. H. M. Beijersbergen, Q. Hui, and M. Takami: "Spectroscopy and Dynamics of Trapped Alkaline Earth Atoms in Superfluid Helium", *Phys. Lett.*, **A181**, 393 (1993).

W. G. Jin, M. Wakasugi, T. T. Inamura, T. Murayama, T. Wakui, H. Katsuragawa, T. Ariga, T. Ishizuka, M. Koizumi, and I. Sugai: "Isotope Shift and Hyperfine Structure in LuI and WI", *Phys. Rev. A*, **49**, 762 (1994).

J.-Z. Tang, Y. Wakabayashi, M. Matsuzawa, S. Watanabe, and I. Shimamura: "Critical Study of Photodetachment of $H^-$ at Energies up to the $n = 4$ Threshold", *ibid.*, p. 1021.

K. Hino, M. Nagase, H. Okamoto, T. Morishita, M. Matsuzawa, and M. Kimura: "Double-Electron Excitation of $H^-$ by Fast Proton and Antiproton Impact", *ibid.*, p. 3753.

M. Kimura, I. Shimamura, and M. Inokuti: "Single and Double Ionization of Helium by Slow Protons and Antiprotons", *ibid.*, p. R4281.

J.-Z. Tang and I. Shimamura: "Mechanism of the Enhancement of Some High-Lying Resonance Series in the Photoionization Spectra of Excited Helium", *ibid.*, **50**, 1321 (1994).

W. G. Jin, M. Wakasugi, T. T. Inamura, T. Murayama, T. Wakui, H. Katsuragawa, T. Ariga, T. Ishizuka, and I. Sugai: "Laser-rf Double-Resonance Spectroscopy of Refractory Elements: $^{183}$WI and $^{181}$TaI", *ibid.*, p. 1920.

N. Toshima: "Ionization and Charge Transfer of Atomic Hydrogen in Collision with Multiply Charged Ions", *ibid.*, p. 3940.

I. Shimamura and M. Kimura: "Analysis of the Lifetimes and Fractions of Antiprotons Trapped in Metastable States of Antiprotonic Helium", *ibid.*, p. 5346.

R. Kadono, A. Matsushita, K. Nagamine, K. Nishiyama, K. Chow, R. F. Kiefl, A. MacFarlane, D. Schumann, S. Fujii, and S. Tanigawa: "Charge State and Diffusivity of Muonium in n-type GaAs", *Phys. Rev. B*, **50**, 1999 (1994).

K. H. Chow, R. L. Lichti, R. F. Kiefl, S. Dunsiger, T. L. Estle, B. Hitti, R. Kadono, W. A. MacFarlane, J. W. Schneider, D. Schumann, and M. Shelley: "Identification of Neutral Bond-Center Muonium in n-Type Semiconductors by Longitudinal Muon Spin Relaxation", *ibid.*, p. 8918.

R. Kadono, A. Matsushita, R. M. Macrae, K. Nishiyama, and K. Nagamine: "Muonium Centers in Crystalline Si and Ge under Illumination", *Phys. Rev. Lett.*, **73**, 2724 (1994).

E. Yagi: "Lattice Location Study on Hydrogen in Metals by Means of Channelling Method Utilizing Nuclear Reaction $^1$H($^{11}$B, $\alpha$)$\alpha\alpha$", *RIKEN Rev.*, No. 4, p. 49 (1994).

R. Kadono: "Muonium Centers in Semiconducors under Illumination", *Solid State Physics* (Kotai Butsuri), **29**, 817 (1994).

M. Terasawa, T. Mitamura, T. Kohara, K. Ueda, H. Tsubakino, A. Yamamoto, Y. Awaya, T. Kambara, Y. Kanai, M. Oura, and Y. Nakai: "High Energy Heavy Ion Irradiation Effects on Electron Transport Property in $La_{2-x}Sr_xCuO_4$", *Trans. Mat. Res. Soc. Jpn.*, **17**, 393 (1994).

## 4. Radiochemistry, radiation chemistry, and radiation biology

Y. Itoh, K. Lee, T. Nakajyo, A. Goto, A. Nakanishi, M. Kase, I. Kanazawa, Y. Yamamoto, and N. Oshima: "Slow Positron Production Using the RIKEN AVF Cyclotron", *Appl. Surf. Sci.*, **85**, 165 (1994).

W. Li, Y. Ohkubo, S. Ambe, Y. Kobayashi, M. Iwamoto, H. Maeda, and F. Ambe: "Study on the Nuclear Reactions of $^{93}$Nb, $^{181}$Ta, and $^{197}$Au Induced by Secondary Neutrons in $^{40}$MeV/nucleon

$^{40}$Ar Ion Collisions", *Chem. Lett.*, **1994**, 277.
Y. Itoh, H. Murakami, and A. Kinoshita: "Positron Annihilation Study on Nanometer Cavities in Porous Silicon", *Hyperfine Interact.*, **84**, 121 (1994).
Y. Kobayashi, K. Asai, T. Okada, and F. Ambe: "Mössbauer and Magnetization Studies on the Ferromagnet $Fe_{3-x}Ru_xSi$", *ibid.*, p. 131.
K. Ando: "Present Status and Future Prospect of Particle Radiobiology", *Isotope News*, No. 471, p. 2 (1993).
S. Ambe: "Mössbauer Study of Iron in Soybean Hulls and Cotyledons", *J. Agric. Food Chem.*, **42**, 262 (1994).
K. Ando: "Current Status of Biological Studies for Heavy Particle Radiotherapy", *J. Jpn. Soc. Ther. Radiol. Oncol.*, **6**, 1 (1994).
K. Asai, Y. Ohkubo, T. Okada, Y. Yanagida, Y. Kawase, S. Uehara, S. Ambe, and F. Ambe: "A Study on Hyperfine Magnetic Field at $^{117}In(\rightarrow^{117}Cd)$ in $Fe_3O_4$ by $\gamma$-$\gamma$ Time-Differential Perturbed Angular Correlation", *J. Phys. Soc. Jpn.*, **63**, 1677 (1994).
Y. Itoh, H. Murakami, and A. Kinoshita: "Characterization of Porous Silicon by Positron Annihilation", *J. Phys.*, (Paris), **3**, 193 (1993).
S. Y. Chen, S. Ambe, and F. Ambe: "Preparation of a Radioactive Multitracer Solution from Iron Foil Irradiated by 80 MeV/nucleon $^{16}O$ Ions", *J. Radioanal. Nucl. Chem. Lett.*, **186**, 113 (1994).
K. Kimura: "A Fast Decay Measurement of Ion Induced Luminescence: Competition between Radiative and Nonradiative Annihilations of STE Produced by Ion Irradiation of $BaF_2$ Single Crystal", *Nucl. Instrum. Methods Phys. Res.*, **B90**, 100 (1994).
Y. Minai, Y. Takahashi, T. Ozaki, M. Ishibashi, S. Ambe, M. Iwamoto, M. Yanokura, H. Maeda, N. Takematsu, F. Ambe, and T. Tominaga: "Multitracer Study on Formation of Metal-humate Complexes and Their Adsorption on Minerals", Proc. Int. Trace Analysis Symp. '94, p. 71 (1994).
M. Yanaga, S. Enomoto, R. Hirunuma, R. Furuta, K. Endo, S. Ambe, and F. Ambe: "Study on Uptake and Excretion of Radioactive Nuclides in Rats Using the Multitracer Technique", *ibid.*, p. 73.
S. Enomoto, M. Yanaga, R. Hirunuma, R. Furuta, K. Endo, S. Ambe, and F. Ambe: "Multitracer Study on Distribution of Radioactive Nuclides in Rats", *ibid.*, p. 77.
K. Ando, S. Koike, M. Iizuka, T. Aruga, N. Hori, W. Shimizu, T. Sugita, S. Murayama, T. Kanai, S. Minohara, M. Sudou, and F. Yatagai: "Effects of High LET Radiation on Murine Skin and Tumors", Proc. 3rd Workshop on Physical and Biological Research with Heavy Ions, eds. K. Ando and T. Kanai, NIRS-M-99, HIMAC-006, Natl. Inst. Radiol. Sci., p. 61 (1993).
Y. Hyodo-Taguchi, T. Kanai, S. Minohara, and Y. Furusawa: "Effects of Accelerated Carbon-Ion on the Induction of Dominant Lethality in the Teleost Fish, *Oryzias latipes*", *ibid.*, p. 77.
K. Kimura: "Track-Depth and Time Resolved Dynamics of Excited States Created in Ion Tracks", *Radiat. Chem.*, **58**, 33 (1994).
S. Ambe, T. Ohkubo, Y. Kobayashi, M. Iwamoto, M. Yanokura, H. Maeda, and F. Ambe: "Transport of Tc(VII) and Re(VII) through a Supported Liquid Membrane", *Radiochim. Acta*, **63**, 49 (1993).
M. Kikuchi, S. Kitayama, S. H. Sjarief, and H. Watanabe: "Plasmids in Several Strains of *Deinococcus radiodurans*", *Radiat. Res.*, **139**, 123 (1994).
F. Ambe: "Development and Applications of Multitracers", *RIKEN Rev.*, No. 4, p. 31 (1994).
K. Ando, K. Fukutsu, H. Tatsuzaki, and F. Yatagai: "Downsizing Effect of Irradiated Volume on Normal Tissue Injuries", *ibid.*, p. 43.

## 5. Material analysis

J. Kawai and K. Maeda: "K X-Ray Measurements of Iron Compounds Using Imaging-Plate X-Ray Emission Spectrometer", *Adv. X-Ray Chem. Anal. Jpn.*, **25**, 1 (1994).
K. Maeda and J. Kawai: "Interfering Line in Trace Analysis by X-Ray Spectrometry: Radiative Auger Satellites", *ibid.*, p. 25.
J. Kawai, T. Nakajima, T. Inoue, H. Adachi, M. Yamaguchi, K. Maeda, and S. Yabuki: "Chemical Effects on the Intensity of Ti K$\eta$ (Radiative Auger Satellite) X-Ray Fluorescence Spectra", *Analyst*, **119**, 601 (1994).
S. Takagi, T. Nakamura, T. Kohno, N. Shiono, and F. Makino: "Observation of Space Radiation Environment with EXOS-D", *IEEE Trans. Nucl. Sci.*, **40**, 1491 (1993).
T. Doke, M. Fujii, M. Fujimoto, K. Fujiki, T. Fukui, F. Gliem, W. Guttler, N. Hasebe, T. Hayashi, T. Ito, K. Itsumi, T. Kashiwagi, J. Kikuchi, T. Kohno, S. Kokubun, S. Livi, K. Maezawa, H. Moriya, K. Munakata, H. Murakami, Y. Muraki, H. Nagoshi, A. Nakamoto, K. Nagata, A. Nishida, R. Rathje, T. Shino, H. Sommer, T. Takashima, T. Terasawa, S. Ullaland, W. Weiss, B. Wilken, T. Yamamoto, T. Yanagimachi, and S. Yanagita: "The Energetic Particle Spectrometer HEP Onboard the GEOTAIL Spacecraft", *J. Geomag. Geoelectr.*, **46**, 713 (1994).
K. Tazaki, M. Aratani, S. Noda, P. J. Currie, and W. S. Fyfe: "Microstructure and Chemical Composition of Duckbilled Dinosaur Eggshell", *Sci. Rep. Kanazawa Univ.*, **39**, 17 (1994).
J. Kawai, H. Adachi, S. Hayakawa, S. Y. Zhen, K. Kobayashi, Y. Gohshi, K. Maeda, and Y. Kitajima: "Depth Selective X-Ray Absorption Fine Structure Spectrometry", *Spectrochim. Acta*, **49B**, 739 (1994).

# VIII. LIST OF PREPRINTS

1994

RIKEN-AF-NP

161 T. Horibata and N. Onishi: "Tilted Axis Rotating in $^{182}$Os Yrast"

162 S. Midorikawa, T. Kubo, and T. Cheon: "Folded Bifurcation in Coupled Asymmetric Logistic Maps"

163 S. A. Goncharov and A. A. Korsheninnikov: "Elastic and Inelastic Scattering p + $^{8}$He at $E_{C.M.}$ = 65 MeV"

164 H. Suganuma, S. Sasaki, and H. Toki: "Color Confinement, Quark Pair Creation and Dynamical Chiral-Symmetry Breaking in the Dual Ginzburg-Landau Theory"

165 T. Nakamura, S. Shimoura, T. Kobayashi, T. Teranishi, K. Abe, Y. Doki, M. Fujimaki, N. Inabe, N. Iwasa, K. Katori, T. Kubo, H. Okuno, T. Suzuki, I. Tanihata, Y. Watanabe, A. Yoshida, and M. Ishihara: "Coulomb Dissociation of a Halo Nucleus $^{11}$Be at $^{72}$A MeV"

166 I. Tanihata, D. Hirata, and H. Toki: "Are All Nucleus Spherical at the Drip Line?"

167 M. Sano and M. Wakai: "Hypernuclear Production in High-Energy Nuclear Collisions"

168 T. Otsuka, M. Ishihara, N. Fukunishi, T. Nakamura, and M. Yokoyama: "Neutron Hallo Effect on Direct Neutron Capture and Photo Disintegration"

169 A. A. Korsheninnikov, M. V. Zhukov, M. Smedgerg, and T. Kobayashi: "Neutron Momentum Distributions from Fragmentation of the Exotic Nucleus $^{8}$He"

170 H. Okuno, K. Asahi, H. Sato, H. Ueno, J. Kura, M. Adachi, T. Nakamura, T. Kubo, N. Inabe, A. Yoshida, Y. Kobayashi, Y. Ohkubo, M. Iwamoto, F. Ambe, T. Shimoda, H. Miyatake, N. Takahashi, J. Nakamura, D. Beaumel, D. J. Morrissey, W. D. Schmidt-Ott, and M. Ishihara: "Systematic Behavior of Ejectile Spin Polarization in the Projectile Fragmentation Reaction"

171 H. Toki, H. Suganuma, and S. Sasaki: "Magnetic Monopole Condensation for Confinement and Chiral Symmetry Breaking"

172 S. Sasaki, H. Suganuma, and H. Toki: "Dual Ginzburg-Landau Theory with QCD Monopoles for Dynamical Chiral-Symmetry Breaking"

173 "TMU/RIKEN Summer Institute on Unstable Nuclei"

174 I. Tanihata, D. Hirata, and H. Toki: "Are All Nucleus Spherical at the Drip Line?"

175 A. A. Korsheninnikov, E. Yu. Nikolskii, T. Kobayashi, D. V. Aleksandrov, M. Fujimaki, H. Kumagai, A. A. Ogloblin, A. Ozawa, I. Tanihata, Y. Watanabe, and K. Yoshida: "Excited States in $^{12}$Be, Exotic Cluster Structure?"

176 H. Ichie, H. Suganuma, and H. Toki: "QCD Phase Transition at Finite Temperature in the Dual Ginzburg-Landau Theory"

177 S. Shimoura, T. Nakamura, M. Ishihara, N. Inabe, T. Kobayashi, T. Kubo, R. H. Siemssen, I. Tanihata, and Y. Watanabe: "Coulomb Dissociation Reaction and Correlations of Two Halo Neutrons"

178 A. A. Ogloblin: "Some Results and Open Problems in Spectroscopy of the Neutron Drip-line Nuclei"

179 K. Varga, Y. Suzuki, and I. Tanihata: "Microscopic Four-Cluster Description of the $^{9}$Li and $^{9}$C Mirror Nuclei"

180 S. Momota: "Mechanism of the Polarization Production by Means of the Tilted-Foil Technique Studied by $\beta$-Radioactive Nuclei"

181 K. Arai, Y. Suzuki, and K. Varga: "Neutron-Proton Halo Structure of the 3.563 MeV $O^+$ State in $^6$Li"

182 S. Kim and S. Ohta: "Lattice QCD Calculation Using VPP500"

183 T. Morikawa, Y. Gono, K. Morita, T. Kishida, T. Murakami, E. Ideguchi, H. Kumagai, G. H. Liu, A. Ferragut, A. Yoshida, Y. H. Zhang, M. Oshima, M. Sugawara, H. Kusakari, M. Ozawa, M. Nakajima, H. Tsuchida, S. Mitarai, A. Odahara, M. Kidera, M. Shibata, J. C. Kim, S. J. Chae, Y. Hatsukawa, and M. Ishihara: "Coulomb Excitation of $^{174}$Hf-Isomer-$\gamma$-Ray Spectroscopy with High-Spin Isomer Beam"

# IX. PAPERS PRESENTED AT MEETINGS

## 1. Accelerator development and accelerator physics

M. Niimura: "Plausible EM-Noise Source in the Space", URSI Int. Symp., Tokyo, May (1994).

Y. Yano, T. Katayama, and RARF Accelerator Group: "Present Status and Future Plan of RIKEN Accelerator Research Facility", 4th European Particle Accel. Conf., London, U.K., June (1994).

O. Kamigaito, A. Goto, Y. Miyazawa, T. Chiba, M. Hemmi, S. Kohara, M. Kase, and Y. Yano: "Design of a New Type of Variable-Frequency RFQ Linac with a Folded-Coaxial Resonator", 19th Linear Accelerator Meeting in Japan, Tokai, July (1994).

O. Kamigaito, A. Goto, Y. Miyazawa, T. Chiba, M. Hemmi, S. Kohara, M. Kase, and Y. Yano: "Design of a New Type of Variable-Frequency RFQ Linac with a Folded-Coaxial Resonator", 17th Int. Linac Conf., Tsukuba, Aug. (1994).

H. Okamura, N. Sakamoto, T. Uesaka, H. Sakai, K. Hatanaka, A. Goto, M. Kase, N. Inabe, and Y. Yano: "Technique for Rotating the Spin Direction at RIKEN", 8th Int. Symp. on Polarization Phenomena in Nuclear Physics, Indiana, U.S.A., Sept. (1994).

M. Niimura and H. Amemiya: "A Compact Pulsed-Power Ion Source for Plasma Potential Diagnostics", Fall Meet. Phys. Soc. Jpn., Shizuoka, Sept. (1994).

M. Kase, N. Inabe, and I. Yokoyama: "A Beam Phase Monitor with Use of a Micro-Channel Plate for the RIKEN Ring Cyclotron", Beam Instrumentation Workshop, Vancouver, Canada, Oct. (1994).

Y. Yano, T. Katayama, and RARF Accelerator Group: "RIKEN RI Beam Factory Project", Tamura Symp. on Accelerator Physics, Austin, U.S.A., Nov. (1994).

## 2. Nuclear physics and nuclear instrumentation

I. Tanihata: "Study of Light Exotic Nuclei Using Radioactive Nuclear Beams", Int. School-Seminar on Heavy Ion Physics, Dubna, Russia, May (1993).

A. A. Ogloblin: "Current Situation and Some New Approaches in Studying of Exotic Nuclei", *ibid.*

T. Matsuzaki and K. Ishida: "Muon Facility at RAL and Methods of Muonic X-ray Detection", RIKEN Symp. on Muon Science 1993 (II): Medical and Biological Applications of Nondestructive Elemental Analysis Using Muons, Wako, Dec. (1993).

H. Kitagawa and A. Ozawa: "Beta-Decays of A = 17 Isobars and Isospin Symmetry", Symp. on Science of Beams of Short Life Nuclei '93, Tanashi, Dec. (1993).

K. Asahi: "Production of Spin-polarized Radioactive Nuclear Beams and Investigation of Probe Isotopes Applicable to Material Science", Symp. on Science with Radioactive Nuclear Beams, Tokyo, Dec. (1993).

H. Okuno: "Mechanizm of Spin Polarization in Projectile Fragmentation Reaction", *ibid.*

H. Ueno: "Measurement of Magnetic Moment for Neutron-halo Nucleus $^{17}$B", *ibid.*

H. Izumi: "Measurement of Electric Quadrupole Moments for Neutron-rich Nuclei $^{14}$B and $^{15}$B", *ibid.*

H. Suganuma, S. Sasaki, and H. Toki: "Color Confinement, Quark Pair Creation and Dynamical Chiral-Symmetry Breaking in the Dual Ginzburg-Landau Theory", YITP Workshop on Dynamics of Quarks and Hadrons, Kyoto, Dec. (1993).

H. Kitagawa, S. Tadokoro, Y. Nishino, and T. Suzuki: "Distributions of Perturbative Gluons in the MIT Bag Model", *ibid.*

H. Kitagawa, A. Ozawa, and I. Tanihata: "Reaction Cross Sections of Isobars (A = 17) in the Glauber Model", *ibid.*

K. Ishida: "RIKEN/RAL Muon Facility: Expected Beam Properties and the Experimental Equipments", ISIS Muon Users Group Meeting, Abindton, U.K., Feb. (1994).

S. Yamaji: "Vibrations in Hot Nuclei", RIKEN Symp. on Dynamics in Hot Nuclei, Wako, Feb. (1994).

H. Kitagawa, A. Ozawa, and I. Tanihata: "Isospin Symmetry in Light Isobars (A = 17)", 49th Ann. Meet. Phys. Soc. Jpn., Fukuoka, Mar. (1994).

T. Motobayashi: "Excitation Energy Spectrum for $^{14}$O Dissociation Reaction", *ibid.*

N. Fukunishi: "Effective Interaction in Asymmetric Nuclear Matter", *ibid.*

K. Sagara, A. Motoshima, T. Sugimitsu, H. Nakamura, and S. Morinobu: "Trial Experiment on a Blow-in Type Gas Jet Target", *ibid.*

H. Suganuma, S. Sasaki, and H. Toki: "Color Confinement, $\bar{q}$-$q$ Pair Creation and Dynamical Chiral-Symmetry Breaking in the Dual Ginzburg-Landau Theory", *ibid.*

M. Yokoyama, T. Otsuka, and H. Sagawa: "Multipole Giant Resonances in Neutron-rich Nuclei", *ibid.*

T. Suzuki and T. Otsuka: "Beta Decay and Magnetic Moment in Neutron-rich Nuclei", *ibid.*

K. H. Kim, T. Otsuka, and M. Tohyama: "Variation of Nucleon Density in Reactions between Stable and Unstable Nuclei", *ibid.*

A. Odahara, Y. Gono, S. Mitarai, E. Ideguchi, M. Kidera, M. Shibata, T. Morikawa, T. Kishida, Y. H. Zhang, A. Ferragut, K. Morita, A. Yoshida, T. Murakami, M. Oshima, H. Kusakari, M. Sugawara, B. J. Min, J. C. Kim, and S. J. Chae: "High-Spin Isomer and Level Structure of $^{145}$Sm", *ibid.*

E. Ideguchi, A. Odahara, T. Shizuma, M. Kidera, M. Shibata, S. Mitarai, Y. Gono, T. Morikawa, M. Oshima, Y. Hatsukawa, and S. Hamada: "High-Spin Isomer of $^{146}$Eu", *ibid.*

Y. Gono, M. Shibata, E. Ideguchi, A. Odahara, M. Kidera, S. Mitarai, T. Morikawa, M. Oshima, Y. Hatsukawa, H. Iimura, M. Shibata, and S. Hamada:

"High-Spin States of $^{147}$Eu", *ibid.*

T. Horibata and N. Onishi: "Tilted Axis Rotating States in $^{182}$Os Yrast", *ibid.*

T. Horibata and N. Onishi: "Tilted Axis Rotating States in $^{182}$Os Yrast", Int. Symp. on Frontiers of Nuclear Structure Physics, Wako, Mar. (1994).

H. Ueno: "Static Moments of Neutron-rich Nuclei Measured with Spin-polarized Radioactive Beams", *ibid.*

M. Tohyama: "E1 and E2 Giant Resonances in $^{22}$O", *ibid.*

H. Ueno: "Abrasion-induced Spin Polarization as a Tool to Study Neutron-rich Nuclei", Int. Symp. on Spin-Isospin Responses and Weak Process in Hadrons and Nuclei, Osaka, Mar. (1994).

T. Ichihara, M. Ishihara, H. Ohnuma, T. Niizeki, Y. Tajima, T. Yamamoto, K. Kato, S. Katoh, T. Yamashita, Y. Fuchi, S. Kubono, M. H. Tanaka, H. Okamura, S. Ishida, T. Uesaka, Y. Satou, and T. Fujita: "($^{12}$C,$^{12}$N) Reaction at $E/A$ = 135 MeV as a Probe of Spin-Isospin Excitation", *ibid.*

T. Kishida: "ACQ System for New Detector Array of Ge", RIKEN Symp. on Nuclei under Extreme Conditions: Physics of High-Spin Isomer Beams, Wako, Mar. (1994).

H. Okuno, K. Asahi, H. Sato, H. Ueno, J. Kura, M. Adachi, T. Nakamura, T. Kubo, N. Inabe, A. Yoshida, T. Ichihara, Y. Kobayashi, Y. Ohkubo, M. Iwamoto, F. Ambe, T. Shimoda, H. Miyatake, N. Takahashi, J. Nakamura, D. Beamel, D. J. Beaumel, W.-D. Schmidt-Ott, and M. Ishihara: "Polarization Mechanism of Projectile Fragment", 1994 Spring Meet. Phys. Soc. Jpn., Fukuoka, Mar. (1994).

T. Wakui, M. Wakasugi, W. G. Jin, T. T. Inamura, T. Murayama, H. Katsuragawa, T. Ariga, T. Ishizuka, M. Koizumi, and I. Sugai: "Precise Measurement of Hyperfine Structure and Nuclear Moments in $^{180m}$Ta by Means of Laser-rf Double Resonance Spectroscopy", *ibid.*

A. Muta and T. Otsuka: "Study of Unstable Nuclei by Deformed Woods-Saxon Potential", *ibid.*

H. Okuno: "Mechanism of Spin Polarization in Projectile Fragmentation Reaction", *ibid.*

H. Ueno: "Measurement of Magnetic Moment for $^{17}$B by Using Spin Polarization in Projectile Fragmentation Reaction", *ibid.*

K. Sumiyoshi, H. Kuwabara, H. Toki, and H. Suzuki: "Various Equations of State at Finite Temperature and the Evolution of Protoneutron Stars", *ibid.*

N. Aoi: "Beta Decay of Neutron Rich Nucleus $^{14}$Be", *ibid.*

N. Nakao et al.: "Spectrometry of Several Tens MeV Neutrons Penetrating Shields Using Organic Liquid Scintillator at 90 MeV AVF Cyclotron Facility, TIARA", 8th Int. Conf. on Radiation Shielding, Arlington, Texas, U.S.A., Apr. (1994).

H. Suganuma: "Glueballs, Hybrids and Exotics", RCNP Workshop on Hadron Physics with Cooled Stored GeV Proton Beams, Osaka, May (1994).

S. Yamaji: "Vibrations in Hot Nuclei on the Basis of Self-consistent Transport Theory", YITP Symp. on Dynamics of Fluctuations, Kyoto, May (1994).

T. Ichihara, M. Ishihara, H. Ohnuma, T. Niizeki, T. Yamamoto, K. Katoh, T. Yamashita, Y. Hara, Y. Fuchi, S. Kubono, M. H. Tanaka, H. Okamura, S. Ishida, T. Uesaka, and Y. Satou: "Spin-flip and Non-spin-flip Isovector Excitations Observed in the ($^{12}$C,$^{12}$N) Reactions at $E/A$ = 135 MeV and the ($^{13}$C,$^{13}$N) Reactions at $E/A$ = 100 MeV", Nucleus Nucleus Collisions V, Taormina, Italy, May/June (1994).

A. Ozawa, G. Raimann, R. N. Boyd, J. J. Kolata, F. Chloupeck, K. Yoshida, M. Fujimaki, T. Kobayashi, Y. Watanabe, I. Tanihata, S. Kubono, and K. Kimura: "Beta-Delayed Neutron Decay of $^{19}$C and Its Astrophysical Implications", *ibid.*

A. Ozawa, I. Tanihata, T. Kobayashi, O. Yamakawa, K. Omata, N. Takahashi, T. Shimoda, K. Sugimoto, D. Olson, W. Christie, and H. Wieman: "Interaction Cross Sections and Radii of $^{11}$C and $^{12}$N and Effective Deformation Parameters in Light Mirror Nuclei", *ibid.*

K. Sugawara-Tanabe: "The Revival of L-S Coupling Scheme in Superdeformation", Int. Conf. in Perspectives for the Interacting Boron Bode, Padova, Italy, June (1994).

A. A. Korsheninnikov: "Experimental Study of Neutron Rich Helium Isotopes and Observation of $^{10}$He", Symp. on Science of Short-Lived Nuclear Beam, INS, Tokyo, June (1994).

T. Kishida: "High Spin Isomer Beam at RIKEN: Current Status and Future Plan", Physics Seminar of Lund Univ., Lund, Sweden, July (1994).

K. Masuda, T. Doke, J. Kikuchi, and H. Okada: "Performance of an Ionization Chamber Filled with Liquid Xenon Doped with Organic Molecules as a Gamma-Ray Detector", SPIE's 1994 Int. Symp. on Optics, Imaging, and Instrumentation, San Diego, U.S.A., July (1994).

T. Kishida: "Current Status on Crystal Balls in Europe", 2nd Workshop on $\gamma$-spectroscopy Collaborations of the JAERI Tandem Booster, Tokai, July (1994).

W. G. Jin, T. Ariga, M. G. Hies, T. T. Inamura, T. Ishizuka, H. Katsuragawa, T. Murayama, J. Z. Ruan, I. Sugai, M. Wakasugi, and T. Wakui: "Nuclear Moments of $^{179}$Ta and $^{180m}$Ta", 2nd China Japan Joint Symp. on Nuclear Physics, Beijing, China, Aug./Sept. (1994).

J. Kasagi: "Hot Nuclei; Gamma-ray and Particle Emission", *ibid.*

Y. Gono: "Production and Application of High-Spin Isomer Beams", *ibid.*

T. Horibata and N. Onishi: "Tilted Axis Rotation

Studied by Self-consistent Cranking Model", *ibid.*

M. Kurokawa: "Study of $\alpha$ Decays in the $^{40}Ar + ^{232}Th$ Reaction Using the RIKEN Gas-Filled Separator II-High Resolution Position Sensitive Detector", Tours Symp. on Nuclear Physics II, Tours, France, Aug. (1994).

T. Motobayashi: "Coulomb Dissociation Experiments of Astrophysical Interest", *ibid.*

H. Okada, M. Shinoda, T. Komiyama, K. Hasuike, J. Kikuchi, T. Doke, K. Masuda, M. Suzuki, and S. Konno: "Time Stability of Liquid Xenon Photoionization Detectors", Fall Meeting Phys. Soc. Jpn., Shizuoka, Sept. (1994).

N. Ishida, K. Masuda, H. Okada, T. Komiyama, and T. Doke: "Measurements of Attenuation Lengths of Scintillation Light in Liquid Rare Gases", *ibid.*

T. Ariga, M. Wakasugi, W. G. Jin, T. T. Inamura, T. Wakui, T. Murayama, T. Ishizuka, H. Katsuragawa, J. Z. Ruan, and I. Sugai: "Measurement of Nuclear Moments in $^{179}Ta$", *ibid.*, Yamagata, Sept./Oct. (1994).

T. Morikawa, Y. Gono, T. Kishida, E. Ideguchi, K. Morita, A. Yoshida, H. Kumagai, G. H. Liu, Y. H. Zhang, A. Ferragut, M. Ishihara, T. Murakami, M. Oshima, Y. Hatsukawa, M. Sugawara, H. Kusakari, M. Ogawa, M. Nakajima, H. Tsuchida, S. Mitarai, A. Odahara, M. Kidera, M. Shibata, J. C. Kim, and S. J. Chae: "First Observation of K-Isomer COULEX with $^{174}Hf$ Isomer Beam", *ibid.*

T. Morikawa and Y. Gono: "Nuclear Spectroscopy by Means of Short Lived Isomer Beams", *ibid.*

E. Ideguchi, A. Odahara, M. Kidera, M. Shibata, S. Mitarai, Y. Gono, T. Kishida, T. Morikawa, M. Oshima, Y. Hatsukawa, S. Hamada, S. Iimura, H. Iimura, M. Shibata, and Y. Kimura: "High-Spin Isomer of $^{148}Tb$", *ibid.*

H. Kitagawa and A. Ozawa: "Beta-Decay of Neutron-Rich Nuclei, $^{17}B$ and $^{19}C$", *ibid.*

A. Motoshima, K. Sagara, H. Nakamura, T. Sugimitsu, and S. Morinobu: "Development of a High-Pressure Gas-Jet Target", *ibid.*

Y. Sugaya, D. Ashery, J. Chiba, H. Ito, K. Kimura, Yu. T. Kieselev, S. Kouda, K. Miyano, T. Murakami, T. Nagae, Y. Nakai, M. Nomachi, H. Ochiishi, S. Sawada, M. Sekimoto, T. Suzuki, K. H. Tanaka, M. K. Vlasov, Y. Yamanoi, K. Yasuda, and Y. Yoshimura: "Subthreshold Antiproton Production in $\alpha$A Reaction", *ibid.*

Y. Satou: "Deuteron Polarimeter at RIKEN", *ibid.*

A. Muta and T. Otsuka: "Structure of $^{11}Be$", *ibid.*

H. Sato: "Polarization of Xe Nuclear Spin by Using the Optical Pumping Method", *ibid.*

N. Nishimori, T. Fujita, A. Motoshima, F. Wakamatsu, H. Akiyoshi, K. Maeda, H. Nakamura, K. Sagara, and T. Nakashima: "Polarization Measurement of 12 MeV Polalized Neutron Beam", *ibid.*

D. Hirata: "Study of the Triaxial Deformation Using the Relativistic Mean Field Theory", *ibid.*

K. Matsuta, T. Minamisono, M. Fukuda, Y. Nojiri, M. Tanigaki, M. Mihara, T. Onishi, T. Yamaguchi, A. Harada, M. Sasaki, T. Miyake, S. Fukuda, K. Yoshida, A. Ozawa, T. Kobayashi, I. Tanihata, J. R. Alonso, G. F. Krebs, and T. J. M. Symons: "Magnetic Moment of Proton-Rich Nucleus $^{9}C$", *ibid.*

K. Matsuta, T. Minamisono, M. Fukuda, Y. Nojiri, S. Fukuda, T. Izumikawa, M. Tanigaki, M. Nakazato, M. Mihara, T. Onishi, T. Yamaguchi, T. Miyake, M. Sasaki, A. Harada, T. Ohtsubo, K. Yoshida, A. Ozawa, T. Kobayashi, I. Tanihata, J. R. Alonso, G. F. Krebs, and T. J. M. Symons: "Asymmetry Parameter of $^{23}Mg$ Beta Decay", *ibid.*

Y. Sugahara: "A New Parameter Set with Mass Number Dependence in the Relativistic Mean Field Theory", *ibid.*

N. Fukunishi: "Effective Interaction in Asymmetric Nuclear Matter II", *ibid.*

M. Yokoyama, T. Otsuka, H. Sagawa, and N. Fukunishi: "Octupole Giant Resonances in Unstable Nuclei", *ibid.*

K. Sumiyoshi and H. Toki: "Equation of State of Supernova Matter and Protoneutron Stars", *ibid.*

A. Ozawa, G. Raimann, R. N. Boyd, J. J. Kolata, F. Chloupeck, K. Yoshida, M. Fujimaki, T. Kobayashi, Y. Watanabe, I. Tanihata, S. Kubono, and K. Kimura: "Beta-Delayed Neutron Decay of $^{19}C$ and $^{17}B$", *ibid.*

T. Horibata and N. Onishi: "Signature Mixing in Tilted Axis Rotating States", *ibid.*

T. Ichihara, M. Ishihara, H. Ohnuma, T. Niizeki, Y. Yamashita, T. Yamamoto, Y. Fuchi, S. Kubono, M. H. Tanaka, H. Okamura, S. Ishida, S. Miyamoto, and H. Toyokawa: "Spin-dipole Resonance of $^{12}B$ Observed in the Charge-Exchange Reaction $^{12}C(^{12}C,^{12}N)^{12}B$ at $E/A = 135$ MeV", *ibid.*

K. Asahi: "Nuclear Magnetic Dipole and Electric Quadrupole Moments of Neutron-rich Nuclei", *ibid.*

H. Ueno: "Measurement of Magnetic Moment for $^{17}N$ by Using Spin Polarization in Projectile Fragmentation Reaction", *ibid.*

H. Suganuma, H. Ichie, and H. Toki: "Multi-flux-tube System in the Dual Ginzburg-Landau Theory and Quark-Gluon-Plasma Formation", *ibid.*

T. Suzuki and T. Otsuka: "Beta Decay in A = 11 Nuclei", *ibid.*

H. Okamura, S. Ishida, N. Sakamoto, H. Otsu, T. Uesaka, T. Wakasa, Y. Satou, S. Fujita, H. Sakai, T. Niizeki, K. Katoh, T. Yamashita, Y. Hara, H. Ohnuma, T. Ichihara, and K. Hatanaka: "Tensor Analyzing Power of the $^{12}C(d,^{2}He)^{12}B$ Reaction at 270 MeV", *ibid.*

A. A. Korsheninnikov: "Spectroscopic Studies of Light Systems Far from Stability Valley and Beyond Drip Line. Results", *ibid.*

E. Yu. Nikolskii: "Spectroscopic Studies of Light Systems Far from Stability Valley and Beyond Drip Line. Experimental System", *ibid.*

T. Ichihara: "Nuclear Reactions and Spectroscopies using the Spectrograph SMART", Jpn. Phys. Soc. Meet., Symp. of Frontier of the Nuclear Spectroscopy, Yamagata, Sept./Oct. (1994).

H. Okamura, S. Ishida, N. Sakamoto, H. Otsu, T. Uesaka, T. Wakasa, Y. Satou, S. Fujita, H. Sakai, T. Niizeki, K. Katoh, T. Yamashita, Y. Hara, H. Ohnuma, T. Ichihara, and K. Hatanaka: "Tensor Analyzing Power of the $^{12}$C(d,$^{2}$He)$^{12}$B Reaction at 270 MeV", 8th Int. Symp. on Polarization Phenomena in Nuclear Physics, Indiana, U.S.A., Sept. (1994).

S. Ishida: "Construction of the Deuteron POLarimeter DPOL at RIKEN", *ibid.*

K. Matsuta, S. Fukuda, T. Izumikawa, M. Tanigaki, M. Fukuda, M. Nakazato, M. Mihara, T. Onishi, T. Yamaguchi, T. Miyake, M. Sasaki, A. Harada, T. Ohtsubo, Y. Nojiri, T. Minamisono, K. Yoshida, A. Ozawa, T. Kobayashi, I. Tanihata, J. R. Alonso, G. F. Krebs, and T. J. M. Symons: "Spin Polarization of $^{23}$Mg in $^{24}$Mg + Au, Cu and Al Collisions at 91 $A$ MeV", *ibid.*

H. Suganuma, S. Sasaki, H. Ichie, and H. Toki: "Dual Higgs Mechanism on Color Confinement and Glueballs", RCNP Symp. on Quark Nuclear Physics with GeV Cooler-Ring Protons and Beyond, Osaka, Sept. (1994).

T. Nakagawa, K. Yuasa-Nakagawa, Y. Futami, K. Furutaka, K. Matsuda, K. Yoshida, T. Mizota, Y. Honjo, N. Tomita, T. Suomiyervi, W. Q. Shen, J. Kasagi, T. Matsuse, and S. M. Lee: "Pre- and Post-Scission Charged Particle Multiplicity in Binary Decay Process for Medium Mass Nuclei", 3rd IN2P3-RIKEN Symp. on Heavy Ion Collisions, Sinrinkohen, Oct. (1994).

T. Motobayashi: "Applications of Coulomb Excitation at Intermediate Energies", *ibid.*

J. Kasagi: "Excitation Energy and Temperature of Hot Nuclei Produced in Incomplete Fusion", *ibid.*

T. Ichihara: "Spin-Flip and Non-spin-flip Isovector Excitation Observed in the ($^{12}$C,$^{12}$N) at $E/A$ = 135 MeV and ($^{13}$C,$^{13}$N) at $E/A$ = 100 MeV Charge-Exchange Reactions", *ibid.*

Y. Gono: "Study of High-Spin States with Isomer Beams", Joint France-Japanese Meet. Within the IN2P3-RIKEN Agreement", *ibid.*

T. Otsuka: "Nuclear Structure Studies of Unstable Nuclei", *ibid.*

H. Kitagawa and A. Ozawa: "Beta-Decay of Neutron-Rich Nuclei, $^{17}$B and $^{19}$C", 1st Int. Workshop on Strucutre and Dynamics of Quantum Many-Body Systems, Non-Linearity and Collective Motions, Aizu-Wakamatsu, Oct. (1994).

A. A. Korsheninnikov: "Experimental Studies of Light Neutron Rich Nuclei", Int. Symp. on Physics of Unstable Nuclei, Niigata, Oct./Nov. (1994).

A. Yoshida: "Measurement of Fusion Cross Section with Neutron Halo Nuclei", *ibid.*

M. Tohyama: "E1 and E2 Giant Resonances in $^{22}$O", *ibid.*

H. Izumi: "Electric Quadrupole Moments of $^{14}$B and $^{15}$B and Magnetic Moment of $^{17}$B", *ibid.*

K. Asahi: "Electromagnetic Moments of Unstable Nuclei Studied with Polarized Projectile Fragments", *ibid.*

T. Otsuka: "Structure of Nuclei Far from Stability", *ibid.*

K. H. Kim, T. Otsuka, and M. Tohyama: "Transfer and Fusion Reactions of Unstable Nuclei", *ibid.*

Y. Gono: "Gamma Spectroscopy with High-Spin Isomer Beams", *ibid.*

T. Motobayashi: "Coulomb Dissociation of $^{8}$B and Solar Neutrino Problem", *ibid.*

H. Toki: "Relativistic Many Body Theory for Unstable Nuclei and Supernovae", *ibid.*

K. Matsuta, M. Fukuda, M. Tanigaki, T. Minamisono, Y. Nojiri, M. Mihara, T. Onishi, T. Yamaguchi, A. Harada, M. Sasaki, T. Miyake, S. Fukuda, K. Yoshida, A. Ozawa, T. Kobayashi, I. Tanihata, J. R. Alonso, G. F. Krebs, and T. J. M. Symons: "Magnetic Moment of Proton Drip-Line Nucleus $^{9}$C", *ibid.*

H. Sato: "Development of Polarized Xe Solid as a Polarizer for Unstable Nuclei", 5th Int. Workshop on Ion-Guide Based Isotope Separation, Hakone, Nov. (1994).

H. Ueno: "Magnetic Moments of $^{17}$N and $^{17}$B and Structure of Nuclei with Large Neutron Excess", *ibid.*

H. Izumi: "Measurement of Electric Quadrupole Moments of Neutron-rich Nuclei $^{14}$B and $^{15}$B", *ibid.*

K. Sumiyoshi: "Structure of Unstable Nuclei and Its Applications", RIKEN Symp. on Use of Supercomputers and Visualization, Wako, Nov. (1994).

H. Suganuma, S. Sasaki, H. Toki, and H. Ichie: "Dual Higgs Mechanism for Quarks in Hadrons", YITP Workshop on From Hadronic Matter to Quark Matter: Evolving View of Hadronic Matter, Kyoto, Nov. (1994).

H. Okuno, K. Asahi, H. Sato, H. Ueno, J. Kura, M. Adachi, T. Nakamura, T. Kubo, N. Inabe, A. Yoshida, T. Ichihara, Y. Kobayashi, Y. Ohkubo, M. Iwamoto, F. Ambe, T. Shimoda, H. Miyatake, N. Takahashi, J. Nakamura, D. Beamel, D. J. Beaumel, W.-D. Schmidt-Ott, and M. Ishihara: "Polarization Mechanism of Projectile Fragment", Symp. on Science of Short-lived Nuclei 93, Tanashi, Dec. (1994).

## 3. Atomic and solid-state physics

M. Takami and J. H. M. Beijersbergen: "Laser Spectroscopy of Atoms and Molecules in Superfluid Liquid Helium I", 48th Ann. Meet. Phys. Soc. Jpn., Sendai, Mar. (1993).

J. H. M. Beijersbergen and M. Takami: "Laser Spectroscopy of Atoms and Molecules in Superfluid Helium II", *ibid.*

J. H. M. Beijersbergen, Q. Hui, and M. Takami: "Laser Spectroscopy of Clusters in Superfluid Helium", 1993 Fall Meet. Phys. Soc. Jpn., Okayama, Oct. (1993).

I. Shimamura: "Properties of Exotic Helium", Symp. on the Theory of Dynamic Processes Involving Exotic Atoms, Yugawara, Feb. (1994).

T. Okada, K. Asai, N. Yamada, T. Matsumoto, Y. Yamada, and Y. Kodama: "$^{57}$Fe Mössbauer Studies of $YBa_2Cu_{3.928}Fe_{0.072}O_8$ Oriented with a High Magnetic Field II", 49th Ann. Meet. Phys. Soc. Jpn., Fukuoka, Mar. (1994).

R. Kadono, A. Matsushita, K. Nishiyama, K. Nagamine, S. Fujii, and S. Tanigawa: "Charge State and Diffusivity of Muonium in n-type GaAs", *ibid.*

Q. Hui, J. L. Persson, J. H. M. Beijersbergen, and M. Takami: "Radiative Lifetimes of Atoms in Liquid Helium", *ibid.*

J. L. Persson, Q. Hui, J. H. M. Beijersbergen, and M. Takami: "Atoms in Liquid Helium: Two Different Sites", *ibid.*

Y. Matsui, I. Ida, M. Koide, N. Nakamura, Y. Kanai, Y. Awaya, T. Nagata, T. Kambara, T. Takayanagi, K. Wakiya, and S. Otani: "Measurement of Ejected Electron Spectra from $Ne^{6+**}$", *ibid.*

I. Ida, Y. Matsui, M. Koide, N. Nakamura, Y. Kanai, Y. Awaya, T. Nagata, T. Kambara, T. Takayanagi, K. Wakiya, and S. Otani: "Measurement of Ejected Electron Spectra from $O^{6+**}$ Produced by $O^{6+}$ + Ne, Ar, $N_2$", *ibid.*

J.-Z. Tang, Y. Wakabayashi, M. Matsuzawa, S. Watanabe, and I. Shimamura: "Calculations of Photodetachment from $H^-$ Using the Hyperspherical Close-Coupling Method", *ibid.*

K. Ando, T. Kambara, Y. Kanai, M. Oura, N. Nakai, Y. Awaya, and Z. Yaming: "Lifetimes of Ne-Like Fe Ion Measured by Beamfoil Spectroscopy", *ibid.*

E. Yagi: "Channelling Method: Studies on the State of Hydrogen and Inert Gas Atoms in Metals", Symp. on the Characterization of Defects, *ibid.*

I. Shimamura: "Properties of Exotic Helium", Int. School Phys. Exotic Atoms, Erice, Sicily, Italy, Mar. (1994).

R. Kadono: "Quantum Tunneling Diffusion of Muon in Solids at Ultra-low Temperature-Atomic Diffusion by its Wave Character", 67th Natl. Meet. Chem. Soc. Jpn. (Spring), Tokyo, Mar. (1994).

M. Terasawa, T. Mitamura, H. Tsubakino, A. Yamamoto, T. Kohara, K. Ueda, Y. Awaya, T. Kambara, Y. Kanai, M. Oura, and Y. Nakai: "Influence of High Energy Heavy Ion Irradiation on Magnetic Flux Pinning in Oxide-Superconductors", 1994 Spring Ann. Meet. of Atomic Energy Society of Japan, Tsukuba, Mar. (1994).

M. Kimura, I. Shimamura, and M. Inokuti: "Double and Single Ionization of He in Collisions with Antiprotons and Protons at Low-keV Energies", Ann. Meet. Div. Atom. Molec. Opt. Phys., Amer. Phys. Soc., Crystal City, Virginia, U.S.A. Apr. (1994).

Y. Awaya and M. Oura: "Present Status of SPring-8 and the Concept of the Atomic Physics Undulator Beamline at SPring-8", Workshop on Atomic Physics at High Brilliance Synchrotron Sources, Argonne, U.S.A., Apr. (1994).

M. Kimura, I. Shimamura, and M. Inokuti: "Double and Single Ionization of He by Slow Protons and Antiprotons", 14th Int. Conf. Few Body Prob. Phys., Williamsburg, Virginia, U.S.A., May (1994).

J. H. M. Beijersbergen, Q. Hui, and M. Takami: "Alkaline-earth Atoms in HeII: the Existence of Bubble States", Symp. at the Int. Wissenschaftsforum Heidelberg, Heidelberg, Germany, May (1994).

J. L. Persson, Q. Hui, and M. Takami: "Spectroscopy and Dynamics of Neutral Atoms in Superfluid Helium", *ibid.*

Y. Awaya: "Studies of Atomic Physics at the RIKEN Accelerator Facility", Int. Workshop on Iron Group Atoms in the Laboratory and Space, Lund, Sweden, June (1994).

R. Hutton, S. Huldt, B. Nyström, I. Martinson, K. Ando, T. Kambara, Y. Kanai, Y. Nakai, Y. Awaya, and J. Sugar: "Experimental Lifetimes of the $3p^2P$ Levels in Na-like $Nb(Nb^{30+})$", 14th Int. Conf. on Atomic Physics (ICAP-XIV), Corolado, U.S.A., July/Aug. (1994).

J. L. Persson, Q. Hui, and M. Takami: "Spectroscopy of Metal Atoms in Superfluid Helium", *ibid.*

M. Terasawa, T. Mitamura, T. Kohara, K. Ueda, H. Tsubakino, A. Yamamoto, Y. Awaya, T. Kambara, Y. Kanai, and M. Oura: "Influence of High Energy Heavy Ion Irradiation on Magnetic Flux Pinning in $La_{1.85}Sr_{0.15}CuO_4$", 4th Int. Conf. on Materials and Mechanism of Superconductivity, and High Temperature Superconductors, Grenoble, France, July (1994).

M. Takami: "Laser Spectroscopy in Superfluid Helium: Exotic Properties of Atoms, Molecules and Superfluids", U.S.-Japan Seminar on Quantum Electronic Devices and States of Matter, Napa, U.S.A., Aug. (1994).

Q. Hui, J. L. Persson, M. Nakamura, and M. Takami: "Spectroscopy of Alkaline Earth Dimers in Liquid Helium", Fall Meet. Phys. Soc. Jpn., Shizuoka, Sept. (1994).

J. L. Persson, Q. Hui, M. Nakamura, and M. Takami: "Ionization Potential of Atoms in Superfluid Helium", *ibid.*

N. Watanabe, S. Kravis, M. Oura, T. Kojima, Y. Awaya, K. Okuno, and M. Kimura: "Characteristics of the RIKEN EBIS", *ibid.*

I. Shimamura and M. Kimura: "General Properties of Adiabatic Potentials for Exotic Atoms", *ibid.*

T. Kambara, Y. Awaya, Y. Kanai, Y. Nakai, T. Kojima, O. Jagutzki, and H. Schmidt-Böcking: "Recoil Ion Momentum Analysis in 8 MeV $O^{n+}$-He Collisions", *ibid.*

Y. Bito, A. Ito, M. Imai, N. Imanishi, Y. Nakai, T.

Kambara, Y. Kanai, T. Kojima, and Y. Awaya: "Fragmentation of $C_{60}$ by Highly Charged Heavy Ion Impact", *ibid.*

Y. Kanai, T. Kambara, Y. Nakai, M. Oura, S. Kravis, and Y. Awaya: "Incident Charge-State Dependence of Binary Encounter Peak Energy II", *ibid.*

T. Okada, Y. Noro, H. Kitazawa, Y. Kobayashi, and F. Ambe: "$^{61}$Ni Mössbauer in Spinel Chromite", *ibid.*

N. Yamada, Y. Kobayashi, T. Okada, and T. Tatsumi: "Mössbauer Effect of $^{57}$Fe in $YSr_2Cu_{3-x}Fe_xO_{7-\delta}$", *ibid.*

Y. Kanai, T. Kambara, Y. Awaya, H. Ida, Y. Matsui, T. Takayanagi, K. Wakiya, N. Nakamura, M. Koide, and S. Ohtani: "Ejected Electron Spectra from Triplet States of Double Excited $O^{4+}$ and $Ne^{6+}$", 7th Int. Conf. on Physics of Highly Charged Ions(HCI-94), Wien, Australia, Sept. (1994).

R. Hutton, S. Huldt, B. Nyström, I. Martinson, K. Ando, T. Kambara, Y. Kanai, Y. Nakai, Y. Awaya, and J. Suger: "Beam-Foil Measurements on Highly Ionized Nb and Zr at RILAC", *ibid.*

Y. Kanai, T. Kambara, M. Oura, Y. Nakai, and Y. Awaya: "Binary Encounter Electron Peaks for 0° Electrons in Collisions of $Bi^{q+}$", *ibid.*

Y. Yamazaki, K. Komaki, S. Sataka, M. Imai, H. Tawara, K. Kawatsura, Y. Kanai, D. R. Schultz, and C. O. Reinhold: "Binary Encounter Electrons Observed at Zero Degree in 1 MeV/u Au + He", *ibid.*

Y. Awaya, K. Ando, Y. Kanai, T. Kambara, M. Oura, and Y. Nakai: "Atomic Physics Studies at the RIKEN Accelerator Research Facility", 2nd Asian Int. Seminar on Atomic and Molecular Physics, Beijing, China, Oct. (1994).

I. Shimamura and M. Kimura: "Interactions of Atoms with Antiprotons and Negative Mesons", *ibid.*

I. Shimamura: "Antiprotonic Atoms", 19th Meet. of the Soc. for Atomic Collision Research, Tokyo, Oct. (1994).

Y. Zou, Y. Awaya, C. P. Bhalla, T. Kambara, Y. Kanai, M. Oura, Y. Nakai, K. Ando, A. Hitachi, and S. Kravis: "L-Subshell Vacancy Production of Fast Argon Ions in Solids", Int. Conf. on the Application of Accelerators in Research and Industry, Denton, U.S.A., Nov. (1994).

I. Shimamura: "Bound States and Collision Processes Due to Coulomb Interactions between Atoms and Negatively Charged Hadrons", Symp. on Strong Interactions in Exotic Atoms, Tanashi, Nov. (1994).

## 4. Radiochemistry, radiation chemistry, and radiation biology

K. Ando et al.: "Relative Biological Effectiveness of Accelerated Carbon Ions on Experimental Tumors", 41st Ann. Meet. of Radiat. Res. Soc., Dallas, U.S.A., Apr. (1993).

K. Ando: "Japanese Radiobiological Experience of Heavy Ions", NIRS Int. Symp. on Heavy Charged Particle Therapy, Chiba, June (1993).

Y. Hyodo-Taguchi, T. Kanai, S. Minohara, and Y. Furusawa: "Effects of Accelerated Carbon-Ion on the Induction of Dominant Lethality in the Teleost Fish, *Oryzias latipes*", 36th Ann. Meet. Jpn. Radiat. Res. Soc., Hiroshima, Oct. (1993).

Y. Otsu, H. Murakami, and Y. Itoh: "Positron Annihilation in Porous Grasses", 49th Ann. Meet. Phys. Soc. Jpn., Fukuoka, Mar. (1994).

K. Kimura: "Luminescence Efficiencies of Auger-free Luminescence and Self-Trapped Exciton of $BaF_2$, and Projectile-ion Dependence on the Efficiencies", *ibid.*

R. Hirunuma, R. Furuta, S. Enomoto, K. Endo, A. Tanaka, M. Yanaga, S. Ambe, Y. Ohkubo, Y. Kobayashi, M. Iwamoto, H. Maeda, and F. Ambe: "Study on Distribution of Radioactive Nuclides in Rats Using a Multitracer Technique", RIKEN Symp. on New Techniques for Utilization of RI as Tracers '94, Wako, Mar. (1994).

S. Ambe, Y. Ohkubo, Y. Kobayashi, M. Iwamoto, H. Maeda, and M. Yanokura: "Study on Transport and Distribution of Elements in Plants", *ibid.*

S. Shibata, K. Watari, Y. Noda, S. Ambe, M. Iwamoto, H. Maeda, and F. Ambe: "Simultaneous Analysis on Solid-Liquid Adsorption Behavior of Various Elements Using Radioactive Multitracer: Non-ionic Macro-reticular Copolymer and Activated Carbon Fiber", *ibid.*

K. Ando et al.: "Homogeneity and Heterogeneity of Carbon-12 Spread-Out-Bragg-Peak in Tumor Cell Kill and Tumor Growth Delay", 42nd Ann. Meet. of Radiat. Res. Soc., Nashville, U.S.A., Apr. (1994).

S. Y. Chen, S. Ambe, Y. Ohkubo, Y. Kobayashi, M. Iwamoto, H. Maeda, N. Takematsu, and F. Ambe: "Adsorption Study of Metal Ions Using Radioactive Multitracers", 3rd Int. Conf. on Methods and Applications of Radioanalytical Chemistry, Kailua-Kona, U.S.A., Apr. (1994).

S. Ambe, Y. Ohkubo, Y. Kobayashi, M. Iwamoto, H. Maeda, and Y. Yanokura: "Multitracer Study on Transport and Distributions of Metal Ions in Plants", *ibid.*

S. Ambe, S. Y. Chen, Y. Ohkubo, Y. Kobayashi, H. Maeda, M. Iwamoto, M. Yanokura, and F. Ambe: "Multitracer, a New Tracer Technique: Its Principle, Features and Application", *ibid.*

R. Hirunuma, R. Furuta, S. Enomoto, A. Tanaka, K. Endo, M. Yanaga, S. Ambe, Y. Ohkubo, Y. Kobayashi, M. Iwamoto, H. Maeda, and F. Ambe: "Studies on the Uptake and Distribution of Radioactive Nuclides in Organs of Rats Using a Multitracer Technique", 67th Natl. Meet. Chem. Soc. Jpn. (Spring), Tokyo, Mar./Apr. (1994).

Y. Takahashi, Y. Minai, S. Ambe, Y. Kobayashi, Y. Ohkubo, M. Iwamoto, M. Yanokura, H. Maeda, S. Shibata, N. Takematsu, F. Ambe, and T. Tominaga: "Multitracer Study on Behaviors of Metal Ions in the

Aqueous System Containing Humic Acid and Clay Minerals or Silicagel", *ibid.*

Y. Sato, J. Kurachi, K. Soga, A. Shinohara, M. Furukawa, S. Kojima, Y. Ohkubo, F. Ambe, K. Mukai, A. Yokoyama, T. Saito, and H. Baba: "Differential Recoil Ranges of Reaction Products in the Interaction of Copper with Intermediate Energy $^{40}$Ar, $^{14}$N Ions", *ibid.*

K. Mukai, A. Yokoyama, T. Saito, H. Baba, Y. Ohkubo, A. Shinohara, M. Furukawa: "Incomplete Fusion in the $^{141}$Pr + $^{40}$Ar System", *ibid.*

Y. Itoh, H. Murakami, and A. Kinoshita: "Positronium Formation and Annihilation in Porous Silicon", 10th Int. Conf. on Positron Annihilation, Beijing, China, May (1994).

Y. Itoh, K. Lee, T. Nakajyo, A. Goto, A. Nakanishi, M. Kase, I. Kanazawa, Y. Yamamoto, and N. Oshima: "Slow Positron Production Using the RIKEN AVF Cyclotron", 6th Int. Workshop on Slow-Positron Beam Techniques for Solids and Surfaces, Makuhari, May (1994).

R. Hirunuma, K. Endo, M. Yanaga, S. Enomoto, S. Ambe, and F. Ambe: "Studies on the Distribution of Various Elements in Organs of Rats Using a Multitracer Technique", 9th Symp. on Biofunctional Chemistry, Tokyo, May (1994).

M. Yanaga, R. Hirunuma, R. Furuta, S. Enomoto, K. Endo, A. Tanaka, S. Ambe, Y. Ohkubo, Y. Kobayashi, M. Iwamoto, H. Maeda, and F. Ambe: "Multitracer Studies on Uptake and Distribution of Radioactive Nuclides in Organs of Rats", 31st Ann. Meet. on Radioisotopes in the Physical Sciences and Industries, Tokyo, July (1994).

M. Iwamoto, S. Ambe, Y. Ohkubo, Y. Kobayashi, H. Maeda, M. Yanokura, and F. Ambe: "Production of Multitracer Nuclides by Irradiation with a $^{84}$Kr Beam", *ibid.*

Y. Itoh, K. Lee, A. Goto, N. Nakanishi, M. Kase, N. Oshima, T. Nakajyo, I. Kanazawa, and Y. Ito: "Slow Positron Production Using RIKEN AVF Cyclotron", *ibid.*

S. Ambe, K. Takeshita, Y. Ohkubo, Y. Kobayashi, H. Maeda, M. Iwamoto, and F. Ambe: "Multitracer Study on Adsorption of Metal Ions on $\alpha$-$Fe_2O_3$", *ibid.*

K. Eguchi-Kasai, M. Murakami, H. Itsukaichi, K. Fukutsu, T. Kanai, Y. Furusawa, K. Sato, H. Ohara, and F. Yatagai: "The Role of DNA Repair on Cell Killing by Charged Particles", 30th COSPAR Meet., Hamburg, Germany, July (1994).

K. Kimura: "Excitation-Density Dependent Competition between Radiative and Nonradiative Annihilations of Core- and Self-trapped-Excitons Produced by Ion Irradiation of a Single Crystal of $BaF_2$", Gordon Conf., Newport, U.S.A., July (1994).

K. Kimura: "Track-Depth Resolved Dynamics of Helium Excimers along 4 MeV/amu N-ion Tracks in Near-Liquid and Liquid Helium", *ibid.*

R. Hirunuma, K. Endo, M. Yanaga, S. Enomoto, S. Ambe, and F. Ambe: "Multitracer Study on Behavior of Trace Elements in Rats", Hiroshima Int. Mini Symp. on Molecular Recognition Involving Metal Complexes, Hiroshima, July (1994).

M. Yanaga, S. Enomoto, R. Hirunuma, R. Furuta, K. Endo, S. Ambe, and F. Ambe: "Study on Uptake and Excretion of Radioactive Nuclides in Rats Using the Multitracer Technique", Int. Trace Analysis Symp. '94, Hakodate and Sapporo, Aug. (1994).

S. Enomoto, M. Yanaga, R. Hirunuma, R. Furuta, K. Endo, S. Ambe, and F. Ambe: "Multitracer Study on Distribution of Radioactive Nuclides in Rats", *ibid.*

K. Kimura and T. Yoshikane: "Formation Efficiencies and Decays of Outermost Core- and Self-trapped Excitons in Ion-Excited $BaF_2$ Single Crystal", 37th Conf. Radiat. Chem., Sapporo, Sept. (1994).

K. Kimura: "A Prize Talk of This Society: Track-Depth and Time Resolved Dynamics of Excited States Created in Ion Tracks", *ibid.*

H. Shibata, T. Furusawa, and K. Kimura: "Study on Luminescence Mechanisms of $BaF_2$ by Means of Electron-Pulse Radiolysis", *ibid.*

S. Ambe and F. Ambe: "Mössbauer Isomer Shifts of Defect $^{119}$Sn Atoms with Ligands from Silver to Iodine", Eötvös Workshops in Science: Nuclear Techniques in Structural Chemistry, Budapest, Hungary, Sept. (1994).

Y. Ohkubo, Y. Kobayashi, S. Ambe, K. Asai, T. Okada, and F. Ambe: "Local Structure and Valence of Impurity Ions in Oxides by TDPAC and Mössbauer Emission Spectroscopy", *ibid.*

K. Kimura and T. Yoshikane: "Formation Efficiencies and Decay Mechanisms of Outermost-core and Self-trapped Excitons in Ion-Irradiated $BaF_2$", 1994 Fall Meet. Phys. Soc. Jpn., Shizuoka, Sept./Oct. (1994).

K. Kimura and T. Yoshikane: "Track-depth Resolved Dynamics of Excited States in Dense Argon at Low Temperature", *ibid.*

Y. Hama, K. Hamanaka, H. Matsumoto, H. Kudoh, T. Sasuga, and T. Seguchi: "Inhomogeneous Degradation of Polymers by X-rays, Gamma-rays and Ion-beam as Studied by Micro-FT-IR", 9th Int. Meet. on Radiation Processing, Istanbul, Turkey, Sept. (1994).

S. Ambe, T. Shinonaga, H. Maeda, M. Iwamoto, S. Uchida, and H. Yasuda: "Determination of Selective Absorption Coefficient for Elements in Plants by a Radioactive Multitracer Technique.", 38th Symp. on Radiochemistry, Shizuoka, Sept. (1994).

S. Shibata, K. Watari, Y. Noda, S. Ambe, M. Iwamoto, H. Maeda, and F. Ambe: "Simultaneous Analysis on Solid-Liquid Adsorption Behavior of Various Elements Using Radioactive Multitracer: Non-ionic Macro-reticular Copolymer and Activated Carbon Fiber", *ibid.*

N. Ito, N. Aoki, H. Harakawa, Y. Saito, K. Kimura,

S. Ambe, M. Iwamoto, H. Maeda, and F. Ambe: "Study on the Ion Exchange Adsorption and Application to Analytical Chemistry on Superacid Resin NAFION Using a Multitracer", *ibid.*

S. Ambe, Y. Iijima, M. Iwata, M. Takeda, M. Takahashi, H. Maeda, M. Iwamoto, and F. Ambe: "Study on Extraction of Various Elements with Crownether Using the Multitracer Technique", *ibid.*

S. Ambe, Y. Ohkubo, Y. Kobayashi, M. Iwamoto, H. Maeda, and M. Yanokura: "Multitracer Study on Transport and Distribution of Metal Ions in Plants", *ibid.*

K. Mukai, K. Takesako, H. Kusawake, Y. Sato, T. Inoue, R. Kasuga, A. Yokoyama, T. Saito, H. Baba, Y. Ohkubo, A. Shinohara, and M. Furukawa: "Incomplete Fusion of Intermediate Energy Induced by Heavy Ions", *ibid.*

M. Iwamoto, S. Ambe, Y. Ohkubo, Y. Kobayashi, H. Maeda, M. Yanokura, and F. Ambe: "Production of Multitracer Nuclides by Irradiation with an $^{40}$Ar Beam", *ibid.*

M. Yanaga, R. Hirunuma, K. Endo, S. Enomoto, S. Ambe, and F. Ambe: "Study on Distribution of Various Trace Elements in Rats Using the Multitracer Technique (1): Uptake and Excretion Behaviour", *ibid.*

S. Enomoto, S. Ambe, F. Ambe, M. Yanaga, R. Hirunuma, and K. Endo: "Study on Distribution of Various Trace Elements in Rats Using the Multitracer Technique (2): Metabolisms and Accumulations of Trace Elements in Various Tissues, Organs and Body Fluids", *ibid.*

T. Ozaki, Y. Takahashi, Y. Minai, S. Ambe, M. Iwamoto, H. Maeda, F. Ambe, S. Takematsu, and T. Tominaga: "Anomalous Adsorption Behavior of Rare Earths", *ibid.*

A. Shinohara, J. Kurachi, K. Mukai, Y. Sato, S. Kiryu, S. Kojima, T. Saito, A. Yokoyama, Y. Ohkubo, M. Furukawa, and F. Ambe: "Angular Distribution of Recoil Products in the Heavy-Ion Reaction of Gold in the Intermediate Energy Range", *ibid.*

K. Kikuchi, S. Nakanishi, K. Sueki, H. Nakahara, S. Enomoto, and F. Ambe: "Pharmacokinetics Study of Water-Miscible Fullerene by $^{14}$C Labeling", *ibid.*

M. Murakami, K. Eguchi-Kasai, H. Itsukaichi, K. Fukutsu, K. Sato, F Yatagai, and T. Kanai: "Biological Effects of Heavy-Ion Irradiation on DNA Double-Strand Breaks Repair Deficient Mutant Cell Line", 37th Ann. Meet. Jpn. Radiat. Res. Soc., Fukuoka, Oct. (1994).

Y. Kagawa, F. Yatagai, M. Suzuki, Y. Kase, A. Kobayashi, M. Watanabe, and F. Hanaoka: "Analysis of Mutations in the Human *HPRT* Gene Induced by Accelerated Heavy-ion Irradiation", *ibid.*

S. Kitayama, H. Takagi, M. Kohroku, and H. Ito: "RecA Gene and Radioresistance of *Deinococcus radiodurans*", *ibid.*

H. Maezawa, T. Mori, F. Yatagai, T. Kanai, S. Inokuchi, and H. Hanada: "Radiosensitivity of Human Skin Cells Irradiated with Heavy-Ion Beams", *ibid.*

M. Yanaga, S. Enomoto, R. Hirunuma, K. Endo, S. Ambe, and F. Ambe: "Study on Uptake and Distribution of Various Elements in Rats Using the Multitracer Technique (1)", 68th Natl. Meet. Chem. Soc. Jpn. (Fall), Nagoya, Oct. (1994).

R. Hirunuma, K. Endo, M. Yanaga, S. Enomoto, S. Ambe, and F. Ambe: "Study on Uptake and Distribution of Various Elements in Rats Using the Multitracer Technique (2)", *ibid.*

Y. Hama, K. Hamanaka, H. Matsumoto, H. Kudoh, T. Sasuga, and T. Seguchi: "Relationship between Energy Profile and Chemical Structural Change in Polymers Irradiated by Ion-beams", 6th Japan-China Bilateral Symp. on Radiation Chemistry, Tokyo, Nov. (1994).

K. Kimura: "Enhanced Decay Rates of Core Excitons in Ion Irradiated $BaF_2$ and CsCl Single Crystals and Ion Dependent Luminescence Efficiencies", *ibid.*

S. Kitayama, H. Takagi, M. Kohroku, and H. Ito: "RecA of *Deinococcus radiodurans*", 17th Ann. Meet. Jpn. Mol. Biol. Soc., Kobe, Dec. (1994).

## 5. Material analysis

K. Maeda and J. Kawai: "Analysis of Aqueous Solution by Ion-Induced X-Ray Spectrometry", 49th Ann. Meet. of Phys. Soc. Jpn., Fukuoka, Mar. (1994).

N. Arai, W. Sakamoto, and K. Maeda: "An Atempt at Analysis of Trace Elements in Otoliths by PIXE", Spring Meet. Jpn. Soc. Sci. Fisheries, Tokyo, Apr. (1994).

N. Arai, W. Sakamoto, and K. Maeda: "Correlation between Trace Element Concentrations and Ambient Seawater Temperature in Red Sea Bream", *ibid.*

K. Sato, H. Honda, J. Jyunji, M. Yanokura, and M. Aratani: "Analysis of Gas Tables as Fire Cause by Means of the Heavy-Ion Rutherford Scattering", Japan Fire Society, Tokyo, May (1994).

K. Sato, H. Honda, J. Ushimaru, M. Yanokura, and M. Aratani: "A Proof for the Gas Range under Operation as a Cause of Fire by Heavy-Ion Rutherford Scattering", Symp. Fire Science and Engineering, Tokyo, May (1994).

A. S. Yukimatsu, S. Takagi, T. Terasawa, T. Kohno, F. Makino, and M. Ejiri: "Structural Variation of Radiation Belt Associated with Solar Flare and SC Event Observed by Radiation Monitor (RDM) Aboard Akebono (EXOS-D)", 8th Int. Symp. on Solar Terrestrial Physics Dedicated to Solar Terrestrial Energy Symp. (STEP), Sendai, June (1994).

A. S. Yukimatsu, M. Ejiri, S. Takagi, T. Terasawa, T. Kohno, and F. Makino: "Structural Variations of Radiation Belts Observed by Radiation Monitor (RDM) Aboard Akebono (EXOS-D)", Taos 10th

Workshop on the Earth's Trapped Particle Environment, New Mexico, U.S.A., Aug. (1994).

K. Sato, H. Honda, J. Jyunji, M. Yanokura, and M. Aratani: "Heavy-Ion Rutherford Scattering Applied to the Fire Investigation", 38th Symp. Radiochemistry, Shizuoka, Sept. (1994).

K. Sato, H. Honda, J. Jyunji, M. Yanokura, and M. Aratani: "Analysis of Gas Tables as Fire Cause by Means of the Heavy-Ion Rutherford Scattering", 42th Conf. Natl. Fire Engineer, Tokyo, Oct. (1994).

K. Maeda and J. Kawai: "Satellite X-Rays Caused by Radiative Auger Effect (RAE)", 12th PIXE Symp., Ikeda, Oct. (1994).

J. Kawai and K. Maeda: "Vertical Beam Line of RIKEN Heavy Ion Linear Accelerator", *ibid.*

N. Arai, W. Sakamoto, and K. Maeda: "Trace Element Hard Tissues in Maline Life", *ibid.*

T. Kohno: "Observation of Anomalous and Solar Cosmic Rays in the Magnetosphere (ORCAS)", Workshop on Participation Oppotunity on the Brazillian Scientific Microsatellite, Sao Jose Dos Campos, Brazil, Oct. (1994).

J. Kawai, S. Hayakawa, S. Y. Zhen, K. Kitajima, K. Maeda, A. Nakao, H. Adachi, and Y. Gohshi: "Total Reflection X-Ray Absorption Fine Structure of Semiconductor Wafers", 5th Workshop on Total Reflection X-Ray Fluorescence Spectroscopy and Related Spectroscopical Methods, Tsukuba, Oct. (1994).

# X. LIST OF SYMPOSIA

(Jan.–Dec. 1994)

1) Dynamics of Hot Nuclei
21–22 Feb., Wako, RIKEN, Cyclotron Lab.

2) New Techniques for Utilization of RI as Tracers '94
28 Mar., Wako, RIKEN, Nuclear Chemistry Lab.

3) Third IN2P3 Symposium in Heavy Ion Collisions
24–28 Oct., Shinrin-Koen, Saitama, Radiation Lab.

4) 5th International Workshop on Ion-guide Based Isotope Separation
5–7 Nov., Hakone-Gora, Cyclotron Lab.

5) Advanced Positron Technologies and Their New Application
15–16 Dec., Wako, RIKEN, Nuclear Chemistry Lab.

# XI. LIST OF SEMINARS

(Jan.–Dec. 1994)

## Radiation Lab., Cyclotron Lab., and Linear Accelerator Lab.

1) T. Horibata, Aomori Univ./RIKEN (Aomori /Saitama), 17 Jan.
"Tilted Axis Rotating States in $^{128}$Os Yrast"

2) H. Suganuma, RIKEN (Saitama), 3 Feb.
"Color Confinement, Quark Pair Creation and Dynamical Chiral-Symmetry Breaking in the Dual Ginzburg-Landau Theory"

3) S. Nonose, Univ. Tokyo (Tokyo), 16 Feb.
"Cluster Collision"

4) S. Midorikawa, Meiji Univ. (Tokyo), 23 Feb.
"Folded Bifurcation in Coupled Asymmetric Logistic Maps"

5) K. Varga, RIKEN (Saitama), 6 Apr.
"Microscopic Multicluster Description of the Neutron-rich Helium Isotopes"

6) K. Tanaka, RCNP, Osaka Univ. (Osaka), 8 Apr.
"Higher Order Quantum Correction on the Relativistic Many-Body Problem and Behavior of High Density Matter"

7) N. Ohnishi, Univ. Tokyo (Tokyo), 18 Apr.
"Periodic Solution and Quantization"

8) Y. Yoshii and T. Kajino, NAO, Theoretical Astrophysics (Tokyo), 10 May
"The Creation of Light Elements – Cosmology and Cosmic Rays"

9) Dr. S. Kim, Argonne Natl. Lab. (USA), 16 May
"Quenched QCD Spectrum Calculation"

10) G. Mathews, NAO, Theor. Astrophys. / Lawrence Livermore Natl. Lab. (Tokyo/USA), 17 May
"Cosmic Phase Transitions and Primordial Nucleosynthesis"

11) Y. Ogawa, INS/RIKEN (Tokyo/Saitama), 24 May
"Momentum Distribution of a Fragment from Breakup Reaction of $^{11}$Li and Neutron Correlation"

12) A. Ono, Kyoto Univ. (Kyoto), 20 May
"Fragment Flow on Heavy Ion Reactions"

13) Y. Batygin, RIKEN (Saitama), 27 May
"Computer Simulation of High Current Beam Dynamics in Particle Accelerator"

14) D. J. Rowe, Univ. of Toronto (USA), 11 July
"A Vector Coherent State Representation of the Five-Dimensional Harmonic Oscillator: Algebraic Models of Nuclear Collective Motion"

15) J. R. Bennett, Tohoku Univ. (Sendai), 12 July
"Interacting Boson Model Description of Dissipation in Fusion and Fission"

16) H. Schuessler, Texas A&M Univ./INS (USA/ Tokyo), 1 Aug.
"Charged Particle Crystals and On-line Spectroscopy"

17) M. Fujiwara, RCNP (Osaka), 4 Aug.
"Microscopic Structures of Spin-Isospin Excitations in Nuclei"

18) Y. T. Ogaessian, Dubna Joint Inst. Nucl. Res. (Dubna), 29 Sept.
"Synthesis of Super Heavy Element at Dubna"

19) N. D. Dang, Vietnam Atomic Energy Commission/INS (Vietnam/Tokyo), 17 Oct.
"Width of Giant Dipole Resonance in Hot Nuclei"

20) H. C. Flocard, Div. Phys. The. I. P. N. Orsay (Orsay), 12 Oct.
"Microscopic Calculations of Superdeformed Bands"

21) S. S. Kapoor, Bhabha Atomic Res. Cent. (India), 18 Oct.
"Study of Dynamics in Heavy Ion Fusion Fission Reactions"

22) C. Bertulani, Inst. Fisica Univ. Federal do Rio de Janeiro (Brazil), 7 Nov.
"Multiphonon Excitation of Giant Resonance"

23) A. Shirokov, Inst. Nucl. Phys., Moscow State Univ. (Moscow), 8 Nov.
"J-Matrix Approach and Three-Body Structure of $^{11}$Li"

24) T. Izumoto, Rikkyo Univ. (Tokyo), 21 Nov.
"Coupled Channels Analyses of Scattering and Fusion Cross Sections of $^{16}$O + $^{152,154}$Sm, $^{186}$W System at Sub- and Near-Barrier Energies"

25) W. von Oertzen, Hahn-Meitner Inst. (Germany),

22 Nov.
"Spectroscopy of $^{10}$He and Other Neutron Rich Nuclei by Two Body Reactions"

26) L. Zhang, IMPAS (China), 22 Nov.
"Possibility of Study the Neutron-Rich Nuclides of Heavy Mass Region with IGISOL"

27) N. Van Giai, Inst. Phys. Nucl., Univ. Paris-Sud (Orsay), 1 Dec.
"Particle Decay of Isovector Giant Resonances"

28) S. Nagamiya, Columbia Univ. (USA), 6 Dec.
"High Energy Frontier in Heavy Ion Physics"

29) E. Suraud, Univ. of Toulouse (France), 16 Dec.
"Multifragmentation in Heavy-Ion Collisions – Mean Field and Fluctuations"

30) T. Suzuki, Fukui Univ./RIKEN (Fukui/Saitama), 19 Dec.
"The Macroscopic Model of Giant Resonance States in Neutron-rich Nuclei"

31) K. Sumiyoshi, RIKEN (Saitama), 20 Dec.
"The Relativistic Mean Field Theory for Unstable Nuclei and the Birth of Neutron Stars"

32) R. Boyd, Ohio State Univ. (USA), 27 Dec.
"Recent Studies in Primordial and Stellar Nucleosynthesis"

### Atomic Physics Lab.

1) M. Stockli, Kansas State Univ. (USA), 10 Jan.
"The KSU-CRYEBIS: Its Status, Its Potential, and Its Applications"

2) Chii-Dong Lin, Kansas State Univ. (USA), 13 Jan.
"Orientation and Alignment in Ion-atom Collisions"

3) H. Marxer, Oxford Univ. (UK), 7 Feb.
"R-Matrix Calculations for Atoms in Crossed Fields"

4) B. Zhou, Kansas State Univ. (USA), 7 Feb.
"Photodetachment of $H^-$ in Static Electric Field"

5) C. Zhu, Inst. Mol. Sci. (Aichi), 15 Feb.
"The Two-State Curve-Crossing Problem"

6) I. A. Sellin, Univ. of Tennessee (USA), 15 Apr.
"Double Ionization in He at Intermediate and High Photon Energy"

7) L. P. Presnyakov, Lebev Phys. Inst. (Russia), 16 May
"Interactions of Highly Charged Ions with Electrons, Atoms, and Negative Ions"

8) Sung-Ho Suck Salk, Pohang Univ. Sci. Technol. (Korea), 3 June
"Berry Phase in Atom-Diatom Collisions"

9) R. I. Hall, Univ. Pierre et Marie Curie (France), 10 Aug.
"One-Photon Double Ionization of Rare-Gas Atoms in the Threshold Region"

10) E. E. Nikitin, Israel Inst. of Tech. (Israel), 7 Oct.
"Quasiclassical Theory of Scattering of Polarized Atoms"

11) J. Eichler, Hahn Meitner Inst. (Germany), 14 Nov.
"Radiative Electron Capture in Relativistic Atomic Collisions"

### Nuclear Chemistry Lab.

1) K. Lee, Univ. of Texas Arlington (USA), 13 Jan.
"Study of Metal Overlayer System Using Positron ($e^+$) Beam"

2) A. N. Garg, Nagpur Univ. (India), 26 Apr.
"Nuclear Analytical Methods in Environmental and Biomedical Studies"

3) R. Amano, Kanazawa Univ. (Kanazawa), 30 Apr.
"RI and Radiopharmaceuticals"

4) A. Weiss, Univ. of Texas Arlington (USA), 18 May
"Study of Ultrathin Metal Films on Metal Using Positron Annihilation Induced Auger Electron Spectroscopy (PAES)"

5) G. Zhang, Shanghai Inst. Nucl. Res. (China), 28 July
"Buckyball and Iron Nanoparticles"

6) K. Kikuchi, Tokyo Metropol. Univ. (Tokyo), 28 July
"Fullerene Family"

7) J. V. Kratz, Johannes Gutenberg-Univ. Mainz (Germany), 14 Sept.
"Periferal and Central Heavy-ion Collisions at Around 1 GeV/A Studied with the Large Area Neutron Detector LAND"

8) P. Gütlich, Johannes Gutenberg-Univ. Mainz (Germany), 30 Sept.
"Recent Development in Spin-crossover and LIESST/NIESST Research"

9) K. Yoshihara, Tohoku Univ. (Sendai), 12 Oct.
"Chemistry of Technetium and Rhenium"

10) Y. Hamajima, Kanazawa Univ. (Kanazawa), 19 Oct.
"Analysis of Complex Gamma-ray Spectra"

11) H.-E. Mahnke, Hahn-Meitner Inst. (Germany), 4 Nov.
"Radioactive Nuclei in Material Science Research"

12) S. Kondo, Nihon Mediphysics (Chiba), 7 Dec.
"Radiopharmaceuticals with Tc-99m: Present and Future"

# XII. LIST OF PERSONNEL

**RIKEN Accelerator Research Facility**

ISHIHARA Masayasu 石原正泰 (Facility Director)
AWAYA Yohko 粟屋容子 (Vice Facility Director)
YANO Yasushige 矢野安重 (Vice Facility Director)

**Linac Division**

CHIBA Toshiya 千葉利哉
CHIBA Yoshiaki 千葉好明
HEMMI Masatake 逸見政武
IKEZAWA Eiji 池沢英二
KASE Masayuki 加瀬昌之
KOHARA Shigeo 小原重夫
MIYAZAWA Yoshitoshi 宮沢佳敏*1

**Ring Cyclotron Division**

FUJITA Jirou 藤田二郎
GOTO Akira 後藤 彰*1
IKEGAMI Kumio 池上九三男
INABE Naohito 稲辺尚人
KAGEYAMA Tadashi 影山 正
KAMIGAITO Osamu 上垣外修一
KASE Masayuki 加瀬昌之
KOHARA Shigeo 小原重夫
KUBO Toshiyuki 久保敏幸
NAGASE Makoto 長瀬 誠
NAKAGAWA Takahide 中川孝秀
OGIWARA Kiyoshi 荻原 清
YOKOYAMA Ichiro 横山一郎

**Experimental Support Division**

ICHIHARA Takashi 市原 卓
KAMBARA Tadashi 神原 正
KANAI Yasuyuki 金井保之
KOBAYASHI Toshio 小林俊雄*1
KUMAGAI Hidekazu 熊谷秀和
MATSUZAKI Teiichiro 松﨑禎市郎
MORITA Kosuke 森田浩介
OKUBO Yoshitaka 大久保嘉高
WATANABE Yasushi 渡邊 康
YATAGAI Fumio 谷田貝文夫

**Radioisotope Facilities Division**

AMBE Fumitoshi 安部文敏*1
IWAMOTO Masako 岩本正子
KOBAYASHI Yoshio 小林義男

**Radiation Protection Group**

FUJITA Shin 藤田 新
NAKAJIMA Shunji 中島諄二
NAKANISHI Noriyoshi 中西紀喜*1

**Secretariat**

NAKAMURA Toshiko 中村とし子
YOSHIDA Tohru 吉田 徹*2

**Steering Committee**

AMBE Fumitoshi 安部文敏
AWAYA Yohko 粟屋容子
CHIBA Yoshiaki 千葉好明
GOTO Akira 後藤 彰
HANAOKA Fumio 花岡文雄
INAMURA Takashi T. 稲村 卓
ISHIHARA Masayasu 石原正泰
KAMITSUBO Hiromichi 上坪宏道
KATSUMATA Koichi 勝又紘一
KIRA Akira 吉良 爽
KOBAYASHI Toshio 小林俊雄
KUMAGAI Noritaka 熊谷教孝
MATSUOKA Masaru 松岡 勝
MIYAZAWA Yoshitoshi 宮沢佳敏
NAGAMINE Kanetada 永嶺謙忠
TAKAHASHI Tan 高橋 旦
TAKAMI Michio 高見道生
TANIHATA Isao 谷畑勇夫*3
YAGI Eiichi 八木栄一
YANO Yasushige 矢野安重

*1 Group Leader, *2 Manager, *3 Chairperson

## Scientific and Engineering Personnel

### Cosmic Radiation Laboratory

IMAI Takashi 今井 喬　　KOHNO Tsuyoshi 河野 毅

(Visitors)
HASEBE Nobuyuki 長谷部信行 (Fac. Gen. Educ., Ehime Univ.)
KASHIWAGI Toshisuke 柏木利介 (Fac. Eng., Kanagawa Univ.)
KATO Chihiro 加藤千尋 (Fac. Sci., Shinshu Univ.)
MUNAKATA Kazuoki 宗像一起 (Fac. Sci., Shinshu Univ.)
MURAKAMI Hiroyuki 村上浩之 (Fac. Sci., Rikkyo Univ.)
NAGATA Katsuaki 永田勝明 (Fac. Eng., Tamagawa Univ.)
NAKAMOTO Atsushi 中本 淳 (Fac. Sci., Rikkyo Univ.)
YANAGIMACHI Tomoki 柳町朋樹 (Fac. Sci., Rikkyo Univ.)

(Students)
FUJIKI Kenichi 藤木謙一 (Fac. Sci., Ehime Univ.)
ITO Tomoyuki 伊藤朋行 (Fac. Sci. Eng., Waseda Univ.)
ITSUMI Norifumi 逸見憲史 (Fac. Sci. Eng., Waseda Univ.)
SHINO Tomoaki 篠 智彰 (Fac. Sci. Eng., Waseda Univ.)
YAMAGIWA Iwao 山極 巌 (Grad. Sch. Sci. Eng., Saitama Univ.)

### Cyclotron Laboratory

FUJITA Jirou 藤田二郎
GOTO Akira 後藤 彰*1
INABE Naohito 稲辺尚人
KAGEYAMA Tadashi 影山 正
KITAGAWA Hisashi 北川 尚
KUBO Toshiyuki 久保敏幸
NAGASE Makoto 長瀬 誠
NAKAJIMA Shunji 中島諄二
OGIWARA Kiyoshi 荻原 清
SUGANUMA Hideo 菅沼秀夫
UESAKA Tomohiro 上坂友洋
YAMAJI Shuhei 山路修平*1
YOKAYAMA Ichiro 横山一郎
FUJITA Shin 藤田 新
IKEGAMI Kumio 池上九三男
JIN Wei-Guo 金 衛国
KAMIGAITO Osamu 上垣外修一
KOHARA Shigeo 小原重夫
MORITA Kosuke 森田浩介
NAKAGAWA Takahide 中川孝秀
NAKANISHI Noriyoshi 中西紀喜
OTSUKA Takaharu 大塚孝治*2
SUZUKI Toshio 鈴木敏男*2
WAKASUGI Masanori 若杉昌徳
YANO Yasushige 矢野安重*3

*1 Senior Scientist, *2 Senior Visiting Scientist, *3 Chief Scientist

(Visitors)
ABE Yasuhisa 阿部恭久 (Uzi Res. Cent., Yukawa Inst. Theor. Phys., Kyoto Univ.)
AKUTSU Takao 阿久津亮夫 (NASDA)
AOKI Jiro 青木司郎 (NASDA)
ARAI Eiichi 新井栄一 (Res. Lab. Nucl. Reactors, Tokyo Inst. Technol.)
ARAKAWA Kazuo 荒川和夫 (JAERI, Takasaki)
BABA Shinji 馬場信次 (NASDA)
BATYGIN Yuri (Elect. Phys. Dept., Moscow Eng. Phys. Inst.)
DATÉ Schin 伊達 伸 (JASRI)
DEY Ranadhir (Variable Energy Cycl. Cent.)
EJIRI Hiroyasu 江尻宏泰 (Dept. Phys., Osaka Univ.)
ENYO Hideto 延与秀人 (Dept. Phys., Kyoto Univ.)
FUJIOKA Manabu 藤岡 学 (Cyclotron Radioisot. Cent., Tohoku Univ.)
FUJISAWA Takashi 藤沢高志 (Denki Kogyo Co. Ltd.)
FUJITA Yoshitaka 藤田佳孝 (Dept. Phys., Osaka Univ.)
FUJIWARA Mamoru 藤原 守 (RCNP, Osaka Univ.)
FUKUDA Mitsuhiro 福田光宏 (JAERI, Takasaki)

FUKUMOTO Sadayoshi 福本貞義 (KEK)
FURUNO Kohei 古野興平 (Inst. Phys. Tandem Accel. Cent., Univ. Tsukuba)
HADA Takashi 羽田尚志 (NASDA)
HAMA Hiroyuki 浜 広幸 (I.M.S.)
HASHIMOTO Osamu 橋本 治 (Inst. Nucl. Study, Univ. Tokyo)
HATANAKA Kichiji 畑中吉治 (RCNP, Osaka Univ.)
HATSUKAWA Yuichi 初川雄一 (JAERI, Tokai)
HATTORI Toshiyuki 服部俊幸 (Res. Lab. Nucl Reac., T.I.T.)
HAYANO Ryugo 早野龍五 (Dept. Phys., Univ. Tokyo)
HEIGUCHI Kazuhiko 平口和彦 (Graduate Sch. Sci. Technol., Niigata Univ.)
HIES Markus G. (Dept. Phys., Mainz Univ.)
HIRAO Yasuo 平尾泰男 (N.I.R.S)
HIRASAWA Shokichi 平沢正吉
HONMA Toshihiro 本間寿広 (Cyclotron Radioisot. Cent., Tohoku Univ.)
HORIBATA Takatoshi 堀端孝俊 (Fac. Eng., Aomori Univ.)
HORIGUCHI Takayoshi 堀口隆良 (Dept. Phys., Hiroshima Univ.)
HORIUCHI Hisashi 堀内 昶 (Dept. Phys., Kyoto Univ.)
HOSONO Kazuhiko 細野和彦 (RCNP, Osaka Univ.)
IGARASHI Toshio 五十嵐敏雄 (NASDA)
IKEDA Kiyomi 池田清美 (Dept. Phys., Niigata Univ.)
IKEDA Nobuo 池田伸夫 (Inst. Nucl. Study, Univ. Tokyo)
IKEGAMI Hidetsugu 池上栄胤 (RCNP, Osaka Univ.)
IKEZOE Hiroshi 池添 博 (JAERI, Tokai)
IMAI Kenichi 今井憲一 (Dept. Phys., Kyoto Univ.)
IMAMURA Mineo 今村峯雄 (Inst. Nucl. Study, Univ. Tokyo)
INOUE Makoto 井上 信 (Inst. Chem. Res., Kyoto Univ.)
ISHII Takayuki 石井孝幸 (NASDA)
ISHIZUKA Takeo 石塚武男 (Dept. Phys., Saitama Univ.)
IWAMOTO Akira 岩本 昭 (JAERI, Tokai)
IWASHITA Yoshihisa 岩下芳久 (Inst. Chem. Res., Kyoto Univ.)
IZUMOTO Toshiaki 泉本利章 (Coll. Sci., Rikkyo Univ.)
JEONG S. C. (Inst. Nucl. Study, Univ. Tokyo)
KAJI Harumi 鍛冶東海 (Dept. Phys., Tohoku Univ.)
KAMEYAMA Hirofumi 亀山浩文 (Dept. Phys., Chiba Keizai Jr. Coll.)
KAMIMURA Masayasu 上村正康 (Dept. Phys., Kyushu Univ.)
KANAZAWA Mitsutaka 金沢光隆 (N.I.R.S.)
KANMURI Tetsuo 冠 哲夫 (Dept. Phys., Osaka Univ.)
KANNO Tooru 菅野 徹 (NASDA)
KATSURAGAWA Hidetsugu 桂川秀嗣 (Dept. Phys., Toho Univ.)
KATAYAMA Ichiro 片山一郎 (Inst. Nucl. Study, Univ. Tokyo)
KATAYAMA Takeshi 片山武司 (Inst. Nucl. Study, Univ. Tokyo)
KATO Kiyoshi 加藤幾芳 (Dept. Phys., Hokkaido Univ.)
KATORI Kenji 鹿取謙二 (Dept. Phys., Osaka Univ.)
KATOU Shouhei 加藤昌平 (Dept. Phys., Osaka Univ.)
KAWAGUCHI Takeo 川口武男 (Mitsubishi Electric Co., Ltd.)
KAWAGUCHI Hideo 川口秀夫 (Tokyo Denshi Co., Ltd.)
KAWAI Mitsuji 河合光路 (Dept. Phys., Kyushu Univ.)
KIKUCHI Fumio 菊池文男 (Coll. Arts Sci., Univ. Tokyo)
KONDO Michiya 近藤道也 (RCNP, Osaka Univ.)
KOSAKO Toshiso 小佐古敏荘 (Atomic Energy Res. Cent., Univ. Tokyo)
KOTAJIMA Hisaya 古田島久哉 (Fac. Eng., Tohoku Univ.)
KOUMOTO Toshirou 河本敏郎 (Dept. Phys., Kyoto Univ.)
KUBOYAMA Satoshi 久保山智司 (NASDA)
KUDO Hisaaki 工藤久昭 (Dept. Chem., Niigata Univ.)
KUROYANAGI Tokihiro 黒柳登喜大 (Dept. Phys., Kyushu Univ.)
LEE Kong Ok 李 康玉 (Rika Women's Coll.)
LEE Sang Mu 李 相茂 (Dept. Phys., Univ. Tsukuba)
LIN Ching-Liang 林 清涼 (Taiwan Univ.)

MAEDA Kazuhide 前田和秀 (Dept. Phys., Kyushu Univ.)
MARUMORI Toshio 丸森寿夫 (Fac. Sci. Technol., Sci. Univ. Tokyo)
MATSUDA Sumio 松田純夫 (NASDA)
MATSUI Yoshiko 松井芳子 (Fac. Technol., Tokyo Univ. Agr. Technol.)
MATSUKI Seishi 松木征史 (Inst. Chem. Res., Kyoto Univ.)
MATSUSE Takehiro 松瀬丈浩 (Dept. Phys., Shinshu Univ.)
MATSUYANAGI Kenichi 松柳研一 (Dept. Phys., Kyoto Univ.)
MIAKE Yasuo 三明康郎 (Inst. Phys., Univ. Tsukuba)
MIDORIKAWA Shoichi 緑川章一 (Fac. Eng., Aomori Univ.)
MINAMISONO Tadanori 南園忠則 (Dept. Phys., Osaka Univ.)
MITSUMOTO Toshinori 蜜本俊典 (Sumitomo Heavy Industries, Ltd.)
MIURA Iwao 三浦 岩 (RCNP, Osaka Univ.)
MIYAMURA Osamu 宮村 修 (Fac. Sci., Osaka Univ.)
MIYATAKE Hiroari 宮武宇也 (Fac. Sci., Osaka Univ.)
MIZOTA Takeshi 溝田武志 (Inst. Phys., Univ. Tsukuba)
MIZUNO Yoshiyuki 水野義之 (RCNP, Osaka Univ.)
MORI Yoshiharu 森 義治 (KEK)
MURAKAMI Tetsuya 村上哲也 (Dept. Phys., Kyoto Univ.)
MURAYAMA Toshiyuki 村山利幸 (Tokyo Univ. Mercantile Marine)
MUROTANI Shin 室谷 心 (Sch. Sci. Eng., Waseda Univ.)
NAGAI Yasuki 永井泰樹 (Dept. Appl. Phys., Tokyo Inst. Technol.)
NAITOU Ichiro 内藤一郎 (NASDA)
NAKAHARA Hiromichi 中原弘道 (Dept. Chem., Tokyo Metrop. Univ.)
NAKAI Koji 中井浩二 (KEK)
NAKAJIMA Masato 中島真人 (NASDA)
NAKAMURA Ichiro 中村市郎 (Dept. Phys., Saitama Univ.)
NAKAMURA Masao 中村正夫 (NASDA)
NAKAMURA Takashi 中村尚司 (Cyclotron Radioisot. Cent., Tohoku Univ.)
NEMOTO Norio 根本規生 (NASDA)
NIIMURA Masanobu 新村正信 (Sch. Sci. Eng., Waseda Univ.)
NIITA Koji 仁井田浩二 (JAERI, Tokai)
NODA Akira 野田 章 (Inst. Chem. Res., Kyoto Univ.)
NODA Kouji 野田耕司 (N.I.R.S.)
NOMURA Toru 野村 亨 (Inst. Nucl. Study, Univ. Tokyo)
OGATA Hiroshi 小方 寛 ( RCNP, Osaka Univ.)
OGAWA Kengo 小川健吾 (Fac. Educ., Chiba Univ.)
OKABE Shigetou 岡部成玄 (Cent. Inf. Proc. Educ., Hokkaido Univ.)
OKAMURA Hiroyuki 岡村弘之 (Dept. Phys., Univ. Tokyo)
OKUMURA Susumu 奥村 進 (JAERI, Takasaki)
ONISHI Naoki 大西直毅 (Coll. Arts Sci., Univ. Tokyo)
OOHIRA Hideharu 大平秀春 (NASDA)
OOTSUKI Tsutomu 大槻 勤 (Lab. Nucl. Sci., Tohoku Univ.)
OOURA Akio 大浦昭夫 (NASDA)
OOYA Jirou 大矢次郎 (NASDA)
OSUGA Toshiaki 大須賀敏明 (Coll. Arts Sci., Chiba Univ.)
PU Yuehu 蒲 越虎 (Inst. Nucl. Study, Univ. Tokyo)
QUAN Zhuo-Shu 全 卓樹 (Dept. Phys., Hosei Univ.)
ROA Yi Nong (Inst. Modern Phys., Academia Sinica, China)
SAGARA Kenji 相良建至 (Dept. Phys., Kyushu Univ.)
SAKAI Hideyuki 酒井英行 (Dept. Phys., Univ. Tokyo)
SASAGAWA Tatsuya 笹川辰弥 (Coll. Eng., Nihon Univ.)
SATO Yukio 佐藤幸夫 (N.I.R.S.)
SATOU Kenichi 佐藤憲一 (Dept. Phys., Tohoku Coll. Pharm.)
SATOU Kenji 佐藤健次 (N.I.R.S.)
SEBE Takashi 瀬部 孝 (Dept. Phys., Hosei Univ.)
SEKINE Toshiaki 関根俊明 (JAERI, Tokai)
SHIBATA Tokushi 柴田徳思 (Inst. Nucl. Study, Univ. Tokyo)
SHIKAZONO Naoki 鹿園直基 (JAERI, Tokai)

SHIMANO Yosuke 嶋野洋介 (NASDA)
SHIMIZU Akira 清水 昭 (RCNP, Osaka Univ.)
SHIMOMURA Koichiro 下村浩一郎 (Meson Sci. Lab., KEK Brunch, Univ. Tokyo)
SHIN Kazuo 秦 和夫 (Fac. Eng., Kyoto Univ.)
SHIN Seung Ai 辛 承愛 (Rika Women's Coll.)
SHINOZUKA Tsutomu 篠塚 勉 (Cyclotron Radioisot. Cent., Tohoku Univ.)
SHIRAI Toshiyuki 白井敏之 (Res. Inst. Fund. Phys., Kyoto Univ.)
SUEKI Keisuke 末木啓介 (Dept. Chem., Tokyo Metrop. Univ.)
SUGAI Isao 菅井 勲 (Inst. Nucl. Study, Univ. Tokyo)
SUGIYAMA Hiroki 杉山大樹 (NASDA)
SUMIYOSHI Hiroyuki 住吉広行 (Matsusho-Gakuen Jr. Coll.)
SUZUKI Toshio 鈴木敏男 (Dept. Phys., Fukui Univ.)
SUZUKI Toshio 鈴木俊夫 (Dept. Phys., Nihon Univ.)
TAGISHI Yoshihiro 田岸義宏 (Tandem Accel. Cent., Univ. Tsukuba)
TAJIMA Naoki 田嶋直樹 (Coll. Arts Sci., Univ. Tokyo)
TAKADA Kenjiro 高田健次郎 (Dept. Phys., Kyushu Univ.)
TAKEMASA Tadashi 武政尹士 (Kyoto Univ. Educ.)
TAKEUCHI Suehiro 竹内末広 (JAERI, Tokai)
TAKIGAWA Noboru 滝川 昇 (Dept. Phys., Tohoku Univ.)
TAMAGAKI Ryozou 玉垣良三 (Dept. Phys., Kyoto Univ.)
TAMURA Takashi 田村高志 (NASDA)
TANABE Kazuko 田辺和子 (Otsuma Women's Coll.)
TANAKA Jinichi 田中仁市 (Inst. Nucl. Study, Univ. Tokyo)
TANAKA Kazuhiro 田中和廣 (Dept. Phys., Hiroshima Univ.)
TANAKA Yasushi 田中保志 (Kyokuto Boeki Kaisha, Ltd.)
TANIKAWA Masashi 谷川勝至 (Dept. Chem., Univ. Tokyo)
TOHYAMA Mitsuru 遠山 満 (Kyorin Univ.)
TOMIMASU Takio 富増多喜夫 (FEL Res. Inst. Inc.)
TOMITANI Takehiro 富谷武浩 (N.I.R.S.)
TOMOTA Toshiaki 友田敏章 (Fac. Eng., Aomori Univ.)
TORIYAMA Tamotsu 鳥山 保 (Dept. Phys., Musashi Inst. Technol.)
TSUNEMOTO Hiroshi 恒元 博 (N.I.R.S.)
UESUGI Masato 上杉正人 (NASDA)
UTSUNOMIYA Hiroaki 宇都宮弘章 (Fac. Sci., Konan Univ.)
UWAMINO Yoshitomo 上簑義朋 (Inst. Nucl. Study, Univ. Tokyo)
WADA Michiharu 和田道治 (Inst. Nucl. Study, Univ. Tokyo)
WADA Takahiro 和田隆宏 (Osaka Dental Coll.)
WAKAI Masamichi 若井正道 (Dept. Phys., Osaka Univ.)
WAKUTA Yoshihisa 和久田義久 (Fac. Eng., Kyushu Univ.)
WANG Zhei 王 真 (Inst. Modern Phys., Acad. Sinica)
XIA Jiawen 夏 佳文 (Inst. Modern Phys., Acad. Sinica)
YAMADA Taiichi 山田泰一 (Coll. Eng., Kanto Gakuin Univ.)
YAMAMOTO Yasuo 山本安夫 (Tsuru Univ.)
YAMANOUCHI Mikio 山内幹雄 (Tandem Accel. Cent., Univ. Tsukuba)
YAMAZAKI Hirohito 山崎寛仁 (Lab. Nucl. Sci., Tohoku Univ.)
YAMAZAKI Takashi 山崎 魏 (RCNP, Osaka Univ.)
YOSHIDA Noriaki 吉田宣章 (Fac. Eng., Kansai Univ.)
YOSHIDA Shiro 吉田思郎 (Dept. Phys., Ishinomaki Senshu Univ.)
YOSHINAGA Naotaka 吉永尚孝 (Dept. Phys., Saitama Univ.)
YOSHIOKA Yasuhiro 吉岡康弘 (NASDA)
YOSHIZAWA Yasukazu 吉沢康和 (Fac. Eng., Kyushu Univ.)
YUAN You-Jin (Inst. Modern Phys., Acad. Sinica, China)
ZHANG Li 張 立 (Inst. Modern Phys., Acad. Sinica, China)

(Students)
AKAZAWA Takashi 赤澤 貴 (Dept. Phys., Saitama Univ.)
AOKI Yuka 青木由香 (Dept. Phys., Tohoku Univ.)
ARIGA Takehiro 有賀健博 (Dept. Phys., Saitama Univ.)

FURUYA Shinji 古谷信司 (Dept. Phys., Tokyo Inst. Technol.)
FUTAMI Yasuyuki 二見康之 (Dept. Phys., Univ. Tsukuba)
HAMADA Shingo 浜田真悟 (Inst. Chem. Res., Kyoto Univ.)
HIRAI Masahide 平井政秀 (Dept. Phys., Sophia Univ.)
HONJYOU Yoshio 本城義夫 (Dept. Phys., Univ. Tsukuba)
HONMA Hiroyuki 本間裕之 (Dept. Appl. Phys., Tokyo Inst. Technol.)
INOUE Jirou 井上次郎 (Dept. Phys., Sophia Univ.)
ITAGAKI Shouhei 板垣松平 (Dept. Phys., Saitama Univ.)
KANGYO Yoshitsugu 観行愛嗣 (Coll. Sci., Chuo Univ.)
KASHIWABARA Taketo 柏原健人 (Dept. Phys., Toho Univ.)
KIM Eun Ju (Dept. Phys., Tohoku Univ.)
KUMAGAI Kenji 熊谷健二 (Dept. Phys., Hiroshima Univ.)
KURIHARA Kaori 栗原 香 (Dept. Phys., Univ. Tsukuba)
KURITA Tetsuro 栗田哲郎 (Dept. Phys., Univ. Tsukuba)
KUROSAWA Tadahiro 黒沢忠弘 (Dept. Phys., Tohoku Univ.)
MABUCHI Hideyuki 馬渕英之 (Fac. Sci., Konan Univ.)
MARUYAMA Toshiki 丸山敏毅 (Dept. Phys., Kyoto Univ.)
MATSUMOTO Norihiro 松本典洋 (Fac. Sci., Kounan Univ.)
MINEMURA Toshiyuki 峯村俊行 (Coll. Sci., Chuo Univ.)
MIURA Takashi 三浦 崇 (Dept. Phys., Univ. Tsukuba)
NAKAGAWA Keiko 中川恵子 (Dept. Phys., Tohoku Univ.)
NAKAO Noriaki 中尾徳晶 (Cyclotron Radioisot. Cent., Tohoku Univ.)
NISHIMORI Nobuyuki 西森信行 (Dept. Phys., Kyushu Univ.)
ODA Ayato 織田彩人 (Tokyo Univ. Mercantile Marine)
OGAWA Izumi 小川 泉 (Int. Chem. Res., Kyoto Univ.)
OOSAKI Toshiro 大崎敏郎 (Dept. Appl. Phys., Tokyo Inst. Technol.)
OZAWA Shuiti 小澤修一 (Coll. Sci., Rikkyo Univ.)
RYU Shin (Dept. Phys., Univ. Tsukuba)
SASAKI Reiji 佐々木玲仁 (Dept. Phys., Tohoku Univ.)
SATOU Eiko 佐藤英子 (Dept. Phys., Univ. Tsukuba)
SEINO Satoshi 清野 聡 (Dept. Appl. Phys., Tokyo Inst. Technol.)
SENO Kenichi 妹尾賢一 (Dept. Appl. Phys., Tokyo Inst. Technol.)
SHINOZAKI Akihisa 篠崎章久 (Dept. Phys., Tohoku Univ.)
TAGAYA Yu 多加谷 祐 (Dept. Phys., Univ. Tokyo)
TAKADA Masashi 高田真志 (Cyclotron Radioisot. Cent., Tohoku Univ.)
TAKAHASHI Takumi 高橋琢巳 (Coll. Sci., Chuo Univ.)
TAKEDA Kenji 竹田賢志 (Dept. Appl. Phys., Tokyo Inst. Technol.)
TOMITA Shigeo 富田成夫 (Dept. Phys., Univ. Tsukuba)
TOMOHISA Yasuhiko 友久保彦 (Dept. Phys., Univ. Tsukuba)
UMETSU Youitiro 梅津陽一郎 (Dept. Phys., Tohoku Univ.)
UTIYAMA Kouji 内山浩志 (Dept. Phys., Saitama Univ.)
WAKUI Takashi 湧井崇志 (Dept. Phys., Toho Univ.)
WATANABE Koutarou 渡邊康太郎 (Dept. Appl. Phys., Tokyo Inst. Technol.)
YAMAGAMI Munetaka 山上宗隆 (Fac. Sci., Konan Univ.)
YAMASHITA Ayako 山下亜矢子 (Dept. Phys., Toho Univ.)
YORITA Tetsuhiko 依田哲彦 (Dept. Phys., Tohoku Univ.)
YUKI Hideyuki 結城秀行 (Dept. Phys., Tohoku Univ.)

**Linear Accelerator Laboratory**

CHIBA Toshiya 千葉利哉
CHIBA Yoshiaki 千葉好明
FUJIMAKI Masaki 藤巻正樹
FUKUDA Moichi 福田茂一
HEMMI Masatake 逸見政武
HIRENZAKI Satoru 比連崎 悟
IKEZAWA Eiji 池沢英二
KASE Masayuki 加瀬昌之
KOBAYASHI Toshio 小林俊雄*
KUMAGAI Hidekazu 熊谷秀和
MIYAZAWA Yoshitoshi 宮沢佳敏
MOMOTA Sadao 百田佐多生
OZAWA Akira 小沢 顕
SUZUKI Takeshi 鈴木 健

TANIHATA Isao 谷畑勇夫**　　TONUMA Tadao 戸沼正雄
YANOKURA Minoru 矢野倉実　　YOSHIDA Koichi 吉田光一

* Senior Scientist, ** Chief Scientist

(Visitors)
ALEKSANDROV D. V. (Kurchatov Inst., Russia)
ARATANI Michi 荒谷美智 (Inst. Enviromental Sci.)
BOLBOT Michael D. (Notre Dame Univ., U.S.A.)
BOYD Richard (Ohio State Univ., U.S.A.)
BROCKMANN Rolf (Inst. Phys. Univ. Mainz, Germany)
CARLSON Brett (CTA, Inst. Estudos Avancados, Brazil)
CHLOUPEK Frank (Ohio State Univ., U.S.A.)
DEMYANOVA Alla S. (Kurchatov Inst. Atomic Energy, Russia)
FENG Jun 馮軍 (Shanghai Inst. Nucl. Res., China)
FUJIWARA Mamoru 藤原守 (RCNP, Osaka Univ.)
FURUYA Keiichi 古谷圭一 (Fac. Sci., Sci. Univ. Tokyo)
HIRATA Daisy (CTA, Inst. Estudos Avancados, Brazil)
ITO Noriaki 伊藤憲昭 (Dept. Cryst. Mater., Nagoya Univ.)
KAIMAN Varga* (Atomki, Debrecen, Hungary)
KANAZAWA Kenichi 金澤健一 (KEK)
KATORI Kenji 鹿取謙二 (Fac. Sci., Osaka Univ.)
KIKUCHI Jun 菊池順 (Sci. Eng. Res. Lab., Waseda Univ.)
KIMURA Kikuo 木村喜久雄 (Fac. Eng., Nagasaki Inst. Appl. Sci.)
KOLATA James (Notre Dame Univ., U.S.A.)
KORSHENINNIKOV A. A. (Kurchatov Inst., Russia)
MATSUTA Kensaku 松多健策 (Fac. Sci., Osaka Univ.)
MATUOKA Nobuyuki 松岡伸行 (Res. Cent. Nucl. Phys., Osaka Univ.)
MOCHIZUKI Keiko 望月圭子 (Fac. Sci., Osaka Univ.)
MOON Chang-Bun (Seoul Natl. Univ., Korea)
MURAOKA Mitsuo 村岡光男 (Coll. Arts Sci., Chiba Univ.)
NIKOLSKI Evgenini Y. (Kurchatov Inst., Russia)
NOJIRI Yoichi 野尻洋一 (Fac. Sci., Osaka Univ.)
OGAWA Kengo 小川建吾 (Coll. Arts Sci., Chiba Univ.)
OGLOBLIN Alexei A. (Kurchatov Inst., Russia)
OJIMA Minoru 小嶋稔 (Fac. Sci., Osaka Univ.)
OMATA Kazuo 小俣和夫 (Inst. Nucl. Study, Univ. Tokyo)
RAIMANN Gerhard (Ohio State Univ., U.S.A.)
SAGAWA Hiroyuki 佐川弘幸 (Fac. Sci., Univ. Tokyo)
SAKAI Hideyuki 酒井英行 (Fac. Sci., Univ. Tokyo)
SATO Kazuhiro 佐藤和広 (Tokyo Fire Dept.)
SUDA Toshimi 須田利美 (Fac. Sci., Tohoku Univ.)
SUGAWARA Masahiko 菅原昌彦 (Fundam. Sci., Chiba Inst. Technol.)
SUZUKI Yasuyuki 鈴木宣之 (Fac. Sci. Niigata Univ.)
TOKI Hiroshi 土岐博 (Fac. Sci., Tokyo Metrop. Univ.)
WADA Takahiro 和田隆宏 (Osaka Dentist Univ.)
YAMAGUCHI Hiromi 山口裕美 (Sci. Eng. Res. Lab., Waseda Univ.)
ZAHAR Mohamed (Dept. Phys., Notre Dame Univ., U.S.A.)

* STA Fellow

(Students)
HARADA Akihiko 原田昭彦 (Fac. Sci., Osaka Univ.)
IZUMIKAWA Takuji 泉川卓司 (Fac. Sci., Osaka Univ.)
MATSUSHITA Kenichi 松下健一 (Fac. Sci., Sci. Univ. Tokyo)
MIHARA Mototsugu 三原基嗣 (Fac. Sci., Osaka Univ.)
MIYAKE Toru 三宅徹 (Fac. Sci., Osaka Univ.)
MIYAMOTO Shinya 宮本真哉 (Fac. Sci., Tokyo Metrop. Univ.)

NAKAZATO Masahisa 中里真久 (Fac. Sci., Osaka Univ.)
ONISHI Takashi 大西 崇 (Fac. Sci., Osaka Univ.)
SASAKI Makoto 佐々木 誠 (Fac. Sci., Osaka Univ.)
TANIGAKI Minoru 谷垣 実 (Fac. Sci., Osaka Univ.)
YAMAGUCHI Takayuki 山口貴之 (Fac. Sci., Osaka Univ.)

**Radiation Laboratory**

FUKUNISHI Nobuhisa 福西暢尚
ISHIHARA Masayasu 石原正泰*
KISHIDA Takashi 岸田 隆
NAKAMURA Takashi 中村隆司
TAKAHASHI Tan 高橋 旦
WATANABE Yasushi 渡邉 康
ICHIHARA Takashi 市原 卓
IZUMO Koichi 出雲光一
KONNO Satoshi 金野 智
OKUNO Hiroki 奥野広樹
TENDOW Yoshihiko 天道芳彦
YOSHIDA Atsushi 吉田 敦

* Chief Scientist

(Visitors)
ABE Yasuhisa 阿部恭久 (Yukawa Inst. for Theor. Phys., Kyoto Univ.)
ADACHI Minoru 足立 實 (Fac. Sci., Tokyo Inst. Technol.)
ANDO Yoshiaki 安藤嘉章 (Coll. Sci., Rikkyo Univ.)
ARTUKH Anatoly (Flerov Lab. Nucl. Reactions, Joint Inst. Nucl. Res., Dubna, Russia)
ASAHI Koichiro 旭 耕一郎 (Fac. Sci., Tokyo Inst. Technol.)
BECK F. A. (Groupe RSN, Strasbourg, France)
BROGLIA R. (Univ. Milano & INFN, Italy)
CASTEN Rick (Phys. Dept., Brookhaven Nat. Lab., USA)
DELBAR Thierry (Univ. Catholique de Louvain, Belgium)
DOKE Tadayoshi 道家忠義 (Sci. Eng. Res. Lab., Waseda Univ.)
ENYO Hideto 延与秀人 (Fac. Sci., Kyoto Univ.)
FLOCARD Hubert (Div. Phys. Theor., Inst. Phys. Nucl., Orsay, France)
FRANCE Ralf (Yale Univ., USA)
FUCHI Yoshihide 渕 好秀 (Inst. Nucl. Study, Univ. Tokyo)
FUJIOKA Manabu 藤岡 学 (Cyclotron and Radioisot. Cent., Tohoku Univ.)
FUKUDA Tomokazu 福田共和 (Inst. Nucl. Study, Univ. Tokyo)
FUKUDA Mitsunori 福田光順 (Fac. Sci., Osaka Univ.)
GAI Moshe (Yale Univ., USA)
GONO Yasuyuki 郷農靖之 (Fac. Sci., Kyushu Univ.)
HAHN Kevin I. (California Inst. Technol.)
HASEGAWA Takeo 長谷川武夫 (Fac. Eng., Miyazaki Univ.)
HOSAKA Masahito 保坂将人 (Inst. Nucl. Study, Univ. Tokyo)
ICHIMURA Munetake 市村宗武 (Coll. Arts and Sci., Univ. Tokyo)
IEKI Kazuo 家城和夫 (Coll. Sci., Rikkyo Univ.)
IMAI Kenichi 今井憲一 (Fac. Sci., Kyoto Univ.)
ISHIDA Nobumichi 石田伸道 (Seikei Univ.)
KASAGI Jirota 笠木治郎太 (Lab. Nucl. Sci., Tohoku Univ.)
KATAYAMA Ichiro 片山一郎 (Inst. Nucl. Study, Univ. Tokyo)
KATO Seigo 加藤静吾 (Fac. Ed., Yamagata Univ.)
KATORI Kenji 鹿取謙二 (Fac. Sci., Osaka Univ.)
KAWAKAMI Hirokane 川上宏金 (Inst. Nucl. Study, Univ. Tokyo)
KAWASHIMA Hideo 川島英雄 (Inst. Nucl. Study, Univ. Tokyo)
KIKUCHI Jun 菊池 順 (Sci. Eng. Res. Lab., Waseda Univ.)
KIM Jong Chan (Dept. Phys., Seoul Natl. Univ., Korea)
KITAO Kensuke 喜多尾憲助 (Data Eng. Inc.)
KUBONO Shigeru 久保野 茂 (Inst. Nucl. Study, Univ. Tokyo)
KUBOTA Shinzo 窪田信三 (Coll. Sci., Rikkyo Univ.)
KUSAKARI Hideshige 草刈英榮 (Fac. Ed., Chiba Univ.)
LEE Sang Mu 李 相茂 (Inst. Phys., Univ. Tsukuba)
LIPNIK Peter (Univ. Catholique de Louvain, Belgium)

LIU Guanhua 劉 冠華 (Inst. Modern Phys., Acad. Sinica, China)
MAEDA Kazushige 前田和茂 (Coll. Gen. Ed., Tohoku Univ.)
MASUDA Kimiaki 増田公明 (Saitama Coll. Health)
MATSUYANAGI Kenichi 松柳研一 (Fac. Sci., Kyoto Univ.)
MENGONI Alberto (ENEA, Ente Nazionale, Italy)
MICHOTTE Carine (Univ. Catholique de Louvain, Belgium)
MIN Byung-Joo 閔 丙珠 (Korea Atomic Energy Res. Inst., Korea)
MITARAI Shiro 御手洗志郎 (Fac. Sci., Kyushu Univ.)
MIYACHI Takashi 宮地 孝 (Inst. Nucl. Study, Univ. Tokyo)
MIYATAKE Hiroari 宮武宇也 (Coll. Gen. Ed., Osaka Univ.)
MORIKAWA Tsuneyasu 森川恒安 (JAERI)
MORINOBU Shunpei 森信俊平 (Fac. Sci., Kyushu Univ.)
MOTOBAYASHI Toru 本林 透 (Coll. Sci., Rikkyo Univ.)
MOTTELSON Ben R. (NORDITA, Copenhagen, Denmark)
MUELLER Ludwig (Univ. Padova, Italy)
MURAKAMI Takeshi 村上 健 (Natl. Inst. Radiol. Sci.)
NAGAI Yasuki 永井泰樹 (Fac. Sci., Tokyo Inst. Technol.)
NAGASHIMA Yasuo 長島泰夫 (Inst. Phys., Univ. Tsukuba)
NAKAJIMA Mitsuo 中島充夫 (Grad. Sch. Nagatsuta, Tokyo Inst. Technol.)
NAKAMURA Shogo 中村正吾 (Fac. Ed., Yokohama Natl. Univ.)
NAKAYAMA Shintaro 中山信太郎 (Coll. Gen. Ed., Tokushima Univ.)
NIIZEKI Takashi 新関 隆 (Fac. Sci., Tokyo Inst. Technol.)
NORO Tetsuo 野呂哲夫 (Res. Center Nucl. Phys., Osaka Univ.)
OGAWA Masao 小川雅生 (Graduate Sch. Nagatsuta, Tokyo Inst. Technol.)
OKAMURA Hiroyuki 岡村弘之 (Fac. Sci., Univ. Tokyo)
ONUMA Hajime 大沼 甫 (Fac. Sci., Tokyo Inst. Technol.)
ORIHARA Hikonojyo 織原彦之丞 (Cyclotron and Radioisot. Cent., Tohoku Univ.)
OSHIMA Masumi 大島真澄 (JAERI)
OTSUKA Takaharu 大塚孝治 (Fac. Sci., Univ. Tokyo)
OYAIZU Michihiro 小柳津充広 (Inst. Nucl. Study, Univ. Tokyo)
PENIONZHKEVICH Yuri (Flerov Lab. Nucl. Reactions, Joint Inst. Nucl. Res., Dubna, Russia)
PETER Jean Jean Peter (Caen Univ., France)
RUAN (GEN) Jian-Zhi 阮 建治 (Coll. Sci., Rikkyo Univ.)
SAGAWA Hiroyuki 佐川弘幸 (Cent. Math. Sci., Univ. Aizu)
SAKAGUCHI Harutaka 坂口治隆 (Fac. Sci., Kyoto Univ.)
SAKAI Mitsuo 坂井光夫 (Inst. Nucl. Study, Univ. Tokyo)
SAKURAGI Hiroyuki 櫻木弘之 (Fac. Sci., Osaka City Univ.)
SAKURAI Hiroyoshi 櫻井博儀 (Fac. Sci., Univ. Tokyo)
SATO Hiroshi 佐藤 竑 (Seikei Univ.)
SCARLASSARA Fernando (Univ. Padova, Italy)
SCHMIDT-OTT Wolf-Dieter (II Physicalisches Inst. Univ., Göttingen, Germany)
SHIBAMURA Eido 柴村英道 (Saitama Coll. Health)
SHIBATA Toshiaki 柴田利明 (Fac. Sci., Tokyo Inst. Technol.)
SHIMIZU Yoshifumi 清水良文 (Fac. Sci., Kyushu Univ.)
SHIMIZU Hajime 清水 肇 (Fac. Ed. Yamagata Univ.)
SHIMODA Tadashi 下田 正 (Coll. Gen. Ed., Osaka Univ.)
SHIMOURA Susumu 下浦 享 (Coll. Sci., Rikkyo Univ.)
SHIRATO Shoji 白土鈔二 (Coll. Sci., Rikkyo Univ.)
SIGNORINI Cosimo (Phys. Dept., Inst. Nazionale di Fisica Nucl., Italy)
SUGAWARA Masahiko 菅原昌彦 (Chiba Inst. Technol.)
SUZUKI Masayo 鈴木昌世 (Japan Synchrotron Radiat. Res. Inst.)
SUZUKI Yasuyuki 鈴木宜之 (Fac. Sci., Niigata Univ.)
TAKADA Eiichi 高田栄一 (Natl. Inst. Radiol. Sci.)
TAKAHASHI Tadayuki 高橋忠幸 (Fac. Sci., Univ. Tokyo)
TAKAHASHI Noriaki 高橋憲明 (Coll. Gen. Ed., Osaka Univ.)
TAKAKU Seisaku 高久清作 (Inst. Nucl. Study, Univ. Tokyo)
TAKIGAWA Noboru 滝川 昇 (Fac. Sci., Tohoku Univ.)
TANAKA Masahiko 田中雅彦 (Inst. Nucl. Study, Univ. Tokyo)

TANOKURA Atsushi 田野倉 敦 (Fac. Sci. Technol., Sophia Univ.)
TERAKAWA Atsuki 寺川貴樹 (Cyclotron and Radioisot. Cent., Tohoku Univ.)
TOKI Hiroshi 土岐 博 (Res. Cent. Nucl. Phys., Osaka Univ.)
TOYOKAWA Hidenori 豊川秀訓 (Res. Cent. Nucl. Phys., Osaka Univ.)
UNO Masahiro 宇野正宏 (Ministry of Education, Sci. Culture)
YAMAMOTO Sukeyasu 山本祐靖 (Fac. Sci. Technol., Sophia Univ.)
YAMAYA Takashi 山屋 堯 (Fac. Sci., Tohoku Univ.)
YOSHINAGA Naotaka 吉永尚孝 (Coll. Lib. Arts, Saitama Univ.)
YOSOI Masaru 與曽井 優 (Fac. Sci., Kyoto Univ.)

(Students)
AOI Nori 青井 考 (Fac. Sci., Univ. Tokyo)
CHAE Soo Joh 蔡 洙祚 (Dept. Phys., Seoul Natl. Univ., Korea)
DOI Masashi 土井雅史 (Fac. Sci., Tokyo Inst. Technol.)
DOKI Yasuhiro 土記康博 (Fac. Sci., Univ. Tokyo)
FUJITA Tetsushi 藤田哲史 (Fac. Sci., Univ. Tokyo)
HANAKI Hidenobu 花木秀信 (Fac. Sci., Tokyo Inst. Technol.)
HASUIKE Katsuhito 蓮池勝人 (Sci. Eng. Res. Lab., Waseda Univ.)
HARA Yosuke 原 洋介 (Fac. Sci., Tokyo Inst. Technol.)
HARADA Masaki 原田昌樹 (Fac. Sci., Tokyo Inst. Technol.)
HIRAI Masaaki 平井正明 (Fac. Sci., Univ. Tokyo)
HORI Yoichi 堀 陽一 (Fac. Sci., Tokyo Inst. Technol.)
HORI Masaki 堀 正樹 (Fac. Sci., Univ. Tokyo)
HORI Junichi 堀 順一 (Coll. Sci., Rikkyo Univ.)
HOSOMICHI Kazuo 細道和夫 (Fac. Sci., Univ. Tokyo)
ICHIGE Masayuki 市毛正之 (Sci. Eng. Res. Lab., Waseda Univ.)
IDEGUCHI Eiji 井手口栄治 (Fac. Sci., Kyushu Univ.)
IKEDA Yasufumi 池田泰文 (Coll. Sci., Rikkyo Univ.)
INOUE Masahiro 井上昌宏 (Coll. Sci., Rikkyo Univ.)
ISHIDA Satoru 石田 悟 (Fac. Sci., Univ. Tokyo)
ITO Mikihiko 伊藤幹彦 (Fac. Sci., Tokyo Inst. Technol.)
ITO Tomoyuki 伊藤朋行 (Sci. Eng. Res. Lab., Waseda Univ.)
IWAMOTO Susumu 岩本 晋 (Coll. Sci., Rikkyo Univ.)
IWASA Naohito 岩佐直仁 (Coll. Sci., Rikkyo Univ.)
IWATA Yoshiyuki 岩田佳之 (Coll. Sci., Rikkyo Univ.)
IZUMI Hideaki 出水秀明 (Fac. Sci., Tokyo Inst. Technol.)
KAMIMURA Kazuto 上村和人 (Coll. Sci., Rikkyo Univ.)
KANEDA Naoya 金田直也 (Fac. Sci., Kyushu Univ.)
KATO Kenichi 加藤健一 (Fac. Sci., Tokyo Inst. Technol.)
KATO Toshiyuki 加藤俊幸 (Sci. Eng. Res. Lab., Waseda Univ.)
KAWAGUCHI Tsutomu 川口 勉 (Coll. Sci., Rikkyo Univ.)
KIDERA Masanori 木寺正憲 (Fac. Sci., Kyushu Univ.)
KIKUCHI Tadashi 菊地 正 (Coll. Sci., Rikkyo Univ.)
KOBAYASHI Misaki 小林美咲 (Sci. Eng. Res. Lab., Waseda Univ.)
KOBINATA Hideo 小日向秀夫 (Fac. Sci., Univ. Tokyo)
KOMIYAMA Tatsuto 込山立人 (Sci. Eng. Res. Lab., Waseda Univ.)
KUBO Madoka 久保 円 (Fac. Sci. Technol., Sophia Univ.)
KUROKAWA Meiko 黒川明子 (Coll. Sci., Rikkyo Univ.)
MATSUDA Kiyohide 松田清秀 (Fac. Sci., Tokyo Inst. Technol.)
MATSUZAKI Keiichi 松崎恵一 (Fac. Sci., Univ. Tokyo)
MINEGISHI Junichi 峰岸純一 (Coll. Sci., Rikkyo Univ.)
MITSUOKA Shinichi 光岡真一 (Kyushu Univ.)
MIYAZAKI Kousuke 宮崎光介 (Fac. Sci., Kyushu Univ.)
MIZOI Yutaka 溝井 浩 (Inst. Nucl. Study, Univ. Tokyo)
MOCHINAGA Kensuke 持永建介 (Fac. Sci., Tokyo Inst. Technol.)
MORIYA Shingo 守屋慎吾 (Coll. Sci., Rikkyo Univ.)
MURATA Tomoki 村田知樹 (Fac. Sci. Technol., Sophia Univ.)
NAGATA Kazuhiko 長田和彦 (Fac. Sci., Tokyo Inst. Technol.)

NAKAMURA Tadashi 中村 正 (Sci. Eng. Res. Lab., Waseda Univ.)
NAKANO Jo 中野 譲 (Inst. Nucl. Study, Univ. Tokyo)
NISHIO Teiji 西尾禎治 (Coll. Sci., Rikkyo Univ.)
NONAKA Takamasa 野中敬正 (Fac. Sci., Univ. Tokyo)
NOTANI Masahiro 野谷将広 (Fac. Sci., Univ. Tokyo)
ODAHARA Atsuko 小田原厚子 (Fac. Sci., Kyushu Univ.)
OGAMI Hiroshi 尾上博司 (Fac. Sci., Tokyo Inst. Technol.)
OGAWA Hiroshi 小川博嗣 (Fac. Sci., Tokyo Inst. Technol.)
OGAWA Hideto 小川秀人 (Coll. Sci., Rikkyo Univ.)
OGAWA Shinsuke 小川真資 (Coll. Sci., Rikkyo Univ.)
OKADA Hiroyuki 岡田宏之 (Sci. Eng. Res. Lab., Waseda Univ.)
OTSU Hideaki 大津秀暁 (Fac. Sci., Univ. Tokyo)
OTSUKA Takanori 大塚貴徳 (Fac. Sci., Univ. Tokyo)
SAITO Tomoki 斎藤知樹 (Seikei Univ.)
SAITO Yoshitaka 齋藤芳隆 (Fac. Sci., Univ. Tokyo)
SAKAMOTO Naruhiko 坂本成彦 (Fac. Sci., Univ. Tokyo)
SASAKI Mitsuru 佐々木 充 (Fac. Sci., Osaka Univ.)
SATO Hiroyasu 佐藤弘康 (Seikei Univ.)
SATO Hiromi 佐藤広海 (Fac. Sci., Tokyo Inst. Technol.)
SATO Yoshiteru 佐藤義輝 (Fac. Sci., Univ. Tokyo)
SATO Masaru 佐藤 優 (Sci. Eng. Res. Lab., Waseda Univ.)
SAWADA Shinya 澤田真也 (Fac. Sci., Kyoto Univ.)
SEKINE Takashi 関根 隆 (Fac. Sci., Tokyo Inst. Technol.)
SHIBATA Masataka 柴田雅隆 (Fac. Sci., Kyushu Univ.)
SHIMURA Masakatsu 志村正勝 (Fac. Sci. Technol., Sophia Univ.)
SHINODA Morihiko 篠田守彦 (Sci. Eng. Res. Lab., Waseda Univ.)
SHIRAKI Tadashi 白木正志 (Coll. Sci., Rikkyo Univ.)
SHIRAKURA Tetsuya 白倉徹也 (Fac. Sci., Osaka Univ.)
SHIZUMA Toshiyuki 静間俊行 (Fac. Sci., Kyushu Univ.)
SUZUKI Kiyoshi 鈴木清詞 (Fac. Sci., Univ. Tokyo)
SUZUKI Masataka 鈴木正恭 (Coll. Sci., Rikkyo Univ.)
TAJIMA Yasuhisa 田島靖久 (Fac. Sci., Tokyo Inst. Technol.)
TERANISHI Takashi 寺西 高 (Fac. Sci., Univ. Tokyo)
TERASAWA Kazuhiro 寺沢和洋 (Sci. Eng. Res. Lab., Waseda Univ.)
TSUCHIDA Naohiko 土田有彦 (Fac. Sci., Univ. Tokyo)
TUCHIDA Hideo 土田英夫 (Graduate Sch. Nagatsuta, Tokyo Inst. Technol.)
UCHIBORI Takeshi 内堀武司 (Coll. Sci., Rikkyo Univ.)
UENO Hideki 上野秀樹 (Fac. Sci., Tokyo Inst. Technol.)
UESAKA Tomohiro 上坂友洋 (Fac. Sci., Univ. Tokyo)
WAKASA Tomotsugu 若狭智嗣 (Fac. Sci., Univ. Tokyo)
WATANABE Yutaka 渡辺 裕 (Fac. Sci., Univ. Tokyo)
WATANABE Akira 渡辺 明 (Sci. Eng. Res. Lab., Waseda Univ.)
YAMAMOTO Takuhisa 山本琢久 (Fac. Sci., Tokyo Inst. Technol.)
YAMASHITA Toshiyuki 山下利幸 (Fac. Sci., Tokyo Inst. Technol.)
YANAGISAWA Yoshiyuki 柳沢善行 (Coll. Sci., Rikkyo Univ.)
YONEDA Kenichiro 米田健一郎 (Fac. Sci., Univ. Tokyo)
YOSHIDA Takuji 吉田拓司 (Coll. Sci., Rikkyo Univ.)
YOSHIMI Akihiro 吉見彰洋 (Fac. Sci., Tokyo Inst. Technol.)

**Atomic Physics Laboratory**

ANDO Kozo 安藤剛三
AWAYA Yohko 粟屋容子*
KAMBARA Tadashi 神原 正**
KANAI Yasuyuki 金井保之
KOJIMA Takao M. 小島隆夫
NAKAI Yoichi 中井陽一
NISHIDA Masami 西田雅美
OURA Masaki 大浦正樹
SHIMAMURA Isao 島村 勲**
SOEJIMA Kouichi 副島浩一

TANG Jianzhi 唐 建志　　WATANABE Naoki 渡部直樹
YOSHIDA Takashi 吉田高志

---

* Chief Scientist, ** Senior Scientist

(Visitors)
AZUMA Toshiyuki 東 俊行 (Coll. Arts Sci., Univ. Tokyo)
DANJO Atsunori 壇上篤徳 (Dept. Phys., Niigata Univ.)
DEPAOLA Brett D. (Kansas State Univ., U.S.A.)
FUJIMA Kazumi 藤間一美 (Fac. Eng., Yamanashi Univ.)
FUKUDA Hiroshi 福田 宏 (Sch. Administration and Informatics, Univ. Shizuoka)
HARA Shunsuke 原 俊介 (Dept. Gen. Educ., Tsukuba Coll. Technol.)
HARSTON Michael R. (Dept. Math., Univ. Nottingham, U.K.)
HINO Kenichi 日野健一 (Dept. Appl. Phys. Chem., Univ. Electro-Commun.)
HULDT Sven (Univ. Lund, Sweden)
HUTTON Roger (Univ. Lund, Sweden)
ISHII Keishi 石井慶之 (Dept. Eng. Sci., Kyoto Univ.)
ISOZUMI Yasuhito 五十棲泰人 (Inst. Chem. Res., Kyoto Univ.)
ITO Shin 伊藤 真 (Radioisot. Res. Cent., Kyoto Univ.)
ITOH Akio 伊藤秋男 (Fac. Eng., Kyoto Univ.)
ITOH Yoh 伊藤 陽 (Fac. Sci., Josai Univ.)
JAGUTZKI Ottmar (Univ. Frankfurt, Germany)
KAWATSURA Kiyoshi 川面 澄 (Kyoto Inst. Technol.)
KIMURA Mineo 季村峯生 (Argonne Natl. Lab., U.S.A.)
KOBAYASHI Nobuo 小林信夫 (Dept. Phys., Tokyo Metrop. Univ.)
KOHARA Takao 小原孝夫 (Fac. Sci., Himeji Inst. Technol.)
KOIKE Fumihiro 小池文博 (Sch. Med., Kitasato Univ.)
KOIZUMI Tetsuo 小泉哲夫 (Dept. Phys., Rikkyo Univ.)
KOMAKI Kenichiro 小牧研一郎 (Coll. Arts Sci., Univ. Tokyo)
KOWARI Kenichi 小割健一 (Dept. Chem., Tokyo Inst. Technol.)
KRAVIS Scott (Dept. Phys., Rikkyo Univ.)
KUROKI Kenro 黒木健郎 (Natl. Res. Inst. Police Sci.)
MARTINSON Indrek (Univ. Lund, Sweden)
MATSUO Takashi 松尾 崇 (Dept. Pathol., Tokyo Med. Dent. Univ.)
MATSUZAWA Michio 松澤通生 (Dept. Appl. Phys. Chem., Univ. Electro-Commun.)
MITAMURA Tohru 三田村 徹 (Fac. Eng., Himeji Inst. Technol.)
MIZOGAWA Tatsumi 溝川辰巳 (Nagaoka Coll. Technol.)
MUKOYAMA Takeshi 向山 毅 (Inst. Chem. Res., Kyoto Univ.)
NYSTROEM Bosse (Univ. Lund, Sweden)
OHTANI Shunsuke 大谷俊介 (Inst. Laser Sci., Univ. Electro-Commun.)
OKUNO Kazuhiko 奥野和彦 (Dept. Phys., Tokyo Metrop. Univ.)
O'ROURKE Franceska (Dept. Appl. Math., Queen's Univ. Belfast, U.K.)
PAPP Tibor (Inst. Nucl. Res., Hungarian Academy Sci., Hungary)
RICHARD Patrik (Kansas State Univ., U.S.A)
SALK Sung-Ho Suck (Pohang Univ. Sci. & Tech., Korea)
SATO Hiroshi 佐藤浩史 (Dept. Phys., Ochanomizu Univ.)
SCHMIDT-BÖCKING Horst (Univ. Frankfurt, Germany)
SEKIOKA Tsuguhisa 関岡嗣久 (Fac. Eng., Himeji Inst. Technol.)
SHIBATA Hiromi 柴田裕実 (Res. Cent. Nucl. Sci., Univ. Tokyo)
SHIMA Kunihiro 島 邦博 (Tandem Accel. Cent., Univ. Tsukuba)
SHIMAKURA Noriyuki 島倉紀之 (Dept. Chem., Niigata Univ.)
STOKLI Martin P. (Kansas State Univ. U.S.A)
SUGER Jack (Natl. Inst. Stand. Technol., U.S.A.)
SULIK Bela (Inst. Nucl. Res., Hungarian Academy Sci., Hungary)
SUZUKI Hirosi 鈴木 洋 (Inst. Laser Sci., Univ. Electro-Commun.)
TAKAYANAGI Toshinobu 高柳俊暢 (Dept. Phys., Sophia Univ.)
TAWARA Hiroyuki 俵 博之 (Natl. Inst. Fusion Sci.)
TERASAWA Mititaka 寺澤倫孝 (Fac. Eng., Himeji Inst. Technol.)

TOSHIMA Nobuyuki 戸嶋信幸 (Inst. Appl. Phys., Univ. Tsukuba)
TSURUBUCHI Seiji 鶴淵誠二 (Fac. Technol., Tokyo Univ. Agric. Technol.)
WAKIYA Kazuyoshi 脇谷一義 (Dept. Phys., Sophia Univ.)
WATANABE Shinichi 渡辺信一 (Dept. Appl. Phys. Chem., Univ. Electro-Commun.)
YAMAZAKI Yasunori 山崎泰規 (Coll. Arts Sci., Univ. Tokyo)
YOSHINO Masuhiro 吉野益弘 (Lab. Phys., Shibaura Inst. Technol.)
ZORAN I. Valeriu (Inst. Phys. Nucl. Eng., Romania)
ZOU Yaming 邹 亚明 (Jiao Tong Univ., China)

(Students)
BITO Yasunori 尾藤康則 (Fac. Eng., Kyoto Univ.)
KAGAWA Makoto 香川 真 (Dept. Phys., Sophia Univ.)
KAGEYAMA Hiroyoshi 影山拓良 (Kyoto Inst. Technol.)
KAKUTANI Nobukazu 角谷暢一 (Coll. Arts Sci., Univ. Tokyo)
KIMURA Yasuyuki 木村恭之 (Dept. Eng. Sci., Kyoto Univ.)
NISHIDA Tetsuo 西田哲朗 (Dept. Eng. Sci., Kyoto Univ.)
SANO Mutsumi 佐野 睦 (Dept. Phys., Rikkyo Univ.)
TAKAHASHI Ryohei 高橋竜平 (Kyoto Inst. Tecnol.)
TANABE Kunihiro 田辺邦浩 (Dept. Phys., Sophia Univ.)

**Muon Science Laboratory**

ISHIDA Katsuhiko 石田勝彦
KINO Yasushi 木野康志
MATSUZAKI Teiichiro 松崎禎市郎
WATANABE Isao 渡邊功雄
KADONO Ryosuke 門野良典
KOYAMA Akio 小山昭雄
NAGAMINE Kanetada 永嶺謙忠*
YAGI Eiichi 八木栄一**

* Chief Scientist, ** Senior Scientist

(Visitors)
AKAISHI Yoshinori 赤石義紀 (Fac. Sci., Hokkaido Univ.)
FUJIOKA Manabu 藤岡 学 (Cyclotron Radioisot. Cent., Tohoku Univ.)
JONES E. Steven (Dept. Phys. Astronomy, Brigham Young Univ., U.S.A.)
KAMIMURA Masayasu 上村正康 (Fac. Sci., Kyushu Univ.)
KUMAGAI Kenichi 熊谷健一 (Fac. Sci., Hokkaido Univ.)
MACRAE Roderick Malcolm*
MATSUSHITA Akira 松下 明 (Res. Dev. Co. Ltd., Japan)
MINAMISONO Tadanori 南園忠則 (Fac. Sci., Osaka Univ.)
MIYAKE Yasuhiro 三宅康博 (Meson Sci. Lab., Univ. Tokyo)
MORITA Masato 森田正人 (Fac. Sci., Josai Univ.)
STRASSER Partrick**
TORIKAI Eiko 鳥養映子 (Fac. Eng., Yamanashi Univ.)
WATANABE Tsutomu 渡部 力 (ICU)

* STA Fellow, ** Postdoctral Researcher

(Students)
DAWSON Wayne (Fac. Sci., Univ. Tokyo)

**Magnetic Materials Laboratory**

KITAZAWA Hideaki 北澤英明
OKADA Takuya 岡田卓也*

* Senior Scientist

**Plasma Physics Laboratory**

OYAMA Hitoshi 大山 等
YANO Katsuki 矢野勝喜

**Microwave Physics Laboratory**

MINOH Arimichi　箕曲在道

**Semiconductor Laboratory**

(Visitors)

AONO Keiko　青野桂子　(Coll. Liberal Arts, Kitasato Univ.)

**Inorganic Chemical Physics Laboratory**

AMBE Shizuko　安部静子
MAEDA Kuniko　前田邦子
MATSUO Yukari　松尾由賀利
TAKAMI Michio　高見道生*

* Chief Scientist

(Visitors)

ARAI Nobuaki　新井修亮　(Dept. Fisheries, Kyoto Univ.)
ISHII Keizo　石井慶造　(Cyclotron Radioisot. Cent., Tohoku Univ.)
KAWAI Jun　河合　潤　(Dept. Metallurgy, Kyoto Univ.)

**Nuclear Chemistry Laboratory**

AMBE Fumitoshi　安部文敏*
ENOMOTO Shuichi　榎本秀一
ITOH Yoshiko　伊東芳子
IWAMOTO Masako　岩本正子
KOBAYASHI Yoshio　小林義男
MAEDA Haruka　前田はるか
OHKUBO Yoshitaka　大久保嘉高

* Chief Scientist

(Visitors)

AMANO Ryohei　天野良平　(Sch. Allied Med. Prof., Kanazawa Univ.)
ASAI Kichizo　浅井吉蔵　(Univ. Electro-Commun.)
BABA Hiroshi　馬場　宏　(Fac. Sci., Osaka Univ.)
ENDO Kazutoyo　遠藤和豊　(Showa Coll. Pharm. Sci.)
FURUKAWA Michiaki　古川路明　(Fac. Sci., Nagoya Univ.)
HARAKAWA Hiroaki　原川裕章　(Coll. Sci. Eng., Aoyamagakuin Univ.)
HASSLEIN Helmut　(Shizuoka Inst. Sci. Technol.)
HIRUNUMA Rieko　蛭沼利江子　(Showa Coll. Pharm. Sci.)
ITO Yasuo　伊藤泰男　(Res. Cent. Nucl. Sci. Technol., Univ. Tokyo)
KANAZAWA Ikuzo　金沢育三　(Fac. Educ., Gakugei Univ.)
KIMURA Kan　木村　幹　(Coll. Sci. Eng., Aoyamagakuin Univ.)
KOBAYASHI Takayuki　小林貴之　(Sch. Hygien. Sci., Kitasato Univ.)
KOJIMA Sadao　小島貞男　(Nucl. Med. Cent., Aichi Medical Univ.)
MINAI Yoshitaka　薬袋佳孝　(Fac. Sci., Univ. Tokyo)
MURAKAMI Hideoki　村上英興　(Tokyo Gakugei Univ.)
NASU Saburo　那須三郎　(Fac. Eng. Sci., Osaka Univ.)
SAITO Tadashi　斎藤　直　(Fac. Sci., Osaka Univ.)
SHIBATA Sadao　柴田貞夫　(Natl. Inst. Radiol. Sci.)
SHIBATA Seiichi　柴田誠一　(Inst. Nucl. Study, Univ. Tokyo)
SHINOHARA Atsushi　篠原　厚　(Fac. Sci., Nagoya Univ.)
SHINONAGA Taeko　篠永妙子　(Fac. Sci., Tokyo Metrop. Univ.)
TANAKA Akira　田中　章　(Showa Coll. Pharm. Sci.)
YAITA Tsuyoshi　矢板　毅　(JAERI, Tokai)
YANAGA Makoto　矢永誠人　(Jikei Univ. Sch. Med.)
YOKOTA Yuko　横田裕子　(Coll. Sci. Eng., Aoyamagakuin Univ.)
YOKOYAMA Akihiko　横山明彦　(Fac. Sci., Osaka Univ.)
YOSHIDA Yutaka　吉田　豊　(Shizuoka Inst. Sci. Technol.)

(Students)
AOKI Naoki 青木尚樹 (Coll. Sci. and Eng., Aoyamagakuin Univ.)
FURUTA Riko 古田理子 (Showa Coll. Pharm. Sci.)
HAGIWARA Tetsuya 萩原徹也 (Fac. Sci. and Eng., Tokyo Denki Univ.)
HARUTA Hiroshi 春田博司 (Showa Coll. Pharm. Sci.)
IIJIMA Yoshihide 飯島由英 (Fac. Sci., Toho Univ.)
INOUE Takakazu 井上貴和 (Fac. Sci., Osaka Univ.)
ITOH Naoya 伊藤直弥 (Coll. Sci. and Eng., Aoyamagakuin Univ.)
IWATA Maki 岩田真紀 (Fac. Sci., Toho Univ.)
KASUGA Ryouichi 春日良一 (Fac. Sci., Osaka Univ.)
KIKUCHI Yasuhisa 菊池康久 (Fac. Sci. and Eng., Tokyo Denki Univ.)
KIRYU Shigetoshi 桐生繁利 (Fac. Sci., Nagoya Univ.)
KOBAYASHI Kanako 小林香奈子 (Fac. Sci., Tokyo Metrop. Univ.)
KOIZUMI Yukiyo 小泉幸世 (Tokyo Gakugei Univ.)
KUWABARA Kazunori 桑原和憲 (Shizuoka Inst. Sci. Technol.)
MINAMI Hiroshi 南 浩 (Showa Coll. Pharm. Sci.)
MIYABAYASHI Kyoko 宮林京子 (Showa Coll. Pharm. Sci.)
MUKAI Kazuhiko 向 和彦 (Fac. Sci., Osaka Univ.)
MUROYAMA Toshiharu 室山俊浩 (Fac. Sci., Nagoya Univ.)
NAKAGAWA Akihiro 中川彰宏 (Shizuoka Inst. Sci. Technol.)
NAKAJO Terunobu 中條晃伸 (Tokyo Gakugei Univ.)
NAKAMURA Jin 中村 仁 (Univ. Electro-Commun.)
ODA Hirotaka 小田寛貴 (Fac. Sci., Nagoya Univ.)
OHTSUKA Hiroshi 大塚博史 (Fac. Sci., Univ. Tokyo)
ONIZUKA Nobuyuki 鬼塚信之 (Tokyo Gakugei Univ.)
OSHIMA Nagayasu 大島永康 (Tokyo Gakugei Univ.)
OTSU Yoko 大津庸子 (Tokyo Gakugei Univ.)
OZAKI Takuo 尾崎卓郎 (Fac. Sci., Tokyo Univ.)
SASAKI Jin 佐々木 仁 (Tokyo Gakugei Univ.)
SATO Yoshihiko 佐藤嘉彦 (Fac. Sci., Nagoya Univ.)
SUZUKI Akihiro 鈴木章浩 (Shizuoka Inst. Sci. Technol.)
TAKAHASHI Yoshio 高橋嘉夫 (Fac. Sci., Univ. Tokyo)
TAKESAKO Kazuhiro 竹迫和浩 (Fac. Sci., Osaka Univ.)
TAKESHITA Kazutaka 竹下和孝 (Fac. Sci., Toho Univ.)
TSUKAHARA Kazuhiro 塚原和弘 (Shizuoka Inst. Sci. Technol.)

**Chemical Dynamics Laboratory**

KIMURA Kazuie 木村一宇

(Visitors)
KAZAMA Shigeo 風間重雄 (Dept. Phys., Chuo Univ.)

(Students)
YOSHIKANE Takao 吉兼隆生 (Dept. Phys., Chuo Univ.)

**Cellular Physiology Laboratory**

HANAOKA Fumio 花岡文雄*
KITAYAMA Shigeru 北山 滋
YATAGAI Fumio 谷田貝文夫**

* Chief Scientist, ** Senior Scientist

(Visitors)
ANDO Koichi 安藤興一 (Natl. Inst. Radiol. Sci.)
FUKUMURA Akifumi 福村明史 (Natl. Inst. Radiol. Sci.)
FURUSAWA Yoshiya 古澤佳也 (Natl. Inst. Radiol. Sci.)
HAMA Yoshimasa 浜 義昌 (Sci. Eng. Res. Lab., Waseda Univ.)

HASHIMOTO Shozo 橋本省三 (Fac. Med., Keio Univ.)
HOSHINO Kazuo 星野一雄 (Natl. Inst. Radiol. Sci.)
IIZUKA Masayuki 飯塚正之 (Natl. Inst. Radiol. Sci.)
ITO Hisao 伊東久夫 (Fac. Med., Keio Univ.)
ITOH Hiroko 伊藤浩子 (Natl. Inst. Radiol. Sci.)
ITSUKAICHI Hiromi 五日市ひろみ (Natl. Inst. Radiol. Sci.)
KANAI Tatsuaki 金井達明 (Natl. Inst. Radiol. Sci.)
KASAI Kiyomi 笠井清美 (Natl. Inst. Radiol. Sci.)
KAWACHI Kiyomitsu 河内清光 (Natl. Inst. Radiol. Sci.)
KIKUCHI Masahiro 菊地正博 (JAERI, Takasaki)
KIMOTO Masafumi 木元正史 (Natl. Inst. Radiol. Sci.)
KOBAYASHI Yasuhiko 小林泰彦 (JAERI, Takasaki)
KOHNO Toshiyuki 河野俊之 (Natl. Inst. Radiol. Sci.)
KOIKE Sachiko 小池幸子 (Natl. Inst. Radiol. Sci.)
KOJIMA Eiichi 小島栄一 (Natl. Inst. Radiol. Sci.)
KOSAKA Toshifumi 小坂俊文 (Dept. Vet. Radiol., Nihon Univ.)
KUBOTA Nobuo 窪田宜夫 (Fac. Med., Yokohama City Univ.)
MATSUFUJI Naruhiro 松藤成弘 (Natl. Inst. Radiol. Sci.)
McINTYRE Cindy L. (Radiobiol. Unit, Med. Res. Counc., U.K.)
MINOHARA Shinichi 簑原伸一 (Natl. Inst. Radiol. Sci.)
MIYAHARA Nobuyuki 宮原信幸 (Natl. Inst. Radiol. Sci.)
MURAISO Chidori 村磯知採 (Natl. Inst. Radiol. Sci.)
MURAKAMI Masahiro 村上正弘 (Natl. Inst. Radiol. Sci.)
NAKAI Hirokazu 中井弘和 (Dept. Agric., Shizuoka Univ.)
OHARA Hiroshi 大原 弘 (Dept. Gen. Cult., Okayama Univ.)
OKUMURA Toshiyuki 奥村敏之 (Fac. Med., Univ. Tsukuba)
SASAKI Hiroshi 佐々木 弘 (Fac. Med. Kyushu Univ.)
SOGA Fuminori 曽我文宣 (Inst. Nucl. Study, Univ. Tokyo)
SUDO Michio 須藤美智雄 (Natl. Inst. Radiol. Sci.)
TAGUCHI Yasuko 田口泰子 (Natl. Inst. Radiol. Sci.)
TAKATUJI Toshihiro 高辻俊宏 (RI Cent., Nagasaki Univ.)
TANAKA Kaoru 田中 薫 (Natl. Inst. Radiol. Sci.)
TATSUZAKI Hideo 立崎英夫 (Fac. Med., Univ. Tsukuba)
TOMURA Hiromi 外村浩美 (Natl. Inst. Radiol. Sci.)
TSUBOI Atsushi 坪井 篤 (Natl. Inst. Radiol. Sci.)
TSUBOUCHI Susumu 坪内 進 (Suzuka Med. Technol. Univ.)
WATANABE Hiroshi 渡辺 宏 (JAERI, Takasaki)
WATANABE Masami 渡辺正己 (Fac. Pharm., Nagasaki Univ.)
YAMASHITA Shoji 山下昌次 (Natl. Saitama Hospital)

(Students)
FUJI Hiroshi 藤 浩 (Fac. Med., Univ. Tsukuba)
KAWASHIMA Mitsuhiko 河島光彦 (Fac. Med., Univ. Tsukuba)
TAKAHASHI Hideyuki 高橋英幸 (Fac. Med., Univ. Tsukuba)

**Microbial Toxicology Laboratory**
YAMAGUCHI Isamu 山口 勇*

---

* Chief Scientist

(Visitors)
WATANABE Tadakazu 渡部忠一 (Agro-Kanesho Co. Ltd.)

(Students)
MATSUMOTO Ken-ichi 松本健一 (Shimane Univ.)

**Safety Center**

HARASAWA Kaoru 原沢 薫
INAMURA Takashi T. 稲村 卓*
INOUE Yoshio 井上義夫
KAGAYA Satoru 加賀屋 悟
KATOU Hiroko 加藤博子
KOTOU Takeo 加藤武雄
MATSUZAWA Yasuhide 松沢安秀
MIYAGAWA Makoto 宮川真言
SAKAMOTO Ichiro 坂本一郎
SHINOHARA Shigemi 篠原茂己
TAKI Kenro 滝 剣朗
UWAMINO Yoshitomo 上蓑義朋

* Head

**Surface Characterization Center**

IWAKI Masaya 岩木正哉*
KUMAGAI Makoto 熊谷 信

* Head

**Radioisotope Technology Division**

NAKANO Kazushiro 中野和城
YATAGAI Fumio 谷田貝文夫*

* Head

(Visitors)
IJIRI Kenichi 井尻憲一 (Radioisot. Cent., Univ. Tokyo)
ISHIKAWA Masanobu 石川雅紀 (Tokyo Univ. Fisheries)
KASE Youko 加瀬陽子 (Natl. Inst. Radiol. Sci.)
KAGAWA Yasuhiro 香川康浩 (Toray Research Center Inc.)
MAEZAWA Hiroshi 前澤 宏 (Fac. Med., Tokai Univ.)
OGURA Koichi 小倉紘一 (Coll. Ind. Technol., Nihon Univ.)
OHARA Hiroshi 大原 弘 (Dept. Gen. Cult., Okayama Univ.)
SUZUKI Masao 鈴木雅雄 (Fac. Pharm., Nagasaki Univ.)
YATO Osamu 矢頭 治 (Kagoshima Agr. Exp. Stn.)

(Students)
HAMANAKA Kenichi 浜中健一 (Fac. Sci. Eng., Waseda Univ.)
MATSUMOTO Hideya 松本英哉 (Fac. Sci. Eng., Waseda Univ.)

# AUTHOR INDEX

**RIKEN Accelerator Progress Report Vol. 28**

理化学研究所加速器年次報告　第28巻　(1995)

印　刷　平成7年 (1995) 3月23日
発　行　平成7年 (1995) 3月31日

発行者　理化学研究所
代表者　有馬朗人
〒351-01　埼玉県和光市広沢2番1号
電話　(048) 462−1111

編集者　理化学研究所加速器研究施設
運営委員会

印刷所　株式会社ユニバーサル・アカデミー・プレス
〒113　東京都文京区本郷6丁目16番2号BR本郷5ビル

定価5,000円
(消費税別)

**理化学研究所**

埼玉県　和光市　広沢